Respiratory Society/World Association of Sarcoidosis and other Granulomatous Disorders. *Sarcoidosis Vasc Diffuse Lung Dis* 1999; 16: 149–173.

5 Huez S, Retailleau K, Unger P, *et al.* Right and left ventricular adaptation to hypoxia: a tissue Doppler imaging study. *Am J Physiol Heart Circ Physiol* 2005; 289: H1391–H1398.

6 Garcia MJ, Rodriguez L, Ares M, *et al.* Myocardial wall velocity assessment by pulsed Doppler tissue imaging: characteristic findings in normal subjects. *Am Heart J* 1996; 132: 648–656.

7 Lindqvist P, Waldenström A, Wikström G, *et al.* The use of isovolumic contraction velocity to determine right ventricular state of contractility and filling pressures: A pulsed Doppler tissue imaging study. *Eur J Echocardiogr* 2005; 6: 264–270.

8 Nunes H, Humbert M, Capron F, *et al.* Pulmonary hypertension associated with sarcoidosis: mechanisms, haemodynamics and prognosis. *Thorax* 2006; 61: 68–74.

9 Lamberto C, Nunes H, Le Toumelin P, *et al.* Membrane and capillary blood components of diffusion capacity of the lung for carbon monoxide in pulmonary sarcoidosis: relation to exercise gas exchange. *Chest* 2004; 125: 2061–2068.

10 Hunter KS, Lee PF, Lanning CJ, *et al.* Pulmonary vascular input impedance is a combined measure of pulmonary vascular resistance and stiffness and predicts clinical outcomes better than pulmonary vascular resistance alone in pediatric patients with pulmonary hypertension. *Am Heart J* 2008; 155: 166–174.

DOI: 10.1183/09031936.00065210

Interferon-γ release assays in tuberculosis contacts: is there a window period?

The tuberculin skin test (TST) is the established procedure for diagnosis of latent tuberculosis infection (LTBI) among the contacts of an infectious tuberculosis (TB) case. TST may convert to positive $\leqslant$8 weeks after *Mycobacterium tuberculosis* infection, an interval that is usually referred to as the ‘‘window period’’. A negative TST obtained $<$8 weeks before does not exclude infection, and a second test is recommended [1, 2]. However, TST has some limitations, such as cross-reactivity with Bacille Calmette–Guérin (BCG) and with nontubercular mycobacterial infections.

T-cell interferon-γ release assays (IGRA) are emerging as new screening tools for LTBI diagnosis. IGRAs incorporate specific antigens of *M. tuberculosis* that are absent in BCG strains and in the majority of nontubercular mycobacteria, offering enhanced specificity for detecting *M. tuberculosis* infection [3]. In addition, their use has been approved for screening of infection in contacts [1, 4]. Most TB contact studies have shown a better correlation of IGRA with the intensity of *M. tuberculosis* exposure than that obtained using TST, particularly in patients previously vaccinated with BCG [5]. Yet, to our knowledge, no study has considered carefully the window period after *M. tuberculosis* exposure while simultaneously evaluating responses for TST and IGRA. The aim of this study was to find out which of the two tests converts earlier to positive in persons with recent infection after contact with an infectious TB case.

We used a longitudinal prospective analysis to study 184 healthy adults, all having had recent contact with a microbiologically confirmed pulmonary TB index patient. The setting was a specialized TB clinic in Pontevedra, Spain, where the incidence of TB has historically been among the highest in Western Europe. In 1996, a TB control programme was established, and incidence has steadily dropped from 72.3 to 32.6 per 100,000 in 2008.

TST and a commercially available IGRA, Quantiferon®-TB Gold In-Tube (QFT; Cellestis, Carnegie, Australia), were both carried out at the first visit of the contacts to our clinic after TB exposure (time 0: TST0 and QFT0, respectively). The attending physician was blind to the QFT result, and medical advice was offered to the patient only on the basis of the TST result. Patients with positive TST were offered to start LTBI chemotherapy after active TB was excluded. For those contacts with a negative TST0, a repeat TST and QFT were undertaken 2 months later (time 2: TST2 and QFT2, respectively), at the end of the window period. In addition, patients with a positive TST0 but negative QFT0 were recalled to have a second QFT 2 months later, irrespective of whether the patient was receiving treatment for LTBI.

Peripheral blood was processed for the QFT assay according to the manufacturer’s instructions. Samples were frozen and stored at -70°C for analysis 3–4 weeks later. The cut-off value for a positive test was $0.35\ \text{IU}\cdot\text{mL}^{-1}$. TST was carried out according to the Mantoux method, with 2 units of tuberculin RT-23 (purified protein derivative; State Serum Institute, Copenhagen, Denmark), following the standardised protocol. A positive TST was defined as an induration of $\geqslant$5 mm. We excluded from the study HIV-infected persons or those with other immunosuppressive conditions, pregnant females, and those with a previous documented positive TST. Institutional ethical approval was obtained from the Ethical Committee of Clinical Research (Xunta de Galicia, Spain). All participants included in the study gave their written informed consent.

Initially, 184 participants, recent contacts of microbiologically confirmed pulmonary TB patients were enrolled in the study, but 32 were excluded due to a history of a previous positive TST (28 cases) or because of incomplete data for the index TB case (four cases). The remaining 152 participants had a median age of 44 yrs (interquartile range 32–55 yrs) and were contacts of 48 different index TB patients. None had ever previously received TB or LTBI treatment. 55 (36.2%) contacts had had a previous BCG vaccination. For 137 (90.1%) contacts, the index TB case was acid-fast bacilli positive.

The results of our study are summarised in figures 1 and 2. At the first visit, 62 (40.8%) contacts showed a positive TST0, while 57 (37.5%) contacts had a positive QFT0. A total of 90 contacts with an initial negative TST0 (0 mm) were called 2 months later for TST2 and QFT2 studies, which were finally performed on 81 patients (nine patients did not return after 2 months). Of those contacts, 24 converted to a positive TST2, representing 29.6% (95% CI 19.1–40.2%). It is worth noting that nine of them (37.5%, 95% CI 16.0–59.0%) had already been positive in QFT0, suggesting an earlier conversion of QFT than TST.

In 80 participants with an initial negative QFT0 (12 with positive TST0 and 68 with negative TST0), a second QFT2 was also carried out. Of this group, 17 converted to positive (21.2%, 95% CI 11.7–30.8%), including three who had had a positive TST0 (17.6%, 95% CI 3.8–43.4%), while a further 12 showed both TST and QFT conversion. In two cases, negative at TST0 and TST2, both had QFT2 results slightly above the diagnostic cut-off limit suggested by the manufacturer (0.37 and 0.45 IU·mL^{-1}, respectively).

Our results indicate that, as for TST, QFT has a window period of conversion after exposure to *M. tuberculosis*. Time of conversion may differ between the two, but still has to be clearly determined for QFT. Nevertheless, QFT conversion preceded that of TST in 37.5% of participants with documented TST conversion, while TST was found to be positive at the first visit after exposure in only three out of 17 cases with QFT conversion, suggesting that an earlier TST conversion is also possible. In at least two of these cases, we cannot rule out that a positive TST0 could be related to previous TB infections or BCG vaccination.

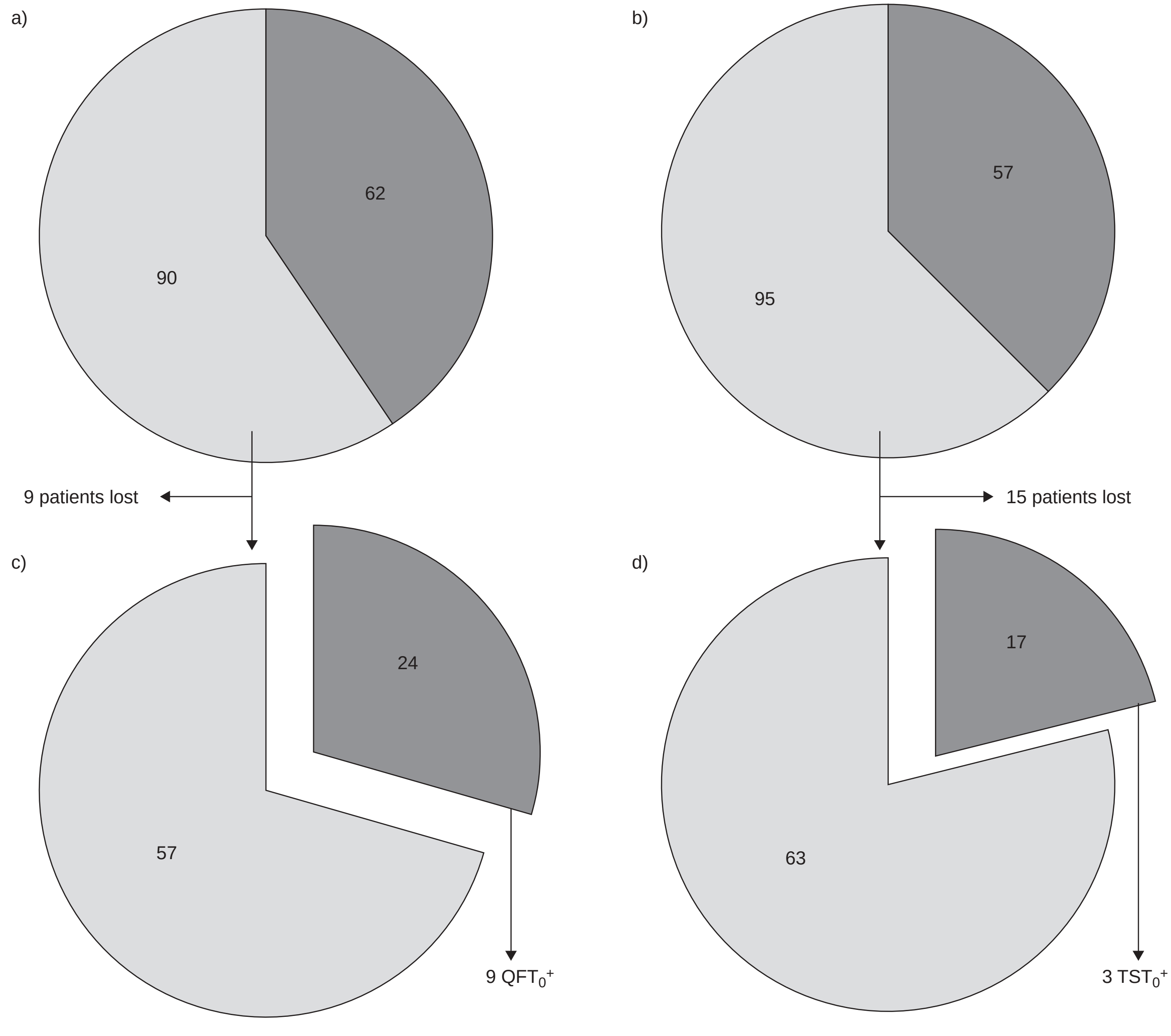

FIGURE 1. Results of a, c) tuberculin skin test (TST) and b, d) Quantiferon®-TB Gold In-Tube (QFT) assay after a, b) recent contact with a tuberculosis index case (TST0 and QFT0) and c, d) after the 2-month window period (TST2 and QFT2). a) n=152. b) n=152. c) n=81. d) n=80. Data are presented as contacts n. □: negative test result; ■: positive test result.

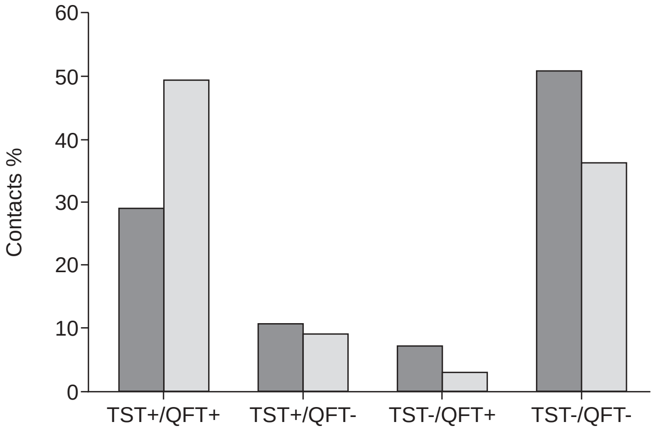

FIGURE 2. Results of tuberculin skin test (TST) and Quantiferon®-TB Gold In-Tube assay (QFT) after recent contact with a tuberculosis index case (■) and 8 weeks later (□).

Our findings suggest that IGRAs could be a valid alternative to TST in the study of TB contacts, especially with increasing evidence that a positive IGRA result is a predictive factor for progression to TB [6, 7]. Nevertheless, to the best of our knowledge, this is the first study that simultaneously compares TST and an IGRA, looking for a possible conversion in both tests. Although the time of QFT conversion still has to be clearly determined, our work contributes towards clarifying the time for studying contacts with IGRAs.

Our study has some limitations that deserve comment. First, there is some concern about the possibility that a prior skin test could boost the response of subsequent IGRAs [8]. In theory, this could invalidate some of the positive IGRA responses obtained 2 months after the TST, but other authors have reported no effect [9]. A second limitation is that QFT reversion to negative in patients with an initial positive QFT0 cannot be ruled out. In addition to the spontaneous reversion reported for TST responses, IGRA reversion has also been described in TB contacts, and its significance is still a matter of debate [10].

From the results of our study, we conclude that QFT has a ‘‘window period’’ after exposure to *M. tuberculosis*. Therefore, for those cases with an initially negative result with QFT after recent exposure, a later second test must be carried out to definitely exclude infection. Alternatively, when QFT is the only technique used, the last possible exposure time to the index case can be assessed, and blood is only drawn for the QFT after an 8-week interval.

L. Anibarro*, M. Trigo#, C. Villaverde¶, A. Pena*, S. Cortizo#, D. Sande*, R.A. Pazos* and Á. González-Fernández+

*Tuberculosis Unit, Dept of Infectious Diseases and Internal Medicine, #Dept of Microbiology, Pontevedra Hospital Complex, Pontevedra, ¶Dept of Statistics and Operational Research, and +Immunology and Joint Immunology Unit, Vigo University Teaching Hospital, University of Vigo, Vigo, Spain.

Correspondence: L. Anibarro, Unidade de Tuberculose, Complexo Hospitalario de Pontevedra, Hospital Provincial, Rúa Loureiro Crespo no. 2. 36001-Pontevedra, Spain. E-mail: luis.anibarro.garcia@sergas.es

Support Statement: The study received financial support from the SUDOE-FEDER (IMMUNONET-SOE1/1P1/E014) and Spanish Ministry of Science and Innovation (Consolider Ingenio 2010, CSD2006-12, NANOBIOMED).

Statement of Interest: None declared.

REFERENCES

1 National Tuberculosis Controllers Association, Centers for Disease Control and Prevention, Guidelines for the investigation of contacts of persons with infectious tuberculosis. Recommendations from the National Tuberculosis Controllers Association and CDC. *MMWR Recomm Rep* 2005; 54: 1–47.
2 Menzies D. Interpretation of repeated tuberculin tests. Boosting, conversion, and reversion. *Am J Respir Crit Care Med* 1999; 159: 15–21.
3 Pai M, Zwerling A, Menzies D. Systematic review: T-cell-based assays for the diagnosis of latent tuberculosis infection: an update. *Ann Intern Med* 2008; 149: 177–184.
4 Ruiz-Manzano J, Blanquer R, Calpe J, *et al.* [Diagnosis and treatment of tuberculosis]. *Arch Bronconeumol* 2008; 44: 551–566.
5 Arend S, Thijsen S, Leyten E, *et al.* Comparison of two interferon-γ assays and tuberculin skin test for tracing tuberculosis contacts. *Am J Respir Crit Care Med* 2007; 175: 618–627.
6 Diel R, Loddenkemper R, Meywald-Walter K, *et al.* Predictive value of a whole blood IFN-γ assay for the development of active tuberculosis disease after recent infection with *Mycobacterium tuberculosis*. *Am J Respir Crit Care Med* 2008; 177: 1164–1170.
7 Kik S, Franken W, Mensen M, *et al.* Predictive value for progression to tuberculosis by IGRA and TST in immigrant contacts. *Eur Respir J* 2010; 35: 1346–1353.
8 van Zyl-Smit R, Zwerling A, Dheda K, *et al.* Within-subject variability of interferon-γ assay results for tuberculosis and boosting effect of tuberculin skin testing: a systematic review. *PLoS One* 2009; 4: e8517.
9 Leyten E, Prins C, Bossink A, *et al.* Effect of tuberculin skin testing on a *Mycobacterium tuberculosis*-specific interferon-γ assay. *Eur Respir J* 2007; 29: 1212–1216.
10 Pai M, Joshi R, Dogra S, *et al.* T-cell assay conversions and reversions among household contacts of tuberculosis patients in rural India. *Int J Tuberc Lung Dis* 2009; 13: 84–92.

DOI: 10.1183/09031936.00030610

Morales-Kastresana *et al. Journal for ImmunoTherapy of Cancer* 2013, **1**:3
http://www.immunotherapyofcancer.org/content/1/1/3

Journal for ImmunoTherapy of Cancer

SHORT REPORT **Open Access**

Essential complicity of perforin-granzyme and FAS-L mechanisms to achieve tumor rejection following treatment with anti-CD137 mAb

Aizea Morales-Kastresana[1], Elena Catalán[2], Sandra Hervás-Stubbs[1], Asis Palazón[1], Arantza Azpilikueta[1], Elixabet Bolaños[1], Alberto Anel[2], Julián Pardo[3†] and Ignacio Melero[1*†]

Abstract

Background: Treatment with agonist anti-CD137 (4-1BB) immunostimulatory monoclonal antibodies elicits complete tumor regressions in a number of transplanted hematological and solid malignancies in mice. Rejection is mainly dependent on cytotoxic T lymphocytes (CTL) and IFNγ, although a role for NK cells and dendritic cells has been observed in some tumor models. Rejection of EG7-derived thymomas has been shown to be CTL-dependent but not NK-dependent.

Findings: In this therapeutic setting, we show that both the perforin-granzyme and FasL effector systems are readily expressed by $CD8^+$ T lymphocytes infiltrating the EG7 lymphomas which are undergoing rejection. Using knock-out mice, we demonstrate that both effector cytolytic systems are involved in the execution of complete immune rejections against EG7 established tumors. In accordance, EG7 tumor cells were susceptible *in vitro* to both killing mechanisms acting in a synergistic fashion.

Conclusions: CD137-elicited rejection of EG7-derived tumors involves the interplay of at least two final effector cytolytic mechanisms that act in cooperation.

Findings

Introduction

CD137 agonists hold promise to augment antitumor immune responses in a clinically significant fashion [1] and two fully human monoclonal antibodies (mAbs) are currently undergoing clinical development (BMS-663513 and PFZ-05082566). Hematological malignancies are not exception to the therapeutic effects of anti-CD137 mAbs and activity has been reported on experimental models of lymphoma, myeloma and mastocytomas [2-4]. The mechanism of action depends mainly on cytolytic T lymphocytes (CTLs) since depletion of CD8β T cells completely abrogates the therapeutic effect [5]. The train of events is complex and needs antigen priming by dendritic cells [5] and in some tumor models the participation of natural killer (NK) lymphocytes as observed in selective depletion experiments [6]. More recently, evidence has been published in the sense that anti-CD137 mAb enhances NK-mediated antibody-dependent cell-mediated cytotoxicity (ADCC) [7,8], in a way that can be exploited to enhance the antitumor activity of Herceptin and Rituximab.

Evidence has been reported showing that activated $CD8^+$ tumor infiltrating lymphocytes (TILs) express CD137 [9] and therefore are amenable to receive artificial costimulation by agonist anti-CD137 mAbs within the malignant tissue microenvironment. The execution of tumor rejection requires production of interferon (IFN) γ by CTLs as demonstrated by neutralizing mAbs [10] and with T cells derived from $IFN\gamma^{-/-}$ mice [10]. However, little is known about the final effector mechanisms that mediate tumor cell killing. CTLs and NK cells may kill using perforin-granzyme, FasL and TNF-related apoptosis inducing ligand (TRAIL) as the executioner molecules [11-14]. Experiments performed in the EG7 tumor model whose successful treatment does not require NK cells [5] clearly show that both the cytolytic

---

* Correspondence: imelero@unav.es
†Equal contributors
[1] CIMA, Gene therapy and Hepatology Unit, University of Navarra, Pamplona, Navarra, Spain
Full list of author information is available at the end of the article

granule and the FasL-mediated killing mechanisms were synergistically involved in achieving complete rejections of these lymphomas.

Results and discussion

Perforin, granzymes A and B and FasL are involved in tumor rejection elicited by anti-CD137 mAbs

As previously published, tumors derived from the EG7 cell line (EL4 stably transfected with ovalbumin [15]) are readily rejected following treatment with anti-CD137 mAb [5]. Treatment of 8-day established tumors with 1D8 mAb achieved complete rejections in six out of six tumors, while the tumors in the control group lethally progressed upon treatment with irrelevant rat IgG (Figure 1A).

Experiments performed in perforin and granzyme A and B triple knockout mice (PAB$^{-/-}$) indicated that although the therapeutic activity was reduced, a residual beneficial effect remained, resulting in two out of six complete rejections (Figure 1B). Conceivably, the FasL-Fas route could also be involved in the execution of rejection by CTLs. Indeed, performing the experiment in mice deficient for FasL (gld mice) also resulted in partial loss of the immunotherapeutic activity of anti-CD137 mAb (Figure 1C). These results are interpreted in the sense that pore-forming and granzyme entrance to malignant cells need to be complemented by FasL-mediated induction of apoptosis in order to optimally achieve tumor rejection.

Next, we explored if both killing mechanisms were available in T cells at the site of tumor rejection. As can be seen in Figure 2A, expression of intracellular granzyme B is observed in a good number of CD8^{+} TILs but not in the CD4^{+} counterparts (Figure 2A left). It is of note that 6.7 ± 1.5% of CD8^{+} TILs stained positive with H-2K^{b}-SIINFEKL tetramers clearly indicating the presence of antigen specificity in the lymphocyte infiltrate (Figure 2A right). Perforin expression in cytolytic granules could not be explored due to the lack of satisfactory mAbs for staining this protein in mice. FasL (CD95L) was detected on the surface of both CD8^{+} and CD4^{+} TILs (Figure 2B).

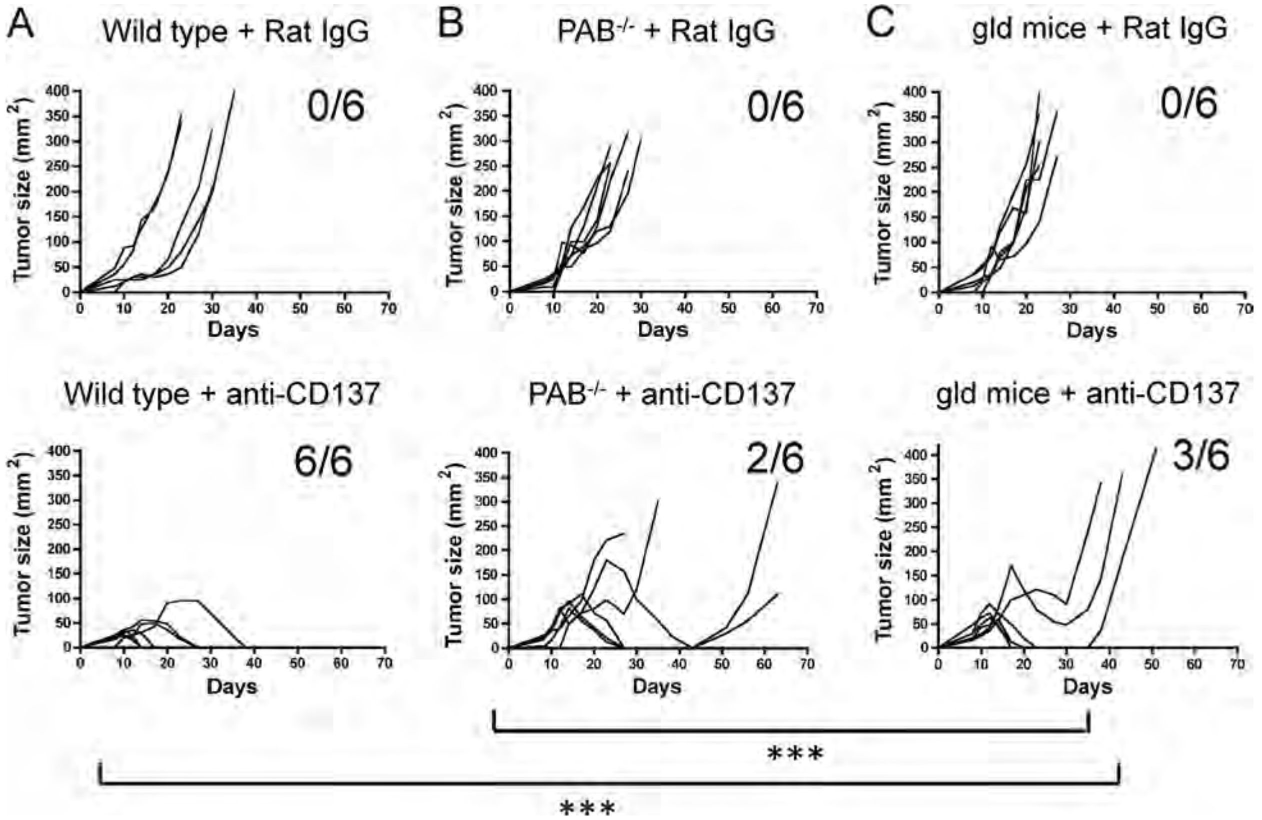

Figure 1 Both perforin-granzyme and FasL pathways contribute to rejection of EG7 tumors upon treatment with anti-CD137 mAbs. Wild type (**A**), perforin and granzyme A and B knockout (PAB$^{-/-}$) (**B**) and FasL-mutant gld (**C**) mice were injected s.c. with 5×10^5 EG7 tumor cells and treated i.p. with 100 μg of control Rat IgG or anti-CD137 mAb on days 8, 10, 12 and 14 after tumor cell challenge. Mean tumor diameters were sequentially measured 2-3 times per week. 6 mice per group were included. Statistical comparisons were performed using a nonlinear regression statistical method (Y= (MaxVol * exp(X-TimeO))/(1 + exp((X-TimeO)/RateGrowth)) with GraphPad software. ***, P<0.001 were considered statistically significant.

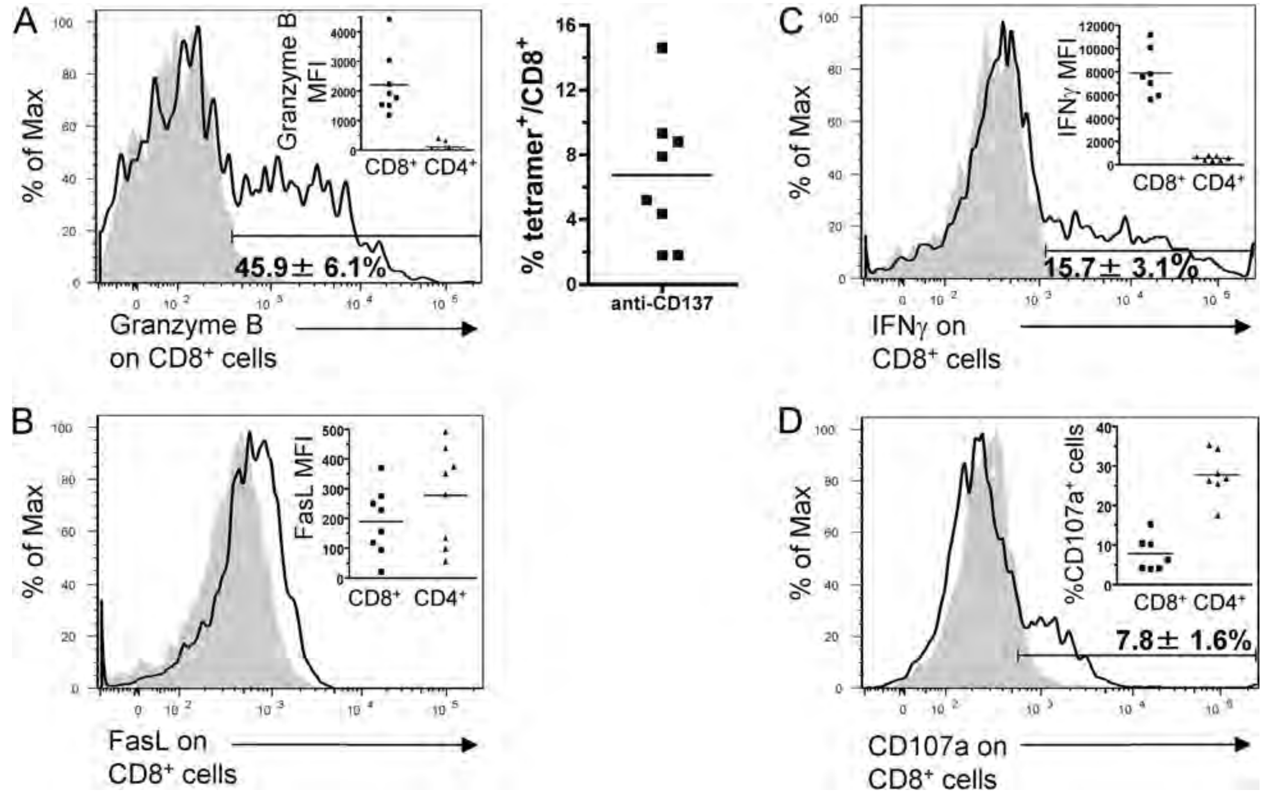

Figure 2 The cytotoxic mechanisms responsible for EG7 tumor rejection are present in TILs after treatment with anti-CD137 mAb. Mice were challenged s.c. with 5 × 10^5 EG7 cells and treated i.p. with anti-CD137 mAb on days 9 and 11. Two days later, tumors were removed and TILs were analyzed by flow cytometry for intracellular granzyme B (**A** left) and percentage of H-$2K^b$-SIINFEKL tetramer$^+$ cells (**A** right), surface FasL (**B**), intracellular IFNγ (**C**) and surface CD107a (**D**) expression on gated CD8$^+$ and CD4$^+$ T lymphocytes. Histograms show CD8$^+$ gated T cells that come from a representative experiment. Grey histograms represent isotype-matched control antibody stainings and open histograms protein-specific surface or intracellular stainings from representative cases. The insets in each histogram show the mean fluorescense intensity (MFI) after subtracting the background staining or the percentage of CD107a positive cells (**D**) for the indicated immunostainings on CD8$^+$ and CD4$^+$ T cells from individual tumors. The experiment was performed with 7-8 mice per group and mean±SEM is included in each histogram.

Previously published evidence had shown that CTL production of IFNγ was required for tumor rejection [10] and we observed that 15.7 ± 3.1% of CD8$^+$ TILs intracellularly express this cytokine without need for any *ex vivo* restimulation of the intratumoral lymphocytes (Figure 2C).

CD107a (LAMP.1) is a cytolytic granule transmembrane protein which emerges at killing synapses and remains transiently on the plasma membrane of effector cells. 7.8 ± 1.6% of CD8$^+$ TILs were caught expressing surface CD107a, thus demonstrating that they were actively degranulating at the time of tumor harvest (Figure 2D). The fact that they are holding this "smoking gun" tells of their active participation in cytotoxicity and tumor rejection. In a separate experiment we were able to gate onto T lymphocytes stained with CD8$^+$ and H^{-2} K^b-SIINFEKL tetramers and analyze the expression of effector molecules in this subset. As can be seen in Additional file 1: Figure S1, these CTLs co-express Granzyme B, IFNγ and CD107a.

EG7 tumor cells are synergistically killed by the perforin-granzyme and the FasL pathways

EG7 cells express surface Fas (Additional file 2: Figure S2A inset) and hence anti-Fas agonistic antibody kills these cells in 18 h as happens in Fas-transfected L1210 cells but not in control untransfected cells. To assess the involvement of these pathways in CTL killing of EG7 cells, anti-lymphocytic choriomeningitis virus (LCMV) derived gp33 CTLs that are directed to a peptide presented by H-$2K^b$ were elicited by immunization with LCMV-WE virus. Recovered CD8$^+$ splenocytes from immunized wild type (WT) mice 8 days after infections showed 71% killing at 10:1 effector:target ratio on EG7 cells pulsed with the gp33 synthetic peptide (Figure 3A). Under these experimental conditions optimal immunization allows us to focus on the effector phase of CTL activity. This activity was only reduced by about one half when immunized mice were deficient in PAB. Conversely, FasL neutralization with MFL3 mAb during the 4 h cytotoxicity experiment did not hamper killing. Interestingly, this anti-

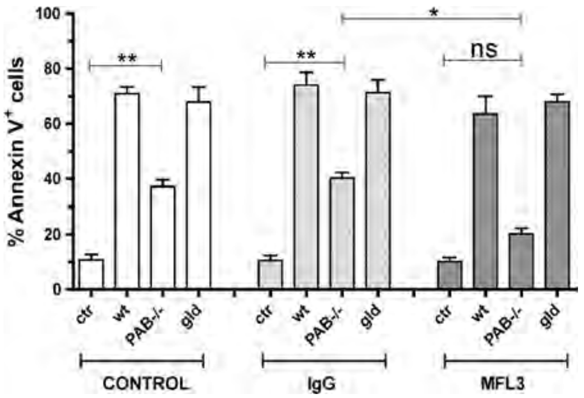

Figure 3 Fas-FasL pathway and perforin-granzyme machineries synergistically kill EG7 cell line. 5×10^4 EG7 cells were pre-pulsed with LCMV gp33 peptide and cocultured in vitro for 4 h with 5×10^5 $CD8^+$ T cells from LCMV immunized wild type (WT), perforin and granzymes A and B knockout (PAB$^{-/-}$) or gld mice in the presence or absence of 1 μg/ml of FasL blocking antibody (MFL3). Cell death was determined by annexin V staining in CD8 negative population by flow cytometry. Ctr, control with target cells without gp33 peptide. Data in the graphs are represented as mean±SEM of three independent experiments. Statistical comparisons were performed using Student's t test with GraphPad software. *, *P*<0.05; **, *P*<0.01; ***, P<0.001; ns, no significant. P<0.05 were considered significant.

FasL mAb completely abolished cytotoxicity when used on effector CTL from PAB$^{-/-}$ mice. CTLs from gld mice were as effective as WT mice in accordance with the results with FasL single blockade and, as expected, the MFL3 mAb did not have any effect under these conditions, further confirming the selectivity of the blocking mAb.

Therefore at least under these conditions, FasL and the cytolytic granule machinery seem to synergistically operate to bring about death of these lymphoma cells. TRAIL engagement of its death promoting receptors could have also been involved, but this was ruled out since EG7 is not killed by 1μg of a recombinant form of TRAIL that readily killed Jurkat cells as a positive control (Additional file 2: Figure S2B).

Materials and methods

Mice and cell lines

C57BL/6 wild type mice (6-8 weeks old) were purchased from Harlan Laboratories. Mice deficient for perforin and granzymes A and B (PAB$^{-/-}$ [16]) or with a mutation in FasL (gld mice) were a kind gift of Markus Simon (Max-Planck Institute of Immunobiology, Freiburg, Germany). PAB$^{-/-}$ and gld mice were bred into the BL/6 background. Animal experimentation followed FELASA guidelines and approval of the Ethics Committee for Animal Experimentation from CITA (2011-01) and University of Navarra (study number 066/10). The murine thymoma cell line EG7 was a kind gift from Dr. Claude Leclerc (Institut Pasteur, Paris, France) and was authenticated using the master cell banks by RADIL (Case number: 6592-2012). Jurkat cells, L1210 and Fas-transfected L1210 have been described [17,18].

In vivo tumor growth

5×10^5 EG7 cells were subcutaneously injected into the flank of WT, PAB$^{-/-}$ or gld mice. Mice were intraperitoneally treated with 100 μg/dose of anti-CD137 or control Rat IgG on days 8, 10, 12 and 14 following tumor cell inoculation. Rat IgG antibody was purchased from Sigma-Aldrich and anti-CD137 clon 1D8 [2] was from Bristol-Myers Squibb (Lawrenceville, NJ). Mice and tumor size were monitored twice a week and mice were sacrificed when the tumor size reached 300 mm^2.

Preparation of cell suspensions from EG7 tumors

Tumors were excised and incubated for 15 minutes at 37°C in a solution containing Collagenase-D+DNase-I (Roche) in RPMI. Afterwards, tumors were disrupted mechanically and passed through a 70-μm cell strainer (BD Falcon). Erythrocytes from cell suspensions were lysed with potassium ammonium chloride lysing buffer.

Flow cytometry

Single-cell suspensions were pretreated with FcR-Block (anti-CD16/32 clone 2.4G2). Anti-CD3ε, anti-CD8α, anti-CD4, anti-FasL, anti-IFNγ, anti-granzymeB and isotype Rat IgG and Hamster IgG isotype controls were all purchased from Biolegend; anti-CD107a, anti-Fas, mouse IgG isotype control and Apoptosis Detection Kit-I were from BD Pharmingen; and anti-TRAIL mAb was from eBioscience. H-2K^b-SIINFEKL tetramers were purchased from Beckman Coulter. For intracellular stainings, cells were fixed and permeabilized with Cytofix/Cytoperm (BD Biosciences). Cells were studied with FACSCanto II or FACSCalibur and were analyzed using FlowJo (TreeStar software). Specific mean fluorescense intensity (MFI) and percentage values in graphs are represented after subtraction of the control isotype-matched signal.

Fas and TRAIL induced cell death assays

10^5 cells were cultured with human recombinant TRAIL, purified anti-Fas antibody (clone Jo2) or isotype control (both from BD Biosciences) for 18 h. Human recombinant TRAIL functional on human and mouse receptors was produced in *E.coli* and purified as previously described [19]. Cell death was analyzed by Annexin V and 7-aminoactinomycin D (7-AAD) double staining.

Generation of *ex vivo* gp33-specific $CD8^+$ cells

Mice were infected with 10^5 pfu LCMV-WE i.p. as described [17]. On day eight after infection, $CD8^+$ cells were positively selected from spleen using anti-CD8-MicroBeads

(Miltenyi Biotec). Purity of selected CD8$^+$ cells was higher than 95%.

Ex vivo cytotoxicity assay

Target cells were pre-incubated with the LCMV-immunodominant peptide gp33 (acquired from Neosystem Laboratory) and effector CD8$^+$ cells were stained with CellTracker Green (Invitrogen). Effector and target cells were incubated at a ratio of 10:1 (effector:target) during 4 hours. In certain experiment anti-FasL blocking antibody (clone MFL3) (BD Biosciences) was added during the 4 h cytotoxicity assay. Gated CellTracker Green-negative targets were analyzed for annexin V and 7-AAD double staining.

Conclusions

As a whole, we have demonstrated using a tumor model amenable to successful immunotherapy with anti-CD137 mAb that the FasL and perforin-granzyme killing machineries act non-redundantly and synergistically to execute complete tumor rejections upon therapy with agonist anti-CD137 mAb.

Additional files

Additional file 1: Figure S1. Experiments as in figure 2 but in this case TILs from five EG7 tumors were pooled and stained with the H-^{2}K^{b} SIINFEKL tetramer. Gated CD8$^+$ Tetramer+ T lymphocytes were analyzed for expression of the indicated effector molecules as depicted in the corresponding histograms.

Additional file 2: Figure S2. The EG7 cell line is susceptible to being killed by anti-Fas antibody but not by recombinant TRAIL. (A) 1 × 10^5 EG7 cells per well were cultured 18 h with 5 μg/ml of soluble anti-Fas antibody. Cell death was determined by annexin V staining by flow cytometry. The inset histogram shows surface Fas expression by the EG7 cell line. The gray histogram represents isotype-matched control antibody and open histogram Fas-specific surface staining. (B) EG7 or positive control Jurkat cells were incubated for 18 hours with 0 to 1 μg/ml human recombinant TRAIL (hrTRAIL) and cell death was analyzed by flow cytometry using 7-AAD and annexin V staining. Dead cells are represented as the percentage of both Annexin V single positive and Annexin V/7-AAD double positive. Data in the graphs are represented as mean±SEM of three independent experiments. Statistical comparisons were performed using Student's t test with GraphPad software. *, $P<0.05$; **, $P<0.01$; ***, $P<0.001$; ns, no significant. $P<0.05$ were considered significant.

Abbreviations

mAb: Monoclonal antibody; CTL: Cytotoxic T lymphocyte; NK: Natural killer; IFN: Interferon; ADCC: Antibody-dependent cell-mediated cytotoxixity; TIL: Tumor infiltrating lymphocyte; TRAIL: TNF-related apoptosis inducing ligand; PAB: Perforin and granzyme A and B; LCMV: Lymphocoriomeningitis virus; WT: Wild type; MFI: Mean fluorescense intensity; 7-AAD: 7-Aminoactinomycin D.

Competing interests

IM has received research grants and consultant honoraria from Bristol Myers Squibb. The rest of the authors do not have conflict of interests to declare.

Authors' contributions

IM and JP were the main investigators and take primary responsibility for the paper. AMK and AP performed the in vivo experiments, AMK, EC, AA and EB carried out the in vitro experiments. The tumor infiltration analysis was performed by AMK and SHS. SHS, AA, JP and IM co-ordinated the research and performed laboratory work. IM and AMK wrote the paper. All authors read and approved the final manuscript.

Acknowledgements

The authors would like to thank to Luis Martinez Lostao and Diego de Miguel for providing recombinant human TRAIL protein. We are grateful to Dr. Maria Jure-Kunkel (Bristol Myers Squibb) for kindly providing 1D8 monoclonal antibody.
This work was supported by grants from MEC/MICINN of Spain (SAF2008-03294; SAF2011-22831; SAF2011-25390), Departamento de Educación and Departamento de Salud del Gobierno de Navarra, Redes temáticas de investigación cooperativa RETIC (RD06/0020/0065), European commission VII framework program (ENCITE), SUDOE-IMMUNONET and "UTE for project FIMA". JP is supported by Aragón I+D (ARAID) and Gobierno de Aragón/ Fondo Social Europeo. AMK and EC receive an FPI scholarship from MEC (Spain), AP a scholarship from FIS from MSC (Spain) and SHS is supported by a Ramon y Cajal contract from MICINN (Spain).

Author details

[1]CIMA, Gene therapy and Hepatology Unit, University of Navarra, Pamplona, Navarra, Spain. [2]Departamento de Bioquímica y Biología Molecular y Celular, Universidad de Zaragoza, Zaragoza, Spain. [3]Instituto de Investigaciones Sanitarias de Aragón. Departamento de Bioquímica y Biología Molecular y Celular, Fac. Ciencias, Instituto de Nanociencia de Aragón (INA). Fundación Aragón I+D (ARAID) Universidad de Zaragoza, Zaragoza, Spain.

Received: 6 November 2012 Accepted: 5 February 2013
Published: 29 May 2013

References

1. Ascierto PA, Simeone E, Sznol M, Fu YX, Melero I: **Clinical experiences with anti-CD137 and anti-PD1 therapeutic antibodies.** *Semin Oncol* 2010, **37:**508–516.
2. Melero I, Shuford WW, Newby SA, Aruffo A, Ledbetter JA, Hellstrom KE, Mittler RS, Chen L: **Monoclonal antibodies against the 4-1BB T-cell activation molecule eradicate established tumors.** *Nat Med* 1997, **3:**682–685.
3. Wilcox RA, Flies DB, Zhu G, Johnson AJ, Tamada K, Chapoval AI, Strome SE, Pease LR, Chen L: **Provision of antigen and CD137 signaling breaks immunological ignorance, promoting regression of poorly immunogenic tumors.** *J Clin Invest* 2002, **109:**651–659.
4. Murillo O, Arina A, Hervas-Stubbs S, Gupta A, McCluskey B, Dubrot J, Palazon A, Azpilikueta A, Ochoa MC, Alfaro C, *et al*: **Therapeutic antitumor efficacy of anti-CD137 agonistic monoclonal antibody in mouse models of myeloma.** *Clin Cancer Res* 2008, **14:**6895–6906.
5. Murillo O, Dubrot J, Palazon A, Arina A, Azpilikueta A, Alfaro C, Solano S, Ochoa MC, Berasain C, Gabari I, *et al*: **In vivo depletion of DC impairs the anti-tumor effect of agonistic anti-CD137 mAb.** *Eur J Immunol* 2009, **39:**2424–2436.
6. Melero I, Johnston JV, Shufford WW, Mittler RS, Chen L: **NK1.1 cells express 4-1BB (CDw137) costimulatory molecule and are required for tumor immunity elicited by anti-4-1BB monoclonal antibodies.** *Cell Immunol* 1998, **190:**167–172.
7. Kohrt HE, Houot R, Goldstein MJ, Weiskopf K, Alizadeh AA, Brody J, Muller A, Pachynski R, Czerwinski D, Coutre S, *et al*: **CD137 stimulation enhances the antilymphoma activity of anti-CD20 antibodies.** *Blood* 2011, **117:**2423–2432.
8. Kohrt HE, Houot R, Weiskopf K, Goldstein MJ, Scheeren F, Czerwinski D, Colevas AD, Weng WK, Clarke MF, Carlson RW, *et al*: **Stimulation of natural killer cells with a CD137-specific antibody enhances trastuzumab efficacy in xenotransplant models of breast cancer.** *J Clin Invest* 2012, **122:**1066–1075.
9. Palazon A, Martinez-Forero I, Teijeira A, Morales-Kastresana A, Alfaro C, Sanmamed MF, Perez-Gracia JL, Penuelas I, Hervas-Stubbs S, Rouzaut A, *et al*: **The HIF-1alpha hypoxia response in tumor-infiltrating T lymphocytes induces functional CD137 (4-1BB) for immunotherapy.** *Cancer Discov* 2012, **2:**608–623.
10. Wilcox RA, Flies DB, Wang H, Tamada K, Johnson AJ, Pease LR, Rodriguez M, Guo Y, Chen L: **Impaired infiltration of tumor-specific cytolytic T cells in**

the absence of interferon-gamma despite their normal maturation in lymphoid organs during CD137 monoclonal antibody therapy. *Cancer Res* 2002, **62**:4413–4418.

11. Lopez JA, Brennan AJ, Whisstock JC, Voskoboinik I, Trapani JA: Protecting a serial killer: pathways for perforin trafficking and self-defence ensure sequential target cell death. *Trends Immunol* 2012, **33**:406–412.
12. Pardo J, Aguilo JI, Anel A, Martin P, Joeckel L, Borner C, Wallich R, Mullbacher A, Froelich CJ, Simon MM: The biology of cytotoxic cell granule exocytosis pathway: granzymes have evolved to induce cell death and inflammation. *Microbes Infect* 2009, **11**:452–459.
13. Vesely MD, Kershaw MH, Schreiber RD, Smyth MJ: Natural innate and adaptive immunity to cancer. *Annu Rev Immunol* 2011, **29**:235–271.
14. Kagi D, Vignaux F, Ledermann B, Burki K, Depraetere V, Nagata S, Hengartner H, Golstein P: Fas and perforin pathways as major mechanisms of T cell-mediated cytotoxicity. *Science* 1994, **265**:528–530.
15. Brossart P, Goldrath AW, Butz EA, Martin S, Bevan MJ: Virus-mediated delivery of antigenic epitopes into dendritic cells as a means to induce CTL. *J Immunol* 1997, **158**:3270–3276.
16. Simon MM, Waring P, Lobigs M, Nil A, Tran T, Hla RT, Chin S, Mullbacher A: Cytotoxic T cells specifically induce Fas on target cells, thereby facilitating exocytosis-independent induction of apoptosis. *J Immunol* 2000, **165**:3663–3672.
17. Pardo J, Balkow S, Anel A, Simon MM: The differential contribution of granzyme A and granzyme B in cytotoxic T lymphocyte-mediated apoptosis is determined by the quality of target cells. *Eur J Immunol* 2002, **32**:1980–1985.
18. Pardo J, Perez-Galan P, Gamen S, Marzo I, Monleon I, Kaspar AA, Susin SA, Kroemer G, Krensky AM, Naval J, Anel A: A role of the mitochondrial apoptosis-inducing factor in granulysin-induced apoptosis. *J Immunol* 2001, **167**:1222–1229.
19. Martinez-Lostao L, Garcia-Alvarez F, Basanez G, Alegre-Aguaron E, Desportes P, Larrad L, Naval J, Martinez-Lorenzo MJ, Anel A: Liposome-bound APO2L/TRAIL is an effective treatment in a rabbit model of rheumatoid arthritis. *Arthritis Rheum* 2010, **62**:2272–2282.

doi:10.1186/2051-1426-1-3
Cite this article as: Morales-Kastresana *et al.*: Essential complicity of perforin-granzyme and FAS-L mechanisms to achieve tumor rejection following treatment with anti-CD137 mAb. *Journal for ImmunoTherapy of Cancer* 2013 **1**:3.

OPEN ACCESS Freely available online

PLoS one

Group B Streptococcus GAPDH Is Released upon Cell Lysis, Associates with Bacterial Surface, and Induces Apoptosis in Murine Macrophages

Liliana Oliveira[1,2,3,4], Pedro Madureira[1,2], Elva Bonifácio Andrade[1,2], Abdelouhab Bouaboud[3,4], Eric Morello[5], Paula Ferreira[1,2], Claire Poyart[3,4], Patrick Trieu-Cuot[5], Shaynoor Dramsi[5]*

1 Universidade do Porto, ICBAS-Instituto de Ciências Biomédicas de Abel Salazar, Porto, Portugal, **2** IBMC-Instituto de Biologia Molecular e Celular, Porto, Portugal, **3** Institut Cochin, Université Paris Descartes, Sorbonne Paris Cité, Faculté de Médecine, Centre National de la Recherche Scientifique (UMR 8104), Paris, France, **4** Institut National de la Santé et de la Recherche Médicale, U1016, Paris, France, **5** Institut Pasteur, Unité de Biologie des Bactéries Pathogènes à Gram-positif, CNRS URA 2172, Paris, France

Abstract

Glyceraldehyde 3-phosphate dehydrogenases (GAPDH) are cytoplasmic glycolytic enzymes that, despite lacking identifiable secretion signals, have been detected at the surface of several prokaryotic and eukaryotic organisms where they exhibit non-glycolytic functions including adhesion to host components. Group B Streptococcus (GBS) is a human commensal bacterium that has the capacity to cause life-threatening meningitis and septicemia in newborns. Electron microscopy and fluorescence-activated cell sorter (FACS) analysis demonstrated the surface localization of GAPDH in GBS. By addressing the question of GAPDH export to the cell surface of GBS strain NEM316 and isogenic mutant derivatives of our collection, we found that impaired GAPDH presence in the surface and supernatant of GBS was associated with a lower level of bacterial lysis. We also found that following GBS lysis, GAPDH can associate to the surface of many living bacteria. Finally, we provide evidence for a novel function of the secreted GAPDH as an inducer of apoptosis of murine macrophages.

Citation: Oliveira L, Madureira P, Andrade EB, Bouaboud A, Morello E, et al. (2012) Group B Streptococcus GAPDH Is Released upon Cell Lysis, Associates with Bacterial Surface, and Induces Apoptosis in Murine Macrophages. PLoS ONE 7(1): e29963. doi:10.1371/journal.pone.0029963

Editor: F. Gisou van der Goot, Ecole Polytechnique Federale de Lausanne, Switzerland

Received April 7, 2011; **Accepted** December 9, 2011; **Published** January 23, 2012

Funding: This work was supported by grants from the Fondation pour La Recherche Médicale (to C.P), from the Agence Nationale de la Recherche "ERA-NET PathoGenoMics ANR-06-PATHO-001-01" (to P.T.-C.) and from SUDOE-FEDER IMMUNONET SOE1/P1/E014 (to P.F.). L. Oliveira was supported by PhD FCT fellowship SFRH/BD/38121/2007. The funders had no role in study design, data collection and analysis, decision to publish, or preparation of the manuscript.

Competing Interests: The authors have declared that no competing interests exist.

* E-mail: shaynoor.dramsi@pasteur.fr

Introduction

Group B Streptococcus (GBS, also known as *Streptococcus agalactiae*) is a common colonizer of the gastro-intestinal and urogenital tracts of up to 40% of healthy individuals. However, under certain circumstances, it may turn into a life-threatening pathogen causing sepsis and meningitis in newborn infants [1]. Mortality due to neonatal GBS infection remains high (up to 10%) despite antibiotic treatment and 25–50% of surviving infants are left with permanent neurological sequelae [2]. GBS is also responsible for invasive infections in adults with underlying diseases and in the elderly [1].

Glyceraldehyde 3-phosphate dehydrogenases (GAPDHs) are essential cytoplasmic enzymes involved in the glycolytic pathway which, despite the lack of secretion signals, have been found localized at the surface of several bacteria, fungi, and even protozoans (reviewed in [3]). In this unexpected location, GAPDH exhibits various adhesive functions thereby facilitating colonization and invasion of host tissues (reviewed in [3]). Like GAPDH, several other cytosolic proteins have been associated with the bacterial surface where they play a different role as referred to their original function and thus have been called "moonlighting proteins" (for review see [4]). Examples of moonlighting proteins include α-enolase [5], glucose-6-phosphate isomerase [6], glutamine synthetase [7], ornithine carbamoyltransferase [6] and fibronectin-binding proteins (PavA of *Streptococcus pneumoniae* [8], FbpA of *Listeria monocytogenes* [9], Fbp54 of *Streptococcus pyogenes* [10]).

Surface-localized GAPDH was originally identified in the Gram-positive pathogen *S. pyogenes* and subsequently found in other streptococcal groups B, C, E, G, H, and L [11]. *S. pyogenes* GAPDH is an ADP-ribosylating enzyme [12] that binds a number of human proteins, including plasmin(ogen) [13,14], lysozyme, myosin, actin, fibronectin [11] and uPAR/CD87 on pharyngeal cells [15]. GAPDH has also been reported on the surface of Gram-negative bacteria such as enterohemorrhagic and enteropathogenic *Escherichia coli* where it binds to human plasminogen and fibrinogen suggesting a role in pathogenesis [16]. It is generally assumed that the release of such cytoplasmic proteins is due to cell lysis, although the involvement of specific export processes has been suggested [17,18]. Nevertheless, the mechanism by how these proteins are exported, secreted or become surface associated is still a matter of debate.

GAPDH was also identified as a surface exposed and enzymatically active protein in GBS [19]. We have demonstrated that GAPDH is detected in the culture supernatants of GBS and acts as a virulence–associated immunomodulatory protein that exerts stimulatory effects on B lymphocytes and induces an early

IL-10 production that facilitates host colonization [20]. We have also reported that surface-localized GAPDH interacts with the human plasminogen system to increase the proteolytic activity of the bacterial surface [21]. These results highlight the contribution of the extracellular form of GAPDH to GBS virulence.

Here, we addressed the question of GAPDH export to the cell surface of GBS strain NEM316. Overall, our data suggest that GAPDH presence in the extracellular medium is due to bacterial lysis. We also found that GAPDH is a very "sticky" protein that, following lysis, can associate to the surface of many living bacteria. Evidence for a novel function for GBS GAPDH as an inducer of apoptosis of murine macrophages is also provided.

Results

Surface display of GAPDH is impaired in pilus mutants of GBS

We previously showed that GAPDH is present in the culture supernatant of GBS strain NEM316 [20] and immunogold electron microscopy revealed the presence of GAPDH on the surface of wild-type (WT) GBS strain NEM316 (Fig. 1A). However the mechanism of export of this abundant cytoplasmic protein devoid of signal sequence remains unknown. Screening our collection of *Himar1* transposon mutants [22] for the presence of surface displayed GAPDH, we found that the non-piliated PilB$^-$ mutant [23], used as control, had an impairment in the presence of exposed GAPDH. Screening of additional mutants of the PI-2a pilus locus [23] unexpectedly revealed that mutants of the major pilin PilB$^-$ and of both accessory proteins PilA/C$^-$ exhibited a significant decrease in the amount of GAPDH present at the bacterial surface (Fig. 1B). In addition, we observed a significantly reduced level of GAPDH in the supernatants of these pilus mutants as compared to the WT strain (Fig. 1C). As an internal control for equal loading in western blots, we used antibodies specific for the CAMP factor, a known secreted GBS protein [24] and the GAPDH to CAMP ratio is shown in Fig. 1D. Of note, Western blot of these supernatant extracts with antibodies to the manganese-dependent superoxyde dismutase SodA, another GBS cytoplasmic protein [25], revealed that SodA protein is also found more abundantly in the culture supernatant of the WT strain compared to the pilus mutants (Fig. 1C). The presence of other cytoplasmic proteins was detected in the WT strain's culture supernatant using the available antibodies in the laboratory specific for known cytoplasmic proteins like D-alanine-D-alanyl carrier ligase (DltA) [26], NADH oxidase (Nox-2) [27], and elongation factor (EF-Tu) (Figure S1).

Some moonlighting proteins of *Mycobacterium tuberculosis* and *Listeria monocytogenes* were reported to be secreted *via* the accessory secretion machinery SecA2 [17,18,28] and we therefore tested the possibility that GAPDH export in GBS could be SecA2-dependent. FACS analysis and immunoblotting of culture supernatant proteins revealed that the GAPDH was slightly more abundant at the surface and in the culture supernatant of the SecA2 mutant as compared to the WT strain, thereby excluding the involvement of this secretion pathway in the export of this protein (data not shown).

GBS pilus mutants display a lower level of bacterial lysis

We hypothesized that the secreted GAPDH both present on the surface and in the extracellular medium of the WT strain could result from bacterial lysis or to increased cellular permeability in membrane-compromised bacteria. We thus used the LIVE/DEAD bacterial viability kit for FACS to quantify bacterial lysis in WT and isogenic PilB$^-$ and PilA/C$^-$ pilus mutants. We found that the "Dead/Live" ratio was significantly higher in the WT strain compared to both pilus mutant strains (Fig. 2A). Thus, the WT strain appears more susceptible to lysis than PilB$^-$ and PilA/C$^-$ mutants. Of note, the *in vitro* growth curves of WT and pilus mutant strains were not significantly different (Figure S2). We compared the autolysis of GBS to that of *Staphylococcus aureus*, a bacterial species for which autolysis has been extensively studied including its impact on the release of cytoplasmic proteins [29]. In both species, autolysis was followed over time by measuring the decrease in turbidity of bacteria recovered in PBS (Fig. 2B). The graph shows a slow decrease in turbidity for GBS with a 20% decrease over 5 h. In contrast, a sharp decrease in turbidity was observed for *S. aureus*, dropping from 100 to ≈30% in the same time period. We estimated that the amount of GAPDH found in the supernatant of WT GBS represent approximately 5% of the amount of GAPDH present in total protein extracts (data not shown). Furthermore, in zymograms assays carried out with GBS, *Enterococcus faecalis* or *Micrococcus luteus* substrate gels, autolysin activity in GBS protein extracts was seen as a single faint hydrolysis band of about 60 kDa whereas *S. aureus* extracts gave 5–7 clear bands (data not shown). Thus, the low level of GBS autolysis, as demonstrated above, very likely accounts for the quantity of GAPDH found in the culture supernatant.

Soluble GAPDH can associate to the bacterial surface of several Gram-positive and Gram-negative bacteria

The possibility that these housekeeping enzymes could become surface exposed by a process of reassociation was proposed previously [30]. In order to test the capacity of soluble GAPDH to bind to the bacterial surface, we performed an ELISA assay in which heat-inactivated GBS were used as a target to bind recombinant histidyl-tagged GAPDH (rGAPDH) added at different concentrations. The interaction between heat-inactivated GBS and rGAPDH was detected using a mouse anti-5×His antibody. The results indicated that rGAPDH interacts with the bacterial surface in a dose dependent manner and that this binding can be inhibited by anti-GAPDH antibodies (Fig. 3A). In addition, we performed another assay in which rGAPDH was added to exponentially growing bacteria including GBS strains from different serotypes, unrelated Gram-positive bacteria (*S. pyogenes*, *L. lactis*, and *S. aureus*), and *E. coli* as a Gram-negative prototype. Following 2 h of incubation at 37°C, bacteria were pelleted by brief centrifugation, washed three times with PBS, and protein extracts were analyzed by immunoblotting using a pentaHis antibody to detect the rGAPDH. This analysis showed that exogenous rGAPDH could efficiently bind to the surface of all the strains tested, including the phylogenetically remote Gram-negative bacterium, confirming the high propensity of this protein to interact with unrelated bacterial surface components (Fig. 3B).

GAPDH can bind to the pilus structural subunits

To test whether pilus subunits can act as GAPDH reassociation partner on the surface of GBS, we examined the direct interaction of GAPDH with purified histidyl-tagged pilus proteins, PilA-6×His, PilB-6×His, and PilC-6×His by ELISA. As control for specificity, we used another histidyl tagged protein His-HvgA S10 (S10 domain of HvgA protein [31]). Fig. 4 shows that although GAPDH was able to bind to all three pilus structural proteins, PilA, PilB and PilC, in a dose dependent manner, it similarly binds to the control protein S10-HvgA. These results indicate that GBS GAPDH is a very "sticky" protein that binds non-specifically to structurally unrelated surface proteins.

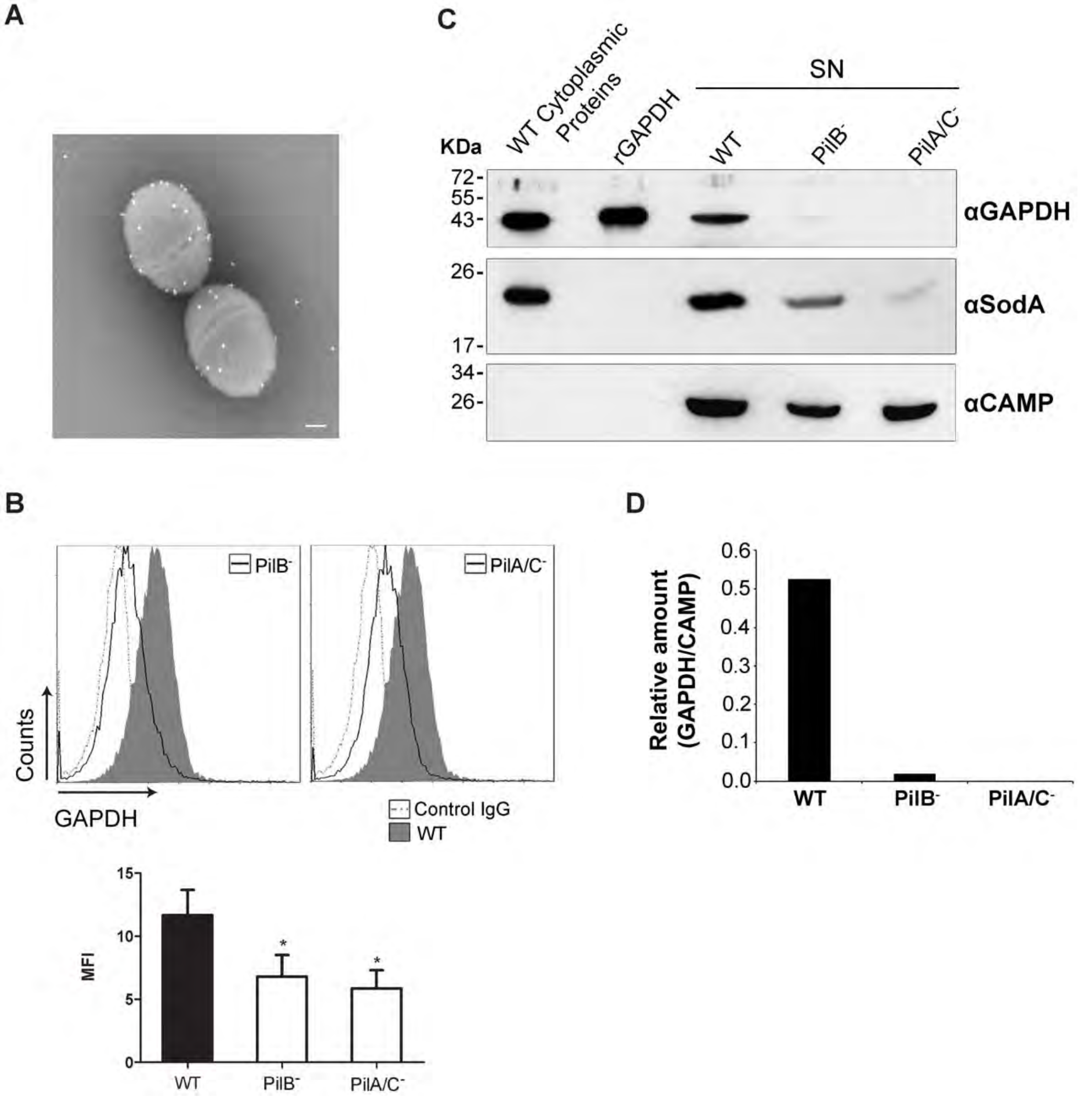

Figure 1. Evaluation of surface-bound and extracellular GAPDH levels in GBS strain NEM316 (WT) and pilus mutant strains. A) Immunoelectron microscopy (IEM) picture of the surface-bound GAPDH in NEM316. Scale bar, 100 nm. B) Fluorescence-activated cell sorter analysis (FACS) of WT, PilB$^-$ and PilA/C$^-$ incubated with a polyclonal rabbit anti-GAPDH IgG (grey filled histogram for WT or black line histogram for PilB$^-$ and PilA/C$^-$ strains) or normal rabbit IgG (control IgG-grey dotted histogram). Mean Fluorescence Intensity (MFI) in lower panel is reported relative to control IgG. C) Western Blot detection of GAPDH in culture supernatants (SN) of exponentially growing WT, PilB$^-$ and PilA/C$^-$ strains. 25 μL of each concentrated supernatant, 10 ng of rGAPDH or 2 μg of WT total proteins were loaded in the gel. After transfer to a membrane, proteins were detected using a polyclonal rabbit anti-rGAPDH IgG antibody, rabbit anti-SodA antibody and rabbit anti-CAMP antibody followed by HRP-conjugated goat anti-rabbit antibody. D) Quantifications of GAPDH relative to the loading control protein (CAMP) in the supernatant of WT, PilB$^-$ and PilA/C$^-$ strains, were performed with ImageJ software. Results shown are representative of three independent experiments. *, $P<0.05$.

doi:10.1371/journal.pone.0029963.g001

Induction of bacterial lysis increases the amount of surface GAPDH

To substantiate the hypothesis that secretion of GAPDH results from cell lysis, we investigated whether induced GBS lysis resulted in increased amount of surface exposed GAPDH. For that purpose, GBS WT or the isogenic SodA mutant were incubated in the presence of 0.1% Triton X-100 for 45 min. As shown in Fig. 5A, Triton treatment increased by approximately 60-fold and 35-fold the amount of GAPDH detected by FACS analysis at the surface of the WT and SodA$^-$ strains, respectively. Immunoblotting of supernatant proteins showed that Triton treatment increased by approximately 500-fold and 350-fold the amount of GAPDH detected in the culture medium of WT and SodA$^-$ strains, respectively, as compared to the non-treated cultures (Fig. 5B). Interestingly, a 220-fold increase in the amount of SodA was also detected in the culture supernatant of the WT strain

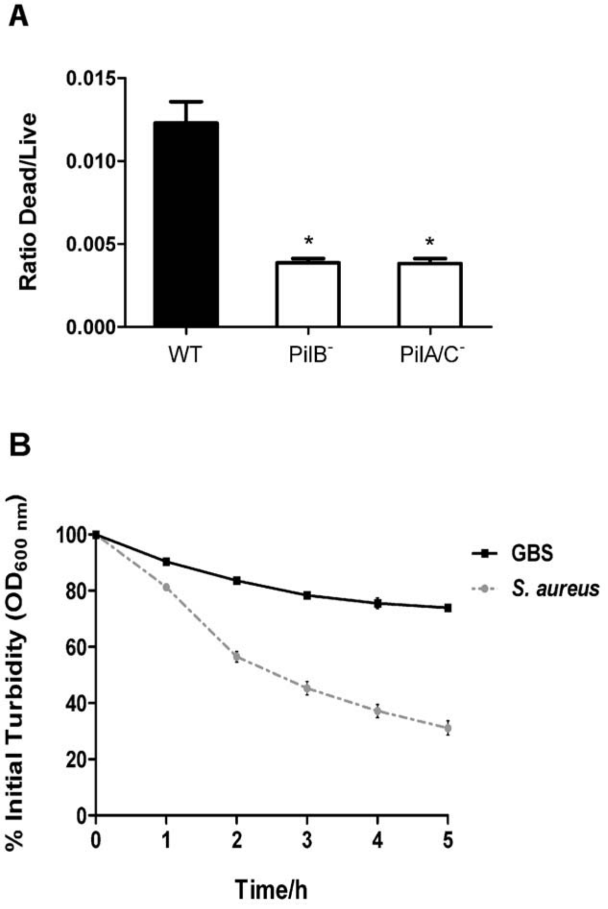

Figure 2. Quantification of bacterial lysis. A) 10 μL of bacterial culture of GBS WT, PilB$^-$ and PilA/C$^-$ were stained with Syto9 and propidium iodide (PI). The bacterial suspensions were then subjected to FACS and counted using the LIVE/DEAD® *Bac*Light^{TM} kit. B) OD$_{600\ nm}$ measurement of GBS or *S. aureus* suspensions in PBS at 37°C over 5 h. The graphic expresses the % in OD in different time points relative to the time 0. Results shown are representative of two independent experiments. *, $P<0.05$.
doi:10.1371/journal.pone.0029963.g002

following Triton treatment. However, as shown in Fig. 5A, the moonlighting protein SodA does not reassociate to the bacterial surface.

We then reasoned that antibiotics targeting the cell wall, such as penicillins, and inducing cell lysis should also increase the release of GAPDH. Similar experiments were therefore performed with penicillin G (PenG), an antibiotic commonly used to treat GBS infections. Incubation for 12 h of exponentially growing GBS with PenG at a final concentration of 6.4 μg/mL (i.e. a therapeutic concentration corresponding to 100 times the MIC) resulted in a CFU/mL decrease of 5×10^6 to 2×10^4. Accordingly, after this treatment, there was approximately a 10-fold increase in the amount of GAPDH detected both at the cell surface (Fig. 5C) and in the culture supernatant (Fig. 5D).

To further confirm that GAPDH is secreted upon cell lysis we overexpressed one putative GBS autolysin, an N-acetyl muramidase, encoded by the gene *gbs0093*, in the WT and PilB$^-$ mutant. Our first attempts in cloning *gbs0093* on high- and low-copy plasmid pOri23 and pTCV-*erm* respectively were unsuccessful. We therefore choose to assay an inducible system that has been used in closely related Gram-positive species using the pMSP3545 vector [32]. We first validated the functionality of this system in GBS NEM316 using the secreted staphylococcal nuclease NucB as a reporter. Addition of nisin in the culture medium allowed the detection of secreted NucB in the supernatant in a dose dependent manner without impairing bacterial growth (Figure S3).

Cloning of *gbs0093* in plasmid pMSP3545 was performed in *E. coli* and the resulting vector was introduced in WT and PilB$^-$ GBS strains. We confirmed the overexpression of the autolysin after a 3 h induction with nisin by semi-quantitative RT-PCR with RNA extracted from both strains (data not shown). We next analyzed the amount of surface bound GAPDH by FACS and observed a significant increase of this protein in the PilB$^-$ mutant after the overexpression of the autolysin following an overnight induction (Fig. 5E). In the WT strain, which display a higher level of bacterial lysis than the PilB$^-$ mutant, the effect of autolysin overexpression was not statistically significant. We also verified by immunoblotting that GAPDH accumulated at higher levels in the culture supernatant of the PilB$^-$ strain (Fig. 5F). Similarly, the amount of the SodA protein, used as control, also increased in the culture supernatant of the PilB$^-$ strain when the autolysin was overexpressed.

rGAPDH induces apoptosis in macrophages

It was previously shown that GBS induces apoptosis of macrophages [33] and that eukaryotic GAPDH plays a role in the induction of cell death of different cell lines (reviewed in [34,35]). Therefore, we investigated whether streptococcal GAPDH could induce apoptosis in both immortalized murine macrophages (RAW264.7) and primary bone marrow-derived macrophages from C57BL/6 mice. As shown in Fig. 6A, rGAPDH or culture supernatant from GBS WT strain induced efficient apoptosis in RAW264.7 at 24 h as determined by using a fluorometric TUNEL assay. As polymyxin B was added in the media containing recombinant proteins and bacterial culture supernatants to neutralize traces of LPS, we observed that its presence at the same concentration (10 μg/ml) in the medium only did not increase the levels of apoptotic cells (data not shown). In addition, immunodepletion of the GAPDH from the culture supernatant significantly decreased apoptosis level. This reduction in apoptosis level was not observed by immunodepleting the SodA protein (Fig. 6A). This result shows that native GAPDH found in the bacterial supernatant of GBS is a potent inducer of apoptosis in this murine cell line. Furthermore, we tested the capacity of the GAPDH present in the supernatant from both pathogenic (*S. pyogenes* and *S. aureus*) and non-pathogenic bacteria (*L. lactis*) to induce apoptosis of macrophages. Interestingly, the GAPDH of both *S. pyogenes* and *S. aureus* plays a significant role in macrophage apoptosis (Fig. 6A). In contrast, the culture supernatant from *L. lactis* was unable to cause apoptosis of macrophages. Similar results were obtained in primary bone marrow-derived macrophages where rGAPDH induced a marked pro-apoptotic effect which was shown to be dose-dependent (Fig. 6B). Moreover, the immunofluorescence images of C57BL/6 bone marrow-derived macrophages that were treated with rGAPDH (Fig. 6C) show the nuclear TUNEL staining and the classical morphological characteristics of apoptosis such as decreased size, a marked round shape and condensed nuclei.

Discussion

Several reports in the last decade have shown that housekeeping enzymes, including glycolytic enzymes such as GAPDH, α-enolase (Eno), phosphoglycerate kinase (PGK), fructose 1,6-biphosphate aldolase (FBA), can mediate a variety of unrelated functions

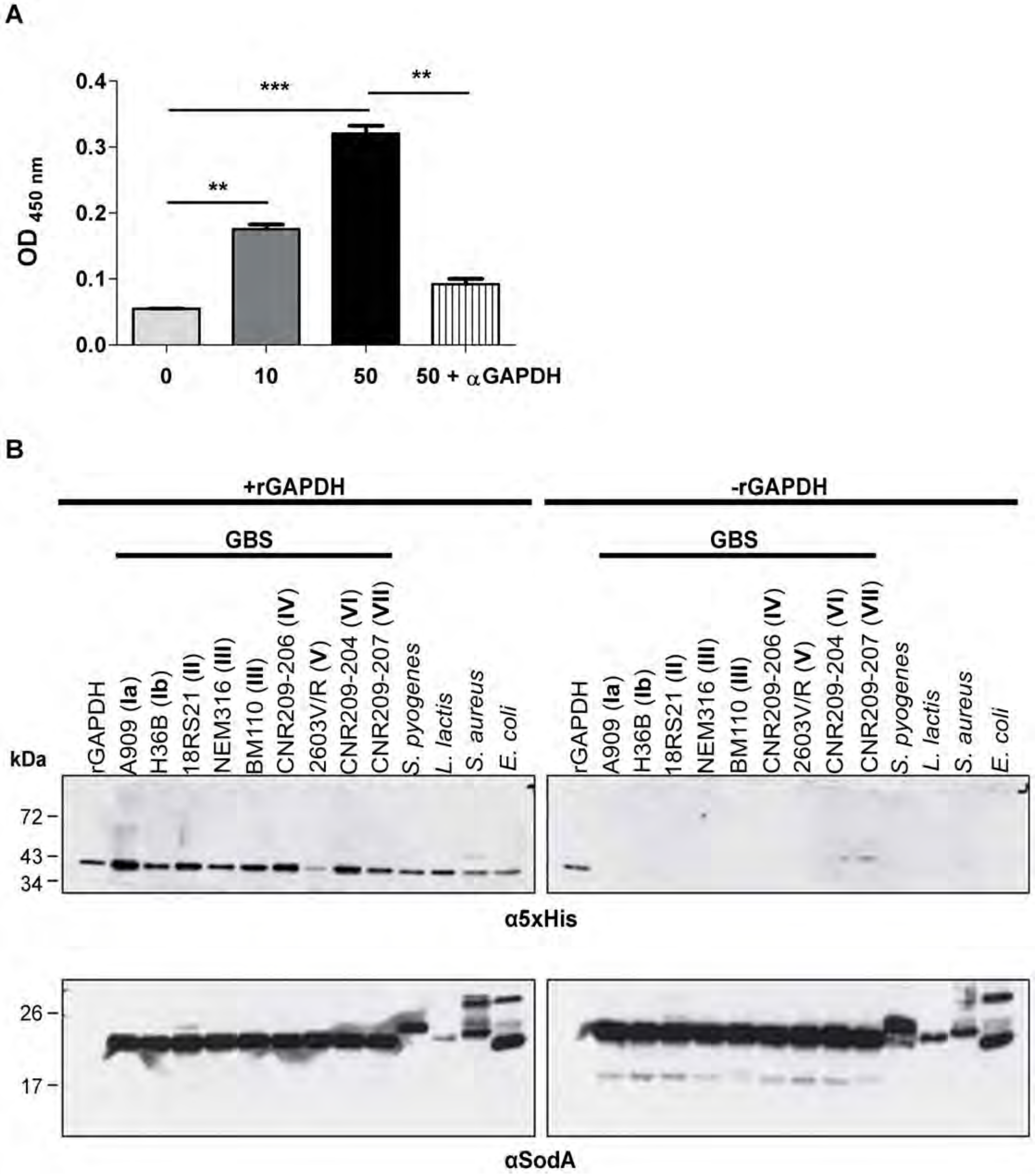

Figure 3. Reassociation capacity of rGAPDH. A) ELISA plates were coated with 6.5×10^7 CFU/well of heat inactivated NEM316 overnight at 4°C. They were incubated with 100 µL/well of different amounts of rGAPDH (0, 10 or 50 µg/mL) or rGAPDH 50 µg/mL with 75 µg of rabbit anti-rGAPDH IgG pAb (50+αGAPDH). rGAPDH was detected using a HRP coupled mouse pentaHis antibody. After revelation, the OD_{450} was registered using a microplate reader. B) 200 µg of rGAPDH (+rGAPDH) or PBS (−rGAPDH) was added to an exponentially grown culture of several GBS strains belonging to different serotypes (Ia, Ib, II, III, IV, V, VI, and VII), *S. pyogenes*, *L. lactis*, *S. aureus*, and *E. coli*. After incubation, total proteins extracts were subjected to SDS-PAGE followed by transfer to nitrocellulose membrane (rGAPDH: 10 ng; Total proteins +/− rGAPDH: 8 µg). This membrane was incubated with an HRP-coupled mouse pentaHis antibody or rabbit anti-SodA antibody (loading control) followed by HRP-conjugated goat anti-rabbit secondary antibody. Results shown are representative of two independent experiments. **, $P<0.01$; ***, $P<0.001$.
doi:10.1371/journal.pone.0029963.g003

depending on their location in the cell and are therefore collectively referred to as "moonlighting proteins". These cytoplasmic enzymes, which lack typical signature sequences for their transport to the cell surface and/or anchoring mechanisms to the cell wall have been observed at the surface of bacteria, yeast, fungi and protozoa (reviewed in [3]).

Seifert *et al.* first characterized GBS GAPDH as an anchorless surface adhesin conferring to the bacteria the ability to bind plasminogen and fibrinogen [19]. We next reported that GAPDH isolated from culture supernatant of GBS strain NEM316 has immunomodulatory properties, contributing to GBS evasion from the host immune system [20]. Interestingly, a GBS strain overexpressing GAPDH showed increased virulence as compared with the wild-type strain in C57BL/6 mice [20]. Furthermore, maternal vaccination with GAPDH conferred protection against GBS infection in neonatal mice [36].

NEM316 pilus, encoded by the PI-2a locus (i.e., *gbs1479-1474*), is composed of three structural subunit proteins: PilA (Gbs1478), PilB (Gbs1477), and PilC (Gbs1474) whose assembly involves two class C sortases (SrtC3 and SrtC4). PilB, the *bona fide* pilin, is the

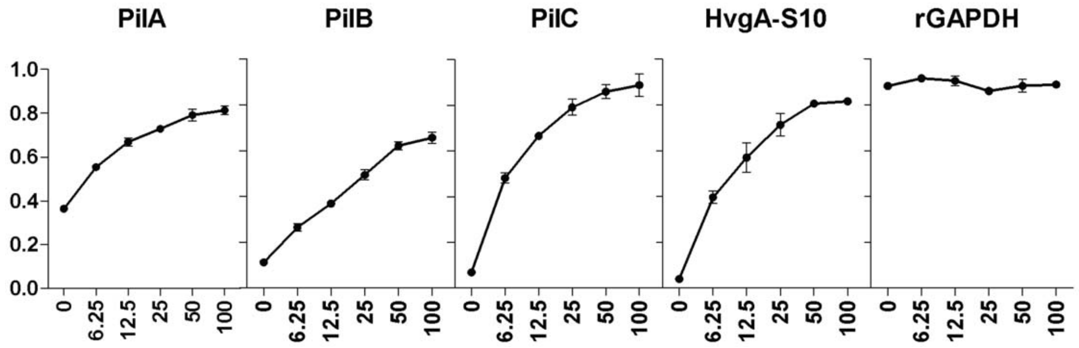

Figure 4. Interaction of rGAPDH with pilus structural subunits. ELISA plates were coated with 10 µg/mL of PilA, PilB, PilC, S10 domain of HvgA (HvgA-S10) or rGAPDH proteins. These plates were incubated with 100 µL/well of different amounts of rGAPDH (0, 6.25, 12.5, 25, 50 or 100 µg/mL). GAPDH was detected using a rabbit anti-rGAPDH IgG pAb. After the revelation, the OD_{450} was registered using a microplate reader. Results shown are representative of two independent experiments.
doi:10.1371/journal.pone.0029963.g004

major component; PilA, the pilus associated adhesin, and PilC, are both accessory proteins incorporated into the pilus backbone. In this work, we unexpectedly found that the non-piliated PilB$^-$ mutant derived from the WT strain NEM316 displays a decrease in surface GAPDH and decided to understand the molecular bases underpinning this observation.

GAPDH presence on the cell surface is associated with bacterial lysis

Here we showed that the reduced amount of surface GAPDH, in both PilB$^-$ and PilA/C$^-$ strains, was due to a lower level of lysis compared to the parental strain NEM316 as determined by dead/live ratio. By comparing the amount of GAPDH found in the cytoplasm and supernatant, we estimated that ≈5% of bacterial lysis would account for the amount of extracellular GAPDH detected in the culture medium. This low level of autolysis is consistent with our turbidity assay showing a 20% decrease over 5 h (Fig. 2B). However, no significant difference in autolysis was observed between GBS WT strain NEM316 and the PilB$^-$ and PilA/C$^-$ mutants using the turbidity or zymogram assays which might simply reflect the poor sensitivity of these techniques. There is circumstantial evidence that some moonlighting proteins from *Mycobacterium tuberculosis* [17] and *L. monocytogenes* [18,28] might be secreted *via* the SecA2 pathway. In staphylococci and streptococci including GBS, where it has been extensively studied, the SecA2 pathway is required for export of a serine-rich repeat protein, Srr1, containing a long atypical signal sequence [37,38,39,40]. Interestingly, the secretion of two major autolysins with signal peptides (MurA and P60) identified in *L. monocytogenes* is SecA2-dependent [18,41]. We therefore hypothesized that the release of moonlighting proteins (SodA, GAPDH, DNAK, GroEL, EF-Tu) in this bacterial species is a direct consequence of the cell lysis resulting from the activity of these SecA2-dependent autolysins, as recently demonstrated for the SecA-dependent autolysin Atl in *S. aureus* [29]. Indeed, Atl was recently reported to play a crucial role in the excretion of 22 cytoplasmic proteins, including GAPDH [29]. Our results rule out the possibility that the SecA2 machinery is involved in the export of GBS GAPDH (data not shown). Furthermore, we were able to detect several other classical cytoplasmic proteins like DltA, Nox-2 and EF-Tu in the supernatant of wild-type strain reinforcing our hypothesis of autolysis (Figure S1).

Interestingly, we found that addition of penicillin G significantly increased the amount of GAPDH in the culture supernatant (Fig. 5D) confirming that bacterial lysis contributes to GAPDH presence extracellularly. ß-lactam-induced toxin release is well-documented in streptococci and staphylococci and there is a recommendation to use these antibiotics in association with an inhibitor of protein synthesis, such as clindamycin, to suppress endotoxin release by bacteria [42]. Penicillin G, an antibiotic commonly used to treat GBS infections might therefore exert an antagonist effect to its bactericidal activity by favoring GAPDH display on the bacterial surface that in turn may favor invasive GBS colonization, an hypothesis that remains to be tested *in vivo*.

The autolytic process and its molecular bases have not been studied in GBS. *In silico* analysis of the NEM316 genome revealed the existence of five genes encoding putative autolysins: *gbs0092* (similar to D,D-carboxypeptidase), *gbs0093* (similar to N-acetyl muramidase), *gbs0678* (similar to beta-N-acetylglucosaminidase), *gbs1540* (similar to amidase or hydrolase), and *gbs1660* (similar to putative amidase). Our transcriptome data on strain NEM316 indicate that *gbs0093* is highly expressed which is confirmed by analysis of surface proteome (our unpublished data). We therefore decided to explore the role of this gene in autolysis using two approaches: construction of an in-frame deletion mutant of *gbs0093* in strain NEM316 and overexpression of this gene in the WT and PilB$^-$ strains. The *Δgbs0093* mutant was not significantly different from the WT strain for surface display of GAPDH (data not shown) suggesting that some of these putative autolysins have redundant activities. In contrast, overexpression of *gbs0093* in the PilB$^-$ mutant, a mutant displaying a lower level of bacterial lysis than the WT strain, led to an increased amount of GAPDH in the culture supernatant that perfectly correlated with a higher level of surface GAPDH in this strain (Fig. 5E, 5F). All together, these results indicate that GBS GAPDH is released following bacterial lysis and can then bind or remain attached to the surface of viable bacteria.

GAPDH interacts with various proteins and many bacterial surfaces

GAPDH is a very "sticky" protein and its ubiquitous adhesive properties were characterized with a recombinant GAPDH that efficiently bind to pilus subunits, PilA, PilB and PilC and to other unrelated surface proteins, such as HvgA (Fig. 4). Of note, *S. pyogenes* GAPDH was shown to be associated with the M or M-like protein and this association may allow GAPDH to indirectly acquire plasmin generated by the M-protein/fibrinogen-mediated fibrinolytic complex [14]. We similarly reported that GAPDH-mediated interaction with human plasminogen system turns on GBS surface proteolytic activity and enhances bacterial virulence in a mouse model [21]. It remains to be demonstrated whether

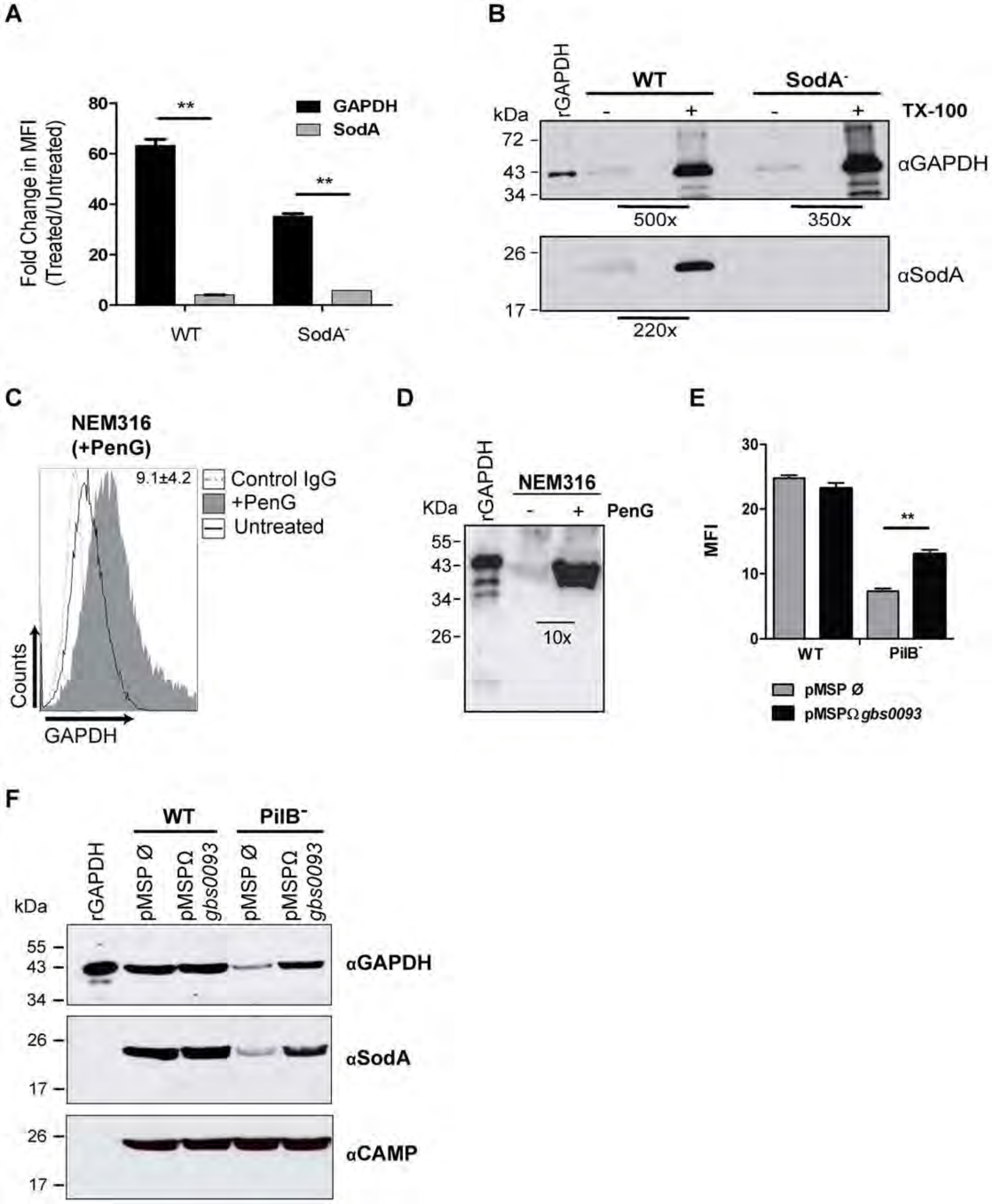

Figure 5. Release of cytoplasmic proteins upon induced bacterial lysis. A, B) NEM316 WT or SodA mutant cultures were treated (+) with 15 U/mL mutanolysin and 0.1% Triton X-100 or left untreated (−). The amount of surface GAPDH or SodA was determined by FACS with a rabbit IgG anti-rGAPDH pAb or anti-SodA followed by AlexaFluor 488-conjugated anti–rabbit antibody (A). The graphic expresses the fold change in MFI after treatment. B) Western Blot analysis of GAPDH and SodA proteins from NEM316 WT or SodA mutant detected using a rabbit anti-rGAPDH IgG pAb or rabbit anti-SodA followed by HRP-conjugated goat anti-rabbit antibody. rGAPDH: 10 ng; supernatants from untreated bacteria: 25 μL; supernatants from Triton-treated bacteria: 1 μL. Numbers in the western blot represent the fold increase of GAPDH or SodA amount after Triton treatment, as determined densitometrically and corrected for sample amount. C, D) 5×10^6 CFU/mL of NEM316 were treated for 12 h with Penicillin G (+PenG) at 100× MIC (6.4 μg/mL) or left untreated. The bacteria were then subjected to FACS analysis as previously described (C). The numbers in the histogram represent the fold change in MFI after the treatment with PenG. D) Western blot analysis of GAPDH protein from NEM316 WT detected using a rabbit anti-GAPDH IgG pAb followed by HRP-conjugated goat anti-rabbit antibody. rGAPDH: 10 ng; supernatants: 25 μL. Numbers in the western blot represent the fold increase of GAPDH amount after PenG treatment, as determined densitometrically. E,F) GBS WT and PilB$^-$ strains containing the inducible vector pMSP3545 empty (pMSP Ø) or encoding *gbs0093* (pMSPΩ*gbs0093*) were subjected to overnight induction with 20 ng/μL nisin after reaching an $OD_{600}=0.3$. After this period, the amount of surface exposed GAPDH was quantified by FACS using anti-GAPDH antibodies (E) and 15 μL of supernatant extracts were analyzed for the presence of GAPDH, SodA, and CAMP by western blot (F). Results shown are representative of at least three independent experiments. **, $P<0.01$.

doi:10.1371/journal.pone.0029963.g005

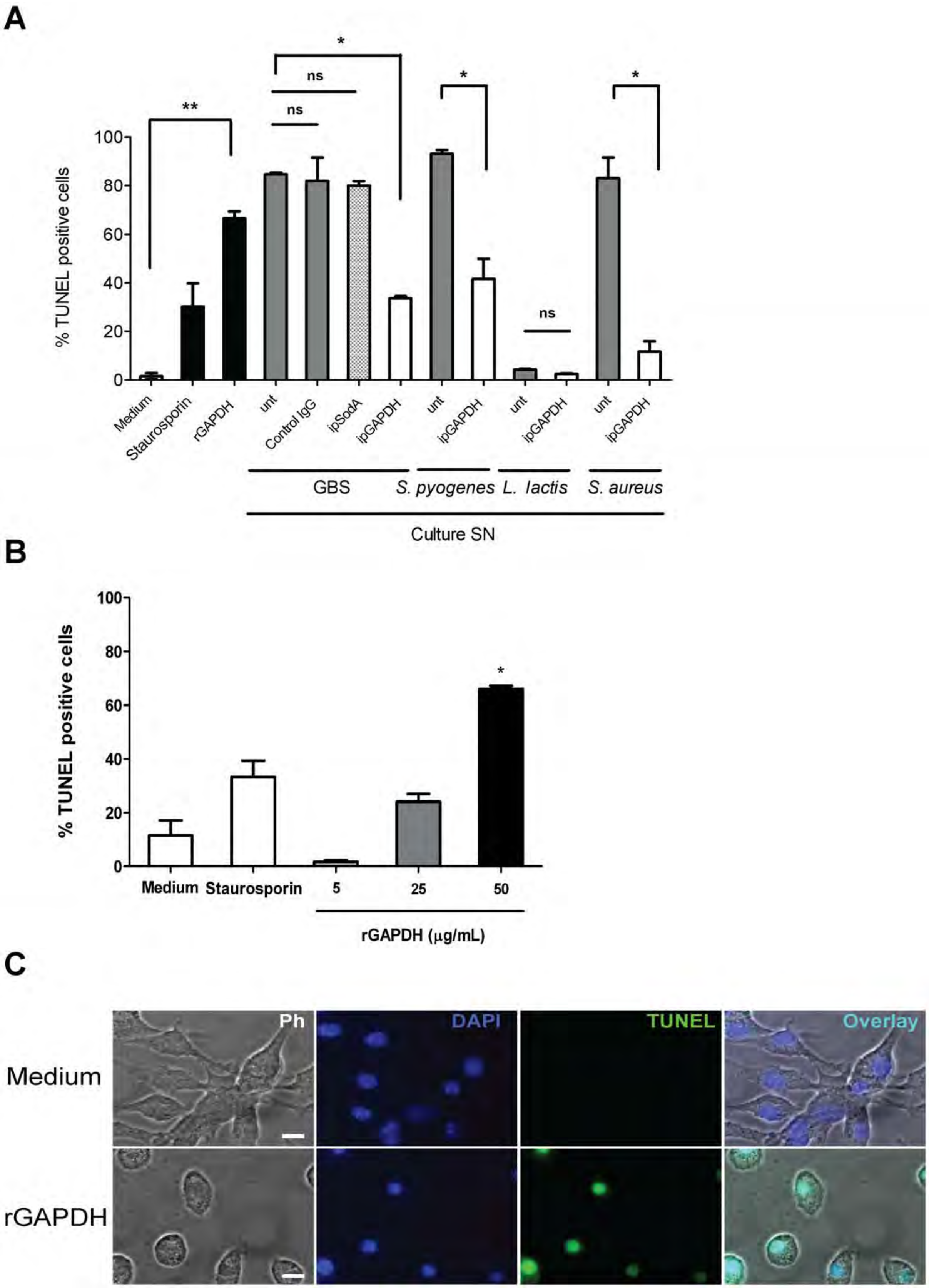

Figure 6. Induction of apoptosis mediated by (r)GAPDH. A) 5×10^5 RAW264.7 murine macrophages were left untreated (Medium) or treated for 24 h with 1 μM staurosporin or 50 μg/mL rGAPDH, or 200 μL of culture supernatant from GBS, *S. pyogenes*, *L. lactis* or *S. aureus* left untreated (unt) or immunoprecipitated with rabbit anti-GAPDH IgG pAb (ipGAPDH), with rabbit anti-SodA IgG pAb (ipSodA) or with a normal rabbit IgG (control IgG).

B) 5×10^5 Bone marrow-derived macrophages from C57BL/6 mice were left untreated (Medium) or treated for 24 h with 1 μM staurosporin, or rGAPDH at the indicated concentrations. After treatment, the macrophages were fixed and stained for TUNEL using the Promega DeadEnd™ Fluorometric TUNEL kit. Samples were acquired and the % of cells that incorporated fluorescein-dUTP (TUNEL positive cells) was quantified. C) For IF, 1×10^5 C57BL/6 bone marrow-derived macrophages were left untreated or treated for 24 h with 50 μg/mL rGAPDH. After that period, cells were fixed and stained as mentioned in B) and visualized in a fluorescence microscope. Scale bars, 15 μm. Results shown are representative of two independent experiments. ns, non-significant; *, $P<0.05$; **, $P<0.01$.
doi:10.1371/journal.pone.0029963.g006

pilus proteins, the major GBS surface proteins, are key players for GAPDH interactions *in vivo*.

A mechanism explaining how these cytoplasmic proteins became surface associated was proposed by Bergmann *et al.* who demonstrated that the pneumococcal enolase protein reassociated on the bacterial surface after secretion [30]. The reassociation of secreted proteins without typical membrane anchor seems to be a general phenomenon and has been observed with a number of other such proteins [3]. In agreement with this model of secretion/reassociation, we demonstrated that purified rGAPDH is able to bind heat-inactivated GBS cells in a dose dependent manner (Fig. 3A). In addition, we showed that rGAPDH can bind to various GBS serotypes, to other Gram-positive bacteria such as *S. pyogenes*, *L. lactis*, *S. aureus*, and even to the phylogenetically remote Gram-negative bacterium *E. coli* indicating that rGAPDH can interact with very diverse cell surfaces (Fig. 3B).

Uncovering a new role for GBS GAPDH

GBS was shown to induce apoptosis of microglia [43], murine macrophages [33], and human epithelial pulmonary A549 cells [44]. In murine macrophages, two distinct pathways leading to apoptosis were induced by GBS. Early apoptosis was shown to be caspase independent [33], being rather mediated by the Ca^{2+}-dependent cysteine proteases, calpains [45]. The GBS β-hemolysin was shown to be important in this early stage apoptosis [33]. In contrast, late apoptosis was characterized as being β-hemolysin independent [46], and characterized by the release of cytochrome c and the activation of caspase 3 and 9 [47]. In a separate study, GBS-induced late stage apoptosis of macrophages was also found to be nitric oxide dependent [48]. Recently, eukaryotic GAPDH have been implicated as a regulator of cell death that participates in the apoptosis of several cell lines (reviewed in [34,35]). It was also previously suggested that *S. pyogenes* GAPDH can cause DNA condensation, a penultimate stage of apoptosis upon direct contact with human pharyngeal cells [49]. Here, we demonstrate for the first time that a prokaryotic GAPDH is able to induce apoptosis of immortalized and primary murine macrophages in a dose-dependent manner (Fig. 6). By immunoprecipitating GAPDH from culture supernatants of GBS, *S. pyogenes* and *S. aureus* we partially but significantly inhibited the apoptosis induced by these culture supernatants. As others factors, such as β-hemolysin have also been shown to induce macrophage apoptosis [33], this may explain the incomplete neutralization of the apoptotic effect of GAPDH-depleted GBS supernatant. These results extend our findings on the role of GAPDH as a potent inducer of macrophage apoptosis to two other important human pathogens, i.e. *S. pyogenes* and *S. aureus*. Our results, by demonstrating that GBS GAPDH is another key element for GBS-mediated induction of apoptosis, ascribe to this enzyme a new role independent from its glycolytic function. Further studies aiming at characterizing the underlying mechanisms of apoptosis induced by GBS GAPDH will be carried out in the future.

GBS GAPDH is a surface-exposed moonlighting protein. We provide strong evidence that GAPDH is non-specifically released in the culture medium as a result of cell lysis and reassociates to the bacterial surface. Our results also suggest that penicillin G, a bacteriolytic antibiotic commonly used to treat GBS infections may have a Janus-faced behavior, by killing the pathogen and by increasing its virulence through enhanced GAPDH release. Furthermore, a new role for this protein beside its previous immunomodulatory activities has been uncovered in this study, i.e. inducer of murine macrophages apoptosis.

Methods

Ethics statement

All of the animal experiments described in the present study were conducted in accordance with guidelines of Cochin Institute, in compliance with the European animal welfare regulation (http://ec.europa.eu/environment/chemicals/lab_animals/home_en.html) and were approved by the Institut Cochin animal care and use committee.

Bacterial strains and growth conditions

The main characteristics of bacterial strains and plasmids used in this study are listed in Table S1. *E. coli* and *S. aureus* were cultured in Trypticase soy (TS) broth or agar. GBS, *S. pyogenes and L. lactis* were cultured in Todd-Hewitt (TH) broth or Columbia agar supplemented with 5% horse blood (COH). Antibiotics were used at the following concentrations: for *E. coli*, kanamycin was used at 50 μg/mL and erythromycin at 150 μg/mL; for GBS kanamycin was used at 500 μg/mL and erythromycin at 10 μg/mL. All incubations were performed at 37°C.

Mice

Wild-type C57BL6/J female mice, 8–12 weeks old, were purchased from Charles River Laboratories.

General DNA techniques

Standard recombinant techniques were used for nucleic acid cloning and restriction analysis [50]. Plasmid DNA from *E. coli* was prepared by rapid alkaline lysis using the QIAprep Spin Miniprep Kit (Qiagen). Genomic DNA from *S. agalactiae* was prepared using the DNeasy Blood and Tissue Kit (Qiagen). PCR was carried out using *Pfu* turbo DNA polymerase (Agilent Technologies) or AmpliTaqGold DNA polymerase (Applied Biosystems) according to the manufacturer's specifications. Amplification products were purified with QIAquick PCR Purification Kit (Qiagen) and verified by sequencing.

Construction of the deletion mutant *PilA/C*$^-$

This double mutant was constructed as previously described [23] by replacing *pilC* into the NEM316:PilA$^-$ *with a pilC allele* interrupted with a kanamycin-resistance gene.

Overexpression constructs

The promoter region and the *gbs0093* coding region (http://genolist.pasteur.fr/SagaList/) were amplified with the primer pairs gbs0093_BamHI (GTTATggatccTGGCATTACCGCTATGTTGG) and gbs0093_PstI (AAACCctgcagCCTCTCGGTCTTTCTGAAAT) (the restriction sites used for cloning are written in lower case). The resulting amplicon was cloned in pCR-Blunt

(Invitrogen) to originate pCR-Blunt*Ωgbs0093*. This latter was digested with *Spe*I and *Xho*I, and ligated into the inducible vector pMSP3545 to give pMSP3545*Ωgbs0093*. This plasmid and pMSP3545 were electroporated in GBS NEM316 WT or PilB$^-$ to generate strains overexpressing *gbs0093*. These strains were cultured until $OD_{600\ nm} = 0.3$ and *gbs0093* expression was induced overnight with 20 ng/mL of nisin (Sigma-Aldrich).

Growth curves

Overnight cultures of GBS strain NEM316 (WT), PilB$^-$ and PilA/C$^-$ in TH broth were diluted in fresh media at different concentrations: 1/50 to 1/500 and 150 µl were distributed in 96 wells plate with 5 replicates per strain tested. The microplate was incubated at 37°C with constant shaking in the BioTek Synergy plate reader and the $OD_{600\ nm}$ was recorded every 20 min for 7 h.

Immunogold electron microscopy

For scanning electron microscopy (SEM) analysis, bacteria were fixed and stained with rabbit anti-rGAPDH IgG pAb followed by anti-rabbit secondary antibody conjugated to 10 nm colloidal gold as previously described [23].

Supernatant and total protein extracts

Bacteria were grown in TH medium at 37°C and harvested for protein analysis during exponential ($OD_{600} = 0.4$) or stationary ($OD_{600} = 0.9$) phase of culture. For the preparation of culture supernatants used in the apoptosis experiments, bacteria were grown ($OD_{600} = 0.9$) in RPMI without phenol red supplemented with 0.1 M HEPES, 1% Glucose, amino acids solution (1×) and vitamins solution (1×) (Sigma-Aldrich). The culture supernatant was collected, filtered through 0.2 µm, and concentrated 50 times using Amicon® Ultracel 10 k centrifugal filters (Millipore) in the presence of a complete protease inhibitor cocktail (Roche Diagnostics). Total protein extracts from bacteria were prepared as previously described [23].

Western Immunoblots

For analysis of GAPDH expression, bacterial proteins were separated into supernatant and total protein extracts (see above). Proteins were resolved on SDS-PAGE gels and transferred to nitrocellulose membrane (Pall). Detection of GAPDH [20], Nox-2 [27], SodA, DltA, and CAMP were performed using rabbit-specific polyclonal antibodies available in the laboratory. Horseradish peroxidase (HRP)-coupled goat anti-rabbit secondary antibody (Zymed) was added and detection was performed with enhanced chemiluminescence (ECL Reagent, GE Healthcare).

Fluorescence-activated cell sorter analysis (FACS)

To analyze surface-exposed GAPDH, bacteria were collected and washed twice in phosphate buffered saline (PBS) before fixation in PBS containing 1% paraformaldehyde. After the incubation period of 20 min at 4°C, fixed bacteria were then washed twice with PBS and incubated for 45 min with rabbit anti-rGAPDH IgG diluted in PBS with 1% BSA or normal rabbit IgG at room temperature. After three washings with PBS, samples were incubated for 30 min with AlexaFluor488-conjugated goat anti-rabbit immunoglobulin (Molecular Probes, Invitrogen). Cells were washed and resuspended in PBS. Samples were acquired on a Beckman Coulter Cytomics FC500 apparatus and data were analyzed using Cytomics RXP software.

ELISA binding assays

To analyze the interaction of rGAPDH with pili subunits, polystyrene microtiter plates (Nunc) were coated overnight at 4°C with 10 µg/ml of PilA, PilB, PilC (production of these recombinant proteins described in [23]) and rGAPDH or the domain S10 of HvgA [31] as controls. The wells were then saturated for 1 h with 2% BSA in PBS at room temperature. rGAPDH was added at 0, 6.25, 12.5, 25, 50, or 100 µg/mL and the plates were incubated for 2 h at room temperature. After washing 5 times in PBS containing 0.1% Tween 20 (Sigma-Aldrich), anti-rGAPDH IgG was added, incubated 2 h at room temperature followed by HRP-conjugated goat anti-rabbit antibody. After incubation for 1 h and extensive washing, the plates were revealed with a citrate solution containing o-Phenylenediamine dihydrochloride (OPD) (Sigma-Aldrich) and H_2O_2. After 20 min at room temperature, the reaction was stopped with 10% SDS and the absorbance was measured at 450 nm with a Biotek Chromoscan.

Interaction of rGAPDH with whole-GBS cells was analyzed as follows: 6.5×10^7 CFU/mL of heat-inactivated NEM316 cells were seeded onto microtiter plates and incubated overnight at 4°C. After blocking 1 h with 2% BSA in PBS at room temperature, rGAPDH was added at various concentrations: 0, 10 or 50 µg/mL or rGAPDH at 50 µg/mL plus 75 µg of anti-rGAPDH IgG antibodies for 2 h at room temperature. After washing, mouse anti-pentaHis antibody (Qiagen) was added and the plates were revealed as described above.

Live/Dead assay

To analyze the proportion of dead/live cells in a culture of NEM316 WT, PilB$^-$ and PilA/C$^-$ these strains were stained using LIVE/DEAD® *Bac*Light™. Bacterial viability and counting kit for flow cytometry (Molecular Probes, Invitrogen) according to the manufacturer's instructions. Briefly, 1 mL of bacterial suspension was washed in NaCl 0.9% and 10 µL of this were added to a FACS tube containing 1 µL of Syto9, 1 µL of propidium iodide (PI) and 978 µL of NaCl 0.9%. The same procedure was used to the 70% isopropanol treated cells that were used as control for dead cells. After incubation (15 min) in the dark at room temperature, 10 µL of beads were added to the tubes. Samples were acquired by a Beckman Coulter Cytomics FC500 apparatus and data were analyzed using Cytomics RXP software.

Turbidity assays

GBS NEM316 and *S. aureus* were grown to exponential phase and the bacterial pellet obtained by centrifugation was washed and resuspended in PBS. The OD_{600} of both bacterial suspensions was recorded and arbitrarily set as 100%. These suspensions were incubated at 37°C without agitation and the decrease in OD was measured hourly for 5 h.

Induction of lysis with Triton X-100 and Penicillin G

To analyze the GAPDH increase in the supernatant and surface of GBS after lysis induction, NEM316 WT or SodA$^-$ were grown until exponential phase and 0.1% Triton X-100 and 15 U/mL of mutanolysin or PBS (control) were added. After incubation on ice for 45 min, the bacterial culture was centrifuged at 4000 *g*, the supernatant was collected and processed for immunoblotting analysis as mentioned above. The cell pellet was recovered, washed and stained for FACS analysis as detailed above. For treatment with Penicillin G, 5×10^6 CFU/mL of NEM316 were treated for 12 h with Penicillin G at 100× MIC (6.4 µg/mL) or left untreated. After this time, the supernatant and cell pellet were collected for immunoblot and FACS analysis, respectively.

rGAPDH reassociation assay

For analysis of the reassociation of rGAPDH to bacterial cells, 200 µg of rGAPDH or PBS (negative control) diluted in 500 µL of TH was added to 500 µL of an exponentially grown culture of several GBS strains belonging to different serotypes, *S. pyogenes*, *L. lactis*, *S. aureus* and *E. coli*. After an incubation period of 45 min at 37°C, total proteins were extracted by Fastprep and subjected to immunoblotting analysis.

Cell culture techniques and apoptosis quantification by TUNEL assay

Murine macrophage cell line RAW264.7 was obtained from American Type Culture Collection and was used in passages between 13 to 16 for the assays. Bone marrow-derived macrophages from C57BL/6 mice were obtained and cultured as previously described [25]. RAW264.7 macrophages were seeded at 5×10^5 cells/well in 24w cell culture Nunc plates 12 h before the assay. These macrophages were then treated for 24 h with 1 µM of staurosporin, 50 µg/mL of rGAPDH, or 200 µl of 50× concentrated supernatant from NEM316. We also used supernatant from other Gram-positive bacteria grown in the same conditions, i.e. *S. pyogenes*, *L. lactis* and *S. aureus* (strains are listed in Table S1). Supernatants were depleted from either GAPDH or SodA using the corresponding polyclonal antibody followed by immunoprecipitation with protein A Sepharose (GE Healthcare) according to manufacturer's instructions. As an additional immunoprecipitation control, culture supernatant was subjected to treatment with an irrelevant antibody (control IgG, normal rabbit IgG, Santa Cruz Biotechnology). Similarly, 5×10^5 bone marrow-derived macrophages/well in 24w cell culture Nunc plates were treated for 24 h with 1 µM of staurosporin, various concentrations of GAPDH (5, 25, 50 µg/mL) or left untreated as negative control. In all treatments with rGAPDH or culture supernatant, polymyxin B was also added at 10 µg/mL to avoid side effects due to LPS contamination. After the treatments, both types of macrophages were detached gently using a cell scraper and stained using the DeadEnd Fluorometric TUNEL System (Promega) following the manufacturer's instructions. Samples were analyzed by FACS using a Beckman Coulter Cytomics FC500. For immunofluorescence staining, 5×10^5 bone marrow-derived macrophages were seeded into 8-well culture slides (BD) and subjected to 50 µg/mL rGAPDH treatment or left untreated for 24 h as mentioned above. Following *in situ* TUNEL staining, the slides were visualized in a Zeiss Axiovert 200 microscope.

Statistical analysis

Unpaired two-tailed t-test was used to analyze the differences between groups. A P value<0.05 was considered statistically significant.

Supporting Information

Figure S1 Detection of GBS cytoplasmic proteins in NEM316 culture supernatant. Western Blotting of DltA, Nox-2, EF-Tu, SodA and GAPDH in total protein extracts (TP) or culture supernatants (SN) of NEM316 WT strain. 5 µg of NEM316 total proteins or 15 µL of each concentrated supernatant were loaded in the gel. After transfer to a membrane, proteins were detected using a polyclonal rabbit anti-anti-DltA, anti-Nox-2, anti-EF-Tu, anti-SodA or anti-rGAPDH IgG antibodies followed by HRP-conjugated goat anti-rabbit antibody.
(TIF)

Figure S2 Bacterial growth curves of GBS strains used in this study. Overnight cultures were diluted in fresh TH medium to give approximately 10^6 CFU/ml. The inoculated broths were distributed (150 µl) in 96 wells plate incubated at 37°C with constant shaking in a plate reader and the OD_{600} was recorded every 20 minutes for 7 hours. Blank values (medium alone) were subtracted from experimental values to eliminate background readings. The y- axis is drawn in log10 scale. Results represent the mean and SD of 5 replicates.
(TIF)

Figure S3 The nisin inducible expression system in GBS NEM316. A) Effect of nisin on bacterial growth: pre-warmed TH broth containing or not nisin at the indicated concentration ranging from 31.25 to 500 ng/mL was inoculated with overnight NEM316/pMSP3545 strain to give approximately 10^7 CFU/ml. The inoculated broth was distributed (150 µL) in 96 wells plate, incubated at 37°C with constant shaking in a plate reader and the OD_{600} was recorded every 20 minutes for 12 hours. Blank values (TH) were subtracted from experimental values to eliminate background readings. B) Production of the secreted staphylococcal nuclease NucB reporter induced by nisin: three nisin concentrations that did not affect bacterial growth were used to induce expression of NucB. Supernatant of overnight growth cultures of NEM316 containing pMSP3545 (control) or pMSP3545Ω*nucB* were collected by centrifugation and 10-fold concentrated by TCA precipitation. Equivalent of 100 µl of culture medium was spotted onto nitrocellulose membrane and analyzed for NucB content by dot-blot analysis using specific primary rabbit antibody.
(TIF)

Table S1 Bacterial strains and plasmids used in this study.
(DOC)

Acknowledgments

We are grateful to Agnès Fouet for helpful discussions, Samuel Bellais and Asmaa Tazi for providing the HvgA-S10 protein and Isabelle Tardieux for technical expertise in microscopy. We thank the J.D. Chiche team at the Institute Cochin for their helpful assistance in mice handling. We thank the University of Minnesota and Dr Garry Dunny's laboratory for the permission to use plasmid pMSP3545. We thank Olivier Dussurget for the kind gift of rabbit anti-*Listeria* EF-Tu and Philippe Langella for the gift of anti- *S. aureus* nuclease antibodies. We thank the Flow Cytometry Core Facility of the Institut Cochin for technical support. We thank Adeline Mallet for carrying out the experiments of scanning electron microscopy (Imagopole, PFMU, Institut Pasteur).

Author Contributions

Conceived and designed the experiments: LO PF CP PT-C SD. Performed the experiments: LO PM EBA AB SD. Analyzed the data: LO PF CP PT-C SD. Contributed reagents/materials/analysis tools: EM. Wrote the paper: LO PF CP PT-C SD.

References

1. Phares CR, Lynfield R, Farley MM, Mohle-Boetani J, Harrison LH, et al. (2008) Epidemiology of invasive group B streptococcal disease in the United States, 1999–2005. JAMA 299: 2056–2065.
2. Edwards MS, Baker CJ, eds. (2005) Group B streptococcal infections: Saunders. pp 1091–1156.
3. Pancholi V, Chhatwal GS (2003) Housekeeping enzymes as virulence factors for pathogens. Int J Med Microbiol 293: 391–401.
4. Jeffery CJ (2009) Moonlighting proteins–an update. Mol Biosyst 5: 345–350.
5. Pancholi V, Fischetti VA (1998) alpha-enolase, a novel strong plasmin(ogen) binding protein on the surface of pathogenic streptococci. J Biol Chem 273: 14503–14515.
6. Hughes MJ, Moore JC, Lane JD, Wilson R, Pribul PK, et al. (2002) Identification of major outer surface proteins of *Streptococcus agalactiae*. Infect Immun 70: 1254–1259.

7. Suvorov AN, Flores AE, Ferrieri P (1997) Cloning of the glutamine synthetase gene from group B streptococci. Infect Immun 65: 191–196.
8. Holmes AR, McNab R, Millsap KW, Rohde M, Hammerschmidt S, et al. (2001) The pavA gene of *Streptococcus pneumoniae* encodes a fibronectin-binding protein that is essential for virulence. Mol Microbiol 41: 1395–1408.
9. Dramsi S, Bourdichon F, Cabanes D, Lecuit M, Fsihi H, et al. (2004) FbpA, a novel multifunctional *Listeria monocytogenes* virulence factor. Mol Microbiol 53: 639–649.
10. Courtney HS, Dale JB, Hasty DI (1996) Differential effects of the streptococcal fibronectin-binding protein, FBP54, on adhesion of group A streptococci to human buccal cells and HEp-2 tissue culture cells. Infect Immun 64: 2415–2419.
11. Pancholi V, Fischetti VA (1992) A major surface protein on group A streptococci is a glyceraldehyde-3-phosphate-dehydrogenase with multiple binding activity. J Exp Med 176: 415–426.
12. Pancholi V, Fischetti VA (1993) Glyceraldehyde-3-phosphate dehydrogenase on the surface of group A streptococci is also an ADP-ribosylating enzyme. Proc Natl Acad Sci U S A 90: 8154–8158.
13. Winram SB, Lottenberg R (1996) The plasmin-binding protein Plr of group A streptococci is identified as glyceraldehyde-3-phosphate dehydrogenase. Microbiology 142(Pt 8): 2311–2320.
14. D'Costa SS, Boyle MD (2000) Interaction of group A streptococci with human plasmin(ogen) under physiological conditions. Methods 21: 165–177.
15. Jin H, Song YP, Boel G, Kochar J, Pancholi V (2005) Group A streptococcal surface GAPDH, SDH, recognizes uPAR/CD87 as its receptor on the human pharyngeal cell and mediates bacterial adherence to host cells. J Mol Biol 350: 27–41.
16. Egea L, Aguilera L, Gimenez R, Sorolla MA, Aguilar J, et al. (2007) Role of secreted glyceraldehyde-3-phosphate dehydrogenase in the infection mechanism of enterohemorrhagic and enteropathogenic *Escherichia coli*: interaction of the extracellular enzyme with human plasminogen and fibrinogen. Int J Biochem Cell Biol 39: 1190–1203.
17. Braunstein M, Espinosa BJ, Chan J, Belisle JT, Jacobs WR, Jr. (2003) SecA2 functions in the secretion of superoxide dismutase A and in the virulence of *Mycobacterium tuberculosis*. Mol Microbiol 48: 453–464.
18. Lenz LL, Mohammadi S, Geissler A, Portnoy DA (2003) SecA2-dependent secretion of autolytic enzymes promotes *Listeria monocytogenes* pathogenesis. Proc Natl Acad Sci U S A 100: 12432–12437.
19. Seifert KN, McArthur WP, Bleiweis AS, Brady LJ (2003) Characterization of group B streptococcal glyceraldehyde-3-phosphate dehydrogenase: surface localization, enzymatic activity, and protein-protein interactions. Can J Microbiol 49: 350–356.
20. Madureira P, Baptista M, Vieira M, Magalhaes V, Camelo A, et al. (2007) *Streptococcus agalactiae* GAPDH is a virulence-associated immunomodulatory protein. J Immunol 178: 1379–1387.
21. Magalhaes V, Veiga-Malta I, Almeida MR, Baptista M, Ribeiro A, et al. (2007) Interaction with human plasminogen system turns on proteolytic activity in *Streptococcus agalactiae* and enhances its virulence in a mouse model. Microbes Infect 9: 1276–1284.
22. Forquin MP, Tazi A, Rosa-Fraile M, Poyart C, Trieu-Cuot P, et al. (2007) The putative glycosyltransferase-encoding gene cylJ and the group B Streptococcus (GBS)-specific gene cylK modulate hemolysin production and virulence of GBS. Infect Immun 75: 2063–2066.
23. Dramsi S, Caliot E, Bonne I, Guadagnini S, Prevost MC, et al. (2006) Assembly and role of pili in group B streptococci. Mol Microbiol 60: 1401–1413.
24. Podbielski A, Blankenstein O, Lutticken R (1994) Molecular characterization of the cfb gene encoding group B streptococcal CAMP-factor. Med Microbiol Immunol 183: 239–256.
25. Poyart C, Pellegrini E, Gaillot O, Boumaila C, Baptista M, et al. (2001) Contribution of Mn-cofactored superoxide dismutase (SodA) to the virulence of *Streptococcus agalactiae*. Infect Immun 69: 5098–5106.
26. Poyart C, Lamy MC, Boumaila C, Fiedler F, Trieu-Cuot P (2001) Regulation of D-alanyl-lipoteichoic acid biosynthesis in *Streptococcus agalactiae* involves a novel two-component regulatory system. J Bacteriol 183: 6324–6334.
27. Yamamoto Y, Pargade V, Lamberet G, Gaudu P, Thomas F, et al. (2006) The Group B Streptococcus NADH oxidase Nox-2 is involved in fatty acid biosynthesis during aerobic growth and contributes to virulence. Mol Microbiol 62: 772–785.
28. Archambaud C, Nahori MA, Pizarro-Cerda J, Cossart P, Dussurget O (2006) Control of Listeria superoxide dismutase by phosphorylation. J Biol Chem 281: 31812–31822.
29. Pasztor L, Ziebandt AK, Nega M, Schlag M, Haase S, et al. (2010) Staphylococcal major autolysin (atl) is involved in excretion of cytoplasmic proteins. J Biol Chem 285: 36794–36803.
30. Bergmann S, Rohde M, Chhatwal GS, Hammerschmidt S (2001) alpha-Enolase of *Streptococcus pneumoniae* is a plasmin(ogen)-binding protein displayed on the bacterial cell surface. Mol Microbiol 40: 1273–1287.
31. Tazi A, Disson O, Bellais S, Bouaboud A, Dmytruk N, et al. (2010) The surface protein HvgA mediates group B streptococcus hypervirulence and meningeal tropism in neonates. J Exp Med 207: 2313–2322.
32. Bryan EM, Bae T, Kleerebezem M, Dunny GM (2000) Improved vectors for nisin-controlled expression in gram-positive bacteria. Plasmid 44: 183–190.
33. Fettucciari K, Rosati E, Scaringi L, Cornacchione P, Migliorati G, et al. (2000) Group B Streptococcus induces apoptosis in macrophages. J Immunol 165: 3923–3933.
34. Colell A, Green DR, Ricci JE (2009) Novel roles for GAPDH in cell death and carcinogenesis. Cell Death Differ 16: 1573–1581.
35. Chuang DM, Hough C, Senatorov VV (2005) Glyceraldehyde-3-phosphate dehydrogenase, apoptosis, and neurodegenerative diseases. Annu Rev Pharmacol Toxicol 45: 269–290.
36. Madureira P, Andrade EB, Gama B, Oliveira L, Moreira S, et al. (2011) Inhibition of IL-10 Production by Maternal Antibodies against Group B Streptococcus GAPDH Confers Immunity to Offspring by Favoring Neutrophil Recruitment. PLoS Pathog 7.
37. Bensing BA, Sullam PM (2002) An accessory sec locus of *Streptococcus gordonii* is required for export of the surface protein GspB and for normal levels of binding to human platelets. Mol Microbiol 44: 1081–1094.
38. Plummer C, Wu H, Kerrigan SW, Meade G, Cox D, et al. (2005) A serine-rich glycoprotein of *Streptococcus sanguis* mediates adhesion to platelets via GPIb. Br J Haematol 129: 101–109.
39. Siboo IR, Chambers HF, Sullam PM (2005) Role of SraP, a Serine-Rich Surface Protein of *Staphylococcus aureus*, in binding to human platelets. Infect Immun 73: 2273–2280.
40. Mistou MY, Dramsi S, Brega S, Poyart C, Trieu-Cuot P (2009) Molecular dissection of the secA2 locus of group B Streptococcus reveals that glycosylation of the Srr1 LPXTG protein is required for full virulence. J Bacteriol 191: 4195–4206.
41. Machata S, Hain T, Rohde M, Chakraborty T (2005) Simultaneous deficiency of both MurA and p60 proteins generates a rough phenotype in *Listeria monocytogenes*. J Bacteriol 187: 8385–8394.
42. Nau R, Eiffert H (2002) Modulation of release of proinflammatory bacterial compounds by antibacterials: potential impact on course of inflammation and outcome in sepsis and meningitis. Clin Microbiol Rev 15: 95–110.
43. Lehnardt S, Wennekamp J, Freyer D, Liedtke C, Krueger C, et al. (2007) TLR2 and caspase-8 are essential for group B Streptococcus-induced apoptosis in microglia. J Immunol 179: 6134–6143.
44. Da Costa AF, Pereira CS, Santos Gda S, Carvalho TM, Hirata R, Jr., et al. Group B Streptococcus serotypes III and V induce apoptosis and necrosis of human epithelial A549 cells. Int J Mol Med 27: 739–744.
45. Fettucciari K, Fetriconi I, Mannucci R, Nicoletti I, Bartoli A, et al. (2006) Group B Streptococcus induces macrophage apoptosis by calpain activation. J Immunol 176: 7542–7556.
46. Ulett GC, Bohnsack JF, Armstrong J, Adderson EE (2003) Beta-hemolysin-independent induction of apoptosis of macrophages infected with serotype III group B streptococcus. J Infect Dis 188: 1049–1053.
47. Ulett GC, Maclean KH, Nekkalapu S, Cleveland JL, Adderson EE (2005) Mechanisms of group B streptococcal-induced apoptosis of murine macrophages. J Immunol 175: 2555–2562.
48. Ulett GC, Adderson EE (2005) Nitric oxide is a key determinant of group B streptococcus-induced murine macrophage apoptosis. J Infect Dis 191: 1761–1770.
49. Pancholi V, Fischetti VA (1997) Regulation of the phosphorylation of human pharyngeal cell proteins by group A streptococcal surface dehydrogenase: signal transduction between streptococci and pharyngeal cells. J Exp Med 186: 1633–1643.
50. Sambrook J, Fritsch EF, Maniatis T (1989) Molecular Cloning: A Laboratory Manual. Cold Spring Harbor, NY: Cold Spring Harbor Laboratory Press.

Modulation of IL-17 and Foxp3 Expression in the Prevention of Autoimmune Arthritis in Mice

Joana Duarte[1,2], **Ana Agua-Doce**[1,2], **Vanessa G. Oliveira**[1,2], **João Eurico Fonseca**[1,3], **Luis Graca**[1,2]*

1 Instituto de Medicina Molecular, Faculdade de Medicina, University of Lisbon, Lisbon, Portugal, **2** Instituto Gulbenkian de Ciência, Oeiras, Portugal, **3** Rheumatology Department, Hospital de Santa Maria, Lisbon, Portugal

Abstract

Background: Rheumatoid Arthritis (RA) is a chronic immune mediated disease associated with deregulation of many cell types. It has been reported that different T cell subsets have opposite effects in disease pathogenesis, in particular Th17 and Treg cells.

Methodology and Findings: We investigated whether non-depleting anti-CD4 monoclonal antibodies, which have been reported as pro-tolerogenic, can lead to protection from chronic autoimmune arthritis in SKG mice – a recently described animal model of RA – by influencing the Th17/Treg balance. We found that non-depleting anti-CD4 prevented the onset of chronic autoimmune arthritis in SKG mice. Moreover, treated mice were protected from the induction of arthritis up to 60 days following anti-CD4 treatment, while remaining able to mount CD4-dependent immune responses to unrelated antigens. The antibody treatment also prevented disease progression in arthritic mice, although without leading to remission. Protection from arthritis was associated with an increased ratio of Foxp3, and decreased IL-17 producing T cells in the synovia. *In vitro* assays under Th17-polarizing conditions showed CD4-blockade prevents Th17 polarization, while favoring Foxp3 induction.

Conclusions: Non-depleting anti-CD4 can therefore induce long-term protection from chronic autoimmune arthritis in SKG mice through reciprocal changes in the frequency of Treg and Th17 cells in peripheral tissues, thus shifting the balance towards immune tolerance.

Citation: Duarte J, Agua-Doce A, Oliveira VG, Fonseca JE, Graca L (2010) Modulation of IL-17 and Foxp3 Expression in the Prevention of Autoimmune Arthritis in Mice. PLoS ONE 5(5): e10558. doi:10.1371/journal.pone.0010558

Editor: Derya Unutmaz, New York University, United States of America

Received February 26, 2010; **Accepted** April 16, 2010; **Published** May 10, 2010

Funding: This work was funded by SUDOE, grant number IMMUNONET-SOE1/1P1/E014, and supported by a research grant from Fundação para a Ciência e Tecnologia (FCT), Portugal (FCT/POCI/SAU-MMO/55974/2004). JD, AA-D, and VGO are funded with scholarships from FCT (SFRH/BD/23631/2005, SFRH/BD/49093/2008, and SFRH/BPD/22575/2005). The funders had no role in study design, data collection and analysis, decision to publish, or preparation of the manuscript.

Competing Interests: The authors have declared that no competing interests exist.

* E-mail: lgraca@fm.ul.pt

Introduction

Rheumatoid arthritis (RA) is a common chronic autoimmune inflammatory disease characterized by destruction of the synovial joints, leading to progressive disability, increased co-morbidity and premature mortality [1,2]. Both genetic and environmental factors are known to contribute to the development of the disease [3]. RA is characterized by a complex immune mediated response with the participation of many cell types including CD4$^+$ T cells [4,5,6], such as the IL-17 producing Th17 subset, which have been shown to play an important role in the pathogenesis of the disease [7,8,9]. The participation of CD4$^+$ T cells in the pathogenesis of RA, namely by influencing other key cellular mediators of the disease (such as B cells or macrophages), has prompted the development of therapeutic strategies targeting this lymphocyte population [10,11,12,13]. Monoclonal antibodies (MAbs) targeting key T cell molecules (such as co-receptor and co-stimulation) have been suggested as drugs capable of achieving long-term protection from the disease, with the potential of leading to immune tolerance, following a short treatment [14]. Indeed long-term transplantation tolerance can be induced in mice following CD4 or co-stimulation blockade [15,16,17].

The most commonly used mouse models for autoimmune arthritis – such as collagen-induced arthritis – have been instrumental in the development of new therapies, such as the blockade of key cytokines, such as TNF. However, arthritis in these mice is self-limited and, as such, pre-clinical studies of putative tolerogenic regimens aiming for long-term effects have been hampered by the lack of suitable animal models of chronic autoimmune arthritis that are not TCR transgenic.

SKG mice, harboring a mutation in ZAP-70 rendering T cells more resistant to activation and thus interfering with appropriate negative selection in the thymus, have been recently described as developing chronic autoimmune arthritis with several characteristics resembling RA [18]. Arthritis in SKG mice has a centripetal course starting with small finger joints, eventually leading to histological changes and bone destruction similar to RA [19]. The incidence and severity of the disease is greater in females, with most mice developing rheumatoid factor (RF), and some animals displaying extra-articular lesions similar to rheumatoid nodules and pneumonitis [18]. Although CD4$^+$ T cells, and its Th17 subset, are important in the pathogenesis of arthritis in SKG mice, other cell populations, such as B cells, participate in the disease as suggested by the production of RF in these animals [18].

Our data reports the long-term protection from chronic autoimmune arthritis following a short course of non-depleting anti-CD4 MAb in SKG mice, associated with decreased IL-17 and increased Foxp3 expression in the synovial tissue. Furthermore, the non-depleting nature of the therapeutic MAb preserves the immune competence of treated mice.

Methods

Ethics Statement

All experiments involving animals were approved by the Animal User and Ethical Committees at the Instituto Gulbenkian de Ciencia, according with directives from Direccao Geral Veterinaria (PORT 1005/92). Mice were bred and maintained under specific pathogen free (SPF) conditions.

Mice

BALB/c, DO11.10.RAG1$^{-/-}$, and SKG mice (generously provided by Professor Shimon Sakaguchi, Kyoto, Japan). Experimental animals were between 8–10 weeks of age and sex matched.

Autoimmune arthritis induction and anti-CD4 treatment

BALB/c and SKG mice were injected intraperitoneally (i.p.) with a single shot of 3mg curdlan per mouse. Treated mice were injected with 1 mg anti-CD4 on days 0 (the day of curdlan injection), 2 and 4. Mice treated at disease onset, were injected with 3 shots of 1 mg anti-CD4 every other day, from the day they have reached a clinical score of 0.5.

Clinical assessment of arthritis

Joint swelling was monitored in blinded cages by two independent observers and scored as described elsewhere [18]: 0, no joint swelling; 0.1, swelling of one finger joint; 0.5, mild swelling of wrist, ankle, or base of tail; and 1.0, severe swelling of wrist, ankle or base of tail. Scores for all joints were totaled for each mouse (with a maximum score of 5 corresponding to severe swelling of the four paws and base of tail).

Antibodies and reagents

Curdlan (Wako, Japan) and Zymosan-A (Sigma-Aldrich, USA) were dissolved in sterile PBS at 15 mg/ml and 20 mg/ml, respectively. Non-depleting anti-CD4 (YTS177) and the isotype control anti-dog CD4 (YKIX302) MAbs were produced in our laboratory using Integra CL1000 flasks (IBS, Chur, Switzerland), purified by 50% ammonium sulfate precipitation, dialyzed against PBS, and purity checked by native and SDS gel electrophoresis. The hybridomas were generously provided by Professor Herman Waldmann (Oxford, UK).

Cytokine analysis

Evaluation of serum cytokines was performed using the mouse inflammation cytometric bead array (BD Biosciences, San Diego, CA), with beads specific for IL-6, TNF, IFN-γ, monocyte chemoattractant protein-1 (MCP-1), and IL-10. IL-17 was quantified by ELISA using a kit from R&D Systems. Cytokine concentrations were measured in duplicates, and compared with standard curves, according to manufacturer instructions.

Quantification of rheumatoid factors

Serum levels of rheumatoid factor were measured by ELISA as previously described [18], using 5 μg/ml mouse IgG to coat the plates, and 1 μg/ml anti-mouse-IgM-HRP for detection (Southern Biotech, Birmingham, USA).

Determination of ovalbumin-specific immune responses

On day 30 following anti-CD4 treatment, or treatment with an isotype control, the mice were immunized with two injections two weeks apart, of 20 μg ovalbumin (OVA, grade V; Sigma, St Louis, USA), in 2.0 mg of endotoxin-free aluminum hydroxide (alum, Alu-gel-S, Serva, Heidelberg, Germany), and sacrificed one week after the last immunization. Non-immunized (naïve) mice were maintained as negative controls. The serum concentration of OVA-specific immunoglobulins was determined by ELISA using an OVA-specific IgG1 kit (SouthernBiotech, Birmingham, USA) with anti-OVA IgG1 standard from Serotec (Oxford, UK).

Histology

Ankle and metatarso-phalangical (MTP) joints were collected and cryopreserved in OCT (Sakura, NL). Cryosections were stained with hematoxilin-eosin according to standard procedures.

Flow cytometry

Cells were stained for flow cytometric analysis with the following fluorochrome-labeled monoclonal antibodies: CD3 (145-2C11), CD4 (RM4-5), CD25 (PC61.5), and Foxp3 (FJK-16s) from eBiosciences or BD Biosciences. Intracellular cytokines were investigated in lymphocytes activated for three hours in PMA-ionomycin in the presence of Brefeldin-A. Monoclonal antibodies specific for IFN-γ (XMG1.2), IL-17A (eBio17B7), and IL-10 (JES5-16E3) were used (all from eBiosciences).

Th17-polarization assays

OVA-specific CD4^{+} T cells from DO11.10.RAG1$^{-/-}$ mice were purified by magnetic separation with CD4 (L3T4) microbeads (Miltenyi Biotec, Germany). Cell purities were between 92–96%. The T cells were cultured for 5 days with bone marrow derived DCs, 0.1 μM OVA peptide (New England Peptide LLC, USA), and 10 μg/ml anti-CD4 (YTS177) in IMDM 5% FBS (Invitrogen), 1% Pen/Strep (GibCo), 0.1% β-Mercaptoethanol (GibCo), 1 ng/ml TGF-β (R&D systems), 20 ng/ml IL-6 (R&D systems), 10 ng/ml IL-1β (Ebiosciences), and 10 μg/ml anti-INFγ (R46A2). At the end of the culture the cells were harvested, and processed for flow cytometry.

RNA extraction and real time PCR

Total RNA was extracted from synovial tissue, dissected from ankle joints, using lysis buffer, and following the tissue RNA kit instructions (Omega bio-tek, USA). Foxp3 and IL-17 were quantified by real time PCR, performed on the ABI Prism® 7000 sequence detection system (Applied Biosystems, USA). The relative mRNA levels of the target genes were normalized against CD3. CD3, Foxp3 and IL-17 primers are described elsewhere [20,21,22].

Statistics

Statistical significance was determined using the two-tailed non-parametric Student's t test (Mann-Whitney U). *P* values <0.05 were deemed significant.

Results

SKG mice develop chronic autoimmune arthritis upon systemic curdlan immunization

Although initial reports have suggested that SKG mice develop chronic autoimmune arthritis spontaneously [18], it was later confirmed that disease induction requires exposure to yeast wall extract (zymosan) or purified β-glucans, like curdlan or laminarin, acting through the pattern recognition receptor Dectin-1 [23].

We confirmed that a single intraperitoneal injection of 2 mg Zymosan (not shown) or 3 mg Curdlan is sufficient to induce chronic disease in SKG mice, but not in wild-type controls (Figure 1A). Both male and female mice developed arthritis, although the disease was more severe in females (Figure 1B). Based on these data we decided to use curdlan in female SKG mice in subsequent experiments.

Non-depleting anti-CD4 treatment prevents the onset of autoimmune arthritis

To assess whether non-depleting anti-CD4 MAbs, suggested in previous studies as having tolerogenic potential, can lead to long-term beneficial effects in chronic autoimmune arthritis, female SKG mice were treated with non-depleting anti-CD4 together with curdlan. Anti-CD4 treatment was effective in preventing the development of autoimmune arthritis ($n = 5$, $P<0.001$, Figure 2A). Since arthritic SKG mice are known to produce high titres of RF (IgM anti-IgG), we quantified serum RF. We found that serum RF were below the limit of detection in all mice treated with anti-CD4 (Figure 2B).

Furthermore, animals treated with anti-CD4 not only remained without clinical manifestations of the disease, but their joints were free from inflammatory cell infiltrates. Indeed, histological sections of ankle and MTP joints from anti-CD4 treated mice showed normal joint tissues, without inflammatory infiltration or bone erosions, compared to the curdlan induced arthritic mice (Figure 2C).

We also evaluated the presence of pro-inflammatory cytokines in arthritic mice compared to anti-CD4 treated animals. We observed a significant decrease in the concentration of IL-6, TNF, MCP-1 and IFN-γ in sera from anti-CD4 treated mice, suggesting that a treatment targeting T cells can have an impact on additional cell types producing those cytokines (Figure 2D). It should be noted that IL-6, which has been associated with Th17 differentiation, is known to be critical for the pathogenesis of chronic autoimmune arthritis in SKG mice [24], and was not detectable in any of the anti-CD4 treated animals. Despite the reported association of IL-17 with arthritis in SKG mice, this cytokine was not detected in sera from arthritic animals, remaining below detection level in all groups (Figure 2E). This observation is in accordance with the proposed local effect of this inflammatory mediator.

Previous studies have suggested a protective role for IL-10 in this murine model of autoimmune arthritis [25]. However, we did not find any significant difference in the serum levels of IL-10, between arthritic and anti-CD4 treated mice ($n = 10$, $P>0.05$, Figure 2E).

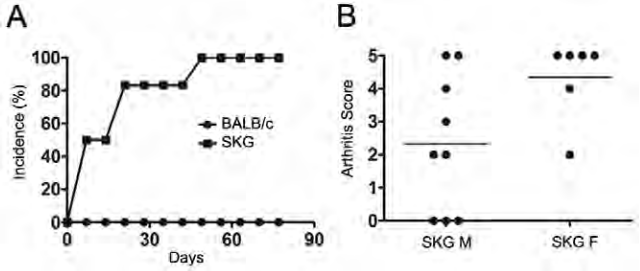

Figure 1. SKG mice develop chronic autoimmune arthritis upon induction with curdlan. (A) Arthritis incidence in female SKG and BALB/c mice after a single i.p. injection of 3 mg curdlan ($n = 6$). Curdlan was able to induce chronic arthritis in SKG but not in BALB/c mice. Each point represents the median per group. (B) Clinical score of 5 month-old male (M) and female (F) SKG mice 90 days following disease induction with curdlan. Data are from two independent experiments.
doi:10.1371/journal.pone.0010558.g001

Non-depleting anti-CD4 alters the balance of Treg/Th17 cells in the synovial tissue and draining LNs

It has been reported that the anti-CD4 MAb used in our study (YTS177) has a non-depleting isotype [26]. We confirmed the non-depleting nature of the MAb as neither the splenic frequency (Figure 3A and B) nor the total number (not shown) of $CD4^+$ T cells were reduced in animals treated with anti-CD4.

Transplantation tolerance achieved with non-depleting anti-CD4 has been associated with the induction of Treg cells, both in the spleen and within tolerated transplants [27,28,29]. We investigated if changes in Treg frequency could be seen in the spleen of anti-CD4 treated mice. We found that there was no change in T cell subpopulations of anti-CD4-treated animals, namely $Foxp3^+$ Treg cells, with a similar frequency of these cells in mice exposed to curdlan in the presence or absence of anti-CD4 treatment (Figure 3A and B). In addition, the frequency of IL-17, IFN-γ or IL-10-producing T cells, identified by intracellular cytokine staining, remained constant in all groups of animals, and below 2% of the $CD4^+$ T cells (not shown).

As our data show that anti-CD4 treatment can prevent joint inflammation, even though T cell subpopulations in secondary lymphoid organs appear to be unaffected, we investigated whether anti-CD4 treatment was leading to alterations in the T cell subpopulations within the synovial tissue of protected animals. Given the technical limitations for the direct enumeration of individual T cells from mouse synovial tissue, we used the expression of Foxp3 and IL-17 mRNA as surrogate markers for the relative frequency of, respectively, Tregs and Th17 cells. For this purpose Foxp3 and IL-17 mRNA expression was measured by quantitative real time PCR and normalized to CD3 expression (thus controlling for different numbers of infiltrating T cells in different samples, as the arthritic synovium contains greater numbers of T cells). This method, of using CD3 expression for normalization of different numbers of infiltrating T cells in tissues with few lymphocytes has been established for other tissues with small numbers of T cells, such as skin grafts in mice [22]. We observed that while IL-17 expression among synovial T cells (i.e. IL-17/CD3 mRNA ratio) was reduced in mice treated with anti-CD4 and consequently protected from inflammatory manifestations of the disease, the expression of Foxp3 among synovial T cells was increased in the same conditions ($n = 4$, $P<0.05$, Figure 3C). Thus, the Foxp3/Th17 ratio in the synovial tissue is substantially shifted following anti-CD4 treatment. In addition, the analysis of popliteal LNs, draining affected joints, showed a reduction in the frequency of $IL\text{-}17^+$ T cells in anti-CD4-treated mice ($n = 8$, $P<0.05$) while the frequency of $Foxp3^+$ cells remained similar in both groups of animals (Figure 3D).

CD4-blockade prevents *in-vitro* Th17 polarization while favoring Foxp3 expression

Although non-depleting anti-CD4 has been widely studied for the induction of transplantation tolerance its exact mechanism of action has not been fully characterized. In experiments performed with TCR-transgenic mice devoid of $Foxp3^+$ Treg cells, it was previously shown that CD4-blockade could directly lead to peripheral conversion of T cells towards $Foxp3^+$ Treg cells thus achieving transplantation tolerance [22]. However, it was never assessed whether CD4-blockade could directly interfere with Th17 polarization, or whether a reduction in Th17 cells (as we observed *in vivo*) would be secondary to Treg-mediated suppression.

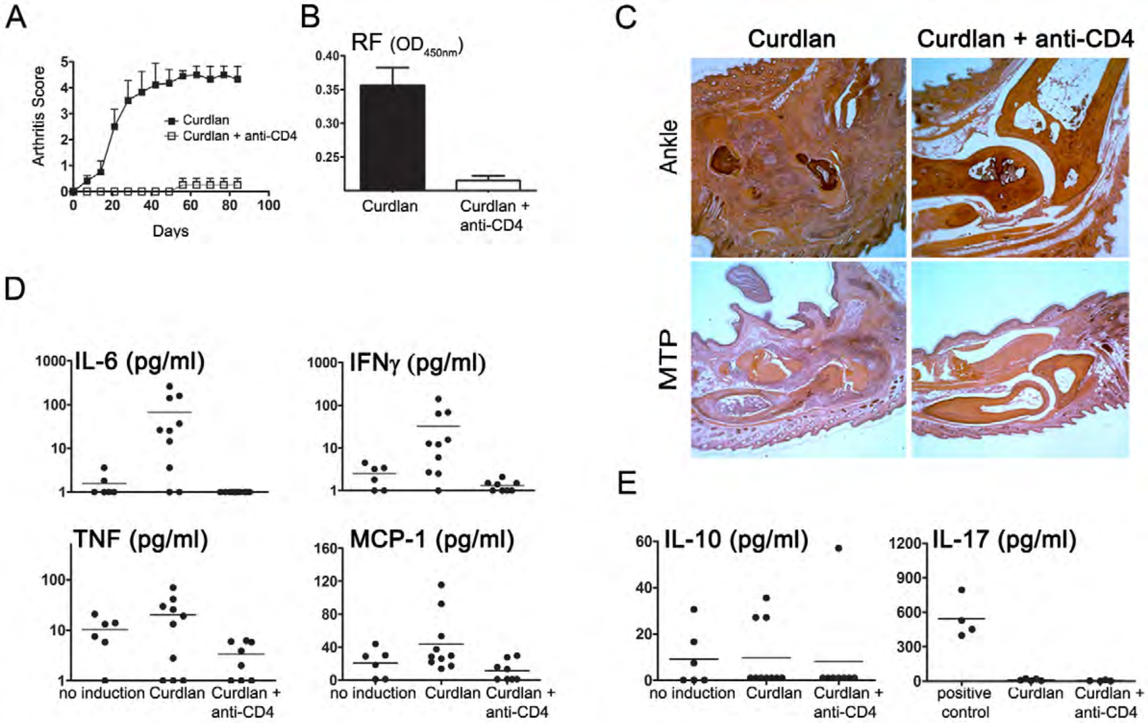

Figure 2. Non-depleting anti-CD4 MAb prevents the onset of autoimmune arthritis. (A) Female SKG mice were immunized with 3mg curdlan i.p. together with 1 mg non-depleting anti-CD4 or an isotype control. The MAb was administered again on days 2 and 4. Anti-CD4 treated mice were protected from the development of autoimmune arthritis (n = 6, $P<0.001$). Data, represented as mean ± SEM, are from two independent experiments. (B) Serum concentration of rheumatoid factor (RF) was measured by ELISA. Mice treated with anti-CD4 showed significantly lower levels of RF (n = 6, $P<0.001$) (C) Histological sections stained with eosin-hematoxilin from the ankle and metatarso-phalangical joints from SKG mice in the absence and in the presence of anti-CD4 treatment, 90 days following curdlan immunization. (D) Serum concentration of IL-6, IFN-γ, TNF and MCP-1 in naive SKG mice, SKG mice exposed to curdlan, or curlan and anti-CD4. Naive SKG mice were age matched and did not develop arthritis in the absence of curdlan immunization (no induction). The serum levels of IL-6 ($P<0.05$), IFN-γ ($P<0.01$) and MCP-1 ($P<0.01$) were significantly lower in anti-CD4 treated mice compared with animals injected with curldan in the absence of tolerizing MAbs. Differences in TNF concentration did not reach statistical significance. (E) The serum concentration of IL-10 and IL-17 in SKG mice exposed to curdlan, or curlan and anti-CD4 remained similar in the different experimental groups. Culture supernatants from Th17 cell culture were used as positive control.
doi:10.1371/journal.pone.0010558.g002

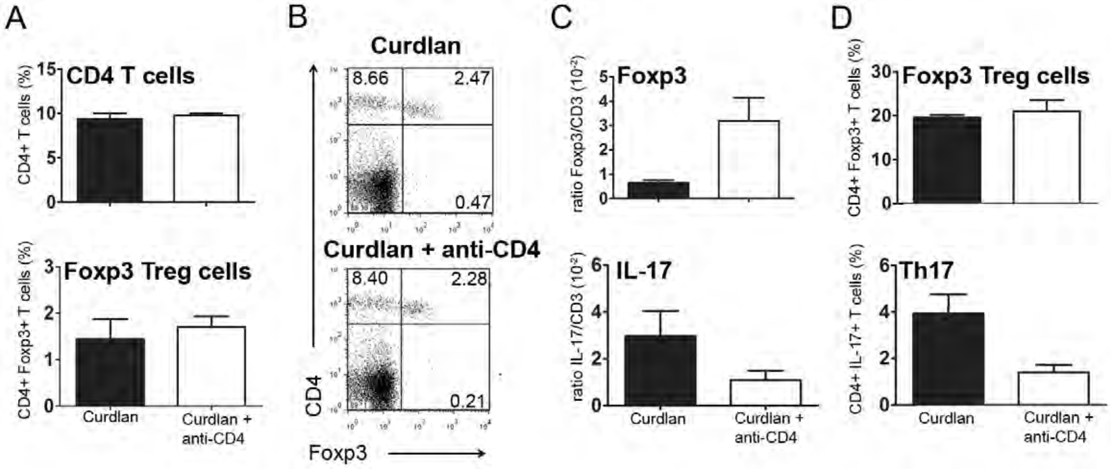

Figure 3. Anti-CD4 MAb influences the local balance of Th17/Treg cells. (A) Frequency of splenic $CD4^+$ T cells or $CD4^+Foxp3^+$ Treg cells from SKG mice exposed to curdlan, or curdlan + anti-CD4 treatment. No significant difference was observed between the two populations of animals. (B) Representative dot plots showing the frequency of splenic $CD4^+Foxp3^+$ T cells from SKG mice exposed to curdlan, or curdlan + anti-CD4 treatment. No significant difference was observed, as represented in panel A. (C) Foxp3 and IL-17 mRNA expression from the synovial membrane of SKG mice exposed to curdlan, or curdlan + anti-CD4 (mRNA expression levels were normalized to CD3 expression). (D) Frequency of $Foxp3^+$ and $IL\text{-}17^+$ T cells within draining LNs of SKG mice exposed to curdlan, or curdlan + anti-CD4.
doi:10.1371/journal.pone.0010558.g003

To address this issue we investigated whether CD4-blockade could prevent *in vitro* Th17 polarization. We used OVA-specific TCR-transgenic CD4$^+$ T cells sorted from DO11.10.RAG$^{-/-}$ mice. We stimulated these cells *in vitro*, for five days, in the presence of DCs loaded with the appropriate peptide and under culture conditions promoting optimal Th17 polarization (in presence of TGF-β, IL-6, IL-1β, and anti-IFN-γ)[30]. We observed that addition of anti-CD4 led to a significant reduction of Th17 cells (n = 6, $P<0.05$, Figure 4). In spite of the presence of cytokines that promote Th17 polarization (cytokines that are known to prevent Foxp3 induction) the addition of anti-CD4 resulted in a significant increase in the frequency of Foxp3$^+$ T cells (n = 6, $P<0.05$, Figure 4).

Non-depleting anti-CD4 induces long- term protection from autoimmune arthritis

To assess whether protection from arthritis induced with anti-CD4 treatment had a long-term effect, SKG mice initially injected with curdlan and non-depleting anti-CD4 were challenged with curdlan 60 days following the initial treatment. Animals exposed to curdlan in the presence of the putative tolerogenic anti-CD4 MAb at day 0 were protected from the induction of arthritis following curdlan administration at day 60, unlike the age-matched controls that did not receive any treatment at day 0 (n = 6, $P<0.05$, Figure 5A).

However, it should be noted, that some anti-CD4 treated mice developed mild manifestations of arthritis following curdlan challenge at day 60, although without progressing to the severe manifestations of the disease observed in control groups.

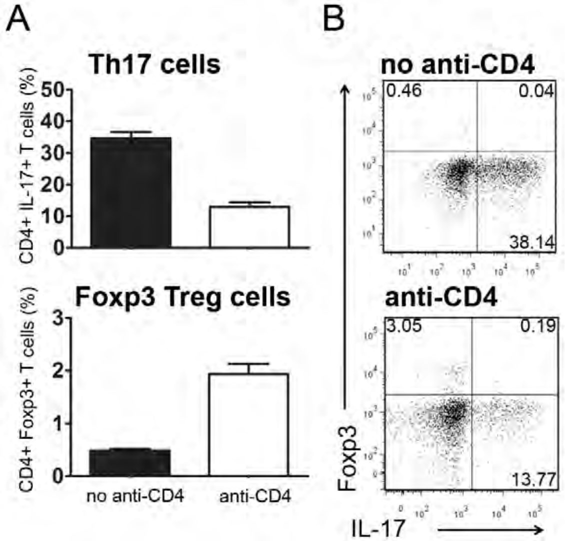

Figure 4. CD4-blockade prevents Th17 polarization. (A) Sorted TCR-transgenic cells were stimulated *in vitro* with peptide-loaded DCs under culture conditions known to preferentially polarize Th17 cells, with the addition of recombinant TGF-β, IL-6, IL-1β, and anti-IFN-γ. After 5 days of culture we observed a significant reduction of IL-17$^+$ cells in the presence of anti-CD4 (n = 6, $P<0.05$). In contrast, anti-CD4 addition led to an increased frequency of Foxp3$^+$ T cells (n = 6, $P<0.05$). (B) Representative dot plots from the two different culture conditions. An independent experiment was performed with a peptide dose of 0.3 μM with similar results.

doi:10.1371/journal.pone.0010558.g004

Non-depleting anti-CD4 prevents progression of established autoimmune arthritis

Given the fact that non-depleting anti-CD4 treatment prevents the onset of autoimmune arthritis, we tested the effectiveness of a similar course of anti-CD4 for the treatment of established arthritis in SKG mice. Female SKG mice were immunized with curdlan and when the clinical score reached 0.5 the arthritic mice were randomly included in a group treated with anti-CD4 MAb or a control group. Mice treated with non-depleting anti-CD4 showed a long-term benefit with slower disease progression and less severe clinical scores (n = 5, $P<0.05$, Figure 5B). However, remission was only achieved in a minority of the treated animals.

Anti-CD4 treated mice remain immunocompetent

A concern of immunomodulatory or tolerogenic therapeutic strategies is their long-term impact on the overall immune response. We therefore assessed the immune competence of anti-CD4-treated BALB/c mice (same genetic background as the SKG mice, but without the ZAP70 point mutation) to mount CD4$^+$ T cell-dependent immune responses towards an unrelated antigen. For this purpose, mice treated with anti-CD4 were sensitized with 20 μg OVA-alum 30 days following anti-CD4 treatment. The quantification of OVA-specific immunoglobulins in the serum was determined one week following sensitization. Our data show that the concentration of OVA-specific immunoglobulins was similar in immunized mice, regardless of previous anti-CD4 treatment, and considerable higher than in naive controls (n = 5, $P<0.05$, Figure 5C). Moreover, we confirmed the same results in SKG mice, subjected to the same protocol (n = 2, not shown). Of note, if OVA was administered at the time of anti-CD4 treatment in BALB/c mice, the animals became unable to produce OVA-specific immunoglobulins following subsequent OVA immunization (n = 6, $P<0,05$, Figure 5D), thus proving that OVA-specific IgG production is CD4-dependent, and that tolerance is only imposed over the antigens present at the time of tolerance induction.

Discussion

Our data show that a short course of non-depleting anti-CD4 can lead to long-term protection from the development of autoimmune arthritis, in a murine model of chronic disease. We have shown that our non-depleting antibody (clone YTS177) is not affecting T cells in the spleen, but seems to be preventing autoimmune arthritis, acting locally at the site of inflammation. It is likely that by targeting CD4$^+$ T cells, the pathogenic cycle of events leading to synovial inflammation and progressive joint destruction is abrogated, as other cellular players are not recruited towards the articular tissue to cause inflammation. This impact of CD4-blockade on other cell types is well illustrated by the marked decrease of pro-inflammatory cytokines produced by dendritic cells (DCs) and macrophages in anti-CD4 treated animals. In addition, given Th17 cells have been described as involved in the production of autoantibodies in experimental autoimmune arthritis [31,32], our observation that anti-CD4-treated mice do not produce RF is in line with the hypothesis that by maintaining pathogenic T cell clones under control the B cells will not receive the necessary stimuli for the production of autoantibodies. We cannot exclude, at this time, a direct effect of non-depleting anti-CD4 MAbs on innate cells expressing CD4, namely natural killer T (NKT) cells that have been reported as being able to provide "help" to B cells, and to influence autoimmune arthritis [33].

In our experiments, we found a limited efficacy for tolerance induction once the animals became overtly arthritic. Although we

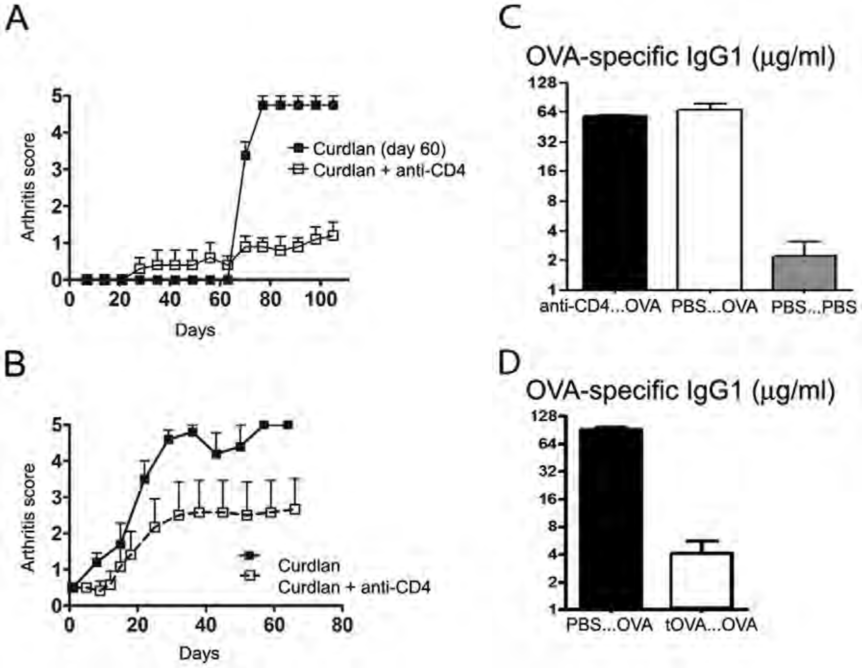

Figure 5. Long-term protective effect of non-depleting anti-CD4 treatment does not affect immune competence. (A) Female SKG mice were injected with 3 mg curdlan i.p. on day 0 and anti-CD4 on days 0, 2, and 4. Animals treated with anti-CD4 displayed long term protection from arthritis (n = 5, $P<0.05$). On day 60, anti-CD4 treated mice and age matched SKG were challenged with 3 mg curdlan i.p. Mice previously treated with anti-CD4 remained protected from the development of autoimmune arthritis (n = 5, $P<0.05$). (B) Female SKG mice were injected with 3 mg curdlan i.p. and, when the clinical score reached 0.5, some of the animals initiated treatment with three i.p. administrations of 1 mg anti-CD4 on alternate days. Control animals rapidly progressed to severe arthritis unlike the anti-CD4 treated mice (n = 6, $P<0.05$). (C) Mice were treated with non-depleting anti-CD4 30 days before immunization with OVA-alum i.p. (αCD4…OVA). One week following sensitization the serum levels of OVA-specific IgG1 were quantified, and compared with untreated (PBS…OVA) and non-immunized controls (PBS…PBS). Mice treated with anti-CD4 MAbs were competent to produce OVA-specific IgG1 to titres similar to untreated controls, and considerably higher than the non-immunized mice (n = 5, $P<0.05$). (D) OVA-specific IgG1 in mice where OVA was initially administered at the time of anti-CD4 treatment (tOVA…OVA), compared with animals that were not initially treated with anti-CD4 (PBS…OVA). Mice treated with anti-CD4 at the time of sensitization with OVA, became tolerant to the subsequent OVA immunization (n = 6, $P<0.05$).

doi:10.1371/journal.pone.0010558.g005

do not have a complete explanation for this observation, it is possible that such resistance to tolerance induction may be due to the participation of other cell types, besides CD4$^+$ T cells, at that late time. In fact, in transplantation it is known that in pre-sensitized animals a population of Asialo GM1$^+$ CD8$^+$ T cells can create a barrier for tolerance induction with MAbs [34]. Thus, it may be possible to enhance the efficacy of tolerance induction in overt arthritis with reagents targeting other cell types, namely CD8$^+$ T cells and B cells.

It remains to be established whether the long-term protection from arthritis afforded following anti-CD4 treatment, even after a new curdlan challenge at a later time, can be explained by the development of regulatory mechanisms that have been described in other animal models of anti-CD4 induced immune tolerance [28,35]. In fact, it is now established that CD4$^+$ T cell activation in the presence of TGF-β and IL-6 favors T cell conversion towards arthritogenic Th17 cells, while activation in the same environment devoid of IL-6 shifts the differentiation from Th17 towards Foxp3$^+$ Treg cells [30]. SKG autoimmune arthritis development is known to be dependent on Th17 [36].

Our data suggests that protection from arthritis induced with anti-CD4 is associated with an overall decrease of infiltrating T cells in synovial tissue and, within those T cells in the synovium, with an increase in the frequency of synovial Foxp3$^+$ Treg cells. As a consequence, the tissue is endowed with local changes that are likely to prevent the onset of arthritis directly within the local environment where inflammation would occur, even following a later exposure to curdlan at a time (day 60) where anti-CD4 MAbs are no longer present. Moreover, the reciprocal decrease of IL-17 expression at the same time that the expression of Foxp3 increases, in the joints of anti-CD4 treated mice, supports the hypothesis that indeed the balance between Treg and Th17 can determine the decision between prevention or onset of autoimmune arthritis. The observation that IL-6 decreases in the serum of anti-CD4 treated mice is also in agreement with this hypothesis. It should be noted, however, that the number of T cells is markedly reduced in the synovium of treated mice, as can be seen in the histological sections (and confirmed with greater CD3 expression in the synovia by RT-PCR – thus the need to use CD3, rather than a housekeeping gene, to normalize our gene expression studies). It was recently reported that IL-17A can be produced by mast cells in rheumatoid arthritis synovia [37]. Although we did not investigate this possible source of IL-17, the overall quantification of IL-17 transcripts was significantly reduced in anti-CD4 treated animals, where T cells were also less abundant. As a consequence, the shift in the Treg/Th17 balance in the synovial tissue is likely to be also influenced by tissue accessibility to different types of effector T cells.

We have also shown that CD4-blockade can directly inhibit T cell polarization towards an IL-17-producing Th17 phenotype, even when the most appropriate cytokine environment is provided. In addition, our data show that even in the presence of those cytokines known to inhibit Foxp3 induction (namely IL-6), CD4-blockade can facilitate the peripheral conversion of Foxp3$^+$ Treg cells. Taken together, our data complements previous studies on the mechanism of tolerance induction in transplantation with anti-CD4 (where peripheral induction of Foxp3$^+$ Treg cells have been shown critical), by demonstrating that CD4-blockade can also lead to a direct inhibition of Th17 polarization – a critical factor for the arthritis pathogenesis, namely in SKG mice [36].

Given the essential role of CD4$^+$ T cells in the pathogenesis of RA, both directly and by recruiting and activating other participating cell types (such as B cells, DCs and macrophages), the therapeutic targeting of CD4$^+$ lymphocytes has been extensively pursued [38]. Depleting and non-depleting anti-CD4 MAbs have been tested in several animal models of autoimmune arthritis [39,40,41,42], and in clinical trials with RA patients [43,44,45]. In spite of promising results in pre-clinical studies, the therapeutic effectiveness of anti-CD4 in clinical trials was modest and short-term, possibly due to transient immunosuppression and not tolerance. In retrospect, those unimpressive results are not too surprising due to technical details related with dosing and MAb characteristics. In fact the immunogenicity of the mouse or chimeric MAb used was well documented as leading to their rapid clearance and consequent loss of efficient CD4 blockade [46]. The reduction of the number of CD4$^+$ T cells was also associated with a concern of possible increased susceptibility to infection.

Our data show that non-depleting anti-CD4 can be effective in preventing chronic autoimmune arthritis while preserving immune competence, as treated mice remain able to mount a CD4-dependent immune response against a different antigen (OVA). OVA immunization is a well established protocol for the induction of CD4-dependent production of OVA-specific immunoglobulins. Moreover, administration of anti-CD4 together with OVA prevents the effectiveness of subsequent immunizations with the same antigen. Taken together, these data suggest that anti-CD4 prevents immune responses towards antigens present at the time of treatment, without hampering immune responses to unrelated antigens introduced in the organism at a later time, therefore preserving immunocompetence. It should be noted that these types of studies, on the long-term immunocompetence of treated mice have been difficult to perform in animal models that, unlike SKG mice, do not develop a chronic form of arthritis.

In summary, we show that therapeutic strategies leading to synovial accumulation of Treg cells and reduction of Th17 are capable of protecting from the onset of autoimmune arthritis, as well as to prevent long-term disease progression, without leading to overall immune suppression.

Acknowledgments

We thank Margarida Souto Carneiro and Marta Monteiro for helpful suggestions. We are grateful to Professor Shimon Sakaguchi (Kyoto, Japan) for providing the SKG mice, and to Professor Herman Waldmann (Oxford, UK) for providing reagents used in this study.

Author Contributions

Conceived and designed the experiments: JD JEF LG. Performed the experiments: JD AAD VO. Analyzed the data: JD AAD VO JEF LG. Wrote the paper: JD JEF LG.

References

1. Chehata JC, Hassell AB, Clarke SA, Mattey DL, Jones MA, et al. (2001) Mortality in rheumatoid arthritis: relationship to single and composite measures of disease activity. Rheumatology (Oxford) 40: 447–452.
2. Gabriel SE, Crowson CS, Kremers HM, Doran MF, Turesson C, et al. (2003) Survival in rheumatoid arthritis: a population-based analysis of trends over 40 years. Arthritis Rheum 48: 54–58.
3. Firestein GS (2003) Evolving concepts of rheumatoid arthritis. Nature 423: 356–361.
4. Banerjee S, Webber C, Poole AR (1992) The induction of arthritis in mice by the cartilage proteoglycan aggrecan: roles of CD4+ and CD8+ T cells. Cell Immunol 144: 347–357.
5. Breedveld FC, Dynesius-Trentham R, de Sousa M, Trentham DE (1989) Collagen arthritis in the rat is initiated by CD4+ T cells and can be amplified by iron. Cell Immunol 121: 1–12.
6. Van Boxel JA, Paget SA (1975) Predominantly T-cell infiltrate in rheumatoid synovial membranes. N Engl J Med 293: 517–520.
7. Chabaud M, Durand JM, Buchs N, Fossiez F, Page G, et al. (1999) Human interleukin-17: A T cell-derived proinflammatory cytokine produced by the rheumatoid synovium. Arthritis Rheum 42: 963–970.
8. Kotake S, Udagawa N, Takahashi N, Matsuzaki K, Itoh K, et al. (1999) IL-17 in synovial fluids from patients with rheumatoid arthritis is a potent stimulator of osteoclastogenesis. J Clin Invest 103: 1345–1352.
9. Ziolkowska M, Koc A, Luszczykiewicz G, Ksiezopolska-Pietrzak K, Klimczak E, et al. (2000) High levels of IL-17 in rheumatoid arthritis patients: IL-15 triggers in vitro IL-17 production via cyclosporin A-sensitive mechanism. J Immunol 164: 2832–2838.
10. Choy EH, Connolly DJ, Rapson N, Jeal S, Brown JC, et al. (2000) Pharmacokinetic, pharmacodynamic and clinical effects of a humanized IgG1 anti-CD4 monoclonal antibody in the peripheral blood and synovial fluid of rheumatoid arthritis patients. Rheumatology (Oxford) 39: 1139–1146.
11. Graca L, Waldmann H (2006) Reprogramming the immune system using antibodies. Methods Mol Biol 333: 247–268.
12. Mason U, Aldrich J, Breedveld F, Davis CB, Elliott M, et al. (2002) CD4 coating, but not CD4 depletion, is a predictor of efficacy with primatized monoclonal anti-CD4 treatment of active rheumatoid arthritis. J Rheumatol 29: 220–229.
13. Schulze-Koops H, Burkhardt H, Kalden JR (1999) What we have learned from trials of immunomodulatory agents in rheumatoid arthritis: Future directions. Drugs Today (Barc) 35: 327–351.
14. Isaacs JD (2007) T cell immunomodulation–the Holy Grail of therapeutic tolerance. Curr Opin Pharmacol 7: 418–425.
15. Graca L, Honey K, Adams E, Cobbold SP, Waldmann H (2000) Cutting edge: anti-CD154 therapeutic antibodies induce infectious transplantation tolerance. J Immunol 165: 4783–4786.
16. Graca L, Le Moine A, Cobbold SP, Waldmann H (2003) Antibody-induced transplantation tolerance: the role of dominant regulation. Immunol Res 28: 181–191.
17. Karim M, Bushell AR, Wood KJ (2002) Regulatory T cells in transplantation. Curr Opin Immunol 14: 584–591.
18. Sakaguchi N, Takahashi T, Hata H, Nomura T, Tagami T, et al. (2003) Altered thymic T-cell selection due to a mutation of the ZAP-70 gene causes autoimmune arthritis in mice. Nature 426: 454–460.
19. Caetano-Lopes J, Henriques R, Canhao H, Duarte J, Amaral PM, et al. (2009) Chronic arthritis directly induces quantitative and qualitative bone disturbances leading to compromised biomechanical properties. Clin Exp Rheumatol 27: 475–482.
20. Hori S, Nomura T, Sakaguchi S (2003) Control of regulatory T cell development by the transcription factor Foxp3. Science 299: 1057–1061.
21. Wu Q, Martin RJ, Rino JG, Breed R, Torres RM, et al. (2007) IL-23-dependent IL-17 production is essential in neutrophil recruitment and activity in mouse lung defense against respiratory Mycoplasma pneumoniae infection. Microbes Infect 9: 78–86.
22. Cobbold SP, Castejon R, Adams E, Zelenika D, Graca L, et al. (2004) Induction of foxP3+ regulatory T cells in the periphery of T cell receptor transgenic mice tolerized to transplants. J Immunol 172: 6003–6010.
23. Yoshitomi H, Sakaguchi N, Kobayashi K, Brown GD, Tagami T, et al. (2005) A role for fungal {beta}-glucans and their receptor Dectin-1 in the induction of autoimmune arthritis in genetically susceptible mice. J Exp Med 201: 949–960.
24. Hirota K, Yoshitomi H, Hashimoto M, Maeda S, Teradaira S, et al. (2007) Preferential recruitment of CCR6-expressing Th17 cells to inflamed joints via CCL20 in rheumatoid arthritis and its animal model. J Exp Med 204: 2803–2812.
25. Hata H, Sakaguchi N, Yoshitomi H, Iwakura Y, Sekikawa K, et al. (2004) Distinct contribution of IL-6, TNF-alpha, IL-1, and IL-10 to T cell-mediated spontaneous autoimmune arthritis in mice. J Clin Invest 114: 582–588.
26. Qin SX, Cobbold S, Benjamin R, Waldmann H (1989) Induction of classical transplantation tolerance in the adult. J Exp Med 169: 779–794.
27. Graca L, Thompson S, Lin CY, Adams E, Cobbold SP, et al. (2002) Both CD4(+)CD25(+) and CD4(+)CD25(-) regulatory cells mediate dominant transplantation tolerance. J Immunol 168: 5558–5565.
28. Graca L, Cobbold SP, Waldmann H (2002) Identification of regulatory T cells in tolerated allografts. J Exp Med 195: 1641–1646.

29. Kingsley CI, Karim M, Bushell AR, Wood KJ (2002) CD25+CD4+ regulatory T cells prevent graft rejection: CTLA-4- and IL-10-dependent immunoregulation of alloresponses. J Immunol 168: 1080–1086.
30. Veldhoen M, Hocking RJ, Atkins CJ, Locksley RM, Stockinger B (2006) TGFbeta in the context of an inflammatory cytokine milieu supports de novo differentiation of IL-17-producing T cells. Immunity 24: 179–189.
31. Hsu HC, Yang P, Wang J, Wu Q, Myers R, et al. (2008) Interleukin 17-producing T helper cells and interleukin 17 orchestrate autoreactive germinal center development in autoimmune BXD2 mice. Nat Immunol 9: 166–175.
32. Jacobs JP, Wu HJ, Benoist C, Mathis D (2009) IL-17-producing T cells can augment autoantibody-induced arthritis. Proc Natl Acad Sci U S A 106: 21789–21794.
33. Coppieters K, Dewint P, Van Beneden K, Jacques P, Seeuws S, et al. (2007) NKT cells: manipulable managers of joint inflammation. Rheumatology (Oxford) 46: 565–571.
34. Trambley J, Bingaman AW, Lin A, Elwood ET, Waitze SY, et al. (1999) Asialo GM1(+) CD8(+) T cells play a critical role in costimulation blockade-resistant allograft rejection. J Clin Invest 104: 1715–1722.
35. Graca L, Le Moine A, Lin CY, Fairchild PJ, Cobbold SP, et al. (2004) Donor-specific transplantation tolerance: the paradoxical behavior of CD4+CD25+ T cells. Proc Natl Acad Sci U S A 101: 10122–10126.
36. Hirota K, Hashimoto M, Yoshitomi H, Tanaka S, Nomura T, et al. (2007) T cell self-reactivity forms a cytokine milieu for spontaneous development of IL-17+ Th cells that cause autoimmune arthritis. J Exp Med 204: 41–47.
37. Hueber AJ, Asquith DL, Miller AM, Reilly J, Kerr S, et al. Mast cells express IL-17A in rheumatoid arthritis synovium J Immunol 184: 3336–3340.
38. Isaacs JD (2008) Therapeutic T-cell manipulation in rheumatoid arthritis: past, present and future. Rheumatology (Oxford) 47: 1461–1468.
39. Chu CQ, Londei M (1996) Induction of Th2 cytokines and control of collagen-induced arthritis by nondepleting anti-CD4 Abs. J Immunol 157: 2685–2689.
40. Mauri C, Chu CQ, Woodrow D, Mori L, Londei M (1997) Treatment of a newly established transgenic model of chronic arthritis with nondepleting anti-CD4 monoclonal antibody. J Immunol 159: 5032–5041.
41. Ranges GE, Fortin S, Barger MT, Sriram S, Cooper SM (1988) In vivo modulation of murine collagen induced arthritis. Int Rev Immunol 4: 83–90.
42. Ranges GE, Sriram S, Cooper SM (1985) Prevention of type II collagen-induced arthritis by in vivo treatment with anti-L3T4. J Exp Med 162: 1105–1110.
43. Herzog C, Walker C, Pichler W, Aeschlimann A, Wassmer P, et al. (1987) Monoclonal anti-CD4 in arthritis. Lancet 2: 1461–1462.
44. Horneff G, Burmester GR, Emmrich F, Kalden JR (1991) Treatment of rheumatoid arthritis with an anti-CD4 monoclonal antibody. Arthritis Rheum 34: 129–140.
45. Reiter C, Kakavand B, Rieber EP, Schattenkirchner M, Riethmuller G, et al. (1991) Treatment of rheumatoid arthritis with monoclonal CD4 antibody M-T151. Clinical results and immunopharmacologic effects in an open study, including repeated administration. Arthritis Rheum 34: 525–536.
46. Horneff G, Winkler T, Kalden JR, Emmrich F, Burmester GR (1991) Human anti-mouse antibody response induced by anti-CD4 monoclonal antibody therapy in patients with rheumatoid arthritis. Clin Immunol Immunopathol 59: 89–103.

Anibarro *et al. BMC Infectious Diseases* 2012, **12**:195
http://www.biomedcentral.com/1471-2334/12/195

BMC Infectious Diseases

RESEARCH ARTICLE **Open Access**

Value of the tuberculin skin testing and of an interferon-gamma release assay in haemodialysis patients after exposure to *M. tuberculosis*

Luis Anibarro[1*], Matilde Trigo[2], Diana Feijoó[3], Mónica Ríos[4], Luisa Palomares[3], Alberto Pena[1], Marta Núñez[4], Carlos Villaverde[5] and África González-Fernández[6]

Abstract

Background: Patients with end-stage renal disease (ESRD) and *Mycobacterium tuberculosis* infection pose a high risk of developing active TB disease. It is therefore important to detect latent TB infection (LTBI) to be able to offer treatment and prevent progression to TB disease. We assessed the value of the tuberculin skin test (TST) and of an interferon-gamma release assay (Quantiferon®-TB Gold in-Tube, QFT) for diagnosing LTBI in ESRD patients, after prolonged exposure to a highly contagious TB case in a haemodialysis unit. As a high number of patients presented erythema without induration in the TST response, this type of reaction was also analysed.

Method: The TST and QFT were simultaneously performed twelve weeks after the last possible exposure to a bacilliferous TB patient. If the first TST (TST-1) was negative, a second TST (TST-2) was performed 15 days later to detect a booster response. A comparison was made between the TST responses (including those cases with erythema without induration) and those for the QFT. The correlation with risk of infection and the concordance between tests were both analysed.

Results: A total of 52 patients fulfilled the inclusion criteria. Overall, 11 patients (21.2%) had a positive TST response: 3 for TST-1 and 8 for TST-2, and 18 patients (34.6%) showed a positive QFT response ($p = 0.065$). Erythema without induration was found in 3 patients at TST-1 and in a further 9 patients at TST-2. The three patients with erythema without induration in TST-1 had a positive TST-2 response. Concordance between TST and QFT was weak for TST-1 ($\kappa = 0.21$); it was moderate for overall TST ($\kappa = 0.49$); and it was strong if both induration and erythema ($\kappa = 0.67$) were considered.

Conclusions: In patients with ESRD, erythema without induration in the TST response could potentially be an indicator of *M. tuberculosis* infection. The QFT shows better accuracy for LTBI diagnosis than the TST.

Background

Patients with end-stage renal disease (ESRD) have an increased risk for developing tuberculosis (TB) disease. It is estimated that once the infection is produced, the risk for developing active TB is 6 to 25 times higher than that in the general population [1,2]. It is difficult to diagnose TB disease in such cases, as there are frequently extrapulmonar locations and nonspecific symptoms. Moreover, they present a high mortality rate [3].

Patients with *Mycobacterium tuberculosis* infection after a recent exposure also have an increased risk for developing TB disease [4,5]. Hence, the risk of TB infection and disease is even higher in ESRD patients after a recent exposure to *M. tuberculosis* [6]. It is therefore crucial to detect latent TB infection (LTBI) in these patients and to offer early treatment that can prevent progression to active TB disease.

The Tuberculin Skin Test (TST) is based on a delayed-type hypersensitivity response against a purified protein derivative (PPD) from *M. Tuberculosis,* and has for many years been the standard tool for detecting LTBI. However, the value of this test is limited by its lack of specificity, due to cross-reactive immune responses

---

* Correspondence: luis.anibarro.garcia@sergas.es
[1]Unidade de tuberculose, Servizo de Medicina Interna, Complexo hospitalario de Pontevedra (CHOP). SERGAS, Mourente s/n, Pontevedra 36071, Spain
Full list of author information is available at the end of the article

caused by previous bacille Calmette-Guérin (BCG) vaccination, or by infection with non-tuberculous mycobacteria [7]. Moreover, TST has shown limited sensitivity for detecting *M. tuberculosis* infection in ESRD patients [8-12].

T-cell Interferon-gamma (IFN-γ) release assays, known as IGRAs, are emerging as new screening tools for the detection of *M. tuberculosis* infection. They incorporate specific antigens from *M. tuberculosis* to induce secretion of INF-γ as a marker of immune responses by T-cells. Such specific antigens are absent in the BCG strains and in the majority of non-tuberculous mycobacteria, avoiding antigenic cross-reactivity. IGRAs also incorporate an internal positive control, so that a failure of response may reflect an underlying anergy [13]. Two commercial tests are available: the Quantiferon®-TB Gold In-Tube (QFT) test (Cellestis Ltd, Carnegie, Australia), which uses ELISA to detect INF-γ in the culture supernatants, and the T-SPOT®.TB (Oxford Immunotec, Abindgdon, UK), which is based on the enzyme-linked inmunospot (ELISpot) assay.

As there is no gold-standard method for the diagnosis of LTBI, it is difficult to estimate the value of IGRA (and TST) for detecting asymptomatic *M. tuberculosis* infection. Correlation with the degree of exposure has been proposed as a surrogate marker of infection. In ESRD patients, IGRAs have shown a better correlation with risk factors for *M. tuberculosis* infection, and their use has recently been proposed instead of the TST in the British Thoracic Society Guidelines for prevention and management of TB infection and disease in patients with chronic kidney disease [14]. In addition, IGRAs show better correlation than TST in TB outbreaks in immunocompetent populations [15]. However, very few studies have directly compared the TST with an IGRA in haemodyalisis patients after a prolonged exposure to a bacilliferous patient [16,17].

After the notification of the diagnosis of a bacilliferous pulmonary TB case in a nurse working at a dialysis unit, we evaluated patients with ESRD who were attending the dialysis centre, with the TST and an IGRA test (QFT). The aims of the present study were to compare the results of an IGRA with those for the TST in patients with ESRD after a TB outbreak at the dialysis centre, as well as to identify factors associated with positive test results. The study also included an 18-month follow-up of the cohort of patients.

Methods

Description of the outbreak

A 52-year-old nurse working in a renal dialysis unit was diagnosed with bacilliferous pulmonary TB. Five months before diagnosis, the worker developed a cough and dysphonia. For nine weeks prior to diagnosis, the worker was off sick and she did not attend the work place. Therefore, she had no more contact with the patients attending the dialysis unit. Microscopic examination of sputum was 4+ positive of acid-fast bacilli, indicating infectiousness, and sputum culture yielded *M. tuberculosis* susceptible to all first-line anti-TB medications. The nurse had been working at the renal dialysis unit on week-long alternating morning and evening shifts. Each shift consisted of four hours of contact time with patients on haemodialysis treatment. The worker was considered to be infectious 17 weeks before she left her workplace [4]. All patients who attended the dialysis unit during this period were considered to be contacts and were evaluated. Twelve weeks after the last possible exposure to *M. tuberculosis*, initial screening was undertaken by simultaneously performing the tuberculin skin test (TST) and the QFT assay.

Tuberculin skin test

Trained personnel performed the TST according to the Mantoux method following the standardized protocol: 0.1 mL (2 TU) of purified protein derivative of tuberculin RT 23 (Statens Serum Institute, Copenhagen, Denmark) was injected intradermally to the volar surface of the forearm. The TST results were read after 72 hours, and the maximum transverse diameter of the induration was estimated. TST values ≥ 5 mm were judged positive according to Spanish national guidelines [18]. A two-step TST was performed: if the first TST (TST-1) was negative (<5 mm induration), a second TST (TST-2) was conducted 15 days later to determine the development of a booster phenomenon. Patients without induration in the TST response, but with presence of erythema, were recorded as “erythema without induration”.

Interferon-gamma release assay

Peripheral blood was processed for the IGRA, using the QuantiFERON®-TB Gold in-Tube Assay (QFT) according to the manufacturer’s instructions (Cellestis Ltd, Carnegie, Australia). One ml of whole blood was added to each of the three QFT tubes: TB antigen (containing ESAT-6, CFP-10 and TB7.7 antigens); mitogen positive control (containing phytohemagglutinin); and a negative control. Samples were frozen and stored at −70°C until analysis. The cut-off value for a positive test was 0.35 IU/mL as recommended by the manufacturer. Blood was collected for QFT immediately before TST-1, and before the start of the haemodialysis session.

Data analysis

The following data were obtained: gender, age, body mass index (BMI), laboratory values (haemoglobin, urea, creatinine, albumin), BCG vaccination status, aetiology of renal disease, diabetes mellitus, immunosuppressive therapy, weeks of exposure to the index case, and the presence of old healed TB in chest radiography. BCG vaccination status was evaluated by the careful revision of the BCG scar by an expertise nurse or by the BCG vaccination certificate.

Follow-up

Patients with either a positive TST or a positive QFT response were considered for treatment for LTBI after active TB disease was excluded. No cases of active TB were found during the study period. The possibility of TB symptoms was carefully monitored throughout the long-term 18-month follow-up period.

Statistical analyses

Unless otherwise indicated, data are presented as mean ± standard deviation (SD). Associations between test results and variables were assessed by Pearson's χ^2-square test or Fisher's exact for categorical variables, and with Student's *t* test or Mann-Witney U rank test for continuous variables. All statistically significant factors ($P<0.05$) or clinically relevant factors with a $P<0.2$ determined by univariate analysis were included in models of multivariate logistic regression analysis. Comparison between test results was performed using the McNemar test. All reported *P* values were two-sided. Concordance between TST and QFT was assessed using the Kappa coefficient (κ). Kappa values indicate weak (≤ 0.40), moderate (0.41-0.60), strong (0.61-0.80), or excellent (>0.80) agreement. The SPSS statistical software for Windows (SPSS version 15.0; SPSS Inc, Chicago, IL, USA) was used in the analyses.

Institutional ethical approval was obtained from the Ethical Committee of Clinical Research (*Xunta de Galicia*, Spain) and written informed consent was obtained from the index case.

Results

Characteristics of the contacts

Initially, the contact investigation included 58 patients with ESRD attending the haemodialysis unit during the 17-week infectious period of the TB index case. One patient refused to be included in the study, and a previous positive TST was documented for five other patients, who were also excluded from further analysis. Hence, a total of 52 patients were included in the study.

The mean age of these patients was 62 ±16.8 years. Seven patients (13.5%) had been vaccinated with BCG. The aetiology of the end-stage renal failure was hypertensive nephrosclerosis (31%), diabetic nephropathy (19%), others (29%), and unknown (21%). Eight patients were receiving immunosuppressive therapy. Two patients recalled previous contact with a TB patient, but both had had a negative TST result.

Each patient attended the dialysis ward for about 4 hours for three days a week, except for one patient who had dialysis on a daily basis. A total of 46 patients (88.5%) had been in contact with the index case for the whole 17-week infectious period. The control unit (where the health personnel work) is located at the centre of the room, so the degree of exposure to the index case was considered to be almost identical for all patients. The other 6 patients with a shorter period of exposure had been in contact with the index case for 4, 6, 11, 12 (two patients) and 13 weeks each.

Other demographic, clinical characteristics and laboratory findings are shown in Table 1.

TST and QFT results

TST results

Of the 52 patients who had been in contact with the index case, 3 (5.8%) had a positive TST result for the first test (TST-1) (Figure 1). Fifteen days later, the remaining 49 patients had a second TST (TST-2) and the TST-2 was positive in 8 patients (16.3%). Overall, 11 patients (21.2%) had a final positive TST. In BCG-vaccinated individuals, the TST was positive in only 1 patient, and this was detected at TST-2. In the five patients with radiographic findings suggesting possible old healed TB, the TST was positive in three cases (one at TST-1 and the other two at TST-2). The induration measurement of tuberculin reaction was >10 mm in every patient with a positive result.

Three patients (6.1%) out of 49 with a negative TST-1 only had erythema. The frequency of patients showing erythema without induration even increased at the

Table 1 Basic demographic characteristics of 52 patients with end-stage renal disease from a haemodialysis unit, all contacts of a healthcare worker who had active pulmonary tuberculosis while working at the dialysis centre

CHARACTERISTICS	STUDY GROUP
Age in years, mean ± SD (range)	62 ± 16.8 (24 to 89)
Male gender, n (%)	31 (59.6)
BCG vaccination, yes, n (%)	7 (13.5)
BMI, mean ± SD	27.1 ± 5.0
Hemoglobin (mg/dL), mean ± SD	11.5 ± 1.4
Albumin level (mg/dL) mean ± SD	2.8 ± 0.4
Diabetes mellitus, yes, n (%)	8 (15.4)
Exposure to index case (weeks, %)	
17 week	46 (88.5)
< 17 weeks	6 (11.5)
Radiographic evidence of healed TB, n (%)	5 (9.6)

BMI: Body mass index.
Infectiousness of the Index Case was estimated for 17 weeks before last exposure.

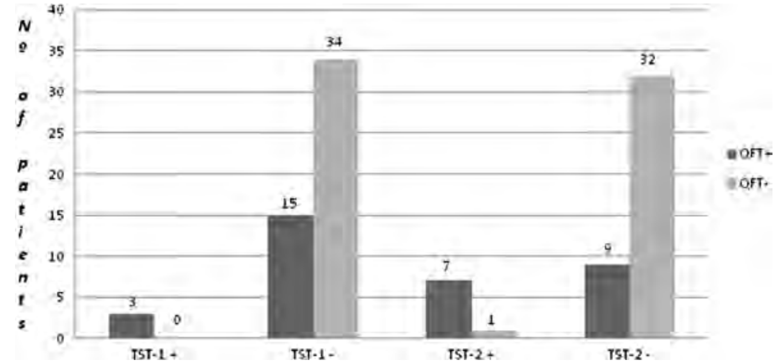

Figure 1 Results of the Tuberculin Skin Test and of the Quantiferon®-TB Gold in-Tube assay. TST-1: Tuberculin skin test result in the first-step testing. TST-2: Tuberculin skin test result in the second-step testing (15 days after TST-1). QFT: Quantiferon®-TB Gold in-tube assay.

second TST, with it being observed in 9 out of the 41 patients with a negative TST-2 (22.0%). It is worth noting that for the three patients with erythema but a negative TST-1, the second TST performed 15 days later was clearly positive (Table 2).

A positive TST result was not associated with any of the variables analysed, although the presence of an old healed TB in chest radiography approached statistical significance (p = 0.057).

QFT results

The QFT was performed at the same time as the TST-1 in all the 52 patients, and it was positive in 18 cases (34.6%). No indeterminate results were found. In BCG-vaccinated individuals, the QFT result was positive in only one patient, who had both negative TST-1 and TST-2 results. In the five patients with radiographic findings suggesting possible old healed TB, QFT was positive in three cases (all with positive TST results) and it was negative in the other two patients, who also had a negative TST result. A positive QFT result was only significantly associated with the presence of old healed TB in chest radiography (p = 0.043).

– Agreement between the TST and QFT results was found to be weak when taking into account only the initial TST (κ = 0.21), whereas it was moderate when both TST results (TST-1 and TST-2) were considered (κ = 0.49) (Table 3).

– Overall, the QFT was positive in 18 patients (34.6%), while the TST was positive in 11 patients (21.2%) (p = 0.065).

Table 2 Relationship between the tuberculin skin test results and erythema

	TST (+)	TST(–) erythema (+)	TST (–) erythema (–)
TST-1	3	3*	46
TST-2	8	9	32

TST-1: Tuberculin skin test result in the first-step testing.
TST-2: Tuberculin skin test result in the second-step testing (15 days after TST-1).
* The three patients with a negative TST-1 result and erythema boosted to a positive TST-2 result.

Value of erythema without induration in the TST response

As an unexpectedly high number of patients presented erythema without any induration in the TST response, we attempted to verify if erythema alone could be a valuable marker for LTBI. Of the 12 patients with erythema and no induration in the TST, 8 had a positive QFT result (2 out of 3 cases with a negative TST-1 result and 6 out of 9 cases with a negative TST-2 result). If both responses (the presence of erythema without induration or a positive TST result) were considered to be positive test results, agreement between the QFT and TST improved to κ = 0.67 (strong agreement), as shown in Table 4.

Contact follow-up

All contacts with a positive result for either the TST or the QFT were considered to have LTBI, after active TB was excluded. Preventive treatment with isoniazid for 9 months was considered for these patients.

Twenty patients (38.5%) were considered to have LTBI (two on the basis of a positive TST result, nine on the basis of a positive QFT result, and nine with positive results for both TST and QFT). Preventive treatment was started for 11 patients, of which 8 patients completed the treatment. Isoniazid treatment was stopped in two patients because of toxicity, and the final patient in this group died during LTBI treatment, from causes unrelated to either TB or isoniazid toxicity. The remaining 9 patients did not start LTBI treatment: four of them due to poor basal performance, while five declined to receive the treatment.

Eighteen months after the outbreak, none of the 20 patients with LTBI developed active TB. Five patients

Table 3 Agreement between the results of tuberculin skin testing with those for the Quantiferon®-TB Gold in-tube assay

			TST-1			Overall TST		
			negative	**positive**	**Total**	**negative**	**positive**	**Total**
QFT	negative	n	34	0	**34**	32	2	**34**
		(%)	65.4%	0%	**65.4%**	61.5%	3.8%	**65.4%**
	positive	n	15	3	**18**	9	9	**18**
		(%)	28.8%	5.8%	**34.6%**	17.3%	17.3%	**34.6%**
	Total	n	49	3	**52**	41	11	**52**
		(%)	94.2%	5.8%	**100%**	78.8%	21.2%	**100%**
kappa value				*0.21*			*0.49*	

TST-1: Tuberculin skin test result in the first-step testing.
Overall TST: Tuberculin skin test result after TST-1 and second-step testing (15 days after first testing).
QFT: Quantiferon®-TB Gold in-tube assay.

died during the follow-up period (one during LTBI treatment and four patients without treatment). No death was related to TB.

The remaining 32 patients with negative results for both QFT and TST were considered to be not infected, and did not receive LTBI treatment. After the 18-month follow-up period of close clinical monitoring, no case of active TB was found among this group. Four patients died during the follow-up period, none of the deaths were related to TB.

Discussion

The present study assessed the value of TST and QFT in haemodialysis patients after prolonged exposure to a highly contagious pulmonary TB patient. The results obtained showed three major findings. First, a single TST has low sensitivity in detecting LTBI and a two-step strategy must be carried out to gain sensitivity. Second, erythema alone (without induration) may be a valuable marker when interpreting TST in haemodialysis patients. And third, the QFT shows better sensitivity than the TST in detecting LTBI in haemodialysis patients.

Table 4 Agreement between the results of tuberculin skin testing and presence of erythema with those for the Quantiferon-TB Gold in-tube assay

			TST/Erythema		
			TST (−) Erythema (−)	**TST (+) or erythema (+)**	**Total**
QFT	**negative**	**n**	29	5	**34**
		%	55.8%	9.6%	**65.4%**
	positive	**n**	3	15	**18**
		%	5.8%	28.8%	**34.6%**
	total	**n**	32	20	**52**
		%	61.5%	38.5%	**100`**
kappa value				***0.67***	

TST: Tuberculin Skin Test.
QFT: Quantiferon®-TB Gold in-Tube assay.

TST has been shown to be unreliable in patients with advanced chronic kidney disease, and although a positive test may be useful for LTBI diagnosis, a negative one cannot be assumed to be a true negative [8,10,11]. Uraemia is a well-known risk factor for impaired immune cellular response [9,19], and this fact is decisive for both a lower sensitivity of the TST and a higher risk of progression from LTBI to TB disease [12]. It has been shown that immune cells can be activated in ESRD patients, but the functionality of these cells is impaired. This is especially true for the subpopulation of T helper 1 (TH1) lymphocytes, which are the cells mainly responsible for cellular immunity and delayed hypersensitivity responses. Moreover, there is a decrease in the number of B cells in a pro-inflammatory environment (complement activation, inflammatory cytokines), together with an imbalance in the ratio of TH1/TH2 lymphocytes [20]. The suppression of the immune TH1 status entails a higher rate of anergy, eventually leading to lower positive TST responses compared to the QFT results. Although limited by the absence of a gold-standard method to confirm LTBI, in our study QFT has shown a higher response than TST, which approaches statistical significance.

Two-step testing in TST has been shown to be crucial for LTBI diagnosis in patients with ESRD, in the absence of a known recent exposure to a contagious index case [21,22]. In our study, 8 patients with an initially negative TST had a second positive TST 15 days later; thereby, highlighting the importance of the booster effect in ESRD patients. The booster effect is believed to result from recall of waned cell-mediated immunity, akin to the anamnestic response. A first tuberculin test may boost cell-mediated immunity in patients with otherwise impaired immune response, such as patients with ESRD [23]. Several studies have addressed the booster phenomenon in ESRD patients without known recent exposure to a TB index case [21,22,24-26]. Cengiz et al. detected a boosted response in a second TST, performed seven days after a first TST, in 24.3% of patients on haemodialysis [22]. Similarly, Habesglu et al. found the booster phenomenon in 29.7% of patients undergoing haemodialysis treatment and with no epidemiologically recognised factors for LTBI [25]. Our study has addressed the booster response in the context of a recent exposure to a highly contagious TB index case. Therefore, it could be difficult to distinguish between a booster effect from a real conversion after the tuberculin "window period". Nevertheless, this is very unlikely, because both TST and QFT were performed 12 weeks after the last possible exposure to the Index Case, which would make very unlikely a conversion attributable to the "window period" [27]. Our findings support the view that two-step TST must be performed in patients with ESRD, even in the context of a recent exposure to *M. tuberculosis*.

An unexpected finding of our study was the high number of patients with erythema, but without induration, in the TST responses. Erythema without induration is not generally considered in the interpretation of the TST in most International Guidelines. However, some Japanese guidelines suggest taking erythema without induration into consideration when the measurement is over 20 mm [28]. In a contact tracing study carried out with 566 BCG-vaccinated school students in Japan, the erythema measurement was correlated with both the induration measurement and the degree of exposure to the index case. These results suggest that erythema (irrespective of the induration response) could have a significant value in the interpretation of the TST results. However, in this study, no concomitant IGRA testing was performed [29]. In our study, joint assessment of induration and erythema has shown better correlation with the QFT results than when only induration was taken into account in the TST response. All 3 patients with erythema, but with a negative result in the initial TST-1, developed a positive TST response 15 days later. Moreover, of the 9 patients with erythema without induration in the second TST, six (66.7%) had a positive QFT result. Overall, our results suggest that in patients with impaired cell-mediated immune response, such as patients with ESRD, erythema without induration could be indicative of a weak immune response to *M. tuberculosis* antigens, even though it did not yield skin induration. Our findings indicate that *M. tuberculosis* infection could be considered in patients with ESRD and with no induration erythema shown in the TST response, particularly in situations of high epidemiological risk of infection. Nevertheless, more studies and a higher number of patients than those presented in our study are required to fully verify this statement.

As there is no gold-standard method to confirm diagnosis of LTBI, the accuracy of tests for evaluating LTBI relies on indirect evidence of infection. There is increasing evidence that IGRA results have a better correlation with known risk factors for LTBI than the TST responses [13]. In addition, several studies have assessed this issue in patients with chronic kidney disease, indicating that for these groups of patients, IGRAs have a greater accuracy than TST in the diagnosis of LTBI [30-34]. However, only a few studies have compared TST and IGRA results in haemodialysis patients after a recent exposure to a bacilliferous TB patient [16,17]. Winthrop et al. found a better correlation with risk exposure using Quantiferon-TB-Gold® test (an older generation of QFT) than when using the TST after exposure to a pulmonary TB patient in a haemodialysis centre [16]. Yet, they found that the rates of positive results using the TST and the IGRA were not significantly different, whereas we found a value close to statistical significance ($p = 0.065$). The conclusion derived from the above cited study and from our current findings (using the new generation of QFT) is that IGRAs may offer greater accuracy for the diagnosis of LTBI in ESRD patients, after exposure to an infectious TB patient [14].

Our study has several limitations that require further comments. First, due to the limited number of patients included in the study, our results must be interpreted with caution, and larger series of patients are necessary to confirm our findings. This is especially true for the value of erythema, as very few studies have previously assessed this item. Second, as there is no gold-standard method for diagnosing true LTBI, it cannot be ruled out that higher positivity rates for the QFT could include some false positive results. Nevertheless, there is increasing evidence about the value of an IGRA as a marker for LTBI, and even as a marker for the risk of progression to active TB [35]. Finally, only one commercial IGRA (QFT) has been evaluated in our study. It has been suggested that the other commercially available IGRA (T-SPOT.TB®) may have an improved sensitivity in patients with immunodeficiency disorders [36]. There are several previous studies that have compared different commercially available IGRAs in ESRD patients [30,32,33]. In a Korean study comparing the performance of TST, QFT and T-SPOT.TB in patients undergoing haemodialysis, the positive rates were 23.5%, 45.9% and 60.4% respectively, suggesting a higher sensitivity for the T-SPOT.TB test. In addition, the frequency of indeterminate results was higher for the QFT compared with the T-SPOT.TB test [32]. In contrast, two other studies failed to demonstrate significantly better sensitivities with the T-SPOT.TB test than with the QFT: 47% vs. 40%, respectively, using an older generation of QFT in a Taiwanese study

[30], or 22% vs. 46%, respectively, in 62 Swiss patients deemed to have LTBI [33].

Conclusions

Our results indicate that the QFT shows better sensitivity than the TST in detecting LTBI in haemodialysis patients, after exposure to *M. tuberculosis*. Nevertheless, if the TST is used for detecting LTBI, a single TST result has low sensitivity and a two-step strategy must be performed to gain sensitivity.

Although the relatively small number of patients included in the present study limits, to some extent, the significance of the conclusions, it can still be emphasized that special care should be taken in patients with ESRD, who show erythema after the TST, because erythema alone (without induration) may be a marker of LTBI when interpreting TST in these patients.

Consent statement

Institutional ethical approval for the study was obtained from the Ethical Committee of Clinical Research (*Xunta de Galicia*, Spain) and written informed consent for publication was obtained from the index case. A copy of the written consent is available for review by the Series Editor of the journal.

Competing interests

The authors declare that they have no competing interests.

Authors' contributions

LA provided patient care and was responsible for data management, design of the study and drafting of the manuscript. MT and AP performed laboratory tests and were involved in writing the draft version. DF, MR, LP and MN made substantial contributions to the acquisition of data, participated in recruitment of subjects, provided patient care and were involved in writing the draft version. CV performed the statistical analysis. AGF revised the draft carefully for important intellectual content. All authors read and approved the final version of the manuscript.

Acknowledgements

We would like to thank the University of Vigo and *SUDOE-FEDER (IMMUNONET*-SOE1/P1/E014) for financial support.

Author details

[1]Unidade de tuberculose, Servizo de Medicina Interna, Complexo hospitalario de Pontevedra (CHOP). SERGAS, Mourente s/n, Pontevedra 36071, Spain. [2]Servizo de Microbioloxía, Complexo hospitalario de Pontevedra (CHOP). SERGAS, Mourente s/n, Pontevedra 36071, Spain. [3]Servizo de Nefroloxía, Complexo hospitalario de Pontevedra (CHOP). SERGAS, Mourente s/n, Pontevedra 36071, Spain. [4]Servizo de Neumoloxía, Complexo hospitalario de Pontevedra (CHOP). SERGAS, Mourente s/n, Pontevedra 36071, Spain. [5]Unidade de estatística. Universidade de Vigo, Campus de Lagoas, Marcosende, Vigo, Pontevedra 36310, Spain. [6]Área de Inmunoloxia, Centro de Investigaciones Biomédicas (CINBIO), Universidade de Vigo, Campus Lagoas Marcosende, Vigo, Pontevedra 36310, Spain.

Received: 28 November 2011 Accepted: 15 August 2012
Published: 20 August 2012

References

1. García-Leoni ME, Martín-Scapa C, Rodeño P, Valderrábano F, Moreno S, Bouza E: **High incidence of tuberculosis in renal patients.** *Eur J Clin Microbiol Infect Dis* 1990, **9**:283–285.
2. Sasaki S, Akiba T, Suenaga M, Tomura S, Yoshiyama N, Nakagawa S, Shoji T, Sasaoka T, Takeuchi J: **Ten years' survey of dialysis-associated tuberculosis.** *Nephron* 1979, **24**:141–145.
3. Segall L, Covic A: **Diagnosis of tuberculosis in dialysis patients: current strategy.** *Clin J Am Soc Nephrol* 2010, **5**:1114–1122.
4. National Tuberculosis Controllers Association, Centers for Disease Control and Prevention: **Guidelines for the investigation of contacts of persons with infectious tuberculosis. Recommendations from the National Tuberculosis Controllers Association and CDC.** *MMWR Recomm Rep* 2005, **54**:1–47.
5. Reichler MR, Reves R, Bur S, Thompson V, Mangura BT, Ford J, Valway SE, Onorato IM, Group CIS: **Evaluation of investigations conducted to detect and prevent transmission of tuberculosis.** *JAMA* 2002, **287**:991–995.
6. (CDC) CfDCaP: **Tuberculosis transmission in a renal dialysis center–Nevada, 2003.** *MMWR Morb Mortal Wkly Rep* 2004, **53**:873–875.
7. Santin M, Dominguez J: **Diagnosis of tuberculosis infection using interferon-gamma based assays.** *Enferm Infecc Microbiol Clin* 2011, **29**:26–33.
8. Shankar MS, Aravindan AN, Sohal PM, Kohli HS, Sud K, Gupta KL, Sakhuja V, Jha V: **The prevalence of tuberculin sensitivity and anergy in chronic renal failure in an endemic area: tuberculin test and the risk of post-transplant tuberculosis.** *Nephrol Dial Transplant* 2005, **20**:2720–2724.
9. Wauters A, Peetermans WE, Van den Brande P, De Moor B, Evenepoel P, Keuleers H, Kuypers D, Stas K, Vanwalleghem J, Vanrenterghem Y, Maes BD: **The value of tuberculin skin testing in haemodialysis patients.** *Nephrol Dial Transplant* 2004, **19**:433–438.
10. Woeltje KF, Mathew A, Rothstein M, Seiler S, Fraser VJ: **Tuberculosis infection and anergy in hemodialysis patients.** *Am J Kidney Dis* 1998, **31**:848–852.
11. Smirnoff M, Patt C, Seckler B, Adler JJ: **Tuberculin and anergy skin testing of patients receiving long-term hemodialysis.** *Chest* 1998, **113**:25–27.
12. Sester M, Sester U, Clauer P, Heine G, Mack U, Moll T, Sybrecht GW, Lalvani A, Köhler H: **Tuberculin skin testing underestimates a high prevalence of latent tuberculosis infection in hemodialysis patients.** *Kidney Int* 2004, **65**:1826–1834.
13. Diel R, Goletti D, Ferrara G, Bothamley G, Cirillo D, Kampmann B, Lange C, Losi M, Markova R, Migliori GB, *et al*: **Interferon-γ release assays for the diagnosis of latent Mycobacterium tuberculosis infection: a systematic review and meta-analysis.** *Eur Respir J* 2011, **37**:88–99.
14. Milburn H, Ashman N, Davies P, Doffman S, Drobniewski F, Khoo S, Ormerod P, Ostermann M, Snelson C, Committee BTSSoCCaJT: **Guidelines for the prevention and management of Mycobacterium tuberculosis infection and disease in adult patients with chronic kidney disease.** *Thorax* 2010, **65**:557–570.
15. Arend S, Thijsen S, Leyten E, Bouwman J, Franken W, Koster B, Cobelens F, van Houte A, Bossink A: **Comparison of two interferon-gamma assays and tuberculin skin test for tracing tuberculosis contacts.** *Am J Respir Crit Care Med* 2007, **175**:618–627.
16. Winthrop KL, Nyendak M, Calvet H, Oh P, Lo M, Swarbrick G, Johnson C, Lewinsohn DA, Lewinsohn DM, Mazurek GH: **Interferon-gamma release assays for diagnosing mycobacterium tuberculosis infection in renal dialysis patients.** *Clin J Am Soc Nephrol* 2008, **3**:1357–1363.
17. Connell DW, Singanayagam A, Charif R, George PM, Molyneaux PL, McCrudden C, Magtoto M, Harden E, Seneviratne SL, Duncan ND, Kon OM: **A comparison between interferon gamma release assays and the tuberculin skin test in the contact tracing of patients with chronic kidney disease.** *Thorax* 2011, **66**:729–730.
18. González-Martín J, García-García J, Anibarro L, Vidal R, Esteban J, Blanquer R, Moreno S, Ruiz-Manzano J: **[Consensus document on the diagnosis, treatment and prevention of tuberculosis].** *Enferm Infecc Microbiol Clin* 2010, **28**:297. e291-e220.
19. Touraine JL, Touraine F, Revillard JP, Brochier J, Traeger J: **T-lymphocytes and serum inhibitors of cell-mediated immunity in renal insufficiency.** *Nephron* 1975, **14**:195–208.
20. Alvarez-Lara MA, Carracedo J, Ramírez R, Martín-Malo A, Rodríguez M, Madueño JA, Aljama P: **The imbalance in the ratio of Th1 and Th2 helper lymphocytes in uraemia is mediated by an increased apoptosis of Th1 subset.** *Nephrol Dial Transplant* 2004, **19**:3084–3090.
21. Dogan E, Erkoc R, Sayarlioglu H, Uzun K: **Tuberculin skin test results and the booster phenomenon in two-step tuberculin skin testing in hemodialysis patients.** *Ren Fail* 2005, **27**:425–428.

22. Cengiz K, Seker A: **Boosted tuberculin skin testing in hemodialysis patients.** *Am J Infect Control* 2006, **34**:383–387.
23. Menzies D: **Interpretation of repeated tuberculin tests. Boosting, conversion, and reversion.** *Am J Respir Crit Care Med* 1999, **159**:15–21.
24. Akcay A, Erdem Y, Altun B, Usalan C, Agca E, Yasavul U, Turgan C, Caglar S: **The booster phenomenon in 2-step tuberculin skin testing of patients receiving long-term hemodialysis.** *Am J Infect Control* 2003, **31**:371–374.
25. Habesoğlu MA, Torun D, Demiroglu YZ, Karatasli M, Sen N, Ermis H, Ozdemir N, Eyuboglu FO: **Value of the tuberculin skin test in screening for tuberculosis in dialysis patients.** *Transplant Proc* 2007, **39**:883–886.
26. Soysal A, Toprak D, Koc M, Arikan H, Akoglu E, Bakir M: **Diagnosing latent tuberculosis infection in haemodialysis patients: T-cell based assay (T-SPOT.TB) or tuberculin skin test?** *Nephrol Dial Transplant* 2012, **27**:1645–1650.
27. Anibarro L, Trigo M, Villaverde C, Pena A, González-Fernández A: **Tuberculin skin test and interferon-γ release assay show better correlation after the tuberculin 'window period' in tuberculosis contacts.** *Scand J Infect Dis* 2011, **43**:424–429.
28. Koike R, Takeuchi T, Eguchi K, Miyasaka N, Rheumatology JCo: **Update on the Japanese guidelines for the use of infliximab and etanercept in rheumatoid arthritis.** *Mod Rheumatol* 2007, **17**:451–458.
29. Toivgoogiin A, Toyota M, Yasuda N, Ohara H: **Validity of using tuberculin skin test erythema measurement for contact investigation during a tuberculosis outbreak in schoolchildren previously vaccinated with BCG.** *J Epidemiol* 2005, **15**:56–64.
30. Lee SS, Chou KJ, Su IJ, Chen YS, Fang HC, Huang TS, Tsai HC, Wann SR, Lin HH, Liu YC: **High prevalence of latent tuberculosis infection in patients in end-stage renal disease on hemodialysis: Comparison of QuantiFERON-TB GOLD, ELISPOT, and tuberculin skin test.** *Infection* 2009, **37**:96–102.
31. Seyhan EC, Sökücü S, Altin S, Günlüoğlu G, Trablus S, Yilmaz D, Koksalan OK, Issever H: **Comparison of the QuantiFERON-TB Gold In-Tube test with the tuberculin skin test for detecting latent tuberculosis infection in hemodialysis patients.** *Transpl Infect Dis* 2010, **12**:98–105.
32. Chung WK, Zheng ZL, Sung JY, Kim S, Lee HH, Choi SJ, Yang J: **Validity of interferon-γ-release assays for the diagnosis of latent tuberculosis in haemodialysis patients.** *Clin Microbiol Infect* 2010, **16**:960–965.
33. Triverio PA, Bridevaux PO, Roux-Lombard P, Niksic L, Rochat T, Martin PY, Saudan P, Janssens JP: **Interferon-gamma release assays versus tuberculin skin testing for detection of latent tuberculosis in chronic haemodialysis patients.** *Nephrol Dial Transplant* 2009, **24**:1952–1956.
34. Passalent L, Khan K, Richardson R, Wang J, Dedier H, Gardam M: **Detecting latent tuberculosis infection in hemodialysis patients: a head-to-head comparison of the T-SPOT.TB test, tuberculin skin test, and an expert physician panel.** *Clin J Am Soc Nephrol* 2007, **2**:68–73.
35. Diel R, Loddenkemper R, Niemann S, Meywald-Walter K, Nienhaus A: **Negative and Positive Predictive Value of a Whole-Blood Interferon-{gamma} Release Assay for Developing Active Tuberculosis: An Update.** *Am J Respir Crit Care Med* 2011, **183**:88–95.
36. Piana F, Codecasa LR, Cavallerio P, Ferrarese M, Migliori GB, Barbarano L, Morra E, Cirillo DM: **Use of a T-cell-based test for detection of tuberculosis infection among immunocompromised patients.** *Eur Respir J* 2006, **28**:31–34.

doi:10.1186/1471-2334-12-195
Cite this article as: Anibarro *et al.*: Value of the tuberculin skin testing and of an interferon-gamma release assay in haemodialysis patients after exposure to *M. tuberculosis*. *BMC Infectious Diseases* 2012 **12**:195.

Available online at www.sciencedirect.com
ScienceDirect
Current Opinion in Biotechnology

Engineering human cells for *in vivo* secretion of antibody and non-antibody therapeutic proteins

David Sánchez-Martín, Laura Sanz and Luis Álvarez-Vallina

Purified proteins such as antibodies are widely used as therapeutic agents in clinical medicine. However, clinical-grade proteins for therapeutic use require sophisticated technologies and are extremely expensive to produce. *In vivo* secretion of therapeutic proteins by genetically engineered human cells may advantageously replace injection of highly purified proteins. The use of gene transfer methods circumvents problems related to large-scale production and purification and offers additional benefits by achieving sustained concentrations of therapeutic protein with a syngenic glycosylation pattern that make the protein potentially less immunogenic. The feasibility of the *in vivo* production of therapeutic proteins by diverse cells/tissues has now been demonstrated using different techniques, such as *ex vivo* genetically modified cells and *in vivo* gene transfer mediated by viral vectors.

Address
Molecular Immunology Unit, Hospital Universitario Puerta de Hierro, 28222 Majadahonda, Madrid, Spain

Corresponding author: Álvarez-Vallina, Luis (lalvarezv.hpth@salud.madrid.org)

Current Opinion in Biotechnology 2011, **22**:924–930

This review comes from a themed issue on
Pharmaceutical biotechnology
Edited by Luis Angel Fernández and Serge Muyldermans

Available online 22nd March 2011

0958-1669/$ – see front matter

DOI 10.1016/j.copbio.2011.03.001

Introduction

Most of the obstacles originally found in monoclonal antibody (mAb)-based therapy have been gradually overcome. The immunogenicity observed in the first mouse mAbs (human anti-mouse antibodies response, HAMA) was initially reduced by using chimeric (which, in turn, originated human anti-chimeric antibodies response, HACA) and humanized antibodies and now can be completely avoided by using fully human antibodies or human recombinant antibodies [1]. There is a plethora of different formats of human recombinant antibodies to choose from, each with some differences over the others in molecular weight, valence, fusion-partners, etc. Thus, half-life and tumour penetration, both pointed at as challenges for antibody-based therapy [2,3], can be fine-tuned by adjusting the format, size, valence, specificity, ligands, etc. (reviewed in [4]).

There remain, however, at least two major concerns: the sheer cost of therapy — partly derived from the costly production process, and the usually long and continued treatments — and the achievement of sustained plasma levels high enough to be effective and low enough so that they are not toxic [3]. Additional concerns arise from different glycosylation patterns (consequence of different expression technologies) that might affect the efficacy of the mAbs (stability, activity, biodistribution, etc.), as well as from the current dosage and administration that involves repeated high-dose bolus injections and a plasma concentration profile that ranges from sub-toxic to sub-therapeutic (Figure 1A).

In order to reduce costs — by avoiding the whole production process — whilst guaranteeing availability in the serum, it has been proposed to produce the antibodies *in vivo* as needed: either by *in vivo* gene modifying target cells or by *ex vivo* modification followed by the return of the cells into the body (Figure 1B). Whichever the alternative, not only the molecule secreted, but also the cell should comply with the original requisites: no immunogenicity, long half-life and effective plasma-levels.

In a pioneering work, Noel *et al.* demonstrated that several cell types (including skin fibroblasts, myogenic cells and hepatocytes), after retroviral gene transfer, could produce *in vivo* an anti-human thyroglobulin mAb used as a model system [5]. An obvious alternative was the use of hybridoma cells as mAb-producer cells, encapsulated in immunoprotective devices to avoid rejection [6]. This cell-based gene therapy approach seemed promising, but faced challenges unsolvable at the time, mainly the low serum levels attained and the short life span of the cells grafted. It took only four more years to obtain an alternative to increase antibody serum levels near 200-fold with the *in vivo* administration of an adenoviral vector coding for the anti-human thyroglobulin mAb [7]. In the same year, the recombinant antibody technology merged with the gene therapy when Sanz *et al.* showed that a single-chain fragment variable (scFv) antibody, secreted by gene-modified cells and directed against an extracellular matrix (ECM) component (laminin), prevented the establishment and growth of sub-cutaneous tumours in mice [8]. This anti-tumour effect was further improved combining a multi-merization strategy with the fusion of the anti-laminin scFv to an endogenous inhibitor of angiogenesis (endostatin) [9]. Afanasieva *et al.* produced evidence that a single systemic administration of recombinant adenovirus encoding a scFv against vascular endothelial growth factor

Figure 1

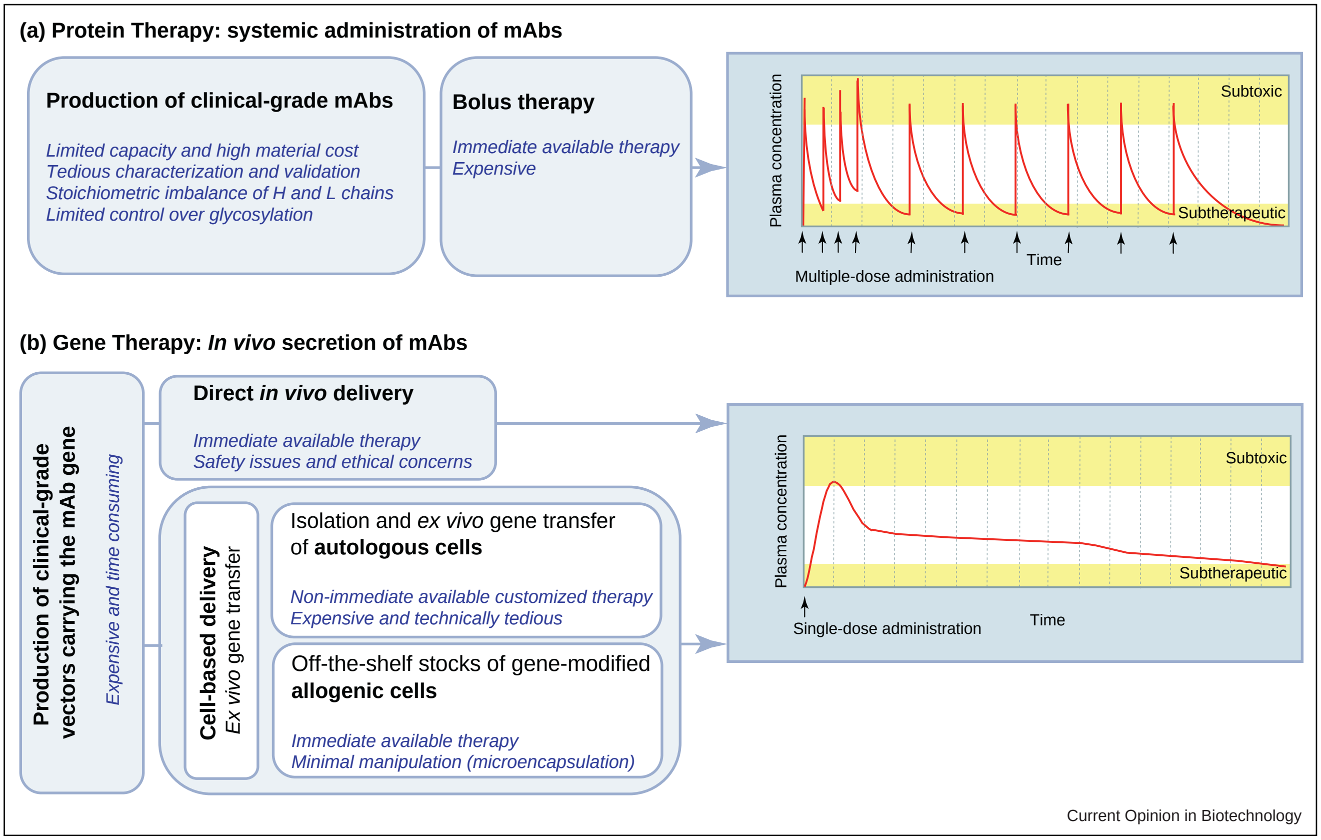

(a) Schematic diagram depicting some limitations associated with the production and use of clinical-grade mAbs, and a simulated pharmacokinetic profile of serum mAb levels after multiple intra-venous doses. **(b)** Schematic diagram of the different genetics strategies aimed at secreting mAbs *in vivo*, and a simulated pharmacokinetic profile of serum mAb levels after a single injection of *ex vivo* gene-modified human cells.

(VEGF) resulted in tumour inhibition and had a similar therapeutic effect as the frequent injections of high amounts of purified anti-VEGF scFv [10]. Alternatives to anti-VEGF antibodies have also been explored, such as expressing instead a full-length VEGFR2-neutralizing mAb using a recombinant adeno-associated virus (AAV) vector that codes for the heavy and light chains of the antibody in the same ORF, spaced by a furin cleavage site and the sequence of the self-processing peptide 2A [11]. This daedal approach produced therapeutic levels of the full-length antibody and the equimolar expression of the heavy and light chains.

In vivo gene therapy: seeking a balance between efficacy and safety

Not surprisingly, the targets most widely used in passive mAb anti-tumour therapy — the VEGF and the human epidermal growth-factor receptor type 2 (HER2) — are also two main targets in gene therapy: Watanabe *et al.* have extensively worked in anti-VEGF gene therapy, and have so far proved that adenoviral vectors and rAAV that codify for a full-length anti-VEGF mAb equivalent to bevacizumab are able to reduce tumour growth, increase survival and reduce metastasis in tumour xenografts models; moreover, they have also suggested its use as a therapy for high-permeability pulmonary oedema [12–14]. Targeting HER2 seems also very promising. Sustained high serum levels (over 1 mg/ml) of a full-length anti-HER2 mAb have been reported after intra-muscular administration of an AAV vector. This strategy was able not only to inhibit tumour growth when AAV was administered before tumour challenge, but also to show anti-tumour efficacy against pre-established tumours [15•]. Also, therapeutic levels of an anti-HER2 antibody have been documented after a single dose of an AAV vector based on the non-human primate AAV serotype rh.10, which reduced tumour growth and increased the survival of mice bearing HER2 positive tumours [16]. Systemic administration of an adenoviral vector has also been used to deliver *in vivo* an immunotoxin comprising an anti-HER2 scFv as targeting moiety [17•]. A different strategy for cancer therapy used a systemically administered lentiviral vector for the *in vivo* production of a full-length mAb directed against the extracellular moiety of the human Met receptor. This approach resulted in an inhibitory activity derived not only from the antibody-induced cleavage of Met expressed at the cell surface, but also from the interference of the mAb with the nascent Met receptor that ultimately results in lower levels of the mature form at the cell surface, a benefit that could not be obtained with standard mAb therapy [18]. However, this approach led to a partial activation of the Met kinase due to antibody-mediated receptor homodimerization, which motivated the authors to design a monovalent Fab version of the same mAb [19].

The resurgence of *ex vivo* gene therapy

In the past years, the use of *ex vivo* gene-modified cells has reemerged due to the combination of two main factors: firstly, viral vectors still need further improvement and secondly, the initial restrictions have been mostly overcome. Adenovirus that do not integrate tend to lower the expression with time, whereas lentiviral vectors that promote the integration of the transgene do it so in an unpredictable pattern which raises safety issues (regarding insertional mutagenesis) and ethical concerns. In addition, viral vectors can elicit an immune response against viral particles or gene products, leading to decreased efficiency of gene transfer [20]. Furthermore, there are now multiple cell types available that have shown long survival times (encapsulated or not), and the serum levels obtained seem to achieve the therapeutic effect. Compte *et al.* transduced human peripheral blood lymphocytes (PBL) with a lentiviral vector to secrete a bispecific anti-CEA × anti-CD3 diabody, which reduced the tumour growth [21] whilst Frank *et al.* overcame the limited penetration of mAbs in the tumour by combining an adenoviral vector that codifies for an anti-HER2 antibody with the tumour tropism of neural stem cells (NSCs), thus rendering it unnecessary the systemic administration of the adenoviral vector [22]. There remains, however, the risk of developing immune response against the viral vector (*in vivo*), the transgene (both, *in vivo* and *ex vivo*) [23,24], and it has been recently reported an immune response against vector-encoded epitopes expressed by the gene-modified cells (independently of the transgene) that should be carefully investigated [25]. These risks raise again the concern of the vector used for gene therapy. Some authors are reporting promising procedures to gene-modify cells using pharmaceutical-grade plasmid vectors that are non-pathogenic and as effective as viral vectors though faster, cheaper and with lower toxicity and immunogenicity [25].

Although NSCs seem promising, the cell type most widely used as a gene therapy cell vehicle is the mesenchymal stem cell (MSC). Compte *et al.* demonstrated that lentiviral-transduced MSCs to express a bispecific anti-CEA × anti-CD3 diabody embedded in a synthetic ECM scaffold supported the release of functional diabody into the bloodstream at detectable levels and inhibited growth of sub-cutaneous human colon cancer xenografts in the presence of systemically administered human PBLs [26•]. Going one step further, the genetic modification of human endothelial cells allowed the formation of neovessels expressing the therapeutic protein (anti-CEA × anti-CD3 diabody) that connected with the host vascular bed and secreted therapeutic antibody levels directly into the blood stream [27].

Even though recombinant antibodies, gene therapy and tumour therapy often go together, there are several works broadening the scope of diseases amenable for the combination of recombinant antibodies and gene therapy (Table 1), such as the neutralization of the West Nile

Table 1

***In vivo* secretion of therapeutic antibodies.**

Target	Format	Cell vehicle	Route of administration	Disease model	Ref.
Cell-based therapy: ex vivo gene transfer:					
CEA × CD3	Diabody	MSCs (h)	s.c. synthetic scaffold	Colon carcinoma (h)	[26•]
CEA × CD3	Diabody	HUVEC	s.c. Matrigel implant	Colon carcinoma (h)	[27]
HER2	IgG1	NSC (h)	i.v.	Fat pad breast cancer (h)	[22]

Target	Format	Viral vector	Route of administration	Disease model	Ref.
Direct delivery: in vivo gene transfer:					
RSV	IgG1	Adenovirus	i.v.	RSV infection	[29]
37/67 kDa laminin receptor	scFv	AAV	Intra-cerebral	Prion disease	[32]
West Nile virus	scFv–Fc	Adenovirus	i.p.	WNV challenge	[28]
Met	IgG2a	Lentivirus	i.v./i.t.	Colon carcinoma (h)	[18]
EGFR	IgG1/k	AAV	i.m.	Squamous cell carcinoma (h)	[15•]
HER2	scFv–toxin	Adenovirus	i.t.	Several erb2(+) (h)	[17•]
Y. pestis V antigen	IgG2b	Adenovirus	i.v.	*Yersinia pestis* challenge	[30]
Y. pestis V antigen	scFv	Adenovirus	i.v.	*Yersinia pestis* challenge	[31]
VEGF	IgG1	Adenovirus	Intra-tracheal	Pulmonary oedema	[12]
VEGF	IgG1	AAV	Intra-pleural	Lung metastasis	[13]
HER2	IgG1	AAV	i.v.	Non-small cell lung cancer (h)	[16]

Abbreviations: AAV, adeno-associated virus; h, human; s.c., sub-cutaneous; i.v., intra-venous; i.t., intra-tumoral; i.p., intra-peritoneal; i.m., intra-muscular.

virus (WNV) after adenovirus-mediated gene transfer of a scFv–Fc fusion derived from a neutralizing antibody [28], or the protective immunity observed in mice against the respiratory syncytial virus (RSV) followed after *in vivo* administration of an adenoviral vector encoding the murine equivalent to palivizumab (a humanized mAb currently in the clinic [29]). The use of adenovirus-codifying antibodies against lethal pathogens has also been proposed as a preventive treatment when no vaccine is available. Although this can certainly raise other ethical concerns, Sofer-Podesta *et al.* showed that pre-treatment of mice with adenovirus coding for a *Yersinia pestis* neutralizing antibody was able to provide with partial protection [30]. This was further improved in a later work using the variable domains from the affinity-maturated scFv [31]. The treatment of prion diseases using scFv-codifying AAV has been suggested as a novel option [32], although it seems to be still far away from becoming a suitable option.

Toward therapeutical neo-organs

Cell-based gene therapy has been proposed as an alternative for the delivery of many other gene products, not only antibodies (Table 2). Its use has been suggested for the therapy of diverse diseases, ranging from ischemia and heart damage [33–38] or bone regeneration [39–45] to diabetes [46,47•], anaemia [48], lung injury [49], retinal degeneration [50] and, of course, for the treatment of cancer [51–57,58•,59–61]. Most of the approaches use free cells, locally implanted or systemically delivered, that can take advantage of the homing properties of these cells. However, recent works suggest that MSCs could play a role in tumour growth and metastasis due to their immunosuppressive and proangiogenic properties, implying a

Table 2

***In vivo* secretion of non-antibody molecules by *ex vivo* gene-modified cells.**

Gene	Cell vehicle	Route of administration	Disease model	Ref.
Angiopoietin-1	MSCs	i.v. (jugular vein)	Acute lung injury	[49]
b-Glucuronidase	MSCs	i.p.	Mucopolysaccharidosis type VII	[67]
BMP-2	BMSCs	Biopolymer	Skull repair	[41]
BMP-2	MSCs	Intra-lesional	Periodontal regeneration	[39]
BMP-2	MSCs	i.v.	Osteopenia	[43]
BMP-2	Fibroblasts	Intra-lesional	Craniotomy defect	[45]
BMP-2 + VEGF	MSCs	i.v.	Segmental bone defect	[44]
BMP-6	MSCs	i.m. (paravertebral muscle)	Posterior spinal fusion	[40]
EPO	MSCs	Matrigel scaffold, s.c.	Anaemia	[48]
EPO	Myoblasts	e-c, s.c.	N/A	[68]
Flt-1 (soluble)	MSCs	i.v.	Lung metastasis	[53]
GDNF	ES	Intra-vitreous	Retinal degeneration	[50]
IFN-a	MSCs	i.v.	Lung metastasis	[55]
IFN-b	MSCs	i.v.	Lung metastasis	[56]
IGF-1	MSCs	Intra-myocardial	Coronary artery occlusion	[33]
IGF-I R (soluble)	MSCs	Matrigel scaffold, s.c.	Liver metastases	[61]
IL-10	MSCs	i.v.	Collagen-induced arthritis	[69]
IL-12	MSCs	i.v.	Lymph node metastasis	[70]
IL-12	MSCs	Matrigel scaffold, s.c.	Breast cancer	[51]
IL-12	MSCs	p.t.	Glioma	[57]
Insulin	Hepatocytes	i.h.	Diabetic pigs	[47•]
Insulin	MSCs	i.p./i.h.	Diabetic mice	[46]
OPG	NSCs	i.v.	Neuroblastoma bone metastasis	[60]
PEX	MSCs	Encapsulated cells, p.t.	Glioblastoma	[64••]
Relaxin	HSCs	i.t.	Breast cancer	[58•]
sFlt-1	MDSCs	Intra-lesional	Articular cartilage repair	[42]
TRAIL	MSCs	i.t.	Glioblastoma	[54]
TRAIL	MSCs	i.v.	Lung metastasis	[59]
TRAIL	MSCs	Intra-craneal	Glioma	[71]
uPA antagonist	MSCs	Co-injection	Osteolytic prostate cancer	[52]
VEGF	Fibroblasts	Intra-myocardial	Cardiac dysfunction	[37]
VEGF	NSCs	Intra-lesional	Spinal cord injury	[72]
VEGF	Fibroblasts	Flap area, wound area	Ischemic flap model	[34]
VEGF	MSCs	i.m.	Hindlimb ischemia	[38]
VEGF	CHO cells	e-c, intra-myocardial	Ischemic myocardium	[73]
VEGF and angipoietin-1	MSCs	i.v.	Cerebral ischemia	[35]
VEGF and angipoietin-1	EPCs	i.v.	Ischemic hind limb	[36]

Abbreviations: s.c., sub-cutaneous; i.v., intra-venous; i.t., intra-tumoral; p.t., peritumoral; i.p., intra-peritoneal; i.h. intra-hepatic; m-e, matrix-embedded; e-c, encapsulated cells, MSC: mesenchymal stem cells, NSC: neural stem cells, HSC: haematopoietic stem cells, MDSC: muscle-derived stem cells, BMSC: bone-marrow stem cells, EPC: endothelial progenitor cell, ES: embryonic stem cells.

potential risk in the use of MSCs in tumour-targeting strategies [62,63]. All in all, to deliver a therapeutic protein, it is sometimes preferred the entrapment of the gene-modified cells in a non-immunogenic synthetic ECM scaffold that allows the free exchange of nutrients and waste products, and also deliver secreted factors into the circulation. Safety of entrapped cells has been recently tested in a series of murine MSC-scaffold combinations and showed that the implanted cells did not spread to other organs [26•]. Goren *et al.* recently presented a hypoimmunogenic platform for the delivery of the hemopexin-like protein based on micro-encapsulated MSC in alginate-poly-L-lysine [64••] and there is currently a vast number of choices for the encapsulation (thoroughly reviewed by Hernandez *et al.* [65•]) that could be readily adapted to accommodate any of the strategies already proposed.

Concluding remarks

In vivo production of antibody and non-antibody-based molecules results in effective and persistent levels of therapeutic protein with syngenic glycosylation patterns, making the proteins potentially less immunogenic and better tolerated. Direct *in vivo* gene therapy offers the advantage of simplicity as one single recombinant viral or non-viral vector could be useful for different patients (Figure 1A). Nonetheless, the use of viruses *in vivo*, albeit modified, still raises questions about safety and immunogenicity. The same applies to non-viral vectors (e.g. plasmid DNA) used *in vivo* plus the short-term expression achieved. *Ex vivo* modification of the cells, on the other hand, can be carried out *in vitro*, under controlled and reproducible conditions, avoiding most of the concerns associated with viral vectors. Autologous cells have the advantage to cause no immune response and therefore are recommended for cell-based gene delivery strategies. However, that would mean that each patient had some cells removed, *ex vivo* modified, screened, amplified, and returned to the host; this is extremely expensive and impossible in some patients. The only potential cost-effective method to bring this approach to the clinical setting would imply the use of stocks of genetically modified allogenic cells ready to be applied in a series of patients. To protect these cells from the immune system and to maintain the survival of the cell inoculum, encapsulation of such cells is a feasible way (Figure 1B). Cell encapsulation offers additional safety and versatility as the cell capsule could be easily removed once the treatment has finished, or in the event of complications in the treatment. Besides, cells should be carefully selected so that they are susceptible for gene modification and so that no further modifications are needed, thus long lasting cells are preferred. One step further is the use not only of amalgamated cells, but cells organized in a tissue-like or organ-like structure where cells have direct access to the blood vessels or the target organ. In this aspect, MSCs are very attractive, as they are currently being used in the clinic (unmodified) for the treatment of unrelated diseases [66], and gene therapy could provide additional or alternative benefits to standard therapy.

Acknowledgements

This study was supported by grants from the Ministerio de Ciencia e Innovación (BIO2008-03233 and PSE-01000-2009-11), the Comunidad Autónoma de Madrid (S-BIO-0236-2006), and the European Union (SUDOE-FEDER. IMMUNONET-SOE1/P1/E014) to L.A-V.; and from the Fondo de Investigación Sanitaria/Instituto de Salud Carlos III (PI08/90856 and PS09/00227) to L.S. D.S-M. was supported by a Comunidad Autónoma de Madrid/Fondo Social Europeo training grant (FPI-000531).

References and recommended reading

Papers of particular interest, published within the period of review, have been highlighted as:

- • of special interest
- •• of outstanding interest

1. Zhang Q, Chen G, Liu X, Qian Q: **Monoclonal antibodies as therapeutic agents in oncology and antibody gene therapy**. *Cell Res* 2007, **17**:89-99.
2. Reichert JM, Rosensweig CJ, Faden LB, Dewitz MC: **Monoclonal antibody successes in the clinic**. *Nat Biotechnol* 2005, **23**:1073-1078.
3. Samaranayake H, Wirth T, Schenkwein D, Raty JK, Yla-Herttuala S: **Challenges in monoclonal antibody-based therapies**. *Ann Med* 2009, **41**:322-331.
4. Cuesta AM, Sainz-Pastor N, Bonet J, Oliva B, Alvarez-Vallina L: **Multivalent antibodies: when design surpasses evolution**. *Trends Biotechnol* 2010, **28**:355-362.
5. Noel D, Pelegrin M, Marin M, Biard-Piechaczyk M, Ourlin JC, Mani JC, Piechaczyk M: **In vitro and in vivo secretion of cloned antibodies by genetically modified myogenic cells**. *Hum Gene Ther* 1997, **8**:1219-1229.
6. Pelegrin M, Marin M, Noel D, Del Rio M, Saller R, Stange J, Mitzner S, Gunzburg WH, Piechaczyk M: **Systemic long-term delivery of antibodies in immunocompetent animals using cellulose sulphate capsules containing antibody-producing cells**. *Gene Ther* 1998, **5**:828-834.
7. Noel D, Pelegrin M, Kramer S, Jacquet C, Skander N, Piechaczyk M: **High in vivo production of a model monoclonal antibody on adenoviral gene transfer**. *Hum Gene Ther* 2002, **13**:1483-1493.
8. Sanz L, Kristensen P, Blanco B, Facteau S, Russell SJ, Winter G, Alvarez-Vallina L: **Single-chain antibody-based gene therapy: inhibition of tumour growth by in situ production of phage-derived human antibody fragments blocking functionally active sites of cell-associated matrices**. *Gene Ther* 2002, **9**:1049-1053.
9. Sanchez-Arevalo Lobo VJ, Cuesta AM, Sanz L, Compte M, Garcia P, Prieto J, Blanco FJ, Alvarez-Vallina L: **Enhanced antiangiogenic therapy with antibody–collagen XVIII NC1 domain fusion proteins engineered to exploit matrix remodeling events**. *Int J Cancer* 2006, **119**:455-462.
10. Afanasieva TA, Wittmer M, Vitaliti A, Ajmo M, Neri D, Klemenz R: **Single-chain antibody and its derivatives directed against vascular endothelial growth factor: application for antiangiogenic gene therapy**. *Gene Ther* 2003, **10**:1850-1859.
11. Fang J, Qian JJ, Yi S, Harding TC, Tu GH, VanRoey M, Jooss K: **Stable antibody expression at therapeutic levels using the 2A peptide**. *Nat Biotechnol* 2005, **23**:584-590.
12. Watanabe M, Boyer JL, Crystal RG: **Genetic delivery of bevacizumab to suppress vascular endothelial growth factor-induced high-permeability pulmonary edema**. *Hum Gene Ther* 2009, **20**:598-610.
13. Watanabe M, Boyer JL, Crystal RG: **AAVrh.10-mediated genetic delivery of bevacizumab to the pleura to provide local anti-VEGF to suppress growth of metastatic lung tumours**. *Gene Ther* 2010, **17**:1042-1051.

14. Watanabe M, Boyer JL, Hackett NR, Qiu J, Crystal RG: **Genetic delivery of the murine equivalent of bevacizumab (avastin), an anti-vascular endothelial growth factor monoclonal antibody, to suppress growth of human tumours in immunodeficient mice**. *Hum Gene Ther* 2008, **19**:300-310.

15. • Ho DT, Wykoff-Clary S, Gross CS, Schneider D, Jin F, Kretschmer PJ, Hermiston TW: **Growth inhibition of an established A431 xenograft tumour by a full-length anti-EGFR antibody following gene delivery by AAV**. *Cancer Gene Ther* 2009, **16**:184-194.

The authors report clinically compatible serum levels of full-length antibody after incorporating the Furin/2A technology to an AAV intramuscular delivered.

16. Wang G, Qiu J, Wang R, Krause A, Boyer JL, Hackett NR, Crystal RG: **Persistent expression of biologically active anti-HER2 antibody by AAVrh.10-mediated gene transfer**. *Cancer Gene Ther* 2010, **17**:559-570.

17. • Liu X, Wu J, Zhang S, Li C, Huang Q: **Novel strategies to augment genetically delivered immunotoxin molecular therapy for cancer therapy**. *Cancer Gene Ther* 2009, **16**:861-872.

This paper shows an effective therapy in a mouse model of human gastric carcinoma mediated by the intratumoral delivery of Ad-e23(scFv)-PE40 immunotoxin directed against c-erb-2/Her-2.

18. Vigna E, Pacchiana G, Mazzone M, Chiriaco C, Fontani L, Basilico C, Pennacchietti S, Comoglio PM: **"Active" cancer immunotherapy by anti-Met antibody gene transfer**. *Cancer Res* 2008, **68**:9176-9183.

19. Pacchiana G, Chiriaco C, Stella MC, Petronzelli F, De Santis R, Galluzzo M, Carminati P, Comoglio PM, Michieli P, Vigna E: **Monovalency unleashes the full therapeutic potential of the DN-30 anti-Met antibody**. *J Biol Chem* 2010, **285**:36149-36157.

20. Nayak S, Herzog RW: **Progress and prospects: immune responses to viral vectors**. *Gene Ther* 2010, **17**:295-304.

21. Compte M, Blanco B, Serrano F, Cuesta AM, Sanz L, Bernad A, Holliger P, Alvarez-Vallina L: **Inhibition of tumour growth in vivo by in situ secretion of bispecific anti-CEA × anti-CD3 diabodies from lentivirally transduced human lymphocytes**. *Cancer Gene Ther* 2007, **14**:380-388.

22. Frank RT, Edmiston M, Kendall SE, Najbauer J, Cheung CW, Kassa T, Metz MZ, Kim SU, Glackin CA, Wu AM *et al.*: **Neural stem cells as a novel platform for tumour-specific delivery of therapeutic antibodies**. *PLoS ONE* 2009, **4**:e8314.

23. Riddell SR, Elliott M, Lewinsohn DA, Gilbert MJ, Wilson L, Manley SA, Lupton SD, Overell RW, Reynolds TC, Corey L *et al.*: **T-cell mediated rejection of gene-modified HIV-specific cytotoxic T lymphocytes in HIV-infected patients**. *Nat Med* 1996, **2**:216-223.

24. Fontana R, Bregni M, Cipponi A, Raccosta L, Rainelli C, Maggioni D, Lunghi F, Ciceri F, Mukenge S, Doglioni C *et al.*: **Peripheral blood lymphocytes genetically modified to express the self-tumour antigen MAGE-A3 induce antitumor immune responses in cancer patients**. *Blood* 2009, **113**:1651-1660.

25. Lamers CH, Willemsen R, van Elzakker P, van Steenbergen-Langeveld S, Broertjes M, Oosterwijk-Wakka J, Oosterwijk E, Sleijfer S, Debets R, Gratama JW: **Immune responses to transgene and retroviral vector in patients treated with ex vivo-engineered T cells**. *Blood* 2011, **117**:72-82.

26. • Compte M, Cuesta AM, Sanchez-Martin D, Alonso-Camino V, Vicario JL, Sanz L, Alvarez-Vallina L: **Tumour immunotherapy using gene-modified human mesenchymal stem cells loaded into synthetic extracellular matrix scaffolds**. *Stem Cells* 2009, **27**:753-760.

The authors present a scaffold of MSCs that systemically secrets a bispecific diabody able to exert an effective antitumor response in distant locations.

27. Compte M, Alonso-Camino V, Santos-Valle P, Cuesta AM, Sanchez-Martin D, Lopez MR, Vicario JL, Salas C, Sanz L, Alvarez-Vallina L: **Factory neovessels: engineered human blood vessels secreting therapeutic proteins as a new drug delivery system**. *Gene Ther* 2010, **17**:745-751.

28. Pereboev A, Borisevich V, Tsuladze G, Shakhmatov M, Hudman D, Kazachinskaia E, Razumov I, Svyatchenko V, Loktev V, Yamshchikov V: **Genetically delivered antibody protects against West Nile virus**. *Antiviral Res* 2008, **77**:6-13.

29. Skaricic D, Traube C, De B, Joh J, Boyer J, Crystal RG, Worgall S: **Genetic delivery of an anti-RSV antibody to protect against pulmonary infection with RSV**. *Virology* 2008, **378**:79-85.

30. Sofer-Podesta C, Ang J, Hackett NR, Senina S, Perlin D, Crystal RG, Boyer JL: **Adenovirus-mediated delivery of an anti-V antigen monoclonal antibody protects mice against a lethal *Yersinia pestis* challenge**. *Infect Immun* 2009, **77**:1561-1568.

31. Van Blarcom TJ, Sofer-Podesta C, Ang J, Boyer JL, Crystal RG, Georgiou G: **Affinity maturation of an anti-V antigen IgG expressed in situ through adenovirus gene delivery confers enhanced protection against *Yersinia pestis* challenge**. *Gene Ther* 2010, **17**:913-921.

32. Zuber C, Mitteregger G, Schuhmann N, Rey C, Knackmuss S, Rupprecht W, Reusch U, Pace C, Little M, Kretzschmar HA *et al.*: **Delivery of single-chain antibodies (scFvs) directed against the 37/67 kDa laminin receptor into mice via recombinant adeno-associated viral vectors for prion disease gene therapy**. *J Gen Virol* 2008, **89**:2055-2061.

33. Haider H, Jiang S, Idris NM, Ashraf M: **IGF-1-overexpressing mesenchymal stem cells accelerate bone marrow stem cell mobilization via paracrine activation of SDF-1alpha/CXCR4 signaling to promote myocardial repair**. *Circ Res* 2008, **103**:1300-1308.

34. Spanholtz T, Maichle A, Niedworok C, Stoeckelhuber BM, Kruger S, Wedel T, Aach T, Middeler G, Hellwig-Burgel T, Bader A *et al.*: **Timing and targeting of cell-based VEGF165 gene expression in ischemic tissue**. *J Surg Res* 2009, **151**:153-162.

35. Toyama K, Honmou O, Harada K, Suzuki J, Houkin K, Hamada H, Kocsis JD: **Therapeutic benefits of angiogenetic gene-modified human mesenchymal stem cells after cerebral ischemia**. *Exp Neurol* 2009, **216**:47-55.

36. Yu JX, Huang XF, Lv WM, Ye CS, Peng XZ, Zhang H, Xiao LB, Wang SM: **Combination of stromal-derived factor-1alpha and vascular endothelial growth factor gene-modified endothelial progenitor cells is more effective for ischemic neovascularization**. *J Vasc Surg* 2009, **50**:608-616.

37. Goncalves GA, Vassallo PF, dos Santos L, Schettert IT, Nakamuta JS, Becker C, Tucci PJ, Krieger JE: **Intramyocardial transplantation of fibroblasts expressing vascular endothelial growth factor attenuates cardiac dysfunction**. *Gene Ther* 2010, **17**:305-314.

38. Yang F, Cho SW, Son SM, Bogatyrev SR, Singh D, Green JJ, Mei Y, Park S, Bhang SH, Kim BS *et al.*: **Genetic engineering of human stem cells for enhanced angiogenesis using biodegradable polymeric nanoparticles**. *Proc Natl Acad Sci U S A* 2010, **107**:3317-3322.

39. Chen YL, Chen PK, Jeng LB, Huang CS, Yang LC, Chung HY, Chang SC: **Periodontal regeneration using ex vivo autologous stem cells engineered to express the BMP-2 gene: an alternative to alveolaplasty**. *Gene Ther* 2008, **15**:1469-1477.

40. Sheyn D, Pelled G, Zilberman Y, Talasazan F, Frank JM, Gazit D, Gazit Z: **Nonvirally engineered porcine adipose tissue-derived stem cells: use in posterior spinal fusion**. *Stem Cells* 2008, **26**:1056-1064.

41. Chang SC, Lin TM, Chung HY, Chen PK, Lin FH, Lou J, Jeng LB: **Large-scale bicortical skull bone regeneration using ex vivo replication-defective adenoviral-mediated bone morphogenetic protein-2 gene-transferred bone marrow stromal cells and composite biomaterials**. *Neurosurgery* 2009, **65**:75-81 discussion 81–73.

42. Kubo S, Cooper GM, Matsumoto T, Phillippi JA, Corsi KA, Usas A, Li G, Fu FH, Huard J: **Blocking vascular endothelial growth factor with soluble Flt-1 improves the chondrogenic potential of mouse skeletal muscle-derived stem cells**. *Arthritis Rheum* 2009, **60**:155-165.

43. Kumar S, Nagy TR, Ponnazhagan S: **Therapeutic potential of genetically modified adult stem cells for osteopenia**. *Gene Ther* 2010, **17**:105-116.

44. Kumar S, Wan C, Ramaswamy G, Clemens TL, Ponnazhagan S: **Mesenchymal stem cells expressing osteogenic and angiogenic factors synergistically enhance bone formation in a mouse model of segmental bone defect**. *Mol Ther* 2010, **18**:1026-1034.

45. Shin JH, Kim KH, Kim SH, Koo KT, Kim TI, Seol YJ, Ku Y, Rhyu IC, Chung CP, Lee YM: **Ex vivo bone morphogenetic protein-2 gene delivery using gingival fibroblasts promotes bone regeneration in rats**. *J Clin Periodontol* 2010, **37**:305-311.

46. Chen NK, Tan SY, Udolph G, Kon OL: **Insulin expressed from endogenously active glucose-responsive EGR1 promoter in bone marrow mesenchymal stromal cells as diabetes therapy**. *Gene Ther* 2010, **17**:592-605.

47. Chen NK, Wong JS, Kee IH, Lai SH, Thng CH, Ng WH, Ng RT,
• Tan SY, Lee SY, Tan ME *et al.*: **Nonvirally modified autologous primary hepatocytes correct diabetes and prevent target organ injury in a large preclinical model**. *PLoS ONE* 2008, **3**:e1734.

The authors present a single, fast, safe and effective procedure for gene-modification of target cells that express the recombinant protein without the aid of virus-derived vectors.

48. Campeau PM, Rafei M, Francois M, Birman E, Forner KA, Galipeau J: **Mesenchymal stromal cells engineered to express erythropoietin induce anti-erythropoietin antibodies and anemia in allorecipients**. *Mol Ther* 2009, **17**:369-372.

49. Xu J, Qu J, Cao L, Sai Y, Chen C, He L, Yu L: **Mesenchymal stem cell-based angiopoietin-1 gene therapy for acute lung injury induced by lipopolysaccharide in mice**. *J Pathol* 2008, **214**:472-481.

50. Gregory-Evans K, Chang F, Hodges MD, Gregory-Evans CY: **Ex vivo gene therapy using intravitreal injection of GDNF-secreting mouse embryonic stem cells in a rat model of retinal degeneration**. *Mol Vis* 2009, **15**:962-973.

51. Eliopoulos N, Francois M, Boivin MN, Martineau D, Galipeau J: **Neo-organoid of marrow mesenchymal stromal cells secreting interleukin-12 for breast cancer therapy**. *Cancer Res* 2008, **68**:4810-4818.

52. Fritz V, Noel D, Bouquet C, Opolon P, Voide R, Apparailly F, Louis-Plence P, Bouffi C, Drissi H, Xie C *et al.*: **Antitumoral activity and osteogenic potential of mesenchymal stem cells expressing the urokinase-type plasminogen antagonist amino-terminal fragment in a murine model of osteolytic tumour**. *Stem Cells* 2008, **26**:2981-2990.

53. Hu M, Yang JL, Teng H, Jia YQ, Wang R, Zhang XW, Wu Y, Luo Y, Chen XC, Zhang R *et al.*: **Anti-angiogenesis therapy based on the bone marrow-derived stromal cells genetically engineered to express sFlt-1 in mouse tumour model**. *BMC Cancer* 2008, **8**:306.

54. Kim SM, Lim JY, Park SI, Jeong CH, Oh JH, Jeong M, Oh W, Park SH, Sung YC, Jeun SS: **Gene therapy using TRAIL-secreting human umbilical cord blood-derived mesenchymal stem cells against intracranial glioma**. *Cancer Res* 2008, **68**:9614-9623.

55. Ren C, Kumar S, Chanda D, Chen J, Mountz JD, Ponnazhagan S: **Therapeutic potential of mesenchymal stem cells producing interferon-alpha in a mouse melanoma lung metastasis model**. *Stem Cells* 2008, **26**:2332-2338.

56. Ren C, Kumar S, Chanda D, Kallman L, Chen J, Mountz JD, Ponnazhagan S: **Cancer gene therapy using mesenchymal stem cells expressing interferon-beta in a mouse prostate cancer lung metastasis model**. *Gene Ther* 2008, **15**:1446-1453.

57. Hong X, Miller C, Savant-Bhonsale S, Kalkanis SN: **Antitumor treatment using interleukin-12-secreting marrow stromal cells in an invasive glioma model**. *Neurosurgery* 2009, **64**:1139-1146 discussion 1146-1137.

58. Li Z, Liu Y, Tuve S, Xun Y, Fan X, Min L, Feng Q, Kiviat N, Kiem HP,
• Disis ML *et al.*: **Toward a stem cell gene therapy for breast cancer**. *Blood* 2009, **113**:5423-5433.

The authors use relaxin, which degrades tumour stroma, to facilitate the access of infiltrating antitumor immune cells to the target tumor cells. The antitumoral effect was achieved after the gene-modification of either tumor cells or HSC cells.

59. Loebinger MR, Eddaoudi A, Davies D, Janes SM: **Mesenchymal stem cell delivery of TRAIL can eliminate metastatic cancer**. *Cancer Res* 2009, **69**:4134-4142.

60. Sims TL Jr, Hamner JB, Bush RA, Fischer PE, Kim SU, Aboody KS, McCarville B, Danks MK, Davidoff AM: **Neural progenitor cell-mediated delivery of osteoprotegerin limits disease progression in a preclinical model of neuroblastoma bone metastasis**. *J Pediatr Surg* 2009, **44**:204-210 discussion 210–201.

61. Wang N, Fallavollita L, Nguyen L, Burnier J, Rafei M, Galipeau J, Yakar S, Brodt P: **Autologous bone marrow stromal cells genetically engineered to secrete an igf-I receptor decoy prevent the growth of liver metastases**. *Mol Ther* 2009, **17**:1241-1249.

62. Sanz L, Santos-Valle P, Alonso-Camino V, Salas C, Serrano A, Vicario JL, Cuesta AM, Compte M, Sanchez-Martin D, Alvarez-Vallina L: **Long-term in vivo imaging of human angiogenesis: critical role of bone marrow-derived mesenchymal stem cells for the generation of durable blood vessels**. *Microvasc Res* 2008, **75**:308-314.

63. Karnoub AE, Dash AB, Vo AP, Sullivan A, Brooks MW, Bell GW, Richardson AL, Polyak K, Tubo R, Weinberg RA: **Mesenchymal stem cells within tumour stroma promote breast cancer metastasis**. *Nature* 2007, **449**:557-563.

64. Goren A, Dahan N, Goren E, Baruch L, Machluf M: **Encapsulated**
•• **human mesenchymal stem cells: a unique hypoimmunogenic platform for long-term cellular therapy**. *FASEB J* 2010, **24**:22-31.

This paper describes the use of microencapsulation of gene-modified human MSCs that secret an inhibitor of angiogenesis to reduce tumor growth.

65. Hernandez RM, Orive G, Murua A, Pedraz JL: **Microcapsules and**
• **microcarriers for in situ cell delivery**. *Adv Drug Deliv Rev* 2010, **62**:711-730.

This review provides an in-depth review on the cell encapsulation field.

66. Garcia-Gomez I, Elvira G, Zapata AG, Lamana ML, Ramirez M, Castro JG, Arranz MG, Vicente A, Bueren J, Garcia-Olmo D: **Mesenchymal stem cells: biological properties and clinical applications**. *Expert Opin Biol Ther* 2010, **10**:1453-1468.

67. Meyerrose TE, Roberts M, Ohlemiller KK, Vogler CA, Wirthlin L, Nolta JA, Sands MS: **Lentiviral-transduced human mesenchymal stem cells persistently express therapeutic levels of enzyme in a xenotransplantation model of human disease**. *Stem Cells* 2008, **26**:1713-1722.

68. Murua A, Orive G, Hernandez RM, Pedraz JL: **Xenogeneic transplantation of erythropoietin-secreting cells immobilized in microcapsules using transient immunosuppression**. *J Control Rel* 2009, **137**:174-178.

69. Choi JJ, Yoo SA, Park SJ, Kang YJ, Kim WU, Oh IH, Cho CS: **Mesenchymal stem cells overexpressing interleukin-10 attenuate collagen-induced arthritis in mice**. *Clin Exp Immunol* 2008, **153**:269-276.

70. Chen X, Lin X, Zhao J, Shi W, Zhang H, Wang Y, Kan B, Du L, Wang B, Wei Y *et al.*: **A tumour-selective biotherapy with prolonged impact on established metastases based on cytokine gene-engineered MSCs**. *Mol Ther* 2008, **16**:749-756.

71. Menon LG, Kelly K, Yang HW, Kim SK, Black PM, Carroll RS: **Human bone marrow-derived mesenchymal stromal cells expressing S-TRAIL as a cellular delivery vehicle for human glioma therapy**. *Stem Cells* 2009, **27**:2320-2330.

72. Kim HM, Hwang DH, Lee JE, Kim SU, Kim BG: **Ex vivo VEGF delivery by neural stem cells enhances proliferation of glial progenitors, angiogenesis, and tissue sparing after spinal cord injury**. *PLoS ONE* 2009, **4**:e4987.

73. Zhang H, Zhu SJ, Wang W, Wei YJ, Hu SS: **Transplantation of microencapsulated genetically modified xenogeneic cells augments angiogenesis and improves heart function**. *Gene Ther* 2008, **15**:40-48.

Award Number: W81XWH-09-1-0698

TITLE: Hybrid Nanotechnologies for Detection and Synergistic Therapies for Breast Cancer

PRINCIPAL INVESTIGATOR: Erkki Ruoslahti, M.D., Ph.D.

CONTRACTING ORGANIZATION: Sanford-Burnham Medical Research Institute, La Jolla, CA 92037

REPORT DATE: October 2012

TYPE OF REPORT: Annual

PREPARED FOR: U.S. Army Medical Research and Materiel Command
Fort Detrick, Maryland 21702-5012

DISTRIBUTION STATEMENT:

Approved for public release; distribution unlimited

REPORT DOCUMENTATION PAGE

Form Approved
OMB No. 0704-0188

1. REPORT DATE *(DD-MM-YYYY)* 1 October 2012

2. REPORT TYPE Annual

3. DATES COVERED *(From - To)* Sept. 21,2011 –Sept.20,2012

4. TITLE AND SUBTITLE
Hybrid Nanotechnologies for Detection and Synergistic Therapies for Breast Cancer

5a. CONTRACT NUMBER

5b. GRANT NUMBER
W81XWH-09-1-0698

5c. PROGRAM ELEMENT NUMBER

6. AUTHOR(S)
Erkki Ruoslahti, M.D., Ph.D.

ruoslahti@sanfordburnham.org

5d. PROJECT NUMBER

5e. TASK NUMBER

5f. WORK UNIT NUMBER

7. PERFORMING ORGANIZATION NAME(S) AND ADDRESS(ES)
Sanford-Burnham Medical Research Institute,
10901 North Torrey Pines Rd., La Jolla, CA 92037 [AND]
UCSB
Bio II, Rm. 3119
Santa Barbara, CA 93106-9610

8. PERFORMING ORGANIZATION REPORT NUMBER

9. SPONSORING / MONITORING AGENCY NAME(S) AND ADDRESS(ES)
U.S. Army Medical Research and Materiel Command
Fort Detrick, MD 2702

10. SPONSOR/MONITOR'S ACRONYM(S)

11. SPONSOR/MONITOR'S REPORT NUMBER(S)

12. DISTRIBUTION / AVAILABILITY STATEMENT

Approved for public release; distribution unlimited

13. SUPPLEMENTARY NOTES

14. ABSTRACT

This is a joint project by two Innovator Awardees and a Scholar to develop a novel nanotechnology platform for the diagnosis and treatment of breast cancer. The prevalence of breast cancer and the large number of deaths from this disease underscore the need for a paradigm shift in the strategies towards developing a cure for breast cancer. Nanotechnology has the potential of causing such a paradigm shift. Current work focuses on the development of novel peptide probes and probe strategies for the targeting of breast cancers, including very early pre-malignant lesions. Another focus is development of drug conjugates, nanomedicines and diagnostic nanosystems for therapeutic and theranostic targeting of breast cancers.

15. SUBJECT TERMS
anti-angiogenesis, phage display, tumor homing peptides

16. SECURITY CLASSIFICATION OF:

a. REPORT	b. ABSTRACT	c. THIS PAGE	17. LIMITATION OF ABSTRACT	18. NUMBER OF PAGES
U	U	U	UU	152

19a. NAME OF RESPONSIBLE PERSON USAMRCC

19b. TELEPHONE NUMBER *(include area code)*

Standard Form 298 (Rev. 8-98)
Prescribed by ANSI Std. Z39.18

Table of Contents

Page

Attachments:

Sanchez-Martin, D., Cuesta, A.M., Fogal, V., Ruoslahti, E., and Alvarez-Vallina, L. The multi-compartmental p32/gCiqR as a new target for antibody based tumor targeting strategies. J Biol Chem 286:5197-5203 (2011) PMC:3037632

Roth, L., Agemy, L., Kotamraju, V.R., Braun, G., T. Teesalu, T, Sugahara, K.N., Hamzah, J., and Ruoslahti E. Transtumoral targeting enabled by a novel neuropilin-binding peptide. *Oncogene*, 31: 3754-3763(2012). PMID: 22179825

Ruoslahti, E. Peptides as targeting elements and tissue penetration devices for nanoparticles. *Adv. Mat.* (review article) 24:3747-3756. (2012). [Epub ahead of print] PMID: 22550056.

Braun G B., Friman, T., Pang, H-B., Kotamraju, VR, Pallaoro, A., Reich, NO.,Teesalu, T. and Ruoslahti, E. Etchable and bright silver nanoparticle probes for cell internalization assays. Submitted

Chen, R., Braun, G.B., Luo, X. Sugahara, K.N., Teesalu, T., Ruoslahti, E. Application of a proapoptotic peptide for an intratumoral-spreading cancer therapy. (2012). Cancer Research, Provisionally accepted.

Alberici L., Roth, L., Sugahara, K.N., Agemy, L., Kotamraju, V.R., Teesalu, T., Bordignon, C., Traversari, C., Rizzardi, G.-P., Rusolahti, E. De Novo Design of a Tumor Penetrating Peptide (2012) Cancer Research, Provisionally accepted.

Collaborative Innovator Grant – W81XWH-09-1-0698
Hybrid Nanotechnologies for Detection and Synergistic Therapies for Breast Cancer
Principal Investigator: Dr. Erkki Ruoslahti; Project PIs: Dr. Roger Tsien and Dr. Shiladitya Sengupta

Progress Report Year 03

INTRODUCTION

This is a joint project by two Innovator Awardees and a Scholar to develop a novel nanotechnology platform for the diagnosis and treatment of breast cancer. The prevalence of breast cancer and the large number of deaths from this disease underscore the need for a paradigm shift in the strategies towards developing a cure for breast cancer. Nanotechnology has the potential of causing such a paradigm shift.

Some clinically used anti-cancer drugs (e.g. Abraxane, Doxil) and imaging agents are already nanoparticle-based. While highly effective, these first generation products do not utilize the full power of nanotechnology; nanoparticles can be “smart,” not just passive carriers of a drug. One such function, which is central to this project, is endowing nanoparticles with an ability to seek out tumors and selectively accumulate in them. This can be accomplished by incorporating a tumor-homing molecule, such as a peptide, aptamer, or antibody to the nanoparticle. A significant recent development has been the realization that nanoparticles can be best targeted into tumors by making use of molecular targets in the vasculature of tumors because these targets, unlike the extravascular tumor tissue, are readily available for circulating nanoparticles. There are numerous targets in tumor vasculature, and they are highly versatile in that they can be pan-tumor markers, or specific to a tumor type (such as breast cancer, specific for a certain stage in tumor development); metastases may have their own markers that depend on the tissue the metastasis resides in. We are making use of the versatility of nanoparticles and vascular homing peptides in developing a seamless, synergistic nanotechnology platform for early detection, monitoring, and therapy of breast cancer.

Synergistic therapies that combine inhibitors of oncogenic signal transduction pathways with cytotoxic chemotherapies have proven effective as nanoparticle-based formulations in animal models. Targeting can then concentrate the therapeutic agent in the tumor, improving the efficacy of the treatment and reducing damage to healthy tissues. The diagnostic and therapy functions will be synergistic in that the diagnostic methods will provide information on the efficacy of individual homing peptides in targeting the tumor. This information makes it possible to select the most effective targeting mechanism for each patient. Incorporating diagnostic and treatment functions into the same particle will enhance the ability to monitor the treatment and reduce the number of procedures the patient is subjected to.

Specifically, we are assembling a panel of breast cancer-homing peptides, which will be then used as recognition elements for nanoparticles. The diagnostic platform technology under development is based on nanoparticles that, when injected into the blood stream, bind to tumor vessels and undergo a change as a result of the binding. This change is then detected in blood samples. We are developing and testing nanoparticles based on polymer and other chemistries to serve as tumor-targeted drug carriers. Cell-penetrating and tumor-penetrating properties of certain homing peptides will be made use of in delivering the drugs-carrying nanoparticles deep into tumor tissue and inside tumor cells. If possible we will distill a single, optimized theranostic nanosystem from these studies. We expect these advances to have a major beneficial effect on the cure rates and quality of life of breast cancer patients.

We are working on a number of biotechnology and pharmaceutical companies that have licensed various aspects of our technologies from our institutions. Thus, there is a high probability that this project will bring advanced nanotechnology closer to clinical reality in breast cancer management (while also creating well-paying jobs).

BODY

The approved Tasks for this grant are:

Task 1.
Establish a panel of homing ligands for the project. (Months 1-36) Investigators: Ruoslahti, Tsien, Soh, Sengupta
1a. Screen an existing panel of tumor-homing peptides for peptides that selectively recognize the vasculature of pre-malignant breast lesions, fully malignant carcinomas, or metastatic lesions. Months 1-18. Investigators: Ruoslahti, Tsien
1b. Screen phage libraries for new peptides that selectively recognize the vasculature of early breast cancer lesions and breast cancer metastases in a given organ. Months 1-36; Investigators: Ruoslahti
1c. Screen aptamer libraries for aptamers that bind to a receptor in tumor vessels where the binding leads to a stable change in conformation that eliminates receptor binding and can be monitored in the blood. Months 1-36; Investigators: Ruoslahti, Soh

Task 2.
Engineer chimeric nanoparticles that deploy signal transduction inhibitors and cytotoxic chemotherapies for synergistic antitumor outcome. (Months 1-30) Investigators: Sengupta, Ruoslahti
2a. Engineer a chimeric nanoparticle from the drug-polymer conjugates. Investigator: Sengupta
Chemically conjugate PD98059 to PLGA. (Months 1-6)
Engineer a polymaleic acid-cisplatin complex (Months 1-24)
Chemically conjugate Doxorubicin-(7KDa) PLGA carbamate conjugate. (Months 1-6)
Engineer a chimeric NP entrapping LY294002 in matrix.(Months 1-24)
2b. Physicochemically characterize the chimeric nanoparticles for size, morphology, and release kinetics of the therapeutic agents. (Months 1-30) Investigator: Sengupta
2c. *In vitro* and *in vivo* characterization of the chimeric nanoparticle in 4T1 and MDA-MB-231 tumor models (Months 6-30) Investigators: Sengupta, Ruoslahti

Task 3.
Validate a minimally invasive bar-coded nanoparticle-based in vivo diagnostic platform for breast cancer detection and staging, and monitoring of therapy. (Months 12-42) Investigators: Ruoslahti, Reich, Tsien, Sengupta
3a. Test a prototype assay in which a mixture of nanoparticles coated with either a tumor-homing peptide or a control peptide is injected into a tumor-bearing mouse and a change in the ratio of the particles in the circulation is monitored. (Months 12-36). Investigators: Ruoslahti, Sengupta
1. Functionalization of magnetic nanoparticles with cleavable Homing-CENDR peptide chimera and physicochemical characterization. (Months 12-30) Investigators: Ruoslahti
2. In vivo evaluation of the prototype nanoparticle (Months 24-42). Investigators: Ruoslahti,

Sengupta
3b. Examine the suitability of surface enhanced Raman spectroscopy (SERS) for *in vivo* detection of barcoded nanoparticles. (Months 18-42) Investigators: Ruoslahti, Reich, Sengupta
3c. Test an alternative prototype in which the nanoparticles are coated with a bipartite tumor homing peptide that is susceptible to proteolytic cleavage by a tumor protease that generates a tumor-binding fragment and a free fragment. The ratio of labels attached to the ends of the peptide is monitored. (Months 12-42). Investigators: Tsien, Ruoslahti, Sengupta

Task 4.
Specific Aim 4. Develop a multifunctional nanoparticle that delivers a drug to tumor vessels and tumor cells, while releasing a diagnostic component into the circulation
(Months: 24-60)
Investigators: Sengupta, Ruoslahti, Tsien
4a. Adapt the barcoded diagnostic technology onto polymer-based drug-loaded multifunctional nanoparticles, and characterize for physicochemical properties. Months 24-48 Investigators: Sengupta, Ruoslahti, Tsien
4b. Characterization of multifunctional nanoparticle in *in vivo* tumor models, including testing for tumor homing, penetration and uptake into tumor cells. Months 36-60 Investigators: Sengupta, Ruoslahti, Tsien
4c. Characterize the antitumor efficacy and mechanism of action of the multifunctional bar-coded nanoparticles *in vivo*. Months 42-60 Investigators: Sengupta

KEY RESEARCH ACCOMPLISHMENTS

We have:

- Used phage library screening to identify a new peptide that detects early changes in the extracellular matrix of premalignant transgenic mouse breast lesions.
- Identified a peptide from our panel of tumor-homing peptides that specifically recognizes the fibroblasts that reside in early premalignant breast lesions.
- Developed (in the Soh laboratory) a new method that may revolutionize aptamer screening and may also allow *in vivo* screening for breast cancer-recognizing aptamers, which has turned out not to be possible with the current technology.
- Shown in a collaborative project between the Sengupta and Ruoslahti laboratories that coating of nanoparticles carrying a platinum compound with the tumor-penetrating peptide iRGD peptide increases the anti-tumor activity of the nanoparticles in a breast cancer model.
- Constructed a functioning hit-and-run assay for tumor detection using iron oxide nanoparticles doped with radiostable gadolinium isotopes.
- Developed a new silver nanoparticle-based assay for accurate measurement of nanoparticle uptake by cells.
- Engineered Cisplatin, Doxorubicin and taxane-based self assembled nanoparticles.
- Engineered PI-828 and PI-103 nanoparticles.
- Extended activatable cell penetrating peptides (ACPPs) to proteases other than matrix metalloproteinases-2 and -9 (elastase and thrombin).

- Shown that RACPPs enable detection of metastases into liver and lymph nodes in a mouse breast cancer model.
- Developed a RACPP-targeted drug conjugates and shown efficacy in a breast cancer model.
- Published and submitted for publication several papers acknowledging this grant and filed patent applications on new inventions.

Task 1. Establish a panel of homing ligands for the project

1a. Screen an existing panel of tumor-homing peptides for peptides that selectively recognize the vasculature of pre-malignant breast lesions, fully malignant carcinomas, or metastatic lesions

Extracellular matrix alteration in pre-malignant lesions
We used phage library screening to identify a new peptide that detects early changes in the extracellular matrix of premalignant transgenic mouse breast lesions in genetically engineered PyMT-MMTV breast cancer mice. The screen that yielded this peptide was based on phage binding to matrigel, which is a basement membrane extract from a mouse tumor. The next and final step was an *in vivo* screen for tumor homing, where we used the MDA-MB-435 xenograft model. We are well aware of the controversy regarding the origin of this tumor, and although the balance seems to have shifted back to this tumor being of breast cancer origin, as shown below, we carefully validate all results using other breast cancer models.

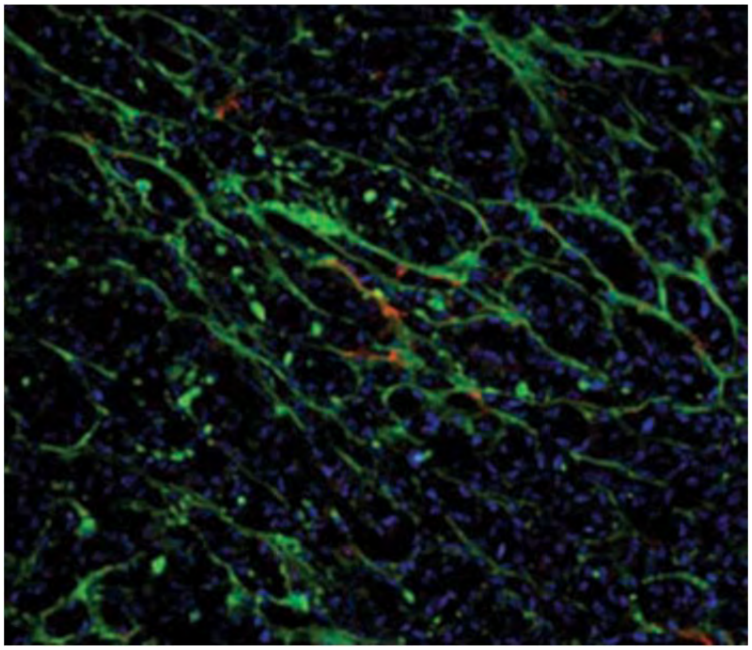

Fig. 1. Specific tumor accumulation of CSG peptide in the MDA-MB-435 breast cancer model. A. Mice bearing MDA-MB-435 xenograft tumors were intravenously injected with fluorescein-conjugated CSG peptide (150 ug/mouse). The mice were anesthetized 2 hours later, perfused through the heart with 4% paraformaldehyde, and the tumors were examined microscopically. B. CSG phage was intravenously injected into MDA-MB-435 tumor-bearing mice, and the phage titers recovered from the tissues after 10 min in circulation were determined. The titers are expressed as fold over control insertless phage.

The peptide, dubbed CSG, is a 9-amino acid peptide with a cyclizing disulfide bond between cysteines at the first and last positions. It avidly and specifically homes to the MDA-MB-435 tumors used to identify it (Fig. 1), and it also homes to mouse 4T1 transplantable, orthotopic breast cancers (Fig. 2). The pattern of homing coincides with extracellular matrix, rather than cells in the tumors.

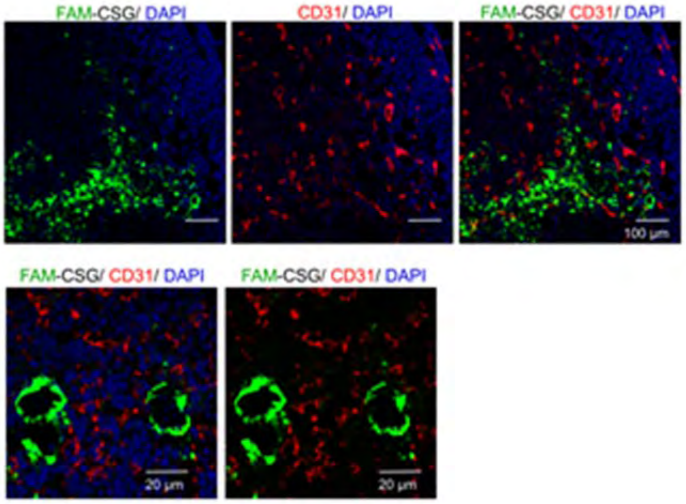

Fig. 2. CSG specifically homes to orthotopic 4T1 mouse breast cancer tumors. FAM-CSG peptide (0.1 µmol) was intravenously injected into tumor-bearing mice and tissues were collected 2 hours later and the peptide was detected in tumor sections by fluorescence microscopy (Green). CSG shows no co-localization with tumor blood vessels (CD31; red). Nuclei were stained with DAPI (blue). Original magnification ×20; scale bars100 µm (upper panels), and ×40; scale bars, 20 µm (lower panels).

The target molecule for CSG appears to be the basement membrane component nidogen, because affinity chromatography on immobilized CSG peptide identifies nidogen-1 as a specific binder of CSG (Fig. 3). This agrees with the matrix localization in tumor-homing studies and its matrigel binding. The identification of nidogen as the relevant receptor will still need to be confirmed with knockdown and antibody inhibition experiments. And it will also be important to determine whether the cancer specificity of CSG comes from over-expression of nidogen-1 in cancer, its abnormal exposure, or some modification of the molecule.

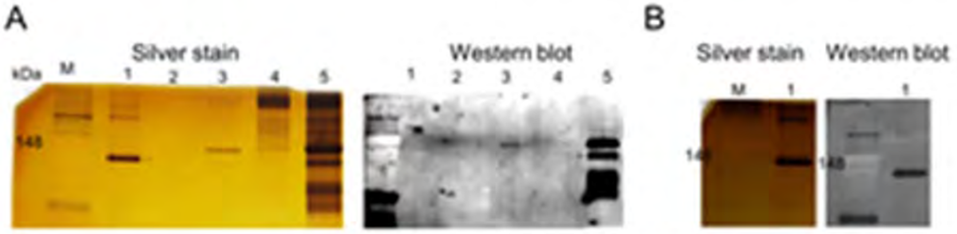

LANE:
1: Recombinant human Nidogen-1
2. Blank
3. Protein bound to agarose-gel linked with CSG from matrigel
4. Purified laminin (>95% purity, free of nidogen-1)
5. Concentrated laminin and nidogen-1 (>90% purity)

Fig. 3. CSG binds to basement membrane protein, nidogen-1/entactin. A. CSG peptide coupled to agarose gel linked with CSG peptide from A. Silver-stained PAGE gel showing the 140-kDa band and immunoblot identification identifying the isolated protein (lane 3) is nidogen-1 using an antibody against mouse nidogen-1. This antibody did not work on recombinant human nidogen-1. B. Silver staining and western blot analysis of recombinant human nidogen-1 using polyclonal antibody raised against human nidogen-1.

A feature of CSG that is particularly relevant to this grant project is that it recognizes early, premalignant breast cancer lesions. We used the well-known PyMT-MMTV models (Fig. 4) for the study of premalignant lesions. Systemically injected CSG recognized the extracellular matrix of the developing mammary glandular tree in the PYMT mice already at a stage where only hypertrophy of the epithelium was evident (Fig. 5), whereas there was no homing to the mammary gland of normal mice of the same strain. We will conduct additional studies on lactating glands, inflamed tissue and, when possible, non-malignant tumors to determine the specificity of this promising peptide for premalignant lesions and fully developed cancer.

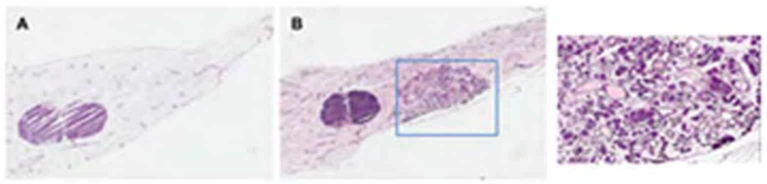

Fig. 4. PyMT-MMTV is a useful model for studying early premalignant breast tumors. H&E images of whole mount sections of mammary fat pad isolated from normal mouse **(**A**)** or 60-day-old PyMT-MMTV (B). Inset shows the hyperplastic lesion in the mouse mammary fat pad.

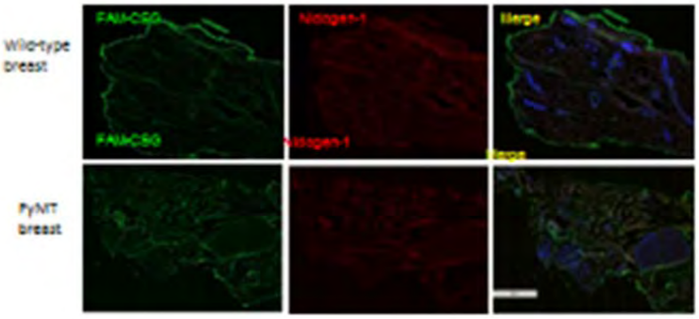

Fig. 5. CSG peptide homes to premalignant hyperplastic lesions in mammary fat pad isolated from PyMT-MMTV animals. Immunofluorescence staining on whole mount sections of mammary fat pad isolated following 1 hour in-vivo circulation of FAM-CSG in normal Blk6 mouse (A) or PyMT-MMTV mouse (B). Green - anti-FAM; Red - anti-nidogen-1, Blue - nuclear stain. Scale bar is 2 microns. The fluorescence around the margins of the sections is non-specific.

Peptide recognizing fibroblasts in premalignant lesions. We have identified a peptide in our panel of tumor-homing peptides that specifically recognizes the fibroblasts that reside in early premalignant breast lesions. This peptide, iRGD, is prototype compound among the tumor-penetrating peptides we have described recently (Sugahara et al., 2009; 2010; Roth et al., 2012; Alberici et al., 2012). Systemically injected iRGD homes to individual cells around the premalignant PyMT glands (Fig. 6). These cells appear to be tumor fibroblasts based on three lines of evidence: They are clearly not tumors cells, their morphology is not that of immune cells, and the iRGD staining co-localizes with the fibroblast marker vimentin (Fig. 6). Moreover, we have found that tumor fibroblasts are strongly positive for iRGD uptake in fully malignant breast cancers (Sugahara et al., unpublished results). Interestingly, iRGD did not home to the blood vessels in the hyperplastic lesions, although it strongly recognizes the blood vessels in breast cancers. This may be an indication that the angiogenic switch (Hanahan and Folkman) has not been turned on at this stage. Even more strikingly, the hyperplastic glandular cells were also not positive for iRGD uptake at this stage. This result indicates that αv integrin and/or neuropilin expression (to be further studied with antibody probes) has not been turned on in the tumor cells or endothelial cells at a stage, when the fibroblasts are already activated.

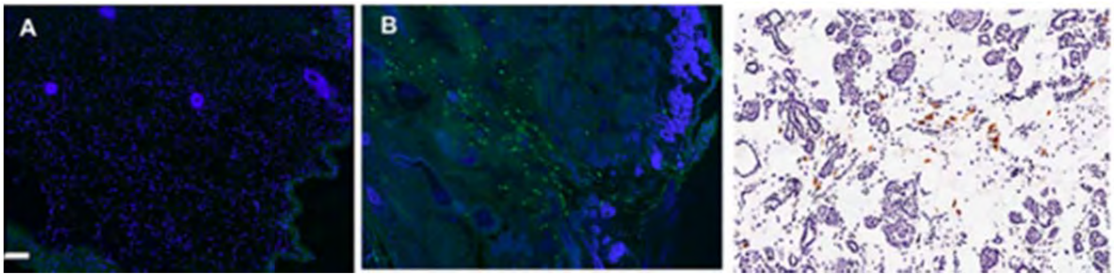

Fig. 6. iRGD homes to early (premalignant) hyperplastic lesions in mammary fat pad isolated from PyMT-MMTV animals. Immunofluorescence staining on whole mount sections of mammary fat pad isolated following 1 hour in-vivo circulation of 0.15 µmol FAM-iRGD in normal Blk6 mouse (A) or day 48 PyMT-MMTV mouse (B). Green – anti-FAM; Blue – DAPI nuclear stain. Scale Bar is 100 micron. (C) Immunohistochemistry staining for FAM on sections of mammary fat pad isolated following FAM-CSG injection in PyMT-MMTV mouse. Note the rare positive cells in the tissue interspersed among the tumor cells.

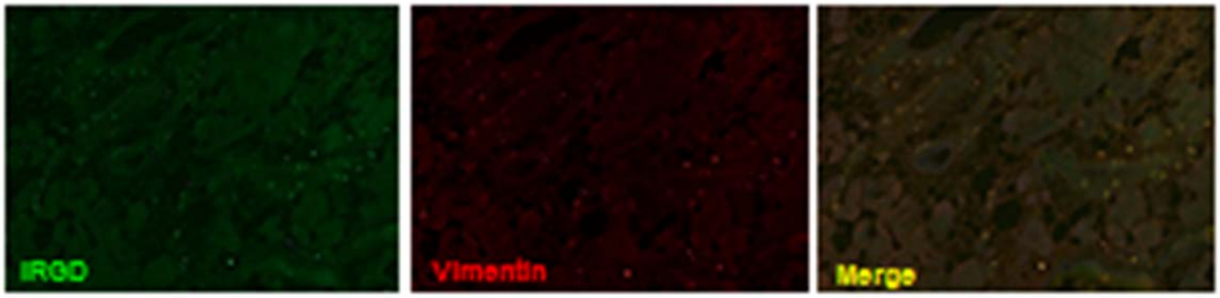

Fig. 7. iRGD colocalizes with fibroblasts in early (premalignant) hyperplastic lesions in mammary fat pad isolated from PyMT-MMTV mice. Immunofluorescence staining on whole mount sections of mammary fat pad isolated following FAM-iRGD injection in PyMT-MMTV mouse. Green - anti-FAM-CSG; Red - anti-vimentin-1, Blue - nuclear stain.

Our results show, to our knowledge for the first time, that changes in the extracellular matrix and resident fibroblasts already occur at the stage of early hyperplasia in breast cancer development, preceding detectable changes in the vasculature. We have initiated phage library screen for peptides that recognize the earliest changes in to-be-breast-cancer tumor cells. The CSG and iRGD peptides may be useful in the diagnosis of early breast cancer. Thus, targeting of nanoparticles with iRGD, such as the nanoparticles carrying a platinum compound developed in a collaborative study between the Sengupta and Ruoslahti laboratories (Task 2) will attack the earliest changes in breast cancer development, in addition to the fully developed cancers. At the other end of the tumor development spectrum, we are working on metastasis targeting and expect to describe the results in the next report.

1b. Screen phage libraries for new peptides that selectively recognize the vasculature of early breast cancer lesions and breast cancer metastases in a given organ.

As described above, we have discovered probes that detect early changes in the extracellular matrix and fibroblasts of premalignant lesions. We are in the process of determining when the blood vessels become detectable with our probes in breast cancer development. Screens for the vasculature of metastases have been initiated.

1c. Screen aptamer libraries for aptamers that bind to a receptor in tumor vessels where the binding leads to a stable change in conformation that eliminates receptor binding and can be monitored in the blood.

Since their initial description (Gold et al., 2012; Keefe et al, 2010), aptamers have shown considerable promise as a synthetic alternative to monoclonal antibodies. Importantly, aptamers, more than any other type of probes, have the capability of altering conformation upon binding of a ligand. In this project, we initially sought to use aptamer screening *in vivo* to identify tumor-homing aptamers that could then be used to develop a cancer test based on conformation-changing aptamers.

As reported previously, we have worked on strategies that would allow us to target angiogenic vasculature. The Soh laboratory used αvβ3 integrin as a target to develop a selection strategy for isolating aptamer pairs that bind to distinct epitopes of a target protein (Gong et al., 2012). They have identified two families of aptamers that specifically recognize the αv and β3 subunits. The isolated aptamers from these families (αv-1 and β3- 1) exhibit low nanomolar affinities for their respective targets, with minimal cross-reactivity to other, closely related integrin homologues. These nuclease-resistant, 2’-F-modified aptamer pairs did not interfere with each other’s binding and could be effectively used as reagents for assays in buffer as well as complex mixtures such as undiluted serum. These aptamers will now be used to determine whether *in vivo* targeting with aptamers is possible.

With an eye toward being able to use aptamer screening *in vivo* akin to what the Ruoslahti laboratory is doing with phage. Our first attempts with conventional aptamer libraries were a failure; no specific binding was detected. We have now devised a new method of generating aptamers that is fundamentally different from the conventional SELEX-based strategies. In our screening method, the affinity of every candidate molecule is individually measured and sorted in a high-throughput fashion. To achieve this, we employ a particle display system that utilizes emulsion PCR (Diehl et al. 2006; Dressman et al., 2003) to transform an aptamer library into a pool of aptamer particles (APs), each displaying multiple copies of a unique aptamer sequence on its surface. We then incubate these APs with fluorescently labeled target protein and use fluorescence-activated cell sorting (FACS) to quantitatively screen each AP based on its mean fluorescence intensity, which is directly proportional to the binding affinity of the aptamer. As previously demonstrated in protein engineering methods based on yeast or bacterial display, the use of FACS to screen the binding properties of individual ligands in a high-throughput manner offers tremendous advantages over conventional selection methods. Through theoretical analysis, we have identified key experimental parameters that enable optimal enrichment of the highest-affinity aptamers, and show that the performance of our particle display system exceeds the theoretical maximum of existing selection methods by many orders of magnitude.

In order to experimentally validate the clear theoretical advantage of our system in isolating high-affinity aptamers, we performed particle display screens against four target proteins—thrombin, ApoE, PAI-1 and 4-1BB—using the optimal conditions identified in our theoretical analysis. It is possible to begin the particle display screen with a large random library, but due to the practical limits of FACS throughput (~10^7 particles per hour), we first performed one round of magnetic bead-based enrichment with a random library of ~10^{14} single-stranded DNA molecules and used this enriched pool to synthesize our initial AP library. Prior to the screen, we performed FACS with APs displaying only the forward primer (FP) to define the reference gate. APs residing in this reference gate exhibited negligible binding to target proteins, and were not collected during the screen.

We performed three rounds (R1–3) of particle display screen for all four targets. Due to the limited initial copy number of each AP, it is important to avoid loss of potentially high-affinity APs in R1; thus, we applied lower screening stringency by setting the sort gate close to the reference gate, such that at least 0.1% of the APs were collected. Aptamers isolated in R1 were PCR amplified and used to synthesize a new set of APs; in this way, ~1000 copies of each AP isolated from R1 were available for R2. In R2 and R3, we used the theoretical optimal screening stringency, setting the sort gate at $F_{max}/3$ and decreasing $[T]$ such that we collected ~0.1–0.2% of the APs. Aptamers isolated in R3 exhibited high affinities for their targets (Fig 8). To estimate average k_d, we considered all APs outside of the reference gate (Fig. 1, blue), and experimentally measured the $[T]$ at which the mean fluorescence of this population is $(F_{max} + F_{bg})/2$. We found the average k_d to be 20 pM, 3 nM, 1 nM and 4 nM for thrombin, ApoE, PAI-1 and 4-1BB, respectively.

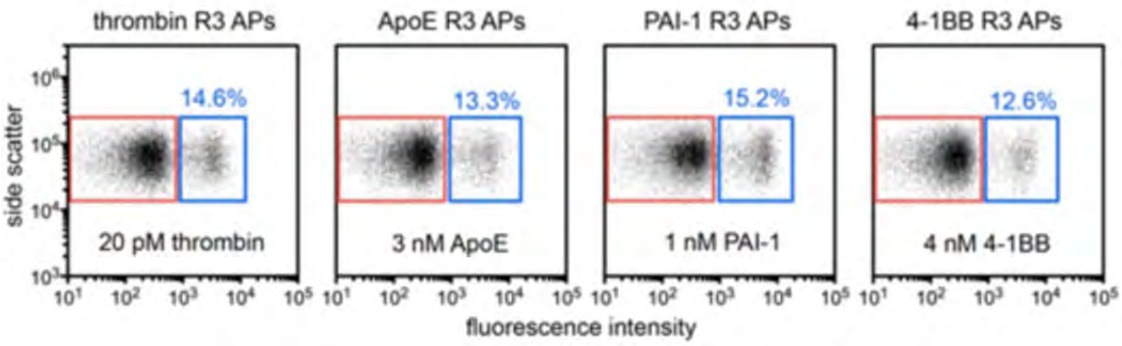

Fig. 8. Particle display screening progress and outcome. Aptamers isolated in R3 exhibited high target affinities. The average k_d of the R3 pools were 20 pM (thrombin), 3 nM (ApoE), 1 nM (PAI-1) and 4 nM (4-1BB), as measured by the mean fluorescence of the APs outside of the reference gate (blue).

Characterization of high-affinity aptamers. To obtain individual aptamer sequences, we cloned the R3 pools into competent bacterial cells and randomly picked and sequenced 20 clones from each. For the best sequences, we present the binding curve and secondary structures as predicted by mfold in Figure 9. The affinities of our aptamers against thrombin and ApoE are significantly higher than any previously reported aptamers. For example, thrombin aptamer Thrombin 03 exhibits a k_d of 7.04 pM (Fig. 9a), which surpasses the values obtained with the same binding assay using aptamers previously reported by approximately two to three orders of magnitude. Similarly, our ApoE aptamer ApoE-06 exhibits a k_d of 938 pM (Fig. 9b), a 4-fold improvement over the aptamer recently isolated by our group using high-stringency microfluidic SELEX20. Importantly, previously reported selections against PAI-1 and 4-1BB have repeatedly failed without the use of modified bases. However, we successfully generated high affinity aptamers for these proteins based entirely on natural DNA; our PAI-1-01 sequence exhibits a k_d of 339 pM (Fig. 9c) and 4-1BB-07shows a k_d of 2.32 nM (Fig. 9d), both comparable to the performance of aptamers generated using modified bases12.

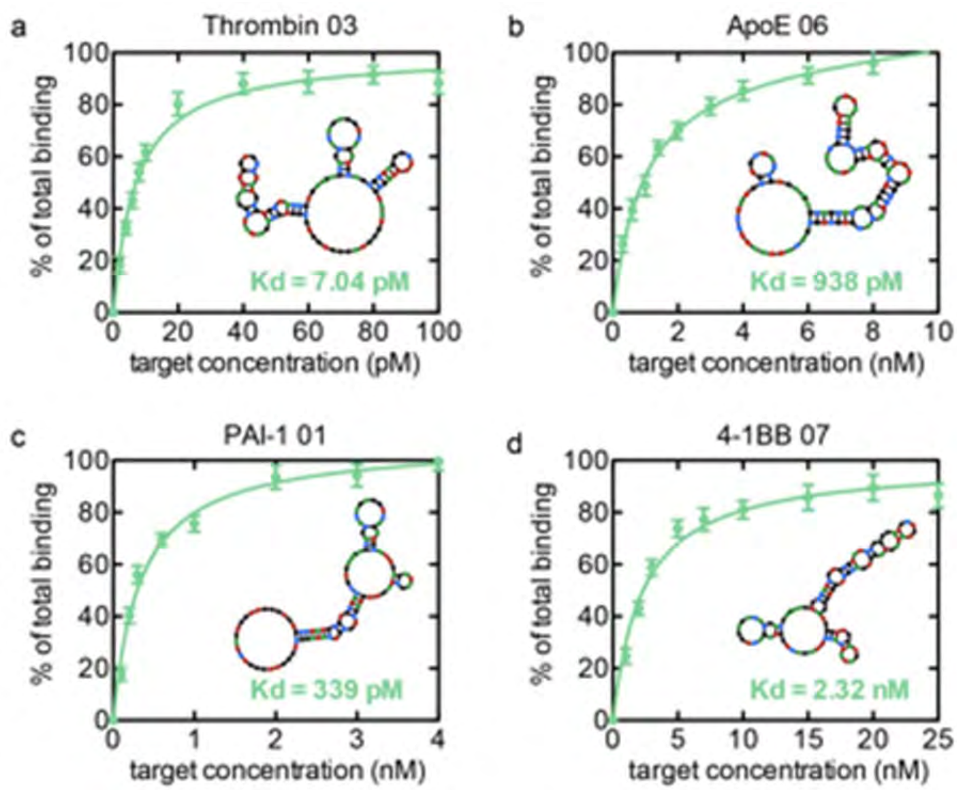

Fig. 9. Affinity measurements of individual aptamers. We used a beadbased fluorescence assay to measure the binding affinity of the top aptamers against (a) thrombin, (b) ApoE, (c) PAI-1 and (d) 4-1BB. We calculated k_d using a Langmuir 1:1 binding model and predicted aptamer secondary structure using mfold.

In conclusion, we report a quantitative screening method for generating high affinity aptamers that offers significant advantages over all previous selection methods. After synthesizing pools of aptamer particles that display ~10^5 copies of a single aptamer sequence, we used FACS to individually measure the affinity of ~10^8 aptamer sequences, enabling isolation of those with highest affinity with unprecedented resolution. Our method offers a critical advantage over conventional SELEX-based methods. Using selection, it is challenging to discard aptamer sequences that proliferate due to factors such as library synthesis bias, non-specific background binding and PCR bias. These effects often lead to the isolation of inferior aptamers or failed selection (Gold et al., 2012). In contrast, our method eliminates the confounding effects of such biases by quantitatively measuring the actual affinity of each individual aptamer for its target at every round, such that aptamers with low affinities are effectively discarded regardless of their copy number.

Through theoretical analysis, we show that these improvements translate to an extraordinary difference in performance, and our particle display method exceeds the theoretical enrichment limit of any selection-based method by orders of magnitude. By performing screens against four different protein targets, we have demonstrated that these significanttheoretical advantages can be realized experimentally, and the affinities of our aptamers against ApoE and thrombin are 4- to 160-fold higher than previously reported sequences. More importantly, we successfully performed particle display screens against two recalcitrant proteins for which selections were reported to repeatedly fail without the use of modified bases12, and generated DNA aptamers with high affinities (PAI-1, k_d = 339 pM and 4-1BB, k_d =2.32 nM). We believe our particle display method should also be compatible with other natural and modified nucleic acid systems, such as natural RNA, 2′-fluoro-modified RNA, 2′-O-methyl-modified RNA and chemically modified DNA. Given that particle display does not require the immobilization of target molecules to a solid support, it is interesting to consider the extension of our method to other molecules in addition to conventional protein targets, including post-translational modifications, lipids, glycans and other classes of biomolecules. Success in doing so may unlock the true potential of nucleic acids as affinity reagents. These capabilities could be particularly relevant in screening for aptamer binders of tumor markers. Even *in vivo* screening for such markers may become possible.

***Task 2*. Engineer chimeric nanoparticles that deploy signal transduction inhibitors and cytotoxic chemotherapies for synergistic antitumor outcome**.

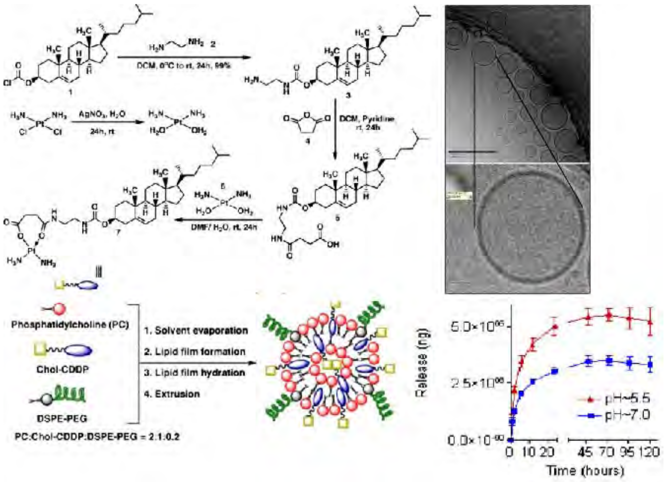

Fig. 10. Synthesis and characterization of SACNs. Scheme for synthesis of cholesterol-cisplatin conjugate from cholesteryl chloroformate. Schematic representation shows synthesis of SACNs by self-assembly from PC, cholesterol-cisplatin conjugate, and DSPE-PEG. High-resolution cryo-TEM image of SACNs at lower magnification (Upper) and magnified image (Lower). (Scale bar, Upper, 500 nm). Graph shows the pH-dependent release of platinum from SACNs as quantified over a 120-h period.

The Sengupta laboratory has demonstrated that rational design of active molecules can facilitate supramolecular assembly in the nanoscale dimension. Using cisplatin as a template, we synthesized a unique platinum (II) tethered to a cholesterol backbone via a unique monocarboxylato and O→Pt coordination environment that facilitates nanoparticle assembly with a fixed ratio of phosphatidylcholine and 1,2-distearoyl-sn-glycero-3-phosphoethanolamine- N-[amino (polyethylene glycol)-2000]. Briefly, cholesterol-tethered cisplatinum (II) amphiphile was engineered, the design of which was inspired by the process of “aquation,” wherein the chloride leaving groups of cisplatin are rapidly displaced to form cis-Pt[(NH3)2(OH2)Cl]+ and cis-Pt[(NH3)2(OH2)2]2+. Indeed, we had demonstrated that Pt chelated to a polyisobutylene maleic acid glucosamine copolymer via a monocarboxylato and an O→Pt coordinate bond release of Pt in a pH-dependent manner, and more efficiently than when the Pt was chelated using dicarboxylato bonds or via a monocarboxylato and an N→Pt coordinate bond. As a result, we rationalized that the introduction of a coordination environment where the Pt was chelated via a monocarboxylato and an O→Pt coordinate bond is critical to the design of an efficacious platinate. As outlined in the given scheme (Fig. 10), we first synthesized cholesterol-ethylenediamine conjugate in near quantitative yield (99.1%) by reacting cholesteryl chloroformate with excess ethylene diamine. Next, we introduced monocarboxylato and amide chelating moiety by reacting cholesterol-ethylenediamine conjugate with succinic anhydride (at 95% yield). Finally, the conjugate was reacted with aquated cis-Pt[(NH3)2(OH2)2]2+ in 1:1 molar ratio in acidic pH (pH = 6.4) to obtain cholesterol-cisplatin conjugate, characterized by monocarboxylato and an O→Pt coordinate bond of an amide, as indicated by an unique single ^{195}Pt NMR peak at −1,621.497 ppm. We engineered the SACNs from the cholesterol-succinic acid-platinum (II) molecule, phosphatidylcholine (PC) and 1,2-distearoyl-sn-glycero-3-phosphoethanolamine-N [amino(polyethylene glycol)-2000] (DSPEPEG) in 1:2:0.2 weight ratio using a lipid-film hydration self assembly method (20)

(Fig. 10). The ultrastructure analysis using cryo-transmission electron microscopy (cryo-TEM) (Fig. 10) revealed the formation of predominantly uni- and rare multilamellar structures less than 200 nm in diameter, with a membrane thickness ~5 nm. Dynamic light scattering further confirmed the size distribution of SACNs with a mean hydrodynamic diameter of 141.4 ± 1.2 nm (n = 9) (Fig. 11C). To validate the kinetics of cisplatin release, SACNs were incubated at acidic pH 5.5 over 120 h, with pH 7 as a reference. As shown in Fig. 11D, SACNs exhibited a pH-dependent sustained release of cisplatin. Interestingly, the rate of release was slower than observed earlier using a polymeric system, indicating that the cholesterol can incorporate into the lipid layer in a manner where the Pt moiety is present both on the outer as well as inner part of the membrane.

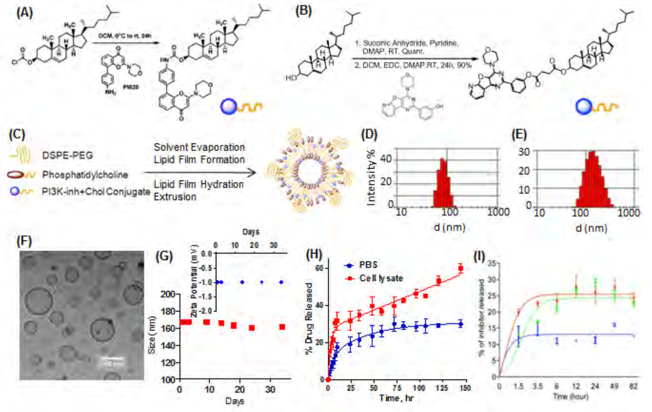

Fig. XX. In vivo antitumor activity of SACNs in 4T1 breast cancer model. (A) Graph shows body weight loss of animals with increasing doses of cisplatin or SACNs (Cisplatin NP). Maximum tolerated dose is calculated at 20% body weight loss. (B) Graph shows change in tumor volume in different treatment groups in 4T1 murine breast cancer model following a single dose of platinum chemotherapy at the MTD platinum dose of cisplatin. (C) Kaplan–Meier curve shows effect of different treatments on survival at MTD platinum dose of cisplatin (P = 0.0189 Logrank test for trend). (D) Multiple dose effects of treatment on 4T1 breast cancer growth. Cells were implanted subcutaneously on day 0. Mice were treated with PBS, carboplatin (3 mg/kg), cisplatin (3 mg/kg and 1 mg/kg), and SACNs (3 mg/kg and 1 mg/kg) (n = 4, doses are Pt equivalent) on days 9, 11, and 13 post-tumor implantation. Upper row shows representative images of excised tumors, and Lower row shows tumor cross sections processed for TUNEL as marker for apoptosis. Images were captured usinga Nikon Ti epifluorescence microscope at 20× magnification to capture a large view field. (E) Growth curves show the effect of the different multiple-dose treatments on tumor volume. (F) Graph shows change in body weight of animals in different treatment groups. (G) Kaplan–Meier curve shows effect of different treatments on survival (P = 0.0022, Logrank Mantel–Cox test).

Self-assembling cholesterol-succinic acid-cisplatinum II-based nanoparticles (SACNs) exhibited increased potency and efficacy in vitro and in vivo, respectively. The maximum tolerated dose (MTD) for the SACNs in BALB/c mice to be 16 mg/kg compared with 9 mg/kg of cisplatin (Fig. 11). We next dosed syngeneic BALB/c mice bearing 4T1 breast tumors (mean tumor volume ~100 mm3) with a single dose of cisplatin (8 mg/kg). Other groups of animals received vehicle, carboplatin, or SACNs, (the latter two received a Pt dose equivalent to 8 mg/kg dose of cisplatin). As shown in Fig. 11, although all of the platinates resulted in significant tumor inhibition compared with the vehicle-treatment, the SACNs exerted the maximal tumor inhibition (P < 0.01 vs. control) followed by cisplatin and carboplatin. Furthermore, although treatment with carboplatin or cisplatin exerted only minor increase in survival over vehicle-treated controls, the SACNs significantly increased overall survival trend (Fig. 11). We next tested the effects of multiple low-dose treatment with cisplatin, carboplatin, or the SACNs, with the highest platinum dose in each case adding up to the levels of Pt delivered at the MTD of cisplatin. Two additional groups were included that were treated with a lower dose of cisplatin or SACNs (equivalent of 1 mg/kg dose of platinum). As shown in Fig. 11 treatment with cisplatin resulted in a dose-dependent inhibition of tumor growth. Interestingly, although at the highest doses the tumor inhibition with the SACNs or cisplatin were identical, at the lower doses the SACNs exerted a superior antitumor effect compared with free cisplatin (P < 0.05, ANOVA). Furthermore, cisplatin resulted in a significant reduction in mean body weight (P < 0.05, ANOVA) compared with the SACN-treated groups (Fig. 11), indicating that the latter can reduce the systemic toxicity associated with cisplatin chemotherapy. Interestingly, even at the lower dose both the SACNs and cisplatin exerted greater tumor inhibition as opposed to the higher dose of carboplatin (Fig. 11). At the higher dose, both cisplatin and SACNs were found to increase survival, although the latter was superior (Fig. 11). These results have recently been published in the PNAS.

We had proposed that we will engineer nanoparticles in which we will entrap PI3K inhibitors. Interestingly, the supramolecular nanoparticle platform can be extended to engineering nanoparticles from PI3K inhibitors. In a recent study, we have engineered such a nanoparticle using PI828 and PI103, potent inhibitors of PI3K. As shown in Fig. 12, we engineered the SNPs from the cholesterol-PI828 or cholesterol-PI103 conjugates, phosphatidylcholine (PC) and 1,2-distearoyl-*sn*-glycero-3-phosphoethanolamine-N-[amino(polyethylene glycol)-2000] (DSPE-PEG2000) at optimized weight ratios using a lipid-film hydration self assembly method. The incorporation efficiency for the cholesterol-PI828 SNPs was 43%, and 60±5% for PI103-cholesterol conjugate SNPs. As shown in Fig. 11D, cholesterol-PI828 conjugates resulted in the formation of SNPs with hydrodynamic diameter of 108 ± 8.9 nm as determined by dynamic light scattering. PI103-SNPs showed a mean particle diameter of 172±1.8 nm. Ultrastructure analysis using cryo-transmission electron microscopy (cryo-TEM) revealed the formation of predominantly unilamellar structures 100 nm or less in diameter. The size difference between TEM and DLS measurements can be attributed to the hydration sphere arising from the PEG coating, which can facilitate the masking from the reticuloendothelial system. Additionally, aliquots of the PI103-SNPs were stored for a period of over a month, and the size and zeta potential was measured periodically as a measure of stability of the nanostructure. As show in **Fig. 12**, no significant temporal variation was observed in either size or zeta potential during this period, indicating that the formulations were stable. To study the temporal kinetics of PI3K inhibitor release, the SNPs were incubated either in phosphate buffer saline or in cell lysate. While the amount of drug released in PBS was saturated at ~20%, a sustained release of drug was observed in cell lysate, consistent with the cleavage of the linkers in acidic and enzymatic (esterase) conditions. Interestingly, while a sustained and increasing drug release was observed with PI103-SNP, the rate of release of PI828 was significantly lower. This is consistent with the carbamate linker between the drug and cholesterol, which is more stable than the ester linkage in the PI103-SNPs.

Fig. 12: Synthetic scheme showing conjugation of **(A)** PI-828 and **(B)** PI103 to cholesterol via carbamate and ester linkages respectively; **(C)** Schematic representation shows assembly of supramolecular nanoparticles (SNPs) from phosphatidylcholine (PC), PI103/PI828-cholesterol conjugate and DSPE-PEG; Distribution of hydrodynamic diameter of **(D)** PI828-SNPs and **(E)** PI103-SNPs measured using dynamic light scattering; **(F)** High resolution cryo-transmission electron microscopy image of PI103-SNPs (Scale Bar = 100 nm); **(G)** Physical stability of PI103-SNPs during storage condition at 4^0C as measured by changes in size. Inset shows changes in Zeta potential of nanoparticles at 4^0C; **(H)** Release kinetics of PI103 from SNPs in PBS, pH 7.4, and in 4T1 breast cancer cell lysate. **(I)** Release kinetics of PI828 from SNPs in PBS, pH 7.4 (blue line), and in lysates from 4T1 cells (red line) and PI3K-overexpressing 4306 ovarian cancer cells (green line). Data shown are mean±SEM (at least triplicates at each condition).

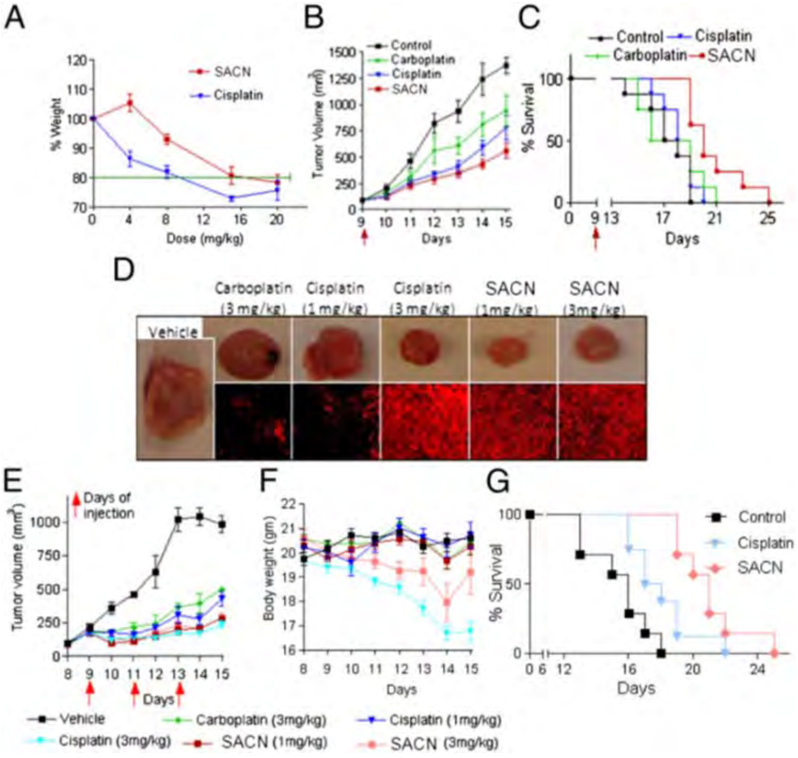

We next investigated the anti-tumor efficacy of PI103-SNPs in 4T1 breast cancer, which is negative for ER and PR, and expresses a low level of the mouse Her2/neu equivalent. Transplanted into syngeneic mice, the 4T1 form aggressive, highly metastatic breast cancers. Mutations in genes that constitute the PI3K pathway occur in >70% of breast cancers. We have previously demonstrated that the 4T1 cells mount a survival response to standard chemotherapy via an upregulation of PI3K signaling. We treated mice with 4T1 tumors with a dose equivalent to 5 mg/kg of PI103 as free drug or as PI103-SNP. The treatment was started when the mean tumor volume had reached 100 mm^3, As shown in **Fig. 13**, treatment with PI103 resulted in tumor growth inhibition relative to PBS-treated controls, but tumor rebound was observed after the treatment was stopped. In contrast, treatment with PI103-SNP resulted in sustained tumor growth inhibition over the study period. This was consistent with the sustained level of the drug in the SNP group. After a single injection, intratumoral Akt phosphorylation was inhibited by both the free drug and PI103-SNP compared to the vehicle-treated group. PI103-SNP seemed more efficient, but the difference was not statistically significant. Interestingly, the phosphorylated forms of downstream signaling molecules, mTOR and 4EBP, were more strongly inhibited in the PI103-SNP-treated group than in the PI103-treated tumors (P<0.05, t test).

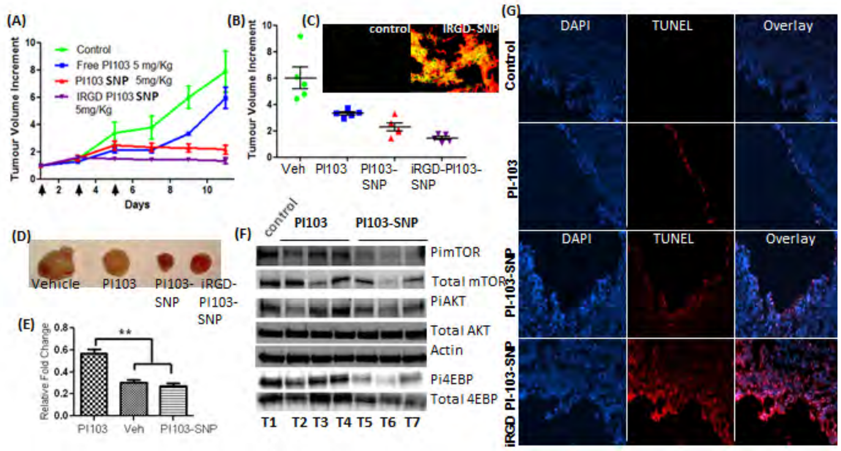

Fig. 13. (A) *In Vivo* efficacy of PI103 or PI103-SNP in syngenic 4T1 breast cancer mouse model. The mice were given 3 injections every other day of PBS (control group), of free PI013, PI103-SNP or iRGD-coated PI103-SNP all 5 mg/kg dose equivalent of PI103. The first day of treatment was considered as Day 1. Tumor volumes were measured every other day for 11 days. The endpoint was tumor size >2000cm^3, or tumor ulceration or necrosis, or death of the animal. **(B)** Distribution of tumor volume increment in different groups at day 11 after the 1st injection. Treatment with PI103-SNP and iRGD-coated PI103-SNP was statistically more effective than treatment with free PI103; **(C)** Immunoflurescence images of frozen sections of tumors from mice treated with PBS or PI103-SNP coated with FAM-labeled iRGD, showing effective tumor targeting with iRGD-coated PI103-SNP. The sections were also labeled for von Willebrand factor (Texas-Red), which delineates the vasculature. **(D)** Pictorial representation of tumor volume from each group; **(E)** Graph showing the effect of PI103 on insulin tolerance. The mice were injected with a single dose of empty SNPs, Free PI-103 (5mg/kg) and PI103-SNP (5 mg/kg). One hour later, the mice were injected with insulin (0.75 units/kg). Blood glucose levels were measured before and 45 min after the insulin injection. Results are mean ± SEM (n = 5). Statistical significance was determined by student t-test. **$p < 0.01$ **(F)** Expression of phospho mTOR, total mTOR, phospho AKT, total AKT, actin, phospho 4EBP and total 4EBP in tumors 72 hours after single dose injection of free PI103 or PI103-SNP at 5mg/kg dose in the 4T1 model. **(G)** Representative epifluorescent images of tumor sections from different treatment groups were labeled for apoptosis using TUNEL (red) and counterstained with DAPI (blue).

To test whether targeting the nanoparticles to the tumor using ‘homing’ peptides increases antitumor efficacy, a separate group of tumor mice were treated with PI103-SNPs that were surface-decorated with iRGD peptide. As shown in Fig. 13, such a treatment resulted in greater tumor inhibition than what was obtained with SNPs that accumulate via passive uptake. Indeed, previous observations have shown that iRGD-coated nanostructures exhibit increased extravasation and tissue penetration in a tumor-specific and neuropilin-1-dependent manner. As shown in **Fig. 13,** epifluorescence imaging of tumor cross-sections revealed significant intra-tumoral localization of FAM-labeled iRGD coated PI103-SNPs. To elucidate the mechanism underlying the increased *in vivo* efficacy, the tumors were excised post-treatment, and processed for terminal deoxynucleotidyl transferase dUTP nick end labeling (TUNEL) as a marker for apoptosis. As shown in **Fig. 13**, treatment with PI103-SNPs resulted in greater apoptosis than treatment with free PI103. iRGD-coated PI103-SNPs induced highest level of apoptosis, followed by PI103-SNPs and free PI103, consistent with the tumor inhibition result.

Task 3. Assay for tumor detection (hit-and-run assay)

3a.Test a prototype assay in which a mixture of nanoparticles coated with either a tumor-homing peptide or a control peptide is injected into a tumor-bearing mouse and a change in the ratio of the particles in the circulation is monitored.

3a.1. Functionalization of magnetic nanoparticles with cleavable homing-CendR peptide chimera and physicochemical characterization.

The Ruoslahti laboratory, in collaboration with the Reich laboratory, has provided the first reduction to practice of the hit-and-run assay. This novel multiplexed nanoparticle platform utilizes iron oxide nanoparticles doped with gadolinium isotopes for in vivo tracking. Blood samples and tissue samples were analyzed using ultra-high sensitivity inductively coupled plasma-mass spectrometry (ICP-MS).

The principle is outlined in **Fig. 14**. The detection and barcoding are based on measurement of radiostable gadolinium isotopes by ICP-MS. Each type of nanoparticle is labeled with a unique isotope and functionalized with a distinct peptide sequence. The mixture of nanoparticles is injected into tumor-bearing and non-tumor bearing (normal) mice. Blood analysis detects the binding of receptors within vascularized, diseased tissue, by monitoring the selective clearance of targeted nanoparticles relative to control nanoparticles.

We have developed materials and methods with reliable multiplexing results across at least four logs of injected dose, validated over several combinations of nanoparticle coatings. In principle the technique may eventually allow multiplexing 10-100 isotopes in a blood or biopsy assay. High atomic mass, stable isotopes, with low biological abundance are ideal. We chose gadolinium since it has been shown to be easy to dope into iron oxide nanoparticles. The main challenges to ICP-MS hit-and-run are 1) the reproducible synthesis of a pair of labeled materials that differ only in the prescribed manner, i.e. outer ligand region. The clearance of materials is the major source of interference in this assay and the dependence on surface chemistry is not well understood. 2) A procedure for digesting and analyzing small volumes of blood. 3) Instrument calibration and stability in multiplexed mode of operation.

We set out to use ratios to monitor selective clearance since that quantity best captures subtle changes in the blood. Ratios correct for certain difficult to control parameters in dosing and collection. The internal standard corrects for differences in injected volume and the blood sampled, dilution/digestion pipetting errors, and instrument sensitivity variation. ICP-MS is very accurate in isotopic ratio analysis, and extremely sensitive in detection. We have explored in depth both ratio and absolute quantities and find the ratio analysis reliable for analyzing large sample sets.

In the experiments described below we detect the presence of a tumor using circulating iRGD peptide carried on nanoparticles and PEG controls. The iRGD pool is depleted in the tumor mouse in a rate and degree related to the particle accumulation in the tumor. This is validated by end-point tissue analysis by ICP-MS and tissue section microscopy.

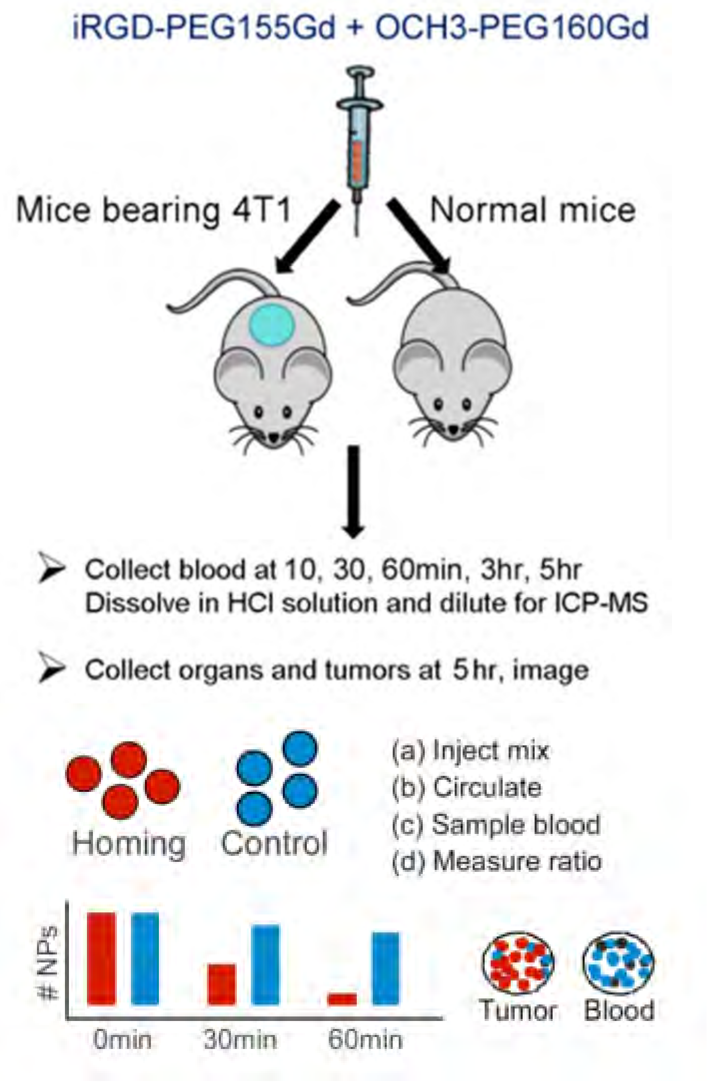

Fig. 14. Targeting with iRGD peptide, versus high molecular weight PEG control particle. Isotope-labeled iron oxide nanoparticles (metals: 5% Gd, 95% Fe) coated with dextran and PEG are functionalized with either a tumor homing peptide (iRGD) or having the inert methoxy group (OCH3), and contain either 155Gd or 160Gd. The two barcoded particles are then mixed at ~1:1 and injected into the tail vein of a mouse. Over the course of a few hours blood is taken and measured for relative nanoparticle content. A sample of the injected solution is analyzed for the 160Gd/155Gd isotopic concentration. Blood values reveal the consumption of homing particles by the tumor.

3a.2. In vivo evaluation of the prototype nanoparticle

The homing properties of the Gd-doped nanoparticles are shown in Figure 15 using the tumor penetrating peptide, iRGD. We could detect the iRGD-Gd-Iron oxide (GDI) across different injection doses (5, 0.5, 0.05 mg/kg) and find that with reduction in the injection dose less nanoparticles accumulate in the tumor and liver. We attribute this to saturation of the sites at the high dosage.

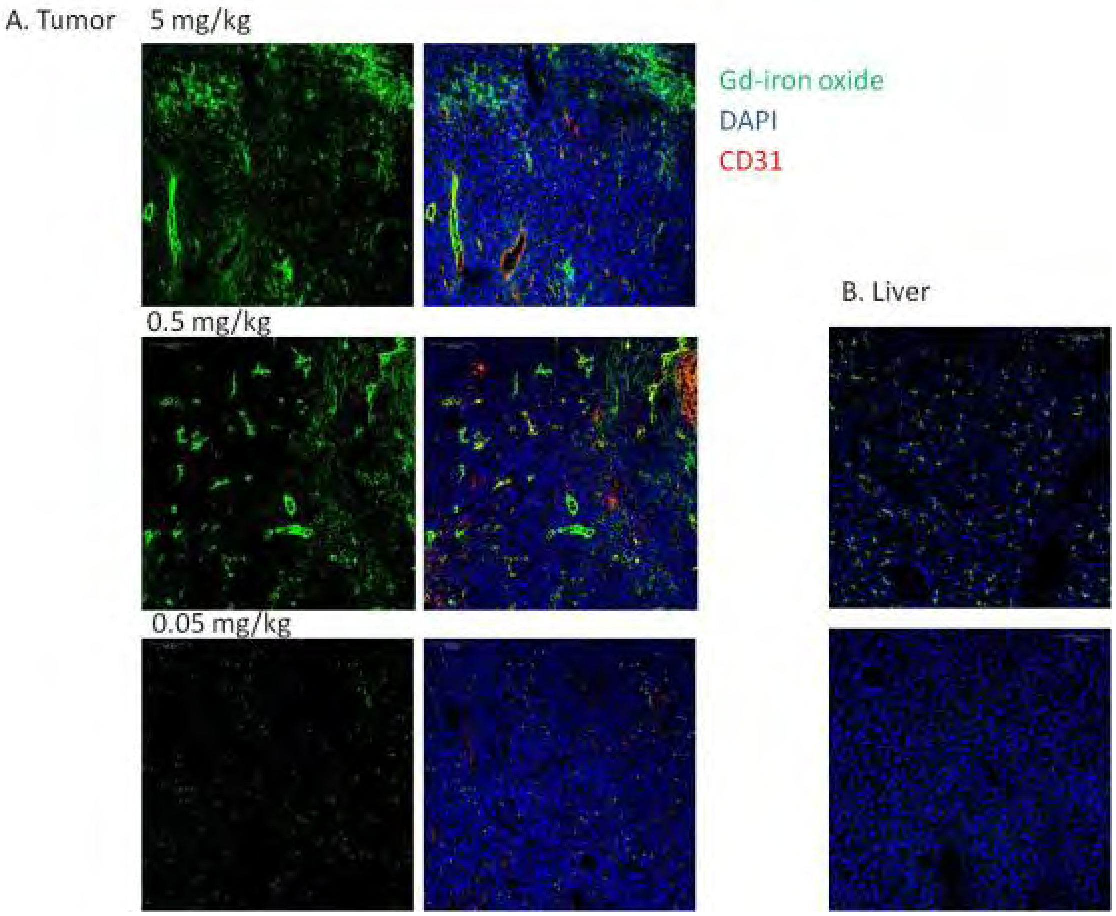

Figure 15. Gd-doped iron oxide (GDI) nanoparticles were conjugated to iRGD through a 5K-PEG linker. After injection the organs were collected and analyzed by confocal microscopy. iRGD-GDI homes and extravasates into the tumor tissue. At lower dose the homing property is retained. Green, FAM-iRGD-GDI; red CD31 staining indicates blood vessels; DAPI shows cell nuclei.

Blood analysis monitors the ratio of the two particles as given by their isotope labels (160Gd and 155Gd). We show here that the rapid phase of clearance of PEGylated and iRGD (targeted) nanoparticles happens during the first 30 min (Figure 16). A difference between the PEG and iRGD non-targeted nanoparticles is detected at ~10 min (Figure 16B). We found this behavior consistent across a range of injected dosage.

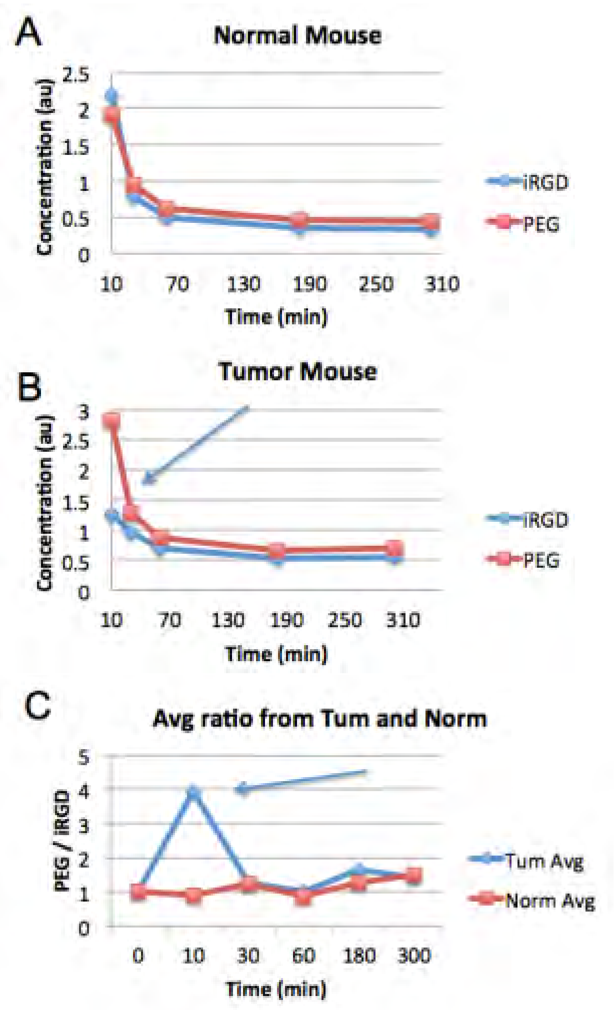

Figure 16. An example experiment using 0.0005 mg/kg Gd-doped iron oxide, coated with either PEG or PEG-iRGD coatings. These are termed PEG and iRGD nanoparticles, respectively. They were mixed and injected into mice with blood samples of 10 µL taken at 10, 30, 60, 180, and 300 min. Multiplexed ICP-MS blood analysis for the concentration of Gd isotopes shows clearance of iRGD nanoparticles is quite similar to PEG nanoparticles in the normal mouse (A), whereas in the tumor-bearing mouse the iRGD selectively disappears from circulation (B). (C) The ratio of PEG/iRGD may be used to capture the difference between the mice. The average of two normal and two tumor mice is plotted, showing a peak difference at ~10 min.

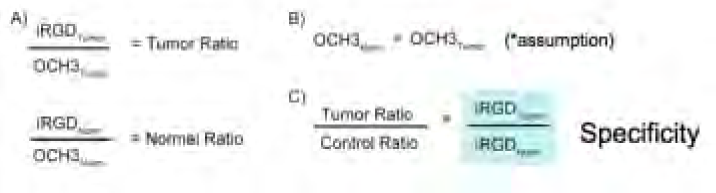

Figure 17. Specificity defined by a ratio of ratios. A) Multiplexed blood ratio value for each time point is acquired. B) We assume a similar relative clearance of the non-targeted OCH3 particle. C) Dividing the tumor-mouse's ratio trace by the trace of the normal mouse gives the specific response of iRGD for the tumor.

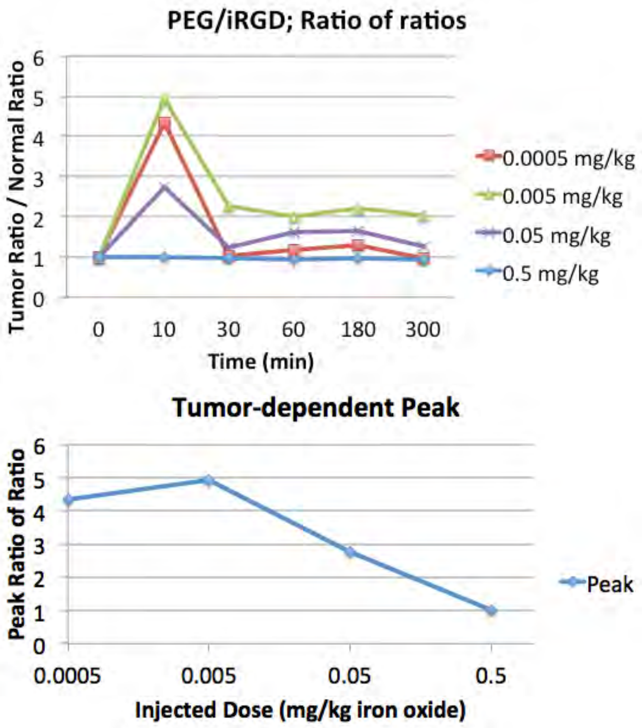

Figure 18. Difference between normal and tumor-bearing mice were quantified at each time by dividing the ratios shown for 0.0005 mg/kg in Figure 16C. Here we look at how the ‘ratio of ratios’ can give insight as we increase the dose in log units. Diagnostic contrast in our tumor mouse model appears when the dose is under 0.05 mg/kg, with iRGD delivery to the tumor showing up as a peak in the ratio of ratios ~10 min post injection. At longer time points the continual clearance of both particles by the liver and spleen (RES) counteracts the differences between the two particles, and the ratio moves back towards a value of one. The quantity of iRGD nanoparticles that bind in the tumor (disappear from blood) is a modest fraction of the total dose only until vascular receptor saturation, shown here and by microscopy in Figure 15 to occur above 0.05 mg/kg. It is considered that receptor recycling, if taking place, is not competitive with the bulk RES interference for this set of nanoparticles.

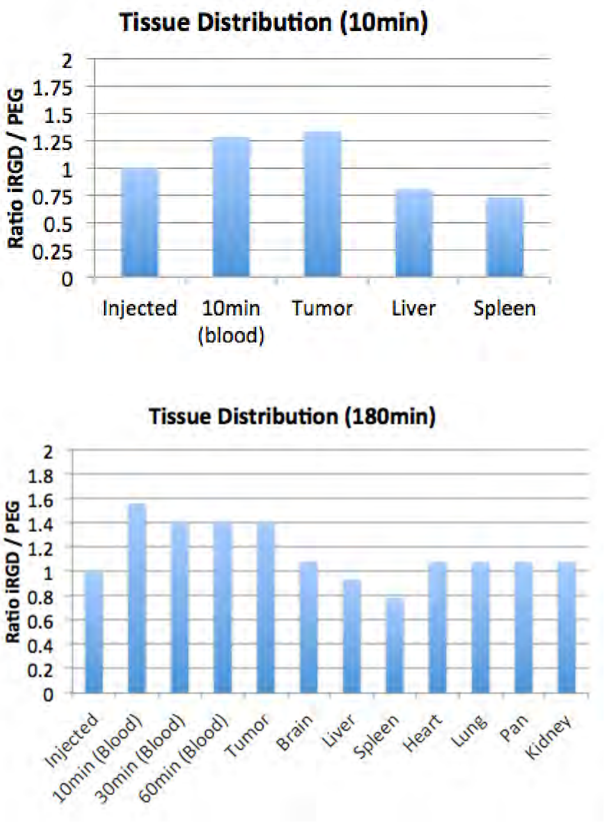

Figure 19. Correlating selective blood clearance of iRGD nanoparticles with end-point perfusion and tissue digestion ICP-MS. PEG nanoparticles serve as control, co-injected as described above. All ratios of 155Gd/160Gd (iRGD/PEG) are normalized to the injected value therefore positive deviations can be converted into preferential iRGD accumulation. At both 10 min and 180 min we detect an excess of iRGD in the tumor. Interestingly, the liver and spleen show the opposite accumulation. Other organs show a neutral value. We note that the absolute signals of brain, heart, lung, pancreas, and kidney were all significantly lower than tumor levels, an indicator of perfusion quality, and the low non-specific uptake of the nanoparticles.

$$Cp = A \cdot e^{-\alpha t} + B \cdot e^{-\beta t}$$

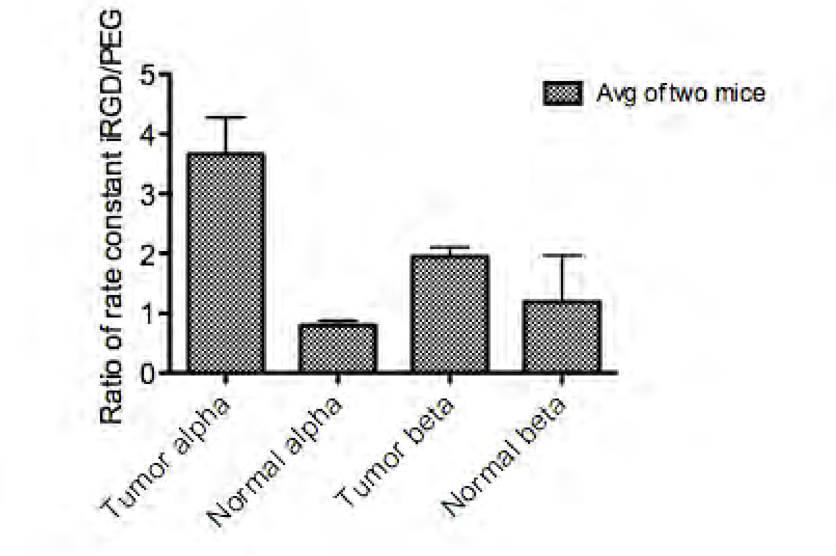

Figure 20. Rate constants were determined using a two-compartment model. Cp is concentration of the nanoparticle in question, alpha and beta are macro rate constants for double-exponential half-life pharmacokinetics as observed. A and B are proportional to initial dosage. Alpha, the faster rate constant, characterizes early clearance from the blood (central compartment), into tissue (peripheral compartment). The ratio of (alpha iRGD) / (alpha PEG) is higher for tumor-bearing mice than for normal mice, as expected for rapid binding assay (liver obscures later phase). We are currently comparing validity of other more complex models.

Using the two-compartment model we have gained insight into the key variables for the assay. For each component of the injected mixture we fitted using the double exponential decay function (Figure 20, Cp formula). When clearance of a given material has both fast and slow decay rates, component alpha defined as the faster rate constant and beta the slower. We calculate alpha and beta for each isotope, by fitting the absolute concentrations in blood over time. PEG alpha value (the faster rate constant) is significantly different from iRGD alpha only in tumor-bearing mice. Beta ratio values were similar between the two isotopes for the two groups. In Figure 20 we have plotted the $\text{alpha}_{iRGD}/\text{alpha}_{PEG}$ ratio values showing the significant difference in tumor-bearing mice (Figure 20). Consistent with this analysis, the early phase 0 to 30 min is where the nanoparticle concentration ratios diverged in Figure 18.

The aim of this project is to diagnose and stage a tumor by injecting a pre-mixed set of nanoparticles where some bind to vascular targets, others do not, and measuring the progressive changes in their blood ratio. Our current data demonstrates the feasibility of detecting a tumor by blood analysis alone. The difficulty in detecting low concentrations of nanoparticles from blood is largely solved by the use of ICP-MS and barcoding nanoparticles with isotopes that are not found in the body, and which are non-toxic. Synthetically the particles should be as similar as one can make them, with long half-lives and high, specific affinity. We use an iron oxide core to minimize potential toxicity of the carrier, although the doses used here are well below those typical for iron oxide or gadolinium based MRI contrast agents.

The multi-valency cyclic peptide has strong affinity (and avidity) which encourages rapid binding, on a time scale least complicated by the liver and spleen RES system. We expect that advances in nanoparticle coatings, driven by a better understanding of RES-nanoparticle interactions will free the hit-and-run assay to include more sophisticated theranostic nanoparticles that may act on longer timescales. We are now testing a peptide control that has D-amino acids in just two positions of the iRGD sequence. We hypothesize that it will behave most similarly to iRGD with respect to RES clearance rates, but the mutations completely remove the integrin binding affinity. Subtle changes such as these should be ideal for detecting the presence of a binding pocket within the complex environment of blood and vascular receptors.

3b. Examine the suitability of surface enhanced Raman spectroscopy (SERS) for *in vivo* detection of barcoded nanoparticles

We encountered problems with high background and low sensitivity of SERS detection of *in vivo* probes and developed the gadolinium-doped iron oxide nanoparticles described in 3a as an alternative.

3c. Bipartite tumor-homing peptides

Most of our effort has been exploiting the discovery reported last year of ratiometric ACPPs (RACPPs) in which cleavage not only unmasks adhesive $(arg)_9$ but disrupts fluorescence resonance energy transfer between Cy5 and Cy7, leading to a large increase in Cy5/Cy7 emission ratios, which in turn allows more rapid and robust discrimination between tumors and surrounding normal tissues. Our optical system for real-time fluorescence-guided surgery required much modification and upgrading to produce continuous pseudocolor-encoded emission ratio images in real time. The major new findings are as follows:
1) *Extension of RACPPs to proteases other than matrix metalloproteinases-2 and -9*: We synthesized RACPPs specific for other enzymes such as elastase and thrombin and found that their FRET responses were practically unchanged despite the necessary changes in substrate sequence. Therefore the RACPP design seems applicable to any protease (and probably any cleavage activity) for which a specific substrate can be designed.
2) *RACPPs Enable Detection of Metastases onto Liver* - Previous single fluorophore labeled ACPPs gave high uptake into normal liver, which made it unlikely that we could distinguish metastases by standard single-wavelength imaging. We have developed a syngeneic model in which GFP-labeled 8119 mammary tumor cells colonize the liver (GFP image, Fig. 21a,e). Gratifyingly, these metastases gave high ratio

Figure 21

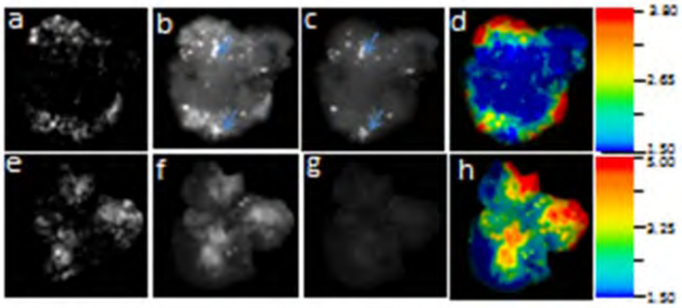

Figure 21. Livers containing PyMT 8119 GFP positive metastases, harvested from mice 2 hr after IV injection of RACPP1 (MMP2,9-selective, a-d) or RACPP3 (elastase-sensitive, e-h). a, e) GFP fluorescence images. b,f) Cy5 fluorescence images obtained by exciting Cy5 at 620 nm. c,g) Cy7 emission images obtained by exciting Cy5, d,h) Cy5/Cy7 emission ratio images. Ratio images showed better correlation with GFP reference emission images than either Cy5 or Cy7 independent images. The ratio contrast for metastases relative to normal liver was higher for RACPP3 (h) than for RACPP1 (d). Arrows exemplify two of the many nontumor regions (as judged by lack of GFP fluorescence) where both Cy5 and Cy7 fluorescence intensities were high, resulting in relatively low ratios.

contrast following RACPP1 injection compared to adjacent normal liver tissue (Fig. 21d). The coregistration between these ratio images and the GFP reference channel (Fig. 21a) is quite good, considering that the wavelengths for RACPP1 penetrate much more deeply than those for GFP. The two individual channels for Cy5 and Cy7 (Fig. 21b,c respectively) show many coincident non-tumor accumulations (two of which are marked by arrows) that are largely canceled with ratioing. When the MMP cleavable sequence PLGC(Me)AG was replaced by an elastase-cleavable sequence, RLQLK(Ac)L, the resulting analog, RACPP3, showed spectra before and after cleavage similar to those of RACPP1. This elastase probe showed an even larger difference in ratio between metastases (ratio= 5.0 ± 0.35, average of 32 GFP positive metastases from 4 mice) and normal liver (1.49 ± 0.1, $p < 10^{-13}$). Ratio images of RACPP3 (Fig. 21h) again correlated much better with GFP reference images (Fig. 21e) than the constituent Cy5 and Cy7 images did (Fig. 21f, g). A nonratiometric analog of RACPP3 lacking Cy7 failed to produce any contrast for liver metastases.

3) *Detection of Lymph Node Metastases Using RACPP* - To evaluate cancer involvement of individual lymph nodes during surgery, mice bearing primary auricular 8119 tumors derived from transgenic mammary tumors were IV injected with RACPP1. Within 1-2 hours, we found significantly increased Cy5/Cy7 ratio in lymph nodes that were involved in cancer compared with lymph nodes that were not (Fig. 22a, Fig 23). Mice injected with the uncleavable control RACPP showed no increased Cy5/Cy7 ratio in either metastatic or normal lymph nodes (Fig. 22b, Fig. 23a). Quantitative analysis of Cy5/Cy7 ratio change showed that RACPP was sensitive enough to detect the presence of metastatic cancer cells even when only a fraction (8-26%) of the lymph node was invaded by cancer (Fig. 22f,h, Fig 23a). Prospective analysis of lymph node metastases in a second set of mice with primary 4T1 tumors injected with RACPP1 using a discrimination threshold (set at ratio of 1.2 or greater) derived from the first set of 8119 lymph node metastases gave specificity=100% (n = 16/16); sensitivity=100% (n = 6/6).

Figure 22

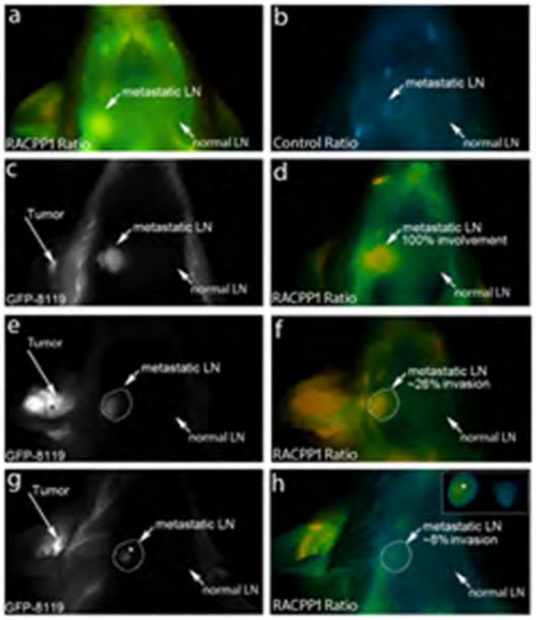

Figure 22. Cy5/Cy7 ratiometric image of mice bearing auricular primary tumors (8119 line) showing increased ratio in pathologically confirmed metastatic LN but not normal LN following IV injection with RACPP1 (a). Mice injected with uncleavable control probe (b) did not show increased ratio in any lymph nodes. Fluorescent images of mice with primary auricular 8119 tumors bearing GFP with ipsilateral lymph node metastases (GFP images in c,e,g) corresponding to increased Cy5/Cy7 ratio following IV injection with RACPP1 (d,f,h). When there was only partial cancer invasion for a given lymph node (e-f, g-h, dotted lines showing LN contour), the area of increased ratio (f,h) localized with GFP signal (asterisk). All ratio images (a,b, d, f,h) were identically scaled over a range of 40 (minimum-maximum = 0.2-8) to accommodate the wide dynamic range provided by RACPP1. Note that although the lymph node with only 8% cancer invasion (h) had lower Cy5/Cy7 ratio in a restricted region (asterisk) compared to lymph nodes with more complete invasion (a,d,f), ratiometric measurements still showed it to be higher than any adjacent normal tissue (insert scale narrowed to visually emphasize the ratiometric change, minimum-maximum = 2-5). h,insert: Ratiometric images *ex vivo* of dissected metastatic LN and contralateral LN.

Our previous best intensity-only probes were ACPPs attached to Cy5-labeled dendrimers (ACPPD). We compared ACPPD and RACPP1 for their sensitivity and specificity of metastasis detection in lymph nodes following IV injection of either probe into mice bearing primary auricular 8119 tumors. After recording fluorescence images from the exposed nodes *in vivo*, the presence or absence of metastasis was verified by independent post mortem histology. Although the ratio of ACPPD Cy5 intensities in nodes vs. adjacent normal tissue was significantly higher ($p = 0.02$) for metastatic than nonmetastatic nodes, there was considerable overlap preventing perfect discrimination at any threshold. The same measure using only Cy5 intensities for RACPP1, i.e. treating it only as a dequenching probe, gave an even more significant difference ($p = 0.0007$) and complete separation according to node status. Even more robust ($p < 10^{-4}$) discriminations of metastatic status were obtained from Cy5/Cy7 ratios of just the node or of the node further ratioed against adjacent normal tissue (Fig. 23b).

Figure 23

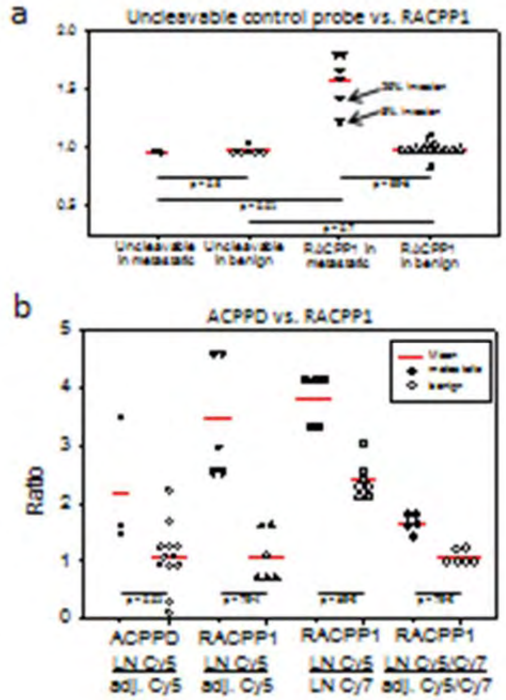

Figure 23. a) Cy5/Cy7 ratio of lymph nodes versus adjacent normal tissue in animals injected intravenously with either control uncleavable probe or RACPP1. Each symbol represents a separate lymph node whose status (solid = metastatic, hollow = non-metastatic) was independently determined by histology. In mice injected with control uncleavable probe, the presence (solid circles) or absence (hollow circles) of cancer invasion did not change the ratio of lymph node Cy5/Cy7 emission ratios relative to adjacent normal tissue, all values being near 1. In mice injected with RACPP1, lymph nodes with cancer invasion (solid triangles) had significantly higher ratios than lymph nodes without cancer invasion (hollow triangles). Interestingly, the ratio of Cy5/Cy7 emission ratios in nodes vs. adjacent normal tissue correlated with the degree of cancer invasion, where the lymph nodes with partial cancer invasion (arrows) showed less ratio increase (albeit still higher than any normal tissue) than lymph nodes with 100% cancer invasion. b) Dot density graph showing higher sensitivity/specificity of RACPP1 compared to ACPPD in the differentiation between lymph nodes bearing cancer invasion (solid symbols) versus adjacent normal tissue (hollow symbols). For ACPPD, although mean Cy5 fluorescence intensity of metastatic lymph nodes relative to adjacent normal tissue (solid circles) is significantly higher ($p = 0.02$) than for lymph nodes without metastasis (open circles), there is overlap which decreases sensitivity/specificity. Metastatic lymph nodes in mice following IV injection of RACPP1 show higher Cy5 intensity relative to adjacent normal tissue (solid triangles), Cy5/Cy7 ratio alone (solid squares) or ratios against adjacent normal tissue (solid diamonds) significantly higher ($p = 7 \times 10^{-4}$, 8×10^{-5}, 7×10^{-6}, respectively) than nonmetastatic nodes (hollow symbols). Because metastatic and benign nodes do not overlap in the RACPP1 ratios, sensitivity and specificity can be 100%.

4) *Ex vivo analysis of patient samples* – Two critical questions in translating these results to patients are
a) what fraction of clinical tumors have enough protease activity to cleave our RACPPs?
b) can we develop a personalized assay from biopsy material to tell whether a given patient's tumor has enough protease activity? Obviously if the patient's tumor lacks activity, we should not attempt to use RACPPs to guide surgery. Both these questions become answerable with RACPPs, because the loss of FRET over time can be measured in homogenates prepared from small amounts of frozen tissue, including banked tissues examined retrospectively. Previous nonratiometric ACPPs could not be assayed ex vivo because the only effect of enzyme activity was to increase pharmacokinetic retention, which can only be tested *in vivo*, not on homogenates from frozen tissue. Preliminary results indicate promising distinction between normal tissues and known tumors (Fig. 24), but we are collecting large numbers of fresh-frozen and banked clinical specimens (including mammary tumors) to achieve sufficient statistics. We are also attempting to extend this principle to a histological assay so that RACPP-cleaving (i.e.

protease) activity can be mapped with high spatial resolution on thin sections.

Fig. 24

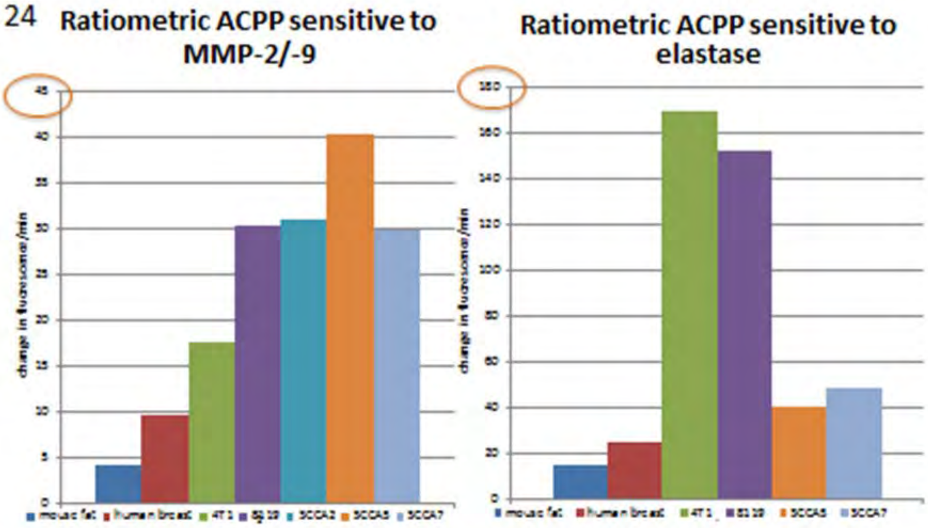

Fig. 24: Ability to cleave RACPPs can be assayed *ex vivo* on frozen tissue samples and may differentiate normal from tumor tissues. Y axis indicates rates of change of Cy5 fluorescence (arbitrary units) over time following addition of MMP- and elastase-sensitive RACPPs to 100 mg homogenized fatty tissue from mouse, normal human breast, two mouse breast cancer grafts (4T1 and 8119), and human head and neck squamous cell carcinoma lines.

Efforts to develop a "hit-and-run" assay to measure intact substrate vs. cleavage products in readily accessible body fluids like blood and urine were suspended due to inconclusive preliminary results and the recruitment by industry of the postdoc skilled in electrophoretic separations of crude samples.

Task 4. **Develop a multifunctional nanoparticle that delivers a drug to tumor vessels and tumor cells, while releasing a diagnostic component into the circulation**

4a. Adapt the barcoded diagnostic technology onto polymer-based drug-loaded multifunctional nanoparticles, and characterize for physicochemical properties

The Ruoslahti laboratory has developed two nanosystems for cancer treatment that are based on iron oxide nanoparticles and shown their efficacy in breast cancer. An intratumorally spreading local tumor treatment effective in breast cancer models has also been developed (Chen et al., *Cancer Res.* in revision). These advances have been reported in detail elsewhere ((W81XWH-08-1-0727 annual report – Oct 2012). The bar-coded detection can easily be incorporated into the nanosystems.

4b. Characterization of multifunctional nanoparticle in *in vivo* tumor models, including testing for tumor homing, penetration and uptake into tumor cells

Last year the Tsien group reported that the ACPPs conjugated to ligands for integrin αvβ3 gave considerably more tumor contrast than either targeting mechanism alone, consistent with literature reports that αvβ3 and MMP-2 form a molecular complex. We have now applied such targeting to chemotherapeutic applications by synthesizing ACPPs with a powerful cytoskeletal inhibitor, monomethyl auristatin E (MMAE), targeted with our best combination, cyclic(RGD) in combination with the MMP-2/-9 cleavable PLGC(Me)AG within the ACPP. The MMAE was attached to the (arg)$_9$ domain via the same cathepsin-sensitive linker as used in the recently FDA-approved antibody-drug conjugate brentuximab vedotin. Fig. 25 shows promising early results in regressing orthotopic MDA-MB-231 xenografts, a model for triple-negative breast cancer. The mice were dosed either with vehicle, 0.2 mg/kg free MMAE, equimolar cRGD-(MMP-sensitive ACPP)-MMAE (6.5 nanomoles peptide), or a control drug conjugate in which both the cyclic(RGD) and ACPP were crippled. Dosing was every three days for a total of four doses and tumor volumes were measured at regular intervals. The dual negative peptide drug conjugate (c(RADfC) and PEG6, green lines) performed worse than unconjugated MMAE (red lines), whereas the dual targeted peptide drug conjugate (c(RGDfC) and PLGC(Me)AG, purple lines) demonstrated a significant (p=3.1x10^{-3}) reduction in average tumor volume and longer survival (p=0.014 by log rank test) compared to unconjugated MMAE (red lines). 2 out of 7 mice seem to have achieved permanent cure. When the dose was increased to 0.32 mg/kg MMAE (peptides still equimolar), the dual targeted peptide caused 4 out of 8 tumors to regress completely, compared to 2 out of 8 for equimolar free MMAE. The ACPPs caused no weight loss or gross toxicity. We are continuing to explore different doses, look more closely for any toxicities, and dissect the relative contributions of the c(RGD) and ACPP targeting mechanisms. ACPPs are much smaller than antibodies, should penetrate solid tumors more easily, and so far have shown much wider applicability across a range of tumor types than any single antibody.

Figure 25

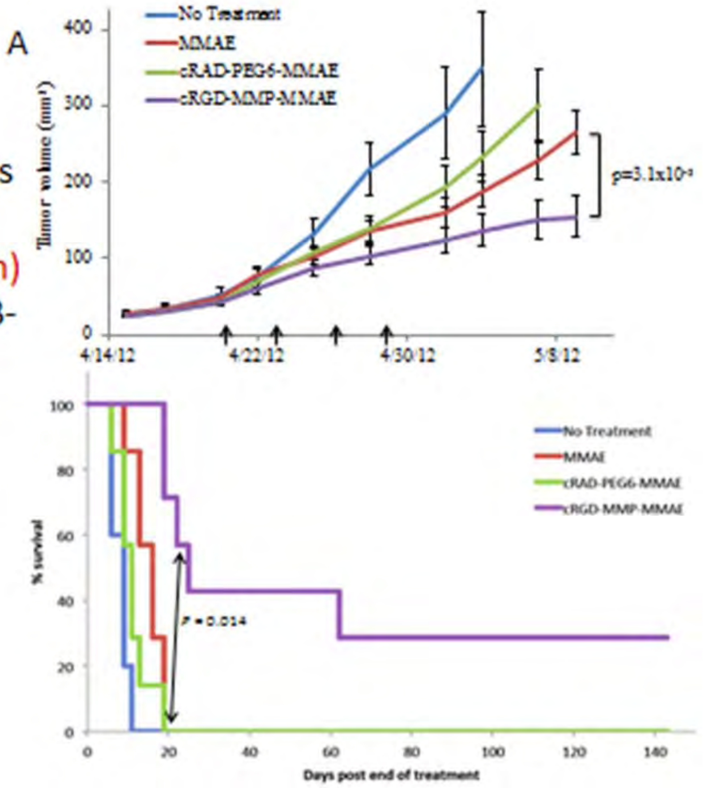

c(RGD)-ACPP-drug conjugate outperforms untargeted drug (monomethylauristatin) in regressing MDA-MB-231 orthotopic xenografts

Jessica Crisp,
Elamprakash Savariar

4c. Characterize the antitumor efficacy and mechanism of action of the multifunctional bar-coded nanoparticles *in vivo* Future work will address this aim.

REPORTABLE OUTCOMES

(1) Papers published, in press, and submitted:
The Ruoslahti laboratory:

Sanchez-Martin, D., Cuesta, A.M., Fogal, V., Ruoslahti, E., and Alvarez-Vallina, L. The multi-compartmental p32/gCiqR as a new target for antibody based tumor targeting strategies. J Biol Chem 286:5197-5203 (2011) PMC:3037632

Roth, L., Agemy, L., Kotamraju, V.R., Braun, G., T. Teesalu, T, Sugahara, K.N., Hamzah, J., and Ruoslahti E. Transtumoral targeting enabled by a novel neuropilin-binding peptide. *Oncogene*, 31: 3754-3763(2012). PMID: 22179825

Ruoslahti, E. Peptides as targeting elements and tissue penetration devices for nanoparticles. *Adv. Mat.* (review article) 24:3747-3756. (2012). [Epub ahead of print] PMID: 22550056.

Braun G B., Friman, T., Pang, H-B., Kotamraju, VR, Pallaoro, A., Reich, NO.,Teesalu, T. and Ruoslahti, E. Etchable and bright silver nanoparticle probes for cell internalization assays. Submitted

Chen, R., Braun, G.B., Luo, X. Sugahara, K.N., Teesalu, T., Ruoslahti, E. Application of a proapoptotic peptide for an intratumoral-spreading cancer therapy. (2012). Cancer Research, Provisionally accepted.

Alberici L., Roth, L., Sugahara, K.N., Agemy, L., Kotamraju, V.R., Teesalu, T., Bordignon, C., Traversari, C., Rizzardi, G.-P., Rusolahti, E. De Novo Design of a Tumor Penetrating Peptide (2012) Cancer Research, Provisionally accepted.

Erkki Ruoslahti and members of his laboratory have given numerous invited seminars and presentations at various national and international conferences.

The Tsien laboratory:

During the year covered by this report, Roger Tsien made presentations related to the above projects at many meetings. The first three sub-areas of progress with RACPPs are covered in two manuscripts, one in press in *Angewandte Chemie* (one of the highest-profile chemistry journals) and one under revision at *Cancer Research*. Provisional and full U.S. patent applications on the RACPPs have been filed. Patent disclosures have been filed with the UCSD Technology Transfer Office covering the improved surgical imaging system and the *ex vivo* personalized protease assay. Avelas Biosciences, UCSD's exclusive licensee for ACPP technology, has developed its own RACPPs closely related to ours, has independently obtained discrimination between metastatic and unaffected lymph nodes similar to Fig. 3, has begun GMP production and preliminary toxicology, and is planning to file an IND and begin Phase I clinical trials in the second half of 2013. The initial indication will be to help decide intraoperatively how many lymph nodes should be removed during resection of breast cancers.

The Sengupta laboratory: Please refer to separate report filed by Dr. Sengupta.

(2) Patents filed:

Title: Truncated LYP-1 Peptides and Methods and Compositions Using Truncated LYP-1 Peptides
Inventor(s): Erkki Ruoslahti, Tambet Teesalu, Kazuki Sugahara, and Lise Roth
Date Reported to iEdison: October 19, 2012

The new peptides reported here will be patented, as well.

Please refer to separate reports filed by Drs. Tsien and Sengupta

CONCLUSION

New peptides recognizing very early changes in breast cancer development have been discovered. Interestingly, the changes detected by these peptides take place before the vasculature in the premalignant lesions is detectably altered. These peptides may be useful in imaging applications. A new aptamer screening technology has been developed under this grant that will help bring the aptamer technology to bear on cancer research and treatment. The Ruoslahti and Sengupta laboratories have developed new nanotechnologies for diagnostic and therapeutic applications in breast cancer. Ratiometric ACPPs from the Tsien laboratory improve the speed and robustness with which tumors can be discriminated from normal background tissues, particularly metastases of mammary tumor cells to liver and to lymph nodes. They enable personalized *ex vivo* assays on patient samples. ACPPs have now shown promise in delivering chemotherapeutic payloads, not just imaging agents. The technologies from all three laboratories have been licensed by the respective institutions to biotech companies that have detailed plans and realistic schedules to begin clinical trials.

References

Alberici, L., Roth, L., Sugahara, K.N., Agemy, L., Kotamraju, V.R., Teesalu, T., Bordignon, C., Traversair, C., Rizzardi, G-P, Ruoslahti, E. *De Novo* Design of a Tumor-Penetrating Peptide. Cancer Research, provisionally accepted. (2012).

Chen, R., Braun, G.B., Luo, X., Sugahara, K.N., Teesalu, T., Ruoslahti, E. Application of a proapoptotic Peptide for an Intratumoral-Spreading Cancer Therapy. Cancer Research, provisionally accepted. (2012).

Diehl, F. et al. BEAMing: single-molecule PCR on microparticles in water-in-oil emulsions. Nature methods 3, 551–9 (2006).

Dressman, D., Yan, H., Traverso, G., Kinzler, K. W. & Vogelstein, B. Transforming single DNA molecules into fluorescent magnetic particles for detection and enumeration of genetic variations. Proc. Natl. Acad. Sci. USA 100, 8817–22 (2003).

Gold, L. et al. Aptamers and the RNA world, past and present. Cold Spring Harbor perspectives in biology 4, (2012).

Gong, Q., Wang, J., Ahmad, K.M., Csordas, A.T., Zhou, J., Nie, J., Stewart, R., Thomson J.A., Rossi, J.J., Soh, H.T. Selection Strategy to Generate Aptamer Pairs that Bind to Distinct Sites on Protein Targets. *Anal. Chem.* 84, 5365−5371 (2012).

Keefe, A. D., Pai, S. and Ellington, A. Aptamers as therapeutics. Nature reviews. Drug discovery 9, 537–50 (2010).

Roth, L., Agemy, L., Kotamraju, V.R., Braun, G., T. Teesalu, T, Sugahara, K.N., Hamzah, J., and Ruoslahti E. Transtumoral targeting enabled by a novel neuropilin-binding peptide. Oncogene, 31: 3754-3763 (2012). PMID: 22179825

Sugahara, K.N., Teesalu T., Karmali P., Kotamraju V.R., Agemy L, Girard O.M., Hanahan D., Mattrey, R.F., and Ruoslahti E. Tissue-penetrating delivery of compounds and nanoparticles into tumors. *Cancer Cell*, 16:510-520, (2009). PMCID: PMC2791543.

Supplemental Material can be found at:
http://www.jbc.org/content/suppl/2010/12/14/M110.161927.DC1.html

THE JOURNAL OF BIOLOGICAL CHEMISTRY VOL. 286, NO. 7, pp. 5197–5203, February 18, 2011

The Multicompartmental p32/gClqR as a New Target for Antibody-based Tumor Targeting Strategies*[S]

Received for publication, July 7, 2010, and in revised form, November 30, 2010 Published, JBC Papers in Press, December 14, 2010, DOI 10.1074/jbc.M110.161927

David Sánchez-Martín[‡1], Ángel M. Cuesta[‡], Valentina Fogal[§2], Erkki Ruoslahti[§¶], and Luis Álvarez-Vallina[‡3]

From the [‡]Molecular Immunology Unit, Hospital Universitario Puerta de Hierro Majadahonda, 28222 Madrid, Spain, the [§]Cancer Research Center, Sanford-Burnham Medical Research Institute, La Jolla, California 92037, and the [¶]Vascular Mapping Center, Sanford-Burnham Medical Research Institute, University of California Santa Barbara, Santa Barbara, California 93106-9610

Tumor-associated cell surface antigens and tumor-associated vascular markers have been used as a target for cancer intervention strategies. However, both types of targets have limitations due to accessibility, low and/or heterogeneous expression, and presence of tumor-associated serum antigen. It has been previously reported that a mitochondrial/cell surface protein, p32/gC1qR, is the receptor for a tumor-homing peptide, LyP-1, which specifically recognizes an epitope in tumor cells, tumor lymphatics, and tumor-associated macrophages/myeloid cells. Using antibody phage technology, we have generated an anti-p32 human monoclonal antibody (2.15). The 2.15 antibody, expressed in single-chain fragment variable and in trimerbody format, was then characterized *in vivo* using mice grafted subcutaneously with MDA-MB-231 human breast cancers cells, revealing a highly selective tumor uptake. The intratumoral distribution of the antibody was consistent with the expression pattern of p32 in the surface of some clusters of cells. These results demonstrate the potential of p32 for antibody-based tumor targeting strategies and the utility of the 2.15 antibody as targeting moiety for the selective delivery of imaging and therapeutic agents to tumors.

The localization of tumors may be accomplished by any of several combinations including computed tomography, ultrasonography, gamma camera examination, and glucose consumption (1, 2). However, targeted localization of the tumors is preferred, mainly using specific probes that bind to tumor-associated cell surface antigens or to markers of angiogenesis expressed by endothelial cells or present in the surrounding extracellular matrix (3–6). Probes that bind to tumor-associated cell surface antigens have some drawbacks (7) such as the heterogeneous expression on the cell surface or the increased serum levels of the antigen as tumors grow, which may act as a trap for the targeting agent. Angiogenesis related targets are readily accessible; however, the relatively low abundance of endothelial cells in tumor tissue makes the molecular imaging of tumor neovessels more challenging. Furthermore, angiogenesis may occur also in a physiological context, thus adding more complexity to the targeting.

With these limitations in mind, we hypothesized as an alternative target a marker selectively expressed in different compartments in the tumor area. One targeting agent specific for the tumor but not restricted to the tumor cells is the tumor homing peptide (LyP-1), which strongly and specifically accumulates in the tumor after systemic administration, localizing preferentially associated to lymphatic markers (8–10). LyP-1-binding protein was characterized as p32 (10), a multiligand and multicompartmental protein that has been independently identified in several contexts and has been named accordingly as SF2P32 (splicing factor SF2-associated protein; 11), HABP-1 (hyaluronic acid binding protein-1; 12), gC1qR (globular domain of C1q receptor; Ref. 13), or HIV TAP (Tat-associated protein; 14). Although p32 is primarily present in the mitochondria, it has been, under certain conditions (15), detected in different cellular compartments (nucleus, cellular surface, endoplasmic reticulum (13, 16–20)) and in different cell types (B lymphocyte (13)), platelets (21), neutrophils (22), eosinophils (23), endothelial cells (24), macrophages and dendritic cells (25, 26), or fibroblasts (27)). p32 has also been recently reported in the surface of tumor cells in hypoxic/nutrient-deprived areas as well as in the cell surface of a tumor-associated macrophage/myeloid cell subpopulation closely linked to tumor lymphatics (10).

In this work, we take advantage of the over-expression of the multicompartmental p32/gClqR (hereafter referred to as p32) associated to tumors (in tumor cells, tumor lymphatics, and tumor-associated macrophages) to generate a human anti-p32 single-chain Fv (scFv)[4] antibody (2.15). This antibody has shown to selectively target solid tumors *in vivo* both as a monovalent and trivalent antibody fragment.

EXPERIMENTAL PROCEDURES

Cells and Culture Conditions—All cells were from the ATCC. HEK-293 cells (human embryonic kidney epithelia; CRL-1573), and MDA-MB-231 (human breast adenocarcinoma; HTB-26) were grown in DMEM supplemented with

---

* This work was supported by grants from the Ministerio de Ciencia e Innovación (BIO2008-03233), the Comunidad Autónoma de Madrid (S-BIO-0236-2006), the European Union (SUDOE-FEDER (IMMUNONET-SOE1/P1/E014; to L. A.-V.), and a grant from the U. S. Department of Defense Breast Cancer Program (to E. R.).

[S] The on-line version of this article (available at http://www.jbc.org) contains supplemental Figs. 1 and 2.

[1] Supported by Comunidad Autónoma de Madrid/Fondo Social Europeo Training Grant FPI-000531.

[2] Supported a fellowship from the Susan Komen Foundation.

[3] To whom correspondence should be addressed: Unidad de Inmunología Molecular, Hospital Universitario Puerta de Hierro, C/Manuel de Falla 1, 28222 Majadahonda, Madrid, Spain. Tel.: 34-911916764; Fax: 34-913160644; E-mail: lalvarezv.hpth@salud.madrid.org.

[4] The abbreviations used are: scFv, single-chain fragment variable; NIP, 4-hydroxy-5-iodo-3-nitrophenyl; rhp32, recombinant human p32.

10% heat-inactivated FCS (all from Invitrogen) in humidified CO_2 (5%) incubator at 37 °C. U-937 cells (human histiocytic lymphoma; CRL-1593.2) and 4T1 cells (mouse breast tumor; CRL-2539) were maintained in RPMI supplemented with 10% FCS. Differentiation of the U-937 cells was induced for the indicated time intervals in fresh culture medium containing 5 nM phorbol myristic acid (Sigma-Aldrich).

Recombinant Proteins, Antibodies, Peptides, and Reactives—Recombinant human p32 (rhp32) was obtained from bacteria and purified by immobilized metal ion affinity chromatography. Recombinant mouse p32 was purchased from United States Biological (USBio). Purified rabbit polyclonal anti-full-length p32 was directed against the N terminus (amino acids 76–93). The mAbs used included mouse anti-p32 (60.11 and 74.5.2), anti-human c-Myc 9.E10, FITC-conjugated anti-human c-Myc 9.E10 (Abcam, Cambridge, UK); anti-human MHC class I molecules W6/32 (eBioscience, San Diego, CA); rat anti-mouse CD31 (BD Biosciences); HRP-conjugated anti-human c-Myc (Invitrogen); and HRP-conjugated anti-M13 bacteriophage (GE Healthcare). The polyclonal antibodies used included an Alexa Fluor 546-conjugated anti-rat IgG (Invitrogen); a phycoerythrin-conjugated goat anti-mouse IgG (Jackson ImmunoResearch Europe, Suffolk, UK); an HRP-conjugated donkey anti-rabbit IgG; and an HRP-conjugated sheep anti-mouse IgG (GE Healthcare). Trypsin, BSA, *o*-phenylenediamine dihydrochloride, and isopropyl-beta-D-thiogalactopyranoside were from Sigma-Aldrich. BSA was conjugated with 4-hydroxy-5-iodo-3-nitrophenyl (NIP; Sigma-Aldrich) in a molar ratio of 10:1 (NIP10-BSA) as described (28). Mouse EHS-laminin (LM111) was from (BD Biosciences).

Selection of scFv Phage Library on rhp32—Recombinant scFv phages (Griffin.1 library, Medical Research Council Cambridge; total diversity, $\sim 1.2 \times 10^9$) (29) were panned for binding on purified antigen (rhp32) as described (30) with slight modifications: immunotubes (Maxisorp, Nunc, Roskilde, Denmark) were coated overnight at 4 °C with 4 ml of rhp32 at a concentration of 10 μg/ml in PBS. After washing twice with PBS, the tubes were blocked for 2 h at 37 °C with 4% BSA in PBS. Meanwhile, 10^{13} phages were blocked with 1 ml 4% BSA in PBS. Preblocked phages were added to the immunotube and incubated at room temperature with continuous rotation for 30 min, followed by 90 min of stationary incubation. The tubes were washed 10 times (in the first round of selection, 20 in the subsequent selections) with PBS containing 0.05% Tween 20 and then with PBS. Bound phages were eluted with 1 ml of trypsin (1 mg/ml in 50 mM Tris-HCl, pH 7.4, 1 mM $CaCl_2$) at room temperature with continuous rotation for 20 min. Eluted phages were recovered by infecting logarithmically growing (A_{600} = 0.5) *Escherichia coli* TG1 (K12, Δ(*lac-pro*), *sup*E, *thi*, *hsdD*5/*F′ traD*36, *pro*A^{+}B^{+}, *lacI*^{q}, *lacZ*ΔM15 (31)) at 37 °C for 30 min. The infected cells were plated on LB agar supplemented with 100 μg/ml ampicillin and 1% glucose and incubated overnight at 37 °C. This enriched library was grown on *E. coli* TG1 and rescued upon infection with the helper phage KM13 (32). Phages displaying scFv fragments were purified from the culture supernatant by precipitation with 20% PEG 6000 and 2.5 M NaCl and were resuspended in sterile cold PBS with 15% glycerol for long term storage at −80 °C and for subsequent rounds of selection.

Screening of Selected Phages by ELISA—Single colonies were screened by ELISA to evaluate the frequency of phage displaying rhp32-binding scFv fragments as described (33). rhp32-binding phages were fingerprinted by amplifying the scFv using primers LMB3 and FdSeq1 (LMB3, 5′-CAG GAA ACA GCT ATG AC-3′; FdSeq1, 5′-GAA TTT TCT GTA TGA GG-3′) followed by digestion with the frequent cutting enzyme BstN-I (New England Biolabs). Molecular characterization was completed by sequencing the variable regions using primers FOR_LinkSeq (V_H; 5′-GCC ACC TCC GCC TGA ACC-3′) and pHEN_Seq (V_L; 5′-CTA TGC GGC CCC ATT CA-3′). Sequences were analyzed and aligned to the VBASE2 database (34) to learn the amino acids forming the loops in the complementarity-determining regions used and type of chains present.

Soluble Antibody Expression and Purification—Phage particles from selected clones were used to infect logarithmically growing (A_{600} = 0.5) *E. coli* HB2151 (nonsuppresser strain (K12, *ara*, Δ(*lac-pro*), *thi*/F′ *pro*A^{+}B^{+}, *lacI*^{q}ZΔM15 (35)), and soluble scFv fragments were obtained as described (33). Purification was performed using the ÄKTAprime plus system (affinity step: HisTrap or HiTrap rProtein A FF columns (GE Healthcare) according to the manufacturer's protocol followed by gel filtration HiPrep 16/60 Sephacryl S100-HR) and checked by ELISA and SDS-PAGE. Either supernatant from isopropyl-beta-D-thiogalactopyranoside-induced HB2151 or purified scFv was used. Competition ELISA was performed as a standard ELISA but with a previous step of blockade using mAb; after blocking with 300 μl 4% BSA in PBS at 37 °C for 1 h, wells were incubated with 100 μl of a 20 μg/ml solution of the appropriate reagent (mAb 60.11, mAb 74.5.2, or control mouse IgG1) for 1 h at room temperature and 30 rpm.

Flow Cytometry—To study the ability of the scFv to detect p32 on the cell surface, unstimulated mouse 4T1 cells and phorbol myristic acid-stimulated human U-937 cells (5 nM for 3, 6, or 12 h prior to the staining) were incubated with anti-p32 mAb (5 μg/ml) or purified scFv (10 μg/ml) and mAb 9E10 (4 μg/ml) in 100 μl for 45 min. After washing, the cells were treated with appropriate dilutions of phycoerythrin-conjugated goat anti-mouse IgG. The samples were analyzed with an EPICS XL (Coulter Electronics, Hialeah, FL).

Construction of Expression Vectors and Purification of Recombinant Multivalent Antibodies—The coding sequence of the scFv 2.15 was amplified using primers ClaI-2.15 (5′-TCA TCG ATG GAG GTG CAG CTG GTG GAG-3′) and FdSeq1 and ligated into pCR2.1 TOPO. The ClaI/NotI-digested fragment was ligated into the ClaI/NotI pCR3.1-L36-NC1^{ES-}-digested plasmid (6) to obtained the pCR3.1–2.15-NC1^{ES-} plasmid. All constructs were verified by sequencing. The details about the plasmid pCEP4-B1.8-NC1^{ES-} containing the B1.8 (anti-NIP) trimerbody and the procedure to obtain purified trimerbodies can be found elsewhere (6).

Antibody Labeling with Cyanine 5—Purified antibodies (scFvs and trimerbodies) were labeled with the near-infrared cyanine 5 (Cy5) *N*-hydroxysuccinimide (NHS) esters (GE

Healthcare) according to the manufacturer's recommendations. One milliliter of the antibody solution (1 mg/ml) was conjugated with 0.1 ml of a 2 mg/ml Cy5 solution for 1 h in the dark at room temperature. Cy5-labeled recombinant antibodies were separated from unconjugated Cy5 dye by gel filtration on Sephadex G-25 Superfine HiTrap Desalting columns (PD-10 columns, GE Healthcare), and concentrated in 10,000 molecular weight cutoff (MWCO) Vivaspin 500 filter (Vivascience) to 1 mg/ml. The labeling ratio of Cy5 to antibody (Cy5:antibody) was calculated as described (36) and was close to 1:(1–2). The functionality of Cy5-labeled antibodies was verified by ELISA against specific antigen.

Infrared Immunophotodetection in Tumor-bearing Mice—Imaging was performed as described (6) with slight modifications. Briefly, wild-type MDA-MB-231 cells (2×10^6) were implanted into the mammary fat pad of 6-week-old female Hsd:athymic nude-*Foxn1*^{nu} mice (Harlan Ibérica, Barcelona, Spain) maintained with a low manganese diet (ssniff Spezialdiäten GMBH, Soest, Germany). Nodule dimensions were used to calculate tumor volume using the formula: width^2 × length × 0.52. When tumors reached a volume of 0.2–0.4 cm^3, mice were injected in the tail vein with 100 μl Cy5-labeled antibody solution in PBS. Mice were imaged using the high resolution charge-coupled device cooled digital camera ORCA-2BT and Hokawo software (Hamamatsu Photonics France, Massy, France) under anesthesia. Three images were acquired for each experiment: a bright field image, a Cy5-specific image (emission, red light filter centered at 632.8 nm; optical filter, 665–680 nm), and an autofluorescence reference image (emission, blue light filtered at 470 nm; optical filter, 665–680 nm). Normalized reference autofluorescence was subtracted from the Cy5-specific image, and the resultant was tinted and merged with the bright-field image (tinted in the GFP blue-shifted spectral (448 nm) for better contrast) using the Hokawo software. Further editing included only cropping, resizing, and rotating the image for a better view of the picture. All mice were handled in accordance with the guidelines of the Hospital Universitario Puerta de Hierro Animal Care and Use Committee and performed in accordance with Spanish legislation.

Immunohistology—Tumors were removed after infrared imaging (2.5 h after i.v. injection), frozen in optimal cutting temperature (OCT) embedding medium (Sakura Tissue Tek, Alphen aan den Rijn, The Netherlands), and sectioned (4–7-μm thickness) using the Leica CM1850 cryostat. Sections were incubated overnight with the primary antibodies (anti-Myc:FITC antibody (1:200) and rat anti-mouse CD31 (1:100)), followed by anti-rat secondary reagents (1:1000), and mounted by using VectaShield mounting media with 4′,6-diamidino-2-phenylindole (Vector Laboratories, Burlingame, CA). Images were acquired using a confocal scanning inverted Leica AOBS/SP2-microscope (Leica Microsystems).

RESULTS

Isolation of Human Anti-rhp32 Antibodies by Panning a scFv Library—The Griffin.1 library was panned against affinity purified recombinant human p32 (rhp32) immobilized in Nunc immunotubes. The frequency of binding clones was studied by ELISA after each round of selection. The percentage of binders was 20% after the first round and 60% after the second. BstN1 fingerprinting of 24 selected clones (by rhp32/BSA ratio (in preliminary 96-well ELISA) > 3) indicated 16 different restriction patterns, which were later confirmed by DNA sequencing.

Biochemical Characterization of scFv Fragments—Ten different clones that were consistent binders were used in a phage-ELISA assay against rhp32 and other unrelated proteins (Fig. 1*A*). Most of the clones were highly specific for rhp32, showing almost no reactivity against other elements present in the selection process (plastic and BSA) or an unrelated protein (LM111). After expression as soluble scFv, although different from clone to clone, there was a significant reactivity of most of the scFvs against rhp32 (Fig. 1*B*). The binding of LyP-1 phage to p32 is inhibited by monoclonal antibody 60.11, which is directed against the C1q binding domain of p32 (10). To identify scFv sharing the epitope with mAb 60.11, four scFv fragments (1.6, 2.9, 2.15, and 2.25) were expressed using the nonsuppressor host *E. coli* HB2151 and purified from the supernatant by standard affinity chromatography procedures. The purified scFv fragments gave rise to a single protein band of expected mobility (Fig. 1*C*, *inset*); a competition ELISA was designed using either mAb 60.11 directed against p32 N-terminal amino acids 76–93 or 74.5.2 directed against amino acids 204–218 from the C terminus of p32. Preincubation with 60.11 but not 74.5.2 greatly diminished the binding of scFv 2.9 and 2.15, indicating overlapping, if not identical, epitopes (Fig. 1*C*). Due to the degree of cross-species conservation between rodents and humans, both in sequence and in the ability to bind C1q (37), we further investigated whether the selected scFv fragments were able to bind immobilized purified recombinant mouse p32. It was found that 2.9 gave no signal on recombinant mouse p32, whereas 2.15 gave comparable signals on both mouse and human p32 immobilized on plastic (Fig. 1*D*).

Reactivity of scFv Fragments to Cell Surface-expressed p32—The ability of the scFv fragments to recognize cell surface-expressed p32 was assessed by flow cytometry using freshly purified soluble scFv. Nonstimulated human U-937 cells reacted minimally with either anti-p32 mAbs (60.11 or 74.5.2) or scFv (2.9 or 2.15) (data not shown). In contrast, U-937 activation with phorbol myristic acid produced a consistently increased p32 expression as reflected by mAbs and scFv fragments. Staining with mAb 60.11 showed that ~50% of stimulated U-937 cells expressed p32 in the surface (Fig. 2*A*). Purified scFv fragments corresponding to 2.9 and 2.15, also stained the U-937 cells, and a slightly higher percentage of the cells were stained than with the 60.11 antibody (Fig. 2*A*). Surface staining of mouse 4T1 cells demonstrated the presence of p32 on the cell surface, in agreement with previous studies (10). The mAb 60.11 produced a small but consistent shift in flow cytometry analysis of live 4T1 cells (Fig. 2*B*). A similar staining pattern was observed in 4T1 cells incubated with the 2.15 scFv. In contrast, incubation of 4T1 cells with 2.9 scFv revealed no staining (Fig. 2*B*). Thus, further corroborating the ability of 2.15 to detect the mouse cell surface p32 to a extent similar to the mAb 60.11.

Tumor Targeting with Mono- and Trivalent Anti-p32 Antibodies—We selected the scFv 2.15 for *in vivo* targeting assays based on its inhibition by the 60.11 mAb as shown by ELISA on its ability to detect p32 expressed in the surface of both human and mouse cells as shown by flow cytometry. Control scFv antibodies included the following: B1.8 (anti-hapten NIP) and L36 (recognizes a conformational epitope of LM111 exposed in several solid tumor models (6)). Antibodies were labeled with the near-infrared fluorochrome Cy5 and injected in the tail vein of nude mice bearing MDA-MB-231 human xenografts. All of the antibodies showed a rapid renal clearance after i.v. injection, with peak signal intensity at 1–2 h and no detectable bladder signal at 24 h post-injection (Fig. 3*B*). The control scFv-B1.8 showed no detectable localization, whereas both 2.15 and L36 localized in the tumors (Fig. 3*A*). Maximum resolution was achieved at ∼2h (Fig. 3*A*), when the ratio of the signal of the 2.15 and that of the B1.8 was near 7 (supplemental Fig. 1). *Ex vivo* imaging of the organs further confirms the specific accumulation of 2.15 and L36 in the tumors, while showing a similar uptake by the kidneys for all the antibodies (Fig. 3*C*). Staining of the tumors from mice that received the scFvs with FITC-conjugated anti-Myc mAb (to detect the injected scFv) and anti-CD31 mAb showed that most of the endothelial cells were negative for the scFv, and most of the scFv staining was dispersed in clusters of cells (Fig. 4, *white arrow*). However, some of the main vessels showed a distinct co-staining in the basal side of the cells (Fig. 4, *arrowhead*).

We have previously reported that the trimerbody format offers advantages over scFv molecules for tumor-targeting applications *in vivo* against a cell surface antigen or an extracellular matrix antigen (LM111) (6). We hypothesized that an anti-p32 trimerbody would also surpass its scFv counterpart for *in vivo* imaging. For this reason, the 2.15 scFv was assembled in the trimerbody format and expressed as a soluble secreted protein in human HEK-293 cells and purified from conditioned medium. The purification scheme yielded antibodies that were >95% pure by SDS-PAGE. The functionality of purified 2.15 trimerbody was demonstrated by ELISA against rhp32 (supplemental Fig. 2). Trimerbodies (2.15 and B1.8) were labeled with Cy5 and injected in the tail vein of nude mice bearing MDA-MB-231 human xenografts. Trimerbodies showed slower clearance than the corresponding scFvs (Fig. 5*B*). The control B1.8 trimerbody showed no detectable localization in the tumor, whereas a strong and selective accumulation was observed in the case of the 2.15 trimerbody. Maximum tumor uptake was detected at 2.5 and 5 h; the signal intensity decreased at 24 h although remained detectable for at least 48 h (Fig. 5*A*), whereas most of the systemic protein was eliminated at 24h (Fig. 5*B*).

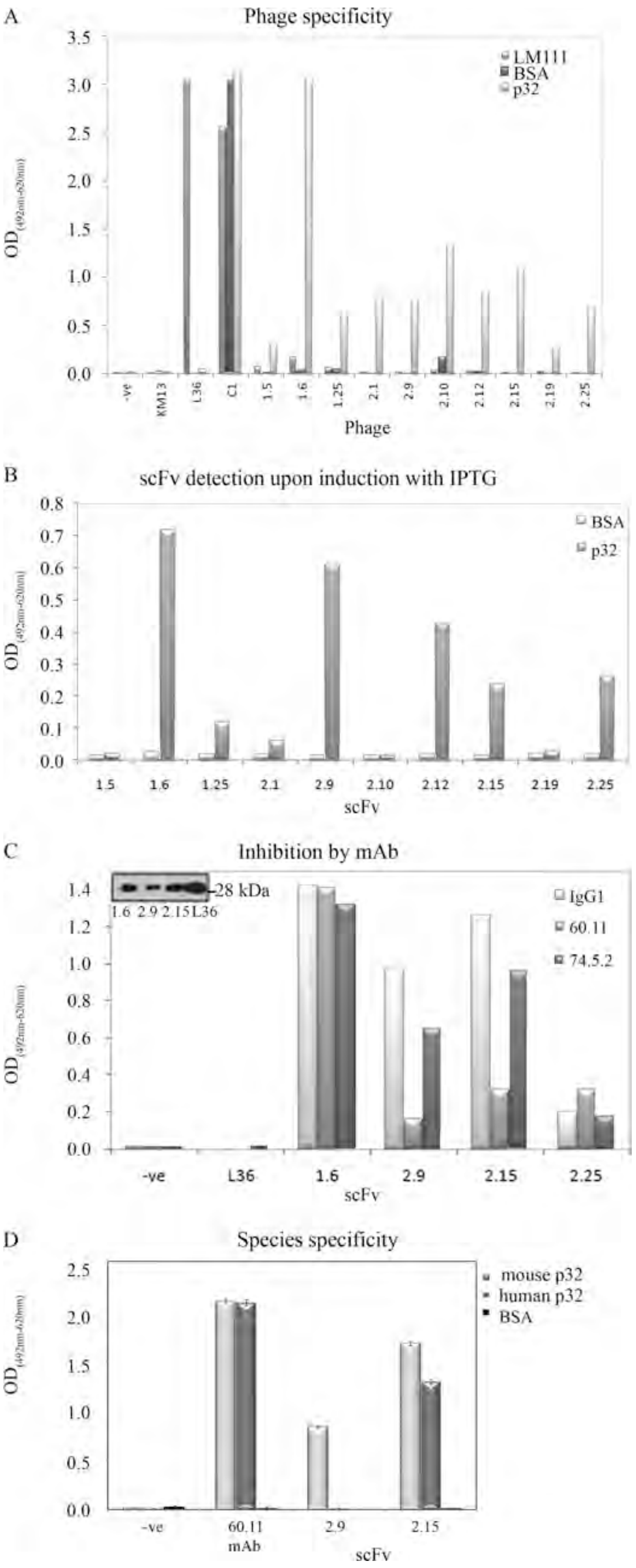

FIGURE 1. **Characterization of anti-p32 phage-derived scFvs.** *A*, specificity of phage scFv fragments from selected clones by ELISA. Reactivity was assessed against the following: elements present in the selection process (BSA); murine laminin-1 (LM111); and the target protein rhp32 (p32). Internal controls were as follows; L36 binds to LM111, but not other proteins; KM13, empty phage, does not bind any protein, whereas C1-phage binds BSA). Phage input was essentially the same for each clone and each ELISA as assessed by phage-ELISA. The *y* axis represents $A_{492\ nm}$ corrected with $A_{620\ nm}$ except otherwise stated. *B*, soluble scFv fragments retained their specificity after cloning in HB2151 and expression after induction with isopropyl-β-D-thiogalactopyranoside (*IPTG*). *C*, mononclonal antibody competition analyses for p32 binding. Binding of 2.9 and 2.15 to rhp32 was diminished after incubation with mAb 60.11, suggesting a common epitope for the scFv and mAb. *Inset*, Western blotting of the purified scFv. *D*, 2.15, but not 2.9, was able to bind to human and mouse p32. *Error bars* represent the standard error of the mean of three different experiments.

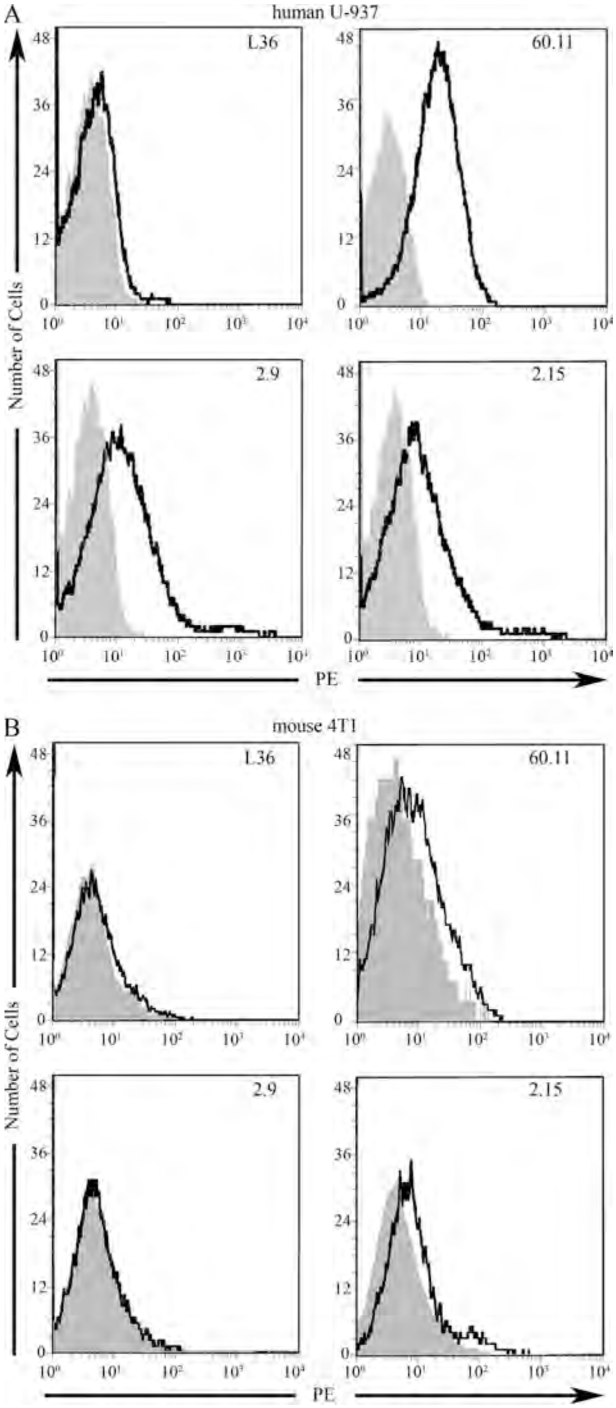

FIGURE 2. **Reactivity of scFv fragments to cell surface expressed p32.** *A*, binding of anti-p32 mAb and purified scFv fragments to phorbol myristic acid-stimulated human U-937 cells by flow cytometry. *B*, binding of anti-p32 mAb and purified scFv fragments to mouse 4T1 cells by flow cytometry. For purified scFv fragments, the bound scFv was detected with sequential incubations with 9E10 anti-Myc mAb and phycoerythrin (*PE*)-labeled goat anti-mouse IgG. FACScan histograms show the binding of each scFv clone (*bold line*) and the backgrounds of phycoerythrin-conjugated secondary antibodies (*gray*).

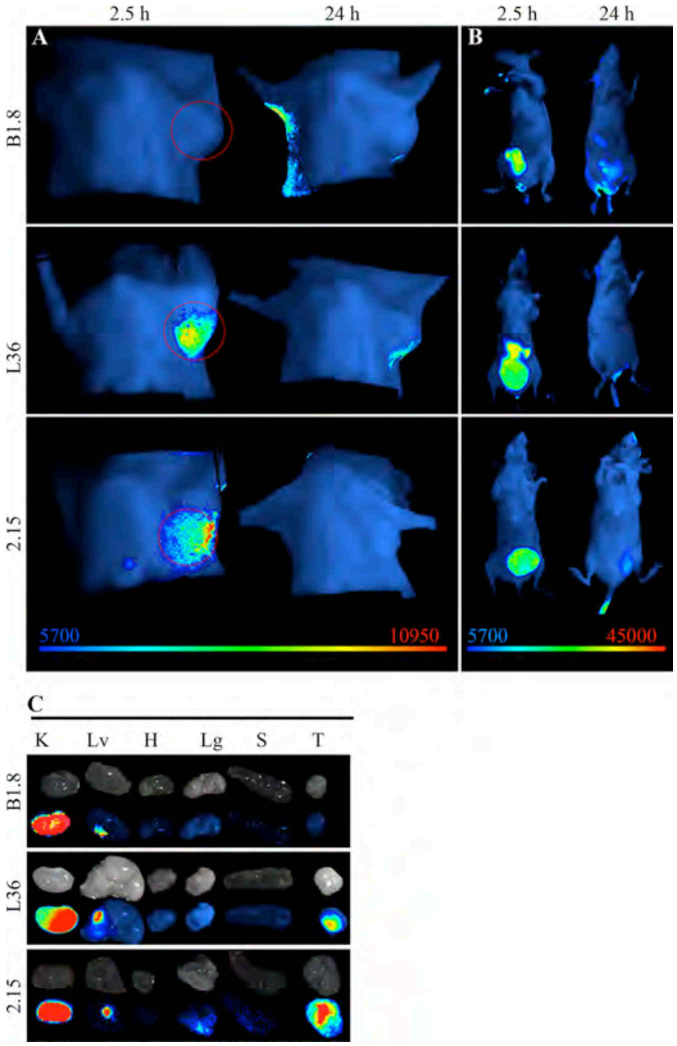

FIGURE 3. **Targeting of fluorescently labeled anti-p32 scFv to human tumors.** Near-infrared fluorescence imaging of nude mice bearing MDA-MB-231 human breast tumor xenografts. *A*, anti-hapten B1.8 did not localize in the tumor, whereas L36 and 2.15 showed a specific signal. A representative image of four mice is shown (2.15 scFv) and three mice (B1.8 and L36). *B*, ventral view shows similar accumulation of the scFv in the bladder. *C*, *ex vivo* imaging of the organs (kidney (*K*), liver (*Lv*), heart (*H*), lung (*Lg*), spleen (*S*), and tumor (*T*)) shows similar uptake of the Cy5-labeled reagent in the kidneys.

DISCUSSION

We have generated a human recombinant antibody against the multicompartmental protein p32/gClqR. We have demonstrated the ability of different formats of this antibody (scFv and trimerbody) to target solid tumors *in vivo*. These results represent a new concept in tumor targeting. So far, antibody-based tumor targeting strategies have been based on tumor-associated cell surface antigens or tumor-associated vascular markers. Antibodies specific to tumor surface antigens, such as HER2-neu (38), carcinoembryonic antigen (39), or prostate-specific antigen (40), among others, have proven useful for *in vivo* localization of solid tumors. However, tumor surface antigens exhibit a high shedding profile and are dependent on tumor dedifferentiation or clonal proliferation. Antigens that are preferentially expressed in the tumor extracellular matrix may be better suited for tumor-targeting applications. In fact, several groups have demonstrated that antibodies specific to components of the extracellular matrix (EDB domain of fibronectin (41), domain C of tenascin C (42), and laminin (6, 33)) were capable of selective targeting of neovascular structures in solid tumors. However, it has been shown that antibodies against tumor-associated vascular

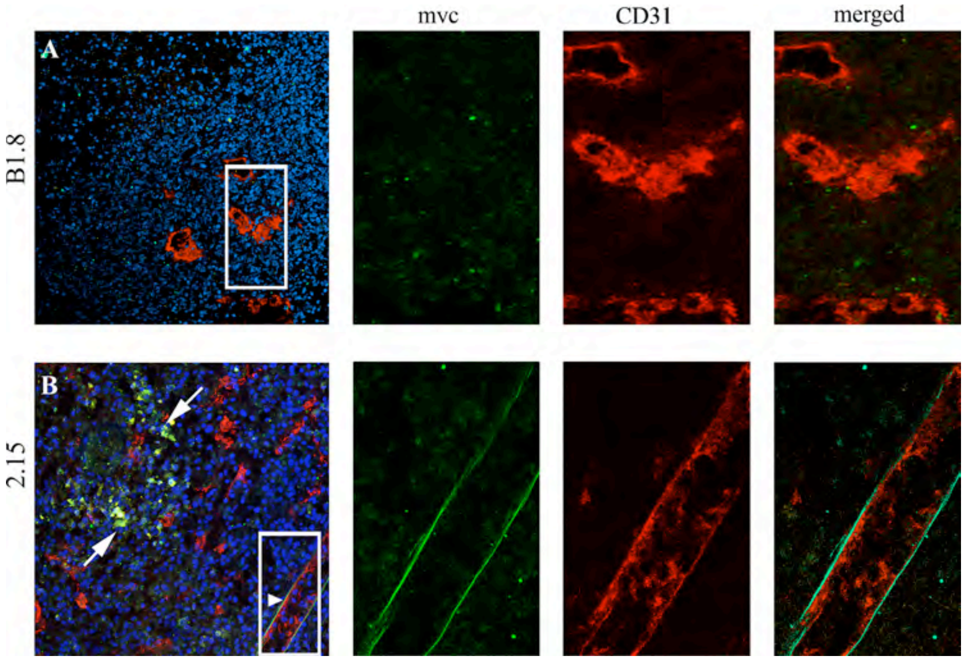

FIGURE 4. **2.15 scFv recognizes dispersed clusters of cells and the basal side of endothelial cells.** After i.v. administration of the scFv, tumors were removed, embedded in OCT, and stained for *myc* (*green*) or for an endothelial marker (CD31, *red*). *A*, B1.8 does not localize in the tumor stroma. It does not localize either associated with vessels (right panel). *B*, 2.15 localizes in the tumor in dispersed clusters of cells (*white arrow*). A distinct co-staining occurred in the basal side of endothelial cells (*arrowhead* and *right panel*).

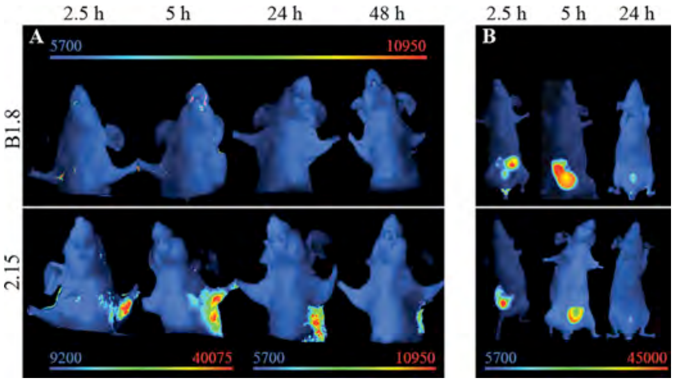

FIGURE 5. **Targeting of fluorescently labeled anti-p32 trimerbody to human tumors.** Near-infrared fluorescence imaging of nude mice bearing MDA-MB-231 human breast tumor xenografts. *A*, an anti-hapten B1.8 trimerbody did not localize in the tumor, whereas the 2.15 trimerbody showed a rapid (2.5 h) and sustained (up to 48 h) localization. Note the different *scale bar* for the early images. *B*, ventral view shows similar trimerbody accumulation in the bladder, as well as some elimination through the liver.

markers fail to accumulate in nonproliferating tumors (43). It is tempting to speculate that this can be a major problem in a proportion of patients as well as certain types of tumors with a very low growth rate.

Although p32 has been reported in the surface of several other cell types under certain circumstances (fibroblasts, neutrophils, endothelial cells, platelets, etc. (15)), the majority of the protein is cytoplasmic and is detectable after permeabilization of the cell membrane (44). Nonetheless, certain cells are able to translocate and release the protein, which can result in the modification of a number of cellular and vascular protein responses (15). The role of cell surface p32 in the tumor remains unclear; however, the unique expression pattern of p32 in tumor cells, tumor lymphatics, and tumor-associated macrophages/myeloid cells makes p32 an ideal target for the diagnosis and therapy of cancer. In fact, it has been reported that p32/gC1qR is the receptor for a tumor-homing peptide, LyP-1. The LyP-1 peptide has been shown to localize in the tumor lymphatics (9), and to effectively target nanoparticles to the tumor (45). In this work, we confirmed that systemically administered 2.15 scFv penetrates the tumor covering a broad population of cells but in a pattern distinct from that of the LyP-1 peptide (8, 9). Although LyP-1 is probably processed as a CendR peptide upon binding to p32 and thus can actively penetrate the tissue (46, 47), the antibody may remain partially bound to the p32 readily accessible from the lumen of the blood vessels and also reach some clusters of cells (probably macrophages) in the stroma nearby.

Multimerization of scFv constructs has important advantages for tumor-targeting applications. Trimerbodies are intermediate-sized molecules that exhibit high stability under physiological conditions and enhanced avidity for the target owing to the trivalent structure (6, 48). In fact, we report that the 2.15 antibody in a trimerbody format stained the tumor more brightly than the 2.15 scFv at all time points. Anti-p32 trimerbody localized rapidly and specifically in the tumors. The tumor uptake reached a maximum at 2.5–5 h post injection and slowly washed out over time. Fluorescence was still detectable in the tumor 48 h after the trimerbody inoculation.

In summary, we have demonstrated that the human anti-p32 antibody 2.15 can selectively localize tumors *in vivo*. These results illustrate the potential of this new antibody for imaging and therapeutic applications and suggest that p32 might be universal target for cancer targeting.

Acknowledgments—We thank Drs. Paloma Sánchez-Mateos and Rafael Samaniego for help with the confocal microscope.

REFERENCES

1. Jacobsson, H., Wallin, G., Werner, S., and Larsson, S. A. (1994) *Eur. J. Nucl. Med.* **21,** 582–586
2. Nguyen, B. D., Roarke, M. C., Karstaedt, P. J., Ingui, C. J., and Ram, P. C. (2009) *Curr. Probl. Diagn. Radiol.* **38,** 68–83
3. Vogel, C. A., Bischof-Delaloye, A., Mach, J. P., Pèlegrin, A., Hardman, N., Delaloye, B., and Buchegger, F. (1993) *Br. J. Cancer* **68,** 684–690
4. Sanz, L., Kristensen, P., Blanco, B., Facteau, S., Russell, S. J., Winter, G., and Alvarez-Vallina, L. (2002) *Gene Ther.* **9,** 1049–1053
5. Steffen, A. C., Orlova, A., Wikman, M., Nilsson, F. Y., Ståhl, S., Adams, G. P., Tolmachev, V., and Carlsson, J. (2006) *Eur. J. Nucl. Med. Mol. Imaging* **33,** 631–638
6. Cuesta, A. M., Sánchez-Martín, D., Sanz, L., Bonet, J., Compte, M., Kremer, L., Blanco, F. J., Oliva, B., and Alvarez-Vallina, L. (2009) *PLoS ONE* **4,** e5381
7. Buchsbaum, G. M., Moll, C., and Duecy, E. E. (2004) *Int. Urogynecol. J. Pelvic. Floor Dysfunct.* **15,** 432–433
8. Laakkonen, P., Akerman, M. E., Biliran, H., Yang, M., Ferrer, F., Karpanen, T., Hoffman, R. M., and Ruoslahti, E. (2004) *Proc. Natl. Acad. Sci. U.S.A.* **101,** 9381–9386
9. Laakkonen, P., Porkka, K., Hoffman, J. A., and Ruoslahti, E. (2002) *Nat. Med.* **8,** 751–755
10. Fogal, V., Zhang, L., Krajewski, S., and Ruoslahti, E. (2008) *Cancer Res.* **68,** 7210–7218
11. Krainer, A. R., Mayeda, A., Kozak, D., and Binns, G. (1991) *Cell* **66,** 383–394
12. Gupta, S., Batchu, R. B., and Datta, K. (1991) *Eur. J. Cell Biol.* **56,** 58–67
13. Ghebrehiwet, B., Lim, B. L., Peerschke, E. I., Willis, A. C., and Reid, K. B. (1994) *J. Exp. Med.* **179,** 1809–1821
14. Yu, L., Loewenstein, P. M., Zhang, Z., and Green, M. (1995) *J. Virol.* **69,** 3017–3023
15. Eggleton, P., Tenner, A. J., and Reid, K. B. (2000) *Clin. Exp. Immunol.* **120,** 406–412
16. Dedio, J., and Müller-Esterl, W. (1996) *FEBS Lett.* **399,** 255–258
17. Braun, L., Ghebrehiwet, B., and Cossart, P. (2000) *EMBO J.* **19,** 1458–1466
18. Kittlesen, D. J., Chianese-Bullock, K. A., Yao, Z. Q., Braciale, T. J., and Hahn, Y. S. (2000) *J. Clin. Invest.* **106,** 1239–1249
19. Mahdi, F., Shariat-Madar, Z., Todd, R. F., 3rd, Figueroa, C. D., and Schmaier, A. H. (2001) *Blood* **97,** 2342–2350
20. Mahdi, F., Madar, Z. S., Figueroa, C. D., and Schmaier, A. H. (2002) *Blood* **99,** 3585–3596
21. Peerschke, E. I., Reid, K. B., and Ghebrehiwet, B. (1994) *J. Immunol.* **152,** 5896–5901
22. Eggleton, P., Ghebrehiwet, B., Sastry, K. N., Coburn, J. P., Zaner, K. S., Reid, K. B., and Tauber, A. I. (1995) *J. Clin. Invest.* **95,** 1569–1578
23. Kuna, P., Iyer, M., Peerschke, E. I., Kaplan, A. P., Reid, K. B., and Ghebrehiwet, B. (1996) *Clin. Immunol. Immunopathol.* **81,** 48–54
24. Peerschke, E. I., Smyth, S. S., Teng, E. I., Dalzell, M., and Ghebrehiwet, B. (1996) *J. Immunol.* **157,** 4154–4158
25. Steinberger, P., Szekeres, A., Wille, S., Stöckl, J., Selenko, N., Prager, E., Staffler, G., Madic, O., Stockinger, H., and Knapp, W. (2002) *J. Leukocyte Biol.* **71,** 133–140
26. Vegh, Z., Goyarts, E. C., Rozengarten, K., Mazumder, A., and Ghebrehiwet, B. (2003) *International Immunopharmacol.* **3,** 345–357
27. Oiki, S., and Okada, Y. (1988) *J. Immunol.* **141,** 3177–3185
28. Hawkins, R. E., Russell, S. J., and Winter, G. (1992) *J. Mol. Biol.* **226,** 889–896
29. Griffiths, A. D., Williams, S. C., Hartley, O., Tomlinson, I. M., Waterhouse, P., Crosby, W. L., Kontermann, R. E., Jones, P. T., Low, N. M., and Allison, T. J. (1994) *EMBO J.* **13,** 3245–3260
30. Nissim, A., Hoogenboom, H. R., Tomlinson, I. M., Flynn, G., Midgley, C., Lane, D., and Winter, G. (1994) *EMBO J.* **13,** 692–698
31. Gibson, T. (1984) *Studies in the Epstein-Barr Virus Genome,* Ph.D. thesis, MRC Laboratory of Molecular Biology, University of Cambridge, Cambridge, UK
32. Kristensen, P., and Winter, G. (1998) *Folding Des.* **3,** 321–328
33. Sanz, L., Kristensen, P., Russell, S. J., Ramirez García, J. R., and Alvarez-Vallina, L. (2001) *Cancer Immunol. Immunother.* **50,** 557–565
34. Retter, I., Althaus, H. H., Münch, R., and Müller, W. (2005) *Nucleic Acids Res.* **33,** D671–674
35. Carter, P., Bedouelle, H., and Winter, G. (1985) *Nucleic Acids Res.* **13,** 4431–4443
36. Birchler, M., Neri, G., Tarli, L., Halin, C., Viti, F., and Neri, D. (1999) *J. Immunol. Methods* **231,** 239–248
37. Lynch, N. J., Reid, K. B., van den Berg, R. H., Daha, M. R., Leigh, L. A., Ghebrehiwet, B., Lim, W. B., and Schwaeble, W. J. (1997) *FEBS Lett.* **418,** 111–114
38. Harries, M., and Smith, I. (2002) *Endocr. Relat. Cancer* **9,** 75–85
39. Begent, R. H., Verhaar, M. J., Chester, K. A., Casey, J. L., Green, A. J., Napier, M. P., Hope-Stone, L. D., Cushen, N., Keep, P. A., Johnson, C. J., Hawkins, R. E., Hilson, A. J., and Robson, L. (1996) *Nat. Med.* **2,** 979–984
40. McDevitt, M. R., Barendswaard, E., Ma, D., Lai, L., Curcio, M. J., Sgouros, G., Ballangrud, A. M., Yang, W. H., Finn, R. D., Pellegrini, V., Geerlings, M. W., Jr., Lee, M., Brechbiel, M. W., Bander, N. H., Cordon-Cardo, C., and Scheinberg, D. A. (2000) *Cancer Res.* **60,** 6095–6100
41. Neri, D., Carnemolla, B., Nissim, A., Leprini, A., Querzè, G., Balza, E., Pini, A., Tarli, L., Halin, C., Neri, P., Zardi, L., and Winter, G. (1997) *Nat. Biotechnol.* **15,** 1271–1275
42. Silacci, M., Brack, S. S., Späth, N., Buck, A., Hillinger, S., Arni, S., Weder, W., Zardi, L., and Neri, D. (2006) *Protein Eng. Des. Sel.* **19,** 471–478
43. Birchler, M. T., Thuerl, C., Schmid, D., Neri, D., Waibel, R., Schubiger, A., Stoeckli, S. J., Schmid, S., and Goerres, G. W. (2007) *Otolaryngol. Head Neck. Surg.* **136,** 543–548
44. van den Berg, R. H., Prins, F., Faber-Krol, M. C., Lynch, N. J., Schwaeble, W., van Es, L. A., and Daha, M. R. (1997) *J. Immunol.* **158,** 3909–3916
45. Karmali, P. P., Kotamraju, V. R., Kastantin, M., Black, M., Missirlis, D., Tirrell, M., and Ruoslahti, E. (2009) *Nanomedicine* **5,** 73–82
46. Ruoslahti, E., Bhatia, S. N., and Sailor, M. J. (2010) *J. Cell Biol.* **188,** 759–768
47. Teesalu, T., Sugahara, K. N., Kotamraju, V. R., and Ruoslahti, E. (2009) *Proc. Natl. Acad. Sci. U.S.A.* **106,** 16157–16162
48. Cuesta, A. M., Sainz-Pastor, N., Bonet, J., Oliva, B., and Alvarez-Vallina, L. (2010) *Trends Biotechnol.* **28,** 355–362

Oncogene (2011) 1–10
© 2011 Macmillan Publishers Limited All rights reserved 0950-9232/11
www.nature.com/onc

ORIGINAL ARTICLE

Transtumoral targeting enabled by a novel neuropilin-binding peptide

L Roth[1,2], L Agemy[1,2], VR Kotamraju[1,2], G Braun[3], T Teesalu[1,2], KN Sugahara[2], J Hamzah[1,2] and E Ruoslahti[1,2]

[1]*Sanford-Burnham Medical Research Institute, Vascular Mapping Laboratory, Center for Nanomedicine, University of California, Santa Barbara, CA, USA;* [2]*Sanford-Burnham Medical Research Institute, Cancer Research Center, La Jolla, CA, USA and* [3]*Institute for Collaborative Biotechnologies, University of California, Santa Barbara, CA, USA*

We have recently described a class of peptides that improve drug delivery by increasing penetration of drugs into solid tumors. These peptides contain a C-terminal C-end Rule (CendR) sequence motif (R/K)XX(R/K), which is responsible for cell internalization and tissue-penetration activity. Tumor-specific CendR peptides contain both a tumor-homing motif and a cryptic CendR motif that is proteolytically unmasked in tumor tissue. A previously described cyclic tumor-homing peptide, LyP-1 (sequence: CGNKRTRGC), contains a CendR element and is capable of tissue penetration. We use here the truncated form of LyP-1, in which the CendR motif is exposed (CGNKRTR; tLyP-1), and show that both LyP-1 and tLyP-1 internalize into cells through the neuropilin-1-dependent CendR internalization pathway. Moreover, we show that neuropilin-2 also binds tLyP-1 and that this binding equally activates the CendR pathway. Fluorescein-labeled tLyP-1 peptide and tLyP-1-conjugated nanoparticles show robust and selective homing to tumors, penetrating from the blood vessels into the tumor parenchyma. The truncated peptide is more potent in this regard than the parent peptide LyP-1. tLyP-1 furthermore improves extravasation of a co-injected nanoparticle into the tumor tissue. These properties make tLyP-1 a promising tool for targeted delivery of therapeutic and diagnostic agents to breast cancers and perhaps other types of tumors.

Oncogene advance online publication, 19 December 2011; doi:10.1038/onc.2011.537

Keywords: tumor homing; tumor penetration; breast cancer; nanoparticles

Introduction

Targeted delivery of therapeutic or diagnostic agents to tumors constitutes a major goal in cancer treatment. By increasing the amount of a drug reaching the tumor, the efficacy is improved while side effects are reduced. This strategy relies on the identification of the molecular signature of tumor vessels, and development of specific affinity ligands to carry payloads to the tumor (Ruoslahti, 2002a, b). Nanoparticles can be used to further improve drug delivery and efficacy by incorporating multiple functions and increasing the payload (Ruoslahti *et al.*, 2010). However, dysfunctional tumor blood vessels and high interstitial pressure tend to prevent penetration of drugs and nanoparticles into the tumor tissue, limiting the efficacy of the treatments (Jain, 1999; Heldin *et al.*, 2004).

We have recently described a technology that provides a way to overcome the limited tissue penetration. C-end Rule (CendR) peptides induce extravasation and tissue penetration via a mechanism that involves cell internalization (Sugahara *et al.*, 2009, 2010; Teesalu *et al.*, 2009). CendR peptides are defined by the presence of the motif (R/K)XX(R/K) (X represents any amino acid), which has to be at the C-terminus for the cell- and tissue-penetration activity. The receptor for the CendR motif was shown to be neuropilin-1 (NRP1) (Teesalu *et al.*, 2009).

NRP1 is a modular transmembrane protein previously identified as a receptor for various forms and isoforms of VEGF (vascular endothelial growth factor) and members of the class 3 semaphorin family (Takagi *et al.*, 1987; He and Tessier-Lavigne, 1997; Kolodkin *et al.*, 1997; Soker *et al.*, 1998). Neuropilin-2 (NRP2), the second member of the neuropilin family, exhibits sequence and structure homology with NRP1, and shares common ligands, among them $VEGFA_{165}$ (Chen *et al.*, 1997; Kolodkin *et al.*, 1997; Gluzman-Poltorak *et al.*, 2000). However, there are also ligands that show selective affinity for one or the other NRP (Chen *et al.*, 1997; Gluzman-Poltorak *et al.*, 2000). Moreover, NRP1 and NRP2 display different expression patterns, with NRP2 (but not NRP1) overexpressed in tumor lymphatics (Caunt *et al.*, 2008). In the CendR pathway, NRP1 appears to be essential for cell internalization and tissue penetration (Teesalu *et al.*, 2009), whereas the role of NRP2 has not been investigated.

Binding to NRP1 requires an exposed C-terminal CendR motif, and peptides with an embedded binding motif in their sequence depend on proteolytic cleavage to activate the CendR internalization pathway. The recently described tumor-penetrating peptide iRGD follows this two-step mechanism. Indeed, iRGD contains an RGD motif for recruitment to angiogenic

---

Correspondence: Professor E Ruoslahti, Sanford-Burnham Medical Research Institute, UCSB Campus, Biology II Building, Room #3119, University of California, Santa Barbara, CA 93106-9610, USA.
E-mail: ruoslahti@sanfordburnham.org
Received 3 September 2011; revised and accepted 18 October 2011

blood vessels and a cryptic CendR motif that is proteolytically unmasked in tumor to trigger extravasation and tissue penetration (Sugahara *et al*., 2009, 2010). As a result of the proteolytic cleavage, iRGD loses its affinity for the integrins, acquires NRP1-binding capacity and induces extravasation (Sugahara *et al*., 2009). Importantly, co-injected drugs or particles penetrate inside the tumor parenchyma along with iRGD, allowing an increase of treatment efficacy in a number of different cancer models (Sugahara *et al*., 2010).

Similar to iRGD, LyP-1 is a tumor-homing cyclic nonapeptide, which contains a cryptic CendR motif (sequence: CGNKRTRGC), and was identified in our laboratory by phage display (Laakkonen *et al*., 2002). LyP-1 homes to tumor lymphatics, tumor cells and tumor macrophages by specifically binding to its receptor p32, a mitochondrial protein expressed on the surface of these cells (Laakkonen *et al*., 2002; Fogal *et al*., 2008). LyP-1 also homes to atherosclerotic plaques and penetrates into their interior (Hamzah *et al*., 2011; Uchida *et al*., 2011). The presence of the cryptic CendR motif suggests the possibility of secondary binding to NRP1 (and perhaps to NRP2 in the lymphatics) and involvement of the CendR pathway. This hypothesis is supported by previous studies showing that LyP-1 is able to extravasate and penetrate the tumor parenchyma (Laakkonen *et al*., 2002; von Maltzahn *et al*., 2008; Karmali *et al*., 2009).

Here, we investigate LyP-1 internalization pathway, and characterize a new peptide derived from LyP-1, with an active CendR element for tumor targeting.

Results

LyP-1 is a cryptic CendR peptide

In order to investigate the role of the CendR motif in LyP-1 peptide, we tested the binding of phage displaying the predicted active CendR fragment CGNKRTR (tLyP-1, for truncated LyP-1) and other truncated forms of LyP-1 to cultured tumor cells. We used DU145 prostate carcinoma cells, because they express only NRP1, and not NRP2 (Supplementary Figures S1A and S2A). As these peptides could have other receptors on the DU145 cells, we used inhibition of cell binding by a function-blocking anti-NRP1 antibody as an indicator of NRP1 dependence of phage binding. The antibody inhibited the cell binding of the phage expressing RPARPAR, the prototypic CendR peptide, by about 70% (Figure 1a). A similar degree of inhibition was obtained for the phage tLyP-1. The NRP1 antibody did not significantly inhibit the binding of the other truncated forms of LyP-1 (Figure 1b). Thus, a single or double basic residue at the C-terminus, as in CGNK or CGNKR, was not enough to confer significant ability to bind to NRP1. CGNKRTRG showed a mild reproducible decrease in DU145 cell binding upon anti-NRP1 treatment, suggesting that the presence of the glycine residue C-terminal of the CendR motif may be compatible with NRP1 binding. This is supported by recent modeling studies showing that glycine-containing peptides (G_7, G_3RG_3 and G_4RG_2) were able to dock in NRP1-binding pocket without major deformation of the receptor structure (Haspel *et al*., 2011). In contrast, the

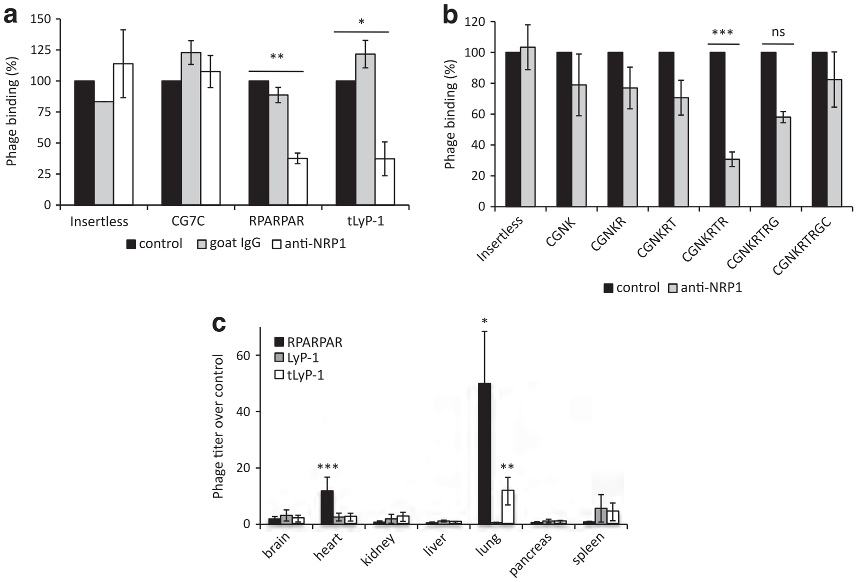

Figure 1 CGNKRTR is the active CendR element of LyP-1. (**a**) DU145 cells were incubated with phage at 4 °C to assess NRP1 binding. Ligand-blocking anti-NRP1 inhibited binding of both CGNKRTR and RPARPAR phage, whereas goat IgG had no effect. Insertless and CG7C control phage binding was not inhibited. Binding is expressed as percentage of binding in control conditions (mean ± s.e.m.; $n = 4$/group; *$P < 0.05$; **$P < 0.01$). (**b**) DU145 cells were incubated with various truncated versions of LyP-1 phage at 4 °C to determine the minimum essential element for NRP1 binding. Ligand-blocking anti-NRP1 inhibited binding of CGNKRTR but not of the other phage. Insertless phage binding was not inhibited. Binding is expressed as percentage of binding in control conditions (mean ± s.e.m.; $n = 5$/group; ***$P < 0.001$; ns, not significant). (**c**) Tissue distribution of intravenously injected phage after 15 min circulation in normal mice. tLyP-1 phage significantly accumulated in the lungs. The titer of phage is expressed as fold over control insertless phage (mean ± s.e.m.; $n = 3$/group; *$P < 0.05$; **$P < 0.01$; ***$P < 0.001$).

binding of full-length LyP-1 to the cells was not inhibited by the anti-NRP1, suggesting that the peptide has to be processed into its CendR form to be able to bind to NRP1.

We next analyzed the distribution of intravenously administered tLyP-1 phage in normal mice after 15 min circulation, and observed that it showed significant accumulation in the lungs (Figure 1c). This finding agrees with previously described accumulation of CendR phage in the lungs, presumably because it is the first vascular bed encountered by intravenously injected substances (Teesalu *et al.*, 2009). Taken together, the binding and inhibition results, and the *in-vivo* phage distribution strongly suggest that tLyP-1 is an active CendR peptide.

NRP1 binds tLyP-1 phage and mediates its internalization

We next tested the binding of tLyP-1 to purified NRP1. The tLyP-1 phage bound to immobilized NRP1 about 120 times more than insertless control phage, whereas phage expressing intact LyP-1 showed no binding (Figure 2a). RPARPAR phage exhibited a 280-fold binding ratio over the control phage, suggesting a higher affinity for NRP1 than tLyP-1.

RPARPAR-displaying phage was originally shown to strongly bind to and internalize into cultured PPC1 prostate carcinoma cells (Teesalu *et al.*, 2009), which express high levels of NRP1 (Supplementary Figure S1A). We found that tLyP-1 phage had a similar activity, whereas LyP-1 phage did not interact with the PPC1 cells (Figure 2b).

As observed with RPARPAR phage, all or almost all the PPC1 cells were positive for tLyP-1 phage uptake. Moreover, tLyP-1 phage co-localized with NRP1 in vesicular structures inside the cells, suggesting that the two proteins co-internalized upon interaction (Figure 2c, arrows). tLyP-1 internalization into the PPC1 cells was inhibited in a dose-dependent manner by oligomeric RPARPAR peptide (Figure 2d), further showing that tLyP-1 internalization follows the CendR pathway.

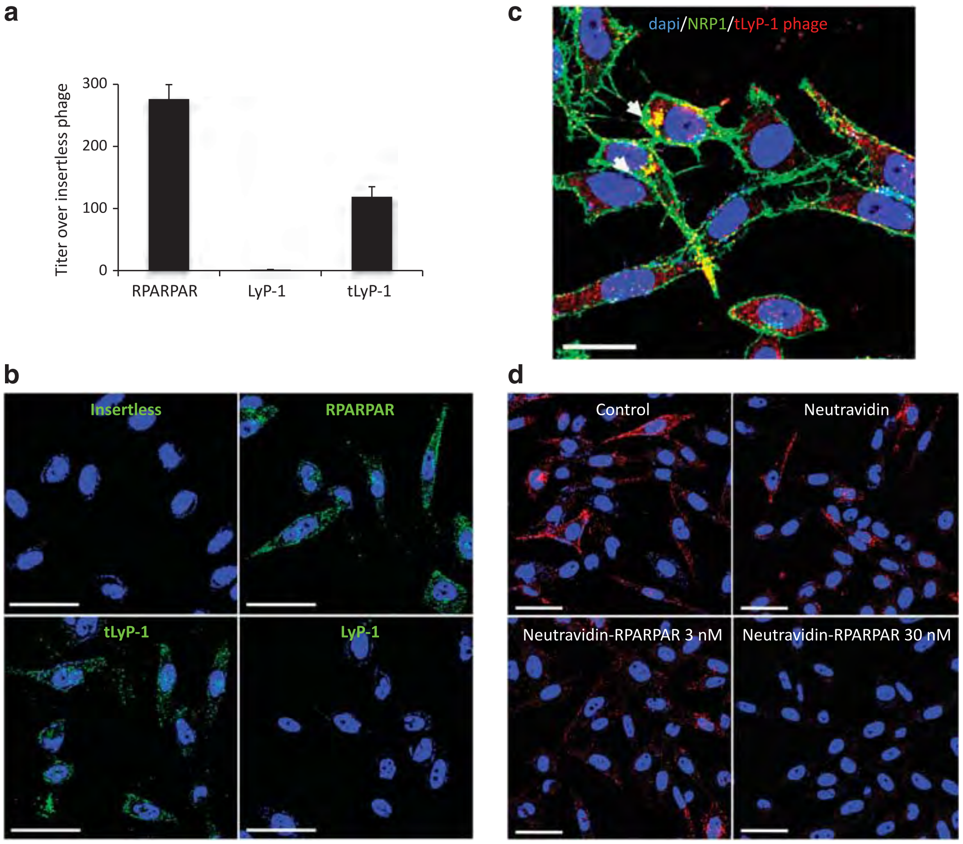

Figure 2 NRP1 binds tLyP-1 and mediates its internalization. (**a**) Purified NRP1 was coated on microtiter wells and the binding of insertless, RPARPAR, LyP-1 and tLyP-1 phage was tested. Binding is expressed as fold over control phage (RPARPAR/insertless = 276, LyP-1/insertless = 1.6, tLyP-1/insertless = 119 ± s.e.m., *n* = 3/group). (**b**) Confocal microscope images of PPC1 cells incubated in the presence of 10^9 p.f.u. of insertless, RPARPAR, LyP-1 or tLyP-1 phage. Phage clones were detected by staining with anti-T7 phage polyclonal antibody (green). Nuclei were stained with DAPI (blue) (original magnification, × 40; scale bars, 50 μm). (**c**) Confocal microscope image of PPC1 cells incubated with tLyP-1 phage (red). Cells were co-stained for NRP1 (green) and nuclei were stained with DAPI (blue). Arrowheads indicate co-localization between tLyP-1 phage and NRP1 (original magnification, × 40; scale bar, 25 μm). (**d**) After 30 min pre-incubation with increasing concentrations of NA-RPARPAR peptide, PPC1 cells were incubated with tLyP-1 phage (red) for 2 h. Nonconjugated NA was used as a control. Nuclei were stained with DAPI (blue). Cells were analyzed by confocal microscopy (original magnification, × 40; scale bars, 50 μm).

NRP2 binds CendR peptides and mediates their internalization

NRP2 involvement in the CendR pathway has not been addressed. Given the homology between NRP1 and NRP2, and the similarities in LyP-1 homing and NRP2 tissue and cell distribution, we hypothesized that NRP2 could also be a CendR receptor. Indeed, tLyP-1 phage bound to purified NRP2 about eight times more than insertless phage (Figure 3a). As observed for NRP1 binding, RPARPAR phage exhibited higher level of binding to NRP2 than tLyP-1 phage (binding ratios over control = 29 versus 8). The binding of both peptides was higher to NRP1 than to NRP2, suggesting that CendR peptides preferentially bind to NRP1. LyP-1 phage did not bind to NRP2 (binding ratio over control = 0.6). We next studied binding and internalization of phage clones into MDA-MB-435 breast carcinoma cells that express only NRP2, and not NRP1 (Supplementary Figure S1A). tLyP-1 phage bound and internalized into these cells, where it co-localized with NRP2 (Supplementary Figure S2B; Figure 3b, arrows). tLyP-1 phage internalization into MDA-MB-435 cells was lower than into PPC1 cells, possibly due to the weaker affinity for NRP2 than for NRP1, or/and to lower total NRP expression in the MDA-MB-435 cells. Using a function-blocking antibody against NRP2, we confirmed that tLyP-1 phage directly bound to NRP2 in MDA-MB-435 cells (Figure 3c). The anti-NRP2 antibody also inhibited RPARPAR phage binding, and oligomeric RPARPAR peptide blocked the binding and internalization of phage tLyP-1 in the cells, further demonstrating the role of NRP2 in the CendR pathway (Figure 3d).

LyP-1 internalization uses the CendR pathway

The MDA-MB-435 cells express the cell surface LyP-1 primary receptor p32, and LyP-1 internalizes into these cells (Fogal *et al.*, 2008). To test whether internalization of tLyP-1 and LyP-1 could occur through p32, we explored tLyP-1 capacity to bind to this receptor. A saturation assay performed with fluorescein-labeled peptides (FAM-peptides) showed low binding of tLyP-1 to purified p32, whereas robust binding was seen with FAM-LyP-1 (Supplementary Figure S3). Moreover, affinity chromatography of 4T1 breast tumor extracts on tLyP-1 revealed no binding of p32 to the tLyP-1 affinity matrix (data not shown). Thus, only the intact LyP-1 peptide binds to p32.

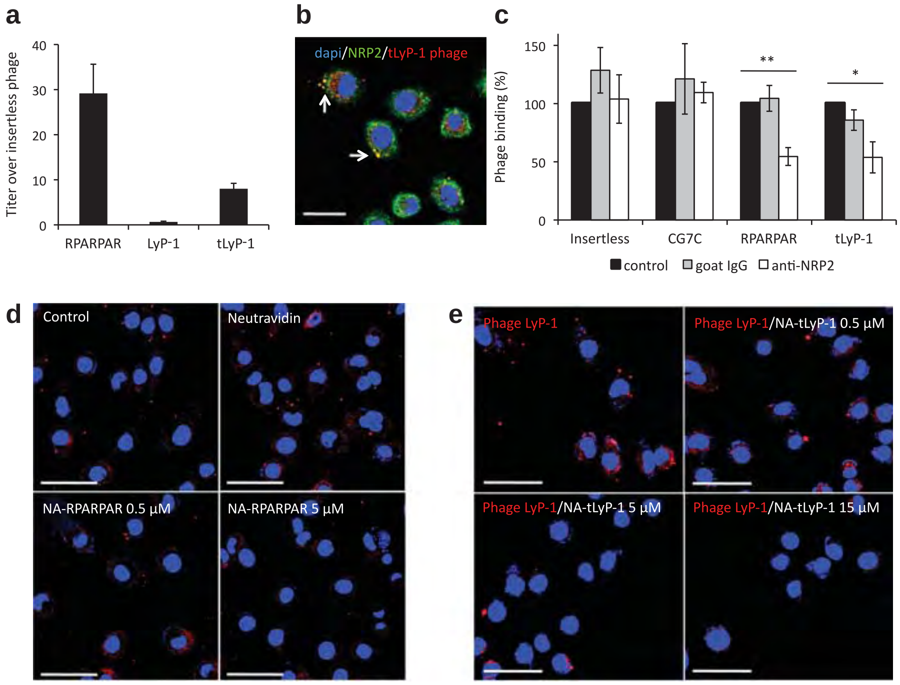

Figure 3 NRP2 binds tLyP-1 and mediates its internalization. (**a**) Purified NRP2 was coated on microtiter wells and the binding of insertless, RPARPAR, LyP-1 and tLyP-1 phage was tested. Binding is expressed as fold over control phage (RPARPAR/insertless = 29, LyP-1/insertless = 0.6, tLyP-1/insertless = 8 ± s.e.m., *n* = 3/group). (**b**) Confocal microscope image of MDA-MB-435 cells cultured for 2 h in presence of tLyP-1 phage (red). Cells were co-stained for NRP2 (green) and nuclei were stained with DAPI (blue). Arrowheads indicate co-localization between tLyP-1 phage and NRP2 (original magnification, × 40, scale bar, 25 μm). (**c**) MDA-MB-435 cells were incubated with phage at 4 °C to assess NRP2 binding. Ligand-blocking anti-NRP2 inhibited binding of both CGNKRTR and RPARPAR phage, whereas goat IgG had no effect. Insertless and CG7C control phage binding was not inhibited. Binding is expressed as percentage of binding in control conditions (mean ± s.e.m.; *n* = 4/group; $^{*}P<0.05$; $^{**}P<0.01$). (**d**) After 30 min pre-incubation with increasing concentrations of NA-RPARPAR peptide, MDA-MB-435 cells were incubated with tLyP-1 phage (red) for 2 h. Nonconjugated NA was used as a control. Nuclei were stained with DAPI (blue) (original magnification, × 40; scale bars, 50 μm). (**e**) After 30 min pre-incubation with increasing concentrations of NA-tLyP-1 peptide, MDA-MB-435 cells were incubated with LyP-1 phage for 2 h. Phage was stained with anti-T7 antibody (red). Nuclei were stained with DAPI (blue) (original magnification, × 40; scale bars, 50 μm).

Having established that (i) tLyP-1 but not LyP-1 binds to NRP1 and NRP2, (ii) LyP-1 but not tLyP-1 binds to p32 and (iii) both LyP-1 and tLyP-1 internalize into MDA-MB-435 cells, we tested the effect of tLyP-1 on LyP-1 cell internalization. Oligomeric tLyP-1 peptide concentration dependently and fully inhibited LyP-1 phage internalization (Figure 3e). This result supports our hypothesis of a common internalization pathway for LyP-1 and tLyP-1, and the likely cleavage of LyP-1 into the CendR form tLyP-1.

We thus hypothesize that LyP-1 internalization mechanism is very similar to what has been documented for the iRGD peptide (Sugahara *et al*., 2009): LyP-1 first binds to cell surface p32 in tumors, which triggers a protease cleavage into the tLyP-1 form, and a shift from p32 to NRP1/2 binding, made possible by the loss of affinity for p32 and newly acquired affinity for the NRPs. The NRP binding then activates the CendR cell internalization pathway (Figure 4).

tLyP-1 specifically homes to breast tumors

Given the high NRP expression in the majority of tumors (Ellis, 2006; Guttmann-Raviv *et al*., 2006; Bagri *et al*., 2009), we set out to study tissue distribution of intravenously injected tLyP-1 in mice bearing orthotopic breast cancers. The mouse 4T1 cells overexpress both NRP1 and NRP2 (Supplementary Figure S1B) and NRP1 and NRP2 exhibit a high sequence homology between mice and humans (93 and 95%, respectively; Chen *et al*., 1997; He and Tessier-Lavigne, 1997). Phage tLyP-1 bound and internalized into 4T1 cells *in vitro* (Supplementary Figure S4). Tumors examined 1 h after the injection of FAM-tLyP-1 were strongly fluorescent under blue light (Figure 5a). Normal tissues, which express NRP1 at lower levels than tumors (Ellis, 2006; Guttmann-Raviv *et al*., 2006; Bagri *et al*., 2009), were negative, with the exception of the kidneys, which reflects the clearance of the peptide through this organ. A control peptide, FAM-ARALPSQRSR (Laakkonen *et al*., 2002), did not accumulate in the 4T1 tumors. Similar results were obtained in human MDA-MB-435 breast cancer xenografts (Figure 5b). Further confocal microscopy analyses confirmed the selective accumulation of FAM-tLyP-1 in 4T1 tumor tissue, and revealed extensive spreading of the label within the tumor (Figure 5c).

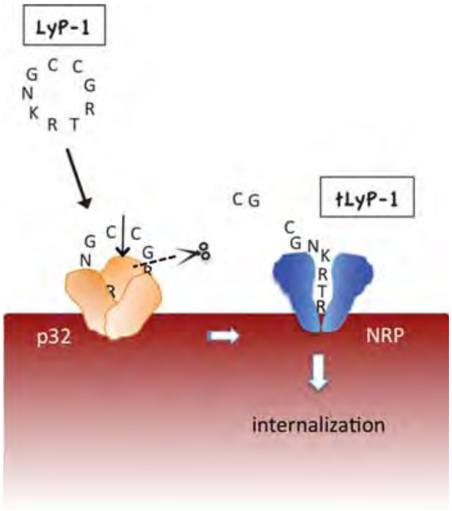

Figure 4 LyP-1 is a cryptic CendR peptide. Cyclic LyP-1 concentrates at the surface of tumor cells by binding to its primary receptor p32. LyP-1 is then proteolytically cleaved into the linear truncated form, tLyP-1, which diminishes its affinity for p32. The exposed C-terminal CendR motif becomes active and triggers binding to NRP1 and/or NRP2, and subsequent cell internalization.

To evaluate the capability of tLyP-1 to deliver nanoparticles into tumors and penetrate into tumor tissue, we conjugated FAM-tLyP-1 to elongated iron oxide nanoparticles dubbed nanoworms (tLyP-1-NWs; dimensions: 30 × 80–100 nm) (Park *et al*., 2009; Agemy *et al*., 2010). Iron oxide nanoparticles have the advantage that they can serve as a contrast agent in magnetic resonance imaging. Examination of tLyP-1-NW biodistribution showed specific homing of tLyP-1-NWs to 4T1 tumors (Figure 6a). As reported previously for various nanoparticles, the NWs nonspecifically accumulated in the liver and spleen to a small extent (Thorek *et al*., 2006), and some were also found in the kidney, presumably reflecting the release of the labeled peptide from the NWs (Supplementary Figure S5). The accumulation of the NWs in the tumor was observed at all time points studied (from 30 min to overnight circulation) (Figure 6a; Supplementary Figure S5). The tLyP-1-NWs also specifically homed to the tumors in a third breast cancer model, human MDA-MB-231 xenografts, which express both NRP1 and NRP2 (Supplementary Figure S6A).

Comparison of tLyP-1-NWs with LyP-1-NWs and RPARPAR-NWs

The tissue distribution profile of tLyP-1-NW was comparable to that of the parental LyP-1-NW with respect to tumor-specific homing, but their spreading patterns were different (Figure 6a). After 4 h of circulation, tLyP-1-NWs showed a significantly wider distribution in the tumor tissue than LyP-1-NWs; the fluorescent surface area in the tumor sections was about four times larger in the tLyP-1 tumors (Figure 6b). The enhanced penetration properties of tLyP-1-NW may be attributable to the exposed CendR motif.

The distribution of the tLyP-1-NWs was strikingly different from NWs coated with the prototypic CendR, RPARPAR. Indeed, besides extensive tumor accumulation, RPARPAR-NWs were also present in each of the other tissues we examined (Figure 6c). The accumulation of the RPARPAR-NWs in the liver, spleen and kidney was higher than that of tLyP-1-NWs or LyP-1-NWs. In addition, the RPARPAR-NWs were present in the heart, lungs and pancreas, which were negative for tLyP-1-NWs. Thus, tLyP-1, even though it is an active CendR peptide, is a specific tumor-homing peptide, possibly because of its lower affinity for NRP receptors compared with RPARPAR.

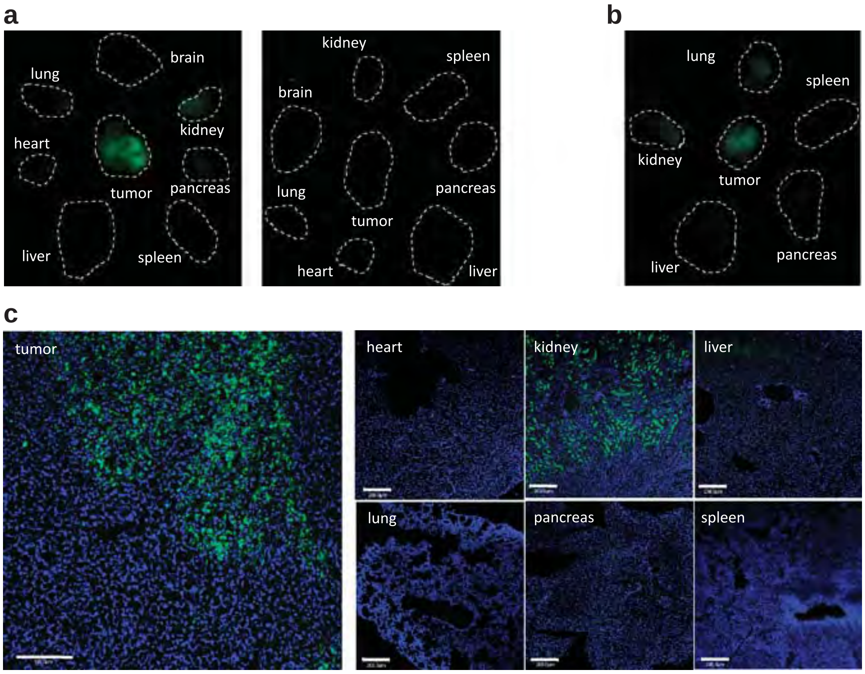

Figure 5 FAM-tLyP-1 homes specifically to breast tumors. (**a**) FAM-tLyP-1 (left panel) or control FAM-ARALPSQRSR (right panel) was intravenously injected into 4T1 tumor-bearing mice. The peptides were allowed to circulate for 1 h and tumors and organs were collected and viewed under blue light. Dotted lines delineate the organs. Representative images of three independent experiments are shown. Note the strong fluorescence in the tumor from the FAM-tLyP-1 injected mouse compared with the other organs, and the absence of fluorescence in the control panel. (**b**) FAM-tLyP-1 was intravenously injected into MDA-MB-435 tumor-bearing mice. The peptide was allowed to circulate for 45 min, and tumor and organs were collected and viewed under blue light. Dotted lines delineate the organs. Representative image of three independent experiments are shown. Note that the fluorescence is only found in the tumor. (**c**) Confocal microscope images of the tumor and of normal organs after 1 h of FAM-tLyP-1 circulation in 4T1 tumor-bearing mice. FAM-tLyP-1: green, nuclei: blue (original magnification, × 20; scale bars, 100 μm (tumor); 10 × ; scale bars, 200 μm (other organs)).

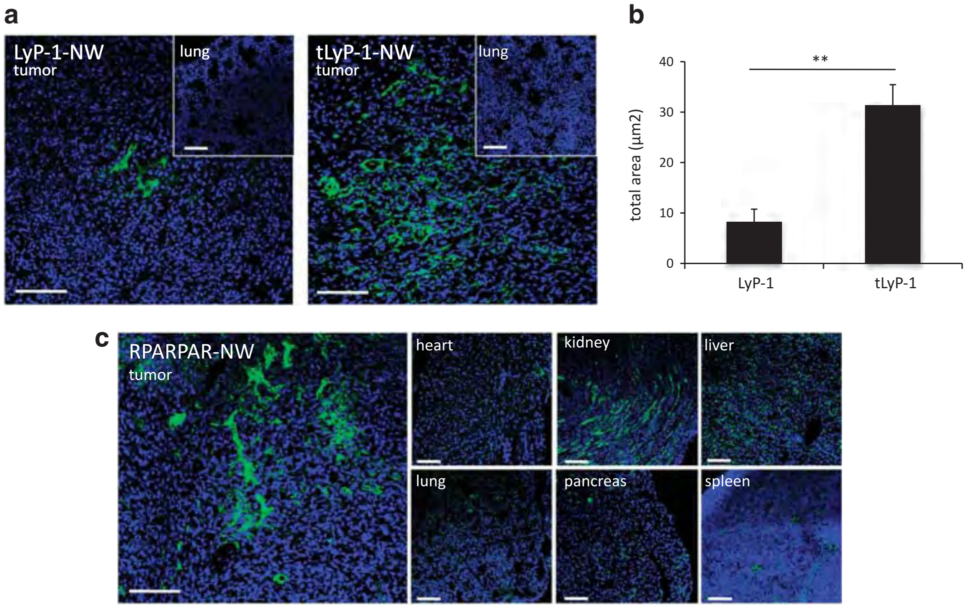

Figure 6 Comparison of tLyP-1-NW homing with LyP-1-NW and RPARPAR-NW homing. (**a**) NWs conjugated to FAM-LyP-1 (left panel) and FAM-tLyP-1 (right panel) peptides were intravenously injected into 4T1 tumor-bearing mice (5 mg iron/kg mouse) and allowed to circulate for 4 h. FAM-peptides: green, nuclei: blue (original magnification, × 20; scale bars, 100 μm). Note the absence of fluorescence in the lungs. (**b**) Fluorescence of 10 fields/tumor was quantified with Image J (mean ± s.e.m.; *n* = *3*/group; ***P* < 0.01) (**c**) NWs conjugated to FAM-RPARPAR peptide were intravenously injected into 4T1 tumor-bearing mice (5 mg iron/kg mouse) and allowed to circulate for 4 h. FAM-RPARPAR: green, nuclei: blue. Note the presence of fluorescence in all the organs (original magnification, × 20; scale bars, 100 μm).

tLyP-1-NWs extravasate into regions positive for NRP1 and NRP2 and tLyP-1 peptide increases tumor penetration of a co-injected compound

To assess tLyP-1-NWs tumor penetration over time, tumor sections were analyzed after different circulation times, and blood vessels were stained with an anti-CD31 antibody (Figure 7a). After 30 min of circulation, tLyP-1-NWs fluorescence co-localized to a high extent with the CD31 staining, showing that the NWs were mainly inside the blood vessels or associated with the blood vessel walls. After 4 h, most of the NWs had extravasated and penetrated the tumor tissue, with only a small fraction still associated with the blood vessels. Similar extravasation pattern was also observed in MDA-MB-231 breast cancer xenografts (Supplementary Figure S6B). tLyP-1-NWs were present in tumor regions where NRP1 and NRP2 were abundantly expressed, and co-localization with anti-NRP1 and anti-NRP2 immunostaining was observed (Figure 7b, arrows). tLyP-1-NWs were still seen in the tumor after overnight circulation, whereas the nonspecific accumulation in the liver, spleen and kidney was no longer detectable (Supplementary Figure S5). For this time point, the tLyP-1-NW signal no longer co-localized with tumor blood vessels and had spread deeper through the tumor tissue.

We also tested the ability of tLyP-1 to trigger tumor penetration of a co-administered compound by activating the CendR pathway (Teesalu *et al*., 2009; Sugahara *et al*., 2010). We injected tLyP-1 peptide together with NWs coated with a tumor-homing peptide (sequence: CGKRK) that is unable to get out of the blood vessels by itself (Hoffman *et al*., 2003; Agemy *et al*., 2011). Confocal microscopy analyses revealed enhanced tumor penetration of CGKRK when injected with tLyP-1 (Figure 7c). Thus, tLyP-1 can also induce penetration of a co-administered compound.

Discussion

Our results show that the tumor-homing peptide LyP-1 (Laakkonen *et al*., 2002) uses the CendR mechanism for cell internalization. More importantly, we document a novel tumor-homing peptide, tLyP-1, which exhibits enhanced penetration capacity within tumor tissue compared with full-length LyP-1, even when tethered

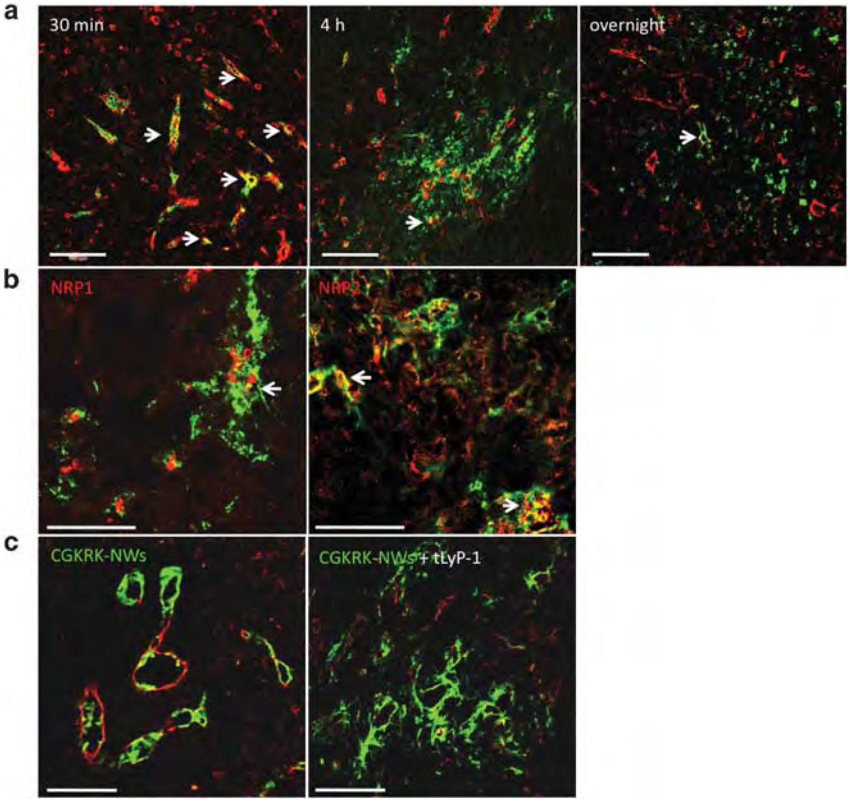

Figure 7 tLyP-1-NWs extravasate into regions positive for NRP1/2 and increase penetration of a co-injected compound. (**a**, **b**) Confocal microscope images of tLyP-1-NWs (green) in comparison with blood vessels and NRPs. (**a**) Blood vessels were stained with anti-CD31 antibody (red). Arrowheads indicate co-localization between the NWs and the blood vessels. Note the spreading of the label in the tumor tissue over time (original magnification, × 20; scale bars, 100 μm). (**b**) tLyP-1-NWs after 4 h of circulation. (Left panel) Tumor sections were stained with anti-NRP1 (red). (Right panel) Tumor sections were stained with anti-NRP2 (red). Arrowheads indicate co-localization between the NWs and the NRP (original magnification, × 40; scale bars, 50 μm). (**c**) CGKRK-NWs (green) were injected alone (left panel) or together with tLyP-1 peptide (right panel) and allowed to circulate for 4 h. Tumor sections were stained with anti-CD31 (red). Note the extravasation in the tumor parenchyma in the presence of tLyP-1 (original magnification, × 20; scale bars, 100 μm).

on nanoparticles. This peptide is furthermore able to induce penetration of a co-injected substance.

A strong body of evidence links LyP-1 to the CendR pathway (Sugahara *et al*., 2009; Teesalu *et al*., 2009). First, we show that exposure of the CendR motif in LyP-1 triggers binding to the established CendR receptor, NRP1. Second, we show that this binding is specific, and follows the CendR rule—the CendR motif 'KRTR' must possess a free C-terminus for the binding to occur. Third, we show that when the CendR motif is exposed, the phage is internalized into cells, where it co-localizes with NRP1. Inhibition of the internalization by the prototypic CendR RPARPAR confirmed the involvement of the CendR pathway. These results strongly suggest that the tumor-penetrating properties of LyP-1 depend on the exposure of the cryptic CendR motif.

The previously identified cryptic CendR peptide, iRGD, loses its affinity for the primary tumor receptor αv integrin after proteolytic cleavage and acquires affinity for NRP1 (Sugahara *et al*., 2009). Similarly, the LyP-1 CendR fragment, tLyP-1, exhibited a weak affinity for the primary receptor p32, suggesting that cryptic CendR peptides follow a general pattern involving loss of affinity for the primary receptor after cleavage, and acquisition of an affinity for NRP1. Hence, the full inhibition of LyP-1 internalization by the CendR fragment tLyP-1 likely indicates that internalization occurs through NRP, and not through p32, even though we cannot entirely rule out the participation of other binding molecules.

$VEGFA_{165}$, which induces vascular permeability through its interaction with NRP1 (Becker *et al*., 2005; Mamluk *et al*., 2005; Acevedo *et al*., 2008), binds to NRP2 as well (Soker *et al*., 1998; Gluzman-Poltorak *et al*., 2000). Interestingly, using cancer cell lines that express selectively one or the other NRP, we were able to show that NRP2 is also a receptor for CendR peptides, although with a lower binding capacity compared with NRP1. NRP2 is expressed in tissues and cells where NRP1 is absent. Thus, ability to bind NRP2 might be crucial for penetration of CendR peptides in these specific tissues, an example of which may be tumor lymphatics, which express high levels of NRP2 and are a specific target of LyP-1 (Laakkonen *et al*., 2002, 2004). The distinct properties of various CendR peptides therefore increase the targeting possibilities offered by this technology.

The most significant and surprising finding in this study was the specific homing of the CendR fragment tLyP-1 to tumors, and its high penetration characteristics. The poor quality and leakiness of tumor vessels can cause extravasation and retention of materials in tumors (Greish, 2007). However, our results show that the accumulation of FAM-tLyP-1 in the tumors is specific. The tLyP-1 peptide alone or conjugated to nanoparticles specifically homed to three different types of breast tumors, and spread widely within the tumor tissue. This significantly enhanced penetration compared with LyP-1 nanoparticles is likely due to the direct exposure of the CendR motif and the absence of proteolytic activity requirement. tLyP-1 was also able to induce co-penetration of CGKRK-NWs, which do not extravasate when injected alone, further demonstrating that it exhibits CendR characteristics *in vivo*.

tLyP-1 showed more specific homing properties than the prototypic CendR peptide RPARPAR. RPARPAR nanoparticles accumulated in all organs analyzed, which is related to its capacity to induce extravasation and tissue penetration through NRP1 binding (Teesalu *et al*., 2009). In contrast, tLyP-1 only accumulated in tumors, both as a free peptide and on nanoparticles. Possible reasons for this difference include the lower affinity of tLyP-1 for NRPs, which should favor binding to tissues with the highest local concentration of NRPs, the tumors (Bagri *et al*., 2009). It is also possible that NRPs are at a higher state of activation in tumors than in normal tissues; regulation of receptor activation is a well-documented phenomenon with other receptors (for example, integrins; Hynes, 2002). Enhanced neuropilin activation could accentuate the effects of the affinity difference between RPARPAR and tLyP-1.

The high expression of both NRP1 and NRP2 in tumors allows one to envision applications for tLyP-1 in tumor targeting. In this study, we show homing and penetration of tLyP-1 to tumors in three different breast cancer models with different patterns of cancer cell NRP expression. Moreover, NRP1 and NRP2 are also present in tumor vessels, where NRP1 is involved in angiogenesis, and NRP2 in lymphangiogenesis (Liang *et al*., 2007; Pan *et al*., 2007; Caunt *et al*., 2008; Dallas *et al*., 2008). Thus, tLyP-1 may be useful in targeting a variety of solid tumors and to deliver therapeutic or diagnostic agents deep inside the tumor tissue. As a proof of principle, we have shown here that tLyP-1 was able to carry fluorescein and superparamagnetic iron oxide nanoparticles to the tumor interior. Moreover, tLyP-1 induced co-penetration of NWs conjugated with a tumor-homing peptide from tumor blood vessels to the tumor parenchyma. Previous studies with another tumor-penetrating peptide, iRGD, have demonstrated the efficacy of these strategies in tumor treatment and imaging (Sugahara *et al*., 2009, 2010). Thus, the strong tumor-homing and penetrating properties of tLyP-1 make it a potentially important addition to the arsenal of targeting agents for drug delivery.

Materials and methods

Antibodies and purified proteins

Purified proteins were used for phage binding assays: recombinant human NRP1 (R&D, Minneapolis, MN, USA) and recombinant human NRP2 Fc chimera (R&D). The ligand-blocking polyclonal antibodies, goat anti-rat NRP1 and goat anti-human NRP2, were purchased from R&D. Goat IgG (AbCam, Cambridge, MA, USA) was used as control. For immunofluorescence, the primary antibodies were (i) monoclonal rat anti-mouse CD31 (BD Biosciences, San Diego, CA, USA), (ii) polyclonal rabbit anti-human NRP1 (Chemicon, Temecula, CA, USA), (iii) polyclonal rabbit anti-human NRP2 (Novus Biologicals, Littleton, CO, USA) and (iv) polyclonal rabbit anti-T7 phage (Teesalu *et al*., 2009). The following secondary antibodies were used: donkey anti-goat 488/546, goat anti-rat 546 and goat anti-rabbit 488/546 (Invitrogen, Carlsbad, CA, USA).

Cell lines and tumors

MDA-MB-435 (Fogal *et al*., 2008), DU145 (purchased from ATCC, Manassas, VA, USA) and PPC1 (Teesalu *et al*., 2009) cells were cultured in Dulbecco's modified eagle medium (Gibco) and 4T1 cells (purchased from ATCC) in IMDM (Gibco). Media were supplemented with 10% fetal bovine serum and 1% penicillin–streptomycin (Gibco, Grand Island, NY, USA). Cells were maintained at 37 °C/5% CO_2.

To produce 4T1 tumors, BALB/c mice were orthotopically injected into the mammary fat pad with 10^6 cells suspended in 100 μl of phosphate-buffered saline (PBS). Experiments were performed 10 days after the tumor cell injection, before the tumors get highly necrotic and hemorrhagic (average tumor size: 300–500 mm^3). To produce MDA-MB-435 tumors, BALB/C athymic nude mice were injected into the mammary fat pad with 2×10^6 cells in 100 μl of PBS, and the mice were used for experiments 4–6 weeks later (average tumor size: 500 mm^3). Before any surgical procedure, mice were anesthetized with intraperitoneal injections of xylazine (10 mg/kg) and ketamine (50 mg/kg). Animal experimentation was performed according to the procedures approved by the Animal Research Committees at the University of California, Santa Barbara.

Peptides and peptide-conjugated NWs

The peptides were synthesized as described (Teesalu *et al*., 2009).

Tetrameric peptides were obtained by conjugation with neutravidin (NA; Pierce, Rockford, IL, USA). NA was dissolved at 5 mg/ml in ultrapure water with 5% glycerol, heated to 37 °C for 1 h, sonicated and filtered. Biotinylated peptide stocks were prepared in water shortly before use, sonicated and added at equal volume to the NA for a final concentration of 250 μM peptide and 40 μM NA. Conjugates were used after 30 min with no additional purification.

NWs coated with peptides were prepared as previously described (Park *et al*., 2009; Agemy *et al*., 2010).

In vitro *phage binding and internalization*

Microtiter wells (Costar, Bloomington, MN, USA) were coated with 5 μg/ml of purified NRP1 or NRP2, blocked with PBS/0.5%. Bovine serum albumin and incubated with 10^8 plaque-forming units (p.f.u.) of phage in 100 μl of PBS/0.05% Tween 20 for 20 h at 37 °C. After six washes in PBS/0.05% Tween 20, bound phage was eluted with 200 μl of 1 M Tris–HCl (pH 7.5)/0.5% sodium dodecyl sulfate for 30 min and quantified by a plaque assay (titration).

To measure phage binding on cells, 2×10^5 suspended cells were incubated with 7×10^8 p.f.u./ml of T7 phage in Dulbecco's modified eagle medium/bovine serum albumin 1% for 1 h at 4 °C. Ligand-blocking antibodies or control goat IgG isotype (10 μg/sample) were added 30 min before phage incubation. The cells were washed four times with Dulbecco's modified eagle medium/bovine serum albumin 1%, and lysed with lysogeny broth/1% Nonidet P-40 (LB/NP40) before phage titration.

Phage, NW and peptide homing in vivo

Normal BALB/c mice were intravenously injected with 10^{10} p.f.u. of phage, which were allowed to circulate for 15 min. The mice were then perfused through the heart with PBS containing 1% Bovine Serum Albumin and tissues were collected and homogenized in 1 ml of LB/NP40 for titration.

4T1 tumor-bearing BALB/c mice and MDA-MB-435 tumor-bearing nude mice were intravenously injected with, respectively, 150 and 100 μl of 1 mM FAM-labeled synthetic peptides. After 1 h circulation, mice were perfused and tissues were collected, observed under blue light (Illumatool Bright Light System LT-9900, Lightools Research, Encinitas, CA, USA) and processed for immunofluorescence analysis.

Peptide-NWs (5 mg iron/kg mouse) were intravenously injected in 4T1 tumor-bearing mice and allowed to circulate for 30 min to 16 h. For co-injection experiments, a mixture of CGKRK-NWs (5 mg iron/kg mouse) and tLyP-1 peptide (1 mM) (peptide:peptide-NWs, 50:50) was intravenously injected in 4T1 tumor-bearing mice. After perfusion, organs were harvested and processed for immunofluorescence analysis.

Immunofluorescence

Tissues were fixed with 4% paraformaldehyde and cryoprotected in 30% sucrose before OCT (optimal cutting temperature, Sakura, Torrance, CA, USA) embedding and freezing. Tissues were sectioned at 7 μm and stained with primary antibodies at 4 °C overnight. Secondary antibodies were incubated for 1 h at 37 °C. Stained tissue sections were mounted in Vectashield DAPI (4′,6-diamidino-2-phenylindole)-containing mounting media (Vector Laboratories, Burlingame, CA, USA) and examined on a Fluoview 500 confocal microscope (Olympus America, Center Valley, PA, USA). To quantify the homing area of peptide-NWs, 10 fields/tumor cryosection were analyzed.

Cells were grown on collagen I-coated coverslips (BD Biosciences) for 24–72 h. After 4% paraformaldehyde fixation, cells were stained with antibodies following the same procedure as for tumor sections, and mounted in DAPI-containing mounting media. For phage binding assay, 10^9 p.f.u. of phage in cell culture medium were incubated for 1–2 h. When NA-peptide inhibitors were used, they were added to the cell medium 30 min before phage incubation. NA alone, at the maximum concentration used in the assay, was used as a control. Cells were examined on a Fluoview 500 confocal microscope.

Statistical analysis

Data were analyzed by two-tailed Student's *t*-test.

Conflict of interest

The authors declare no conflict of interest.

Acknowledgements

We thank Dr Eva Engvall for comments on the manuscript. This work was supported by grant number W81XWH-09-1-0698 and W81XWH-08-1-0727 from the USAMRAA for the Department of Defense (ER). LR was supported by Susan G Komen for the Cure post-doctoral fellowship (KG091411) and GB by a fellowship from the Santa Barbara Cancer Center. ER was supported in part by CA30199 the Cancer Center Support Grant from the NCI.

Author contributions: ER and LR designed the research; LR, LA, TT, KNS and JH performed the research; LA, GB and VRK contributed reagents; LR and ER analyzed the data and wrote the paper. All authors discussed the results and commented on the manuscript.

References

Acevedo LM, Barillas S, Weis SM, Gothert JR, Cheresh DA. (2008). Semaphorin 3A suppresses VEGF-mediated angiogenesis yet acts as a vascular permeability factor. *Blood* **111**: 2674–2680.

Agemy L, Friedmann-Morvinski D, Kotamraju VR, Roth L, Sugahara KN, Girard OM *et al*. (2011). Targeted nanoparticle enhanced proapoptotic peptide as potential therapy for glioblastoma. *Proc Natl Acad Sci USA* **108**: 17450–17455.

Agemy L, Sugahara KN, Kotamraju VR, Gujraty K, Girard OM, Kono Y *et al*. (2010). Nanoparticle-induced vascular blockade in human prostate cancer. *Blood* **116**: 2847–2856.

Bagri A, Tessier-Lavigne M, Watts RJ. (2009). Neuropilins in tumor biology. *Clin Cancer Res* **15**: 1860–1864.

Becker PM, Waltenberger J, Yachechko R, Mirzapoiazova T, Sham JS, Lee CG *et al*. (2005). Neuropilin-1 regulates vascular endothelial growth factor-mediated endothelial permeability. *Circ Res* **96**: 1257–1265.

Caunt M, Mak J, Liang WC, Stawicki S, Pan Q, Tong RK *et al*. (2008). Blocking neuropilin-2 function inhibits tumor cell metastasis. *Cancer Cell* **13**: 331–342.

Chen H, Chedotal A, He Z, Goodman CS, Tessier-Lavigne M. (1997). Neuropilin-2, a novel member of the neuropilin family, is a high affinity receptor for the semaphorins Sema E and Sema IV but not Sema III. *Neuron* **19**: 547–559.

Dallas NA, Gray MJ, Xia L, Fan F, van Buren 2nd G, Gaur P *et al*. (2008). Neuropilin-2-mediated tumor growth and angiogenesis in pancreatic adenocarcinoma. *Clin Cancer Res* **14**: 8052–8060.

Ellis LM. (2006). The role of neuropilins in cancer. *Mol Cancer Ther* **5**: 1099–1107.

Fogal V, Zhang L, Krajewski S, Ruoslahti E. (2008). Mitochondrial/cell-surface protein p32/gC1qR as a molecular target in tumor cells and tumor stroma. *Cancer Res* **68**: 7210–7218.

Gluzman-Poltorak Z, Cohen T, Herzog Y, Neufeld G. (2000). Neuropilin-2 is a receptor for the vascular endothelial growth factor (VEGF) forms VEGF-145 and VEGF-165 [corrected]. *J Biol Chem* **275**: 18040–18045.

Greish K. (2007). Enhanced permeability and retention of macromolecular drugs in solid tumors: a royal gate for targeted anticancer nanomedicines. *J Drug Target* **15**: 457–464.

Guttmann-Raviv N, Kessler O, Shraga-Heled N, Lange T, Herzog Y, Neufeld G. (2006). The neuropilins and their role in tumorigenesis and tumor progression. *Cancer Lett* **231**: 1–11.

Hamzah J, Kotamraju VR, Seo JW, Agemy L, Fogal V, Mahakian LM *et al*. (2011). Specific penetration and accumulation of a homing peptide within atherosclerotic plaques of apolipoprotein E-deficient mice. *Proc Natl Acad Sci USA* **108**: 7154–7159.

Haspel N, Zanuy D, Nussinov R, Teesalu T, Ruoslahti E, Aleman C. (2011). Binding of a C-end rule peptide to the neuropilin-1 receptor: a molecular modeling approach. *Biochemistry* **50**: 1755–1762.

He Z, Tessier-Lavigne M. (1997). Neuropilin is a receptor for the axonal chemorepellent Semaphorin III. *Cell* **90**: 739–751.

Heldin CH, Rubin K, Pietras K, Ostman A. (2004). High interstitial fluid pressure – an obstacle in cancer therapy. *Nat Rev Cancer* **4**: 806–813.

Hoffman JA, Giraudo E, Singh M, Zhang L, Inoue M, Porkka K *et al*. (2003). Progressive vascular changes in a transgenic mouse model of squamous cell carcinoma. *Cancer Cell* **4**: 383–391.

Hynes RO. (2002). Integrins: bidirectional, allosteric signaling machines. *Cell* **110**: 673–687.

Jain RK. (1999). Transport of molecules, particles, and cells in solid tumors. *Annu Rev Biomed Eng* **1**: 241–263.

Karmali PP, Kotamraju VR, Kastantin M, Black M, Missirlis D, Tirrell M *et al*. (2009). Targeting of albumin-embedded paclitaxel nanoparticles to tumors. *Nanomedicine* **5**: 73–82.

Kolodkin AL, Levengood DV, Rowe EG, Tai YT, Giger RJ, Ginty DD. (1997). Neuropilin is a semaphorin III receptor. *Cell* **90**: 753–762.

Laakkonen P, Akerman ME, Biliran H, Yang M, Ferrer F, Karpanen T *et al*. (2004). Antitumor activity of a homing peptide that targets tumor lymphatics and tumor cells. *Proc Natl Acad Sci USA* **101**: 9381–9386.

Laakkonen P, Porkka K, Hoffman JA, Ruoslahti E. (2002). A tumor-homing peptide with a targeting specificity related to lymphatic vessels. *Nat Med* **8**: 751–755.

Liang WC, Dennis MS, Stawicki S, Chanthery Y, Pan Q, Chen Y *et al*. (2007). Function blocking antibodies to neuropilin-1 generated from a designed human synthetic antibody phage library. *J Mol Biol* **366**: 815–829.

Mamluk R, Klagsbrun M, Detmar M, Bielenberg DR. (2005). Soluble neuropilin targeted to the skin inhibits vascular permeability. *Angiogenesis* **8**: 217–227.

Pan Q, Chanthery Y, Liang WC, Stawicki S, Mak J, Rathore N *et al*. (2007). Blocking neuropilin-1 function has an additive effect with anti-VEGF to inhibit tumor growth. *Cancer Cell* **11**: 53–67.

Park JH, von Maltzahn G, Zhang L, Derfus AM, Simberg D, Harris TJ *et al*. (2009). Systematic surface engineering of magnetic nanoworms for *in vivo* tumor targeting. *Small* **5**: 694–700.

Ruoslahti E. (2002a). Specialization of tumour vasculature. *Nat Rev Cancer* **2**: 83–90.

Ruoslahti E. (2002b). Drug targeting to specific vascular sites. *Drug Discov Today* **7**: 1138–1143.

Ruoslahti E, Bhatia SN, Sailor MJ. (2010). Targeting of drugs and nanoparticles to tumors. *J Cell Biol* **188**: 759–768.

Soker S, Takashima S, Miao HQ, Neufeld G, Klagsbrun M. (1998). Neuropilin-1 is expressed by endothelial and tumor cells as an isoform-specific receptor for vascular endothelial growth factor. *Cell* **92**: 735–745.

Sugahara KN, Teesalu T, Karmali PP, Kotamraju VR, Agemy L, Girard OM *et al*. (2009). Tissue-penetrating delivery of compounds and nanoparticles into tumors. *Cancer Cell* **16**: 510–520.

Sugahara KN, Teesalu T, Karmali PP, Kotamraju VR, Agemy L, Greenwald DR *et al*. (2010). Coadministration of a tumor-penetrating peptide enhances the efficacy of cancer drugs. *Science* **328**: 1031–1035.

Takagi S, Tsuji T, Amagai T, Takamatsu T, Fujisawa H. (1987). Specific cell surface labels in the visual centers of Xenopus laevis tadpole identified using monoclonal antibodies. *Dev Biol* **122**: 90–100.

Teesalu T, Sugahara KN, Kotamraju VR, Ruoslahti E. (2009). C-end rule peptides mediate neuropilin-1-dependent cell, vascular, and tissue penetration. *Proc Natl Acad Sci USA* **106**: 16157–16162.

Thorek DL, Chen AK, Czupryna J, Tsourkas A. (2006). Superparamagnetic iron oxide nanoparticle probes for molecular imaging. *Ann Biomed Eng* **34**: 23–38.

Uchida M, Kosuge H, Terashima M, Willits DA, Liepold LO, Young MJ *et al*. (2011). Protein cage nanoparticles bearing the LyP-1 peptide for enhanced imaging of macrophage-rich vascular lesions. *ACS Nano* **5**: 2493–2502.

von Maltzahn G, Ren Y, Park JH, Min DH, Kotamraju VR, Jayakumar J *et al*. (2008). *In vivo* tumor cell targeting with ‘click’ nanoparticles. *Bioconjug Chem* **19**: 1570–1578.

Supplementary Information accompanies the paper on the Oncogene website (http://www.nature.com/onc)

www.MaterialsViews.com
ADVANCED MATERIALS
www.advmat.de

REVIEW

Peptides as Targeting Elements and Tissue Penetration Devices for Nanoparticles

*Erkki Ruoslahti**

The use of nanoparticles in medicine (nanomedicine) has recently become an intensely studied field. Nanoparticles carrying drugs and imaging agents have already reached the clinic, but they are essentially passive delivery vehicles, not what are referred to as "smart" nanoparticles. An important function to add to make nanoparticles smarter is active homing to the target tissue. It makes nanoparticles accumulate in the target tissue at higher concentrations than would be the case without this feature, increasing therapeutic efficacy and reducing side effects. This review discusses the recent developments in the nanoparticle targeting field with emphasis on peptides that home to vascular "zip codes" in target tissues and provide a tissue- and cell-penetrating function.

1. Introduction

Nanoparticles (NPs) are thought to have great potential as drug delivery vehicles in medicine. The first NP drugs are already in the clinic. Examples include a NP composed of albumin-paclitaxel complexes (Abraxane) and liposomes loaded with doxorubicin (Doxil), which are both cancer therapeutics. However, these NPs are essentially passive drug delivery vehicles that do not fully exploit the potential of NPs. By virtue of being particles, NPs can accommodate multiple functions, such as being able to zero in on their target in the body. The targeting can be accomplished by coupling onto the NP a homing element, such as an antibody or peptide that specifically binds to the target tissue. The concept of targeted drug delivery is an old one. The idea is appealing because this approach has some of the advantages of topical application of drugs: high local concentration at the site of the disease process and low systemic exposure. Some of the reasons for the modest success of the approach so far include the early focus on targeting the parenchymal (tumor) cells, which has been largely stymied by poor penetration of the probes into extravascular tissue. The realization that the vasculature is more accessible to molecular probes has been a significant advance. Moreover, the recent emergence of NPs as delivery vehicles and the identification of specific targets in the vasculature have rekindled interest in the targeting approach. We call this mode of drug delivery "synaphic" (Gr. syn, together; aphic, affinity) targeting; it is also referred to as 'active' or 'pathotropic' targeting.

Peptides are particularly well suited for NP targeting because they are small, easy to synthesize and typically non-immunogenic, and because the multivalent presentation of a peptide on a NP provides high avidity for the target. We screen phage libraries in live mice to identify peptides that direct phage homing to a specific target, such as a tumor or the vascular bed of a certain tissue. As the phage is a NP, it is essentially confined to the vessels, and the screening primarily targets differentially expressed endothelial cell markers (vascular "zip codes";[1]). Endothelial marker molecules are readily available for NP binding, and quite frequently the parenchymal cells express the same marker as the endothelium. However, NP access to the extravascular tissue is limited. Recently discovered tumor-penetrating and tissue-penetrating peptides provide a solution to this problem, as they are capable of taking a payload deep into extravascular tissue. Remarkably the NP or drug does not even have to be coupled to the peptide; the peptide activates a bulk transport system that sweeps along any compound that is present in the blood.[2,3] Treatment studies in mice show improved anti-tumor efficacy and less damage to normal tissues. In this review, I discuss the recent advances in NP delivery focusing on the use of molecular markers in the vasculature as the primary target, NP exit from the blood vessels, and their transport through the target tissue.

2. Molecular Specialization of the Vasculature

2.1. Peptides Detecting Vascular Zip Codes

Studies designed to examine the possibility that tissue-specific metastasis of tumors depended on a specific affinity of circulating tumors cells for the vessels of the preferred host tissue suggested molecular heterogeneity of the endothelium.[4] In the early 1990s, I decided to explore the proposed molecular heterogeneity and it role in metastasis by using phage display in vivo. A library of peptides expressed as fusions to a phage surface protein and typically containing about 1 billion different peptides is intravenously injected into live mice under

---

Prof. E. Ruoslahti
Center for Nanomedicine
UCSB, Biology II Bldg., University of California
Santa Barbara, CA 93106-9610, USA
E-mail: ruoslahti@sanfordburnham.org
Prof. E. Ruoslahti
Cancer Center, Sanford-Burnham Medical Research Institute
10901 N. Torrey Pines Rd., La Jolla, CA 92037, USA

DOI: 10.1002/adma.201200454

anesthesia, and 5–10 minutes later, the tissue of interest is collected for phage isolation. By repeating the process a number of times, one obtains a pool of phage enriched in phage clones displaying peptides that selectively home to the target tissue. Sequencing the part of the phage genome that encodes the peptide insert in a sample of phage clones from the enriched pool typically reveals repeated peptide sequences; those are the candidate homing peptides. We initially showed that it was possible to identify homing peptides for brain and kidney vessels.[5] Phage screening has since been used to identify homing peptides for many additional tissues, so many that it seems reasonable to conclude that every tissue puts a specific signature on its vasculature (reviewed in ref. [6]). We also used in vivo phage display to identify a breast cancer cell surface protein that recognizes a lung vascular zip code, promoting metastasis to the lungs.[7] These results support the metastasis hypothesis that inspired the initial in vivo phage display studies.

Various diseases put disease-specific signatures on the vasculature of the diseased tissue, and in vivo phage display has also proven useful in the identification of these disease-specific vascular markers. Cancer, inflammation, atherosclerotic plaques, arthritis, and regenerating tissue are known to induce the expression of new molecular markers in the blood vessels. A major advantage of the in vivo phage screening is that it is unbiased in revealing what works in vivo. Other unbiased methods, such as antibody-based screens,[8] cloning strategies,[9] and in vivo biotinylation[10] have also been used successfully in analyzing tumor vasculature. A major advantage of phage screening is that it recognizes proteins that are expressed at the cell surface in tumors but are entirely intracellular in normal tissues. This expression pattern is quite common in tumors and other activated tissues (see the section on receptors).

Vascular specificities are often shared among cancer, atherosclerosis, inflammation and tissue regeneration. The apparent reason is that they all involve angiogenesis, the sprouting of new blood vessels from existing ones.[11] However, that does not mean that the specificity profiles in different diseases are identical. A striking example of the dependence of vascular marker expression on the nature of the lesion is what happens during tumorigenesis: the vessels of premalignant lesions differ from those of fully malignant lesions (while both differ from normal vessels). In vivo phage display in two de novo transgenic mouse tumor models yielded peptides that recognized the vessels of premalignant lesions, but no longer bound to the vessels in lesions that had turned into fully malignant tumors in the same tumor model. Other peptides displayed the opposite binding pattern, and a third set recognized the vessels in both pre-malignant and fully malignant lesions.[12,13] In addition to the interesting biology, being able to specifically target pre-malignant lesions has potentially important diagnostic and therapeutic implications. It may be possible to image very early incipient malignancies and target them for destruction. Also, when a target receptor and targeting probe are chosen for tumor imaging and therapy, it will be important to know whether the system also recognizes pre-malignant conditions. Comparison of tumor vessels and vessels from regenerating liver by gene expression analysis revealed distinct differences.[14] Similarly, in vivo phage display with tumors as a target has produced different sets of peptides than when wounds[15] or arthritic joints[16] were targeted. One of the wound-homing peptides, a cyclic peptide with the sequence CARSKNKDC, also recognizes tumor vessels, but is much more potent as a homing peptide for wounds and inflamed tissues.[15,17]

Dr. Erkki Ruoslahti is Distinguished Professor and former president of Sanford-Burnham Medical Research Institute and a founder of the Center for Nanomedicine at UCSB. Dr. Ruoslahti is a pioneer in the field of cell adhesion. He now studies specific vascular addresses in directing drugs to sites of disease. He is a member of the U.S. National Academy of Sciences.

2.2. Target Molecules (Receptors) for Homing Peptides

A homing peptide identified by phage screening can be used to identify the corresponding receptor. The most commonly used method for receptor identification is affinity chromatography or "pull-down" on the peptide, followed by mass spectrometry analysis of the bound proteins. Some receptors for tissue-specific vascular homing peptides have been identified.[18–20] More is known about the receptors in tumors. An early phage screening study[21] yielded a tumor-homing peptide with an RGD sequence motif. As RGD is an integrin-binding motif,[22] and RGD-binding integrins such as $\alpha v\beta 3$ and $\alpha v\beta 5$ are specifically expressed in tumor endothelia,[23] this result confirmed the validity of in vivo screening.

New targets identified with homing peptides in tumor vasculature include a form of aminopeptidase N (CD13), which binds peptides containing the NGR motif.[24,25] A peptide representing a 31-amino acid fragment of human high mobility group protein 2, termed F3, is an example of a novel tumor-homing peptide identified by in vivo phage screening of protein fragments encoded by cDNAs.[26] The receptor for F3 is nucleolin expressed at the cell surface. Nucleolin is ubiquitous as an intracellular protein, but is specifically expressed at the cell surface of endothelial cells and tumor cells in vivo.[27,28] Nucleolin was the first example of what appears to be a common phenomenon, expression of intracellular proteins at the cell surface of tumor cells and tumor endothelial cells. Phage display is particularly well suited for the discovery of markers, the accessibility of which at the cell surface makes them tumor specific, rather than high overall expression. Other examples of such markers in tumor vasculature include the cytoplasmic proteins annexin1[29,30] and plectin-1,[31] and the mitochondrial protein p32 (also known as gC1q receptor, and hyaluronic acid binding protein). This protein is the receptor for the tumor homing peptide LyP-1, also originally discovered using in vivo phage display.[32] LyP-1 targets p32 on the cell surface of lymphatic, myeloid, and cancer cells in tumors, whereas normal tissues only express p32 inside the cells, where it is not available for peptide binding.[33]

The fibrin-fibronectin complex in blood clots is a well-recognized target in vascular thrombosis. Less appreciated, but perhaps even more important, is the presence of such complexes in tumors and atherosclerotic plaques. The walls of tumor vessels and the interstitial spaces in tumors contain products of blood clotting, presumably as a result of plasma protein seepage from leaky tumor vessels. Fibrinogen leaked from blood vessels is converted to a fibrin meshwork by tissue procoagulant proteins such as tissue factor.[34–36] Other plasma proteins, plasma fibronectin in particular, become covalently linked or otherwise bound to the fibrin meshwork. These fibrin-fibronectin complexes can be accessed with peptides such as the 9-amino acid cyclic peptide CLT-1[36,37] and the pentapeptide CREKA.[38] Subtle clotting also takes place on the surface of atherosclerotic plaques, and has been made use of in delivering cargo to plaques.[39]

Homing peptides in the clinic. Remarkable success in delivering the cytokine tumor necrosis factor α (TNFα) into tumors has been reported with RGD and NGR peptides; the targeted cytokine was effective in doses as much as 1,000-fold lower than the usual dose, mitigating side effects of this highly toxic cytokine.[40] A TNFα-NGR fusion protein is currently in phase 3 clinical trials.[41] The reasons for this success are likely to be two-fold: TNFα is a trimer and the NGR peptide is attached to each subunit, enhancing binding through an avidity effect. In addition, the chimeric protein has two receptors potentially acting in concert: the receptors for TNFα and the NGR peptide. The same RGD and NGR peptides have also been used to deliver tissue factor in human patients to induce blood clotting specifically in tumor blood vessels, with resulting occlusion of the vessels and tumor infarct.[42]

2.3. Tissue-Penetrating Peptides

We have recently described a tissue-penetrating transport pathway that can be activated with peptides and can be made disease-specific. The key element in the tissue-penetration is the sequence motif R/KXXR/K, which binds to neuropilin-1 (NRP-1), a co-receptor for VEGF. We have named R/KXXR/K the C-end Rule (CendR) motif, because the second arginine or lysine residue has to be C-terminal for the motif to bind to NRP-1.[43] When the CendR peptide binds to NRP-1, a cell internalization and trans-tissue transport pathway is activated. This pathway can transport payloads ranging from small molecules to NPs. Most importantly, it can be activated in a tissue-specific manner by making the CendR motif cryptic and delivering it to the target tissue. The tissue specificity (in this case tumor-specificity) was accomplished with the prototypic peptide of this class, iRGD.[2,3] The sequence of iRGD is CRGDKGPD (the lysine residue can also be an arginine, and the aspartic acid a glutamic acid) and it is cyclized through a disulfide bond between the cysteine residues. This peptide homes to tumors because it contains the integrin-binding RGD motif. What makes it special, however, is the basic residue after the RGD, which creates an internal, cryptic CendR motif (RGDR or RGDK). The multiple steps that make a cryptic CendR peptide a tissue-specific activator of the NRP-1-dependent pathway are as follows:[2] (1) a peptide containing an internal R/KXR/K motif binds to a vascular receptor specific for a target tissue (RGD binding to $\alpha v\beta 3$ and $\alpha v\beta 5$ in the case of iRGD); (2) as a result of this initial binding at the target, the peptide is proteolytically processed to convert the internal R/KXR/K motif into a C-terminal one; (3) the C-terminal R/KXXR/K motif binds to NRP-1, inducing the transport pathway out of the blood vessels and through the extracellular tissue (**Figure 1**). The peptide can carry a payload that is either covalently coupled to the peptide, or the payload can simply be administered together with the peptide because the endocytic bulk transport pathway triggered through neuropilin-1 sweeps along by-stander molecules.[3]

The cell surface binding mediated by the integrin binding is needed for the proteolytic step to occur in cell culture,[2] explaining why the CendR motif of iRGD is only activated in tumors in vivo. The protease that activates iRGD and other cryptic CendR peptides has not been identified. In fact, more than one protease capable of cleaving after a basic residue may be involved, as these peptides can be activated in vitro by trypsin.[43] However, furins are likely candidates because the CendR motif conforms to their consensus substrate. Interestingly, furin expression has been shown to be elevated in tumors and has been used for tumor targeting.[44] NRP-1 is often also highly expressed in tumors.[45] Thus, high furin and NRP-1 may add to the tumor specificity created by the RGD-integrin interaction.

A number of homing peptides described earlier may be tumor-penetrating peptides similar to iRGD. That this is the case with LyP-1 (CGNKRTRGC;[32]) has been shown.[46] Surprisingly, the truncated version of LyP-1 with an active CendR motif exhibited a degree of tumor selectivity.[46] Although RGD peptides with a basic residue following the RGD motif bind poorly to integrins,[2] a peptide resembling the CendR fragment of iRGD (RGDK) has been reported to selectively home to tumors.[47] It may be that a combination of over-expression of neuroplin-1, which is common in tumors, with even a weak binding to a tumor-specific component can render a peptide partially selective for tumor homing. Two other tumor-homing peptides, F3 (KDEPQRRSARLSAKPAPPKPEPKPKKAPAKK[1]) and CRGRRST[13] also contain potential CendR sequences (underlined). We used quantum dots coated with the LyP-1 and F3 peptides in our early NP studies to show the feasibility of in vivo targeting.[48]

Many of the well-known cell-penetrating peptides (CPPs), such as the Tat peptide, contain CendR motifs. However, the CPPs are not cell-type specific,[49] they enter into all types of cells. Likely reasons for the lack of cell type-specificity include the following: First, The CendR motif of a CCP may be irrelevant, because the CPP uses a ubiquitous pathway different from the CendR pathway. Second, The CendR motif may be active (C-terminal) in the CPP causing internalization to all cells expressing NRP-1 (or NRP-2). Third, a CPP may bind to a ubiquitous primary receptor causing activation of its cryptic CendR motif at the surface of all cells. Tumor-homing variations of CPPs have been engineered. In one peptide, the cell-binding activity of the positively charged Tat peptide is neutralized by tethered negatively charged amino acids, until a tumor protease

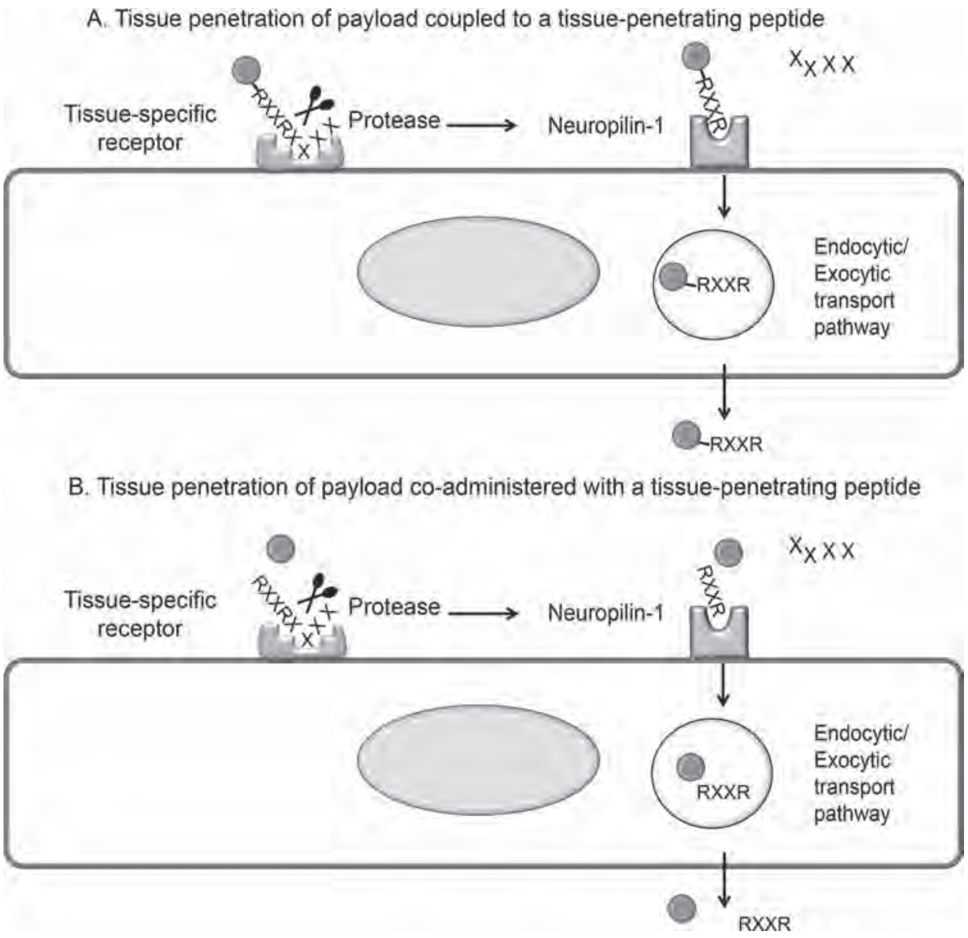

A. Tissue penetration of payload coupled to a tissue-penetrating peptide

B. Tissue penetration of payload co-administered with a tissue-penetrating peptide

Figure 1. Schematic representation of the trans-tissue transport pathway induced by tissue-penetrating peptides of coupled and co-administrated payloads.[43,2,3] Note that the exosome aspect of the pathway shown in the figure is an inference from the properties of the pathway and has not been directly observed. See the text for detail.

cleaves the tether, reversing the blockade.[50] Others have combined a CPP with a tumor-homing peptide, and somewhat surprisingly, the homing peptide activity overrides the universal internalizing properties if the CPP and the chimeric peptides become selective for tumors.[51,52]

We have shown, particularly for the prototype cryptic CendR peptide iRGD, that the delivery of therapeutic and diagnostic agents specifically into tumors can be greatly enhanced with these peptides.[2,3,53,46] This difference is particularly striking when the vascular homing peptide also binds to the cells in tumor parenchyma, as this helps retain the peptide and drive its further spreading within the extravascular tumor tissue. For example, the receptors for iRGD, integrins and NRP-1, are expressed in tumor vessels, as well as on the various other cell types present in the tumor mass, including usually the tumor cells.[2] The studies described above focused on tumor-homing CendR peptides. However, homing peptides for other diseases and tissues exist,[54] and the neuropilin CendR receptors are ubiquitously expressed, albeit that the expression tends to be higher in tumors.[45,46] Thus, there seems to be no reason why disease- and tissue-specific CendR peptides could not be obtained for purposes other than cancer targeting. For example, in addition to tumors, LyP-1 specifically homes to atherosclerotic plaques and penetrates into them, but does not recognize normal vessels.[55]

A major advantage of the CendR system is that by allowing effective extravasation and tissue penetration, a CendR peptide makes more of the target tissue (such as a tumor) available for a therapeutic agent than would be the case with targeting elements that lack the CendR properties. The ability of CendR peptides to promote tissue entry and accumulation of compounds that are not conjugated with the peptide (by-stander effect) provides additional unique advantages: First, it is not necessary to create a new chemical entity to target a drug by CendR peptide co-administration, as is the case when a drug is coupled to a targeting element. This greatly simplifies the path to clinical application. Second, the amount of any given receptor in a target tissue is likely to be quite low, and this is a major limitation of synaphic targeting of drug conjugates.[56] For example, if one assumes that a gram of tumor tissue contains 10^9 cells, and they express an average of 100,000 receptors per cell, there would be roughly 170 pmoles of the receptor in that tumor mass. Only a fraction of the total receptor is likely to be available for the binding of a targeting probe. For many drugs, the required tissue concentration is much higher than a few picomoles per gram of tissue, which means that only a limited amount of a covalently coupled conjugate can be specifically targeted. The by-stander effect does not have this limitation, as the targeted receptor is only used to activate the CendR transport pathway.

The CendR pathway has only been partially characterized so far. It is an endocytic pathway, and marker studies suggest that the CendR endosomes are not related to any of the well-known endosomal vesicles.[43] The fact that this pathway, once activated, sweeps along by-stander molecules and even NPs, suggests a relationship to pinocytosis. Although this has not been directly observed, the CendR vesicles may also be exocytic because it would be difficult to explain the tissue penetration if the payload would only enter cells and not come out of them. The pathway is an active transport pathway; it requires energy and is much faster than what could be explained on the basis of diffusion.[3]

3. Nanoparticle Targeting

3.1. Homing Peptide-Targeted Nanoparticles

NPs can incorporate unique functions that cannot readily be engineered into simple drugs. One such function is selective homing to a target. Coating the surface of NPs with a targeting element, such as a homing peptide, confers the NPs specific affinity to the intended target tissue. NPs with a surface studded with binding elements have been dubbed nanoburrs,[57] a term that coveys the idea of binding, but does not quite cover the specificity of the binding.

Vascular targeting is particularly advantageous with NPs, which have limited ability to exit the vasculature. There is a vast literature on passive NP targeting to tumors through the so-called enhanced permeability and retention (EPR) effect, but EPR is not very effective, and its size-dependency, slow time frame, and variability from tumor to tumor limit its usefulness.[58,59] High interstitial pressure and fibrosis constitute additional barriers to the access of NPs to the interior of tumors.[60–62] Furthermore, EPR is unlikely to operate in non-tumor vascular beds. For these reasons, it is important to design systems that initially target the vasculature, rather than the parenchymal cells.

The luminal side of vessels is fully accessible to NPs circulating in the blood and the vessels can serve as a gateway to the interior of the targeted tissue. NPs are an ideal payload for homing peptides because the presentation of multiple copies of the peptide on the NP surface makes possible multivalent binding. The high avidity resulting from the multivalency compensates the generally moderate affinity of peptides. In addition, elongated shape, such as that of iron oxide nanoworms can enhance homing peptide-mediated binding of NPs to the surface of cells, presumably because more interactions between the two surfaces are possible than when the NP is spherical.[63] Since we use phage display to find homing peptides, and the phage is a NP and the display is multivalent,[6] the peptides identified in this manner are already selected for NP homing.

The “dark” side of NP multivalency is that all surface features in them are presented in a multivalent fashion, providing potential recognition signals for the reticuloendothelial system (RES). RES is also known as the mononuclear phagocyte system (MPS). RES eliminates foreign materials, such as NPs from the circulation by capturing them into the liver and spleen. Minimizing NP uptake by RES is critical to ensure effective drug delivery. Various ‘stealth’ coatings, and modifying the shape and size of the particles can mitigate this problem (e.g. ref. [64]), but only delay the inevitable; NPs eventually end up in the RES. However, any delay in the RES uptake of NPs is important because it gives them more time to reach the intended target. The RES remains a major problem in nanomedicine (reviewed in ref. [56,65]) and better solutions for this problem are likely to come from more complete understanding of the RES phagocytosis process at the molecular level.

3.2. Amplified Tumor Homing of Nanoparticles

While both drugs and NPs can be targeted, NP targeting can be enhanced by engineered more complex, cooperative targeting functions into them. We have described NPs that self-amplify their own homing to tumors. Superparamagnetic iron oxide NPs (SPIO) are coated with a pentapeptide (sequence: CREKA) that binds to fibrin-fibronectin complexes deposited in tumor blood vessels (and tumor stroma) as a result of subtle clotting.[38] These deposits are not present in normal vessels, making the homing tumor specific. The initial accumulation of the CREKA-SPIO in tumor vessels causes additional clotting in these vessels, which creates new binding sites for additional NPs, which causes more clotting, and so on. This self-amplifying homing system occludes about 20% of tumor vessels, and the enhancement factor from the amplification is about six-fold.[38] The amplified NP homing greatly enhanced tumor imaging, but the level of vessel occlusion was not sufficient for significant inhibition of tumor growth. Recent improvements to the system have made it possible to occlude 60–70% of tumor vessels, resulting in tumor necrosis and growth inhibition.[66] A clotting activator (tissue factor) that is targeted to tumors with a homing peptide has been introduced into clinical trials.[42] The CREKA system has the advantage that the NPs could be loaded with a drug to further enhance its anti-tumor potency.

Integrating multiple functions into a single NP can reduce the efficacy of the individual functions. For example, we have found that a two-fold reduction of homing peptide density on an NP can drastically reduce the efficacy of tumor homing.[66] Dividing the functions between two NPs that then cooperate in their functions can circumvent these problems. In one study, we coated two different tumor homing peptides with partially non-overlapping selectivity for tumor vessels onto separate SPIO NPs. Surprisingly, when the two NPs were injected together into the circulation of tumor mice, they completely colocalized producing a wider distribution of each NPs than was obtained with either one alone. This phenomenon, which presumably depends on an attractive force between the NPs, allowed us to greatly increase the number of tumor vessels occluded by the CREKA-SPIO.[66] The clotting promoting activity of CREKA-SPIO in tumors requires three elements: (1) The NP has to be slightly thrombogenic, as is the case with SPIO. Micelles coated with CREKA home to tumors, but do not cause additional clotting. (2) The CREKA peptide is necessary; SPIO coated with another tumor-homing peptide also home to tumors, but have no clotting activity in tumor vessels. (3) The pro-coagulant tumor environment is needed. CREKA-SPIO NPs accumulate in the liver RES, but no occlusion of liver vessels has been observed. CREKA-SPIO also bind to the endothelium over atherosclerotic plaques, where subtle clotting produces fibrin-fibronectin complexes, but cause no additional clotting.[39,66] Thus, this approach to occlude tumor vessel occlusion seems to be safe.

In another strategy, photothermal heating mediated by tumor-targeted gold nanorods increased the expression of the receptor for a homing peptide coated onto a second, drug-carrying NP.[67,68] The clotting cascade also lends itself to cooperating NP designs.[69] A combination therapy with NPs that carry different drugs would be another possible application of cooperating NPs. Designing NPs that aggregate under the influence of a feature of the target tissue, such as the expression of an enzyme, is another way of constructing an amplified targeting system, as aggregated NPs are not likely to wash out from a target tissue. Interestingly, one such system utilizes furin cleavage as the triggering mechanism for NP aggregation,[70,71] which may benefit both from the aggregation and a CendR effect.

In some cases, it will be possible to replace nanosystems that use multiple NPs with multi-compartment NPs, which enable co-presentation of dissimilar properties on the same particle. For example, the requirement of high homing peptide concentration on a NP for optimal homing could be satisfied by coating a compartment of a NP with the peptide, leaving the rest of the surface available for other function.[72]

3.3. Nanoparticle Biocompatibility

In vivo use of NPs for medical purposes places strict requirements on biocompatibility and lack of toxicity. Iron oxide NPs are clinically approved for imaging applications and for the treatment of anemia caused by iron deficiency. Organic NPs (Abraxane and Doxil) are being used in cancer therapy. However, many of the inorganic NPs now studied in animals, such as various types of quantum dots and carbon nanotubes are likely to face high regulatory hurdles. Porous silicon NPs exhibit a favorable toxicity profile as they degrade in vivo producing silicic acid, which is a physiological compound eliminated through the urine.[73] The non-toxicity, high capacity for cargo, and quantum dot-like optical properties make porous silicon NPs a promising material for the design of next generation NPs.

3.4. Tissue-Penetrating Nanoparticles

As discussed above, tissue-penetrating peptides can induce exit from the blood vessels in the target tissue and transport through that tissue, particularly when the receptor for the peptide is shared between the vascular and parenchymal cells. The tumor-homing iRGD peptide is an example of a probe that fulfills these criteria. The results with NP targeting have been particularly striking because NPs are much larger than peptides or proteins, and that hinders their diffusion out of the blood vessels.

Coating of Abraxane with the iRGD or LyP-1 peptide resulted in enhanced accumulation and several-fold higher activity than seen with the original drug.[53,2] It was also shown that the iRGD effect on Abraxane, and on doxorubicin liposomes, could be achieved by simple co-administration of the peptide with the NPs, without having to couple the two together.[3]

Recently, we have used iRGD in the co-administration mode to construct a nanoplatform for the delivery of a drug into glioblastomas.[74] The system consists of elongated iron oxide NPs (nanoworms; NWs;[63] which are coated with a bifunctional peptide through a PEG linker. One branch of the peptide, CGKRK is a tumor-specific vascular homing element,[13] and the other branch is $_D$[KLAKLAK]$_2$, a membrane perturbing pro-apoptotic D-amino acid peptide, which serves as a drug. We have previously shown that the $_D$[KLAKLAK]$_2$ peptide can be targeted to tumors and other disease sites by directly conjugating it to a homing peptide.[75,76] The conjugates were effective, but also highly toxic. Unexpectedly, we found that the NP-bound $_D$[KLAKLAK]$_2$ was hundreds of times more potent in killing cells in culture than the soluble form. Standley et al.[77] have also reported high efficacy of multivalent $_D$[KLAKLAK]$_2$. The greatly increased specific activity of the NP-bound pro-apoptotic peptide was important in that it made it possible to reduce the dose of the peptide. The lower dose in turn brought the dose needed into the range that would not be expected to overwhelm the CGKRK receptors. The resulting improvement in targeting reduced the side effects to a moderate increase in enzyme markers of liver damage, which was reversible upon termination of the treatment. Another significant feature of the CGKRK-$_D$[KLAKLAK]$_2$ system that the homing peptide directs the pro-apoptotic $_D$[KLAKLAK]$_2$ peptide to the subcellular organelle this pro-apoptotic peptide acts on, the mitochondria. CGKRK binds to mitochondria, and it apparently also has cell penetrating properties, because the NWs were seen in association with the mitochondria of the target cells.[74]

The CGKRK-$_D$[KLAKLAK]$_2$ nanosystem eradicated the tumors in one glioblastoma model and significantly extended the life span of the mice in another, more aggressive model;[74] (**Figure 2**). When the nanosystem was combined with iRGD injections, there was a further, highly significant extension of survival of the tumor mice with the aggressive tumors. CGKRK is an internalizing peptide, but it lacks tissue-penetrating properties. Accordingly, the NWs, when injected alone, stayed in the blood vessels. However, when co-injected with iRGD they extravasated (**Figure 3**). Thus, the likely reason for the improvement of the therapy results is that by using iRGD, we had made the tumor cells a secondary target in addition to the vasculature. Importantly, these results also suggest that iRGD can help a therapeutic agent penetrate the blood-brain barrier in glioblastomas, albeit that the barrier may be somewhat compromised in the tumors. A somewhat analogous nanosystem consisting of the membrane-disrupting toxin melittin targeted to tumors with perfluorocarbon NPs coated with an RGD-mimic compound has been described.[78] Interestingly, melittin contains a cryptic CendR motif. It would be interesting to know whether activation of the CendR system contributed to the anti-tumor activity of these NPs.

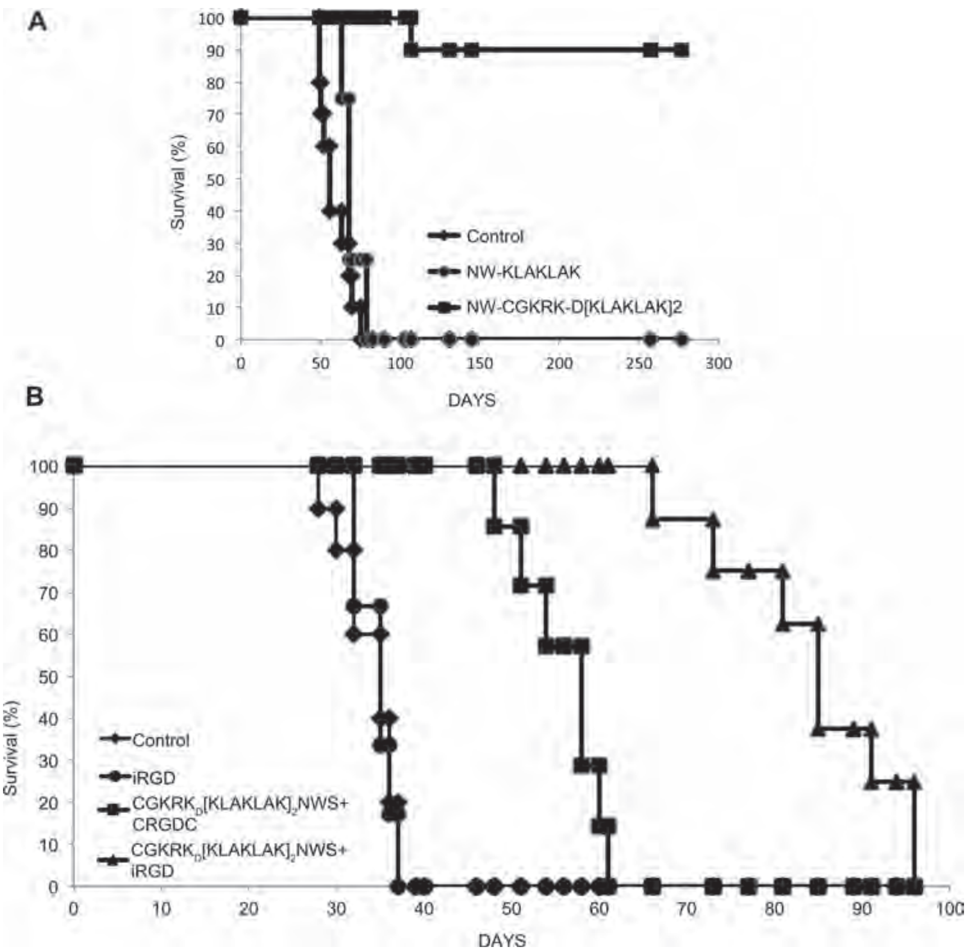

Figure 2. Glioblastoma treatment with CGKRK$_D$[KLAKLAK]$_2$-nanoworms (NWs) in mice. A. Mice bearing lentiviral (H-RasV12-shp53) induced brain tumors[86,87] in the right hippocampus were intravenously injected with iron oxide NWs coated with peptides (5 mg of iron per kg). The particles were administered every other day for 18 days, starting 3 weeks post-viral injection. Survival curves (n = 8–10 mice per group) shows rapid demise of the mice in the control groups and long-term survival of the group treated with CGKRK$_D$[KLAKLAK]$_2$NWs. B. Mice bearing orthotopic 005 tumors implanted 10 days earlier (n = 8–10 mice per group) received every other day for 3 weeks intravenous injections of either CGKRK$_D$[KLAKLAK]$_2$-NWs (5 mg of iron/kg), or CGKRK$_D$[KLAKLAK]$_2$-NWs (5 mg/kg) mixed with 4 mmol/kg of iRGD or PBS. CGKRK$_D$[KLAKLAK]$_2$-NWs have a strong anti-tumor effect, which is further enhanced when the NWs are co-injected with iRGD. In contrast to the CGKRK$_D$[KLAKLAK]$_2$ nanosystem, a number of other treatments, such as various anti-angiogenic agents have shown no activity in these models.[87] Modified with permission.[74] Copyright 2011, The National Academy of Sciences.

3.5. Subcellular Targeting of Nanoparticles

The CGKRK-$_D$[KLAKLAK]$_2$ described above is an example of combined targeting that encompasses systemic delivery of a NP payload to a target tissue (tumor vessels), internalization into cells, and further delivery to a specific subcellular organelle. The entire process was accomplished with one peptide.[74] Similar targeting has been accomplished in cell cultures by coating NPs with cell-penetrating peptides fused with organelle localization signals for the nucleus (e.g. KKKRK[79]) and mitochondria.[80] An important question concerns the delivery of NP payloads into the cytoplasm. Therapies that rely on nucleic acids, such as siRNA, have tremendous potential in making previously "undruggable" molecules accessible as treatment targets. Unfortunately, the application of this technology has been hampered by the unsolved problem of delivering the compounds to the target. The main problem is the instability of these compounds in vivo. A likely solution will come from nanotechnology. NPs can protect the compounds, carry them to the target cells and deliver the intact compound into the cytoplasm. An encouraging advance has been the recent report of successful delivery of siRNA to the tumor of a human patient.[81]

4. Beyond Tumor Penetration

Tissue penetration by peptides has also been observed in tissues other than tumors. LyP-1, which has been shown to be a tumor-penetrating peptide that depends on the CendR mechanism,[46] also homes to atherosclerotic plaques, penetrating into the plaque interior.[55] Iron oxide NPs and protein cage NPs have been show to enter plaques when coated with LyP-1.[55,82] Moreover, peptides in a panel of heart-homing peptides, which were also found to penetrate into extravascular heart tissue, contain CendR sequences,[20] and likely also use the CendR

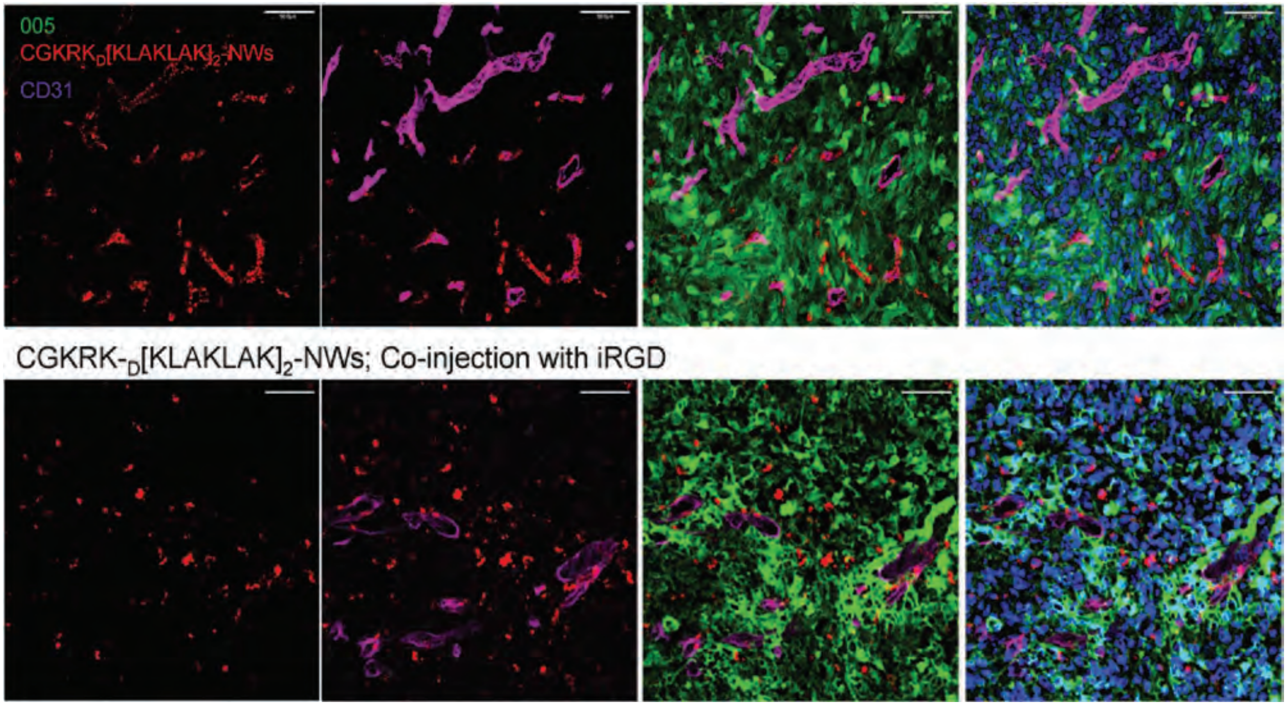

Figure 3. Enhanced penetration of CGKRK$_D$[KLAKLAK]$_2$-NWs co-injected with iRGD into extravascular glioblastoma tissue. Mice bearing orthotopic 005 glioblastomas[87] were intravenously injected with CGKRK$_D$[KLAKLAK]$_2$-NWs (5 mg of iron/kg) in combination with 4 mmol/kg of either non-labeled CRGDC (upper row) or iRGD (lower row) peptide. The tumors and tissues were collected 5–6 hours later, and analyzed by confocal microscopy. CGKRK$_D$[KLAKLAK]$_2$-NWs (red) are found outside the blood vessels (magenta), associated with tumor cells (green) when co-injected with iRGD, but remained associated with blood vessels when co-injected with the conventional RGD peptide, CRGDC, which lacks tumor-penetrating properties. Nuclei were stained with DAPI (blue). Scale bars, 50 mm. Modified with permission.[74] Copyright 2011, The National Academy of Sciences.

pathway. Finally, it is striking that a number of peptides reported to cross the blood-brain barrier also contain cryptic CendR sequences.[83–85] Taken together with the results on glioblastoma discussed above this suggests that CendR sequences activated at the brain endothelium may be able to cross the blood-brain barrier and take a payload, even NPs, with them. **Table 1** lists the many types of NPs and tumor-penetrating peptides that have been used to deliver compounds to various targets.

Table 1. Nanoparticle delivery with tumor-penetrating peptides.

Nanoparticle	Target	Peptide	Reference
Quantum dots	Tumors, lungs	LyP-1, F3[a]	[48]
Micelles	Tumors	LyP-1	[53]
Iron oxide NPs	Tumors, athero-sclerotic plaques	iRGD, LyP-1, F3	[2,3,55,88]
Protein cage NPs	Atherosclerotic plaques	LyP-1	[82]
Albumin-paclitaxel NPs (Abraxane)	Tumors	iRGD	[2,3]
Doxorubicin lipo-somes	Tumors	iRGD, LyP-1	[73,3]
Bismuth sulfide NPs	Tumors	LyP-1	[89]
Hydrogel NPs	Tumors	F3	[90]

[a] F3 contains a CendR motif and internalizes into cells, but the involvement of the CendR pathway in F3 activities has not been formally proven.

5. Conclusion and Future Prospects

Poor tissue penetration of NPs limits the application of NPs to the treatment of disease. The capacity of the receptors at the target tissue poses a further limitation to the number of NPs that can be specifically targeted to a target tissue. The tumor-penetrating peptides we have recently described can solve these problems. These peptides activate a bulk tissue-specific transport pathway in that once activated is not limited by the availability of specific receptors for the targeted NPs. The specificity of the peptide determines the tissue the pathway is activated in, resulting in target specific delivery of compounds that are co-administered with the peptide. A current challenge that is likely to only be resolved by nanomedical approaches is the delivery of nucleic acid-based therapeutics. Substantial progress has already been made in this area, but efficacious subcellular delivery still remains to be resolved. Finally, a major future advance in nanomedicine would be engineering NPs in which binding to a target would elicit an activity, such as release of a drug.

Acknowledgements

I thank Dr. Eva Engvall for comment on the manuscript. Research in the author's laboratory is supported by Innovator Awards W81XWH-08-1-0727, W81XWH-09-0698 from the Department of Defense, and grant CA CA152327 from the National Cancer Institute.

Received: February 1, 2012
Revised: February 29, 2012
Published online: May 2, 2012

---

[1] E. Ruoslahti, *Biochem. Soc. Trans.* **2004**, *32*, 397.
[2] K. N. Sugahara, T. Teesalu, P. P. Karmali, V. R. Kotamraju, L. Agemy, O. M. Girard, D. Hanahan, R. F. Mattrey, E. Ruoslahti, *Cancer Cell* **2009**, *16*, 510.
[3] K. N. Sugahara, T. Teesalu, P. P. Karmali, V. R. Kotamraju, L. Agemy, D. R. Greenwald, E. Ruoslahti, *Science* **2010**, *328*, 1031.
[4] R. Auerbach, W. C. Lu, E. Pardon, F. Gumkowski, G. Kaminska, M. Kaminski, *Cancer Res.* **1987**, *47*, 1492.
[5] R. Pasqualini, E. Ruoslahti, *Nature* **1996**, *380*, 364.
[6] T. Teesalu, K. N. Sugahara, E. Ruoslahti, *Methods Enzymol.* **2012**, *503*, 35.
[7] D. M. Brown, E. Ruoslahti, *Cancer Cell* **2004**, *5*, 365.
[8] B. S. Jacobson, D. B. Stolz, J. E. Schnitzer, *Nat. Med.* **1996**, *2*, 482.
[9] E. B. Carson-Walter, D. N. Watkins, A. Nanda, B. Vogelstein, K. W. Kinzler, B. St Croix, *Cancer Res.* **2001**, *61*, 6649.
[10] B. Borgia, C. Roesli, T. Fugmann, C. Schliemann, M. Cesca, D. Neri, R. Giavazzi, *Cancer Res.* **2010**, *70*, 309.
[11] K. Alitalo, P. Carmeliet, *Cancer Cell* **2002**, *1*, 219.
[12] J. A. Hoffman, E. Giraudo, M. Singh, L. Zhang, M. Inoue, K. Porkka, D. Hanahan, E. Ruoslahti, *Cancer Cell* **2003**, *4*, 383.
[13] J. A. Joyce, P. Laakkonen, M. Bernasconi, G. Bergers, E. Ruoslahti, D. Hanahan, *Cancer Cell* **2003**, *4*, 393.
[14] S. Seaman, J. Stevens, M. Y. Yang, D. Logsdon, C. Graff-Cherry, B. St Croix, *Cancer Cell* **2007**, *11*, 539.
[15] T. A. Jarvinen, E. Ruoslahti, *Am. J. Pathol.* **2007**, *171*, 702.
[16] Y. H. Yang, R. Rajaiah, E. Ruoslahti, K. D. Moudgil, *Proc. Natl. Acad. Sci. USA* **2011**, *108*, 12857.
[17] T. Urakami, T. A. Jarvinen, M. Toba, J. Sawada, N. Ambalavanan, D. Mann, I. McMurtry, M. Oka, E. Ruoslahti, M. Komatsu, *Am. J. Pathol.* **2011**, *178*, 2489.
[18] D. Rajotte, E. Ruoslahti, *J. Biol. Chem.* **1999**, *274*, 11593.
[19] M. G. Kolonin, P. K. Saha, L. Chan, R. Pasqualini, W. Arap, *Nat. Med.* **2004**, *10*, 625.
[20] L. Zhang, J. A. Hoffman, E. Ruoslahti, *Circulation* **2005**, *112*, 1601.
[21] W. Arap, R. Pasqualini, E. Ruoslahti, *Science* **1998**, *279*, 377.
[22] E. Ruoslahti, *Matrix Biol.* **2003**, *22*, 459.
[23] S. M. Weis, D. A. Cheresh, *Nat. Med.* **2011**, *17*, 1359.
[24] R. Pasqualini, E. Koivunen, R. Kain, J. Lahdenranta, M. Sakamoto, A. Stryhn, R. A. Ashmun, L. H. Shapiro, W. Arap, E. Ruoslahti, *Cancer Res.* **2000**, *60*, 722.
[25] A. Corti, F. Curnis, *Curr. Pharm. Biotechnol.* **2011**, *12*, 1128.
[26] K. Porkka, P. Laakkonen, J. A. Hoffman, M. Bernasconi, E. Ruoslahti, *Proc. Natl. Acad. Sci. USA* **2002**, *99*, 7444.
[27] S. Christian, J. Pilch, M. E. Akerman, K. Porkka, P. Laakkonen, E. Ruoslahti, *J. Cell. Biol.* **2003**, *163*, 871.
[28] E. A. Said, B. Krust, S. Nisole, J. Svab, J. P. Briand, A. G. Hovanessian, *J. Biol. Chem.* **2002**, *277*, 37492.
[29] P. Oh, Y. Li, J. Yu, E. Durr, K. M. Krasinska, L. A. Carver, J. E. Testa, J. E. Schnitzer, *Nature* **2004**, *429*, 629.
[30] S. Hatakeyama, K. Sugihara, T. K. Shibata, J. Nakayama, T. O. Akama, N. Tamura, S. M. Wong, A. A. Bobkov, Y. Takano, C. Ohyama, M. Fukuda, M. N. Fukuda, *Proc. Natl. Acad. Sci. USA* **2011**, *108*, 19587.
[31] K. A. Kelly, N. Bardeesy, R. Anbazhagan, S. Gurumurthy, J. Berger, H. Alencar, R. A. Depinho, U. Mahmood, R. Weissleder, *PLoS Med* **2008**, *5*, e85.
[32] P. Laakkonen, K. Porkka, J. A. Hoffman, E. Ruoslahti, *Nat. Med.* **2002**, *8*, 751.
[33] V. Fogal, L. Zhang, S. Krajewski, E. Ruoslahti, *Cancer Res.* **2008**, *68*, 7210.
[34] H. F. Dvorak, D. R. Senger, A. M. Dvorak, V. S. Harvey, J. McDonagh, *Science* **1985**, *227*, 1059.
[35] K. Abe, M. Shoji, J. Chen, A. Bierhaus, I. Danave, C. Micko, K. Casper, D. L. Dillehay, P. P. Nawroth, F. R. Rickles, *Proc. Natl. Acad. Sci. USA* **1999**, *96*, 8663.
[36] J. Pilch, D. M. Brown, M. Komatsu, T. A. Jarvinen, M. Yang, D. Peters, R. M. Hoffman, E. Ruoslahti, *Proc. Natl. Acad. Sci. USA* **2006**, *103*, 2800.
[37] F. Ye, X. Wu, E. K. Jeong, Z. Jia, T. Yang, D. Parker, Z. R. Lu, *Bioconjug. Chem.* **2008**, *19*, 2300.
[38] D. Simberg, T. Duza, J. H. Park, M. Essler, J. Pilch, L. Zhang, A. M. Derfus, M. Yang, R. M. Hoffman, S. Bhatia, M. J. Sailor, E. Ruoslahti, *Proc. Natl. Acad. Sci. USA* **2007**, *104*, 932.
[39] D. Peters, M. Kastantin, V. R. Kotamraju, P. P. Karmali, K. Gujraty, M. Tirrell, E. Ruoslahti, *Proc. Natl. Acad. Sci. USA* **2009**, *106*, 9815.
[40] F. Curnis, A. Gasparri, A. Sacchi, R. Longhi, A. Corti, *Cancer Res.* **2004**, *64*, 565.
[41] V. Gregorc, G. Citterio, G. Vitali, A. Spreafico, P. Scifo, A. Borri, G. Donadoni, G. Rossoni, A. Corti, F. Caligaris-Cappio, A. Del Maschio, A. Esposito, F. De Cobelli, F. Dell'Acqua, A. Troysi, P. Bruzzi, A. Lambiase, C. Bordignon, *Eur J Cancer* **2010**, *46*, 198.
[42] R. Bieker, T. Kessler, C. Schwoppe, T. Padro, T. Persigehl, C. Bremer, J. Dreischaluck, A. Kolkmeyer, W. Heindel, R. M. Mesters, W. E. Berdel, *Blood* **2009**, *113*, 5019.
[43] T. Teesalu, K. N. Sugahara, V. R. Kotamraju, E. Ruoslahti, *Proc. Natl. Acad. Sci. USA* **2009**, *106*, 16157.
[44] K. Hajdin, V. D'Alessandro, F. K. Niggli, B. W. Schafer, M. Bernasconi, *PLoS One* **2010**, *5*, e10445.
[45] A. Bagri, M. Tessier-Lavigne, R. J. Watts, *Clin. Cancer Res..* **2009**, *15*, 1860.
[46] L. Roth, L. Agemy, V. R. Kotamraju, G. Braun, T. Teesalu, K. N. Sugahara, J. Hamzah, E. Ruoslahti, *Oncogene* **2011**.
[47] D. Pramanik, B. K. Majeti, G. Mondal, P. P. Karmali, R. Sistla, O. G. Ramprasad, G. Srinivas, G. Pande, A. Chaudhuri, *J. Med. Chem.* **2008**, *51*, 7298.
[48] M. E. Akerman, W. C. Chan, P. Laakkonen, S. N. Bhatia, E. Ruoslahti, *Proc. Natl. Acad. Sci. USA* **2002**, *99*, 12617.
[49] J. M. Gump, S. F. Dowdy, *Trends Mol. Med.* **2007**, *13*, 443.
[50] T. Jiang, E. S. Olson, Q. T. Nguyen, M. Roy, P. A. Jennings, R. Y. Tsien, *Proc. Natl. Acad. Sci. USA* **2004**, *101*, 17867.
[51] M. Tan, K. H. Lan, J. Yao, C. H. Lu, M. Sun, C. L. Neal, J. Lu, D. Yu, *Cancer Res.* **2006**, *66*, 3764.
[52] H. Myrberg, L. Zhang, M. Mae, U. Langel, *Bioconjug. Chem.* **2008**, *19*, 70.
[53] P. P. Karmali, V. R. Kotamraju, M. Kastantin, M. Black, D. Missirlis, M. Tirrell, E. Ruoslahti, *Nanomedicine* **2009**, *5*, 73.
[54] E. Ruoslahti, *Nat. Rev. Cancer* **2002**, *2*, 83.
[55] J. Hamzah, V. R. Kotamraju, J. W. Seo, L. Agemy, V. Fogal, L. M. Mahakian, D. Peters, L. Roth, M. K. Gagnon, K. W. Ferrara, E. Ruoslahti, *Proc. Natl. Acad. Sci. USA* **2011**, *108*, 7154.
[56] E. Ruoslahti, S. N. Bhatia, M. J. Sailor, *J. Cell Biol.* **2010**, *188*, 759.

[57] J. M. Chan, J. W. Rhee, C. L. Drum, R. T. Bronson, G. Golomb, R. Langer, O. C. Farokhzad, *Proc. Natl. Acad. Sci. USA* **2011**, *108*, 19347.
[58] H. Maeda, J. Wu, T. Sawa, Y. Matsumura, K. Hori, *J. Control Release* **2000**, *65*, 271.
[59] A. K. Iyer, G. Khaled, J. Fang, H. Maeda, *Drug Discov. Today* **2006**, *11*, 812.
[60] R. K. Jain, *Annu. Rev. Biomed. Eng.* **1999**, *1*, 241.
[61] C. H. Heldin, K. Rubin, K. Pietras, A. Ostman, *Nat. Rev. Cancer* **2004**, *4*, 806.
[62] K. P. Olive, M. A. Jacobetz, C. J. Davidson, A. Gopinathan, D. McIntyre, D. Honess, B. Madhu, M. A. Goldgraben, M. E. Caldwell, D. Allard, K. K. Frese, G. Denicola, C. Feig, C. Combs, S. P. Winter, H. Ireland-Zecchini, S. Reichelt, W. J. Howat, A. Chang, M. Dhara, L. Wang, F. Ruckert, R. Grutzmann, C. Pilarsky, K. Izeradjene, S. R. Hingorani, P. Huang, S. E. Davies, W. Plunkett, M. Egorin, R. H. Hruban, N. Whitebread, K. McGovern, J. Adams, C. Iacobuzio-Donahue, J. Griffiths, D. A. Tuveson, *Science* **2009**, *324*, 1457.
[63] J. H. Park, G. von Maltzahn, L. Zhang, A. M. Derfus, D. Simberg, T. J. Harris, E. Ruoslahti, S. N. Bhatia, M. J. Sailor, *Small* **2009**, *5*, 694.
[64] N. Doshi, S. Mitragotri, *PLoS One* **2010**, *5*, e10051.
[65] S. M. Moghimi, A. C. Hunter, J. C. Murray, *Pharmacol. Rev.* **2001**, *53*, 283.
[66] L. Agemy, K. N. Sugahara, V. R. Kotamraju, K. Gujraty, O. M. Girard, Y. Kono, R. F. Mattrey, J. H. Park, M. J. Sailor, A. I. Jimenez, C. Cativiela, D. Zanuy, F. J. Sayago, C. Aleman, R. Nussinov, E. Ruoslahti, *Blood* **2010**, *116*, 2847.
[67] J. H. Park, G. von Maltzahn, M. J. Xu, V. Fogal, V. R. Kotamraju, E. Ruoslahti, S. N. Bhatia, M. J. Sailor, *Proc. Natl. Acad. Sci. USA* **2010**, *107*, 981.
[68] G. von Maltzahn, A. Centrone, J. H. Park, R. Ramanathan, M. J. Sailor, T. A. Hatton, S. N. Bhatia, *Adv. Mater.* **2009**, *21*, 3175.
[69] G. von Maltzahn, J. H. Park, K. Y. Lin, N. Singh, C. Schwoppe, R. Mesters, W. E. Berdel, E. Ruoslahti, M. J. Sailor, S. N. Bhatia, *Nat. Mater.* **2011**, *10*, 545.
[70] G. Liang, H. Ren, J. Rao, *Nat. Chem.* **2010**, *2*, 54.
[71] D. Ye, G. Liang, M. L. Ma, J. Rao, *Angew. Chem. Int. Ed.* **2011**, *50*, 2275.
[72] J. Lahann, *Small* **2011**, *7*, 1149.
[73] J. H. Park, L. Gu, G. von Maltzahn, E. Ruoslahti, S. N. Bhatia, M. J. Sailor, *Nat. Mater.* **2009**, *8*, 331.
[74] L. Agemy, D. Friedmann-Morvinski, V. R. Kotamraju, L. Roth, K. N. Sugahara, O. M. Girard, R. F. Mattrey, I. M. Verma, E. Ruoslahti, *Proc. Natl. Acad. Sci. USA* **2011**, *108*, 17450.
[75] H. M. Ellerby, W. Arap, L. M. Ellerby, R. Kain, R. Andrusiak, G. D. Rio, S. Krajewski, C. R. Lombardo, R. Rao, E. Ruoslahti, D. E. Bredesen, R. Pasqualini, *Nat. Med.* **1999**, *5*, 1032.
[76] W. Arap, W. Haedicke, M. Bernasconi, R. Kain, D. Rajotte, S. Krajewski, H. M. Ellerby, D. E. Bredesen, R. Pasqualini, E. Ruoslahti, *Proc. Natl. Acad. Sci. USA* **2002**, *99*, 1527.
[77] S. M. Standley, D. J. Toft, H. Cheng, S. Soukasene, J. Chen, S. M. Raja, V. Band, H. Band, V. L. Cryns, S. I. Stupp, *Cancer Res.* **2010**, *70*, 3020.
[78] N. R. Soman, S. L. Baldwin, G. Hu, J. N. Marsh, G. M. Lanza, J. E. Heuser, J. M. Arbeit, S. A. Wickline, P. H. Schlesinger, *J Clin Invest* **2009**, *119*, 2830.
[79] B. Kang, M. A. Mackey, M. A. El-Sayed, *J. Am. Chem. Soc.* **2010**, *132*, 1517.
[80] A. M. Derfus, W. Chan, S. N. Bhatia, *Adv. Mater.* **2004**, *16*, 961.
[81] M. E. Davis, J. E. Zuckerman, C. H. Choi, D. Seligson, A. Tolcher, C. A. Alabi, Y. Yen, J. D. Heidel, A. Ribas, *Nature* **2010**, *464*, 1067.
[82] M. Uchida, H. Kosuge, M. Terashima, D. A. Willits, L. O. Liepold, M. J. Young, M. V. McConnell, T. Douglas, *ACS Nano* **2011**, *5*, 2493.
[83] C. Che, G. Yang, C. Thiot, M. C. Lacoste, J. C. Currie, M. Demeule, A. Regina, R. Beliveau, J. P. Castaigne, *J. Med. Chem.* **2010**, *53*, 2814.
[84] P. Kumar, H. Wu, J. L. McBride, K. E. Jung, M. H. Kim, B. L. Davidson, S. K. Lee, P. Shankar, N. Manjunath, *Nature* **2007**, *448*, 39.
[85] C. Rousselle, P. Clair, J. Temsamani, J. M. Scherrmann, *J. Drug Target.* **2002**, *10*, 309.
[86] T. Marumoto, A. Tashiro, D. Friedmann-Morvinski, M. Scadeng, Y. Soda, F. H. Gage, I. M. Verma, *Nat. Med.* **2009**, *15*, 110.
[87] Y. Soda, T. Marumoto, D. Friedmann-Morvinski, M. Soda, F. Liu, H. Michiue, S. Pastorino, M. Yang, R. M. Hoffman, S. Kesari, I. M. Verma, *Proc. Natl. Acad. Sci. USA* **2011**, *108*, 4274.
[88] G. R. Reddy, M. S. Bhojani, P. McConville, J. Moody, B. A. Moffat, D. E. Hall, G. Kim, Y. E. Koo, M. J. Woolliscroft, J. V. Sugai, T. D. Johnson, M. A. Philbert, R. Kopelman, A. Rehemtulla, B. D. Ross, *Clin. Cancer Res..* **2006**, *12*, 6677.
[89] J. M. Kinsella, R. E. Jimenez, P. P. Karmali, A. M. Rush, V. R. Kotamraju, N. C. Gianneschi, E. Ruoslahti, D. Stupack, M. J. Sailor, *Angew. Chem. Int. Ed.* **2011**, *50*, 12308.
[90] I. Winer, S. Wang, Y. E. Lee, W. Fan, Y. Gong, D. Burgos-Ojeda, G. Spahlinger, R. Kopelman, R. J. Buckanovich, *Cancer Res.* **2010**, *70*, 8674.

Science Manuscript Template

Title: Etchable and Bright Silver Nanoparticle Probes for Cell Internalization Assays

Authors: Gary B. Braun[a,b], Tomas Friman[a,b], Hong-Bo Pang[b], Venkata Ramana Kotamraju[a,b], Alessia Pallaoro[c], Norbert O. Reich[c], Tambet Teesalu[a,b,d], Erkki Ruoslahti[a,b]

Affiliations:

a: Sanford-Burnham Medical Research Institute at University of California, Santa Barbara, CA 93106, Center for Nanomedicine, University of California, Santa Barbara, CA 93106
b: Cancer Research Center, Sanford-Burnham Medical Research Institute, La Jolla, CA 92037, USA
c: Department of Chemistry and Biochemistry, University of California, Santa Barbara, CA 93106
d: Laboratory of Cancer Biology, Institute of General and Molecular Pathology, University of Tartu, Estonia

*Correspondence to: ruoslahti@sanfordburnham.org

Abstract: Nanoparticles are often used to deliver drugs and other bioactive compounds to cells *in vitro* and *in vivo*. Fluorescent imaging used to study internalization and subcellular localization of nanoparticles, does not allow unequivocal distinction between cell surface-bound and internalized particles. We have developed a simple technique to rapidly remove silver nanoparticles outside living cells leaving only the internalized pool. Etching is based on the sensitivity of silver to a redox-based destain solution. This strategy, based on dye-labeled silver, can be used to study internalization of nanoparticles by techniques such fluorescence and darkfield microscopy, flow cytometry, and inductively coupled plasma–mass spectrometry (ICP-MS).

One Sentence Summary: We describe a rapid and selective technique to remove bright silver nanoparticles outside living cells leaving only the internalized pool.

Main Text:

Designing nanoparticles for therapeutic, diagnostic and theranostic applications is of pivotal importance in advancing nanomedicine[1, 2]. Nanoparticles (NPs) enter cultured cells at rates determined by their surface coating, size and shape [3-5]. Most of the clinically relevant nanoparticle targets are intracellular and NPs are typically coated with an effector layer to engage cellular receptors and trigger internalization. Cell culture assays are used to gauge the particle internalization by fluorescent, chemical, radioactive, or enzymatic tracers. Distinguishing internalized NPs from cell surface-bound particles typically involves disrupting ligand-protein interactions by exposing cells to low pH or using a competitive ligand, which may have unwanted effects on cells and be challenging for high-avidity nanoparticles. Here we demonstrate a cell-impermeable silver etchant that rapidly dissolves extracellular silver NPs (AgNPs) while leaving internalized AgNPs visible for imaging or quantification.

Silver is increasingly used for biomedical imaging applications because of its unique optical properties including fluorescence and Raman enhancement of near-surface molecules and intense darkfield scattering from the core, each of which arise from size- and shape-dependent plasmonic effects[6-11]. In contrast, gold NPs typically quench fluorescence and are not as well suited for microscopy, and dye-labeled polymer NPs require harsh solvents or etchants to dissolve (e.g. dimethylformamide)[12-14]. Commercial silver etch or 'destain' solutions widely used in photography, and to dissolve silver associated with protein bands in polyacrylamide gels, are well suited for dissolving AgNPs. A typical etchant solution uses the redox agent ferricyanide ($Fe(III)CN_6^{3-}$), which oxidizes Ag^0 to Ag^+, and thiosulfate anion to solubilize the ions[15, 16]. The etchant removes AgNPs in seconds due to their small size (Fig. 1A,B), and the process can be performed in cell culture medium and is well tolerated by mammalian cells (Fig. S1-4)[17]. The Fe(III) complex is reduced to Fe(II), ferrocyanide, but remains ligand-stabilized and thus all reagents are removed upon washing. Notably, gold NPs are resistant to this etchant if hydroxide is absent[18] and ascorbate, known to reduce ferricyanide blocks the etch activity towards Ag (Fig. S5)[17].

C-end rule (CendR) peptides trigger neuropilin-dependent cell and tissue penetration when exposed at the C-terminus of a polypeptide chain[19]. The design of fluorescent dye-labeled AgNPs coated with the prototypic CendR peptide RPARPAR, and their distribution before and after etch in neuropilin-1-expressing PPC-1 prostate cancer cells are shown in Figure 1. Darkfield and fluorescence microscopy (Fig. 1C-D, S1) demonstrate the removal of extracellular particles (those bound to the cell surface and the culture plate surface between cells). Internalized particles protected from etchant by the plasma membrane remain unaltered in intensity. The resonant scattering wavelength in darkfield imaging red-shifts when AgNPs are within one diameter length from each other[8]. This effect is clearly visible in the perinuclear region, presumably due to endosome fusion. Quantification by flow cytometry showed that under these incubation conditions ~60% of the signal from RPARPAR AgNPs could not be etched due to their internalization (Fig. 1D-F). As expected, AgNPs functionalized with RPARPARA (an inactive control peptide with an alanine residue added to the C-terminus of RPARPAR[20, 21]) showed weak surface binding to cells with complete etchability (Fig 1E). Removal of elemental silver from outside the cells was verified using inductively coupled plasma mass spectrometry (Fig. S3). The etch strategy was also used for facile analysis of AgNP coatings. The brightness and photostability of dyes positioned near metal surfaces can increase through a decreased excited state lifetime caused by coupling to surface plasmons, with significant enhancement from AgNPs larger than ~40 nm[8, 9]. The enhancement factor for the dye-labeled coating on the 80 nm AgNPs was 9-fold (Fig. 1F), determined by etching the core at constant volume. Smaller AgNP (~25 nm) showed negligible enhancement with a similar coating [9]. Together, these results illustrate how etchable silver nanoparticle cores with tailored coatings can be a powerful tool in studies of uptake and endosomal trafficking.

References and Notes:

Acknowledgments:

We thank K. N. Sugahara, L. Agemy, R. Chen, and M. Moskovits for helpful discussions, A. Kylander-Clark for assistance and technical support with ICP-MS, J. Wang for flow cytometry assistance, and the NRI-MCDB Microscopy Facility at UCSB. This work was supported by US

DoD awards W81XWH-10-1-0199 and W81XWH-09-0698. G.B.B. was supported by the Cancer Center of Santa Barbara.

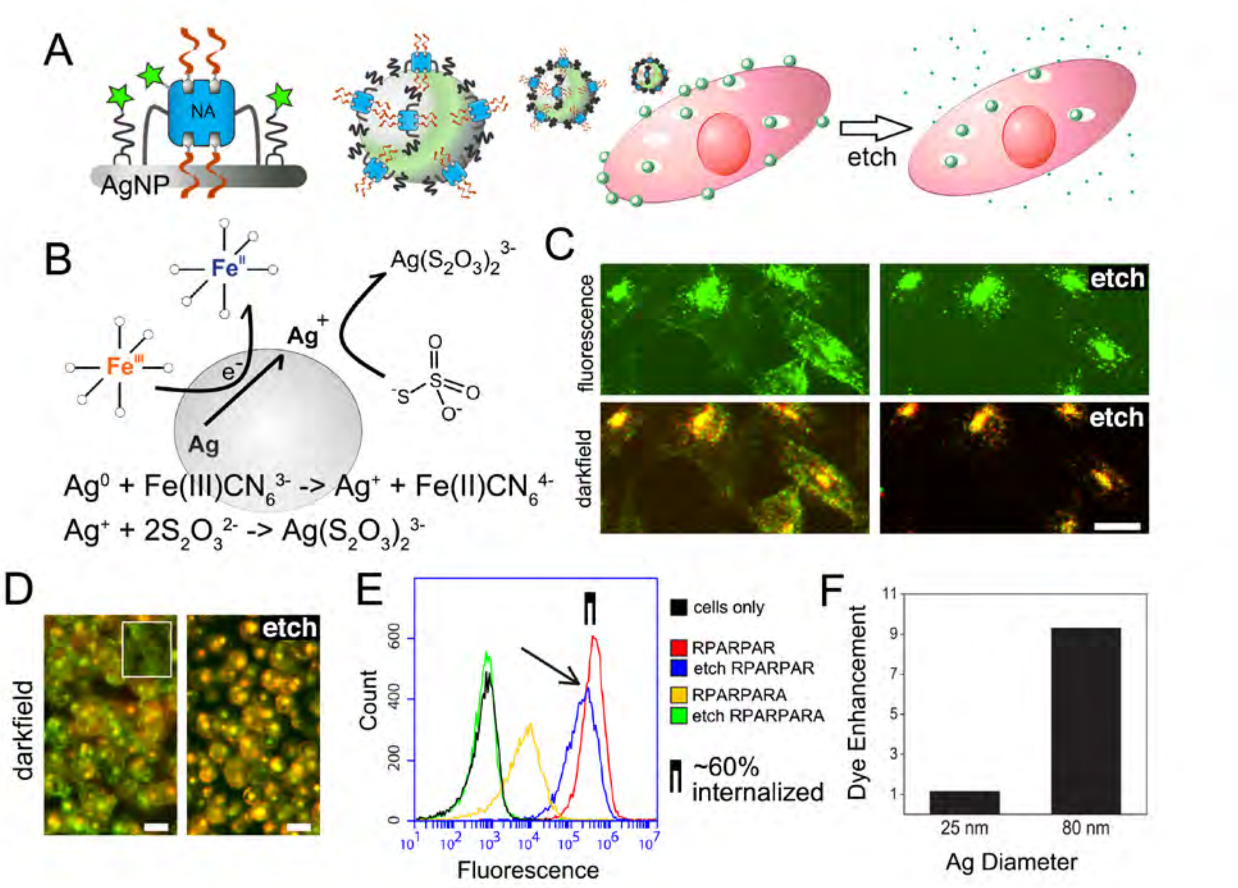

Figure 1. (A) Scheme of silver nanoparticles AgNP with neutravidin (NA) coating, fluorescent dyes (green stars), and internalizing peptide biotin-x-RPARPAR, x is aminohexanoic linker. AgNP-RPARPAR bind to and are taken up by cells, which are treated with brief exposure to etching solution to remove extracellular particles. (B) Etch reagents ferricyanide (10 mM) and thiosulfate (10 mM) oxidize and stabilize silver ions, respectively, releasing components into solution. (C) Fluorescence and darkfield microscopy of cells incubated with dye-labeled AgNP-RPARPAR. Post-etch images show internalized (etch-protected) nanoparticles. Collections of AgNPs in endosomes have the expected red-shifted darkfield scattering. (D) Darkfield images of cell suspensions with AgNP-RPARPAR. Etched cells retain red-shifted signals. Inset shows cells without AgNPs. (E) Flow cytometry fluorescence histograms of cells with AgNP-RPARPAR before (red), and after etching (blue), versus cells without AgNPs (black), and non-internalizing control, biotin-x-RPARPARA AgNPs (yellow, unetched and green, etched). Percent internalization is defined as the ratio of net mean fluorescence signal of etched and unetched populations. (F) AgNP fluorescence enhancement was determined for two Ag diameters by the ratio of solution fluorescence of etched and unetched samples. Strong enhancement is found for the larger Ag.

Supplementary Materials:

Materials and Methods
Figures

Etch solution.

20X Etchant. *Reagent A:* Potassium ferricyanide ($K_3Fe(CN)_6$, Sigma, CAS# 13746-66-2) was dissolved in PBS (Hyclone) at 0.20 M. *Reagent B:* Sodium thiosulfate pentahydrate ($Na_2S_2O_3$: $5H_2O$, Sigma, CAS# 10102-17-7) was also dissolved in PBS at 0.2 M. These were stored at room temperature in 50 mL polypropylene tubes.

Typically the two solutions were combined with PBS or media to form a 2X solution, used within several hours. E.g. 800 μL PBS, 100 μL Reagent A, 100 μL Reagent B. Equal volume was added to the media containing the cells and AgNPs. Etching power was verified using a stock of concentrated silver particles with observation of color change culminating at that given by the ferricyanide solution itself (yellow). See Fig. S5 for typical colors.

Preparation of silver neutravidin nanoparticles.

Neutravidin (NA, Thermo Scientific) for silver nanoparticle coupling was prepared by modification of NA with NHS-PEG5k-OPSS (Jenkem), where OPSS is ortho-pyridyl disulfide. The NA-OPSS was dialyzed against 0.1X PBS ~ pH 6 with 2 mM NaN_3 and assayed for OPSS using reduction by TCEP (tris(2-carboxyethyl)phosphine, 0.5M solution pH 7.0, Sigma). On average 2.2 OPSS were bound per NA, using extinction from pyridyl leaving group of 8.08×10^3 M^{-1} cm^{-1} and 99.6×10^3 M^{-1} cm^{-1} NA (60 kDa).

80 nm silver nanoparticles were prepared using a modification of a method reported by Xia et al. (Sun, Y. G. and Xia, Y. N. J. Am. Chem. Soc. 2004, 126, 3892-3901). First, 0.375 g of $AgNO_3$ and 1.5 g PVP (polyvinylpyrrolidone, M_W = 55000) were dissolved in 150 mL ethylene glycol. This mixture was then heated to 160 ˚C and the reaction proceeded for 1 h. The silver was cooled and precipitated in a large amount of acetone followed by centrifugation at 1000 RCF for 10 min. The precipitates were redispersed in water. Extinction coefficient used was 1.1 x 10^11 M^{-1} cm^{-1}, for 80 nm diameter solid spherical silver nanoparticles.

Neutravidin-OPSS was added to the silver PVP in water (~ pH 6) and incubated overnight, then washed by centrifugation at 3300 RCF, sonicating into PBST, made from PBS (Hyclone) with 0.005% Tween 20 (Sigma). Lipoic PEG amine (3400 g/mol, Nanocs Inc.) was dissolved in 70% ethanol and added to the silver NA at a final concentration of 20 μM and incubated overnight at room temperature and 4 ˚C for 3 days. After centrifuge washing the particles in PBST at 3300 ×g and sonicating, NHS-dyes were added at 50 μM and incubated overnight at 4 ˚C followed by extensive washing. Particles were washed with PBST and biotin peptides were added at 40 μM for >1 h, then washed with PBST. Dye used for Fig. 1C was CF488A-NHS (Biotium, Cat# 92120), Fig 1D-F Alexa Fluor 647-NHS (Invitrogen, Cat# A20106), and in 1S was CF555-NHS (Biotium, Cat# 92130). Biotin peptides were biotin-x-RPARPAR-OH and biotin-x-RPARPARA-OH (the C-terminal alanine abolishes neuropilin-1 binding), synthesized in house as described previously (19), where x indicates aminohexanoic linker.

25 nm AgNP were synthesized similarly as above but using 10 kDa PVP instead of 55 kDa as given for the 20 nm AgNP procedure (9). 20 g PVP 10kDa (Sigma) was first dissolved in 150 mL ethylene glycol at room temperature, and to this solution the 400 mg AgNO3 was added with continuous stirring. The suspension was then stirred at room temperature until complete dissolution of the AgNO3 was achieved. Then, the system was heated up to 120 ˚C using an oil bath, and the reaction was allowed to proceed for 1 h at this temperature. At the end of the reaction period the colloidal dispersion was cooled until the system reached room temperature. Acetone precipitation was performed as for the larger AgNPs.

Darkfield and epifluorescence microscopy.

For Fig. 1C, PPC-1 cells were plated in 96-well plates, incubated overnight in DMEM with 10% FBS and penicillin/streptomycin. Silver NA with peptide were added and incubated at 37 ˚C for 1 h, washed, and imaged before and after etching. For darkfield imaging in Fig. 1C a Leica DM-IRE2 inverted microscope, 20X objective, with darkfield condenser S2 was used. Inserting the DAPI filter set passes blue scattering components ~450 nm to the CCD detector, while the rhodamine filter passes ~570 nm scattered light. Capturing each separately and overlaying identifies monomer silver particles in blue and aggregates in both blue and red. For fluorescence the lamp was used with fluorescein filter set inserted. For visual clarity the darkfield blue channel was pseudocolored green in Figure 1C, such that red-shifted scattering appears yellow in the overlay.

Flow cytometry.

PPC-1 cells were released using enzyme-free dissociation buffer, washed with Hanks buffered saline solution (HBSS, Hyclone) and resuspended in DMEM with 10 μM t-RNA to limit non-specific binding, and aliquoted into tubes. Silver NA, with either biotin-X-RPARPAR or biotin-X-RPARPARA, was added and the tubes were rotated for 1 h. For etched samples an equal volume of 2X etchant in PBS was added followed by centrifuging and resuspension in media. Analysis was performed on an Accuri C6 Flow Cytometer with blue and red (640 nm) laser, where the red was used to detect Alexa Fluor 647 dye on the silver coating, channel FL-4, and the blue was used for forward and side scatter (FSC, SSC).

Fluorescence enhancement test.

Fig. 1F experimental info. AgNP-NA was reacted with Biotium 555-NHS dye as described above, and washed extensively by centrifugation in PBST. 100 μL was aliquoted into wells in a 96 well plate. To control wells, 100 μL PBS was added. Etched samples received 100 μL of 2X etch in PBS. In separate experiments the dye was found to not be affected by the etch solution. Small AgNP had minimal difference between etched and unetched wells, supporting the robustness of the dye and the use of this simple method to compare coatings during synthesis.

Supplemental Figures, methods and legends.

Figure S1. Live imaging of NP internalization using CF488A-dye.

PPC-1 cells were grown on collagen I (BD) coated coverslips (eight chambers, Bioexpress) for two days. The cells were then incubated with cell mask orange (Invitrogen) for 5 min in cell culture media, to visualize the membrane as well as endosomes formed after staining. The cells were washed three times in HBSS and ~10 pM 80 nm CF488 AgNPs was added in cell culture media and incubated for 45 min. Unbound particles were washed off with HBSS. An equal volume of etching solution was then injected into the culture chamber while on the microscope stage (Fluoview 500, Olympus). Time-lapse series of images were collected and movies were produced with Fluoview software (Olympus). Frames were cropped and presented here before and after etch. Cell mask stain in red traces the plasma membrane and endosomal structures, and green for the AgNPs, overlaid. Yellow indicates colocalization.

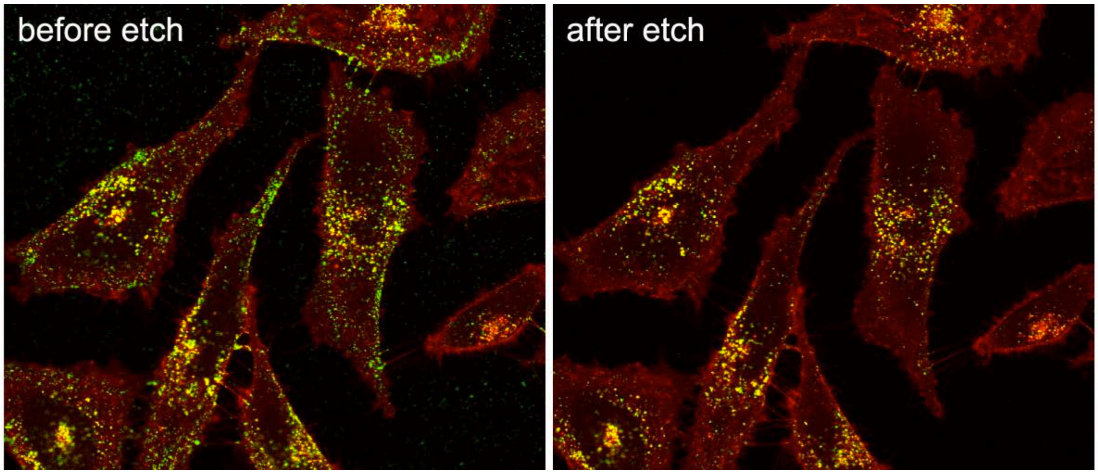

Figure S2. Inductively coupled plasma mass spectrometry (ICP-MS).
Samples were analyzed using a Nu Attom high-resolution ICP-MS in static peak-jumping mode. Cells were incubated with high dose silver NA RPARPAR in 6 well plates, washed with HBSS to saturate uptake and verify removal of silver. Wells were lysed then etch was added to give ‘total’ silver. ‘Internalized’ samples were etched and washed prior to cell lysis, then etched again to recover internalized silver. ICP-MS signals from ‘internalized’ divided by ‘total’ was used to quantify cell uptake. Notably, with this assay format any particles that non-specifically bind the plate will decrease uptake value.

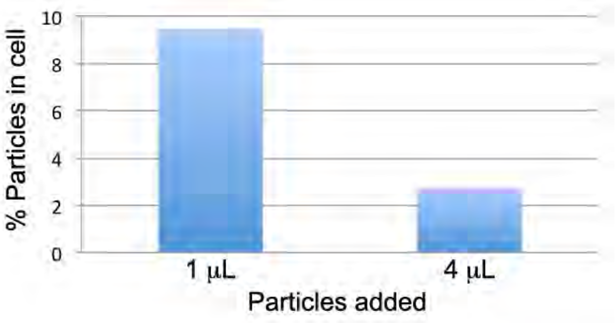

Figure S3. Plate Optimization of Etch Components.
Concentration of the two reagents was optimized in a plate format. Complete etching of a high concentration of silver nanoparticles was judged by visual inspection of the color and reduced scattering, and darkfield microscopy. Ag particles with PVP coating (80 nm diam, 200 optical density at 450 nm) were diluted by 10 in PBS with 0.005% Tween-20 (Sigma). 100 μL was added per well. A variable amount of sodium thiosulfate solution (100 mM in water) and potassium ferricyanide (30mM, or (*)100mM for rows G and H, in water). Boxed wells show the clarified solution at minimum of 8 mM ferricyanide and 8 mM thiosulfate. The lack of particles was verified by depositing solution onto a glass slide for darkfield analysis. A fraction of particles were observed to survive the well for 6.5 mM ferricyanide and 4 mM thiosulfate. Working concentration of 10 mM of each component was chosen for each component.

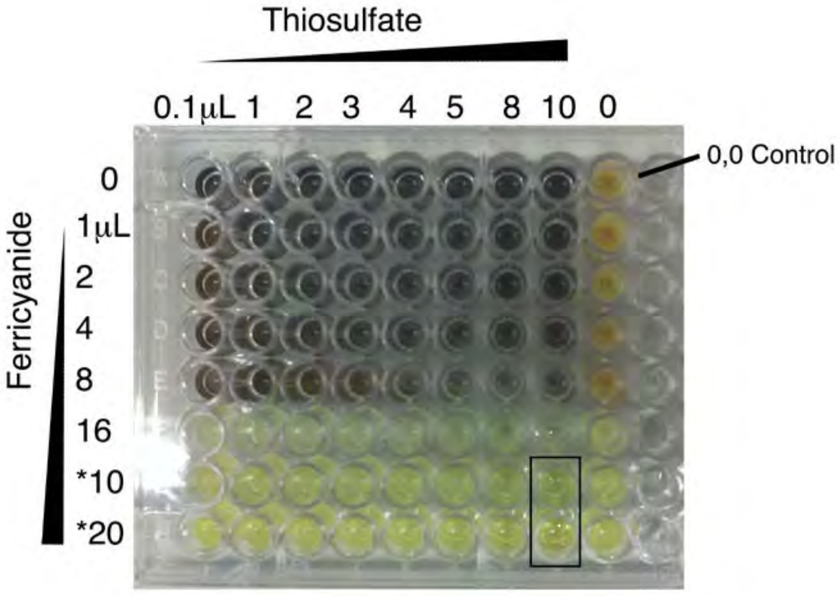

Figure S4. Cell viability after etching. (A) PPC-1 cells were exposed to AgNP with NA and biot-x-RPARPAR-OH for one hour. The etch solution was added, incubated for 1 h, followed by washing and replacing with new media. After overnight culture at 37°C the cell morphology by brightfield analysis was compared to (B) control cells having nothing added.

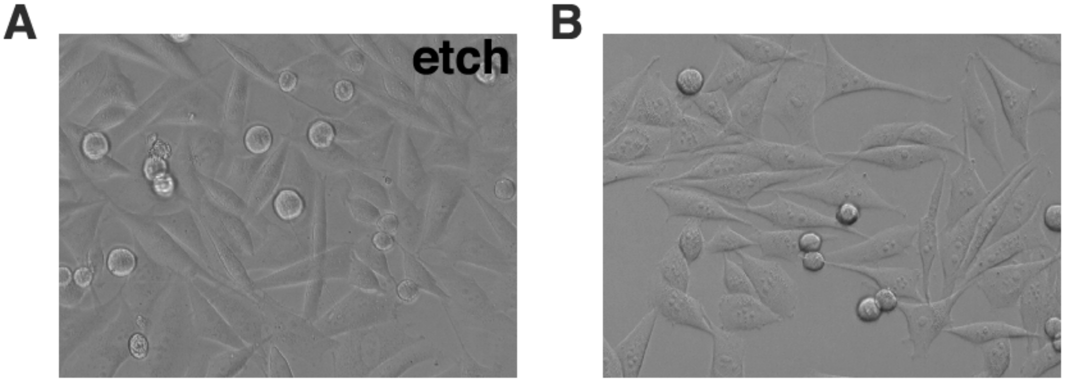

Figure S5. Ascorbate effect on etching. Sodium ascorbate, known for its ability to reduce the ferricyanide, was found to block the etching of AgNPs. The yellow ferricyanide/thiosulfate solution turns clear upon adding ascorbate at a 2:1 molar ratio over the ferricyanide. AgNPs survive the ascorbate blocked etch. This supports the importance of the redox state of ferricyanide, and indicates the use of ascorbate as a quenching agent.

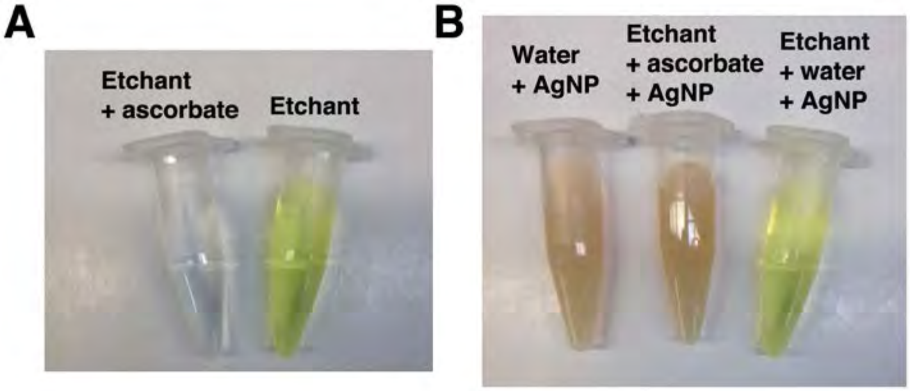

Figure S6. Additional flow cytometry. Dot plots of fluorescence versus forward scatter (FSC) and side scatter (SSC) show all events collected for the data set in Fig. 1D. (A) FSC detects cells but not AgNPs and is used for gating. Cells were identified for Fig. 1D by the FSC window indicated by the blue bar. The color code is the same as for Fig. 1D, where red is AgNP-RPARPAR and blue is with etch. Black is for control cells without AgNP. (B) SSC shows some sensitivity to AgNP, likely due to the overlap of plasmon resonance with the laser (450 nm resonance, 488 nm laser). Fluorescence is found to be linearly proportional to SSC (red streak), for AgNP which are free or bound to debris, or in cells (which have a characteristic SSC given in black). Etch sample in blue shows loss of events below the cell-minimum SCC, consistent with these being cell associated, and a slight loss of the upper-rightmost population, attributed to the loss of membrane bound AgNP.

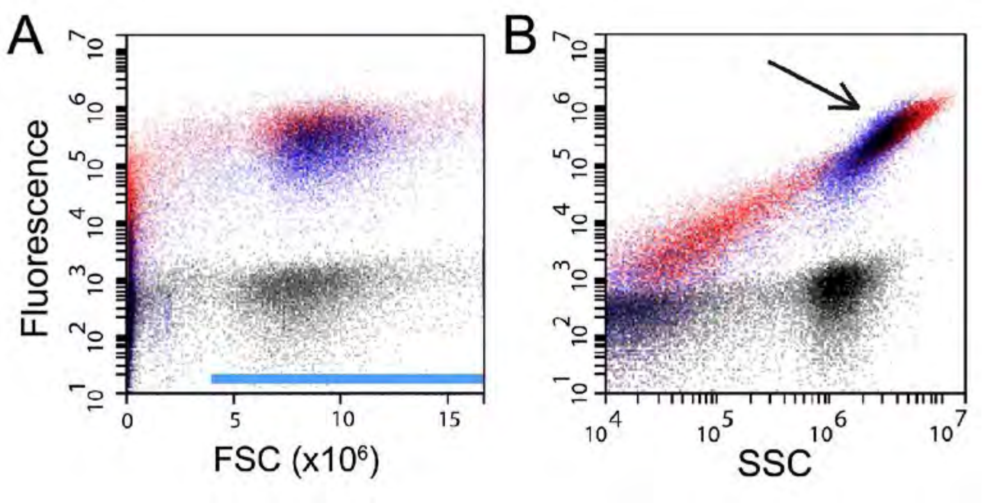

1. Tassa, C., S.Y. Shaw, and R. Weissleder, *Dextran-coated iron oxide nanoparticles: a versatile platform for targeted molecular imaging, molecular diagnostics, and therapy.* Acc Chem Res, 2011. 44(10): p. 842-52.

2. Ruoslahti, E., *Peptides as Targeting Elements and Tissue Penetration Devices for Nanoparticles.* Adv Mater, 2012.

3. Jiang, W., et al., *Nanoparticle-mediated cellular response is size-dependent.* Nat Nanotechnol, 2008. 3(3): p. 145-150.

4. Chithrani, B.D. and W.C. Chan, *Elucidating the mechanism of cellular uptake and removal of protein-coated gold nanoparticles of different sizes and shapes.* Nano Lett, 2007. 7(6): p. 1542-50.

5. Chithrani, B.D., A.A. Ghazani, and W.C.W. Chan, *Determining the size and shape dependence of gold nanoparticle uptake into mammalian cells.* Nano Lett, 2006. 6(4): p. 662-668.

6. Sun, Y. and Y. Xia, *Gold and silver nanoparticles: a class of chromophores with colors tunable in the range from 400 to 750 nm.* Analyst, 2003. 128(6): p. 686-91.

7. Wiley, B., Y. Sun, and Y. Xia, *Synthesis of silver nanostructures with controlled shapes and properties.* Acc Chem Res, 2007. 40(10): p. 1067-76.

8. Lakowicz, J.R., *Radiative decay engineering 5: metal-enhanced fluorescence and plasmon emission.* Anal Biochem, 2005. 337(2): p. 171-94.

9. Zhang, F., et al., *Fabrication of Ag@SiO(2)@Y(2)O(3):Er nanostructures for bioimaging: tuning of the upconversion fluorescence with silver nanoparticles.* J Am Chem Soc, 2010. 132(9): p. 2850-1.

10. Mulvihill, M.J., et al., *Anisotropic etching of silver nanoparticles for plasmonic structures capable of single-particle SERS.* J Am Chem Soc, 2010. 132(1): p. 268-74.

11. Braun, G.B., et al., *Generalized Approach to SERS-Active Nanomaterials via Controlled Nanoparticle Linking, Polymer Encapsulation, and Small-Molecule Infusion.* Journal of Physical Chemistry C, 2009. 113(31): p. 13622-13629.

12. Kim, J.H., et al., *Specific and sensitive detection of nucleic acids and RNases using gold nanoparticle-RNA-fluorescent dye conjugates.* Chem Commun (Camb), 2007(42): p. 4342-4.

13. Goulet, P.J., G.R. Bourret, and R.B. Lennox, *Facile phase transfer of large, water-soluble metal nanoparticles to nonpolar solvents.* Langmuir, 2012. 28(5): p. 2909-13.

14. Cho, E.C., et al., *Understanding the role of surface charges in cellular adsorption versus internalization by selectively removing gold nanoparticles on the cell surface with a I2/KI etchant.* Nano Lett, 2009. 9(3): p. 1080-4.

15. Meywald, T., H. Scherthan, and W. Nagl, *Increased specificity of colloidal silver staining by means of chemical attenuation.* Hereditas, 1996. 124(1): p. 63-70.

16. Scheler, C., et al., *Peptide mass fingerprint sequence coverage from differently stained proteins on two-dimensional electrophoresis patterns by matrix assisted laser desorption/ionization-mass spectrometry (MALDI-MS).* Electrophoresis, 1998. 19(6): p. 918-27.

17. Van Duijn, M.M., *Ascorbate Stimulates Ferricyanide Reduction in HL-60 Cells through a Mechanism Distinct from the NADH-dependent Plasma Membrane Reductase.* Journal of Biological Chemistry, 1998. 273(22): p. 13415-13420.

18. Burdinski, D. and M.H. Blees, *Thiosulfate- and thiosulfonate-based etchants for the patterning of gold using microcontact printing.* Chemistry of Materials, 2007. 19(16): p. 3933-3944.

19. Teesalu, T., et al., *C-end rule peptides mediate neuropilin-1-dependent cell, vascular, and tissue penetration.* Proc Natl Acad Sci U S A, 2009. 106(38): p. 16157-62.

20. Sugahara, K.N., et al., *Tissue-penetrating delivery of compounds and nanoparticles into tumors.* Cancer Cell, 2009. 16(6): p. 510-20.

21. Teesalu, T., K.N. Sugahara, and E. Ruoslahti, *Mapping of vascular ZIP codes by phage display.* Methods Enzymol, 2012. 503: p. 35-56.

Application of a Proapoptotic Peptide for an Intratumoral-Spreading Cancer Therapy

Renwei Chen, Gary B Braun, Xiuquan Luo, Kazuki N. Sugahara, Tambet Teesalu, Erkki Ruoslahti

Center for Nanomedicine, Sanford-Burnham Medical Research Institute at University of California, Santa Barbara, CA 93106 and Cancer Research Center, Sanford-Burnham Medical Research Institute, La Jolla, CA 92037, USA

Correspondence to: Erkki Ruoslahti, M.D., Ph.D. Tel: 1(805)893-5327, Fax: 1(805)893-5805, E-mail: ruoslahti@sanfordburnham.org

Running title: Intratumorally spreading tumor therapy

Key words: Bit1 cell death domain, protein transduction, cell internalization, tissue penetration, tumor therapy

The abbreviations used are: Bit1, Bcl-2 inhibitor of transcription; CDD, cell death domain; Pth2, peptidyl-tRNA hydrolase 2; AES, amino enhancer of split; TLE, transducing-like enhancer of split; CendR, C-end Rule; NRP-1, neuropilin-1; SPDP, N-succinimidyl 3-(2-pyridyldithio)-propionate.

Footnotes: Xiuquan Luo, present address: University of Texas Southwestern Medical Center, Simmons Comprehensive Cancer Center, xiuquan.luo@utsouthwestern.edu

Word count: 4995

Total number of Figures: 6

Grant support: This work was supported by grants W81XWH-10-1-0199 and W81XWH-08-1-0727 from the DOD (E.R.) and Cancer Center Support Grant CA30199 from the NCI.

Competing Interest: KNS, TT and ER are shareholders of CendR Therapeutics Inc, that has rights to some of the technology described in this paper. RC, GB, and XL declare no conflict of interest.

Abstract

Bit1 is a pro-apoptotic mitochondrial protein associated with anoikis. Upon cell detachment, Bit1 is released into the cytoplasm and triggers caspase-independent cell death. Bit1 consists of 179 amino acids; the C-terminal two thirds of the molecule functions as a peptidyl-tRNA hydrolase, while the N-terminus contains a mitochondrial localization signal. Here, we localize the cell death domain (CDD) to the N-terminal 62 amino acids of Bit1 by transfecting cells with truncated Bit1 cDNA constructs. CDD was more potent in killing cells than the full-length Bit1 protein when equivalent amounts of cDNA were transfected. To develop Bit1 CDD into a cancer therapeutic we engineered a recombinant protein consisting of the CDD fused to iRGD, which is a tumor-specific peptide with unique tumor-penetrating and cell-internalizing properties. iRGD-CDD internalized into cultured tumor cells through a neuropilin-1-activated pathway and triggered cell death. Importantly, iRGD-CDD spread extensively within the tumor when injected intratumorally into orthotopically implanted breast tumors in mice. Repeated treatment with iRGD-CDD strongly inhibited tumor growth, resulting in an average reduction of 77% in tumor volume and eradication of some tumors. The caspase independence of Bit1-induced cell death makes CDD a potentially attractive anti-cancer agent because tumor resistance to the main mechanisms of apoptosis is circumvented. Using iRGD to facilitate the spreading of a therapeutic agent throughout the tumor mass may be a useful adjunct to local therapy of tumors that are surgically inoperable or difficult to treat systemically.

Introduction

Cell-matrix interactions are important for cell survival, and failure of cells to adhere to the extracellular matrix results in anoikis (1). Bit1 is a mitochondrial peptidyl-tRNA hydrolase that causes cell death when released into the cytoplasm or experimentally expressed there (2). Bit1 release occurs upon loss of cell attachment, resulting in cell death (2). Bit1 negatively regulates Erk activation, revealing a possible molecular pathway for the anoikis regulation (3, 4). Cytosolic Bit1 interacts with the Groucho family transcriptional co-regulator Amino-terminal Enhancer of Split (AES) to induce caspase-independent cell death (2). These activities and the ability of Bit1 to counteract transducin-like enhancer of split 1 (TLE1), which is an anti-apoptotic oncoprotein, suggest a tumor suppressor role for Bit1 (2, 5, 6). A unique property of Bit1 is that cell attachment through certain integrins can prevent cell death induced by cytoplasmic Bit1, whereas various anti-apoptotic signaling molecules, such as Bcl-2, Bcl-xL, PI-3K, and Akt, can prevent the release of Bit1 from mitochondria, but are unable to rescue the cell death caused by cytoplasmic Bit1 (2).

Bit1 is a 179-amino acid protein in which amino acids 63-179 at the C-terminus of the molecule constitute the catalytic, peptidyl-tRNA hydrolase 2 (Pth2) domain and the N-terminus serves as a mitochondrial localization signal (2, 7). It is also known that the N-terminal domain is needed for the apoptotic activity (2, 7), but the active site has not been mapped in detail and the mechanism whereby Bit1 causes cell death is not fully understood. We undertook this study to define the cell death domain (CDD) of Bit1, delineate its mechanism of action, and explore its use as an anti-tumor drug. To deliver Bit1 CDD protein into tumor cells and deal with the problem of poor penetration of anticancer drugs in solid tumors (8, 9), we employed so-called C-end Rule or CendR peptides. These peptides contain a CendR motif (R/KXXR/K), which binds to neuropilin-1 (NRP-1) triggering a cell internalization and tissue penetration pathway (10, 11). The CendR motif has to be at the C-terminus of the peptide to be active. The iRGD peptide contains a cryptic CendR motif (sequence: CRGDKGPDC; CendR motif underlined). This peptide activates the CendR pathway specifically in tumors because it first binds to αvβ3 and αvβ5 integrins, which are expressed in tumor vessels and various types of other cells within tumors, but not in normal tissues. Having bound to the integrins in a tumor, iRGD is proteolytically cleaved to generate a fragment with a C-terminal CendR motif that binds to NRP-1 and activates the CendR pathway (10).

Materials and Methods

Reagents, cell lines, and tumors

Mouse anti-human NRP-1 monoclonal antibody was purchased from Miltenyi Biotec Inc; rabbit anti-Ki67 polyclonal antibody was from Abcam; mouse anti-β-actin monoclonal antibody was from Sigma-Aldrich; The secondary antibodies used were Alexa Fluor® 488-conjugated goat IgG (Invitrogen Life Technologies) Full-length cDNA for Bit1 in the mammalian expression vector pCMV-myc were generated previously in the lab (2). QuikChange Mutagenesis Kit for Bit1 mutagenesis was purchased from Agilent Technologies. In situ cell death detection kit for terminal deoxynucleotidyl transferase–mediated deoxyuridine triphosphate nick end labeling (TUNEL) and FuGENE®6 Transfection Reagent for overexpression was purchased from Roche Applied Science. MTT for cell viability assay was from Invitrogen Life Technologies.

Human cell lines from Embryonic Kidney (HEK) 293T, PPC1 prostate cancer, M21 melanoma, and MCF-10CA1a breast cancer were maintained in Dulbecco's modified Eagle's medium with glutamine containing 10% FBS, penicillin and streptomycin at 37°C and 5% CO_2. Mouse breast cancer cell line 4T1 was maintained in Iscove's modified Dulbecco's medium with glutamine containing 10% FBS, penicillin and streptomycin.

To produce orthotopic tumors, one million of tumor cells in 100 µl of PBS were injected into the mammary fat pad of mice. Athymic nude mice (Harlan Laboratories) were used for MCF-10CA1a cells and normal Balb/C mice (Charles River) for 4T1 cells. All animal procedures were performed in compliance with the guidelines approved by the Animal Research Committee at the University of California, Santa Barbara.

Construction and production of recombinant CDD proteins

Recombinant CDD proteins were prepared as follows: The CDD sequence was cloned into the bacterial expression vector pRSET containing a hexahistidine tag (Invitrogen Life Technologies). Because CDD harbors a mitochondrial signal peptide, a myc-tag was placed at the N-terminus of CDD to prevent the fusion protein from localizing to mitochondria. To generate cell and tissue-penetrating CDD proteins, oligonucleotides encoding the CendR peptides, RPARPAR (11) or iRGD (sequence: CRGDKGPDC) (10) were synthesized and ligated to the downstream of oligonucleotides encoding the CDD, with a glycine-serine linker placed in between (Supplementary Fig. S1A). All construct sequences were confirmed by DNA sequencing. Proteins were expressed in *E. coli* BL21 (DE3) plysS strain (Novagen) after induction at 30°C for 24 h using MagicMedia™ E. coli Expression Medium (Invitrogen Life Technologies) according to the manufacturer's instructions. The recombinant proteins were purified using Ni-NTA affinity chromatography under native conditions by using ÄKTA™ FPLC system. The bound proteins were eluted with 20 mM sodium phosphate buffer containing 300 mM imidazole, pH 8.0. The eluates were dialyzed against PBS pH 7.4 containing an additional 360 mM NaCl. In some experiments, the his-tag was removed using enterokinase (Invitrogen Life Technologies) according to the manufacturer's instructions. Bit1 CDD proteins migrated as major bands at 13 kDa (CDD) and 16 kDa (RPARPAR-CDD and iRGD-CDD) in Coomassie Blue-stained 4-20 % SDS-PAGE. The protein identities were confirmed by immunoblotting using antibodies against his-tag or myc-tag (Supplementary Fig. S1B). Labeled recombinant proteins were prepared by conjugating with a Dylight 550 NHS ester dye (Dy550) (Pierce Biotechnology) at amine groups. The labeled protein was dialyzed and filtered (0.22 µm). Absorbance measurement was used to determine the dye concentration and degree of labeling, which was somewhat less than an average of one dye group per protein molecule.

Cell internalization of the recombinant proteins

Sub-confluent tumor cells on chamber slides (Nalge Nunc International) were incubated with 3 µM Dy550-labeled protein between 30 min and 24 h. The cells were then washed 3 times with PBS and fixed with ice-cold methanol for 10 min. The specimens were mounted with DAPI-containing Vectashield® media (Vector Laboratories) and analyzed under a confocal microscope, Olympus Fluoview 500.

Peptide-conjugated dextran was used to inhibit peptide-CDD protein for cell internalization. A thiol-reactive dextran conjugate was prepared by modifying amino-dextran 10 kDa (5.1 amines per strand, Invitrogen Life Technologies) with N-succinimidyl 3-(2-pyridyldithio)-propionate (SPDP), and dialyzed using Slide-A-Lyzer Dialysis Cassettes 3,500 MWCO (Pierce Biotechnology). To the SPDP-dextran, an excess Cys-peptide was added, followed by extensive dialysis. Each dextran molecule contained, on average, 5 copies of peptide. Inhibition assays were carried out by incubating 3 µM dextran conjugated peptide and 3 µM Dy550-labeled CDD protein with PPC1 cells for 1 h at 37°C. The cells were then washed, fixed, and analyzed by confocal microscopy as described above.

Tumor tissue penetration ex vivo and in vivo

Protein penetration in tumors was studied *ex vivo* using fresh explants of MCF-10CA1a tumors. Excised tumors were cut into pieces and incubated at 37°C with 20 µM Dy550-labeled proteins in DMEM containing 1% BSA. Binding and entry of proteins to the cut surface were examined by confocal microscopy (Olympus Fluoview 500). *In vivo* protein penetration was analyzed using orthotopic MCF-10CA1a tumor xenografts in mice. Dy550-labeled protein (20 µl of 35 µM solution; approximately 10 µg protein per tumor) was injected into the center of tumor (60-80mm^3) with spheroic shape using 31-gauge needle, and 4 hours later, entire tumors were dissected and fixed in 4% PFA. Five-µm serial sections from entire tumors were stained with DAPI and scanned using ScanScope FL 6114 (Aperio Technologies, Inc).

Tumor treatment

Tumor-bearing mice were assigned to three treatment groups approximately 4 weeks after the inoculation of MCF-10CA1a cells and 9 days after the inoculation of 4T1 cells. The assignment was based on tumor size to ensure there was no statistically significant difference in tumor volume among the groups at the time the treatment began. Tumor volume was calculated from two diameter measurements using a digital vernier caliper and the formula: tumor volume = (length × width^2) / 2. Proteins were diluted in PBS at 0.3 µg/µl and injected intratumorally. The injected volume was one third of the tumor volume (0.33 µl of solution per mm^3 of the tumor) (12). The tip of the needle was advanced to the center of the tumor and the protein solution was injected over the course of 30 seconds. The injections were given every 3 days (a total of 4 injections in the MCF-10CA1a and 3 in the 4T1 model).

Statistical analysis

Data were analyzed by Student t-test, one-way ANOVA, and two-way ANOVA followed by a suitable post hoc test using GraphPad Prism 5 software (Graphy Pad Software, San Diego, CA).

Results

Localization of Bit 1 cell death domain

Forced expression in the cytoplasm of full-length Bit1 has been shown to induce caspase-independent cell death, whereas the C-terminal catalytic domain lacks this activity (2). Hence we focused our analysis on the N-terminal domain. To identify the cell death domain, we expressed a panel of N-terminally myc-tagged Bit1 fragments in HEK 293T cells because the N-terminal tag prevents mitochondrial localization of

Bit1 (2). Transient transfection of full-length Bit1 and the N-terminal 1-62 amino acids (F1-62) caused significant cell death, whereas various shorter fragments from the N-terminal domain showed lesser or no activity (Fig. 1; Supplementary Fig. S2A). The catalytic Pth2 domain did not induce cell death, but instead caused a modest increase in cell viability, providing a possible explanation for the higher activity of F1-62 than full-length Bit1 (Fig. 1). The vector control had no effect on cell viability. Based on these results, we defined the F1-62 fragment as a Bit1 cell death domain (CDD).

The Bit1 CDD includes a conserved transmembrane segment at residues 14-33 (PSTLGLAVGVACGMCLGWSL) in the human Bit1 sequence (Supplementary Fig. S2B). Deleting these residues (Δ14-33) resulted in cytosolic and nuclear expression, whereas the first 13 residues were not required for the mitochondrial localization (Supplementary Fig. S2C). These findings are consistent with the enzymatic Pth2 domain exposed to the cytoplasm (Supplementary Fig. S2D and S2E).

Internalization of CendR-modified Bit1 CDD protein into cells

To deliver Bit1 CDD into cells and potentially into their cytoplasm, we fused CDD to a tumor-penetrating peptide iRGD. For comparison, we also used RPARPAR, a peptide in which the CendR motif is constitutively active. Bit1 CDD with no CendR peptide showed negligible binding to PPC1 cells, a cell line that expresses high levels of NRP-1 (Fig. 2A, panel a). In contrast, both RPARPAR-CDD and iRGD-CDD effectively bound to and were taken up into these cells (Fig. 2A, panels b and c). CDD and RPARPAR-CDD did not bind to or internalize into the NRP-1-deficient melanoma cell line M21 (11) (Fig 2A, panels d and e). iRGD-CDD bound to the surface of the M21 cells but was only weakly internalized (Fig. 2A, panel e), consistent with M21 cells expressing high levels of the relevant integrins (13). Cell entry of RPARPAR-CDD was rapid; after 30-min incubation, the protein was detectable in PPC1 cells, colocalizing with NRP-1 (Fig. 2B). The amount of internalized RPARPAR-CDD peaked around 3 h and much of the protein was found in perinuclear vesicles. Consistent with the 3-step cell entry process, internalization of iRGD-CDD was slower than that of RPARPAR-CDD (Fig. 2C). Twenty-four hours after these proteins were introduced into the cultures, the cells rounded up, shrank, and partially detached, indicating cell death (Fig. 2B and 2C). Dextran-conjugated RPARPAR and iRGD inhibited the internalization of RPARPAR-CDD and iRGD-CDD protein, respectively, whereas dextran alone or dextran conjugated with iRGE (CRGEKGPDC), which does not bind to integrins showed no inhibition of the iRGD-CDD interaction with cells (Fig. 2D). These controls clearly establish the specificity of the CendR peptide-modified CDDs.

Reduction of cell viability by CendR-modified CDD proteins

Treatment of cultured breast cancer cells MCF-10CA1a and 4T1 with iRGD-CDD or RPARPAR-CDD significantly reduced cell viability, whereas non-modified CDD protein had a modest effect at the highest concentrations or no effect at all (Fig. 3A). RPARPAR-CDD was no more cytotoxic to NRP-1-deficient M21 cells than unmodified CDD protein at the highest concentration used (3 µM), indicating that the marginal toxicity at this concentration was not related to the CendR targeting. iRGD-CDD decreased M21 cell viability more than the other two CDD proteins, possibly because of integrin-mediated internalization, but the difference to RPARPAR-CDD and CDD was not statistically significant (Fig. 3A).

Histidine has been shown to enhance endosomal escape, explained in part by a cationic transition at low pH (14-17). Enterokinase cleaves fusion proteins containing the $(Asp)_4$-Lys recognition sequence (18), which is positioned in our construct between the his-tag and the CDD domain. The his-tag in iRGD-CDD was cleaved and removed using enterokinase and Ni-NTA affinity chromatography purification. The removal of the his-tag in the resulting iRGD-CDD was confirmed by SDS-PAGE (Fig. 3B). Cytotoxicity tests in MCF-10CA1a cells showed that the his-tag effect on construct toxicity was not significant (Fig. 3C). Thus, the his-tag plays only a minor role, if any, in the endosomal escape of the iRGD-CDD protein.

Penetration of iRGD-CDD into tumor tissue

The iRGD peptide extravasates and penetrates into extravascular tumor tissue when intravenously injected into tumor-bearing mice (10). We analyzed the penetration ability of the CDD proteins by using fresh MCF-10CA1a tumor explants. CDD showed modest binding to the cut surface of tumor tissue. iRGD-CDD, however, bound strongly and even penetrated several cell layers into the tumor tissue (Fig. 4A).

The tumor penetration activity was also apparent when fluorescently labeled iRGD-CDD was intratumorally injected into MCF-10CA1a tumors in mice. The strong iRGD-CDD signal was detectable in all sections from an entire tumor (Fig. 4B). It exhibited a web-like pattern resembling fibrotic stromal morphology (Fig. 4B, panel 5 inset *a*). Fibrosis is one of the major barriers that prevent drug distribution within tumor tissue. The ability of iRGD to penetrate fibrotic areas in tumors should help overcome this issue and improve local chemotherapy. The wide positive areas along the tumor periphery were presumably caused by outside-in penetration of iRGD-

CDD that overflowed during the injection and the signals were not detectable outside of tumor rim (Fig. 4B, panel 5 inset *b*). Sporadic localized iRGD-CDD signals were detectable throughout the tumor suggesting protein penetration by active transport (Fig. 4B, panel 7 inset). When CDD was injected, significant intratumoral signals were only present near the injection site (Fig. 4C, panels 3 and 4). The CDD protein that overflowed during the injection remained outside the tumor rim (Fig. 4C, panels 1 through 6, and inset), and showed minimal penetration into the tumor tissue (Fig. 4C). The total signal of the CDD protein was lower than that of the iRGD-CDD, possibly because there is no ligand for CDD protein on tumor cells, allowing the protein to be exported from the tumor. These data support the notion that iRGD mediates active tumor penetration of the CDD protein utilizing the NRP-1-dependent CendR pathway.

Inhibitory effect of iRGD-CDD on tumor growth in mice

Two aggressive breast tumor models MCFA-10CA1a and 4T1 were used for evaluation of antitumor effect by the iRGD-CDD protein. Etoposide, a topoisomerase inhibitor that induces caspase-dependent apoptosis in cancer cells (19), was capable of activating caspase 3 in 4T1 cells, but failed in MCF-10CA1a cells, suggesting an impaired caspase cascade signaling in the MCF-10CA1a cells (Supplementary Fig. S3). This lack of correlation between CDD activity and caspase independence agrees with the previously documented caspase independence of cell death induced by the full length of Bit1 protein.

We next sought to determine whether tumor-targeted Bit1 CDD could be used as a therapeutic agent. We initially administered iRGD-CDD or CDD intravenously at 10 mg per kilogram of mouse body weight every other day. The initial results suggested an anti-tumor effect by iRGD-CDD that was not seen with CDD, but symptom of the severe toxicity required euthanasia intervention (Fig. S4). Thus, we turned our attention to local treatment. The MCF-10CA1a tumors grew rapidly in mice treated with intratumoral injections of the PBS or CDD. In the iRGD-CDD treated mice, inhibition of tumor growth was evident as early as 3 days after the treatment began. At the end of treatment on day 12, the tumor volume was reduced by about 77% compared to the PBS and CDD controls (Fig. 5A). Tumor weights at the end of the experiments were in agreement with the size measurements; the mean weight of the tumors in the iRGD-CDD group was 30% of that in the control groups (Fig. 5B). Notably, 2 out of 8 mice (25%) in the iRGD-CDD treated group had too small tumors to be excised after 12 days of treatment. The small nodules at the tumor inoculation site in these two mice disappeared during the following several weeks without any further treatment. No skin abnormalities were observed around the injection sites, suggesting the tumor specific penetration of iRGD-CDD (Fig. 5C). The mice were healthy and had no signs of tumor metastasis during 6 months of observation.

The treatment results in the 4T1 tumor model were also positive, but reflected the greater aggressiveness of these tumors than the MCF-10CA1a tumors. Tumor volume in iRGD-CDD group was about 40% and tumor weight about 50% smaller than in the PBS and CDD control groups (Fig. 5D and 5E).

Hematoxylin and eosin (H&E) stained tumor sections did not show differences among tumors treated with iRGD-CDD, CDD, or PBS (Fig. 6A). Tumors from the iRGD-CDD groups, however, showed significantly stronger TUNEL staining than tumors treated with PBS or CDD, indicating substantial cell death in the iRGD-CDD-treated tumors (Fig. 6B). In agreement with the TUNEL result, staining for the Ki-67 marker of cell proliferation was significantly lower in the iRGD-CDD-treated tumors than in the PBS or CDD controls (Fig. 6C).

Discussion

In this work, we define the Bit1 cell death domain, localize it to the presumed membrane-embedded domain of the protein and show that CDD is more potent than full length Bit1 in causing cell death when tested by cDNA transfection. We also show that the CDD protein is highly active when introduced into tumor cells using protein transduction mediated by the tumor-penetrating and cell-internalizing peptide iRGD, and that the fusion protein is a promising anti-tumor agent capable of spreading within tumor tissue from an intratumoral injection.

Our results place the CDD of Bit1 in the N-terminal domain, which contains the 20-amino acid hydrophobic sequence thought to anchor Bit1 to the mitochondrial outer membrane. Targeting of polypeptides encoded in the nucleus to mitochondria requires the presence of a signal sequence for mitochondrial localization. Most of these sequences contain positively charged amphipathic alpha helical stretch at the N-terminus, followed by a stretch of hydrophobic residues (20). The Bit1 N-terminus fulfills these criteria (Supplementary Fig. S2A). The mitochondrial signal sequences can direct a protein through both of the mitochondrial membranes to the interior of mitochondria, to the space between the outer and inner membranes, or anchor a protein to the outer membrane (21-23). Our results show that Bit1 is available for protease digestion at the surface of intact mitochondria (Supplementary Fig. S2D). Thus, Bit1 membrane-embedded domain likely attaches the protein to the outer mitochondrial membrane without mediating transfer through the membrane.

Recent results provide clues to the mechanisms underlying Bit1 and Bit1 CDD-mediated cell death. Bit 1, when translocated to the cytoplasm from the mitochondria, interacts with the Groucho/TLE family member AES, suggesting that Bit1 may regulate the activities of the anti-apoptotic and oncogenic TLE proteins (2, 6, 24). Other results show that disrupting Bit1 expression with shRNA confers weakly malignant MCF7 cells enhanced anoikis resistance and increased migratory potential. These changes correlated with an increase in active extracellular kinase regulated (Erk) levels and a decrease in Erk-directed phosphatase activity (25), providing another possible mechanism for the reduced viability of cells with increased Bit1 activity.

We demonstrated the CDD activity and specificity using two methods, cDNA transfection and protein transduction. As CDD is thought to act in the cytoplasm and the effects of the protein transduction and cDNA transfection were similar, we infer that the CendR peptides delivered CDD into the cytoplasm. This is the first demonstration that peptides using the CendR pathway can be active in protein transduction.

Traditional cell-penetrating peptides have been used to deliver recombinant proteins to mammalian cells (26, 27), but these peptides are non-selective; they promote entry into all cells. The prototype of these peptides, Tat, resembles our peptides in that it contains several CendR (R/KXXR/K) motifs (11). However, Tat is active whether fused to the N- or C-terminus of a protein, whereas the activity of CendR peptides is position-dependent in that the CendR motif must be exposed at the C-terminus to be active (11). Hence, activation of peptides with cryptic CendR motifs in a target tissue can be used in tissue-specific delivery of payloads. Indeed, our tumor-homing CendR peptides, such as iRGD and LyP-1 are specific for tumors, whereas the Tat-type peptides are not specific of any cell type or tissue (10, 28). Thus, the tumor-specific CendR peptides offer new opportunities for cell type-specific and tissue-specific protein transduction.

The iRGD peptide selectively activates the CendR trans-tissue transport pathway in tumor, taking payloads as large as nanoparticles with it (10, 29-31). Here we show that these peptides can provide a protein with an anti-cancer activity and the ability to penetrate into tumor tissue from a local site without affecting the surrounding normal tissue.

We made use of the tumor penetration activity of iRGD-CDD in a new anti-cancer treatment. Treating-tumor bearing mice with iRGD-CDD effectively inhibited tumor growth *in vivo*, causing nearly 80% reduction in tumor volume of the MCF-10CA1a tumors and 40% reduction in 4T1 tumors. Importantly, 25% of the MCF-10CA1a tumors were eradicated by the iRGD-CDD treatment. Targeting caspase-independency for tumor therapeutics is a promising strategy to eliminate cancer cells because tumor cells often develop resistance to anti-tumor agents by developing defects in caspase activation. Activating a caspase-independent cell death pathway with Bit1 CDD may be an effective way of attacking tumor cells resistant to apoptosis. Caspase activation is blocked in the MCF-10CA1a cells, whereas this pathway is intact in the 4T1 cells. The greater inhibitory effect of Bit1 CDD in the MCF-10CA1a tumor than in the 4T1 tumor suggests an inverse correlation between the activity of the caspase-dependent cell death pathways (32).

Intratumoral treatment may be particularly useful for tumors that are difficult to remove surgically or treated systemically. Advanced tumors in vital organs can be unresectable, and some tumors are protected from systemic chemotherapy by the blood-brain barrier and fibrotic stroma. Indeed, adjuvant local chemotherapy has been applied to malignant glioma and tested in advanced tumors localizing in the lungs, pancreas, and esophagus (33-37). However, poor drug spreading within the tumor tissue has been a limiting factor for successful local tumor therapies (35, 38, 39). iRGD-CDD, the novel tumor-penetrating cell death protein, may significantly advance local tumor therapies and offer new treatment options to cancer patients with locally advanced tumors.

Acknowledgements

We thank Dr. Eva Engvall for comments on the manuscript, Christopher Brunquell for scientific discussions, and Paul Kirsch for editorial assistance. This work was supported by grants W81XWH-10-1-0199 and W81XWH-08-1-0727 from the DOD (E.R.) and Cancer Center Support Grant CA30199 from the NCI.

References

1. Frisch SM, Vuori K, Ruoslahti E, Chan-Hui PY. Control of adhesion-dependent cell survival by focal adhesion kinase. J Cell Biol. 1996;134:793-9.
2. Jan Y, Matter M, Pai JT, Chen YL, Pilch J, Komatsu M, et al. A mitochondrial protein, Bit1, mediates apoptosis regulated by integrins and Groucho/TLE corepressors. Cell. 2004;116:751-62.
3. Biliran H, Jan Y, Chen R, Pasquale EB, Ruoslahti E. Protein kinase D is a positive regulator of Bit1 apoptotic function. J Biol Chem. 2008;283:28029-37.
4. Kairouz-Wahbe R, Biliran H, Luo X, Khor I, Wankell M, Besch-Williford C, et al. Anoikis effector Bit1 negatively regulates Erk activity. Proc Natl Acad Sci U S A. 2008;105:1528-32.

5. Matsuyama A, Hisaoka M, Iwasaki M, Iwashita M, Hisanaga S, Hashimoto H. TLE1 expression in malignant mesothelioma. Virchows Arch. 2010.

6. Sonderegger CK, Vogt PK. Binding of the corepressor TLE1 to Qin enhances Qin-mediated transformation of chicken embryo fibroblasts. Oncogene. 2003;22:1749-57.

7. De Pereda JM, Waas WF, Jan Y, Ruoslahti E, Schimmel P, Pascual J. Crystal structure of a human peptidyl-tRNA hydrolase reveals a new fold and suggests basis for a bifunctional activity. J Biol Chem. 2004;279:8111-5.

8. Hambley TW, Hait WN. Is anticancer drug development heading in the right direction? Cancer Res. 2009;69:1259-62.

9. Minchinton AI, Tannock IF. Drug penetration in solid tumours. Nat Rev Cancer. 2006;6:583-92.

10. Sugahara KN, Teesalu T, Karmali PP, Kotamraju VR, Agemy L, Girard OM, et al. Tissue-penetrating delivery of compounds and nanoparticles into tumors. Cancer Cell. 2009;16:510-20.

11. Teesalu T, Sugahara KN, Kotamraju VR, Ruoslahti E. C-end rule peptides mediate neuropilin-1-dependent cell, vascular, and tissue penetration. Proc Natl Acad Sci U S A. 2009;106:16157-62.

12. Giustini AJ, Ivkov R, Hoopes PJ. Magnetic nanoparticle biodistribution following intratumoral administration. Nanotechnology. 2011;22:345101.

13. Cheresh DA, Spiro RC. Biosynthetic and functional properties of an Arg-Gly-Asp-directed receptor involved in human melanoma cell attachment to vitronectin, fibrinogen, and von Willebrand factor. J Biol Chem. 1987;262:17703-11.

14. Chang KL, Higuchi Y, Kawakami S, Yamashita F, Hashida M. Efficient gene transfection by histidine-modified chitosan through enhancement of endosomal escape. Bioconjug Chem. 2010;21:1087-95.

15. Hatefi A, Megeed Z, Ghandehari H. Recombinant polymer-protein fusion: a promising approach towards efficient and targeted gene delivery. J Gene Med. 2006;8:468-76.

16. Lo SL, Wang S. An endosomolytic Tat peptide produced by incorporation of histidine and cysteine residues as a nonviral vector for DNA transfection. Biomaterials. 2008;29:2408-14.

17. Stevenson M, Ramos-Perez V, Singh S, Soliman M, Preece JA, Briggs SS, et al. Delivery of siRNA mediated by histidine-containing reducible polycations. J Control Release. 2008;130:46-56.

18. Collins-Racie LA, McColgan JM, Grant KL, DiBlasio-Smith EA, McCoy JM, LaVallie ER. Production of recombinant bovine enterokinase catalytic subunit in Escherichia coli using the novel secretory fusion partner DsbA. Biotechnology (N Y). 1995;13:982-7.

19. Kaufmann SH. Induction of endonucleolytic DNA cleavage in human acute myelogenous leukemia cells by etoposide, camptothecin, and other cytotoxic anticancer drugs: a cautionary note. Cancer Res. 1989;49:5870-8.

20. Schmidt O, Pfanner N, Meisinger C. Mitochondrial protein import: from proteomics to functional mechanisms. Nat Rev Mol Cell Biol. 2010;11:655-67.

21. Rapaport D. Finding the right organelle. Targeting signals in mitochondrial outer-membrane proteins. EMBO Rep. 2003;4:948-52.

22. van der Laan M, Hutu DP, Rehling P. On the mechanism of preprotein import by the mitochondrial presequence translocase. Biochim Biophys Acta. 2010;1803:732-9.

23. Waizenegger T, Stan T, Neupert W, Rapaport D. Signal-anchor domains of proteins of the outer membrane of mitochondria: structural and functional characteristics. J Biol Chem. 2003;278:42064-71.

24. Zhang X, Chen HM, Jaramillo E, Wang L, D'Mello SR. Histone deacetylase-related protein inhibits AES-mediated neuronal cell death by direct interaction. J Neurosci Res. 2008;86:2423-31.

25. Karmali PP, Brunquell C, Tram H, Ireland SK, Ruoslahti E, Biliran H. Metastasis of tumor cells is enhanced by downregulation of Bit1. PLoS One. 2011;6:e23840.

26. Wadia JS, Dowdy SF. Modulation of cellular function by TAT mediated transduction of full length proteins. Curr Protein Pept Sci. 2003;4:97-104.

27. Zhou H, Wu S, Joo JY, Zhu S, Han DW, Lin T, et al. Generation of induced pluripotent stem cells using recombinant proteins. Cell Stem Cell. 2009;4:381-4.

28. Roth L, Agemy L, Kotamraju VR, Braun G, Teesalu T, Sugahara KN, et al. Transtumoral targeting enabled by a novel neuropilin-binding peptide. Oncogene. 2011.

29. Ruoslahti E. Peptides as Targeting Elements and Tissue Penetration Devices for Nanoparticles. Adv Mater. 2012.

30. Ruoslahti E, Bhatia SN, Sailor MJ. Targeting of drugs and nanoparticles to tumors. J Cell Biol. 2010;188:759-68.

31. Sugahara KN, Teesalu T, Karmali PP, Kotamraju VR, Agemy L, Greenwald DR, et al. Coadministration of a tumor-penetrating peptide enhances the efficacy of cancer drugs. Science. 2010;328:1031-5.

to the manufacturer's instruction. The vector without Bit1 fragment served as a control. The percentage of cell viability was determined 24 h post-transfection by MTT assay and normalized to vector control. Error bars denote mean ± SEM of 3 separate experiments performed in triplicate of each Bit1 fragment indicated. One-way ANOVA and student t-test were used for statistical analysis. The comparison shown is to the vector control, or between Bit1 and F1-62. **, $p < 0.01$; ***, $p < 0.001$, ns, not significant.

Figure 2. Internalization of CDD fusion proteins into cells. A, human prostate tumor cells PPC1 and human melanoma cells M21 were incubated with 3 μM fusion proteins that had been labeled with the red fluorophor Dy550. The cells were washed 3 times with PBS and fixed with cold methanol for 10 min. Cell nuclei were stained with DAPI (blue). The proteins were visualized by confocal microscopy (red). B and C, comparison of the localization of RPARPAR-CDD (B), and iRGD-CDD (C) with NRP-1 in PPC1 cells at various points of time. After incubation with the Dy550-labeled proteins, the cells were immunostained with an anti-NRP-1 antibody (green). Arrows indicate co-localization of the red CDD proteins and green NRP-1. The arrowheads point at cells with dying cell morphology at the 24-hour time point. D, specific inhibition of peptide-CDD fusion protein uptake into PPC1 cells by dextran (Dex) conjugated peptides. The fusion proteins were incubated with the cells for 1 h at 37°C in the presence of the cognate peptide inhibitors and controls. Unmodified dextran (Dex; upper left panel) and dextran coated with iRGE (Dex-iRGE; lower left panel) served as controls. Arrows point at bound and internalized RPARPAR-CDD or iRGD-CDD (red). Scale bar: 20 μm for all images.

Figure 3. Cytotoxicity of CDD proteins in tumor cell lines. A, breast tumor cell lines from human MCF-10CA1a, mouse 4T1, and human melanoma M21 cells were incubated for 48 h with the recombinant CDD proteins at various concentrations and cell viability was measured by MTT assay. B, iRGD-CDD proteins with or without hexahistidine tag were separated on a gradient SDS-PAGE gel and visualized using Coomassie Blue staining. C, MCF-10CA1a cells were incubated for 48 h with the iRGD-CDD protein with or without a his-tag. Error bars denote mean ± SEM of 3 separate experiments performed in quadruplicate at each concentration of the proteins. Two-way ANOVA was applied for statistical analysis. **, $p < 0.01$; ***, $p < 0.001$; ns, not significant.

Figure 4. Tumor penetration of iRGD-CDD protein. A, penetration into tumor explants. Confocal microscopic view of MCF-10CA1a tumor explants incubated with Dy550-labeled proteins (red). Cell nuclei were stained with DAPI (blue). Scale bar, 100 µm. B and C, penetration through tumor tissue *in vivo.* Scanscopic images of serial sections from MCF-10CA1a tumors injected intratumorally with iRGD-CDD (B) or CDD (C) for 4 hours before harvesting of the tumor. The space between adjacent sections is 400 µm. Thus, the thickness from section 1 through 8 is approximately 3 mm. Tumor rims are surrounded by dotted lines. B, iRGD-CDD is abundant within the tumor, particularly in areas that appear rich in fibrotic stromal tissue (panel 5 insets *a* and *b*), as well as localized signal in parenchymal area (panel 7 inset). No signal was seen outside of tumor rim (panel 5 inset *b*). Arrowhead points to injection site; arrows point to the areas that presumably caused by outside-in penetration of overflowed iRGD-CDD during the injection. C, the only significant signal of CDD within the tumor tissue is around the injection site (panels 3 and 4, arrowheads).

Primarily CDD is located in the tumor rim (panels 3 through 8). Scale bar in panels 1-8, 2 mm and in the insets, 50 μm.

Figure 5. iRGD-CDD inhibits tumor growth in mice. Mice bearing orthotopic MCF-10CA1a (A and B) (n = 8 mice per treatment group) or 4T1 tumors (D and E) (n = 12 per group) were treated by intratumoral injections of PBS, CDD, or iRGD-CDD every 3rd day. The mean tumor volume ± SEM and mean tumor weight ± SEM were plotted. Two-way ANOVA was used for the analysis of tumor volume and one-way ANOVA for the tumor weight. * $p \leq 0.05$, ** $p \leq 0.01$, *** $p \leq 0.001$, ns, not significant. C, eradication of tumor by intratumoral injection of iRGD-CDD. MCF-10CA1a tumor xenograft at 63 mm^3 was injected locally with iRGD-CDD every 3 days for 4 times. By the end of the treatment on day 12 tumor volume reduced to 3 mm^3. The nodule disappeared in the following several weeks with no more treatment. Skin appeared normal around injection site during and after the treatment.

Figure 6. Analysis for cell death and anti-proliferative effect of iRGD-CDD in tumors. A, H&E staining of tumor sections from mice treated with intratumoral injections of PBS, CDD, or iRGD-CDD. B, cell death was analyzed by terminal deoxynucleotidyl transferase–mediated deoxyuridine triphosphate nick end labeling (TUNEL) staining (green). Nuclei were stained with DAPI (blue). TUNEL positivity was quantified by normalizing TUNEL signal to DAPI (right panel). C, cell proliferation was analyzed by immunostaining of tumor sections using a rabbit anti-Ki-67 polyclonal antibody, followed by Alex Flour®-488 conjugated anti-rabbit IgG (green). Nuclei were stained with DAPI (blue). Ki-67 expression was quantified by

normalizing the Ki-67 signal to DAPI signal (right panel). Error bars denote mean ± SEM. * $p \leq 0.05$; ** $p \leq 0.01$; ns, not significant. Scale bar, 100 μm for all images.

Chen et al, Figure 1

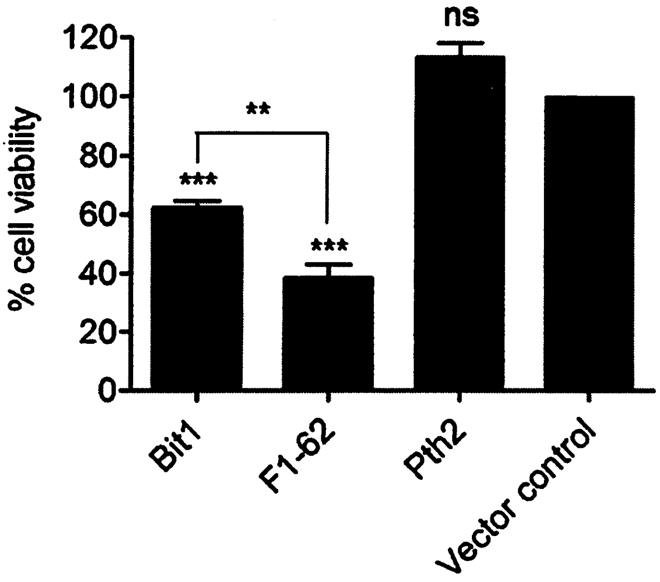

Chen et al, Figure 2

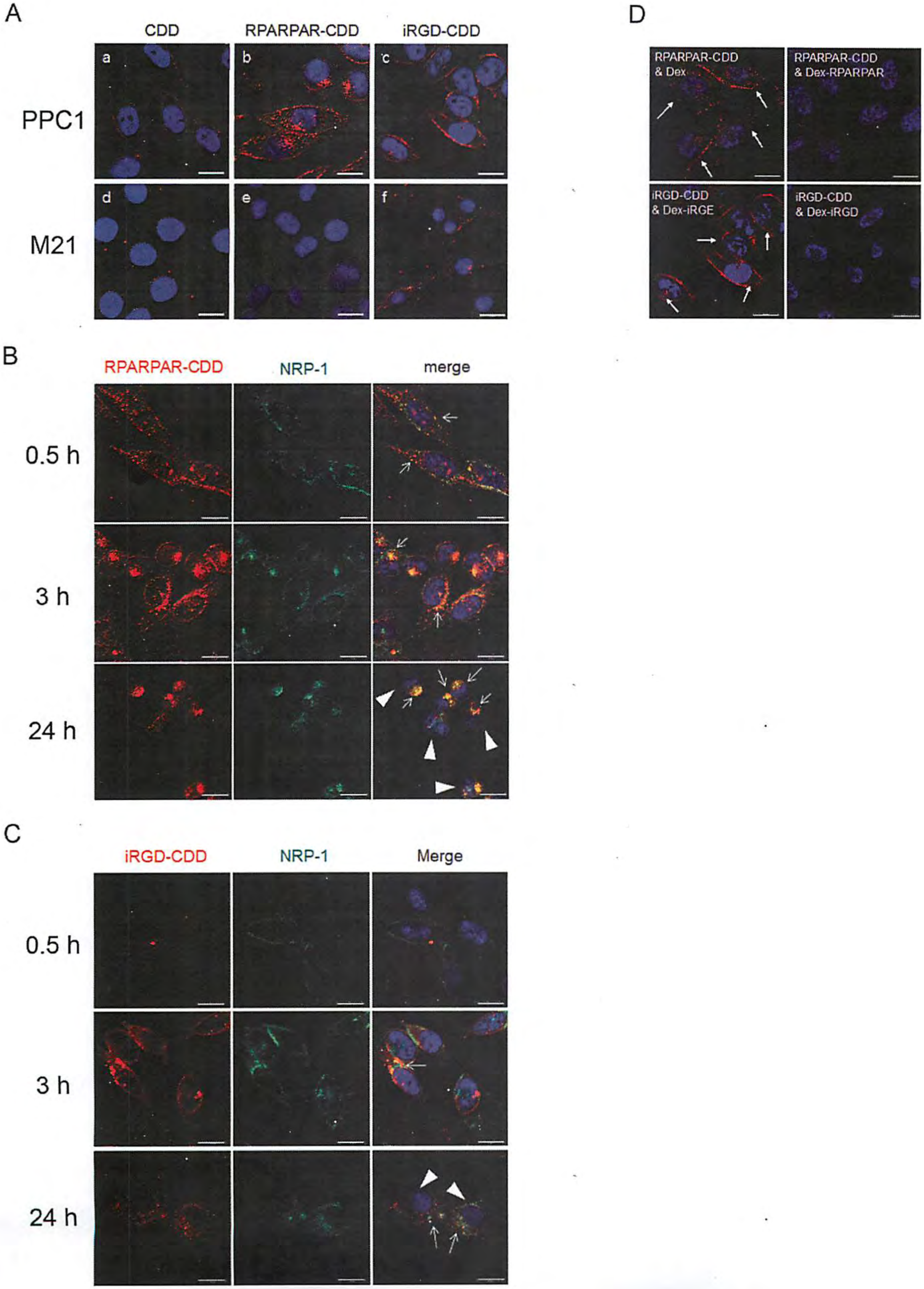

Chen et al, Figure 3

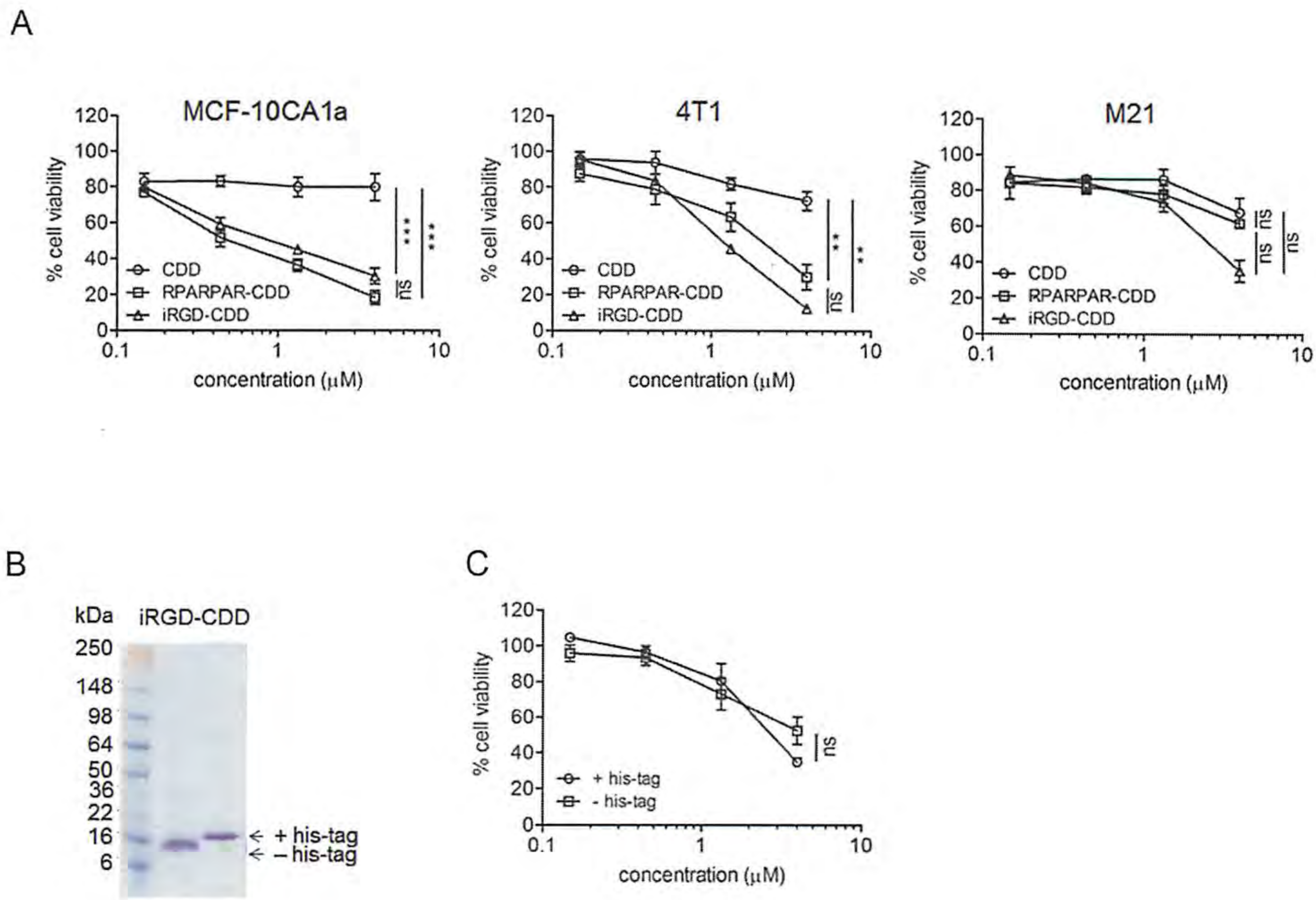

Chen et al, Figure 4

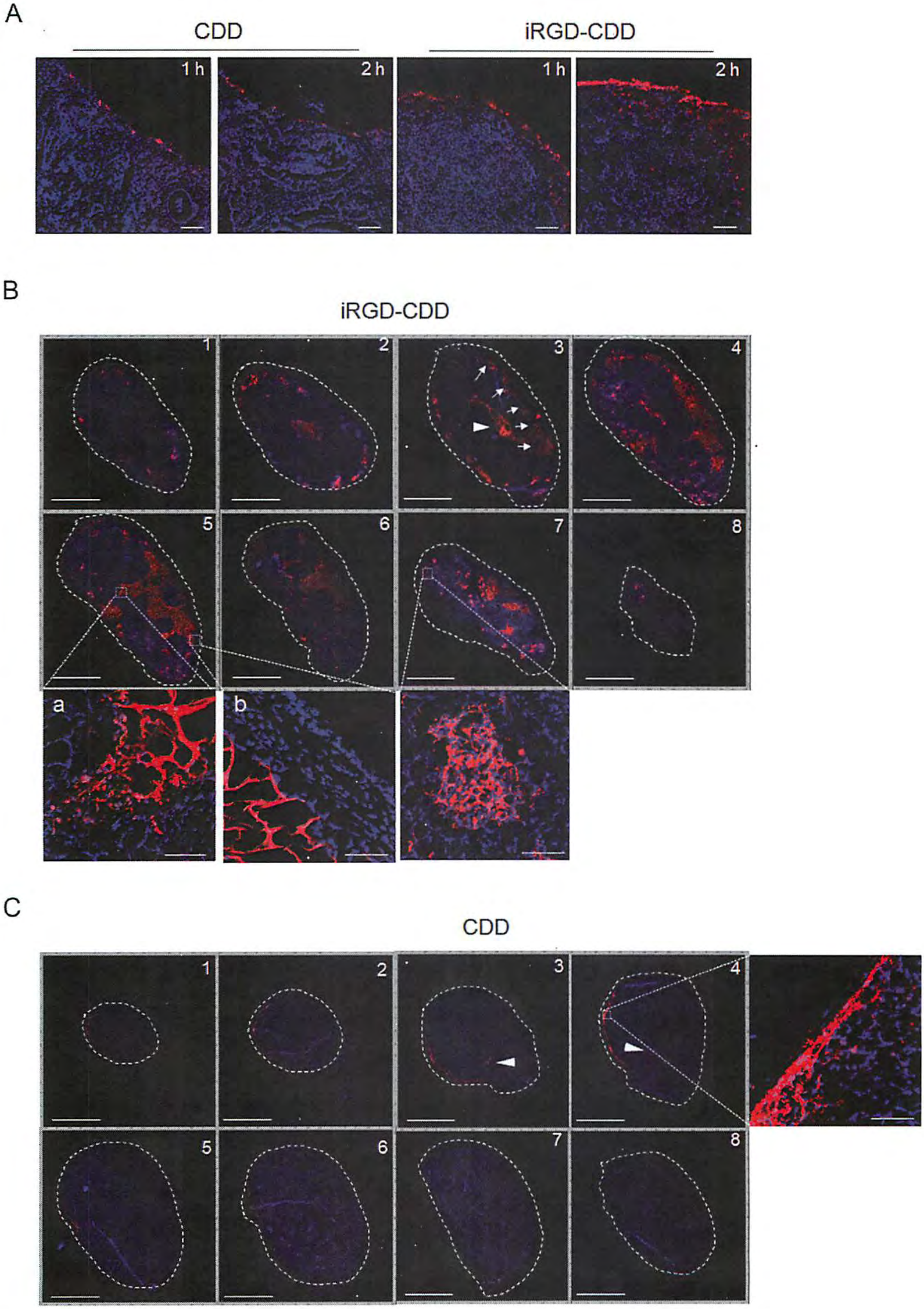

Chen et al, Figure 5

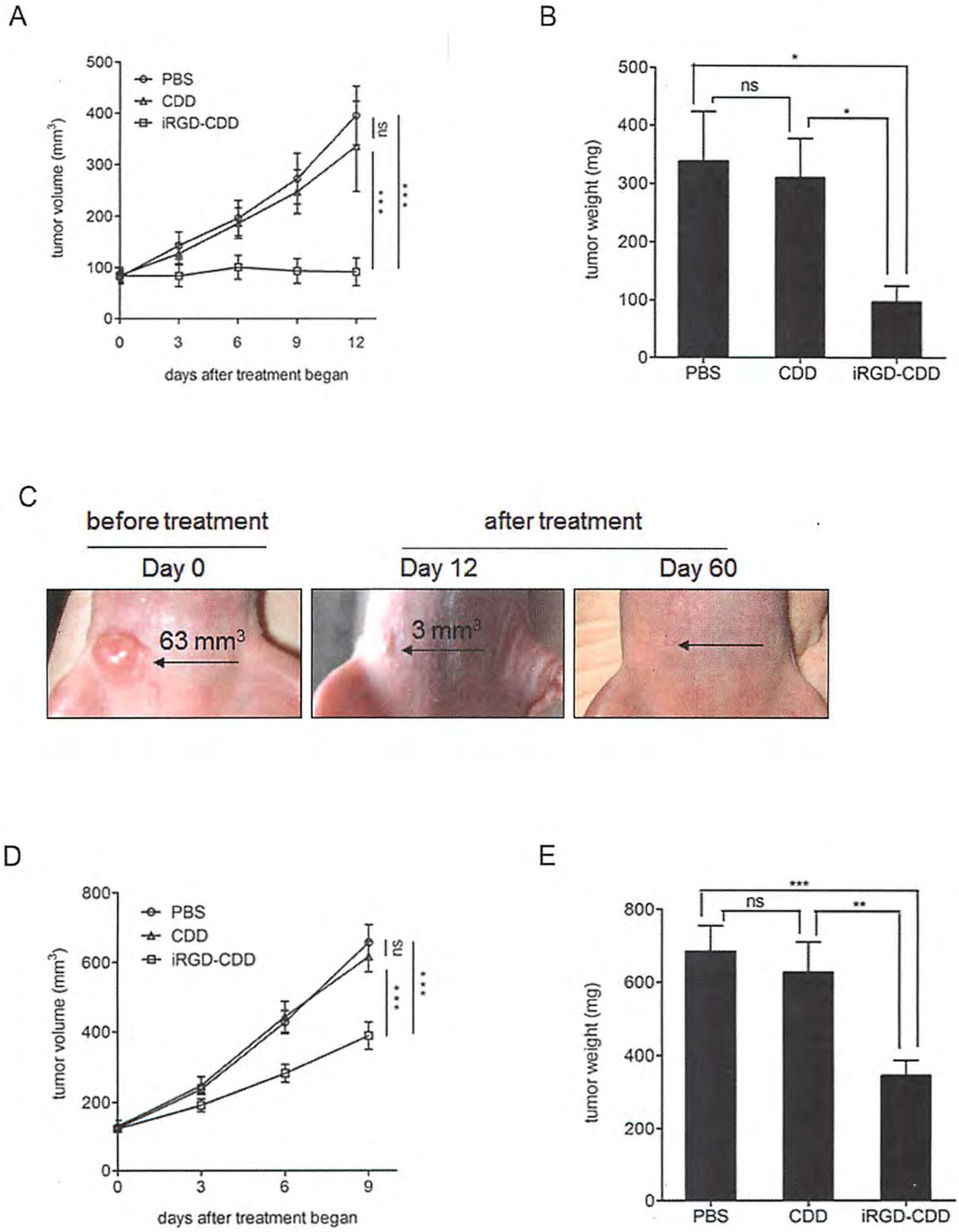

Chen et al, Figure 6

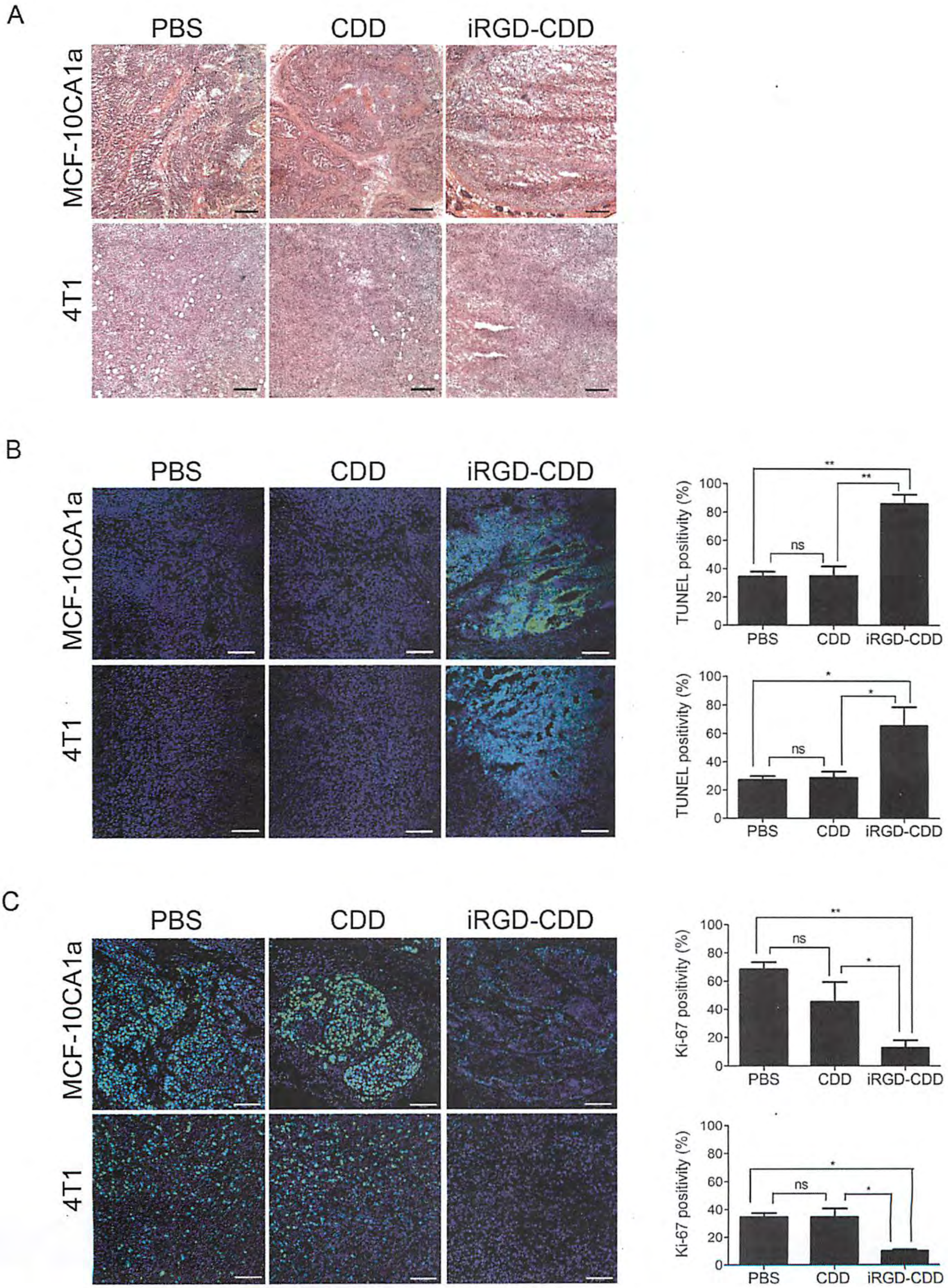

Supplementary data

Application of a Proapoptotic Peptide for an Intratumoral-Spreading Cancer Therapy

Renwei Chen, Gary B Braun, Xiuquan Luo, Kazuki N. Sugahara, Tambet Teesalu, Erkki Ruoslahti

Material and methods

HeLa cervical carcinoma cell line was maintained in Dulbecco's modified Eagle's medium with glutamine containing 10% FBS, penicillin and streptomycin at 37°C and 5% CO_2. Rabbit anti-his-tag polycolonal antibody and rabbit anti-cleaved caspase 3 polyclonal antibody were from Cell Signalling; mouse anti-PARP clone2-10 monoclonal antibody was from BD Pharmingen; rabbit anti-myc-tag polyclonal antibody was from MBL Medical & Biological Laboratories Co., Ltd (Naka-ku Nagoya, Japan); mouse anti-cytochrome c monoclonal antibody was from Santa Cruz Biotech; anti-human Bit1 polycolonal antibody was prepared by immunizing a rabbit with human recombinant Bit1 protein; mouse anti-β-actin monoclonal antibody was from Sigma-Aldrich. The secondary antibodies used were Alexa Fluro® 680-conjugated goat IgG (Invitrogen Life Technologies) and IRDye 800CW-conjugated goat IgG (Li-Cor Biosciences).

To determine the orientation of Bit1 in the mitochondrial membrane, HeLa cells were permeabilized with digitonin which permeabilizes the cholesterol rich plasma membrane but leaves the low cholesterol mitochondrial membrane intact.

Subsequently, cells were treated with trypsin for 15 min to degrade cytosolic proteins and the cytosolic part of membrane proteins on organelles (1). Degradation of Bit1 and cytochrome C was analyzed by immunoblot.

Figure legends

Figure S1. Construction and identification of Bit1 CDD recombinant proteins. A, a schematic diagram of recombinant Bit1 CDD proteins. A hexahistidine tag, an enterokinase cleavable sequence (DDDDK), and a myc-tag were placed at the N-terminus of Bit1 CDD. A tissue-penetrating peptide, RPARPAR or iRGD (CRGDKGPDC), was fused to the CDD C-terminus. B, purified CDD fusion proteins were separated on a gradient SDS-PAGE gel and visualized by staining with Coomassie blue, or immunoblotting with anti-his-tag (red) and anti-myc-tag (green) antibodies.

Figure S2. N-terminal fragments of Bit1 cause cell death. A, HEK 293T cells were transiently transfected with N-terminally myc-tagged truncated Bit1 fragments. The vector without a Bit1 fragment served as a control. The percentage of cell viability was determined 24 h post-transfection by MTT assay and normalized to vector control. Error bars denote mean ± SEM of 3 separate experiments performed in triplicate. One-way ANOVA was used for statistical analysis. The comparisons shown are to the vector control. **, $p < 0.01$; ***, $p < 0.001$; ns, not significant. B, sequence alignment of the N-terminus of Bit1 is from multiple species. The numbers correspond to the human Bit1 sequence (AF151905). Consensus sequences among the indicated species are marked with * at the bottom. A conserved transmembrane domain was identified at amino acids 14-33 in the human Bit1 sequence. C, confocal micrographs of HeLa cells transiently over-expressed with Bit1 or its deletion variants. Red, Bit1 or truncated Bit1; blue, nuclei. Deletion of the N-terminal 13 residues (ΔAAs 1-13) did not alter the mitochondrial localization pattern of Bit1 (2). Deletion of the N-terminal 33 residues (ΔAAs 1-33) or the putative transmembrane domain (ΔAAs 14-33) resulted in cytosolic and nuclear expression. D, immunoblotting of mitochondrial Bit1 and cytochrome C after digitonin and trypsin treatment of the cells. Bit1 was degraded by the treatment of digitonin and trypsin suggesting its localization at mitochondrial outer membrane. Cytochrome C, a protein that localizes to the intermembrane space of mitochondria was not degraded under the same treatment, indicating that the mitochondria had remained intact. Scale bar, 10 µm. E, a schematic diagram showing the proposed localization of Bit1 on the outer membrane of mitochondrion facing the cytosol.

Figure S3. Caspase cascade signaling is impaired in MCF-10CA1a human breast cancer cells. MCF-10CA1a and 4T1 cells were treated with 0.1 µM of etopside or 1 µM of iRGD-CDD protein for 48 h. Cell lysates were immunoblotted with a rabbit anti-cleaved caspase 3 monocloanl antibody (Cell Signaling) and a mouse anti-PARP monoclonal antibody (clone c2-10, BD Pharmingen). Both antibodies react with human and mouse samples. β-actin was used as a loading control.

Figure S4. Tumor volume and body weight. Mice bearing orthotopic 4T1 tumors (n = 5 per group) were treated by intravenously injected of PBS, CDD, or iRGD-CDD at 10 mg/kg of mouse body weight every other day. A, the mean tumor volume ± SEM was plotted and analyzed by two-way ANOVA. * $p \le 0.05$; ** $p \le 0.01$; ns, not significant. B, the body weight before the treatment was used to calculate the mean body weight variation (%). The CDD compounds caused severe toxicity and loss of body weight made it necessary to euthanize these mice on day 6 of the treatment.

References

1. Nguyen M, Millar DG, Yong VW, Korsmeyer SJ, Shore GC. Targeting of Bcl-2 to the mitochondrial outer membrane by a COOH-terminal signal anchor sequence. J Biol Chem. 1993;268:25265-8.
2. Jan Y, Matter M, Pai JT, Chen YL, Pilch J, Komatsu M, et al. A mitochondrial protein, Bit1, mediates apoptosis regulated by integrins and Groucho/TLE corepressors. Cell. 2004;116:751-62.

Chen et al, Supplementary Figure S1

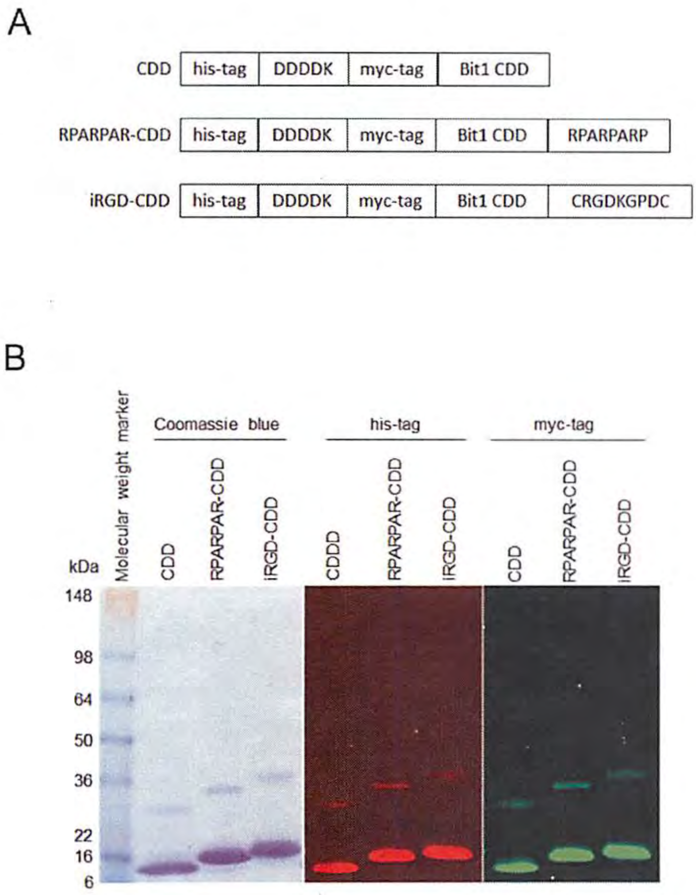

Chen et al, Supplementary Figure S2

A

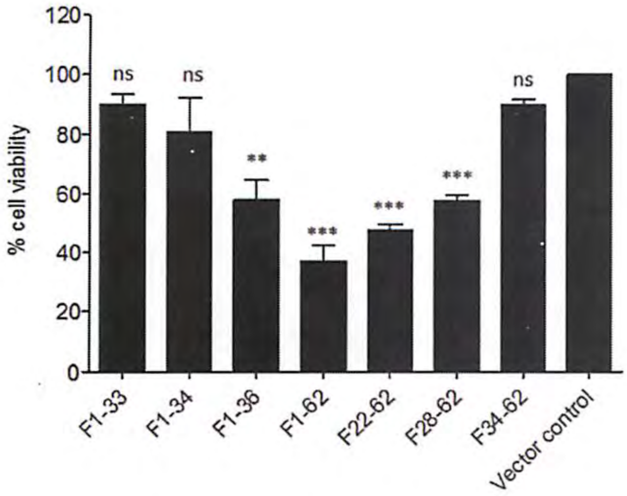

B

```
                                  transmembrane domain
       Amino acids  1         11        21        31        41        51        61
      Homo sapiens  MPSKSLVMEYLAHPSTLGLAVGVACGMCLGWSLRVCFGMLPKSKTSKTHTDTESEASILGDS
    Macaca mulatta  MPSKSLVMEYLAHPSALGLAIGVACGVCLGWSLRVRFGMLPKSKTSKTHTDTESEASILGES
      Mus musculus MMLSKFLTMEYLVHPGTLSLAAGVACGMCLGWGLRSHLGMFPQNSTSEANRDTETGTEASILGE
 Rattus norvegicus  MLSKLLTMEYLVHPGTLSLAAGVACGMCLGWGLRSHLGIFPQNSTSETNRDTEMGTEASILG
Xenopus tropicalis         MDYFTYPGALPLTAGLACGLFLGWSLRGRFGYFRSFSTLATNEVGTEASTMGETGE
     Gallus gallus         MDYLSKPGFLSILAGVACGVCLGWGIRGRFLRQHRAMAASAGSCGTEANVMGESGE
        Bos taurus  MISRSLVMEYLTNPGALSLVAGVACGVCLGWGLRMRFGMLPKSSVRETNPDTETEASILGES
         Consensus         * *   *  *    * ***  *** *
```

C

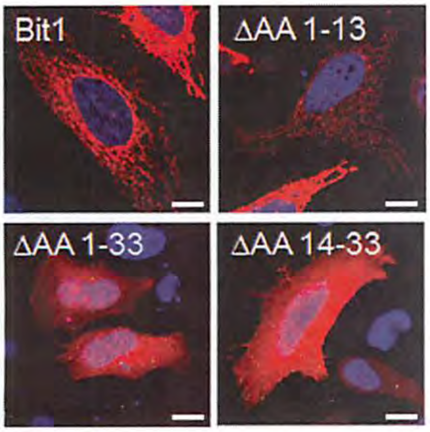

D

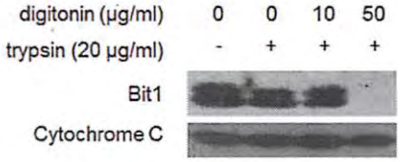

E

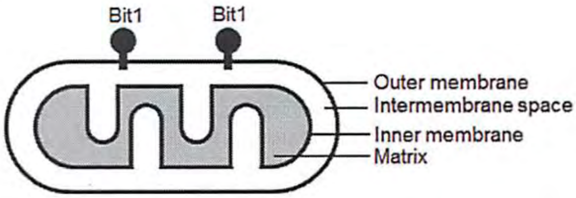

Chen et al, Supplementary Figure S3

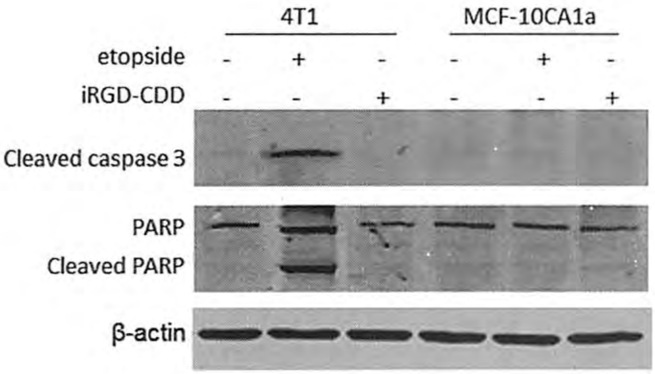

Chen et al, Supplementary Figure S4

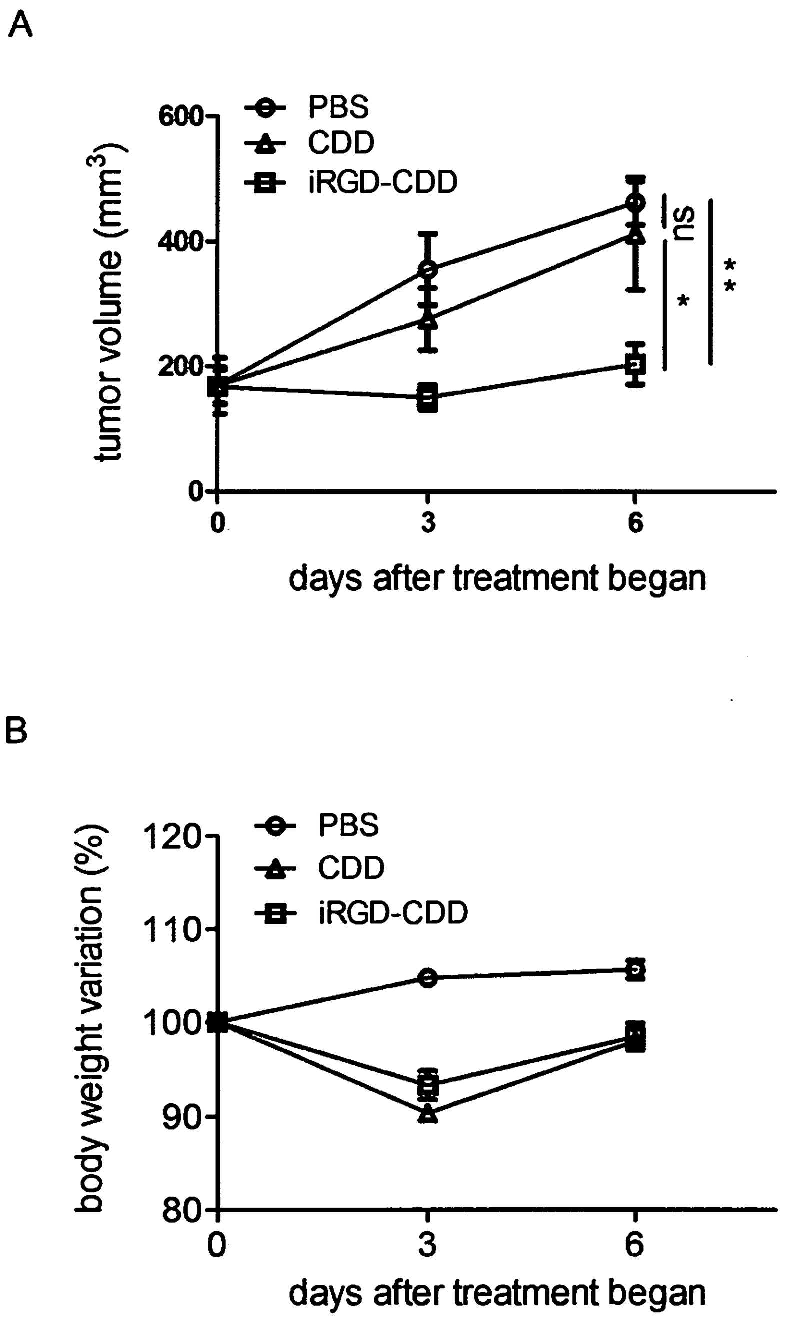

De Novo Design of a Tumor-Penetrating Peptide

Luca Alberici[1,2,3], Lise Roth[4], Kazuki N. Sugahara[1], Lilach Agemy[1], Venkata R. Kotamraju[1], Tambet Teesalu[1], Claudio Bordignon[2,3], Catia Traversari[2], Gian-Paolo Rizzardi[2], Erkki Ruoslahti[1]

[1] Cancer Center, Sanford-Burnham Medical Research Institute, 10901 N. Torrey Pines Rd., La Jolla, CA 92037 U.S.A. and Center for Nanomedicine, Sanford-Burnham Medical Research Institute at University of California, Santa Barbara, CA 93106-9610

[2] MolMed S.p.A., Via Olgettina 58, 20132 Milano, Italy

[3] Università Vita-Salute San Raffaele, Via Olgettina 58, 20132 Milano, Italy

[4] Division of Vascular Oncology and Metastasis, German Cancer Research Center (DKFZ), Im Neuenheimer Feld 280, 69120 Heidelberg, Germany

Running Title: *De Novo* Design of a Tumor-Penetrating Peptide

Keywords: Tissue-penetrating peptide, C-end Rule, NGR, Tumor targeting, Drug delivery

Word count: 4921

Total number of figures: 5

Corresponding Author:

Erkki Ruoslahti, Distinguished Professor
Cancer Center, Sanford-Burnham Medical Research Institute, 10901 N. Torrey Pines Rd., La Jolla, CA 92037 U.S.A.
Phone: 858 795-5023
E-mail: ruoslahti@sanfordburnham.org

Grant Support

This work was partially supported by MolMed S.p.A. (www.molmed.com), and by grants W81XWH-09-1-0698 and W81XWH-08-1-0727 from the USAMRAA of the DoD (ER) and by grant R01 CA 152327 from the National Cancer Institute of the National Institutes of Health. ER is supported in part by CA30199 the Cancer Center Support Grant from the National Cancer Institute of the National Institutes of Health.

Competing Interest

LA, CT, GPR and CB are employees of MolMed S.p.A. KNS, VRK, TT and ER are shareholders of CendR Therapeutics Inc, which has rights to some of the technology described in this paper. LR and LAg declare no conflict of interest.

Abstract

Poor penetration of anti-tumor drugs into the extravascular tumor tissue is often a major factor limiting the efficacy of cancer treatments. Our group has recently described a strategy to enhance tumor penetration of chemotherapeutic drugs through use of iRGD peptide (CRGDK/RGPDC). This peptide comprises two sequence motifs: RGD, which binds to αvβ3/5 integrins on tumor endothelia and tumor cells and a cryptic CendR motif (R/KXXR/K-OH). Once integrin binding has brought iRGD to the tumor, the peptide is proteolytically cleaved to expose the cryptic CendR motif. The truncated peptide loses affinity for its primary receptor and binds to neuropilin-1, activating a tissue-penetration pathway that delivers the peptide along with attached or co-administered payload into the tumor mass. Here we describe the design of a new tumor-penetrating peptide based on the current knowledge of homing sequences and internalizing receptors. The tumor-homing motif in the new peptide is the NGR sequence, which binds to endothelial CD13. The NGR sequence was placed in the context of a CendR motif (RNGR), and this sequence was embedded in the iRGD framework. The resulting peptide (CRNGRGPDC, iNGR) homed to tumor vessels and penetrated into tumor tissue more effectively than the standard NGR peptide. iNGR induced greater tumor penetration of coupled nanoparticles and co-administered compounds than NGR. Doxorubicin given together with iNGR was significantly more efficacious than the drug alone. These results show that a tumor-specific, tissue-penetrating peptide can be constructed from known sequence elements. This principle may be useful in designing tissue-penetrating peptides for other diseases.

Introduction

The vasculature of each tissue is unique in terms of protein expression and these molecular differences are referred to as "vascular zip codes" (1). The selectively expressed proteins provide targets for specific delivery of diagnostic and therapeutic compounds to the vasculature of desired tissues. Currently, a variety of tumor-targeting peptides are in preclinical and clinical development. However, vascular abnormalities, fibrosis and contraction of extracellular matrix contribute to an increased interstitial fluid pressure inside the tumor, which impedes drug delivery into the extravascular tumor tissue (2).

Our group has recently reported the identification of the CendR motif (R/KXXR/K) that is capable of increasing the penetration of peptides, chemicals, and synthetic and biological nanoparticles into tissues through the engagement of neuropilin-1 (NRP-1) (3). Specific penetration into tumors was achieved through the use of an iRGD peptide (CRGDK/RGPDC) (4). iRGD, identified by *in vivo* phage display for tumor homing peptides, combines targeting to tumor vessels and tumor parenchyma through an RGD motif with the cell-internalizing and tissue penetrating properties of a CendR motif RGDK/R in the peptide (4). iRGD mechanism of action involves three steps. First, the RGD sequence binds to αvβ3/5 integrins. Then, a proteolytic cleavage by a yet-to-be-identified host protease(s) exposes the CendR motif, which is now able to interact with NRP-1 to trigger the internalization process. This strategy allows the activation of the CendR motif only in a targeted tissue, avoiding NRP-1 activation in normal vasculature. Interestingly, iRGD triggers a specific tumor penetration of, not only iRGD-coupled compounds, but also of drugs co-administered with free iRGD peptide (5). The CendR motif also activates the penetration pathway through binding to NRP-2 (6).

Potentially, the addition of a cryptic CendR motif could increase the penetration of other tumor targeting peptides, providing more tools to overcome the poor delivery of drugs to tumors. We set out to test this hypothesis using the NGR tumor-homing motif. The NGR sequence was identified by *in vivo* phage display in tumor bearing mice (7). Initially it was thought to bind one or more of the integrins selectively expressed in angiogenic vessels (7, 8). This idea was further supported by the discovery that the asparagine in the NGR motif undergoes a spontaneous deamidation reaction that yields iso-aspartic acid (isoDGR), generating an RGD mimetic (9, 10). However, the unaltered NGR motif also specifically homes to tumor vessels, where it binds to an isoform of aminopeptidase N (CD13) (11, 12). NGR peptides have been used to target a variety of agents into tumors; an NGR conjugate of human tumor necrosis factor α is in advanced clinical trials for cancer therapy (13-16). Here we combined the NGR motif with a CendR motif to create a new tumor-homing peptide with tissue-penetrating properties.

Materials and Methods

Animal use. All procedures on the animals, including those to ensure minimizing discomfort, have been carried out according to the protocol approved at the Sanford-Burnham Medical Research Institute.

Preparation of compounds. Synthetic peptides (4), peptide-coated NWs (17) and peptide-expressing T7 phage (18) were prepared as described elsewhere. DOX was purchased from Sigma-Aldrich (St. Louis, MO). Evan's Blue was purchased from MP Biomedicals (Irvine, CA)

Cell lines and tumor models. HUVECs (Lonza, Allendale, NJ) were cultured in complete EGM-2 medium from Lonza. 4T1 cells were cultured in Dulbecco's Modified Eagle Medium (Thermo Scientific, Rockford, IL) supplemented with 10% fetal bovine serum (FBS) and penicillin/streptomycin (Gibco, Grand Island, NY). All tumor cell lines were bought and authenticated by ATCC (Teddington, UK). Orthotopic 4T1 breast tumors were generated by injecting 10^5 cells into the mammary fat pad of female BALB/c mice at the age of 4-6 weeks (Harlan Sprague-Dawley, Indianapolis, IN).

***In vitro* phage binding and internalization assays**: Phage amplification, purification, titration, sequencing, and UV inactivation were performed as reviewed (18). One million cells were incubated with 10^{10} plaque forming unit (pfu) of purified phage in DMEM-1% BSA at 4°C for binding or 37°C for internalization. The cells were washed with cold DMEM-BSA four times, lysed in lysogeny broth (LB) containing 1% Nonidet P-40 (LB-NP40) and titrated. In internalization assays, the second wash was replaced with an acid wash (500 mM NaCl, 0.1 M glycine, 1% BSA, pH 2.5) to remove and inactivate phage bound to the cell surface. In inhibition assays, the cells were incubated with 1 µg/ml of neutralizing anti-NRP-1 antibody (R&D Systems), control IgG (Santa Cruz Biotechnology), or 10-fold excess of UV-inactivated phage 15 min prior to adding the phage of interest.

***Ex vivo* tumor dipping assays:** The assays were performed as described elsewhere (5, 6). Briefly, 4T1 tumor bearing mice were anesthetized and perfused through the heart with PBS containing 1% BSA. The tumors were excised and incubated with 10^9 pfu of phage in DMEM-1% BSA for 1 hour at 37°C. After extensive washes with PBS, the tumors were lysed in 1 ml of LB-NP40 for phage titration. In some cases, the tumors were fixed in PBS containing 4% paraformaldehyde (PFA) and processed for immunostaining.

Biodistribution of peptides, phage and NWs. *In vivo* tumor homing experiments with peptides, phage, and NWs were performed as described (4, 17). Briefly, 10^9 pfu of phage particles were injected into the tail vein of tumor bearing mice, and allowed to circulate for 40 minutes. The mice were perfused through the heart with PBS containing 1% BSA under deep anesthesia. The tumors and tissues were excised and mechanically homogenized for phage titration or fixed in 4% PFA for immunostaining. In some cases, 50 µg of anti-NRP-1 antibody or control IgG was intravenously injected 15 minutes prior to the phage injection. For the peptide homing studies, 100 µl of 1 mM FAM-labeled peptides were intravenously injected into tumor mice and allowed to circulate for 1 hour. In case of the NWs, particles at a dose of 5 mg/kg of iron were injected into the tail vein of tumor mice and allowed to circulate for 5 hours. After perfusion of the mice, tissues were collected, macroscopically observed under UV light (Illuminatool Bright Light System LT-9900), and processed for immunostaining. Intratumoral accumulation of NWs was quantified with ImageJ.

Immunofluorescence: Immunofluorescence on cells was performed using 10 µM FAM-peptides and following the protocol previously described (19). Immunofluorescence on frozen sections was performed as described earlier (4) using the following antibodies at 1:200 dilution: rat anti-mouse CD31 Alexa-594 (Invitrogen), rabbit anti-T7 phage (3) and donkey anti-rabbit Alexa 488 (Invitrogen). Images were taken using a Fluoview confocal microscope (Olympus, Center Valley, PA).

***In vivo* systemic permeability assay**. Tumor bearing mice were injected intravenously with 4 µmol/kg of peptide combined with 1 mg of Evans Blue, 10 mg/kg of free DOX or 5 mg iron/kg of CGKRK-coated NWs (20). After indicated time of circulation, the mice were perfused through the heart with PBS supplemented with 1% BSA, and tissues were collected. Evans Blue was extracted by incubating the tissues in 1 ml of 2,2 N-methylformamide overnight at 37°C with mild shaking. After centrifugation, the OD_{600} of the supernatant was measured. To assess the extravasation of CGKRK-NWs, tissues were fixed in 4% PFA overnight at 4°C and subjected to immunostaining for CD31-positive blood vessels. For DOX quantification (21), excised tissues were mechanically homogenized in 1 ml of 1% Sodium Dodecyl Sulphate (SDS) containing 1 µM H_2SO_4, and frozen overnight in 2 ml of chloroform/isopropyl alcohol (1:1, v/v). The samples were melted, vortexed and centrifugated at 16,000 g for 15 min, and OD_{490} of the organic (lower) phase was measured.

Tumor treatment studies. Mice bearing orthotopic 4T1 breast tumors at 50 mm^3 received intravenous injections of free DOX (3 mg/kg) or PBS, combined with 4 µmol/kg of peptide every other day. Tumor growth and body weight were monitored every other day. The tumor volume was calculated using the following formula: volume (mm^3) = (d^2 x D)/2, where d is the smallest and D is the largest tumor diameters.

Statistical analysis: All data were analyzed with one-way ANOVA. Tumor treatment studies were analyzed with two-way ANOVA for repeated measurements.

Results

Design of iNGR peptide. We used 3 elements to create the iNGR peptide (CRNGRGPDC): the NGR motif, a CendR motif (RNGR) overlapping with the NGR motif, and a cleavable consensus (GPD) from the iRGD peptide. The cyclic conformation required for high affinity binding of NGR to CD13 (22) was obtained through the addition of cysteines at the N- and C-terminus of the peptide. We also prepared the truncated version of iNGR that is expected to result from proteolytic activation of iNGR (CRNGR), which we refer to as iNGRt. The conventional NGR (CNGRC), RGD (CRGDC), iRGD (CRGDKGDPC) and activated iRGD (CRGDK) peptides were used as controls. The peptides used in this study are summarized in Table S1.

iNGR and NGR bind to the same primary receptor. Human umbilical vein endothelial cells (HUVECs) express on their surface both the NGR receptor CD13 and the CendR receptor NRP-1 (Fig S1). iNGR bound to HUVECs as efficiently as CNGRC, whether tested as FAM-labeled peptide (Fig. 1A) or displayed on phage (Fig. 1B, black columns). As expected, the iNGR phage did not bind $CD13^{+}$ U937 monocytes (Fig. S2A-C), as previously reported for the CNGRC peptide (11). UV-inactivated phage displaying CNGRC inhibited the HUVEC binding of the iNGR phage in a dose-dependent fashion, whereas inactivated CRGDC did not differ from insertless control phage in this regard (Fig. 1C). CNGRC phage did not inhibit the binding of iRGD phage to HUVECs (Fig. S3A). Moreover, only *in vitro* deamidated CNGRC and iNGR phage showed binding to immobilized $\alpha v\beta 3$ integrin (Fig. S3B). These results suggest that CNGRC and iNGR bind to the same primary receptor through the NGR motif and that the conversion of asparagine to aspartate does not take place during phage production, purification, storage, or during the incubations. Therefore the binding of CNGRC and iNGR to cells is not due to isoDGR interacting with αvβ3/5 integrins.

The iNGR CendR motif interacts with NRPs and promotes cell internalization. We constructed phage displaying a truncated version of iNGR in which the CRNGR CendR motif occupies a C-terminal position (iNGRt). This phage bound avidly to HUVECs, likely due to an interaction with NRP-1 (Figs. 1A and 1B). Indeed, iNGRt phage binding to HUVECs was reduced by pre-incubation with a UV-inactivated phage expressing a prototypic CendR motif peptide (RPARPAR) or a neutralizing NRP-1 antibody (Fig. 1B), indicating involvement of the CendR/NRP-1 pathway. Pre-incubation with a phage displaying a peptide with a blocked CendR motif (RPARPARA), and a control antibody, had no effect on iNGRt binding to HUVECs. The binding of intact iNGR was not affected by the UV-inactivated RPARPAR phage or NRP-1 antibody showing that NRP-1 is not involved in the initial binding of the peptide. Measuring phage internalization by incubating phage with HUVECs at 37°C, followed by a wash with a low pH buffer to inactivate extracellular phage, showed stronger internalization of iNGR and iNGRt than CNGRC (Fig. 1D). Inhibition experiments showed that the internalization was mediated by the interaction of the CendR motif with NRP-1. These results suggest that HUVECs express a protease capable of activating the cryptic CendR motif embedded in the iNGR peptide. Indeed, mass spectrometry showed that upon incubation of HUVECs with FAM-iNGR peptide, only the cleaved FAM-CRNGR fragment (m/z: 1076.527), but not the full-length peptide (m/z: 1445.065), was present inside the cells (Fig S4). FAM-CNGRC peptide (m/z: 1020.020) did not penetrate into the cells. Direct proof that the CendR motif within the iNGR peptide is capable of binding to NRPs was provided by

CRNGR phage binding to immobilized NRP-1 (Fig. 1E). This phage also bound to NRP-2 (Fig. 1F). In agreement with the finding that the motif R/KXXR/K has to be in a C-terminal position to bind to NRPs (the Cend-Rule)(3), only phage expressing the iNGRt, and the analogous iRGDt, bound to the NRPs, whereas the corresponding full-length peptides showed only background binding. Interestingly, iNGRt showed higher affinity for NRP-1 and NRP-2 than iRGDt, suggesting that a C-terminal arginine residue (CRNGR) provides higher affinity than lysine (CRGDK).

iNGR penetrates deeper into tumors than NGR. We have previously shown in *ex vivo* tumor penetration assays that iRGD utilizes a CendR-mediated active transport system to cross tumor barriers (5). To investigate the iNGR-mediated penetration pathway, we performed an *ex vivo* tumor penetration assay of phage using explants of orthotopic 4T1 murine breast tumors (positive for expression of CD13 and NRP1/2; Fig 2A). To evaluate the extent of tumor penetration, we titrated the phage recovered from tumors (Fig 2B) and determined the distribution of phage immunoreactivity (Fig 2C). The CendR-containing phage (iNGR and iRGD) penetrated into the explants with resembling patterns, whereas non-CendR phage (CNGRC and control) remained at the outer rim of the explants. These results suggest that iNGR and iRGD share a similar CendR-mediated transport mechanism to penetrate tumor tissue.

Systemic iNGR selectively accumulates and penetrates into tumors. Having determined that the CendR motif within the iNGR peptide can be proteolytically activated to trigger interaction with NRPs and penetration into cells and tissues, we assessed the homing of iNGR *in vivo*. Intravenously administered iNGR phage accumulated within the tumor and penetrated into the tumor stroma more than CNGRC phage (Fig 3A and B upper panels). The iNGRt phage also showed high tumor penetration, presumably because of the high expression of NRP-1 on tumor vasculature and tumor cells, but this phage also accumulated in lungs and heart of the tumor mice. iNGR penetration could be blocked by concomitantly administering a neutralizing anti-NRP-1 antibody, but not a control antibody (Fig 3B lower panels). Vascular targeting of iNGR was not inhibited by the anti-NRP-1 treatment (arrows, Fig 3B left lower panel), supporting the notion that the CendR activation occurs after iNGR accomplishes NGR-dependent vascular targeting. Intravenously injected FAM-iNGR peptide also accumulated in 4T1 breast tumors (Fig. 3C) and BxPC-3 pancreatic tumors (Fig. S5A) more strongly than FAM-CNGRC. FAM-iNGR extravasation within tumor tissue was greater than that of FAM-CNGRC (Fig 3D). FAM-iNGR selectively penetrated into tumors and not in control organs (Fig 3E). Elongated iron oxide nanoparticles (nanoworms; NWs) coated with iNGR also showed higher extravasation than CNGRC-NWs (Fig 3F and S5B). The NWs were less efficient than phage in penetrating the tissue, likely because they are larger in size (NWs, 30 x 70/200 nm; phage, 55nm).

iNGR triggers tumor-specific penetration of co-administered compounds. The engagement of NRP-1 increases vascular permeability (23), and iRGD triggers this phenomenon specifically in tumors (5). We found that iNGR significantly increased extravasation and accumulation of the albumin-binding dye Evans blue in 4T1 tumors, but not in non-tumor tissues. CNGRC or vehicle alone had no effect on the biodistribution of the dye (Fig. 4A, 4B, and S6). iNGR facilitated tumor-specific accumulation of Evans blue in CT26 colon and LLC lung tumor models as well (Fig. S7). We also co-administered iNGR with NWs coated with a tumor homing peptide, CGKRK (20) that brings the NWs to tumor vessels, but does not trigger extravasation. iNGR allowed the NWs to extravasate into the tumor parenchyma (Fig. 4C). Finally, iNGR triggered more penetration of doxorubicin (DOX) into the tumors than DOX alone or DOX combined with CNGRC (Fig. 4D).

iNGR enhances anticancer drug efficacy. Having found that iNGR co-administration increased the local accumulation of DOX within tumors, we investigated the effect of iNGR on the activity of DOX. We treated orthotopic 4T1 breast tumor mice with a combination of DOX (3 mg/kg) and 4 µmol/kg of iNGR, a control peptide, or PBS every other day. As shown in Figure 5A, iNGR, but not CNGRC, enhanced the antitumor effect of DOX. iNGR alone had no effect on the progression of tumor growth. Loss of body weight as an indicator of DOX toxicity was not affected by the peptide co-administration (Fig. 5B). These results demonstrate the potential of iNGR as an adjuvant to increase the efficacy of co-administered anticancer drugs.

Discussion

We report here the design of a new tumor-penetrating peptide, iNGR. The peptide was constructed by combining the tumor-targeting motif NGR and tissue-penetrating CendR motif into a 9-amino acid cyclic peptide. The iNGR peptide, homed to tumor vessels, exited the vessels, and penetrated into the tumor mass. It was able to take both coupled and co-administered payloads with it. When the co-administered payload was a drug (DOX), the efficacy of the drug increased. These results show that it is possible to use the existing knowledge to construct a new tumor-specific, tissue-penetrating peptide.

The mechanisms underlying iNGR activity are similar to those described for iRGD (4, 5). The receptor for the tumor-targeting motif NGR is a variant form of aminopeptidase N (12). The binding of iNGR to cultured cells was specifically inhibited by CNGRC, indicating that iNGR binds to the same receptor. NGR peptides are known to spontaneously undergo slow deamidation of the asparagine residue into isoaspartic acid. The resulting isoDGR peptides, like RGD peptides, bind to αv integrins. Our results exclude integrin involvement in the binding of iNGR peptide and phage to cultured cells. It is also unlikely that isoDGR formation affects the *in vivo* tumor targeting of iNGR because the deamidation process takes several hours (24), whereas the half-life of intravenously injected peptides of the size of iNGR is only minutes (25). Thus iNGR and iRGD bind to different primary receptors on cells.

Upon engagement of the iRGD peptide at the plasma membrane of target cells, a proteolytic cleavage by a yet-to-be-identified enzyme(s) exposes the CendR sequence, which subsequently binds to NRP-1 (4). Our evidence indicates that the same mechanism operates with iNGR. First, phage displaying the predicted CendR product of iNGR, CRNGR (iNGRt) bound to NRP-1 and NRP-2, and did so with a higher affinity than CRGDK fragment of iRGD. The reason for the difference may be that a peptide with a C-terminal arginine binds more efficiently to NRPs than a peptide with a lysine C-terminus (26). Comparison of the tumor-homing efficacy of iRGD with an arginine or a lysine (CRGDK/RGPDC) showed that the lysine-containing form was more effective *in vivo* (4). It may be that other effects of the lysine residue, such as stronger integrin binding or higher susceptibility to protease cleavage, overcome the effect of lower affinity for NRPs. Second, iNGR, both as a synthetic peptide and on phage was taken up by cells in a NRP-dependent manner. Third, we isolated the iNGRt CendR fragment from inside cells treated with the intact iNGR peptide, as has been previously done with iRGD (4). Fourth, the co-injection of iNGR phage with neutralizing anti-NRP-1 antibody resulted in a reduced extravasation of iNGR. These results show that iNGRt, the active form of iNGR, is generated through proteolysis and that the tumor-penetrating properties of iNGR are based on its ability to activate the CendR pathway.

The activation of iNGR into iNGRt appears to take place only in tumors because iNGR only accumulated in tumors. In contrast, the truncated iNGRt form, while showing preferential homing to tumors, also accumulated in the lungs and heart. This homing pattern reflects the expression of NRP-1, which is universal in the blood vessels but particularly high in tumor vessels (27). The reason for the selective activation of the cryptic CendR motif in tumors is likely to be that binding to the primary receptor is needed for activating proteolytic cleavage. Previous work from our laboratory has shown that an iRGD variant that does not bind to integrins, but contains a CendR motif, does not penetrate into cultured cells, whereas iRGD does (4). The nature of the primary receptor does not seem to matter, as long as the receptor is tumor specific. iRGD and iNGR bind to different primary receptors, but both become activated in cell cultures and in tumors. Moreover, we have recently shown that a previously identified tumor-homing peptide, CGNKRTRGC (LyP-1) (28) also penetrates into tumors through the CendR/NRP mechanism (6). The primary receptor for this peptide is p32/gC1qR/ HABP1, a mitochondrial protein expressed at the cell surface in tumors (29). Thus, our results show that at least 3 different primary receptors can initiate the sequence of events that leads to the NRP-dependent activation of the CendR pathway in tumors. Importantly, the difference in the primary receptors allows us to differentially target tumors or tumor areas based on receptor expression patterns, providing multiple options to enhance tumor therapy with tumor-specific CendR peptides.

The experiments with phage, fluorophore-labeled peptide, and nanoparticles showed the ability of iNGR to take coupled payloads into the extravascular tumor tissue. Our results further demonstrate that such enhanced delivery and tumor penetration also applies to compounds co-administered with iNGR. Importantly, we showed this for DOX, the anti-tumor activity of which was increased by injecting the drug together with iNGR.

The co-administration strategy has significant advantages. First, because chemical coupling is not needed, new chemical entities are not created, providing a faster route for clinical development. Second, unlike targeting of compounds chemically coupled to an homing element, the co-administration process is not strictly dependent on the number of available receptors, which seriously limits the amount of a drug that can be delivered to a target (30).

Taken together, our results show that iNGR possesses the same targeting ability as CNGRC, supplemented with cell-internalizing and tumor-penetrating properties. This transformation suggests an important principle: a targeting peptide can be *ad hoc* improved by the addition of a CendR motif, which endows the peptide with tissue-penetrating properties and allows enhanced delivery of co-administered compounds into a target tissue. Rational optimization of targeting peptides in this manner may also have valuable applications in other diseases.

Authors' Contributions

LA, LR, KNS, TT, CT, GPR, CB and ER designed research; LA, LR, KNS, LAg and TT performed research; VRK and LAg contributed new reagents; LA, LR, KNS, LAg, TT and ER analyzed data. LA, KNS, TT and ER wrote the paper.

References

1. Ruoslahti E. Specialization of tumour vasculature. Nat Rev Cancer 2002;2:83-90.
2. Heldin CH, Rubin K, Pietras K, Ostman A. High interstitial fluid pressure - an obstacle in cancer therapy. Nat Rev Cancer 2004;4:806-13.
3. Teesalu T, Sugahara KN, Kotamraju VR, Ruoslahti E. C-end rule peptides mediate neuropilin-1-dependent cell, vascular, and tissue penetration. Proc Natl Acad Sci U S A 2009;106:16157-62.
4. Sugahara KN, Teesalu T, Karmali PP, Kotamraju VR, Agemy L, Girard OM, et al. Tissue-penetrating delivery of compounds and nanoparticles into tumors. Cancer Cell 2009;16:510-20.
5. Sugahara KN, Teesalu T, Karmali PP, Kotamraju VR, Agemy L, Greenwald DR, et al. Coadministration of a tumor-penetrating peptide enhances the efficacy of cancer drugs. Science 2010;328:1031-5.
6. Roth L, Agemy L, Kotamraju VR, Braun G, Teesalu T, Sugahara KN, et al. Transtumoral targeting enabled by a novel neuropilin-binding peptide. Oncogene 2012:31:3754-63.
7. Arap W, Pasqualini R, Ruoslahti E. Cancer treatment by targeted drug delivery to tumor vasculature in a mouse model. Science 1998;279:377-80.
8. Koivunen E, Gay DA, Ruoslahti E. Selection of peptides binding to the alpha 5 beta 1 integrin from phage display library. J Biol Chem 1993;268:20205-10.
9. Curnis F, Longhi R, Crippa L, Cattaneo A, Dondossola E, Bachi A, et al. Spontaneous formation of L-isoaspartate and gain of function in fibronectin. J Biol Chem 2006;281:36466-76.
10. Spitaleri A, Mari S, Curnis F, Traversari C, Longhi R, Bordignon C, et al. Structural basis for the interaction of isoDGR with the RGD-binding site of alphavbeta3 integrin. J Biol Chem 2008;283:19757-68.
11. Curnis F, Arrigoni G, Sacchi A, Fischetti L, Arap W, Pasqualini R, et al. Differential binding of drugs containing the NGR motif to CD13 isoforms in tumor vessels, epithelia, and myeloid cells. Cancer Res 2002;62:867-74.

12. Pasqualini R, Koivunen E, Kain R, Lahdenranta J, Sakamoto M, Stryhn A, et al. Aminopeptidase N is a receptor for tumor-homing peptides and a target for inhibiting angiogenesis. Cancer Res 2000;60:722-7.

13. Corti A, Curnis F. Tumor vasculature targeting through NGR peptide-based drug delivery systems. Curr Pharm Biotechnol 2011;12:1128-34.

14. Corti A, Pastorino F, Curnis F, Arap W, Ponzoni M, Pasqualini R. Targeted drug delivery and penetration into solid tumors. Med Res Rev 2012;32:1078-91.

15. Corti A, Curnis F, Arap W, Pasqualini R. The neovasculature homing motif NGR: more than meets the eye. Blood 2008;112:2628-35.

16. Curnis F, Sacchi A, Borgna L, Magni F, Gasparri A, Corti A. Enhancement of tumor necrosis factor alpha antitumor immunotherapeutic properties by targeted delivery to aminopeptidase N (CD13). Nat Biotechnol 2000;18:1185-90.

17. Agemy L, Sugahara KN, Kotamraju VR, Gujraty K, Girard OM, Kono Y, et al. Nanoparticle-induced vascular blockade in human prostate cancer. Blood 2010;116:2847-56.

18. Teesalu T, Sugahara KN, Ruoslahti E. Mapping of Vascular ZIP Codes by Phage Display. Methods Enzymol 2012;503:35-56.

19. Curnis F, Cattaneo A, Longhi R, Sacchi A, Gasparri AM, Pastorino F, et al. Critical role of flanking residues in NGR-to-isoDGR transition and CD13/integrin receptor switching. J Biol Chem 2010;285:9114-23.

20. Agemy L, Friedmann-Morvinski D, Kotamraju VR, Roth L, Sugahara KN, Girard OM, et al. Targeted nanoparticle enhanced proapoptotic peptide as potential therapy for glioblastoma. Proc Natl Acad Sci U S A 2011;108:17450-5

21. Mayer LD, Dougherty G, Harasym TO, Bally MB. The role of tumor-associated macrophages in the delivery of liposomal doxorubicin to solid murine fibrosarcoma tumors. J Pharmacol Exp Ther 1997;280:1406-14.

22. Colombo G, Curnis F, De Mori GM, Gasparri A, Longoni C, Sacchi A, et al. Structure-activity relationships of linear and cyclic peptides containing the NGR tumor-homing motif. J Biol Chem 2002;277:47891-7.

23. Becker PM, Waltenberger J, Yachechko R, Mirzapoiazova T, Sham JS, Lee CG, et al. Neuropilin-1 regulates vascular endothelial growth factor-mediated endothelial permeability. Circ Res 2005;96:1257-65.

24. Corti A, Curnis F. Isoaspartate-dependent molecular switches for integrin-ligand recognition. J Cell Sci 2011;124:515-22.

25. Werle M, Bernkop-Schnurch A. Strategies to improve plasma half life time of peptide and protein drugs. Amino Acids 2006;30:351-67.

26. Haspel N, Zanuy D, Nussinov R, Teesalu T, Ruoslahti E, Aleman C. Binding of a C-end rule peptide to the neuropilin-1 receptor: a molecular modeling approach. Biochemistry 2011;50:1755-62.

27. Jubb AM, Strickland LA, Liu SD, Mak J, Schmidt M, Koeppen H. Neuropilin-1 expression in cancer and development. J Pathol 2012;226:50-60.

28. Laakkonen P, Porkka K, Hoffman JA, Ruoslahti E. A tumor-homing peptide with a targeting specificity related to lymphatic vessels. Nat Med 2002;8:751-5.

29. Fogal V, Zhang L, Krajewski S, Ruoslahti E. Mitochondrial/cell-surface protein p32/gC1qR as a molecular target in tumor cells and tumor stroma. Cancer Res 2008;68:7210-8.

30. Ruoslahti E, Bhatia SN, Sailor MJ. Targeting of drugs and nanoparticles to tumors. J Cell Biol 2010;188:759-68.

Figure legends

Fig. 1. iNGR shares the same receptor with CNGRC and, upon activation, strongly interacts with NRPs. (A) HUVECs were incubated for 2 hours at 4°C with FAM-labeled ARA (ARALPSQRSR;(28)), CNGRC, iNGR or iNGRt peptides. Cells were fixed and imaged with a Fluoview confocal microscope. Scale bars: 100 μm. (B and D) Tenfold excess of UV-inactivated RPARPAR or RPARPARA phage, or 1 μg/ml of control or neutralizing NRP-1 antibody was used to inhibit the binding (B) or the internalization (D) of CNGRC, iNGR or iNGRt phage in HUVECs. The results are shown as fold increase over insertless phage. * one way ANOVA < 0.05. Error bars: Standard Error. (C) Dose-dependent inhibition of iNGR phage binding to HUVECs by UV-inactivated phage. iNGR phage binding without inhibitors was considered as 100%. Error bars: Standard Error. (E and F) Dose-dependent binding of phage to purified NRP-1 (E) or NRP-2 (F) proteins. The number of phage bound to the proteins was quantified using a combination of a rabbit anti-T7 phage antibody and an HRP-labeled goat anti-rabbit antibody.

Fig. 2. iNGR penetrates deeper to tumors than NGR. (A) Expression of CD13, NRP-1, and NRP-2 on 4T1 cells analyzed by flow cytometry. The profiles represent the values of cells stained with appropriate antibodies (solid lines) or an isotype control (shaded). (B) Explanted 4T1 tumors were incubated with insertless, CNGRC, iNGR or iRGD phage. Phage bound to the tumor surface were removed with acid wash, and the number of phage particles that penetrated into the tumors was quantified by phage titration. Results are shown as fold increase over insertless phage. Each value was normalized against tumor weight. * one way

ANOVA < 0.05. Error bars: Standard Error. (C) Tumor dipping assays were performed as in (B), and frozen tumor sections were stained with an anti-T7 phage antibody (green) and DAPI (blue). Scale bars: 100μm.

Fig. 3. Systemic iNGR selectively accumulates and penetrates tumors. (A-B) *In vivo* phage homing to orthotopic 4T1 tumors. Phage were intravenously injected into 4T1 bearing mice and allowed to circulate for 40 minutes. After perfusion of the mice, tissues were collected and homogenized for phage titration (A) or processed for phage (green) and CD31 (red) immunostaining (B). Blue represents DAPI staining. In some cases, iNGR phage was co-injected with 50 μg of neutralizing NRP-1 or rabbit IgG antibody (B, lower panels). * one way ANOVA < 0.05. Scale bars: 50μm. Error bars: Standard Error (C-E) *In vivo* peptide homing to 4T1 tumors. One hundred micrograms of FAM-peptides (green) were intravenously injected into 4T1 bearing mice. One hour later, the mice were perfused, and tissues were collected and imaged under a UV light table (C and E). Then, the tissues were processed for CD31 (red) and nuclei (blue) staining (D) Scale bars: 50μm. (F) *In vivo* homing of NWs to 4T1 tumors. CNGRC- or iNGR-coated NWs (green) were injected into the tail vein of 4T1 tumor mice. After 4 hours, the mice were perfused, and tumors were collected and subjected to CD31 staining (red). Blue represents DAPI staining. Confocal images at 20x and 40x magnifications are shown. Scale bars: 100μm (20x), 50μm (40x). The arrows point to blood vessels positive for phage (B) or peptide (D). Note that the iNGR phage, peptides, and NWs effectively penetrated 4T1 tumors, and that the anti-NRP-1 antibody inhibited the tumor penetration of iNGR phage.

Fig. 4. iNGR triggers tumor-specific penetration of co-administered compounds. (A and B) One milligram of Evans Blue dye was intravenously co-injected with 4 μmol/kg of peptides or PBS. After 40 minutes of circulation, the mice were extensively perfused, and tumors were collected for imaging under white light (A). Evans blue was extracted from the collected tumors and organs and quantified by OD_{600} measurement (B). (C) Five mg/kg of FAM-CGKRK-conjugated NWs (green) were injected with or without 4 μmol/kg of iNGR peptide into the tail vein of 4T1 bearing mice. After 5 hours of circulation, tumors were collected for CD31 immunostaining (red). Blue represents DAPI staining. Two representative images of three tumors are shown. Scale bars: 100μm. (D) Ten mg/kg of DOX was intravenously co-injected with 4 μmol/kg of the indicated peptides in 4T1-bearing mice. After 1 hour of circulation, the mice were extensively perfused, and the tissues were collected for DOX quantification. Results are shown as fold increase over DOX alone. * one way ANOVA < 0.05. Error bars: Standard Error.

Fig. 5. iNGR enhances efficacy of anticancer drugs without affecting side effects. (A) Mice bearing orthotopic 4T1 tumors were treated every other day with PBS or 3 mg/kg of DOX combined with 4 μmol/kg of CNGRC or iNGR peptide. Tumor growth was assessed every other day. (B) Body weight changes of the tumor mice from the treatment studies in (A). Percent body weight shift is shown. * two-way ANOVA < 0.05. *** two-way ANOVA < 0.001. Error bars: Standard Error.

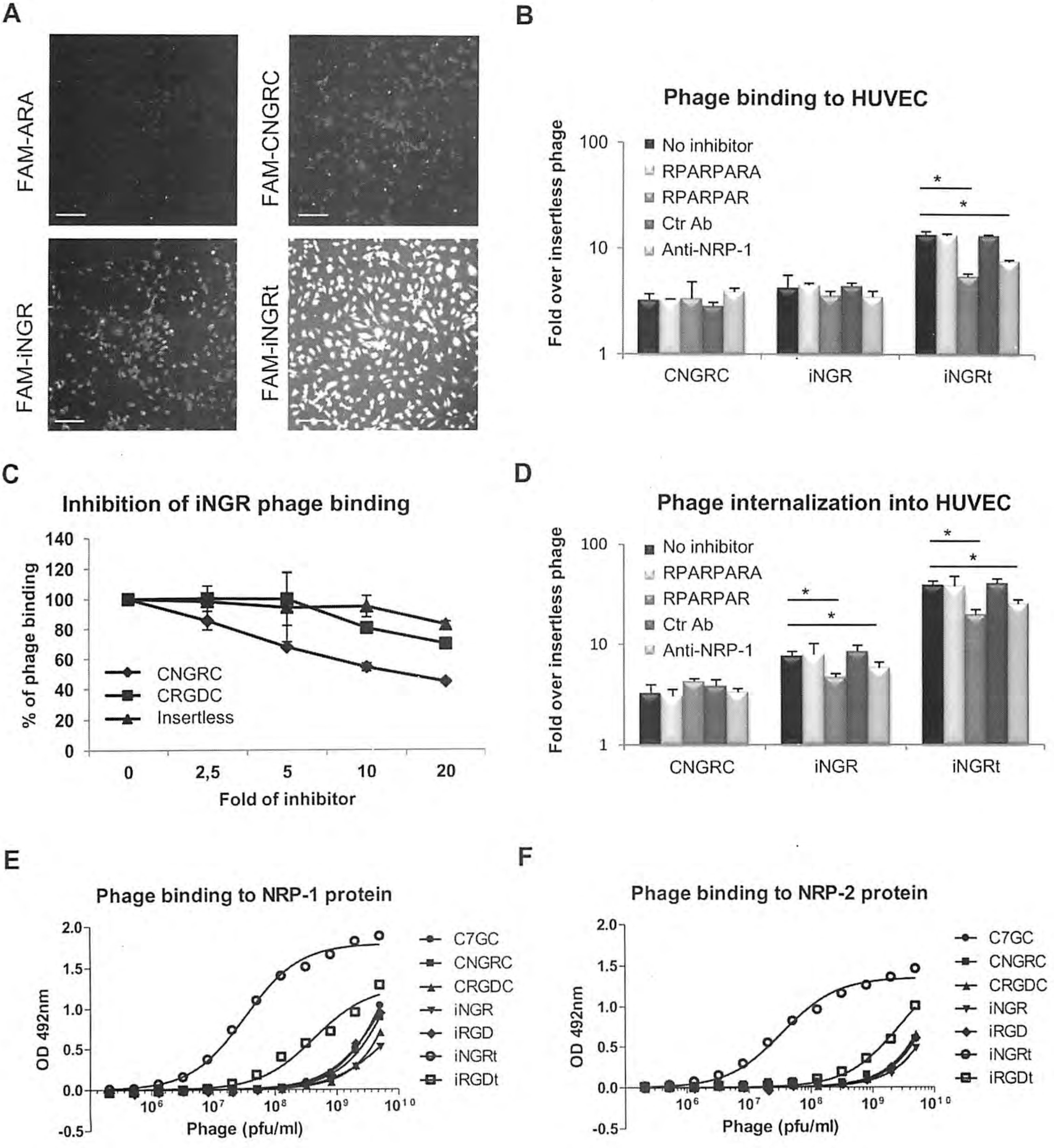
A
FAM-ARA
FAM-CNGRC
FAM-iNGR
FAM-iNGRt
B
Phage binding to HUVEC
Fold over insertless phage
100
10
1
No inhibitor
RPARPARA
RPARPAR
Ctr Ab
Anti-NRP-1
*
*
CNGRC
iNGR
iNGRt
C
Inhibition of iNGR phage binding
% of phage binding
140
120
100
80
60
40
20
0
CNGRC
CRGDC
Insertless
0
2,5
5
10
20
Fold of inhibitor
D
Phage internalization into HUVEC
Fold over insertless phage
100
10
1
No inhibitor
RPARPARA
RPARPAR
Ctr Ab
Anti-NRP-1
*
*
*
*
CNGRC
iNGR
iNGRt
E
Phage binding to NRP-1 protein
OD 492nm
2.0
1.5
1.0
0.5
0.0
-0.5
10^6
10^7
10^8
10^9
10^{10}
Phage (pfu/ml)
C7GC
CNGRC
CRGDC
iNGR
iRGD
iNGRt
iRGDt
F
Phage binding to NRP-2 protein
OD 492nm
2.0
1.5
1.0
0.5
0.0
-0.5
10^6
10^7
10^8
10^9
10^{10}
Phage (pfu/ml)
C7GC
CNGRC
CRGDC
iNGR
iRGD
iNGRt
iRGDt

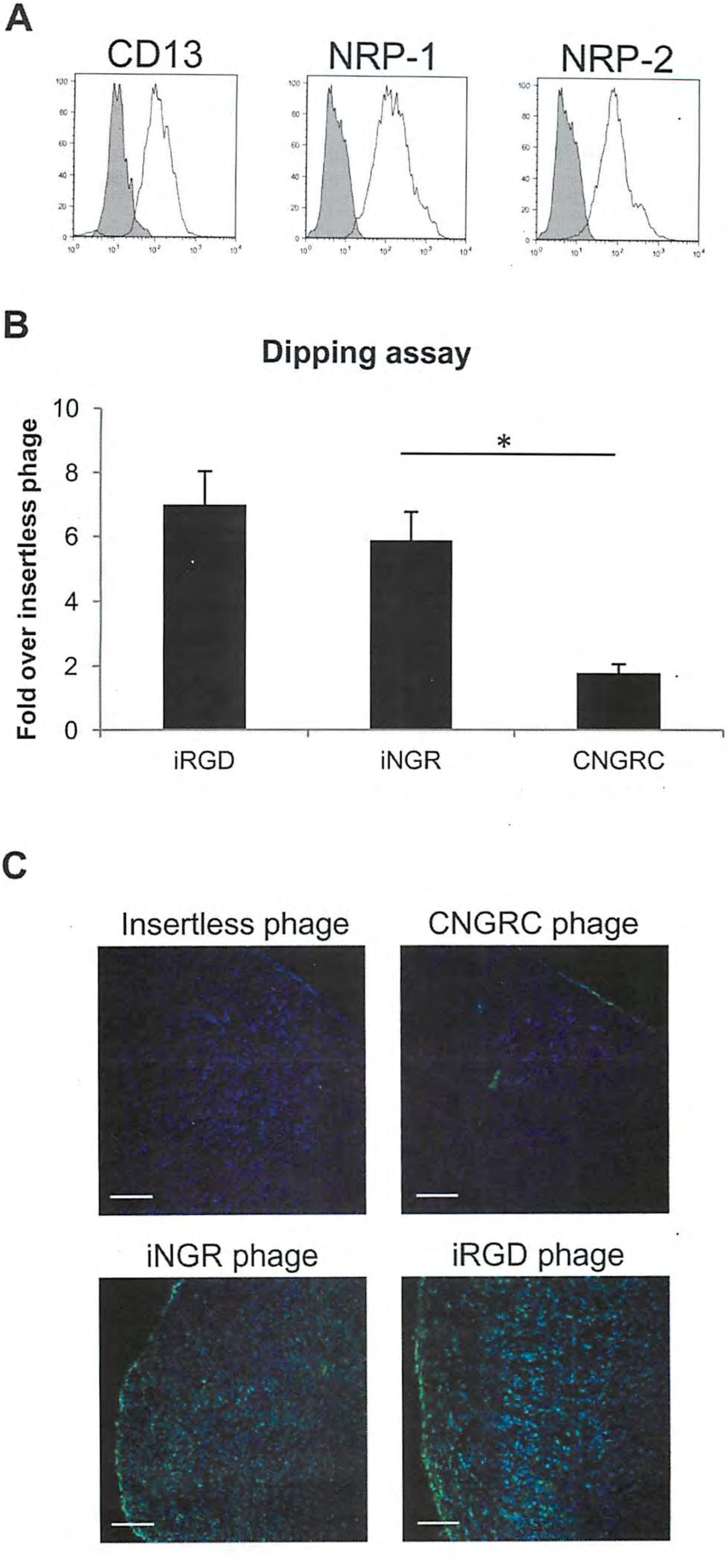
A
CD13
NRP-1
NRP-2
100
80
60
40
20
0
10^0
10^1
10^2
10^3
10^4
B
Dipping assay
Fold over insertless phage
10
8
6
4
2
0
*
iRGD
iNGR
CNGRC
C
Insertless phage
CNGRC phage
iNGR phage
iRGD phage

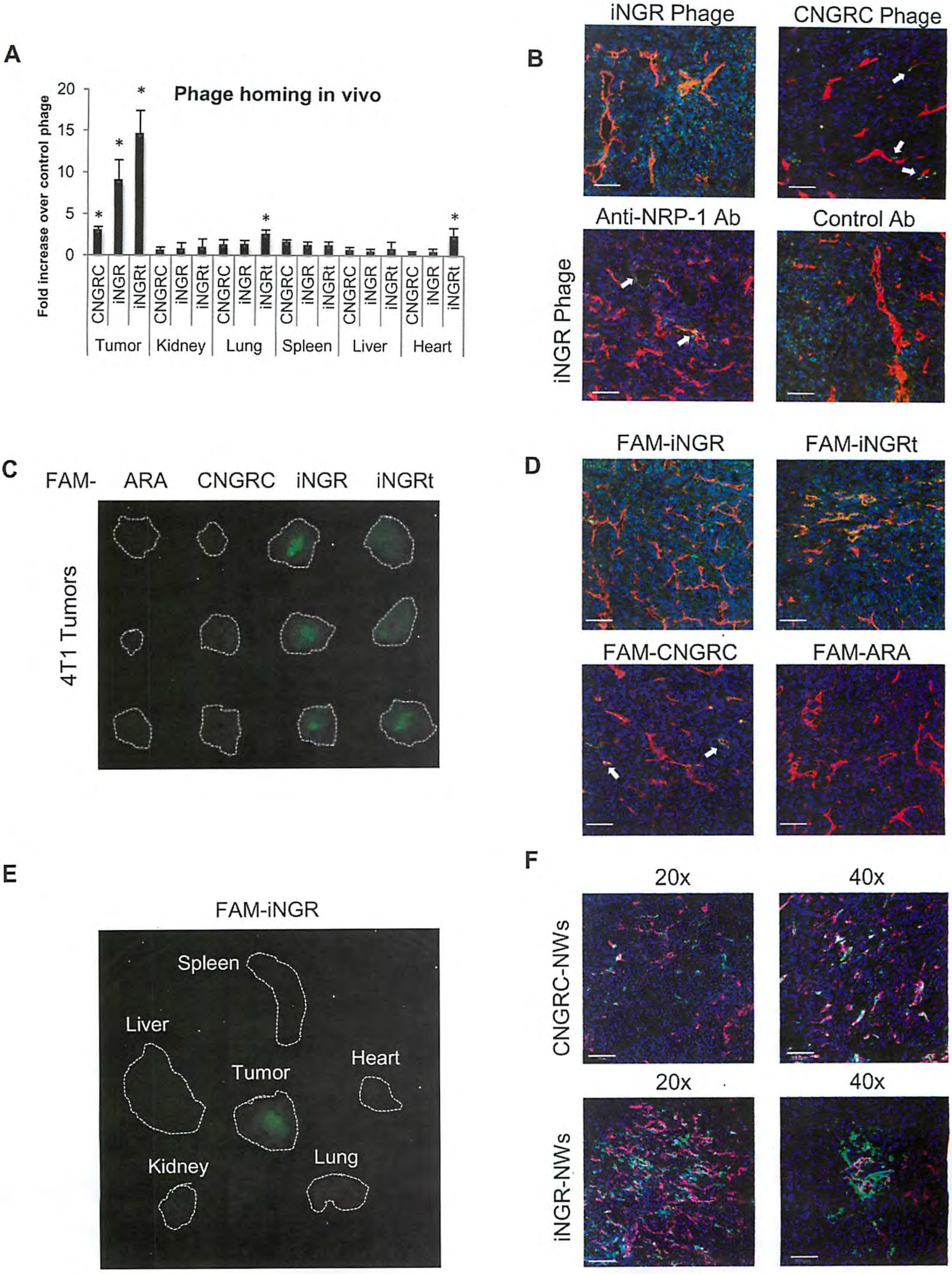
A
Phage homing in vivo
Fold increase over control phage
20
15
10
5
0
*
CNGRC
iNGR
iNGRt
Tumor
Kidney
Lung
Spleen
Liver
Heart
B
iNGR Phage
CNGRC Phage
Anti-NRP-1 Ab
Control Ab
iNGR Phage
C
FAM-
ARA
CNGRC
iNGR
iNGRt
4T1 Tumors
D
FAM-iNGR
FAM-iNGRt
FAM-CNGRC
FAM-ARA
E
FAM-iNGR
Spleen
Liver
Heart
Tumor
Kidney
Lung
F
20x
40x
CNGRC-NWs
iNGR-NWs

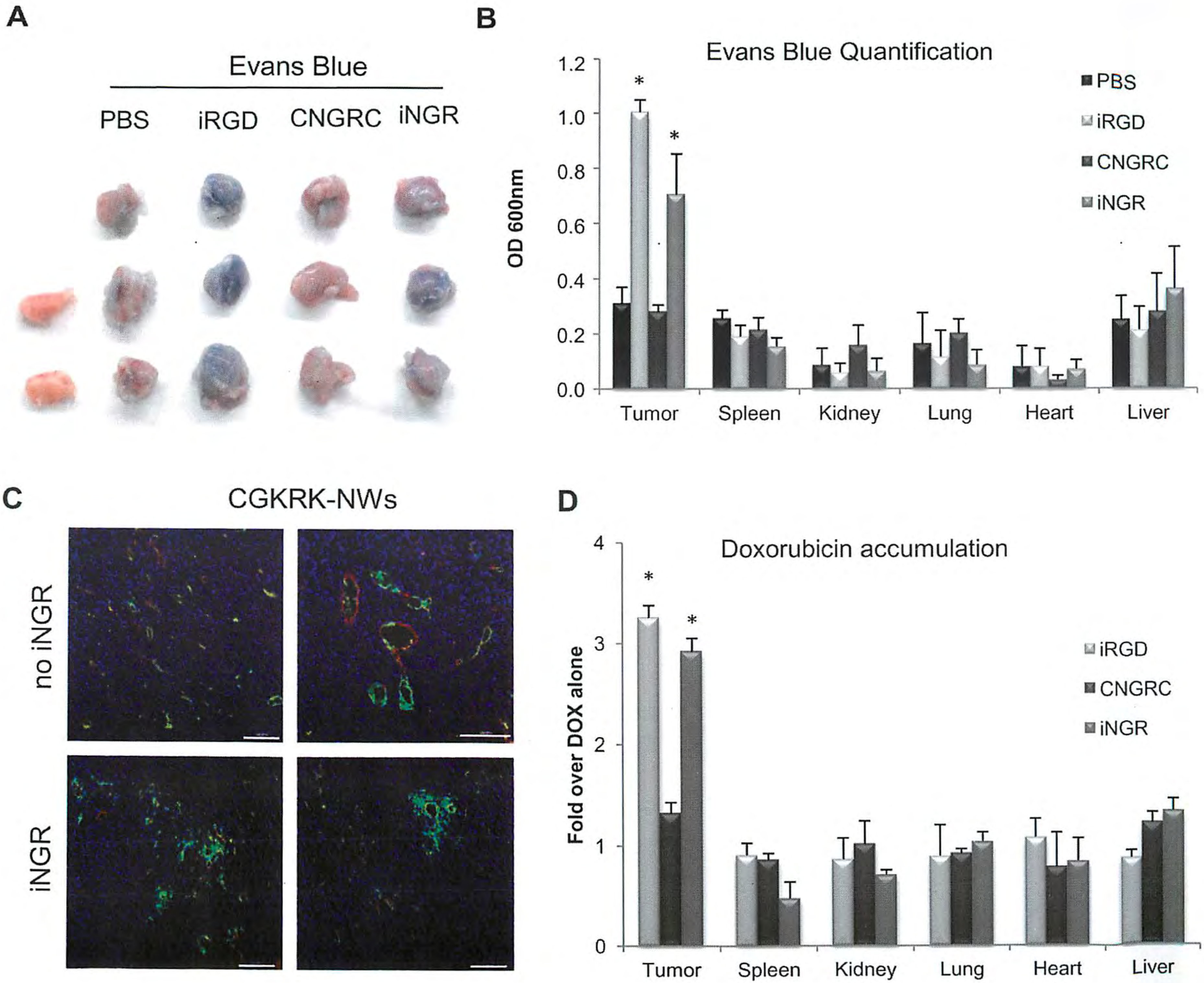
A
Evans Blue
PBS
iRGD
CNGRC
iNGR
B
Evans Blue Quantification
OD 600nm
1.2
1.0
0.8
0.6
0.4
0.2
0.0
*
*
PBS
iRGD
CNGRC
iNGR
Tumor
Spleen
Kidney
Lung
Heart
Liver
C
CGKRK-NWs
no iNGR
iNGR
D
Doxorubicin accumulation
Fold over DOX alone
4
3
2
1
0
*
*
iRGD
CNGRC
iNGR
Tumor
Spleen
Kidney
Lung
Heart
Liver

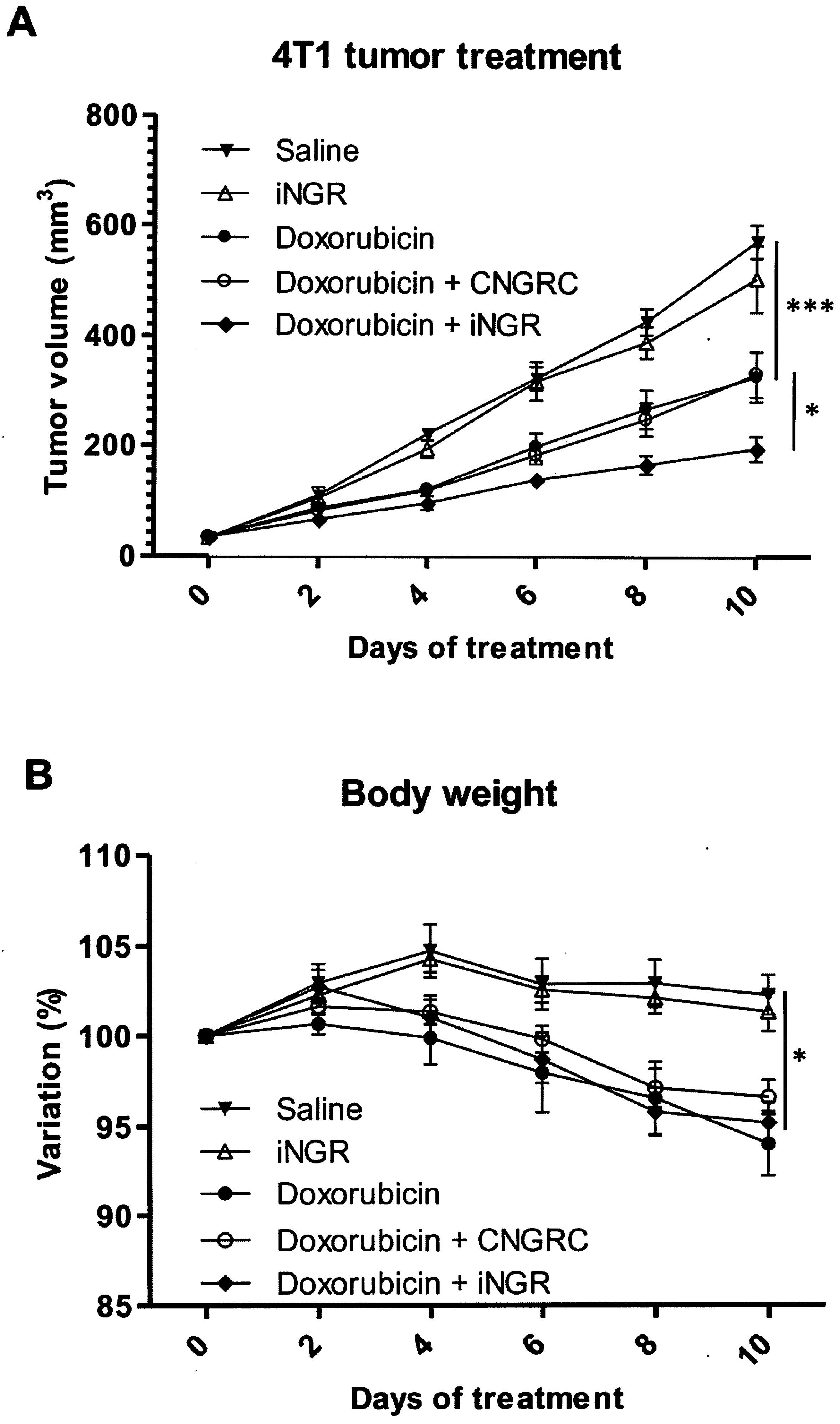
A
4T1 tumor treatment
Tumor volume (mm^3)
800
600
400
200
0
Saline
iNGR
Doxorubicin
Doxorubicin + CNGRC
Doxorubicin + iNGR
***
*
0
2
4
6
8
10
Days of treatment
B
Body weight
Variation (%)
110
105
100
95
90
85
*
Saline
iNGR
Doxorubicin
Doxorubicin + CNGRC
Doxorubicin + iNGR
0
2
4
6
8
10
Days of treatment

Supplementary

De Novo Design of a Tumor-Penetrating Peptide

Luca Alberici[1,2,3], Lise Roth[4], Kazuki N. Sugahara[1], Lilach Agemy[1], Venkata R. Kotamraju[1], Tambet Teesalu[1], Claudio Bordignon[2,3], Catia Traversari[2], Gian-Paolo Rizzardi[2], Erkki Ruoslahti[1]

Materials and Methods

ELISA. MicroTest III Flexible assay plates (BD, San Jose, CA) were coated with 5 µg/ml of recombinant human NRP-1 (R&D Systems, Minneapolis, MN), recombinant human NRP-2 Fc chimera (R&D Systems), or recombinant human integrin αvβ3 (R&D Systems). The coated plates were blocked with 0.5% BSA in PBS for 1 hour, and incubated with serial dilutions of phage for 2 hours at 4°C. The wells were washed with PBS containing 0.05% Tween20, and incubated with a rabbit anti-T7 phage antibody (3). After 1 hour at 4°C, the wells were washed and incubated with an HRP-labeled anti-rabbit antibody (Sigma-Aldrich) for 1 hour at 4°C. o-Phenylenediamine dihydrochloride (SigmaFast OPD; Sigma-Aldrich) was used as a substrate to quantify the amount of the HRP-labeled antibody captured on the microtiter wells. The reaction was stopped using 3 M H_2SO_4 and the absorbance at 492 nm was measured using a Labsystems Multiskan Plus (Fisher Scientific, Pittsburgh, PA).

Flow Cytometry: Adherent cells were detached using enzyme free dissociation buffer (Gibco). Incubations and washes were performed in PBS containing 3% FBS with the following antibodies at the dilution of 1:100. Primary antibodies: rat IgG (Santa Cruz Biotechnology, Santa Cruz, CA), rat anti-mouse CD13 (R363, GeneTex, Irvine, CA), rabbit IgG (Santa Cruz Biotechnology), rabbit anti-mouse NRP-1 (Millipore, Billerica, MA), rabbit anti-mouse NRP-2 (Millipore), mouse IgG (AbD Serotech, Raleigh, NC), mouse anti-human CD13 (WM15, Santa Cruz Biotechnology, Santa Cruz, CA), mouse anti-human NRP-1 (Miltenyi Biotec, Bergisch Gladbach, Germany) and mouse anti-human NRP-2 (R&D Systems). Secondary antibodies: FITC-labeled goat anti-rabbit (Invitrogen, Grand Island, NY), Alexa-488-labeled goat anti-rat (Invitrogen) antibodies and PE-labeled goat anti-mouse (Southern Biotech, Birmingham, AL).. Fluorescence was detected using a FACSort (BD Bioscience, San Jose, CA).

Cell lines and tumor models: The human leukemic monocyte lymphoma cell line U937 was cultured in RPMI supplemented with 10% FBS and penicillin/streptomycin. The Human pancreatic cell line BxPC-3 was cultured in DMEM supplemented with 10% FCS and penicillin/streptomycin. Ectopic BxPC3, tumors were generated by s.c. injection of 10^6 cells into athymic nude mice. Mouse Lewis Lung Carcinoma (LLC) and CT26 colon carcinoma were cultured in standard conditions. LLC ($1x10^5$) and CT26 ($4x10^5$) cells were s.c. injected into syngeneic C57BL/6 mice and BALB/c mice (Charles River Laboratories), respectively.

Peptide fragment isolation and analyses: Peptide fragment isolation and mass spectrometry analyses were performed using the protocol provided for FAM-iRGD isolation from cells (Sugahara et al. Cancer Cell, *16:* 510-520, 2009).

Figure legends

Supplementary Table 1. Peptide description. ID and sequence in single letter amino acid code of each peptide is shown.

Supplementary Fig. 1. HUVECs express NGR and CendR motif receptors. Expression of CD13, NRP-1, and NRP-2 on HUVECs analyzed by flow cytometry. The profiles represent the values of cells stained with appropriate antibodies (solid lines) or an isotype control (shaded).

Supplementary Fig. 2. iNGR does not bind to CD13$^+$ monocytes. (A) Expression of CD13, NRP-1, and NRP-2 on U937 monocytes analyzed by flow cytometry. The profiles represent the values of cells stained with appropriate antibodies (solid lines) or an isotype control (shaded). (B) Binding and (C) internalization of indicated T7 phage into U937 cells. Results are reported as fold increase over insertless phage binding/internalization. Error bars: Standard Error.

Supplementary Fig. 3. iNGR binding is not mediated by αv integrins. (A) Dose-dependent inhibition of iRGD phage binding to HUVECs by UV-inactivated phage. iRGD phage binding without inhibitors was considered as 100%. Error bars: Standard Error. (B) Dose-dependent binding of phage to purified αvβ3 integrin. Some of the phage were pre-incubated in 0.1 M ammonium bicarbonate for 6 hours at 37°C to induce deamidation of asparagine into isoaspartic acid in the peptides and then probed on αvβ3 coated plates. The number of phage that bound to the protein was quantified with ELISA using a combination of a rabbit anti-T7 phage antibody and an HRP-labeled goat anti-rabbit antibody.

Supplementary Fig. 4. iNGR is cleaved upon entering the cells. Mass-Spectrometry of intact FAM-NGR and FAM-iNGR peptides (first 2 lanes) and peptide fragments isolated from inside HUVECs (lanes 3 to 5). HUVECs were incubated without any peptides or with FAM-CNGRC or FAM-iNGR for 1 hour in the presence of a proteasome inhibitor MG132. The cells were lysed, and FAM-peptide fragments were recovered by immunoprecipitation with an anti-FAM antibody from the cell lysates. Note the presence of FAM-CRNGR peptides (m/z: 1076.527) only in the bottom panel. X: 6-aminoesanoic acid used as linker.

Supplementary Fig. 5. iNGR penetrates into extravascular tumor tissue. (A) Peptide accumulation in human pancreatic BxPC3 tumors. FAM-peptides (100 μg; green) were intravenously injected into BxPC3-bearing mice. One hour later, the mice were perfused, and tissues were collected and imaged under a UV light table. Tum, Tumor; B, brain; K, kidney; Lu, lung; H, heart; P, pancreas, S, spleen. (B) FAM-NGR and FAM-iNGR NWs penetration into the tumor was quantified. Results are expressed as μm^2 of NW positive area per field. * $p<0.05$.

Supplementary Fig. 6. iNGR does not increase the penetration of co-administered Evans blue dye into normal organs. Mice bearing 4T1 tumors were intravenously injected with 1 mg of Evans blue combined with PBS or 4 μmol/kg of the indicated peptides. After 40 minutes of circulation, the mice were extensively perfused, and the organs were collected for imaging under white light. T, tumor; S, spleen; K, kidney; Lu, lung; H, heart; Liv, liver.

Supplementary Fig. 7. iNGR enhances tumor penetration of Evans Blue dye. Evans Blue (1 mg) was intravenously co-injected with of peptides (4 μmol/kg) or PBS into mice bearing either LLC (A) or CT26 (B) tumors. After 40 minutes of circulation, mice were extensively perfused and tumors were collected. Evans Blue was extracted from the tumors and kidneys and quantified by OD_{600} measurement. Error bars: Standard Error. * $p<0.05$. **$p<0.005$.

Table S1

Peptide ID	Complete amino acid sequence
ARA	ARALPSQRSR
Insertless	SSVDKLAAALE
NGR	CNGRC (cyclized between the cysteines)
iNGR	CRNGRGPDC (cyclized between the cysteines)
iNGRt	CRNGR
RGD	CRGDC (cyclized between the cysteines)
iRGD	CRGDKGPDC (cyclized between the cysteines)
iRGDt	CRGDK
RPARPAR	RPARPAR
RPARPARA	RPARPARA

Figure S1

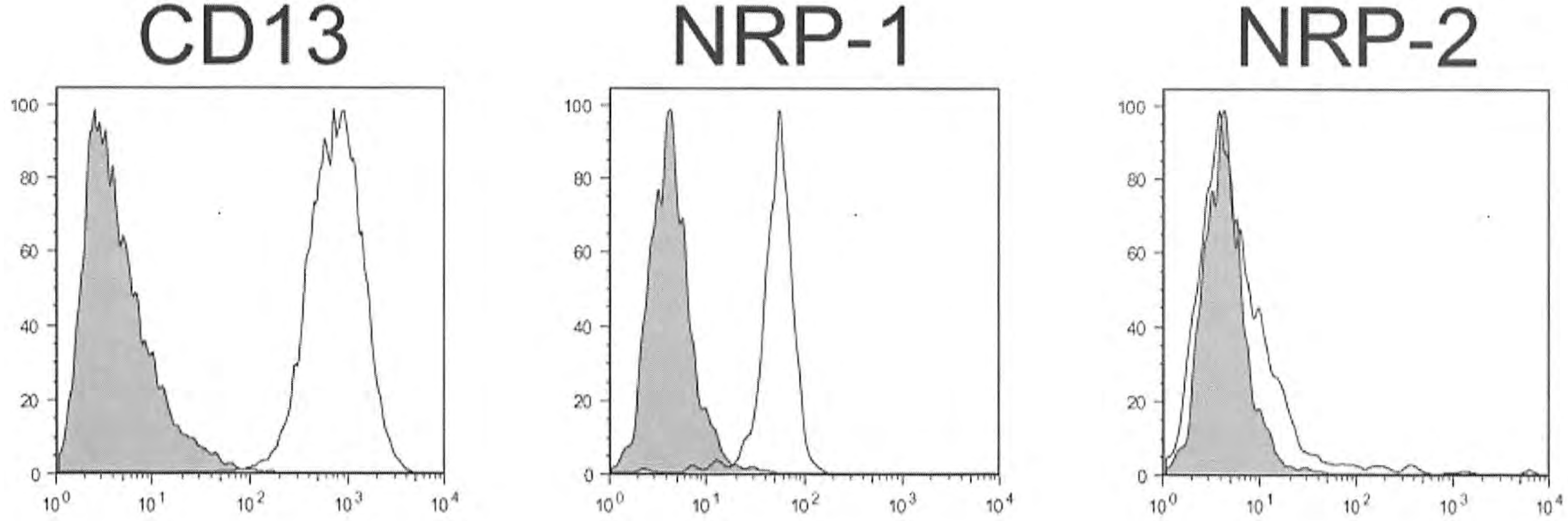

Figure S2

A

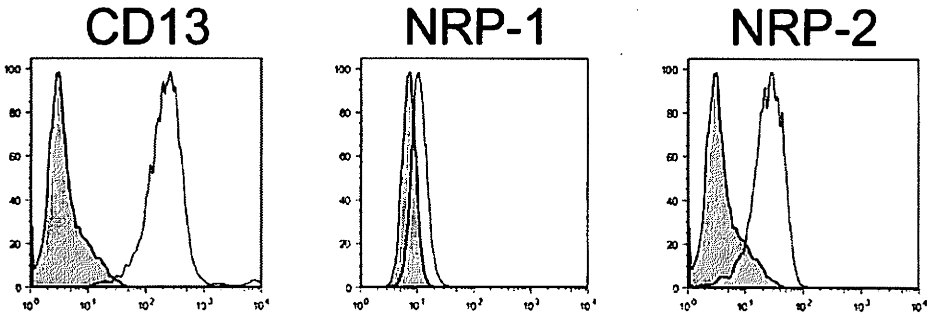

B

Phage binding to U937

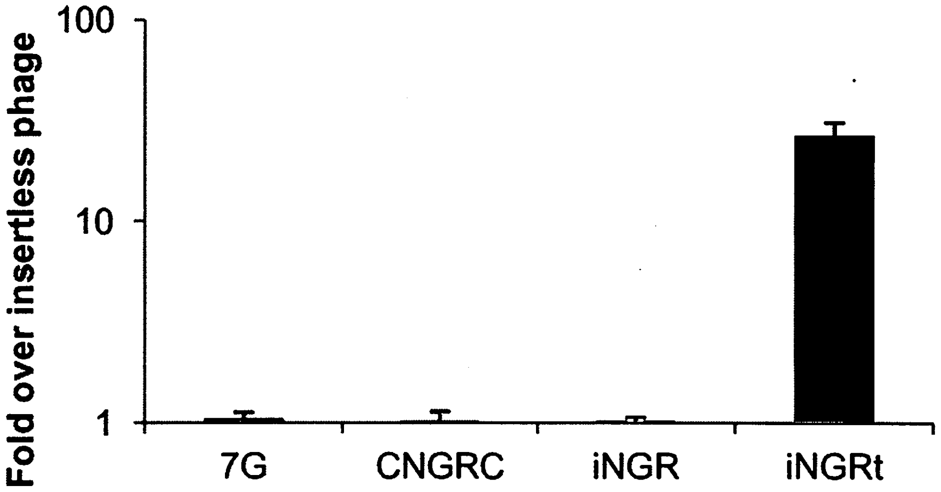

C

Phage internalization into U937

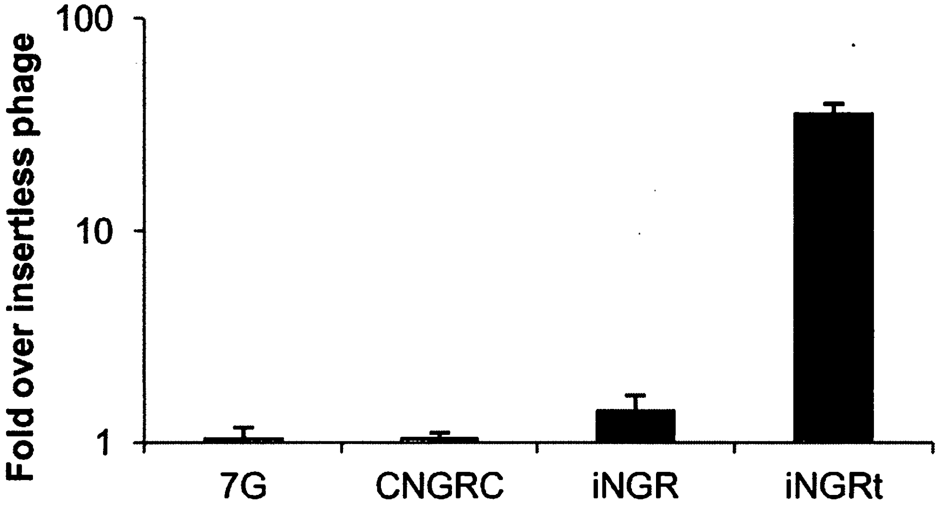

Figure S3

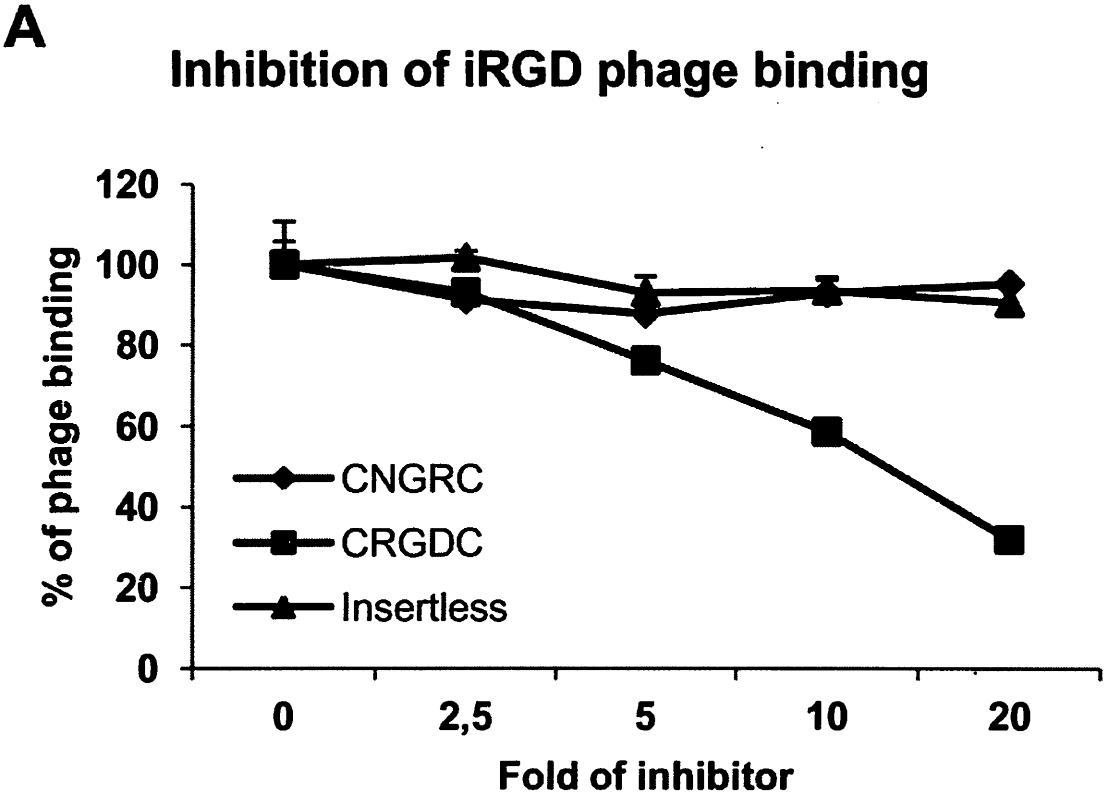
A
Inhibition of iRGD phage binding
% of phage binding
120
100
80
60
40
20
0
CNGRC
CRGDC
Insertless
0
2,5
5
10
20
Fold of inhibitor

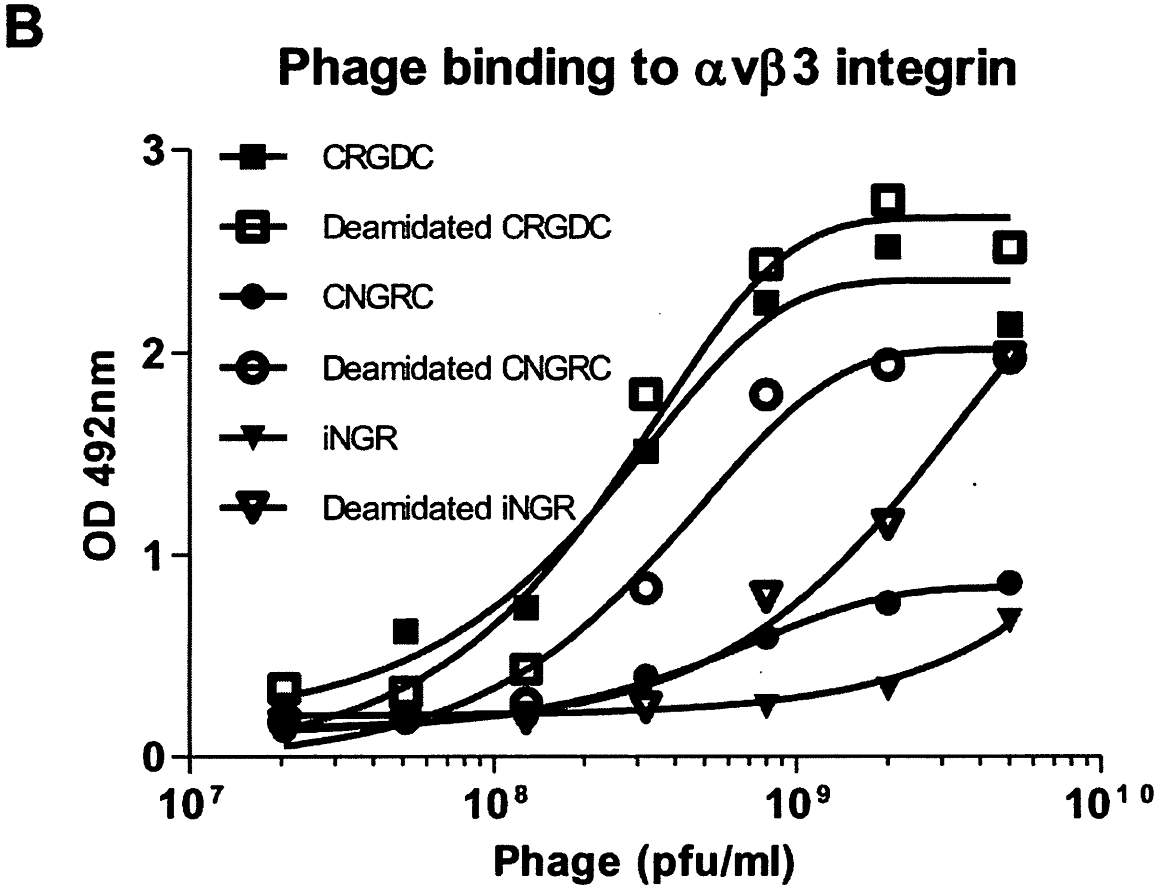
B
Phage binding to αvβ3 integrin
OD 492nm
3
2
1
0
CRGDC
Deamidated CRGDC
CNGRC
Deamidated CNGRC
iNGR
Deamidated iNGR
10^7
10^8
10^9
10^{10}
Phage (pfu/ml)

Figure S4


Purified peptides
FAM-CNGRC
FAM-iNGR
Peptides from cells treated with
No peptide
FAM-CNGRC
FAM-iNGR
1020.020
FAM-X-CNGRC
1003.193
1058.269
1096.254
1165.270
FAM-X-CRNGRGPDC
1445.065
1241.211
1483.257
933.497
949.479
977.536
993.483
1021.539
1037.529
1065.569
1109.604
1125.589
1153.629
1169.586
1197.625
1241.669
1285.665
933.649
949.607
977.665
993.637
1021.676
1037.670
1065.731
1109.752
1153.777
1197.784
1076.527
FAM-X-CRNGR
933.737
977.746
993.792
1021.802
1037.774
1109.842
1154.801
1197.850
1000
1100
1200
1300
1400
1500
m/z

Figure S5

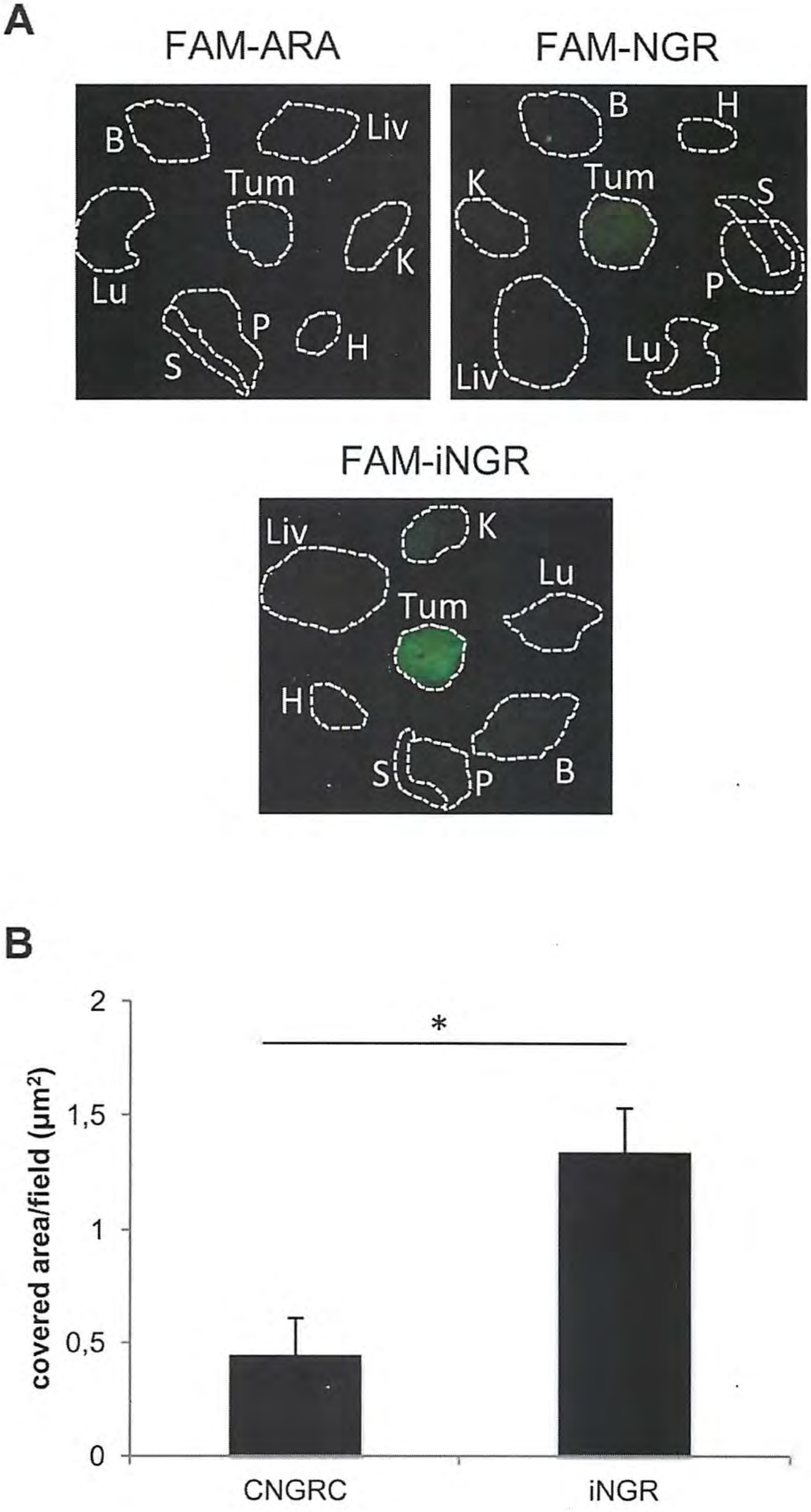
A
FAM-ARA
B
Liv
Tum
Lu
K
S
P
H
FAM-NGR
B
H
K
Tum
S
P
Liv
Lu
FAM-iNGR
Liv
K
Lu
Tum
H
S
P
B
B
covered area/field (µm²)
2
1,5
1
0,5
0
*
CNGRC
iNGR

Figure S6

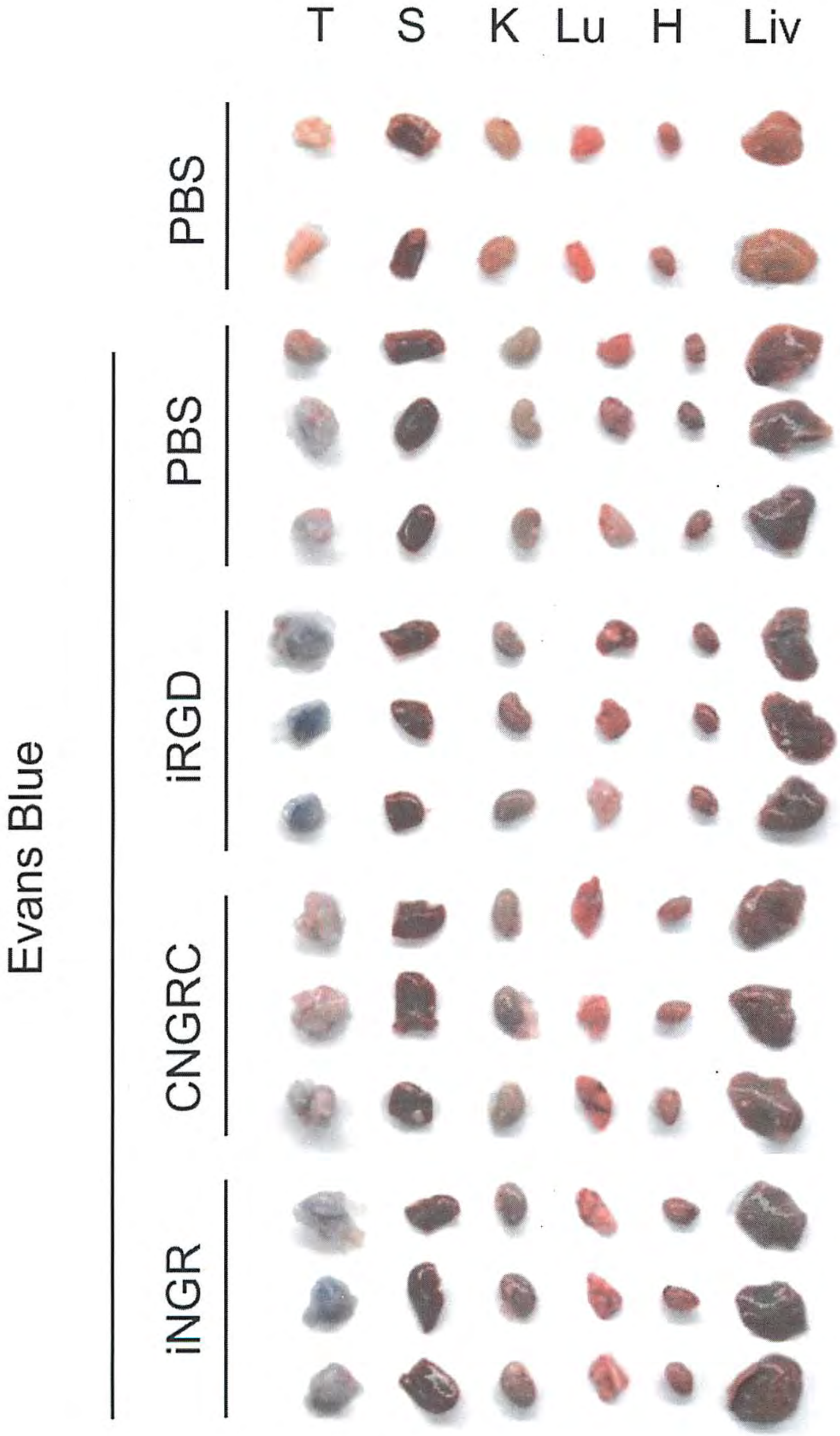

Figure S7

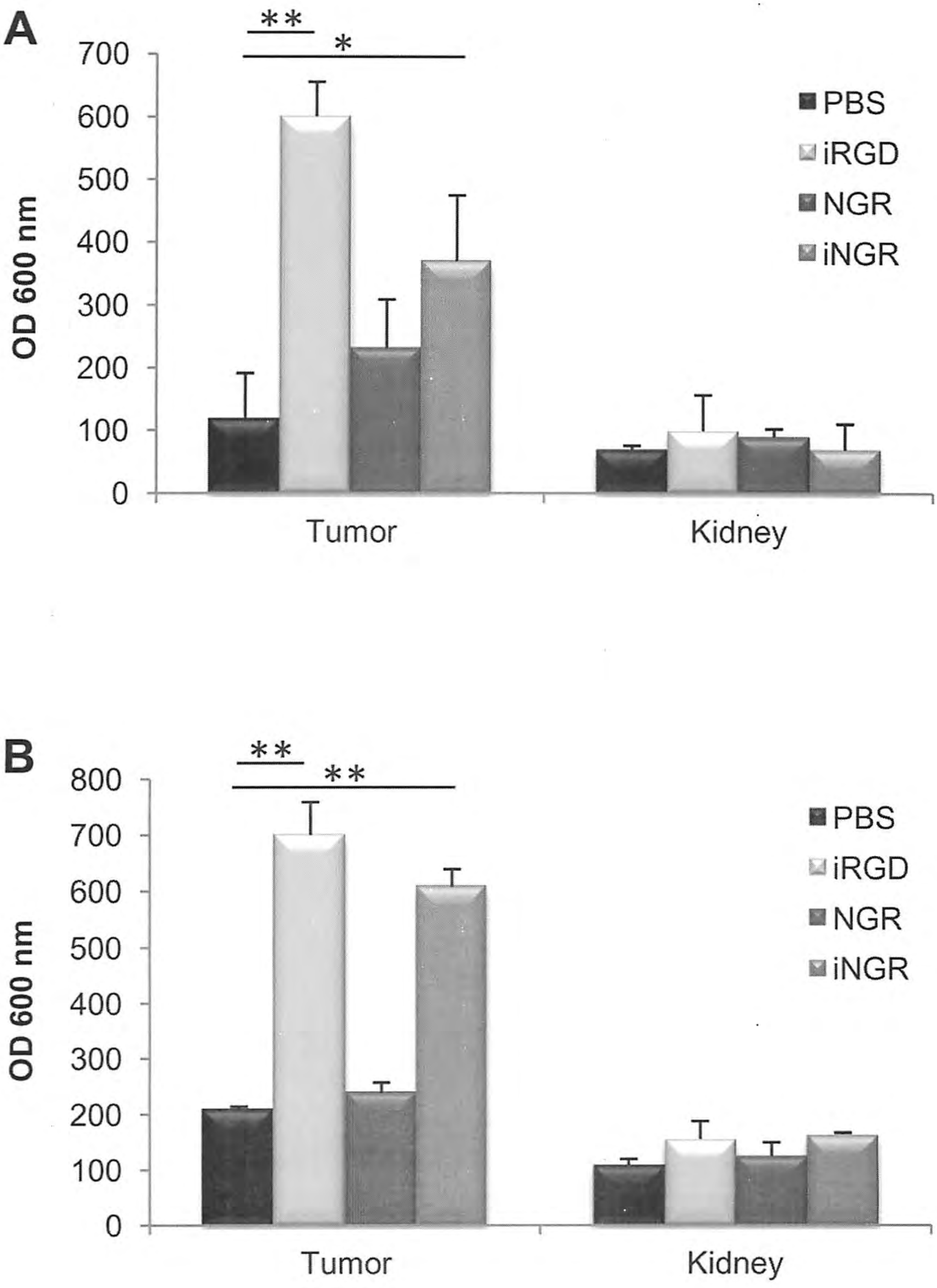
A
**
*
700
600
500
400
300
200
100
0
OD 600 nm
PBS
iRGD
NGR
iNGR
Tumor
Kidney
B
**
**
800
700
600
500
400
300
200
100
0
OD 600 nm
PBS
iRGD
NGR
iNGR
Tumor
Kidney

uicc
global cancer control

IJC
International Journal of Cancer

Intratumoral injection of interferon-α and systemic delivery of agonist anti-CD137 monoclonal antibodies synergize for immunotherapy

Juan Dubrot[1], Asis Palazón[1], Carlos Alfaro[1], Arantza Azpilikueta[1], María Carmen Ochoa[1], Ana Rouzaut[1], Iván Martinez-Forero[1], Alvaro Teijeira[1], Pedro Berraondo[1], Agnes Le Bon[2], Sandra Hervás-Stubbs[1] and Ignacio Melero[1]

[1] CIMA and Clinica Universitaria, Universidad de Navarra, Pamplona, Spain
[2] Faculté Necker, INSERM U591, Paris, France

CD137 artificial costimulation results in complete tumor rejection in several mouse models. Type I interferons (IFN) exert antitumor effects through an array of molecular functions on malignant cells, tumor stroma and immune system cells. The fact that agonist anti-CD137 mAb induce tumor regressions in mice deficient in the unique receptor for Type I IFNs (IFNAR$^{-/-}$) indicated potential for treatment combinations. Indeed, combination of intratumor injections of mouse IFN-α and intraperitoneal injections of anti-CD137 mAb synergized as seen on subcutaneous lesions derived from the MC38 colon carcinoma, which is resistant to each treatment if given separately. Therapeutic activity was achieved both against lesions directly injected with IFN-α and against distant concomitant tumors. Experiments in bone marrow chimeras prepared with IFNAR$^{-/-}$ and WT mice concluded that expression of the receptor for Type I interferons is mainly required on cells of the hematopoietic compartment. Synergistic effects correlated with a remarkable cellular hyperplasia of the tumor draining lymph nodes (TDLNs). Enlarged TDLNs contained more plasmacytoid and conventional dendritic cells (DC) that more readily cross-presented. Importantly, numbers of both DC subtypes inversely correlated with the tumor size. Numbers of CD8 T cells specific for a dominant tumor antigen were increased at TDLNs by each separate treatment but only with slight augments due to the combination. Combined antitumor effects of the therapeutic strategy were also seen on subcutaneous TC-1 tumors established for 24 days before treatment onset. The described strategy is realistic because (*i*) agents of each kind are clinically available and (*ii*) equivalent procedures in humans are feasible.

Multiple genes encoding interferon-α constitute a family of highly homologous cytokines that share with interferon-β a single dimeric receptor expressed by most nucleated cells.[1] Type I interferons are physiologically involved in locally minimizing viral replication and inducing inflammatory and immune responses that control such infections.[2] These interferons are collectively named Type I interferons to distinguish them from interferon-γ or Type II interferon. Systemic interferon-α as a recombinant protein has demonstrated dramatic efficacy in a small fraction of patients suffering melanoma, renal cell carcinoma[3] and some hematological malignancies.[4] Antitumor effects of Type I IFNs are exerted not only on malignant cells[5,6] but also on nonmalignant cells of the tumor-bearing host. Interferon-α inhibits angiogenesis[6–8] and enhances innate[9] and adaptive[10] immune responses. Interestingly, those melanoma cases showing sustained clinical responses show autoimmunity signs.[11] On malignant cells, Type I IFNs induce signaling pathways that can eventually result in cell arrest and apoptosis.[12] On the immune system stimulating effects of Type I interferons are observable on natural killer (NK) cells,[9,13] T cells,[14] dendritic cells[15] and B cells.[16] All these leukocyte subsets are potentially involved in the antitumor activity.[17]

Involvement of Type I IFNs in immunosurveillance[18] against nascent chemically induced tumors has been experimentally described in mice.[19] Immunotherapy of cancer exploits these antitumor properties of IFN-α in an attempt to tackle already established malignancies.[3,8,20] An specialized leukocyte subpopulation termed plasmacytoid DC has been

Key words: Type I interferon, 4-1BB (CD137), combined immunotherapy, immunostimulatory monoclonal antibodies
Additional Supporting Information may be found in the online version of this article.
Grant sponsor: MEC/MICINN; **Grant numbers:** SAF2005-03131, SAF2008-03294; **Grant sponsor:** Redes Temáticas de Investigación Cooperativa RETIC; **Grant number:** RD06/0020/0065; **Grant sponsor:** Fondo de Investigación Sanitaria; **Grant number:** FIS PI060932; **Grant sponsor:** Departamento de Educación del Gobierno de Navarra, Departamento de Salud del Gobierno de Navarra (Beca Ortiz de Landázuri), European Commission VII Famework Program (ENCITE), SUDOE-IMMUNONET, Fundacion Mutua Madrileña, UTE for Project FIMA, Ministerio de Educación y Ciencia
DOI: 10.1002/ijc.25333
History: Received 1 Sep 2009; Accepted 2 Mar 2010; Online 22 Mar 2010

Correspondence to: Ignacio Melero, MD, PhD, Av Pio XII, 55, 31008 Pamplona, Spain, Fax: 34-948-194717, E-mail: imelero@unav.es

described to be in charge of producing large quantities of Type I INFs[21] when these specialized DCs detect biomolecules denoting viral features.[21,22]

CD137 is a surface glycoprotein that belongs to the TNFR family (4-1BB or TNFRSF-9).[23–26] It belongs to the subset of these molecules that do not encompass a death domain[26] and their main function seems to be costimulation of T lymphocytes.[27] It is expressed on activated but not resting T cells and has a clear role at inhibiting programmed cell death and promoting effector differentiation.[24,26,28] CD137 surface expression is not exclusive of activated T cells but is also present on activated NK cells[29] and other leukocyte populations including dendritic cells[30,31] and their precursors.[32] CD137 stimulation with antibodies[33] or other agonist moieties[34] enhances cellular immune responses against tumors achieving the clearance of transplanted malignancies in multiple experimental models.[24,33] Importantly, the efficacy of agonist anti-CD137 monoclonal antibodies can be enhanced by combinations with chemotherapy,[35,36] radiotherapy[37] or various types of cancer vaccines.[38–41] The main antitumor mechanism of action of anti-CD137 seems to be a selective costimulation of cytolytic T lymphocytes that have been primed by tumor antigens.[24,31,39]

Combination of systemic anti-CD137 and interleukin-12 gene transfer to tumor cells exerts synergistic therapeutic effects against several resistant tumors to each separate treatment.[42,43] Combination with other cytokines given either as proteins or genes has not been reported.

This study analyzes local intratumor release of recombinant interferon-α combined with systemic treatment with an agonist anti-CD137 mAb. The synergistic effects were absolutely dependent on Type I IFN receptor expression on the hemopoietic lineages of the tumor bearing hosts and correlated with increased numbers of conventional and plasmacytoid DC in the TDLNs.

Material and Methods

Cell lines and cultures

The murine colon adenocarcinoma cell line MC38 (H-2^b) was obtained from Lieping Chen (Johns Hopkins, Baltimore, MD) verified for identity by Johns Hopkins Genetic Resources Core Facility and cultured in RPMI 1640+Glutamax medium supplemented with 10% fetal calf serum (Gibco, Prat de Llobregat, Spain) and 50 μmol/l 2-mercaptoethanol. TC-1 cell line, a lung epithelial cell line transformed by the HPV-16 E6 and E7 oncogenes,[44] was cultured in the same conditions and verified to contain the HPV-E7 oncogenes and for cell identity.[44] EG.7 was obtained through ATCC and original vials were thawed for the experiments (Manassas, VA, CRL-2113).

Mice

Female C57BL/6 mice (age 6–9 weeks) were obtained from Harlan (Barcelona, Spain). IFNAR$^{-/-}$ mice backcrossed to C57Bl/6 background for 12 generations were obtained through Matthew Albert (Institute Pasteur, Paris, France). OT-I TCR-transgenic mice purchased from Jackson (Barcelona, Spain) are bred in our animal facility as described.[31] All animal handling and tumor experiments were approved by the institutional ethical committee in accordance with Spanish regulations (study 003/2007).

In vivo tumor experiments

For tumor implantation, mice were injected with EG.7, MC38 or TC-1 cells (5×10^5 cells per animal) s.c. in the right flank or in both flanks as detailed in each experiment. Tumor growth was monitored by measuring 2 perpendicular diameters with a digital caliper every 2–4 days. Intratumor injections were performed in 50 μl with 28 G needles.

Anti-CD137 monoclonal antibody and Type I interferon

Anti-CD137 mAb is produced from the 2A hybridoma,[38] kindly provided by Dr. Lieping Chen. The mAb produced by this hybridoma was purified from culture supernatant by affinity chromatography in sepharose protein G columns (GE Healthcare Bio-sciences AB, Uppsala, Sweden) dialized and quality controlled including determinations of lipopolysaccharide (LPS) concentration (Antibody BCN, Barcelona, Spain, as a contractor). Control IgG from rat serum was obtained from Sigma-Aldrich (UK).

Murine IFN-α_4 is obtained from a hybridoma cell line stable transfected with an expression plasmid pEE12 containing IFN-α_4.[15] IFN-α_4 was transfected in the NS0 murine melanoma cell line and cultured in selection media. These cells were subsequently cultured during a 10–15 days period at 5×10^5 cells/ml in serum free media supplemented with cholesterol lipid concentrate (Life Technologies, Carlsbad CA). IFN-α_4 bioactivity and concentration were quantified as described.[15] A culture in which there was not transfectants proliferation was used as control vehicle.

Generation of BM chimeric mice

Bone marrow (BM) chimeric mice were generated by irradiation of recipient mice (C57BL/6) with a single-lethal dose of 700 cGy. Recipient mice were then reconstituted with $2–5 \times 10^6$ donor BM cells. BM chimeric mice were kept on antibiotic-containing drinking water for 15 days and reconstituted for 8–10 weeks before use.

Cell proliferation assay

The 3-(4,5-dimethylthiazol-2-yl)-2,5-diphenyl tetrazolium bromide (MTT) colorimetric assay (Roche, Basel, Switzerland) was used to determine the direct effect of IFN-α on proliferation of MC38 cells. IFN-α was further diluted into a series of 1/2 dilutions (from 2,000 U/ml to 125 U/ml). MC38 cells were seeded at 2×10^3 cells per well in complete medium. The cells were incubated at 37°C in 5% CO_2 for 4 days. At indicated timepoints cultures received 10 μl MTT solution (5 mg/ml) and 4 hr later, 100 μl of solubilization solution were added. After overnight incubation, the optical density (OD) value was determined.

Isolation of mononuclear cells from lymph node and tumors

Ipsilateral tumor draining lymph nodes (TDLNs) from pooled inguinal, brachial and axilar lymph nodes from tumor-bearing mice and subcutaneous tumor nodules were surgically harvested. These organs were incubated in Collagenase-D and DNase-I (Roche Basel, Switzerland) for 15 min at 37°C. Dissociated cells were passed through a 70-μm nylon mesh filter (BD Falcon, BD Bioscience, San Jose, CA) to obtain unicellular cell suspensions. Cell suspensions from minced tumor nodules were similarly obtained.

Dendritic cell separation from tumor draining lymph nodes and cross-presentation assays

Ovalbumin (OVA)-specific T cell proliferation was assessed using CFSE-labeled OT-I T cells as described previously.[31] Briefly, DCs were positively selected from the TDLNs of tumor-bearing mice from the indicated treatment groups using immunomagnetic beads selecting for CD11c$^+$ (CD11c Microbeads mouse, Miltenyi Biotec) and the AUTOMACS cell separation system (Miltenyi Biotec, Gladbach, Germany). Cell purity was >85% in all groups as assessed by flow cytometry. CD8$^+$ OT-1 T cells were purified from the spleen of OT-I TCR transgenic mice. As a negative control CD11c$^+$ cells purified from tumor-free mice were used and as positive control, In that case, cells were pulsed with the synthetic peptide SIINFEKL at 50 ng/ml.[31] We incubated carboxyfluorescein succinimidyl ester (CFSE)-labeled 10^5 CD8$^+$ OT-I T cells with 2×10^5 or 5×10^4 CD11c$^+$ cells in U-bottom 96-well plates for 48 hr and analyzed proliferation by means of CFSE dilution by flow cytometry (FACSCalibur; BD Biosciences).[31]

In vivo killing assay

Splenocytes from naïve C57BL/6 mice were divided into 2 samples. One sample was pulsed with 10 μg/ml of the KSPWFTTL peptide (NeoMPS, Strasbourg, France) or the HPV-16 E7$_{49-57}$ peptide (RAHYNIVTF)[45] for 30 min at 37°C in 5% CO$_2$, washed extensively, and subsequently labeled with high concentration 1.25 μM of CFSE (Sigma-Aldrich, Dorset, UK). The nonpulsed control sample was labeled with low concentration 0.125 μM of CFSE. Then, both CFSE^{high} and CFSE^{low} labeled cells were mixed at 1:1 ratio and injected i.v. (5×10^6 cells of each population) into tumor-bearing mice. Twenty-four hours after transfer, spleens were harvested and specific cytotoxicity was analyzed by flow cytometry. Specific citotoxicity was calculated as follows: 100 − [100 × (% CFSE^{high} tumor bearing mice/% CFSE^{low} tumor bearing mice)/(% CFSE^{high} naïve mice/% CFSE^{low} naïve mice)].

Antibodies and flow cytometry

Single-cell suspensions were pretreated with FcR-Block (anti-CD16/32 clone 2.4G2; BD Biosciences-Pharmigen, San Jose, CA). Afterward, cells were stained with the following antibodies: CD8α fluorescein (FITC) conjugated (53–6.7; eBioscience, San Diego, CA), CD3ε allophycocyanin (APC) conjugated (145-2C11; BD Biosciences-Pharmingen), CD11c APC conjugated (N418; eBioscience), B220 FITC conjugated (RA3-6B2; BD Biosciences-Pharmingen), NK1.1 phycoerythrin (PE) conjugated (12–5,941; eBioscience), H2-K^b FITC conjugated (SF1-1.1; BD Biosciences-Pharmingen), as well as using Mouse regulatory T cell staining kit purchased from e-bioscience (catlog number 88–8,111). To identify specific tumor CD8 T lymphocytes, cells were stained with the iTAg MHC Class I tetramer loaded with the KSPWFTTL synthetic peptide and conjugated with PE (Beckmann Coulter, Madrid, Spain). Cells were analyzed with a FACSCalibur (BD) and FlowJo software.

Results

Combined antitumor effects of intralesional IFN-α and agonist anti-CD137 mAb

The potential for combination of 2 drugs increases if the mechanisms of action are not completely overlapping. For this purpose, we used C57BL/6 mice which had been grafted with the EL-4 lymphoma cells transfected to express chicken ovalbumin (EG.7 cells).[46] We observed that a course of anti-CD137 mAb 2A was able to eradicated most of the tumors[31] either when the mice expressed or not the receptor for Type I IFN (Fig. 1). To obtain this piece of information, we used IFNAR$^{-/-}$[47] mice which had been backcrossed to the C57BL/6 genetic background for 12 generations. Contrary to EG.7 tumors, established MC38 colon carcinomas for 10 days form subcutaneous tumors that are resistant to treatment by anti-CD137 mAbs at this timepoint (Figs. 2*a* to 2*c*). Hence, this provides conditions to test further technical improvements or combinations to refine the efficacy of these strategies. These tumors are also not amenable to treatment with 2 intratumoral doses of 5×10^4 U of IFN-α given on days 10 and 14 (Fig. 2). Intraperitoneal treatment on days 10 and 14 with anti-CD137 mAb at standard doses (100 μg per dose) retarded the growth rate of the tumors for 3–7 days, but did not result in curative effects. In a group of mice treated with both agents on the same days, 2 out of 6 animals completely rejected the tumor, and most tumors showed retardation of growth of about 1 week (Figs. 2*a* and 2*b*). Regressed tumors did not relapse in the cured animals when followed for at least 3 months (Fig. 2*c*). Of note, when IFN-α was injected subcutaneously at the opposite flank, as far away as possible from the tumor lesion, the combined therapeutic effect was not observed, indicating the need of interferon-mediated changes in the malignant tissue/location (data not shown).

Systemic therapeutic effects of the combined treatment

Malignant tumors often develop metastasis and only some of the lesions may be amenable to intratumoral injections. To

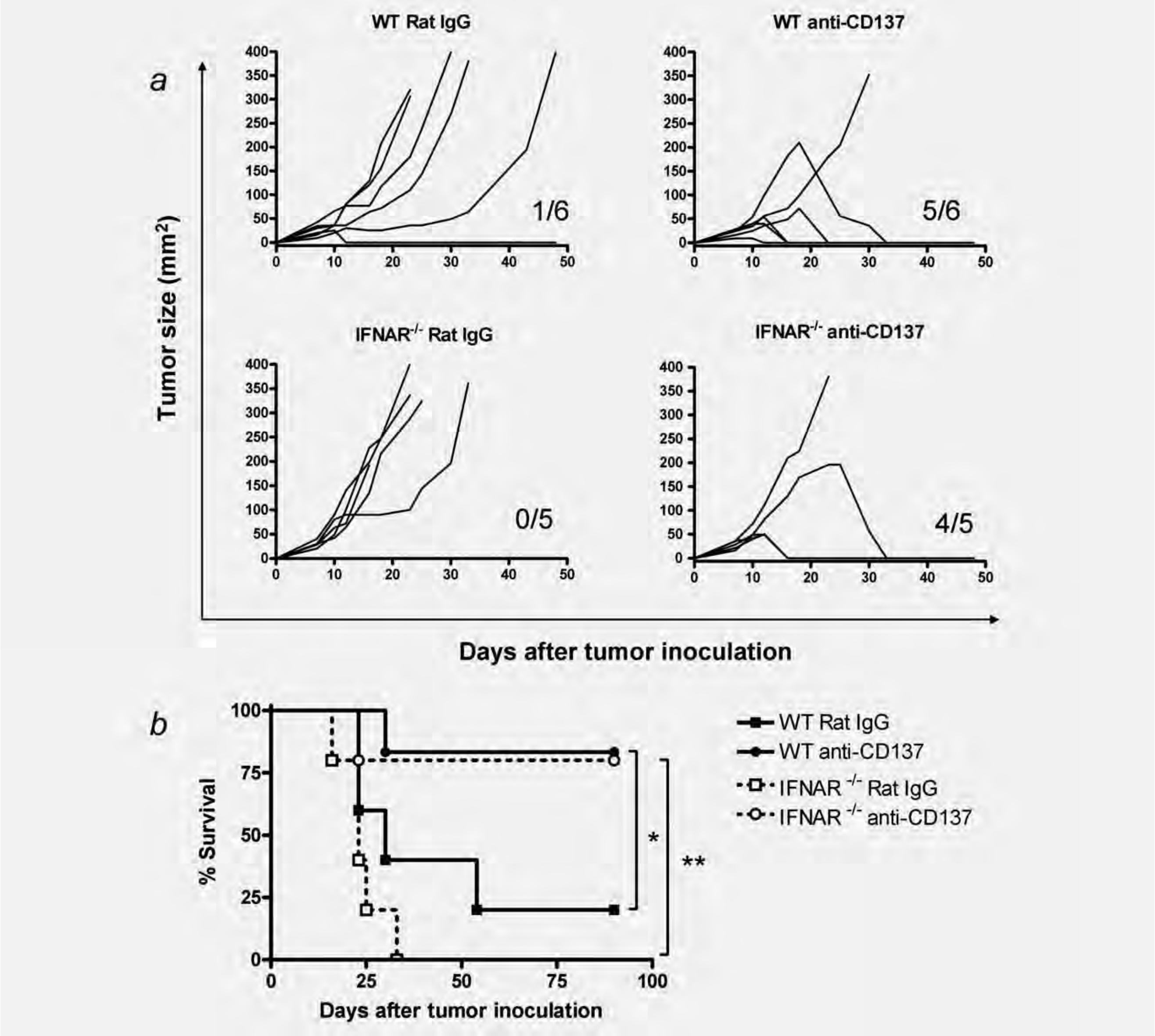

Figure 1. Agonist anti-CD137 mAbs are efficacious in IFNAR$^{-/-}$ mice. (*a*) Follow up of tumor sizes in individual C57BL/6 (WT) or IFNAR$^{-/-}$ mice treated with 2 intraperitoneal doses of 100 μg of rat polyclonal IgG (control) or anti-CD137 (2A) on days 9, 11, 13 and 15 after subcutaneous inoculation of EG.7 lymphoma cells. (*b*) Long-term survival data of the groups of animals (*$p < 0.05$, **$p < 0.01$ according to log rank tests). Results were confirmed in a separate experiment.

model such conditions mice were injected with tumor cells in opposite subcutaneous regions, so they developed bilateral tumor nodules. Under these conditions, the strategy was tested directly injecting with IFN-α only 1 of the tumors. In the set of experiments shown in Figure 2*d*, the growth of the directly treated tumor and the contralateral tumor were sequentially monitored. Treatment was given as late as on days 9, 12 and 15 after tumor cell inoculation. In this case, combination treatment gave rise to 4 bilateral rejections that translated into long-term survival (Fig. 2*e*) in 4 of 6 cases, whereas anti-CD137 mAb treatment only attained 1 complete rejection out of 5 mice. No noticeable antitumor effects were observed in the control and IFN-α single-agent-treated groups. Similar combined effects were obtained in a limited number of mice that hosted liver and subcutaneous concomitant tumors in which anti-CD137 mAb was given systemically and IFNα injected intratumorally in the subcutaneous lesion (data not shown).

If cured mice were rechallenged with MC38 cells 4 to 5 weeks after complete rejection MC38 failed to graft in 5 of 6 cases, whereas it lethally grafted in control naïve mice (Fig. 3, left panel). As a control, these MC38-resistant mice developed tumors in the opposite flank as derived from the antigenically unrelated B16F10 melanoma (Fig. 3, right panel).

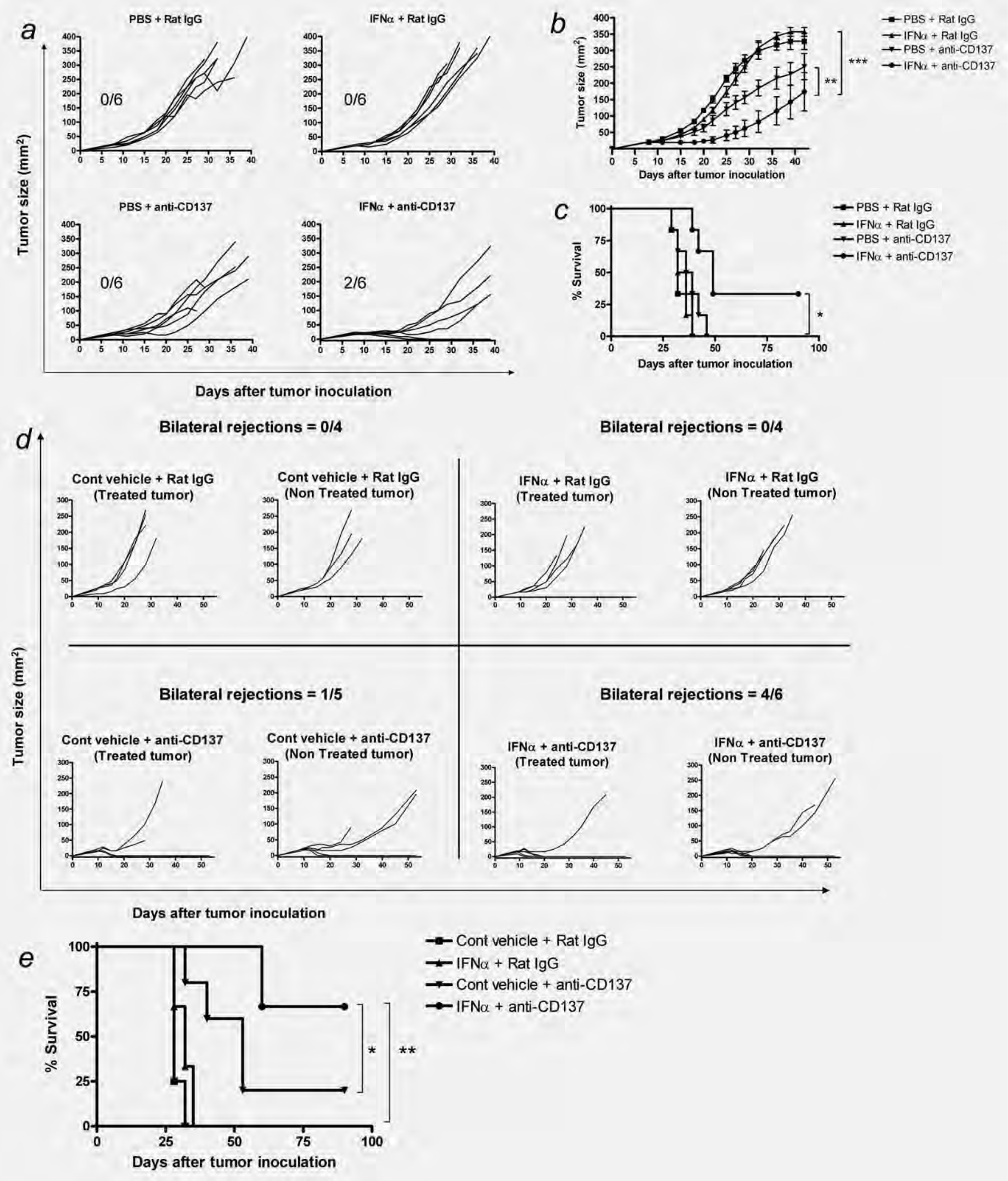

Figure 2. Intratumoral mouse interferon-α and systemic injection of anti-CD137 mAb show therapeutic synergy against MC38-derived colon carcinomas. (*a*) Individual tumor follow up of mice subcutaneously implanted with MC38 cells on day 0 and treated on days 10 and 14 with intraperitoneal 100 μg doses of rat IgG (control) or anti-CD137 2A. Mice also received on same days intratumoral injections of 5×10^4 units of mouse IFN-α4 in 50 μl or an equal volume of saline buffer (PBS) as a control. (*b*) Mean ± SEM of tumor sizes and statistical comparisons based on likelihood ratio tests using Monolix software as previously described.[45] (*c*) Long-term follow up of survival and log rank test comparisons (*$p < 0.05$). (*d*) Groups of mice were injected bilaterally with MC38 cells and treated i.p on days 9, 12 and 15 with either 100 μg of anti-CD137 mAb or rat IgG and intratumoral injections of IFN-α or control vehicle on the same days, but only inside the tumor nodules on the right flank. Graphs represent the evolution of individual tumors indicating the directly injected lesion and the contralateral tumor. Fraction of bilateral complete regression is given above each pair of graphs. (*e*) Long-term survival and statistal differences based on log rank tests (*$p < 0.05$) are depited. Comparable results were obtained in 3 separate experiments.

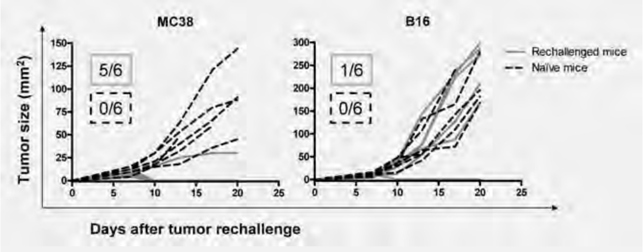

Figure 3. Mice cured by combined treatment resist a second inoculation with MC38 tumor cells. Mice that remained tumor-free after rejection of MC38 tumors upon combined treatment given as in Figure 2*b* were challenged in the left flank with 5×10^5 MC38 cells (left graph) and 5×10^5 B16F10 melanoma cells in the right flank (right graph). As a control an age-matched group of tumor naïve mice was injected with similar inoculi of tumor cells. Individual tumor follow-up of 6 animals per group is shown with the fraction of mice rejecting each tumor type in the control or rechallenged groups indicated by continuous grey lines (rechallenged) and discontinuous lines (naïve).

IFN-α receptor expression in Bone marrow-derived cells is crucial for the antitumor effects

Mice genetically deficient in the alpha chain for the Type I interferon receptor (IFNAR$^{-/-}$) were used to generate bone marrow chimeras. Some of these chimeras would not express this receptor at all, whereas others would express it but only either in tissues derived from bone marrow progenitors or in the nonhematopoietic radio-resistant compartment. In the animals in which the bone marrow donors were defective in the receptor for IFN-α, no bilateral rejections were induced by the combined treatment (Figs. 4*a* and 4*b*). On the contrary, when the donor bone marrow expressed IFN-α receptor there was some antitumor activity (3 of 9 complete rejections), regardless of the absence of the receptors in the rest of the tissues of the mouse (Fig. 4*c*). Interestingly, when both the hematopoietic and nonhematopoietic compartments expressed the receptor, 6 of 9 bilateral complete rejections took place (Fig. 4*d*). The corresponding long-term survival data of the different groups of chimeric mice treated with the combination are shown in Fig. 3*e*.

Direct effects of IFN-α on MC38 tumor cells and on the tumor stroma

Cultured MC38 cells experienced retardation in proliferation upon exposure to different concentrations of mouse IFN-α *in vitro* as assessed by MTT assays (Fig. 5*a*). The reduced number of cells was not related to apoptosis since no changes were noticed in the apoptosis rate of the cultures as FACS-measured by lack of nuclear staining with 7-Amino-actinomycin D (7-AAD) (data not shown). Therefore, the mild cytostatic effect observed was unlikely to explain the antitumor effects.

IFN-α is a strong upregulator of the MHC Class I antigen presentation pathway resulting in high levels of surface expression of MHC Class I molecules. It was noticed that 24 hr following intratumor injections there was a marked upregulation of surface H-2K^b expression on tumor cells, but more markedly on CD45 positive and negative stromal cells (Fig. 5*b*). These MHC expression changes offer more potential for effector CTL cell recognition.

Observations on T cells taken from LN or spleen from these animals did not show higher levels of CD137 expression 24 and 48 hr following IFN-α administration, thereby excluding an obvious synergy mechanism, defined as an increase of available CD137 molecules for the immunostimulatory mAb upon IFN-α intratumoral treatment (Supporting Information Fig. 1A).

CXCL10 chemokine (IP10) concentrations tended to be higher in lysates made from tumor nodules intratumorally injected with IFN-α (Supporting Information Fig. 1B) than in control treated mice. This is not a surprise for IP10 is a prominent gene upregulated by Type I IFNs[48] and may suggest a mechanism of action of intratumoral IFN-α based on the attraction of activated lymphocytes.[49] We do not substantiate any significant reduction in Tregs or myeloid suppressor cell numbers upon combined treatment (not shown).

Events in the tumor draining lymph nodes upon combined treatment

It was remarkable that TDLNs from mice whose tumors were treated with the combination underwent a clear enlargement for which both IFN-α and CD137 mAb contributed. This translates in about 5-fold higher cellularity if compared to untreated mice (Fig. 6*a*).

Such TDLNs were enriched in both conventional/myeloid DC and in plasmacytoid DC by each separate treatment and, very evidently, by combined treatments. Combination treatment resulted in enhanced DC quantities when comparisons were made either in terms of percentages or, more strikingly, when absolute numbers where taken into account (Figs. 6*b* and 6*c*). Importantly, the number of conventional DC and plasmacytoid DC in the LN showed an almost perfect inverse correlation with the tumor size upon sacrifice at day 13 (24 hr after the second treatment doses) and may be predictive indicators for efficacy. To further understand if those DC could be cross-presenting tumor antigens, we switched to the OVA-expressing EG7 subcutaneous tumor model and provided to the mice either the separate treatments or the combined treatment. TDLNs were surgically harvested 2 days after completion of the 2 doses of treatment and CD11c$^+$ cells were purified with immunomagnetic beads. These DCs were seeded at different cell ratios with CFSE-labeled OT-I TCR transgenic T cells that specifically recognize the SIINFEKL OVA epitope. It was found that DCs from the LN of untreated mice did not induce proliferation of OT-1 cells, whereas both systemic anti-CD137 mAb and intratumoral IFN-α injections elicited proliferation as intensely as with DC pulsed with the cognate synthetic peptide (Fig. 7). Combined

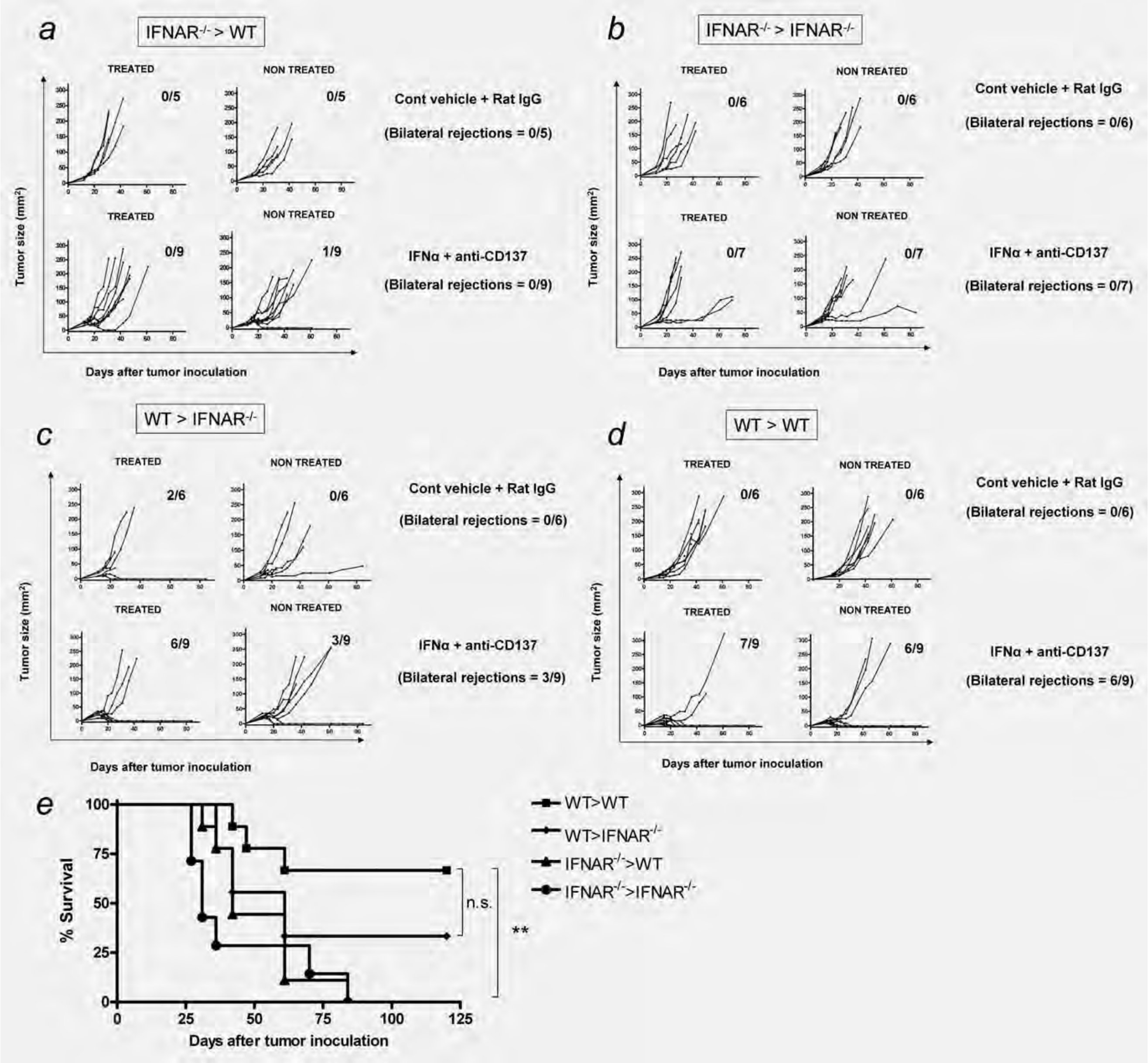

Figure 4. Bone marrow chimeric mice indicate that IFNAR expression is needed in the hemopoietic compartment for the synergy between intratumor injection of IFN-α and anti-CD137 mAb. Different combinations bone marrow chimeric mice of IFNAR$^{-/-}$ and WT as indicated in *a* to *d* were s.c. inoculated with MC38 tumors and treated on days 12, 15 and 18 with rat IgG, anti-CD137 mAb i.p. combined to control vehicle or IFN-α as respectively indicated in the graph legends. Graphs show size follow up of individual tumors either intralesionally treated (treated) with IFN-α and untreated contralateral lesions. Fractions of bilateral complete rejections are recorded. (*e*) Shows long-term survival of the different tumors statistically compared with log rank tests.

treatment only slightly increased the elicited proliferation over each separate treatment.

In the MC38 model, the amount of CD8 T cells specific for an immunodominant determinant of the MC38 tumor cells[50] detected with a MHC tetramer were analyzed in the TDLNs both in terms of percentage and absolute numbers. FACS staining disclosed that some of the animals receiving 2 doses of combined treatments harbored more tumor-specific CD8 T cells but the tendency did not render statistical differences (Fig. 6*d*) and did not correlate well with the tumor size reduction (not shown).

Single treatment with anti-CD137 mAb also quantitatively enhanced the amounts of specific T cells. *In vivo* killing assays using splenocytes pulsed with the relevant peptide showed enhanced killing in the case of mice treated either with CD137 mAb and IFN-α, albeit combined treatment did not result in a further enhancement (Supporting Information Fig. 2). An IFN-γ ELISPOT set up with splenocytes

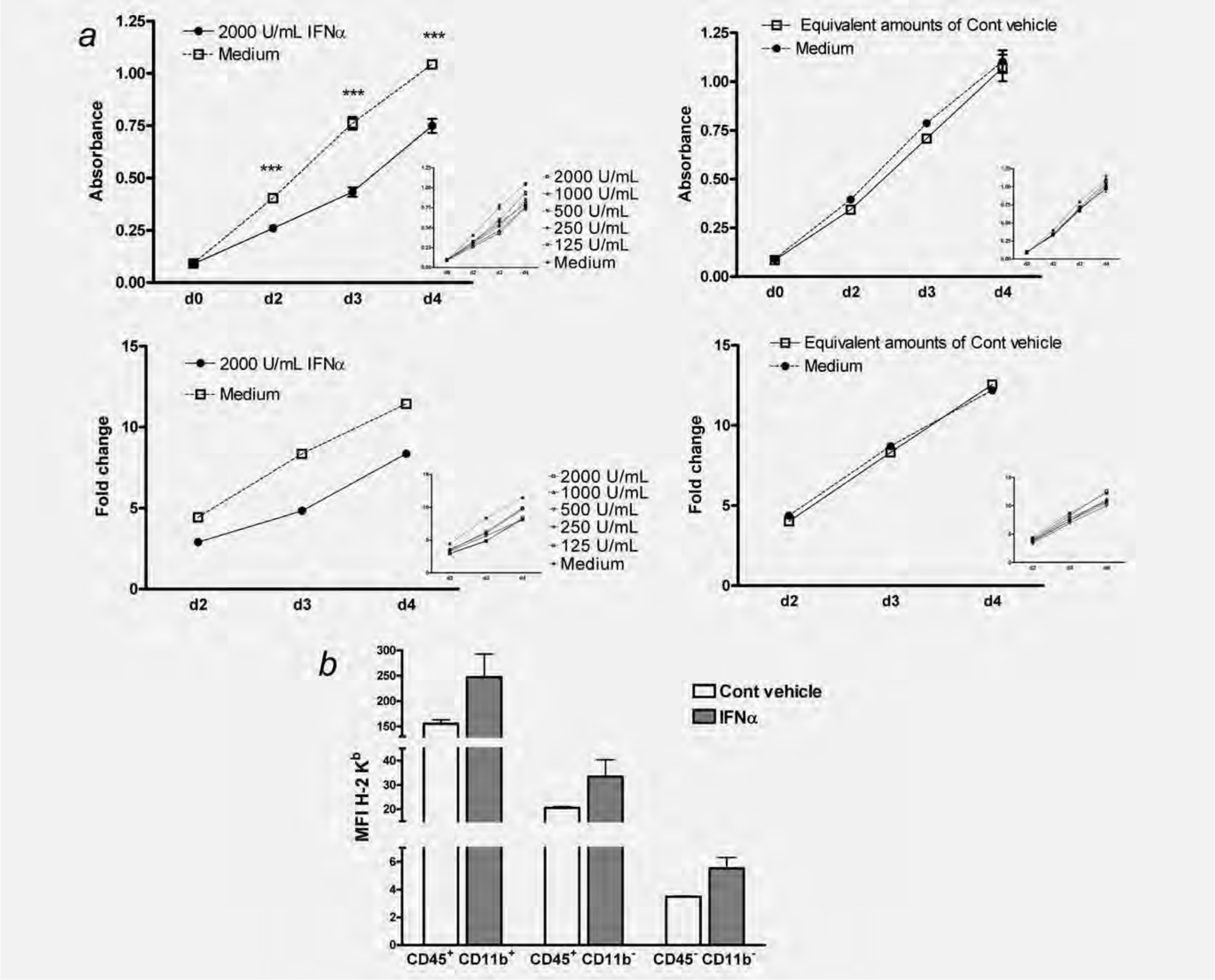

Figure 5. IFN-α decreases in vitro proliferation of MC38 cells in culture and increases the expression of MHC class I molecules on malignant and bone-marrow derived tumor stromal cells in vivo. (*a*) Time course analysis assessment of proliferation with MTT represented as absorbance and the fold change in absorbance over day 0. Data represent mean ± SD of 5 replicate wells containing adherent MC38 cells in the presence of mouse IFN-α at the indicated concentrations or control vehicle. The insets represent the effect of decreasing doses of IFN-α. Data are representative of 2 independent experiments. (*b*) MC38 tumors of 4–7 mm in diameter were injected with 5 × 10^4 IU of IFN-α or control vehicle. Twenty-four hours later a cell suspension was generated from disaggregated tumor nodules and multiple color FACS analysis comparatively quantified the mean intensity of fluorescence for H-$2K^b$ staining in the of the indicated cell subpopulations representing tumor cells ($CD45^-CD11b^-$) and bone marrow ($CD45^+$) derived stroma. Representative results of 3 experiments performed are shown.

stimulated with KSPWFTTL peptide rendered parallel results with increases due to IFN-α and CD137 mAb but lack further increases as a result of the synergistic combination treatment (not shown).

Cells that suppress the antitumor immune response in the tissue microenvironment could be potentially modulated by the combined therapy. Analyses of cell suspensions obtained from tumor nodules on day 4 following treatment onset, indicated that systemic anti-CD137 mAb enhanced the percentage of $CD4^+CD25^+FOXP3^+$ regulatory T cells, whereas intratumoral injection IFN-α did not modify this parameter. Curiously, in mice that received the combined treatment the increase of regulatory T cells due to anti-CD137 mAb was not observable, indicating that IFN-α may counteract this undesired effect of anti-CD137 mAb (Supporting Information Fig. 3A). However, these changes did not take place at the TDLNs (Supporting Information Fig. 3B). We also documented that there were no changes induced by the therapies on the intratumoral percentages of myeloid derived suppressor cells (MDSC) defined as $CD11b^+IL\text{-}4R\alpha^+$ cells at the same timepoint (Supporting Information Fig. 3C).

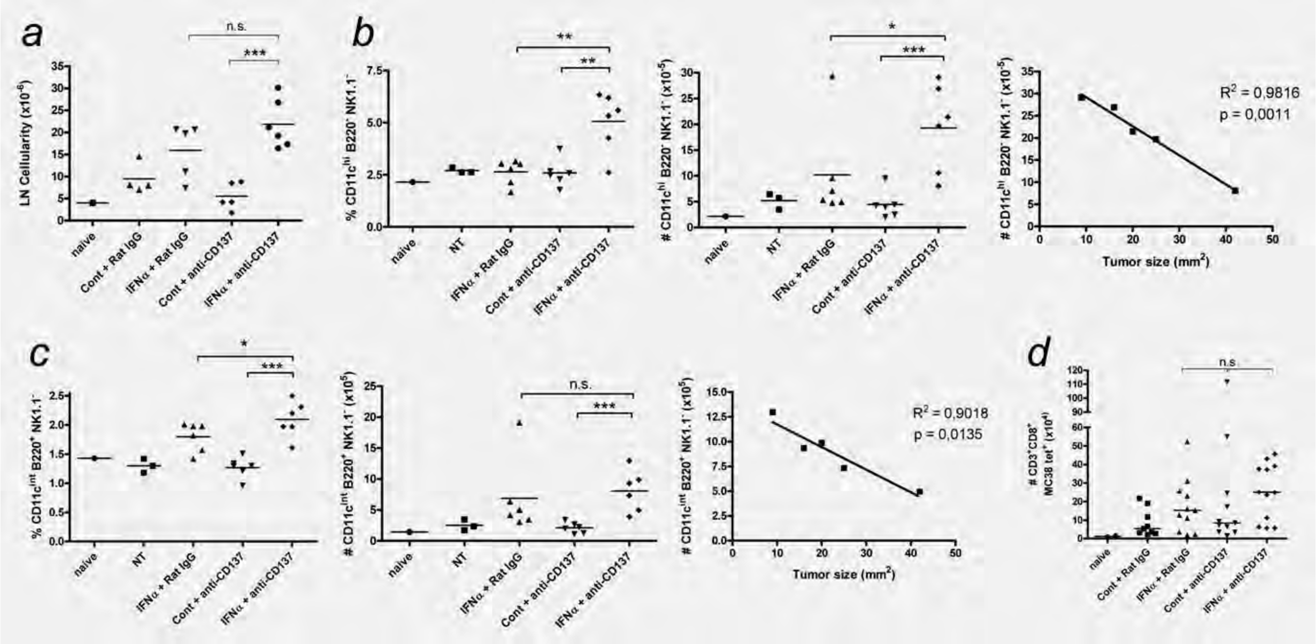

Figure 6. Combined treatment with intratumoral IFN-α and systemic anti-CD137 mAb enlarges TDLNs and increase the number of conventional and plasmacytoid dendritic cells in this location. (*a*) Number of cells in the dissected LN draining subcutaneous MC38 tumors treated as indicated on days 9 and 12 to be excised on day 13. Results are representative of 5 different experiments (*b*) Percentages (left) and numbers (center) of conventional DC in TDLNs assessed by multicolour staining defining them as CD11c^{high} B220$^-$ NK1.1$^-$ cells. The right panel plots an inverse correlation of tumor size and number of cDC on day 13 with the corresponding R^2 and *p* values. (*c*) Percentages (left) and numbers (center) of plasmacytoid DC in TDLNs assessed by multicolor staining as CD11c^{int} B220$^+$ NK1.1$^-$ cells. The right panel plots an inverse correlation of tumor size and number of pDC at day 13 with the corresponding R^2 and p values. (*d*) Individual TDLN CD8 T cell numbers in the indicated treatment groups that specifically recognize the immunodominant MC38 epitope, as stained on day 13 with the H2-K^b tetramer folded in the presence of the KSPWFTTL peptide. Results represent 3 independent experiments.

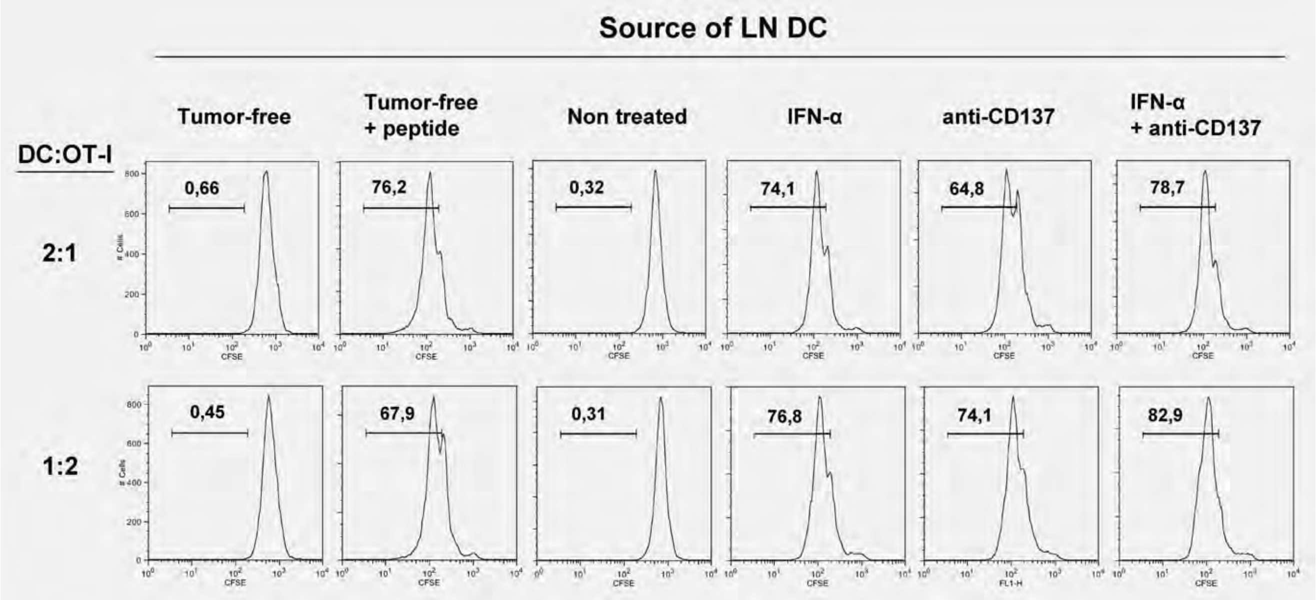

Figure 7. DC recovered from TDLNs of animals treated with anti-CD137 mAb, intratumoral IFNα or the treatment combination display stronger crosspriming of CD8 T cells *in vitro*. EG7 tumor bearing mice were treated on days 9 and 12 after tumor cell inoculation with 100 μg per dose of intraperitoenal anti-CD137 mAb or/and with intratumoral injections 5 × 10^4 units of IFN-α per dose. A control group of mice was left untreated as a control. On day 14, TDLNs were removed and CD11c$^+$ cell purified with immunomagentic beads. DCs were cocultured with CFSE-labeled OT-I TCR-trangenic CD8$^+$ T cells at the indicated ratios and proliferation was monitored by CFSE dilution as seen in the histograms. As a negative control DC from inguinal and axilary LN from tumor-free mice were used. These cells pulsed with 50 ng/ml of SIINFEKL peptide were used as a positive control.

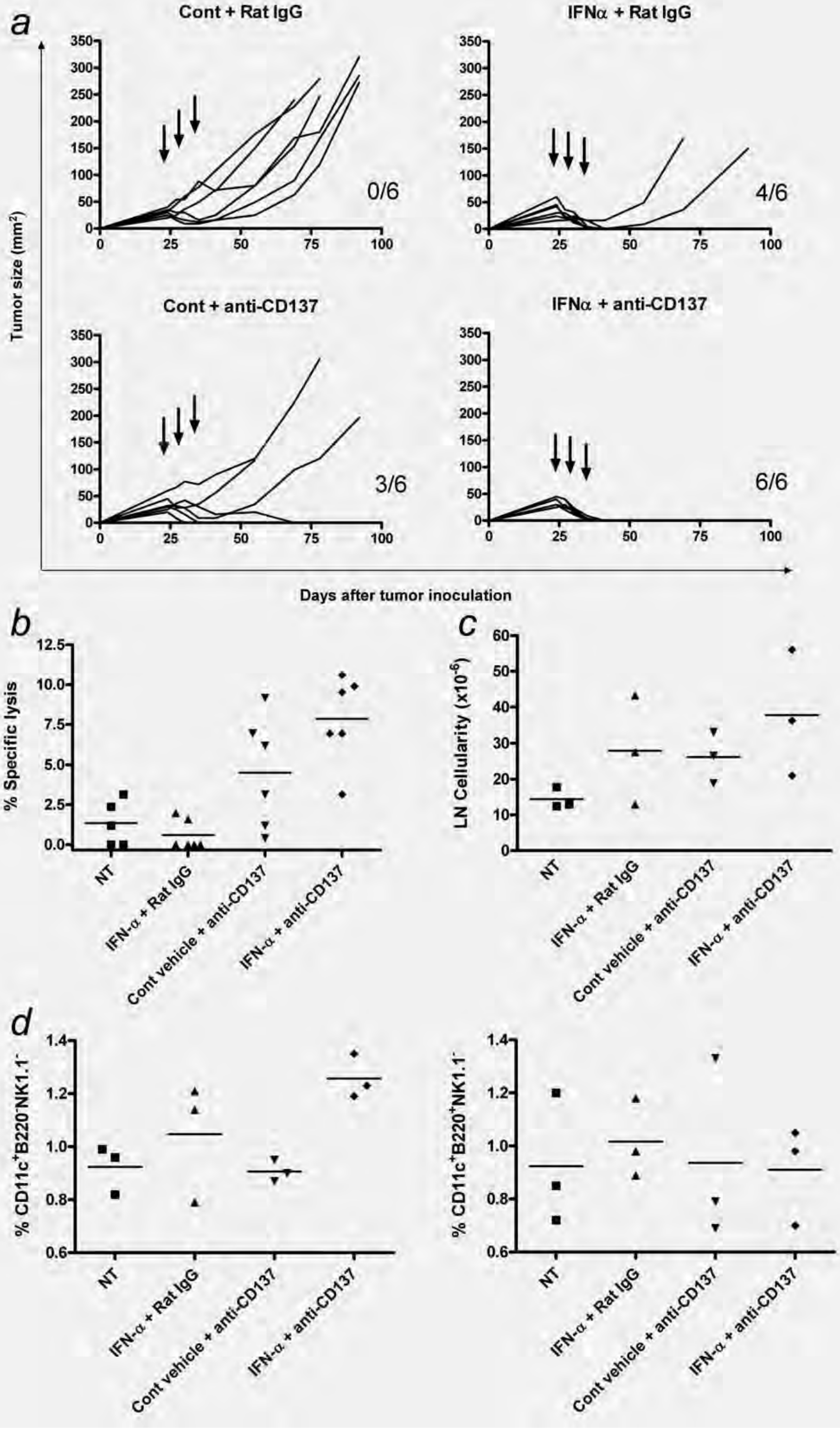

Figure 8. TC-1 derived tumors established for 24 days are cured by the IFN-α + anti-CD137 combination. (*a*) Individual size follow ups of subcutaneous tumor nodules derived from the TC-1 cell line that were established for 24 days without therapy, and then treated on days 24, 27 and 30 with 100 μg of anti-CD137 or rat IgG or/and 5×10^4 IU of mouse IFN-α or control vehicle in 50 μl given intratumorally. Results are representative of 2 independent experiments. (*b*) In mice treated as in A, 1 day after the second dose an in vivo killing assay was performed to assess the specific lysis of splenocytes pulsed with the HPV-16 E7 immunodominant epitope ($E7_{49-57}$). Data were recorded in 6 animals per group of treatment as indicated in the graph. (*c*) Absolute cell numbers in the draining LN in mice treated as in *b*. (*d*) Percentages of conventional (left) and plasmacytoid DC (right) in those TDLNs.

Combined treatment shows intense curative effects on mice bearing TC-1 tumors

Other experimental tumors were studied to test the efficacy of the combination. These tumors had to be resistant to either single-agent treatment. B16 melanoma for instance did not respond to combination treatment in our hands when it was given on days 8 and 10 (not shown). Moreover, a series of MMTV-Her2/Neu transgenic mice[51] treated weekly once mammary tumors became palpable (at 3–4 months of age) did not evidence better survival upon weekly IFN-α injections in the multifocal breast lesions and intraperitoneal delivery of 3 weekly doses of anti-CD137 mAb (Supporting Information Fig. 4). In this experiment, a 2.5 mg/kg dose of cyclophosphamide had been given to the mice to counteract immunosuppressive mechanisms.[45] These failures show that the combination strategy has room for improvement by further addition of other agents.[35,36]

However, tumors derived from the TC-1 cell line, a lung epithelial cell line transformed by the HPV-16 E6 and E7 oncogenes,[44] were sensitive (Fig. 8*a*). Indeed, these tumors were established for 24 days[45] before treatment onset and underwent complete rejections in 6 of 6 cases upon combined treatment. Of note, in this tumor anti-CD137 mAb and intralesional IFN-α given separately displayed partial efficacy. This indicates that the benefit of combined treatment can be extended to other tumors besides MC38. In the TC-1 tumor model, a modest increase in in-vivo killing activity specific against the HPV-16 E7 tumor antigen was observed upon combined treatment (Fig. 8*b*). As shown above in the case of MC38-bearing animals, the TDLNs tended to be enlarged by combined therapy (Fig. 8*c* and data not shown). Figure 8*d* shows that such TDLNs contained more conventional DC but in this case without percentage increases of plasmacytoid DC.

Because of its preclinical activity, relative simplicity and the elicited mechanisms of action, this combined treatment deserves testing in the clinical arena.

Discussion

This study shows preclinical synergistic effects in a clinically feasible combination strategy for cancer treatment. Tumor lesions amenable for injection can be repeatedly perfused with a solution containing Type I interferons, whereas fully human anti-CD137 mAb is in clinical trials and can be combined (NCT00612664, NCT00309023, NCT00351325). Clinical feasibility of the strategy is particularly envisioned for conditions with cutaneous lesions and concurrent visceral metastasis, as frequently observed in patients with Stage IV melanoma. Clinical trials would monitor the evolution of both visceral and directly injected lesions with IFN-α. We have documented that anti-CD137 mAb can cure tumors in IFNAR$^{-/-}$ mice indicating that both immunostimulatory pathways can operate independently, thereby providing the basis for empirical combination of the agents.

The antitumor effects are believed to be mediated by a local enhancement of tumor immunogenicity in the context of potent artificial systemic costimulation for primed T cells as provided by the agonist anti-CD137 mAbs.[24,26] In this context, IFN-α can promote proinflamatory changes in the tumor microenvironment that facilitate rejection. For instance, T cell homing *via* enhanced chemotaxis into the tumor, increased antigen presentation by dendritic cells,[52,53] less active local immunosuppression and direct effects on tumor cells retarding their growth.[3] Data obtained with the IFNAR$^{-/-}$ derived chimera mice indicate that the immune system has a key role in sensing and responding to intralesional IFN-α. In any case, the effects of IFN-α acting locally[53] seem to be very important because subcutaneous injection of the cytokine elsewhere in the mouse was not effective.

The TDLN site deserves much attention because it represents the main point of contact between the tumor and the immune system. It is considered the main site where the antitumor immune response is orchestrated by dendritic cell-mediated crosspresentation of tumor antigens.[54] Intralesional IFN-α mediates changes in cellularity in TDLNs that are amplified when anti-CD137 mAb are given in combination. Intermittent exposure to short-lived recombinant IFN-α protein maybe an advantage because sustained exposure may desensitize the system, for instance promoting SOCS-1 expression that represses the Type I IFN receptor signaling pathways.[55]

Enhancement in the numbers of conventional and plasmacytoid DC were not expected and seem to correlate well with lymph node cellularity and the antitumor effect of the combined treatment. We are actively studying which DC functions are critical for the therapeutic outcome[56] and, in particular, what could be the mechanistic involvement of plasmacytoid DC.[22] This could be especially important for efficient cross-priming of tumor antigens[31,57] that we observe to be upregulated both by IFNα and anti-CD137 mAb. With regard to the T cell compartment, tumor-specific CD8 T cells were readily detectable in TDLNs by tetramer staining and found to be functional by *in vivo* killing assays. Both anti-CD137 mAb and intratumoral IFN-α increased these parameters, but the treatment combination did not result in a clear further enhancement that would explain the therapeutic synergistic effects at least in the MC38 model. In the TC-1 tumor model, a slight increase in *in vivo* killing assays due to the combination treatment was detectable. It is doubtful that mere numeric increases of T cells are the main factor explaining the therapeutic synergy.

It is important to keep in mind that experiments with MHC tetramers with a described immunodominant antigen[50,56] fail to measure subdominant antigens emerging through epitope spreading. However, our chromium-release assays with the MC38 tumor cell line and restimulated splenocytes from the different treatment groups do not support this notion (data not shown).

Conditioning of the tumor lesion for the immune attack *via* upregulation of the Class I antigen presentation pathway in the tumor and in the stroma[58] may be of paramount importance for the successful outcome. Attraction to the lesion of activated T and NK cells *via* the IFN-induced chemokines

CXCL9,CXCL10 and CXCL11 can be of importance too to tilt the balance in the immune tumor microenvironment in favor of rejection.[59]

The TC-1 tumor model when established for more than 3 weeks was amenable for partial treatment efficacy by intratumoral IFN-α and agonist anti-CD137 mAb as single agents but only the combination resulted in complete eradications in all the treated cases.

However, efficacy of the combination is not universal for all mouse models since its weekly application to MMTV-Her2/Neu transgenic mice bearing palpable tumors did not alter the fatal course of the breast carcinomas. This was in spite of pretreatment with cyclophosphamide given 1 day before the onset of combined treatment to tamper with regulatory T cells.[45] Further agents should be incorporated to attain efficacy for this multifocal cancer model.

Recent reports on synergistic effects of anti-CD137 mAb with chemotherapy[35,36] maybe marking the future route to address these resistant preclinical models and eventually patients with metastatic cancer. Transplantable tumors with variable degree of resistance to anti-CD137 mAb treatment provide the testing grounds for stepwise development of immunotherapy combinations. These include B16 melanoma, 4T1 breast cancer and Lewis lung carcinoma which are still unmet models for successful treatment. The immunogenicity of MC38 and RENCA ascribe these tumors to an intermediate level of resistance. Our observations of strong synergy between adoptive T cell transfer and CD137 mAb treatment (Martinez-Forero et al., unpublished) argue in the sense that intrinsic immunogenicity of the tumor determines the amount of T cells amenable to receive costimulation upon treatment with anti-CD137 mAb.

Anti-CD137 mAb are already being tested in cancer patients in combination with standard chemotherapy combinations (NCT00351325). Other concomitant localized tumor-destructive interventions such as radiotherapy and criotherapy could be of interest in these feasible combination strategies. A very recent article provides evidence for a synergy between anti-CD137 mAb and intratumoral injection of TLR-9 agonist oligonucleotides also in the MC38 tumor model. Interestingly, such combined therapeutic effects were lost if the mice were deficient for Type I IFN receptor,[60] thereby providing an interesting parallelism with our data. Results in tumor models are to be interpreted with caution but speak of promising therapeutic efficacy for translational research.

Local release of interferon in tumors has been attained with intralesional injections recombinant adenovirus encoding IFN-β showing good immune-mediated results in rodent models but not in mesothelioma patients.[20] Further combination with anti-CD137 mAb could enhance therapeutic effects as it has been the case with IL-12 also locally delivered by gene therapy.[42] In our hands, anti-CD137 mAb seems to increase regulatory T cells at the MC38 tumor microenvironment. Interestingly, local release of IFNα somehow thwarts such an unwanted phenomenon. The importance of this finding for the therapeutic outcome remains to be defined.

Of much interest is the recent report that an interferon response gene expression signature in human melanoma lesions prior to treatment with a polypeptide vaccine nicely correlated with clinical responses.[59] In a manner, we are exaggerating this situation with our combination strategy involving acute intralesional releases of Type I IFN.

The synergistic mechanisms of action of IFN-α and agonist anti-CD137 are probably multifarious since these treatment impinge on multiple cell types and turns on many plausible mechanisms of action. IFN-α is gaining the reputation of being a powerful as a local adjuvant for vaccination.[53] This is probably due both to the multilayered actions on immune and nonimmune system cells. In a sense, in our strategy, we are turning a tumor nodule into a more immunogenic tissue, with some resemblance to a virally infected territory or a vaccine. In this scenario, amplification of the ensuing cellular immune response with agonist anti-CD137 mAbs is conceivably highly beneficial and evokes the observations on CD137-based therapies combined with tumor and viral vaccines.[38] Safety, simplicity and efficacy make the approach very appealing for development in diseases for which systemic INF-α is approved such as melanoma and renal cell carcinoma.

Acknowledgements

The authors are grateful to Dr. Chen for the kind gift of the 2A hybridoma and Dr. Albert for generously providing IFNAR−/− mice. Ms. Elena Ciordia and Mr. Eneko Elizalde are acknowledged for excellent animal facility management. M.S.-H. receives a Ramon y Cajal contract from Ministerio de Educación y Ciencia and A.P. a scholarship from FIS.

References

1. Krause CD, Pestka S. Historical developments in the research of interferon receptors. *Cytokine Growth Factor Rev* 2007;18:473–82.
2. Sadler AJ, Williams BR. Interferon-inducible antiviral effectors. *Nat Rev Immunol* 2008;8:559–68.
3. Moschos S, Varanasi S, Kirkwood JM. Interferons in the treatment of solid tumors. *Cancer Treat Res* 2005;126:207–41.
4. Bonifazi F, de Vivo A, Rosti G, Guilhot F, Guilhot J, Trabacchi E, Hehlmann R, Hochhaus A, Shepherd PC, Steegmann JL, Kluin-Nelemans HC, Thaler J, et al. Chronic myeloid leukemia and interferon-alpha: a study of complete cytogenetic responders. *Blood* 2001;98: 3074–81.
5. Takaoka A, Taniguchi T. New aspects of IFN-alpha/beta signalling in immunity, oncogenesis and bone metabolism. *Cancer Sci* 2003;94:405–11.
6. Tamura T, Yanai H, Savitsky D, Taniguchi T. The IRF family transcription factors in immunity and oncogenesis. *Annu Rev Immunol* 2008;26: 535–84.
7. Streck CJ, Ng CY, Zhang Y, Zhou J, Nathwani AC, Davidoff AM. Interferon-mediated anti-angiogenic therapy for

neuroblastoma. *Cancer Lett* 2005;228: 163–70.

8. De Palma M, Mazzieri R, Politi LS, Pucci F, Zonari E, Sitia G, Mazzoleni S, Moi D, Venneri MA, Indraccolo S, Falini A, Guidotti LG, et al. Tumor-targeted interferon-alpha delivery by Tie2-expressing monocytes inhibits tumor growth and metastasis. *Cancer Cell* 2008; 14:299–311.
9. Swann JB, Hayakawa Y, Zerafa N, Sheehan KC, Scott B, Schreiber RD, Hertzog P, Smyth MJ. Type I IFN contributes to NK cell homeostasis, activation, and antitumor function. *J Immunol* 2007;178:7540–9.
10. Tough DF. Type I interferon as a link between innate and adaptive immunity through dendritic cell stimulation. *Leuk Lymphoma* 2004;45:257–64.
11. Gogas H, Ioannovich J, Dafni U, Stavropoulou-Giokas C, Frangia K, Tsoutsos D, Panagiotou P, Polyzos A, Papadopoulos O, Stratigos A, Markopoulos C, Bafaloukos D, et al. Prognostic significance of autoimmunity during treatment of melanoma with interferon. *N Engl J Med* 2006;354:709–18.
12. Takaoka A, Hayakawa S, Yanai H, Stoiber D, Negishi H, Kikuchi H, Sasaki S, Imai K, Shibue T, Honda K, Taniguchi T. Integration of interferon-alpha/beta signalling to p53 responses in tumour suppression and antiviral defence. *Nature* 2003;424:516–23.
13. Gidlund M, Orn A, Wigzell H, Senik A, Gresser I. Enhanced NK cell activity in mice injected with interferon and interferon inducers. *Nature* 1978;273: 759–61.
14. Curtsinger JM, Gerner MY, Lins DC, Mescher MF. Signal 3 availability limits the CD8 T cell response to a solid tumor. *J Immunol* 2007;178:6752–60.
15. Le Bon A, Etchart N, Rossmann C, Ashton M, Hou S, Gewert D, Borrow P, Tough DF. Cross-priming of CD8+ T cells stimulated by virus-induced type I interferon. *Nat Immunol* 2003;4: 1009–15.
16. Le Bon A, Tough DF. Type I interferon as a stimulus for cross-priming. *Cytokine Growth Factor Rev* 2008;19:33–40.
17. Arina A, Murillo O, Hervas-Stubbs S, Azpilikueta A, Dubrot J, Tirapu I, Huarte E, Alfaro C, Perez-Gracia JL, Gonzalez-Aseguinolaza G, Sarobe P, Lasarte JJ, et al. The combined actions of NK and T lymphocytes are necessary to reject an EGFP+ mesenchymal tumor through mechanisms dependent on NKG2D and IFN gamma. *Int J Cancer* 2007;121: 1282–95.
18. Gresser I. The antitumor effects of interferon: a personal history. *Biochimie* 2007;89:723–8.
19. Dunn GP, Koebel CM, Schreiber RD. Interferons, immunity and cancer immunoediting. *Nat Rev Immunol* 2006;6: 836–48.
20. Sterman DH, Recio A, Carroll RG, Gillespie CT, Haas A, Vachani A, Kapoor V, Sun J, Hodinka R, Brown JL, Corbley MJ, Parr M, et al. A phase I clinical trial of single-dose intrapleural IFN-beta gene transfer for malignant pleural mesothelioma and metastatic pleural effusions: high rate of antitumor immune responses. *Clin Cancer Res* 2007;13: 4456–66.
21. Diebold SS, Kaisho T, Hemmi H, Akira S, Reis e Sousa C. Innate antiviral responses by means of TLR7-mediated recognition of single-stranded RNA. *Science* 2004;303: 1529–31.
22. Gilliet M, Cao W, Liu YJ. Plasmacytoid dendritic cells: sensing nucleic acids in viral infection and autoimmune diseases. *Nat Rev Immunol* 2008;8: 594–606.
23. Pollok KE, Kim YJ, Zhou Z, Hurtado J, Kim KK, Pickard RT, Kwon BS. Inducible T cell antigen 4-1BB. Analysis of expression and function. *J Immunol* 1993; 150:771–81.
24. Melero I, Murillo O, Dubrot J, Hervas-Stubbs S, Perez-Gracia JL. Multi-layered action mechanisms of CD137 (4-1BB)-targeted immunotherapies. *Trends Pharmacol Sci* 2008;29:383–90.
25. Nam KO, Kang WJ, Kwon BS, Kim SJ, Lee HW. The therapeutic potential of 4-1BB (CD137) in cancer. *Curr Cancer Drug Targets* 2005;5:357–63.
26. Watts TH. TNF/TNFR family members in costimulation of T cell responses. *Annu Rev Immunol* 2005;23:23–68.
27. Croft M. The role of TNF superfamily members in T-cell function and diseases. *Nat Rev Immunol* 2009;9:271–85.
28. Lee HW, Park SJ, Choi BK, Kim HH, Nam KO, Kwon BS. 4-1BB promotes the survival of CD8+ T lymphocytes by increasing expression of Bcl-xL and Bfl-1. *J Immunol* 2002;169:4882–8.
29. Melero I, Johnston JV, Shufford WW, Mittler RS, Chen L. NK1.1 cells express 4-1BB (CDw137) costimulatory molecule and are required for tumor immunity elicited by anti-4-1BB monoclonal antibodies. *Cell Immunol* 1998;190:167–72.
30. Choi BK, Kim YH, Kwon PM, Lee SC, Kang SW, Kim MS, Lee MJ, Kwon BS. 4-1BB functions as a survival factor in dendritic cells. *J Immunol* 2009;182: 4107–15.
31. Murillo O, Dubrot J, Palazon A, Arina A, Azpilikueta A, Alfaro C, Solano S, Ochoa MC, Berasain C, Gabari I, Perez-Gracia JL, Berraondo P, et al. In vivo depletion of DC impairs the anti-tumor effect of agonistic anti-CD137 mAb. *Eur J Immunol* 2009;39: 2424–36.
32. Lee SW, Park Y, So T, Kwon BS, Cheroutre H, Mittler RS, Croft M. Identification of regulatory functions for 4-1BB and 4-1BBL in myelopoiesis and the development of dendritic cells. *Nat Immunol* 2008;9:917–26.
33. Melero I, Shuford WW, Newby SA, Aruffo A, Ledbetter JA, Hellstrom KE, Mittler RS, Chen L. Monoclonal antibodies against the 4-1BB T-cell activation molecule eradicate established tumors. *Nat Med* 1997;3:682–5.
34. McNamara JO, Kolonias D, Pastor F, Mittler RS, Chen L, Giangrande PH, Sullenger B, Gilboa E. Multivalent 4-1BB binding aptamers costimulate CD8+ T cells and inhibit tumor growth in mice. *J Clin Invest* 2008;118:376–86.
35. Kim YH, Choi BK, Kim KH, Kang SW, Kwon BS. Combination therapy with cisplatin and anti-4-1BB: synergistic anticancer effects and amelioration of cisplatin-induced nephrotoxicity. *Cancer Res* 2008;68:7264–9.
36. Kim YH, Choi BK, Oh HS, Kang WJ, Mittler RS, Kwon BS. Mechanisms involved in synergistic anticancer effects of anti-4-1BB and cyclophosphamide therapy. *Mol Cancer Ther* 2009;8:469–78.
37. Shi W, Siemann DW. Augmented antitumor effects of radiation therapy by 4-1BB antibody (BMS-469492) treatment. *Anticancer Res* 2006;26:3445–53.
38. Wilcox RA, Flies DB, Zhu G, Johnson AJ, Tamada K, Chapoval AI, Strome SE, Pease LR, Chen L. Provision of antigen and CD137 signaling breaks immunological ignorance, promoting regression of poorly immunogenic tumors. *J Clin Invest* 2002; 109:651–9.
39. Melero I, Hervas-Stubbs S, Glennie M, Pardoll DM, Chen L. Immunostimulatory monoclonal antibodies for cancer therapy. *Nat Rev Cancer* 2007;7:95–106.
40. Tirapu I, Arina A, Mazzolini G, Duarte M, Alfaro C, Feijoo E, Qian C, Chen L, Prieto J, Melero I. Improving efficacy of interleukin-12-transfected dendritic cells injected into murine colon cancer with anti-CD137 monoclonal antibodies and alloantigens. *Int J Cancer* 2004;110:51–60.
41. Ko E, Luo W, Peng L, Wang X, Ferrone S. Mouse dendritic-endothelial cell hybrids and 4-1BB costimulation elicit antitumor effects mediated by broad antiangiogenic immunity. *Cancer Res* 2007;67:7875–84.
42. Pan PY, Gu P, Li Q, Xu D, Weber K, Chen SH. Regulation of dendritic cell function by NK cells: mechanisms underlying the synergism in the combination therapy of IL-12 and 4-1BB activation. *J Immunol* 2004;172:4779–89.
43. Xu D, Gu P, Pan PY, Li Q, Sato AI, Chen SH. NK and CD8+ T cell-mediated

eradication of poorly immunogenic B16-F10 melanoma by the combined action of IL-12 gene therapy and 4-1BB costimulation. *Int J Cancer* 2004;109: 499–506.

44. Lin KY, Guarnieri FG, Staveley-O'Carroll KF, Levitsky HI, August JT, Pardoll DM, Wu TC. Treatment of established tumors with a novel vaccine that enhances major histocompatibility class II presentation of tumor antigen. *Cancer Res* 1996;56:21–6.
45. Berraondo P, Nouze C, Preville X, Ladant D, Leclerc C. Eradication of large tumors in mice by a tritherapy targeting the innate, adaptive, and regulatory components of the immune system. *Cancer Res* 2007;67:8847–55.
46. Zhu Y, Zhu G, Luo L, Flies AS, Chen L. CD137 stimulation delivers an antigen-independent growth signal for T lymphocytes with memory phenotype. *Blood* 2007;109:4882–9.
47. Muller U, Steinhoff U, Reis LF, Hemmi S, Pavlovic J, Zinkernagel RM, Aguet M. Functional role of type I and type II interferons in antiviral defense. *Science* 1994;264:1918–21.
48. Sanda C, Weitzel P, Tsukahara T, Schaley J, Edenberg HJ, Stephens MA, McClintick JN, Blatt LM, Li L, Brodsky L, Taylor MW. Differential gene induction by type I and type II interferons and their combination. *J Interferon Cytokine Res* 2006;26:462–72.
49. Narvaiza I, Mazzolini G, Barajas M, Duarte M, Zaratiegui M, Qian C, Melero I, Prieto J. Intratumoral coinjection of two adenoviruses, one encoding the chemokine IFN-gamma-inducible protein-10 and another encoding IL-12, results in marked antitumoral synergy. *J Immunol* 2000;164: 3112–22.
50. Sijts AJ, Ossendorp F, Mengede EA, van den Elsen PJ, Melief CJ. Immunodominant mink cell focus-inducing murine leukemia virus (MuLV)-encoded CTL epitope, identified by its MHC class I-binding motif, explains MuLV-type specificity of MCF-directed cytotoxic T lymphocytes. *J Immunol* 1994;152:106–16.
51. Boggio K, Nicoletti G, Di Carlo E, Cavallo F, Landuzzi L, Melani C, Giovarelli M, Rossi I, Nanni P, De Giovanni C, Bouchard P, Wolf S, et al. Interleukin 12-mediated prevention of spontaneous mammary adenocarcinomas in two lines of Her-2/neu transgenic mice. *J Exp Med* 1998;188:589–96.
52. Melero I, Arina A, Murillo O, Dubrot J, Alfaro C, Perez-Gracia JL, Bendandi M, Hervas-Stubbs S. Immunogenic cell death and cross-priming are reaching the clinical immunotherapy arena. *Clin Cancer Res* 2006;12:2385–9.
53. Ferrantini M, Capone I, Belardelli F. Interferon-alpha and cancer: mechanisms of action and new perspectives of clinical use. *Biochimie* 2007;89:884–93.
54. Melief CJ. Mini-review: regulation of cytotoxic T lymphocyte responses by dendritic cells: peaceful coexistence of cross-priming and direct priming? *Eur J Immunol* 2003;33:2645–54.
55. Qin H, Wilson CA, Lee SJ, Benveniste EN. IFN-beta-induced SOCS-1 negatively regulates CD40 gene expression in macrophages and microglia. *FASEB J* 2006; 20:985–7.
56. Chiodoni C, Paglia P, Stoppacciaro A, Rodolfo M, Parenza M, Colombo MP. Dendritic cells infiltrating tumors cotransduced with granulocyte/macrophage colony-stimulating factor (GM-CSF) and CD40 ligand genes take up and present endogenous tumor-associated antigens, and prime naive mice for a cytotoxic T lymphocyte response. *J Exp Med* 1999;190: 125–33.
57. Melero I, Vile RG, Colombo MP. Feeding dendritic cells with tumor antigens: self-service buffet or a la carte? *Gene Ther* 2000;7:1167–70.
58. Zhang B, Zhang Y, Bowerman NA, Schietinger A, Fu YX, Kranz DM, Rowley DA, Schreiber H. Equilibrium between host and cancer caused by effector T cells killing tumor stroma. *Cancer Res* 2008;68: 1563–71.
59. Harlin H, Meng Y, Peterson AC, Zha Y, Tretiakova M, Slingluff C, McKee M, Gajewski TF. Chemokine expression in melanoma metastases associated with CD8+ T-cell recruitment. *Cancer Res* 2009; 69:3077–85.
60. Westwood JA, Haynes NM, Sharkey J, McLaughlin N, Pegram HJ, Schwendener RA, Smyth MJ, Darcy PK, Kershaw MH. Toll-like receptor triggering and T-cell costimulation induce potent antitumor immunity in mice. *Clin Cancer Res* 2009; 15:7624–33.

OPEN ACCESS Freely available online

PLoS one

Carcinoma-Derived Interleukin-8 Disorients Dendritic Cell Migration Without Impairing T-Cell Stimulation

Carlos Alfaro[1]☯, Natalia Suárez[1,2]☯, Ivan Martínez-Forero[1], Asís Palazón[1], Ana Rouzaut[1], Sarai Solano[1], Esperanza Feijoo[1], Alfonso Gúrpide[3], Elixabet Bolaños[1,3], Lorena Erro[1], Juan Dubrot[1], Sandra Hervás-Stubbs[1], Alvaro Gonzalez[2], Jose Luis Perez-Gracia[3]¶, Ignacio Melero[1,3]*¶

1 Gene Therapy and Hepatology Division, Centro de Investigación Médica Aplicada (CIMA), Pamplona, Spain, **2** Biochemistry Department, Clínica Universidad de Navarra, Pamplona, Spain, **3** Medical Oncology Department, Clínica Universidad de Navarra, Pamplona, Spain

Abstract

Background: Interleukin-8 (IL-8, CXCL8) is readily produced by human malignant cells. Dendritic cells (DC) both produce IL-8 and express the IL-8 functional receptors CXCR1 and CXCR2. Most human colon carcinomas produce IL-8. IL-8 importance in malignancies has been ascribed to angiogeneis promotion.

Principal Findings: IL-8 effects on human monocyte-derived DC biology were explored upon DC exposure to recombinant IL-8 and with the help of an IL-8 neutralizing mAb. *In vivo* experiments were performed in immunodeficient mice xenografted with IL-8-producing human colon carcinomas and comparatively with cell lines that do not produce IL-8. Allogenic T lymphocyte stimulation by DC was explored under the influence of IL-8. DC and neutrophil chemotaxis were measured by transwell-migration assays. Sera from tumor-xenografted mice contained increasing concentrations of IL-8 as the tumors progress. IL-8 production by carcinoma cells can be modulated by low doses of cyclophosphamide at the transcription level. If human DC are injected into HT29 or CaCo2 xenografted tumors, DC are retained intratumorally in an IL-8-dependent fashion. However, IL-8 did not modify the ability of DC to stimulate T cells. Interestingly, pre-exposure of DC to IL-8 desensitizes such cells for IL-8-mediated *in vitro* or *in vivo* chemoattraction. Thereby DC become disoriented to subsequently follow IL-8 chemotactic gradients towards malignant or inflamed tissue.

Conclusions: IL-8 as produced by carcinoma cells changes DC migration cues, without directly interfering with DC-mediated T-cell stimulation.

Citation: Alfaro C, Suárez N, Martínez-Forero I, Palazón A, Rouzaut A, et al. (2011) Carcinoma-Derived Interleukin-8 Disorients Dendritic Cell Migration Without Impairing T-Cell Stimulation. PLoS ONE 6(3): e17922. doi:10.1371/journal.pone.0017922

Editor: R. Mosley, University of Nebraska Medical Center, United States of America

Received August 18, 2010; **Accepted** February 17, 2011; **Published** March 14, 2011

Funding: Financial support was from MEC/MICINN (SAF2005-03131 and SAF2008-03294), Departamento de Educación del Gobierno de Navarra, Departamento de Salud del Gobierno de Navarra (Beca Ortiz de Landázuri), Redes temáticas de investigación cooperativa RETIC (RD06/0020/0065), Fondo de investigación sanitaria (FIS PI060932), European commission 7th framework program (ENCITE) and SUDOE-IMMUNONET, Fundacion Mutua Madrileña, and "UTE for project FIMA". CA is supported by Fundación Científica de la Asociación Española Contra el Cáncer (AECC). SH-S receives a Ramon y Cajal contract from Ministerio de Educación y Ciencia and AP a scholarship from FIS. The funders had no role in study design, data collection and analysis, decision to publish, or preparation of the manuscript.

Competing Interests: The authors have declared that no competing interests exist.

* E-mail: imelero@unav.es

☯ These authors contributed equally to this work.

¶ These authors also contributed equally to this work.

Introduction

In a previous study [1] we showed that ^{111}Indium-labeled DC when injected into tumor lesions of patients suffering advanced digestive carcinomas [2] tended to remain inside the injected lesion. An explanation for such a retention was proposed in the sense that the human tumors abundantly produce IL-8 [1,3] and DC express CXCR1 and CXCR2 functional IL-8 receptors on their plasma membrane [1,4,5]. However, no definitive proof was provided for the role of IL-8 in intratumoral retention of DC [1].

An IL-8 homologue is absent from the mouse genome and these precludes incisive definitive genetic experimentation on the role of IL-8 in murine tumor models. However there are reports suggesting that mouse CXCR1 is activated by human IL-8, hence permitting to some extent experiments in xenografts [6].

Chemokine receptors guide DC in physiology and in inflammation [7,8]. DC migration from inflamed/infected [9] or malignant tissues [10,11] is important for the orchestration of immune responses. Chemokine receptors do not only regulate motility but also control other cellular functions such as activation or survival in various cell types [11,12]. Therefore it would not be a surprise if the chemokine microenvironment modified DC functions other than migration [12].

Human tumor cells produce IL-8 in most cases [1,13] as a biological dirty trick played by the malignant tissue to promote angiogenesis [3,13,14,15] and possibly to support the type of smoldering inflammation that promotes tumor progression and metastasis [14,16,17]. Tumor growth in human patients statistically correlates with IL-8 serum concentrations [3,18]. Recently, a role for IL-8 has been described in the resistance to antiangiogenic

VEGF signal blockade with sunitinib [19]. Importantly escape from sunitinib can be thwarted by co-treatment with neutralizing anti-IL8 mAb [19].

IL-8 was originally discovered as a powerful attractor of polymorphonuclear leukocytes (PMNs) [20,21] in acute inflammation [21], but may act on other leukocyte subtypes [1,22] and on endothelial cells [15]. In turn, DC are both responsive to IL-8 [4,5], and produce IL-8 either when inactive or more overtly so, when activated/matured [1]. Injecting DC inside tumors has been intended to enhance antitumor activity for therapeutic purposes in animal models [11,23] and in the clinic [2,24,25]. One of the hurdles faced is that the tumor microenvironment is rich in substances impairing DC functions [11,26]. DC migration into lymph nodes is of critical importance in cancer immunotherapy based on DC [27,28,29]. If retained intratumorally, DC would be prey for tumor microenvironmental factors such as TGF-β for longer periods of time [11], thereby causing damage to the induction of anti-tumor immunity.

Here we show that xenografts of human tumors retain DC inside the injected tumors by means of IL-8-mediated chemoattraction, that can also recruit DC to the malignancy when injected in the subcutaneous connective tissue in the vicinity of the tumor. However, the same functional recombinant IL-8 that attracts DC and PMNs does not impair the abilities of DC to induce T-cell activation and proliferation either *in vitro* or *in vivo*. Interestingly, pre-exposure of DC to IL-8 restrains subsequent migration towards IL-8 chemo-attractive gradients indicating desensitization of the receptors.

Methods

Ethics statement

Animal studies have been performed in accordance with Spanish legislation under specific approval from the institutional ethics board by the *Comité de Ética para la Experimentación Animal of the University of Navarra* (Study 03/007 approval). Human cells are obtained from Blood donors (public blood bank of Navarra) under written informed consent for research.

Dendritic cell generation

Dendritic cells were generated from filter buffy coats (FBC)-derived monocytes donated by healthy donors [30] who explicitly sign a written informed consent. To generate immature DCs from monocytes, human peripheral blood was isolated by Ficoll-Paque gradient centrifugation from FBC. Isolated mononuclear cells from these sources were subjected to positive selection using anti-CD14-conjugated paramagnetic beads and purified using the AutoMacs system according to the manufacturer's instructions (Miltenyi Biotec, Bergisch Gladbach, Germany). Purified monocytes were cultured for 7 days in RPMI-1640 with 5% (v/v) heat inactivated FCS. To differentiate dendritic cells from $CD14^+$ cells, culture medium was supplemented with GM-CSF (1000 U/mL; Novartis, Basel, Switzerland) and IL-4 (500 U/mL; R&D Systems, Minneapolis, MN). DCs were matured adding clinical grade TNF-α (50 ng/mL; Boehringer Ingelheim, Ingelheim, Germany), IFN-α (1,000 IU/mL; Schering-Plough, Kenilworth, NJ) and Poly I:C (10 μg/mL; Ampligen, Bioclones, Tokai, South Africa) for 48 h.

Cell lines and IL-8 concentrations in mouse serum and culture supernatants

HT29, CaCo2 and SW48 colon carcinoma cell lines were obtained from American Type Culture Collection (Rockville, MD). Cell lines were cloned by limiting dilution in 96-well plates and subcultures (10^5 cells) were tested for the concentration of IL-8 in the 24 h supernatants from these subcultures by means of ELISA (BD Biosciences, San Diego, CA). Cyclophosphamide (Cytoxan) was purchased in our hospital pharmacy.

Semiquantitative RT-PCR for IL-8

Total cellular RNA was extracted with Trizol (Invitrogen, Carlsbad, CA) according to the protocol provided by the manufacturer. First-strand cDNA was synthesized from 1 μg total cellular RNA using an RNA PCR kit (Takara Bio Inc., Otsu, Japan) with random primers. Thereafter, cDNA was amplified using 30, and 28 cycles for IL-8 and for β-actin, respectively. The specific primers used were as follows: IL-8, forward primer 5′-ATGACTTCCAAGCTGGCCGTG -3′ and reverse primer 5′-TTATGAATTCTCAGCCCTCTTCAAAAACTTCTC-3′; and for β-actin, forward primer 5′-GTGGGGCGCCCCAGGCACCA-3′ and reverse primer 5′-CTCCTTAATGTCACGCACGATTTC-3′. The product sizes were 300 bp for IL-8, and 548 bp for β-actin. The thermocycling conditions for the targets were as follows: denaturing at 94°C for 30 s for IL-8, and β-actin, annealing at 60°C for 30 s for IL-8 and β-actin, and extension at 72°C for 90 s for IL-8 and β-actin. The PCR products were fractionated on 2% agarose gels and visualized by ethidium bromide staining. The quantity of a band was measured by the area under its intensity profile curve using BioRad Quantity One 1-D Analysis Software (Bio-Rad Laboratories, Hercules, CA, USA). β-actin was employed to normalize the amount of RNA used in each reaction.

Mouse tumors

Nude mice, $Rag^{-/-}$ or $Rag^{-/-}$ IL-2R$\gamma^{-/-}$ were obtained from The Jackson Laboratory. Animal experiments were in accordance to Spanish laws and approval was obtained from the animal experimentation committee of the University of Navarra (Study 03/007 approval). These mice were injected with the tumor cell lines HT29 (5×10^6 cells), CaCo2 (10^7 cells) or SW48 (5×10^6) to induce subcutaneous tumors. IL-8 in serum samples was sequentially measured by ELISA (BD Biosciences). When indicated 3 mg/mouse of cyclophosphamide were injected i.p.

In vivo migration

Female nude mice, $Rag^{-/-}$ or $Rag^{-/-}$ IL-2R$\gamma^{-/-}$ as indicated, were subcutaneously injected with 5×10^6 HT29 (n = 4), 10×10^6 CaCo2 (n = 4) or 10^6 SW48 (n = 3) tumor cells. When tumors reached about 1 cm diameter, 10^6 mature DCs were labelled with 2.5 μM CFSE (Sigma, Barcelona, Spain) or 4×10^{-6} M PKH26 (Sigma), washed and injected intratumorally. Mouse IgG (100 μg, BD Pharmingen) or neutralizing anti-human IL-8 mAb (100 μg, BD Pharmingen) were coinjected within the same syringe into the tumors. In case of HT29 and SW48, cell suspensions from the tumors were generated with the GentleMacs dissociator device (Miltenyi Biotec). Cell suspensions were analysed by FACS and fluorescent cells counted. In the case of CaCo2 xenografts, three days later, tumors were mechanically homogenized. Tissue homogenates were cleared from debris by centrifugation and fluorescence was measured using a plate fluorimeter (Polarstar Galaxy, BMG). Migration was calculated as fluorescence in the tumor divided by total input fluorescence injected (fluorescence was quantified in arbitrary units).

Cytokine production by maturing DC

For *in vitro* stimulations, 10^5 DC were cultured 48 h with medium alone (control), LPS (1 μg/mL) purchased from Sigma, R-848 imidazoquinoline (1 mM) purchased from Pharmatech

(Shangai, China) or sCD40L at 200 ng/mL purchased from Abnova (Taipei, Taiwan). After culture for 48 h, supernatants were collected and the cytokine concentration was determined by immunoassay. Commercially available ELISA kits were used for the detection of IL-12p70 and IL-10 (BD Bioscience).

FACS analysis

FITC and PE-labeled mAb specific for the DC maturation markers: CD80, CD83, CD86 and HLA-DR (BD Bioscience) and isotype-matched labeled controls were used to characterize cell surface phenotypes by flow cytometry. Dendritic cells (10^5) were washed in cold PBS and incubated 15 min at 4°C with specific FITC or PE-labeled Abs. MAbs against IL-8 receptors (CXCR1 and CXCR2) were used by indirect fluorescence developed with a rabbit anti-mouse antiserum tagged with FITC (Jackson ImmunoResearch Labs, West Grove, PA).

In vitro and *in vivo* MLR

In vitro MLR were performed as described [26]. Briefly, a total of 2×10^5 lymphocytes from a distinct donor were added on day 9 at different T cell:DC ratios (1280:1, 640:1, 320:1, 160:1, 80:1 and 40:1). After 3 days, the [methyl-3H]thymidine uptake was determined by the addition of 1 μCi of [methyl-3H]thymidine.

Female Rag$^{-/-}$ IL-2Rγ$^{-/-}$ were subcutaneously injected with 5×10^6 HT29 cells. When tumors reached approximately 1 cm in diameter, these mice and tumor-free mice were intraperitoneally injected with 1×10^6 DC and 5×10^6 PKH2-labeled PBLs. After 4 days, cells were obtained by intraperitoneal lavages and samples were analysed using a FACSCalibur Flow Cytometer (Becton Dickinson). The number of T cell divisions is proportional to the dilution of PKH2 intensity and was found to be negligible in the absence of DC (data not shown). For FACS analysis lymphocytes were gated based on FSC/SSC features.

PMN purification and fluorescence labelling

In vitro neutrophil and DC migration was measured in Transwell Chambers (5 μm; Corning Costar, Corning, NY). PMN cells were enriched by sedimentation of peripheral blood mixed in a dextran (6% v/v) solution. After sedimentation, floating fractions were collected. Red cells in the resuspended pellets were osmotically lysed. The remaining cell suspensions were layered onto Ficoll-Paque gradients and pellets were collected and washed after centrifugation. Neutrophil purity was >95% (CD15$^{\mathrm{bright}}$ neutrophils)

In vitro chemotaxis assay

In vitro neutrophil and DC migration was measured in Transwell Chambers (5 μm; Corning Costar, Corning, NY). Both PKH26-DCs (10^5) and PKH2-labeled neutrophils (10^5) or only PKH2-labeled neutrophils were added to the upper chamber and migration stimuli were placed in the lower chamber. In this experiment IL-8 (R&D Systems) was used at 20 ng/mL as positive control. In other cases PKH26-DCs with or without IL-8 neutralizing mAb or IgG as control (BD Pharmigen) at 20 μg/mL was placed in the lower chamber as indicated. Transmigrated cells in the lower chamber were quantified using a FACSCalibur flow cytometer (BD Biosciences) or fluorescence microscopy imaging of the lower chamber. In some cases the lower chamber contained a subconfluent monolayer of HT29 cells. The chemotactic index was calculated as the number of migrated cells in the experimental conditions divided by number of migrated cells in the negative control, which is complete culture medium. In the experiments with HT29 cell in the lower chamber number of PKH2-fluorescent DC per microscopic field (×20) in the lower chamber were quantitated in triplicate wells by a blinded observer. Recombinant MIP3α was from R&D.

Statistics

Comparisons were made with paired student's t tests. Values of p are given in the corresponding experiments.

Results

HT29 and CaCo2 tumor cell lines xenografted into immunodeficient mice generate tumors that produce IL-8

A panel of human colon carcinomas was tested in order to identify cultures that produce high amounts of IL-8 to the supernatant [1]. All clonal subcultures of HT29 showed high homogeneous outputs of IL-8 while the SW48 cell line did not reach detectable levels in any experiment, and CaCo2 subcultures showed around one half of the production when compared to the levels attained by HT29 cells cultured at identical density for the same period of time (Figure S1). Microenvironment conditions and therapy may modify the ability of tumor cells to produce IL-8. Figure 1A shows that the production of IL-8 secreted to culture supernatants by viable HT29 cells was reduced in 24 h by exposure to low concentrations cyclophosphamide, while cells still preserved membrane integrity (>90% viability by trypan blue exclusion). Interestingly, the low range of cyclophosphamide concentrations was more effective at preventing IL-8 bioproduction and secretion to the supernatant. Gemcitabine and radiation did not or more weakly affected IL-8 secretion (Figure 1A and data not shown). Moreover, in a repeated set of experiments semiquantitative RT-PCR for IL-8 in comparison with the house keeping mRNA β-actin showed that cyclophosphamide inhibits IL-8 production at the mRNA level in a dose-dependent manner (Figure 1B), in such a way that low dose cyclophosphamide was better at mediating this effect than higher concentrations.

These results open the possibility that IL-8 production can be acutely reduced by cyclophosphamide for therapeutic purposes. Indeed, metronomic cyclophosphamide is becoming an attractive alternative for cancer management [31] and potentiation of a variety of immunotherapies [32].

When HT29 was xenografted in athymic nude mice, it gave rise to subcutaneous nodules that grew steadily over time (Figure 1C). Sequential sera samples from such animals contained increasing concentrations of IL-8 (Figure 1C) that correlated with tumor progression as reported in human patients [3].

CaCo2 failed to graft as subcutaneous nodules in two thirds of cases (data not shown), but grafted homogeneously as multiple peritoneal nodules if injected intraperitoneally (Figure S2). CaCo2-grafted animals also showed circulating IL-8 (Figure S2) but at lower concentrations if compared to HT29-bearing mice, as expected from the productions of IL-8 in the cell line cultures. Apart from this quantitative difference, the tendency was similar in tumors from both cell lines.

Importantly, treatment of mice with a single dose of 3 mg/mouse of cyclophosphamide reduced the serum concentration of IL-8 in the next 24 h in a range from 48 to 100% (Figure 1D), while those concentrations rapidly rebound in 48–72 h. It is of note that for this experiment mice with 7-day palpable tumor xenografts were used, so the concentrations of IL-8 in plasma were still low.

In conclusion, xenografted colon carcinomas retain the property of producing high amounts of human IL-8, and our results indicate that such a function could be modified by cyclophosphamide.

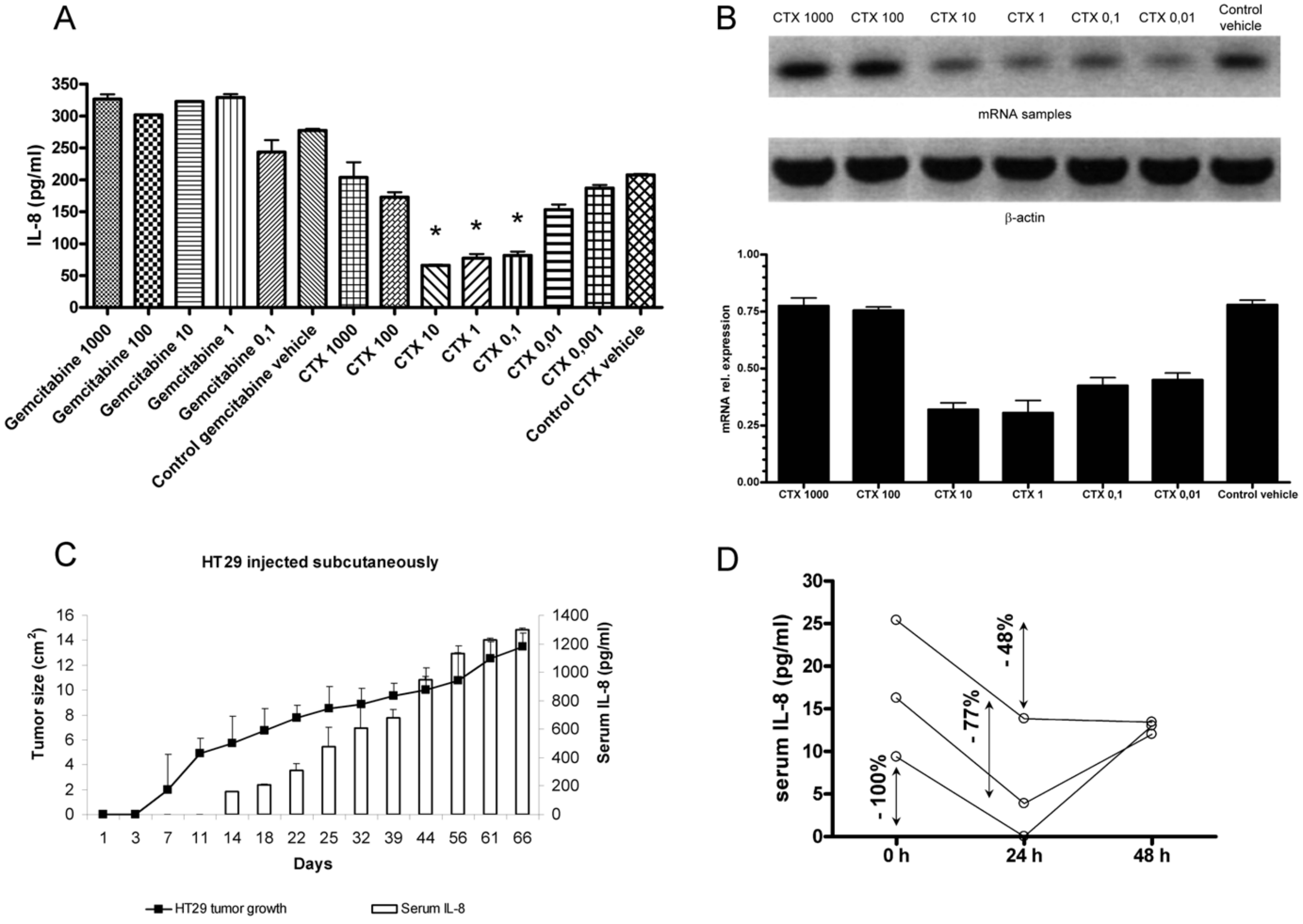

Figure 1. HT29 cells when xenografted secrete IL-8 to the plasma of the mice. ELISA determination of IL-8 in the supernatant of HT29 confluent cultures in the presence of indicated concentrations of cyclophosphamide (1000 to 0.001 µg/mL), or gemcitabine (1000 to 0.1 µg/mL) during the 24 h prior to supernatant collection. When indicated the solution vehicle of both drugs was added at the highest concentration. Results represent mean±SEM from three experiments. (B) Separate set of experiments as in A but in this case HT29 were collected and IL-8 mRNA was quantified by RT-PCR. PCR bands are shown in the upper panel and densitometry quantitative data given in the lower panel representing relative expression of IL-8 mRNA in comparison with β-actin mRNA. (C) Subcutaneously xenografted HT29 cells in Rag$^{-/-}$ IL-2Rγ$^{-/-}$ mice gave rise to progressing tumors (left axis depicting mean tumor diameter) and increasing serial serum concentrations of human IL-8 (right axis). Results represent mean±SEM of three independent experiments with 6 mice per experiment. Similar results were observed with CaCo2 tumors xenografted in the peritoneal cavity (Figure S1). (D) IL-8 serum concentrations of three individual Rag$^{-/-}$ IL-2Rγ$^{-/-}$ mice bearing HT29 tumors for seven days before a single intraperitoneal injection of 3 mg of cyclophosphamide and 24 and 48 h after treatment. The percentages of reduction at 24 h are indicated. Experiments were repeated at least three times with the exception of (D) that was performed with three individual animals.
doi:10.1371/journal.pone.0017922.g001

Exogenously injected human DC inside xenografted HT29 tumors are retained by IL-8 in the tumor microenvironment

In order to study whether IL-8-producing tumors would retain intratumorally DC injected inside the lesion, we first chose the HT29 xenografts because of their higher bioproduction of IL-8.

Human DC were derived from CD14^{+} monocytes in the presence of GM-CSF and IL-4 and labeled with PKH26. Fluorescent DC were injected into HT29 tumor nodules subcutaneously implanted into Rag$^{-/-}$ IL-2Rγ$^{-/-}$ mice. In some of the mice, DC were injected with control polyclonal mouse IgG antibody, while in other cases were resuspended with 100 µg/mL of an anti-human IL-8 neutralizing mAb. 72 h after DC injection, tumors were removed and a single cell suspension was generated. The number of fluorescent human CD11c^{+} cells versus total cells was quantified. As can be seen in figure 2A, IL-8 indeed retained DC intratumorally since the neutralizing anti-IL-8 mAb decreased the number of cells that remained inside the tumor by more than one half (Figure 2A). FACS analysis representing two cases are shown in figure 2B as an example. These results were confirmed in athymic nude mice bearing subcutaneous CaCo-2 tumors (Figure S3) indicating that the phenomenon was not exclusive of HT29-derived tumors.

SW48 cells, that failed to produce IL-8 as shown in figure S1, were xenografted in Rag$^{-/-}$ mice. In this case, the tumors could not retain DC labeled with the fluorescent dye PKH26. Figure 2C shows representative dot plots from three mice 72 h post intratumoral injection along with the fluorescence of input DC (left dot-plot of figure 2C). These results on the colon cancer cell line that does not produce IL-8 further indicate that this chemokine was important for the retention of DC inside the tumor upon intratumoral release.

Lack of IL-8 effects on DC-mediated T-cell stimulation

Functional response to IL-8 involves signalling pathways that might alter DC functions, since these cells are known to express CXCR1 and CXCR2 [1]. We explored this question in detail

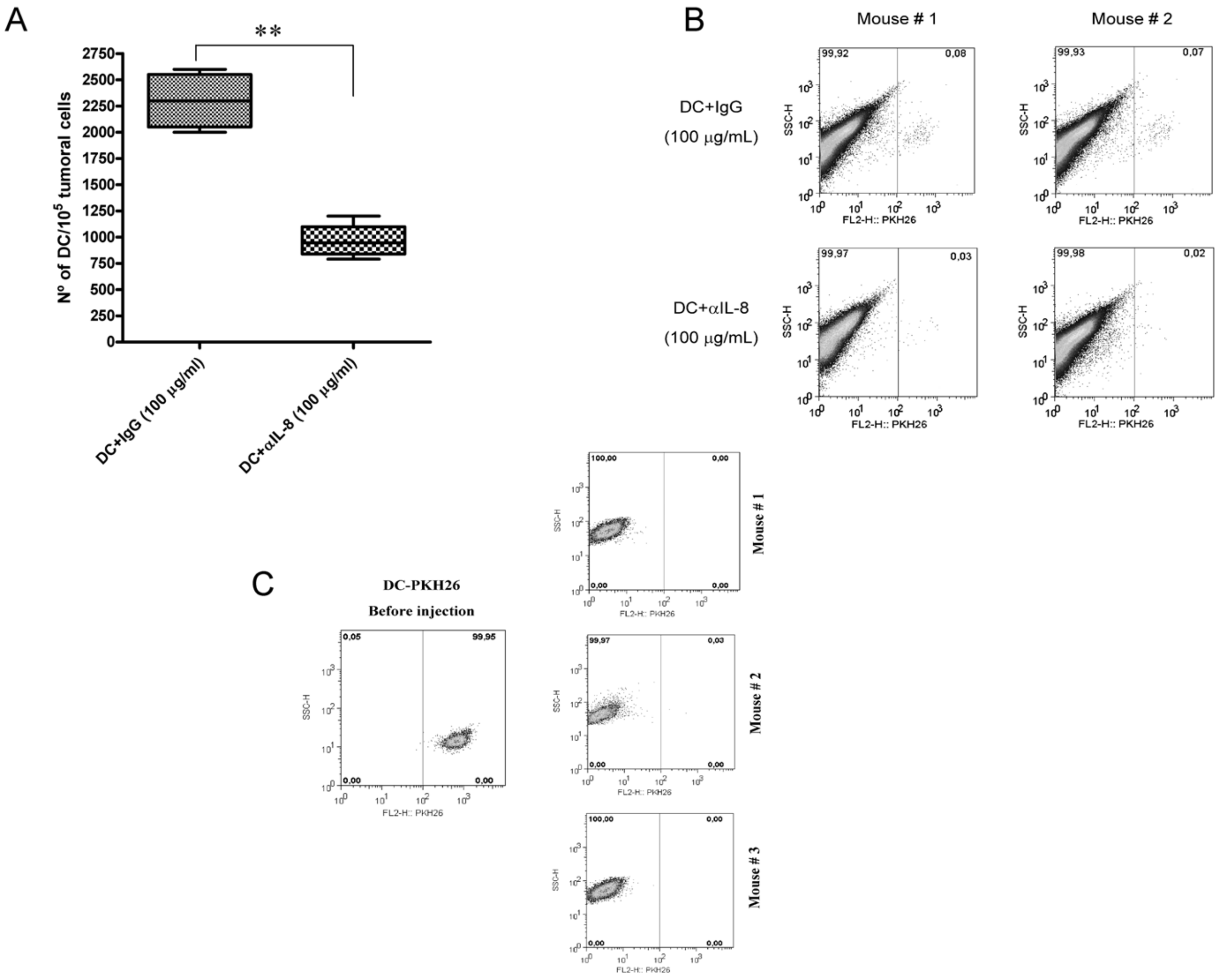

Figure 2. IL-8 produced by tumor cells *in vivo* retains DC inside xenografted tumor nodules. (A) HT29 was xenografted into Rag$^{-/-}$ IL-2R$\gamma^{-/-}$ double KO mice. Tumor nodules, 8–12 mm in diameter, were injected with 5×10^{6} PKH26-labeled monocyte-derived DC. When indicated, the 100 µL DC suspensions contained 100 µg/mL of mouse IgG (control antibody) or anti-IL-8 neutralizing mAb. The figure shows the proportion of PKH26^{+} events with respect to total tumor cells upon FACS analysis, three days after DC injection. Four mice with two bilateral xenografted tumors each per condition were used. Of note, DC cultured in the presence of the anti-IL-8 mAb at 100 µg/mL did not show loss of viability at least in 72 h (data not shown). (B) Representative FACS dot plots from A in two tumor nodules from two mice are shown as an example. Similar data were obtained with xenografts of the CaCo2 cell line (Figure S2). (C) Absence of PKH26-labeled DC in 3 out of 3 SW48 xenografts processed as in A, following injection of fluorescence labeled human DC. In the left dot-plot, the fluorescence intensity of injected PKH26-labeled DC is shown for reference. Dot plots are from representative experiment of two actually performed with three animals per group each.

doi:10.1371/journal.pone.0017922.g002

using Mixed Lymphocyte Reaction (MLR) assays in which DC were co-cultured in decreasing amounts with fully allogeneic Peripheral Blood Mononuclear Cells (PBMC) containing alloreactive T-cells. When added during the MLR reaction, IL-8 did not change the proliferation of T cells (Figure 3A) or the ensuing production of INF-γ to the supernatant (data not shown).

DC were derived from CD14^{+} monocytes in the presence of GM-CSF and IL-4 and during this process we had observed that tumor-derived compounds impair differentiation [26]. However, in the case of IL-8 as a recombinant protein, resulting DC stimulated allogenic MLRs as strongly as those DC derived in the absence of the IL-8 chemokine (Figure 3B).

Alternatively, IL-8 could alter the maturation/activation of DC [29]. To induce maturation, DC were incubated for 48 h with a mixture of INF-α, TNF-α and Poly I:C in the presence or absence of IL-8. No change was observed again in the ability of DC to induce proliferation of allogeneic T lymphocytes (Figure 3C). To rule out alterations of the recombinant protein used, in every case, IL-8 was controlled for functionality since it readily attracted human neutrophils, as shown in chemotaxis assays (Figure S4).

We had previously shown that DC expressed CXCR1 and CXCR2 [1]. We observed that the exposure to the ligand for two hours induced the modulation/internalization of both receptors (Figure 3D) in the very same DC used to set up the T-cell allostimulation experiments. Therefore, the pathways guiding IL-8-directed migration and those governing the capabilities for T-cell stimulation seem to be fairly independent in the DC.

The absence of effects on T cell:DC co-cultures suggested that the molecular factors employed by the DC for T cell activation were not affected by IL-8.

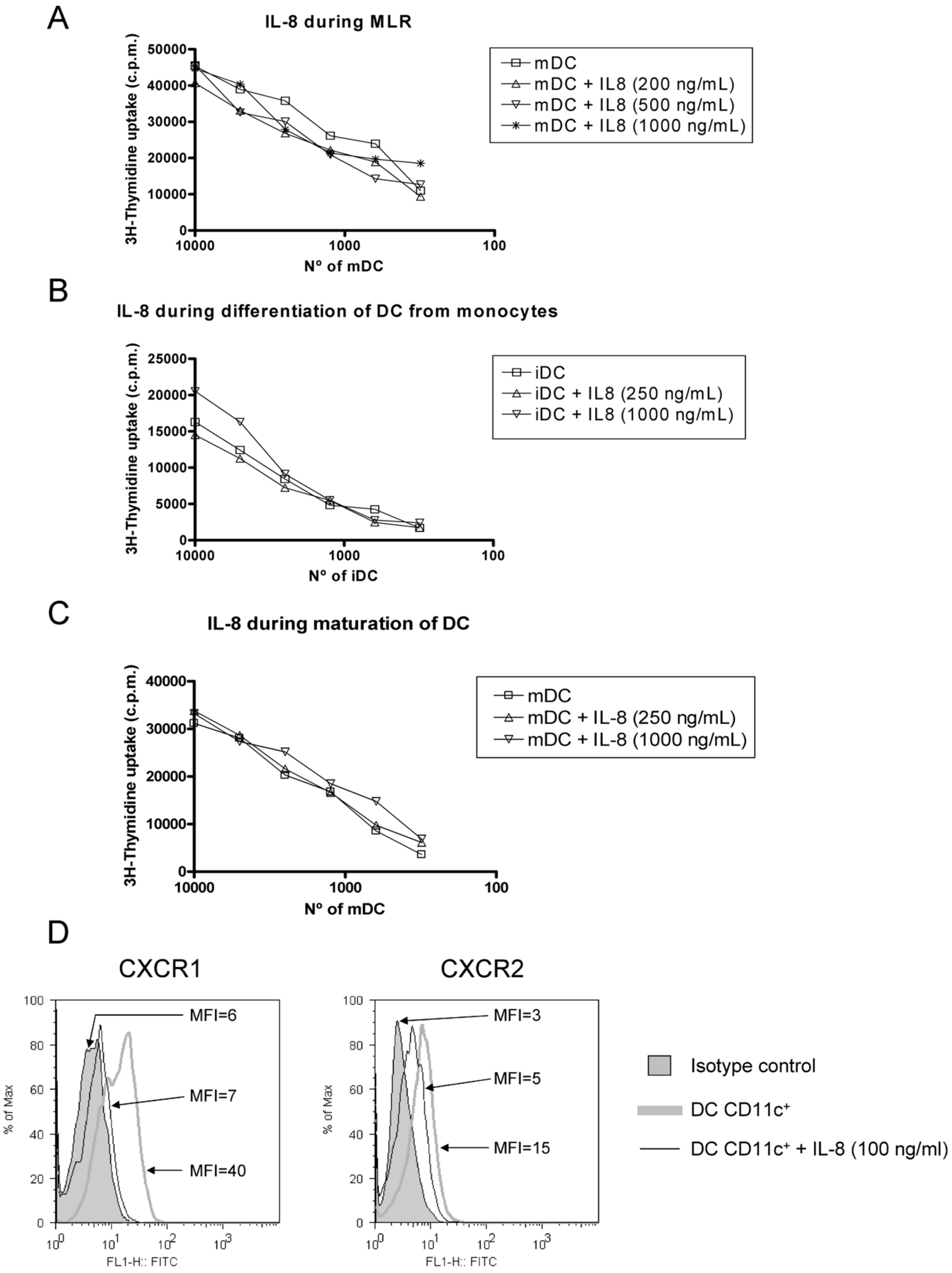
A
IL-8 during MLR
3H-Thymidine uptake (c.p.m.)
50000
40000
30000
20000
10000
0
10000
1000
100
Nº of mDC
mDC
mDC + IL8 (200 ng/mL)
mDC + IL8 (500 ng/mL)
mDC + IL8 (1000 ng/mL)
B
IL-8 during differentiation of DC from monocytes
3H-Thymidine uptake (c.p.m.)
25000
20000
15000
10000
5000
0
10000
1000
100
Nº of iDC
iDC
iDC + IL8 (250 ng/mL)
iDC + IL8 (1000 ng/mL)
C
IL-8 during maturation of DC
3H-Thymidine uptake (c.p.m.)
40000
30000
20000
10000
0
10000
1000
100
Nº of mDC
mDC
mDC + IL-8 (250 ng/mL)
mDC + IL-8 (1000 ng/mL)
D
CXCR1
CXCR2
% of Max
100
80
60
40
20
0
10^0
10^1
10^2
10^3
FL1-H:: FITC
MFI=6
MFI=7
MFI=40
MFI=3
MFI=5
MFI=15
Isotype control
DC CD11c+
DC CD11c+ + IL-8 (100 ng/ml)

Figure 3. IL-8 does not impair T cell stimulation by DC that express functional CXCR1 and CXCR2. (A) Human monocyte-derived DC and T-cells were seeded in the indicated proportions. Functional recombinant IL-8 was added at different concentrations as indicated in the graph legends. T-cell proliferation was measured by ^{3}H-thymidine incorporation 3 days later. A representative case out of three independently performed experiments with cells from different combinations of donors is shown. (B) Experiments as in A, but in this case DC were incubated with the indicated amounts of IL-8 added to monocytes during the 7-day differentiation culture in the presence of GM-CSF+IL-4. A representative experiment out of at least three is shown. (C) Similar experiments as in B but in this case IL-8 at the indicated concentrations was added during the maturation 48 h culture onto differentiated DC matured for 48 h with IFN-α, TNF-α and poly I:C. A representative experiment out of at least three performed is shown. As a control every IL-8 batch was shown to readily attract human PMNs in chemotaxis assays (Figure S3). (D) Mature DC as those used for the MLRs were tested by indirect immunofluorescence for the expression of CXCR1 and CXCR2. Incubation with 100 ng/mL of IL-8 during 2 h resulted in a loss of fluorescence intensity upon immunostaining of the surface receptors indicating receptor internalization. The mean fluorescence intensity (MFI) of each histogram is provided. FACS Experiments were repeated in two occasions with similar results.
doi:10.1371/journal.pone.0017922.g003

Indeed, table S1 shows that IL-8 at various concentrations does not alter the level of expression the maturation markers CD80, CD83, CD86 and MHC class II on mature and immature DC. Moreover, IL-8 did not alter the production of IL-12 and IL-10 upon maturation as induced by lipopolysaccharide (LPS) plus the R-848 imidazoquinoline or recombinant CD40L (Figure S5).

Furthermore, we explored the issue of whether immunodeficient animals bearing IL-8-producing tumors would impair MLR alloreactions of human leukocytes seeded inside their peritoneal cavities. For this purpose, we grafted HT29 tumors for 5–7 weeks and co-injected PKH2-labeled PBL and allogeneic DC inside the peritoneal cavity. As can be seen in figure 4, T cells readily proliferated in tumor-free mice within 4 days and such proliferative responses were clearly downsized by the presence of subcutaneous tumors.

If neutralizing anti-IL-8 mAb was co-injected with the PBL and the allogenic DC, no recovery of proliferation was observed. This is interpreted in the sense that factors other than IL-8 downregulate T-cell proliferation. This is in agreement with the lack of IL-8 effects on DC-mediated T-cell stimulation in the *in vitro* alloreactive co-cultures.

In addition, we performed experiments (shown in figure 4B) that demonstrate that treatment of the HT29-xenografted mice with cyclophosphamide did not improve the alloreactive T-cell stimulation. Moreover SW48 xenografts, that do not produce IL-8, also inhibit the intraperitoneal alloreactive response to an extent comparable to that observed with HT29 (Figure 4B).

Regardless the fact that there is no IL-8 homologue gene in the mouse genome, human IL-8 exerts at least some agonist activity on mouse CXCR1 as described [6]. Indeed, we were able to observe IL-8 chemotactic activity on mouse bone marrow-derived DC (Figure S6A). Therefore we set up experiments in which we activated CD4$^+$ TCR-transgenic OT-2 T cells responding to ovalbumin in the peritoneal cavity of Rag$^{-/-}$ IL-2Rγ$^{-/-}$ mice. DC were pulsed with the cognate peptide and the mice were bearing or not established HT29 subcutaneous tumors. As shown in figures S6B and C, HT29 tumors also suppressed proliferation of the mouse T cells in this setting, although such an inhibition was not affected again by IL-8 neutralizing antibodies. Our data further indicate the existence of immunosuppressive factors in the tumor bearing mice which are different from IL-8.

Pre-exposure of DC to IL-8 disorient DC to subsequently follow IL-8-guided migration

DC in tumor bearing subjects would be chronically exposed to IL-8. As we have shown in figure 3D, exposure of DC to IL-8 determines receptor downregulation. Therefore we hypothesized that pre-incubation of DC with IL-8 could inhibit subsequent responses to IL-8 gradients.

In figure 5, chemotactic experiments were set up plating IL-8-producing HT29 cells in the lower chamber and PKH2-labelled DC in the upper chamber. The colon carcinoma cell line induced migration of DC in 16 h that was abolished by anti-IL8 neutralizing mAb. Interestingly, if DC had been pre-exposed for 24 h to recombinant IL-8, migration was also abolished indicating that desensitized DC could not migrate towards the IL-8-producing carcinoma cells. Data are quantified in figure 5B, which also shows that monolayers of the SW48 (the cell line that does not produce IL-8) also fail to attract DC. Likewise, pre-treatment of the HT29 cells with low concentrations of cyclophosphamide decreased the ability of HT29 to attract DC because of reducing IL-8 secretion (Figure 5C).

Therefore while IL-8 seems to leave T cell stimulation by DC unimpaired, chronic exposure to IL-8 may profoundly affect the migration capabilities of DC towards IL-8 gradients and possibly of other leukocyte subsets as well.

In a previous study we reported that DC produce IL-8 [1]. Figure S7A confirms that DC produce IL-8 at the protein and mRNA level. It was conceivable the autocrine IL-8 may downregulate CXCR1 and CXCR2 expression, as seen in figure 3D with exogenously added IL-8. Indeed, we observed brighter immunofluorescence specific for CXCR1 and CXCR2 when IL-8 was neutralized with a specific mAb (Figures S7B and C) and when DC were cultured at very low cell densities upon agitation to dilute the secreted IL-8 (Figures S7B, C and D). Therefore autocrine IL-8 determines the level of receptor surface expression in DC providing an interesting mode of regulation.

IL-8 produced by DC retains and attracts neutrophils

A function of IL-8 could be to favor a rendezvous between polymorphonuclear (PMN) cells and DC by co-attracting both subsets of leukocytes. In our hands, both immature and mature DC produce abundant IL-8, although mature DC produce about four-five-fold more quantity on a per cell basis (Figure S7).

Classical chemotaxis assays were set up to determine if IL8 could regulate DC and PMN migration in a concerted fashion. As can be seen in figure 6A and figure S4, neutrophils are attracted by recombinant IL-8. However, if neutrophils are seeded together with DC (at 1:1 ratio), neutrophil migration as induced by IL-8 was abolished. These data might indicate that DC have a means to attract and/or retain PMNs that otherwise would migrate away.

If the assays were set up with PMNs in the upper and DC in the lower chamber, neutrophils were attracted by DC seeded into the lower chamber. Importantly, addition of neutralizing anti-IL-8 mAb eliminated most of the attraction of fluorescence-labeled neutrophils by the DC seeded in the lower chamber (Figure 6B) while control antibody exerted no effect.

Our results as a whole indicate that although IL-8, abundantly produced by tumors, would not damage DC-mediated stimulation of T-cells. However, tumor-derived IL-8 would alter migration and interactions with other leukocyte subtypes such as neutrophils. For instance, if DC are prevented from migrating towards MIP3α gradients by HT29 supernatants they would reach the inflamma-

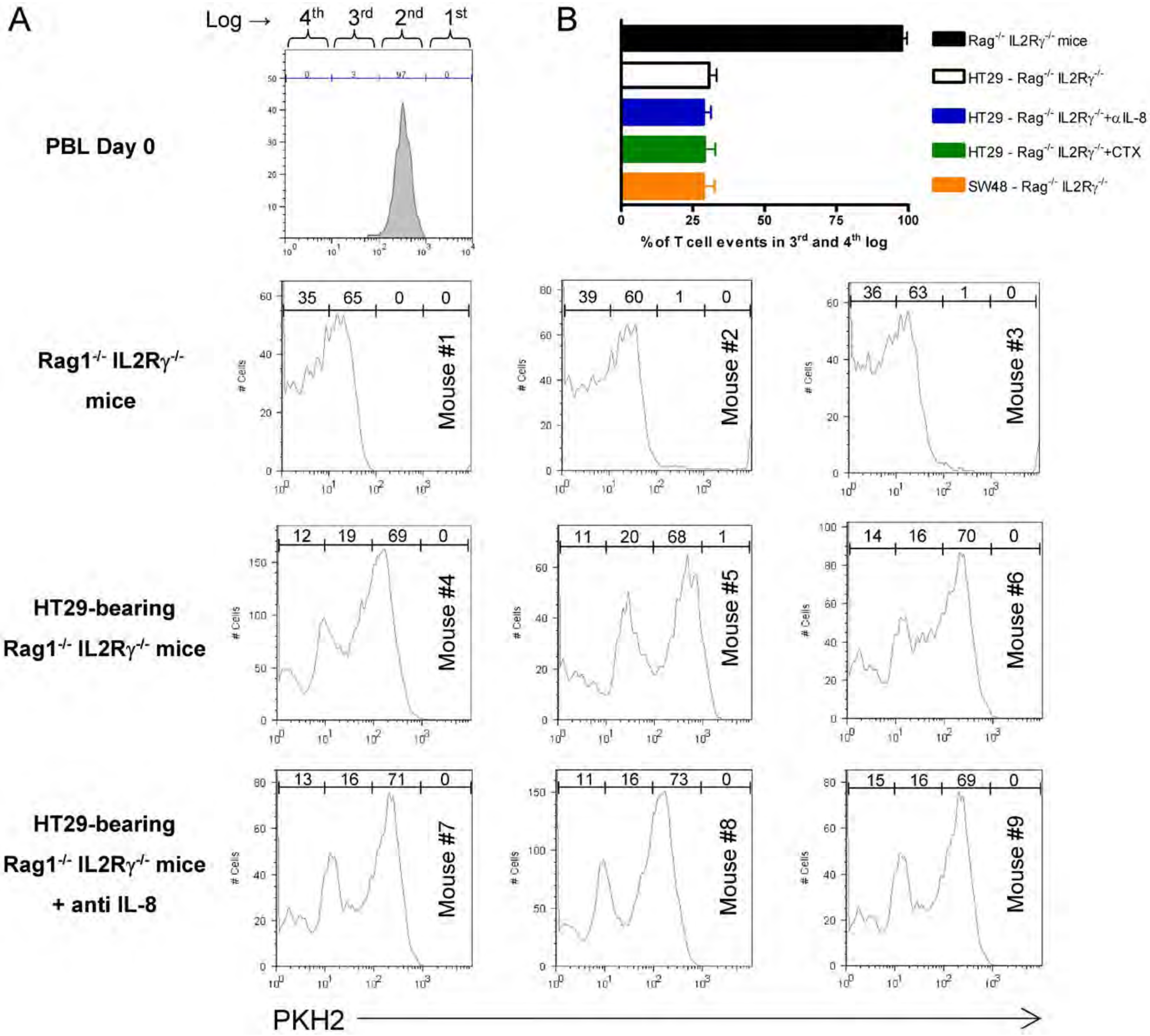

Figure 4. Impairment of DC-induced human T-cell proliferation inside the peritoneum of HT29 xenografted mice. (A) Rag$^{-/-}$ IL-2γR$^{-/-}$ mice (3 per group) were xenografted with HT29 cells or remained tumor-free. Four weeks later mice received intraperitoneal injections of human PKH2-labeled PBLs and fully allogenic mature DC (ratio 5:1 to a total of 6×10^6 cells). Proliferation was monitored four days later by dye dilution on FACS-gated lymphocytes from peritoneal lavages by dilution of the fluorescent dye. In the group of indicated mice an intraperitoneal injection of 100 µg of neutralizing anti-IL-8 mAb was provided immediately following the injection of PBLs and DC. Percentages of dividing lymphocytes in each log cursor interval are shown in the histograms. Fluorescence intensity in the input undivided PBL was over 95% above the third log interval (upper histogram). (B) Similar experiments as in A, quantifying PKH2-dilution as the percentage of cells that reach the 3rd and 4th log scales of the flow cytometry histograms. Log regions are depicted in the upper histogram of A. Data from animals bearing subcutaneous SW48 xenografts, that do not produce IL-8, have been included. Data represent mean±SD.

doi:10.1371/journal.pone.0017922.g004

tory focus in lesser numbers and as a result would stimulate T cells less efficiently (Figure S8). IL-8-disoriented migration could thereby contribute to weaken immune responses to cancer.

IL-8 produced by tumor xenografts attracts DC to the tumor tissue unless they have been desensitized by pre-exposure to IL-8

As seen in figure 1, HT29 xenografts are sites of intense IL-8 production. Therefore we reasoned that DC injected in the subcutaneous tissue 5 mm away from the tumor (Figure 7A) should be attracted to the tumor nodule. Indeed, fluorescence-labelled DC were recovered from the tumor tissue and such migratory behaviour was inhibited if DC were co-injected with the neutralizing anti-IL-8 mAb (Figure 7B). More importantly, pre-exposure of the DC cultures to IL-8 for 24 h prior to injection also greatly impaired the migration towards the tumor. Therefore tumors can attract DC by means of IL-8 but chronic exposure to IL-8 desensitizes DC for this in vivo migration. Owing to these effects, IL-8 produced at malignant lesions profoundly impairs the migratory orientation of DC.

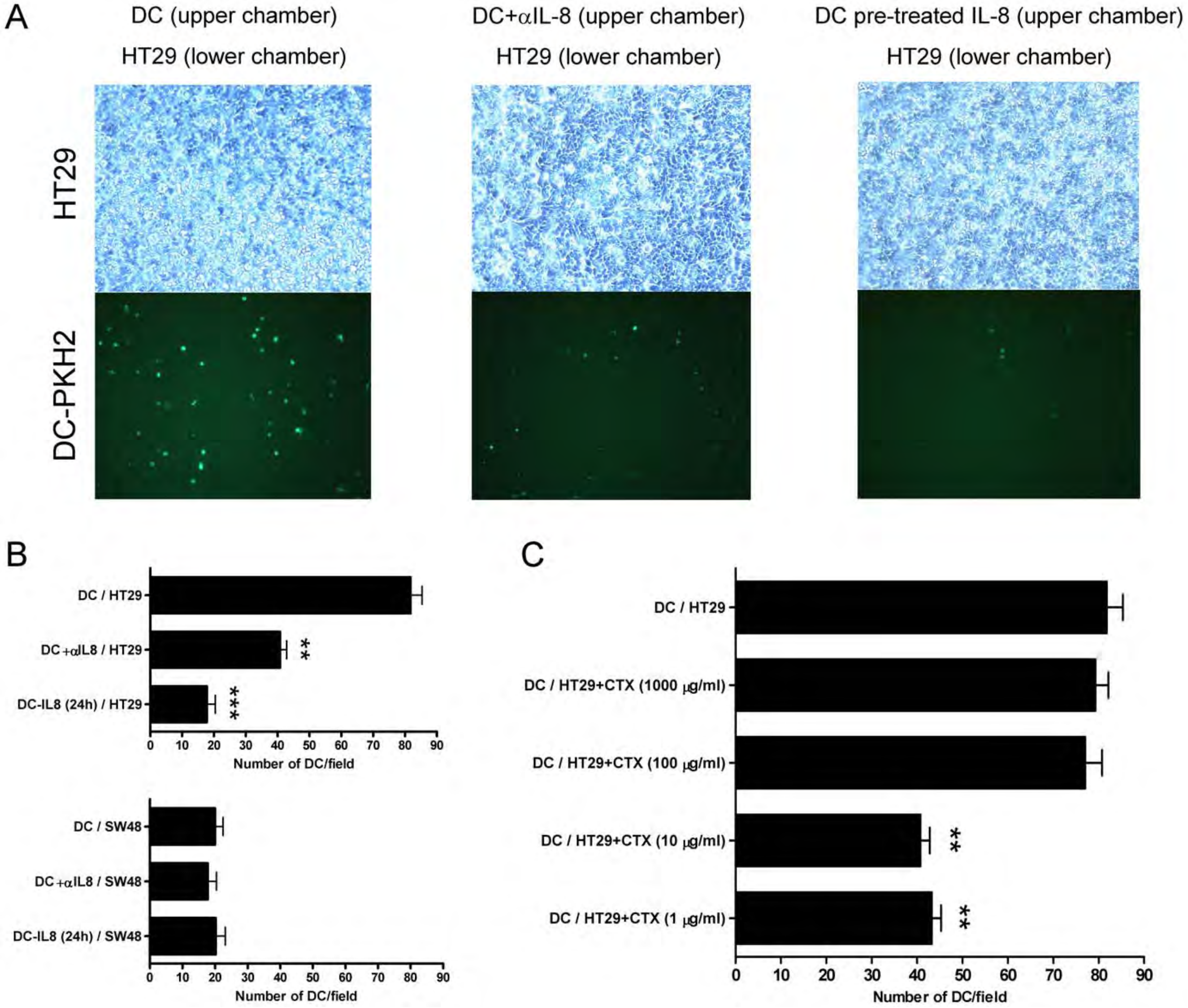

Figure 5. DC pre-exposed to IL-8 become desensitized to respond to carcinoma-derived IL-8 as a chemoattractant. (A) Chemotaxis assays were set up with HT29 confluent monolayers in the lower chamber and fluorescent DC in the upper chamber. Phase contrast microscopy images and the corresponding UV fluorescence microscopic fields of the lower chamber are shown. When indicated the lower chamber contained neutralizing anti-IL-8 mAb (20 μg/mL) or the DC had been pre-exposed for 24 h to recombinant IL-8 (1 μg/mL). (B) In the upper panel representation of data from three independent experiments similarly performed to those in A with HT29 cells represented as mean±SD in which four random fields were counted for each triplicate well. In the lower panel experiments performed as in A, but in this case the confluent monolayers in the lower chamber were formed by SW48 cells that do not produce IL-8. (C) Experiments as in A, but in this case HT29 cells had been pretreated with various cyclophosphamide concentrations for 24 h as indicated in the figure. Results represent mean±SD.
doi:10.1371/journal.pone.0017922.g005

Discussion

By producing IL-8, tumors may profoundly alter the migration-guiding gradients of this important chemokine in the tissues of tumor-bearing hosts [33]. Indeed, the chemokine network is well known to modify cancer biology in multiple ways from metastasis and angiogenesis to the attraction of a nurturing leukocyte infiltrates [33]. In this study, we demonstrate that IL-8 as produced by human tumor cells is capable of attracting (or retaining) human DC *in vivo*, but that IL-8 does not functionally affect the ability of DC to stimulate alloreactive T cells.

We found that at least *in vitro*, IL-8 production by tumor cells can be decreased by low dose cyclophosphamide at the protein and mRNA level. *In vivo* this is reflected by transient decreases in the serum concentration of the chemokine in circulating blood. The rapid decrease and recovery of serum concentrations indicate the rapid turnover in blood of a polypeptide below the renal filtration threshold and with a short half-life [34]. We are exploring the therapeutic implications of low-dose cyclophosphamide effects on IL-8 patho-phisiology. In fact, this effects on IL-8 output can be a factor behind the beneficial effects of the described metronomic dosing of the drug [31,32]. In addition acute reductions in IL-8 output as induced by cyclophosphamide might be exploited to support intratumoral injections of DC in order to favor migration to lymph nodes.

In a clinical trial IL-8 was suspected to mediate intratumoral retention of DC artificially delivered in such locations by image-guided procedures of injection [1]. However, the role of IL-8 at *in*

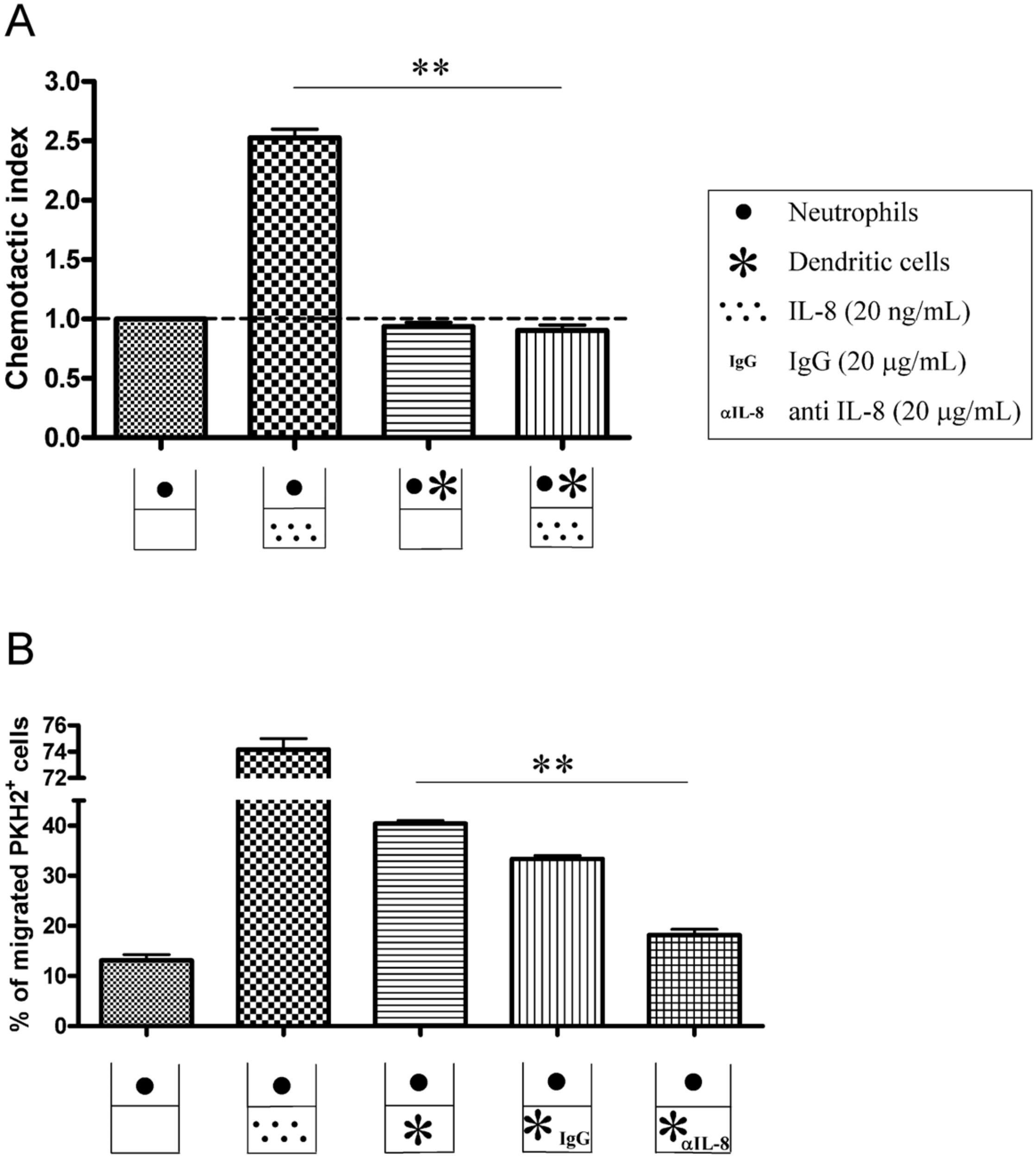

Figure 6. DCs retain neutrophils in migration assays towards IL-8 and attract neutrophils in an IL-8-dependent fashion. (A) Transwell chemotaxis assays were set up with PKH2-labeled neutrophils. Neutrophils migrated to recombinant IL-8 added to the lower chamber. However, if neutrophils are seeded in the upper chamber together with DC (1:1) migration is totally impaired. Of note there is IL-8 by the DC as shown in figure S6A. This experiment is representative of two independently performed in triplicate wells with migration lasting for 120 min. (B) Percentage of migration of PKH2-labeled neutrophils that were seeded into the upper chamber of transwell migration assays towards recombinant IL-8 or DC placed in the lower chamber. When indicated, IL-8-neutralizing mAb (20 μg/mL) was added to the lower chamber along with the DC. Migration was analyzed at 120 minutes. Similar experiments analyzed as early as 60 minutes rendered similar results (data not shown). Results are representative of two separate triplicate experiments independently performed. Asterisks indicate statistical significance $p<0.01$ in student's t tests.

doi:10.1371/journal.pone.0017922.g006

vivo retention could not be experimentally documented. In this study, we observe that DC are retained inside xenografted colon carcinomas by IL-8. The evidence was generated by means of a neutralizing anti-IL-8 mAb injected alongside the DC. These findings further support our interpretations with regard to the apparent retention of intratumorally injected DC in patients according to scintigraphic scans [1,2].

In our mouse xenograft system, we do not yet understand whether migration out of tumors is the result of chemotaxis driven by mouse factors or random migration. What we document is that IL-8 mediates the retention inside the tumor microenvironment. This is not a surprise since IL-8 receptors, CXCR1 and CXCR2, are expressed on DC and are functional in classical chemotaxis assays [1]. The production of IL-8 by DC themselves could be also operating in an autocrine or paracrine fashion in this intratumoral setting. Nonetheless, we clearly observe that HT29 tumor xenografts are capable to chemoattract DC when injected in the connective tissue that surrounds the malignancy.

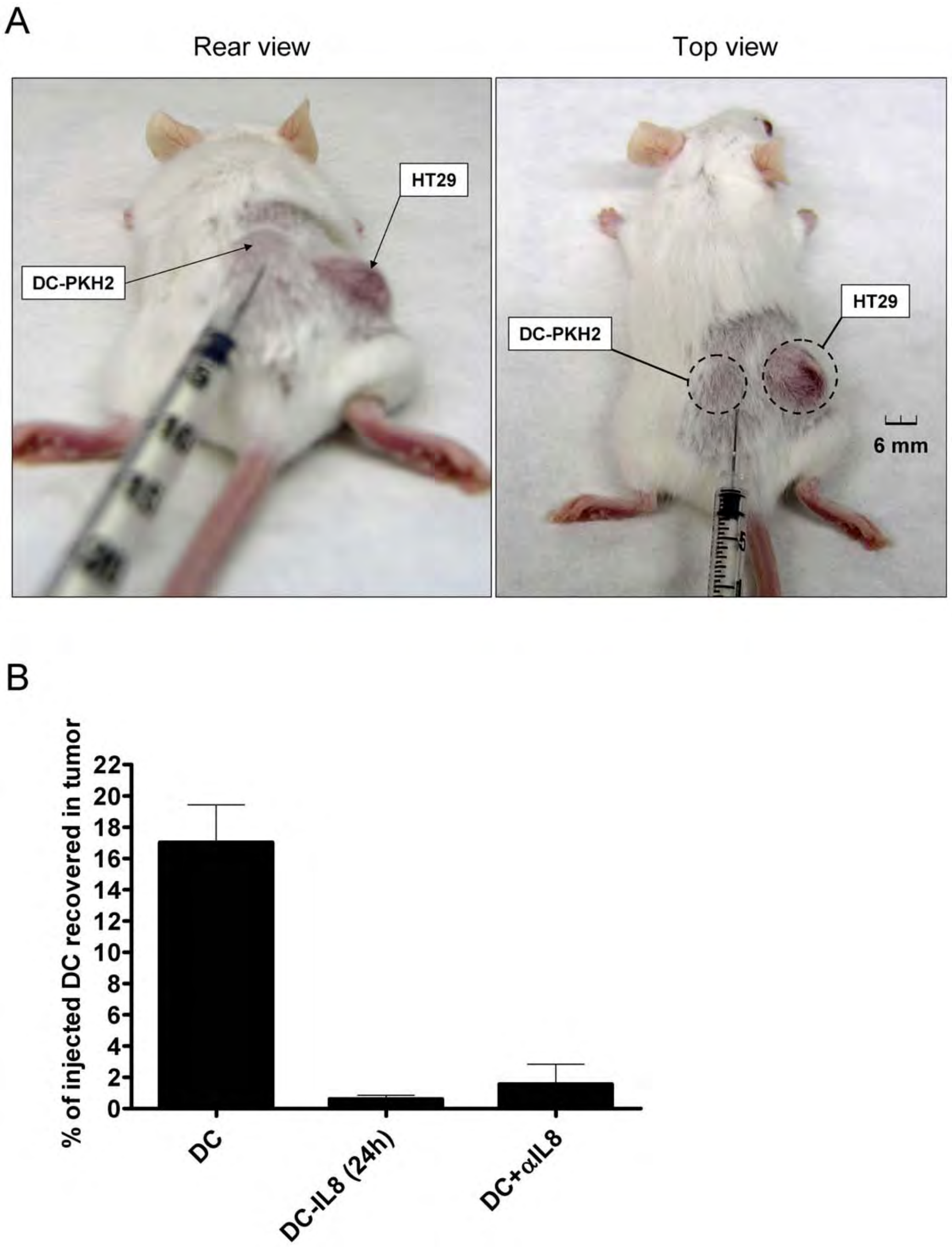

Figure 7. HT29 xenografts attract human DC injected in the subcutaneous tissue which surrounds the tumor. (A) Mice bearing HT29 established xenografts as the one shown in the pictures were injected approximately 5 mm away from the tumor lesion with 5×10^6 human immature DC labelled with PKH2 that were resuspended in 50 µl of saline buffer to form a small subcutaneous bump which disappeared in less than 2 hours. (B) 24 hours later tumors were surgically removed and a cell suspension was obtained in which the number of fluorescent DC were enumerated by flow cytometry and normalized as the percentage of injected DC that were recovered from the tumor. When indicated DC were pre-treated for 24 hours in culture with 1 µg/ml of rIL-8 or DC were co-injected with 100 µg of neutralizing anti-IL8 mAb.
doi:10.1371/journal.pone.0017922.g007

The IL-8 receptors, when ligated, turn on various signaling pathways [35] and rearrange the cytoskeleton [13]. IL-8 could thereby potentially alter the functional performance of DC. Therefore we hypothesized that DC under the influence of IL-8 in the tumor, would be poorer T cell stimulators. However, fully functional IL-8 (as checked in migration assays) was completely incapable of decreasing T-cell allostimulation as mediated by DC. This is in agreement with the fact that IL-8 does not affect the expression of costimulatory receptors or T-cell stimulating cytokines. It remains to be seen if IL-8 alters the antigen presenting machinery or other biological activities of DC that are not required for alloreactive stimulation. Although not formally ruled out, this possibility is considered unlikely.

Nonetheless, if DC were retained in the tumor milieu by IL-8, those DC would remain under the concentrated influence of tumor-derived factors that repress DC functions [26,36,37,38]. Evidence for this phenomenon also comes out from our alloreactive reactions of human lymphocytes inside the peritoneum of immunodeficient mice bearing HT29 and SW48 xenografts [39]. Some of the malignant tissue immunorepressor molecules include TGF-β [40,41], VEGF [42,43], interleukin-13 [44], prostaglandins, kynurerines [40] and most likely other unknown polypeptide moieties [26], as well as certain lipids [45].

Collectively, our data can be interpreted in the sense that IL-8 retains DC in the precise location where such antigen presenting cells are most efficiently damaged in their function by tumor-derived biomolecules. Our results regarding the *in vivo* inhibition of T-cell allostimulation in animals xenografted with human tumors offer a useful experimental system to dissect tumor-dependent mechanisms of inhibition that are operating distantly from the tumor implant. This experimental tool is employed in our laboratory [39].

DC intratumoral retention has been described as an evasion strategy in breast cancers [46]. We can observe in *in vitro* chemotaxis that if HT29 cells prevent DC from migrating to MIP3α mimicking an inflammatory focus then fewer DC reach the location to stimulate T cells and the immune response is accordingly less intense.

These phenomena certainly pose an obstacle for the intratumoral route of DC administration in human immunotherapy [11], an approach that has been described to be very successful in a number mouse models [47,48,49,50]. From the therapeutic point of view, low doses of cyclophosphamide can be useful to reduce IL-8 output by viable tumor cells. Neutralization of IL-8 with mAb could be also therapeutically feasible. This has been recently demonstrated in a situation in which tumor xenografts escape from sunitinib-induced anti-angiogenesis by means of an IL-8-dependent mechanism [19].

IL-8 attracts neutrophils and possibly immature forms such as myeloid derived suppressor cells [37,51]. Interestingly, DC secrete IL-8 that may act in an autocrine fashion [1]. Apart from these largely unexplored autocrine effects that modulate CXCR1 and CXCR2 surface levels; we show that DC are capable of attracting or retaining neutrophils in an IL-8-dependent fashion. The physiological consequences of DC-neutrophil interactions [52] in the tumor context are currently being actively explored in our laboratory, with emphasis on the implications for cross-presentation of tumor antigens [53,54].

What seems also plausible is that under high circulating levels of IL-8, as occurs in HT29-xenografted mice or patients with bulky disease, migration-driving gradients of IL-8 would be disrupted and thereby DC-production of IL-8 might be overwhelmed in its ability to attract neutrophils and other leukocytes. Indeed, we have obtained evidence in the sense that overwhelming pre-exposure to IL-8 results in desensitization of the DC to the chemotactic effects of IL-8. In other words, this could mean that DC chronically exposed to IL-8 in the context of tumor-bearing hosts would become disoriented and thus unable to follow migration cues set up by IL-8 concentration gradients. *In vivo* evidence of desensitization for migration further supports this notion. Such immune disorientation as caused by the abundantly and ectopically expressed chemokine may result in disordered immune responses and ought to have relevant prognostic consequences for patients.

Supporting Information

Figure S1 Colon carcinoma cell lines HT29 and CaCo2 produce high levels of IL-8 in a clonal stable fashion while SW48 does not produce IL-8. Clonal limiting dilution subcultures (four for each cell line) of the colon cancer-derived cell lines HT29, CaCo2 and SW48 were tested for the production of IL-8 as measured in 24 h culture supernatants by ELISA.
(TIF)

Figure S2 CaCo2 carcinoma cells xenografted in immunodeficient mice develop progressive intraperitoneal tumors that correlate with raising serum concentrations of IL-8. Intraperitoneally xenografted CaCo2 cells developed progressive peritoneal colon carcinomas in athymic nude mice (measured as weight increase in the left axis) and accumulated increasing concentrations of serum IL-8 (right axis).
(TIF)

Figure S3 DC are retained inside CaCo2 tumors in a IL-8-dependent fashion. CaCo2 cells were xenografted in athymic nude mice. Only 1/3 of such animals successfully xenografted tumor lesions. Tumor nodules, 8–12 mm in diameter, were injected with CFSE-labeled human DC derived from monocytes, as in A. DC were injected in 100 μL of saline buffer with control antibody or neutralizing anti-IL-8 mAb. In these cases, tumors were homogenated and cleared of debris by centrifugation. Fluorescence in the lysate was measured in a fluorimeter. The amount of fluorescence remaining in the tumor compared to that present in the lysate from an identical number of DC before being injected in the tumor was quantitated. Data are presented as the percentage of fluorescence lost from the tumor. Experiments were performed with four mice bearing a single tumor nodule. The inset shows a correlation of fluorescence (arbitrary units) and number of DC in lysates containing increasing amounts of CFSE-labeled DC.
(TIF)

Figure S4 Recombinant IL-8 rendering negative results at modifying DC functionality is capable of attracting PMNs. Migration transwell assays with purified neutrophils in the upper chamber and different concentrations of the recombinant IL-8 in the lower chamber to prove that IL-8 used in figure 3A, B, C and D was fully functional.
(TIF)

Figure S5 IL-8 does not modify IL-12 nor IL-10 secretion by DC matured in the presence of LPS+R848 or trimerized CD40L. IL-12 and IL-10 were quantified in the supernatant of DC cultures treated with the indicated concentrations of IL-8 during the 48 h maturation culture. Concentrations (mean±SD) represent triplicate wells from a single experiment.
(TIF)

Figure S6 Activation of antigen specific murine CD4 T cells by DC in mice bearing HT29 tumors is suppressed by factors distinct from IL-8. (A) Mouse BM-derived DC [50,55] were subjected to classical transwell chemotaxis assays towards culture medium (control), 10^5 heat-inactivated E. coli bacteria used as a positive control, or recombinant IL-8 as indicated. Data show a modest but reproducible attraction of mouse DC by human recombinant IL-8. (B) Schematic representation of experiments in which HT29-bearing $Rag^{-/-}$ $IL\text{-}2R\gamma^{-/-}$ mice were injected in the peritoneal cavity with 5×10^6 CFSE-labelled CD4 OT-2 cells [56] and 10^6 syngeneic DC pulsed with the OVA323-339 synthetic peptide. (C) Assessment of OT-2 T-cell proliferation by dilution of CFSE as in figure 4. Experiments were performed in mice bearing or not HT29 tumors with or without

cognate peptide stimulation by the DC (n = 3 mice per group). When indicated 100 µg of anti-IL8 mAb were co-injected into the peritoneal cavity.
(TIF)

Figure S7 DC produce IL-8 and such autocrine IL-8 modulates in part the surface expression of CXCR1 and CXCR2. (A) Left axis: IL-8 concentration in the supernatant of mature (mDC) and immature DC (iDC); Right axis: mRNA encoding IL-8 in the corresponding DC cultures assessed by semi quantitative RT-PCR. (B and C) IL-8 concentration in the supernatant (left axes) and CXCR1 (B) and CXCR2 (C) surface expression as mean fluorescence intensity (MFI) analyzed by FACS (right axes). In B and C a mAb neutralising IL-8 (20 µg/ml) was added when indicated, or the DC were cultured under gentle agitation at the cellular densities given. Results are presented as mean±SD from triplicate experiments. IL-8 neutralisation or lower IL8 concentrations in the supernatants correlate with higher MFIs for CXCR1 and CXCR2 on the DC. (D) Shows representative FACS histograms from B and C.
(TIF)

Figure S8 IL-8 in conditioned supernatants from HT29 cells impedes DC from migrating to MIP3α gradients. As a consequence fewer DC reaching the lower chamber results in less T-cell allostimulatory activity at this location. In order to model whether DC-disoriented migration would give rise to less T cell stimulation, we set up in the left panel chemotaxis assays in which DC migrated towards recombinant MIP3α (100 µg/ml). Data are presented as mean±SD of the chemotactic index normalized with culture medium without MIP3α (Neg). DC were seeded in the upper chamber with or without conditioned medium of HT29 cells or SW48 cells as indicated. When indicated an IL-8 neutralising antibody was added. In the right panel DC recovered from the lower chamber were used to stimulate allogenic PBL, and T-cell proliferation was recorded three days later as c.p.m. in ^{3}H-Thy incorporation assays. Data represent three independent replicates.
(TIF)

Table S1 Lack of IL-8 effect on surface expression of dendritic cell maturation markers. Mean fluorescence intensity of the indicated surface markers of DC upon FACS analyses in human DC (mean±SD from three different experiments) using either immature (iDC) or LPS+R848 matured DC (mDC), that were cultured in the absence or the presence of increasing concentrations of IL-8 as indicated in the columns. Experiments are representative of three similarly performed with different donors.
(TIF)

Acknowledgments

Elena Ciordia and Eneko Elizalde are acknowledged for excellent animal facility management, as well as technical help by Arantza Azpilikueta, Manuela González-Aparicio and Ana Larraga.

Author Contributions

Conceived and designed the experiments: IM JLP-G AG CA NS AR. Performed the experiments: CA NS AP LE SS EB JD EF. Analyzed the data: IM SH-S JLP-G IM-F AR AG. Contributed reagents/materials/analysis tools: IM EF AR. Wrote the paper: IM JLP-G CA NS.

References

1. Feijoo E, Alfaro C, Mazzolini G, Serra P, Penuelas I, et al. (2005) Dendritic cells delivered inside human carcinomas are sequestered by interleukin-8. Int J Cancer 116: 275–281.
2. Mazzolini G, Alfaro C, Sangro B, Feijoo E, Ruiz J, et al. (2005) Intratumoral injection of dendritic cells engineered to secrete interleukin-12 by recombinant adenovirus in patients with metastatic gastrointestinal carcinomas. J Clin Oncol 23: 999–1010.
3. Xie K (2001) Interleukin-8 and human cancer biology. Cytokine Growth Factor Rev 12: 375–391.
4. Sallusto F, Palermo B, Lenig D, Miettinen M, Matikainen S, et al. (1999) Distinct patterns and kinetics of chemokine production regulate dendritic cell function. Eur J Immunol 29: 1617–1625.
5. Sozzani S, Luini W, Borsatti A, Polentarutti N, Zhou D, et al. (1997) Receptor expression and responsiveness of human dendritic cells to a defined set of CC and CXC chemokines. J Immunol 159: 1993–2000.
6. Fan X, Patera AC, Pong-Kennedy A, Deno G, Gonsiorek W, et al. (2007) Murine CXCR1 is a functional receptor for GCP-2/CXCL6 and interleukin-8/CXCL8. J Biol Chem 282: 11658–11666.
7. Sallusto F, Lanzavecchia A (1999) Mobilizing dendritic cells for tolerance, priming, and chronic inflammation. J Exp Med 189: 611–614.
8. Martin-Fontecha A, Lanzavecchia A, Sallusto F (2009) Dendritic cell migration to peripheral lymph nodes. Handb Exp Pharmacol. pp 31–49.
9. MartIn-Fontecha A, Sebastiani S, Hopken UE, Uguccioni M, Lipp M, et al. (2003) Regulation of dendritic cell migration to the draining lymph node: impact on T lymphocyte traffic and priming. J Exp Med 198: 615–621.
10. Verdijk P, Aarntzen EH, Punt CJ, de Vries IJ, Figdor CG (2008) Maximizing dendritic cell migration in cancer immunotherapy. Expert Opin Biol Ther 8: 865–874.
11. Huarte E, Tirapu I, Arina A, Vera M, Alfaro C, et al. (2005) Intratumoural administration of dendritic cells: hostile environment and help by gene therapy. Expert Opin Biol Ther 5: 7–22.
12. Bachmann MF, Kopf M, Marsland BJ (2006) Chemokines: more than just road signs. Nat Rev Immunol 6: 159–164.
13. Waugh DJ, Wilson C (2008) The interleukin-8 pathway in cancer. Clin Cancer Res 14: 6735–6741.
14. Murdoch C, Muthana M, Coffelt SB, Lewis CE (2008) The role of myeloid cells in the promotion of tumour angiogenesis. Nat Rev Cancer 8: 618–631.
15. Schraufstatter IU, Trieu K, Zhao M, Rose DM, Terkeltaub RA, et al. (2003) IL-8-mediated cell migration in endothelial cells depends on cathepsin B activity and transactivation of the epidermal growth factor receptor. J Immunol 171: 6714–6722.
16. Lin WW, Karin M (2007) A cytokine-mediated link between innate immunity, inflammation, and cancer. J Clin Invest 117: 1175–1183.
17. Rolny C, Capparuccia L, Casazza A, Mazzone M, Vallario A, et al. (2008) The tumor suppressor semaphorin 3B triggers a prometastatic program mediated by interleukin 8 and the tumor microenvironment. J Exp Med 205: 1155–1171.
18. Ueda T, Shimada E, Urakawa T (1994) Serum levels of cytokines in patients with colorectal cancer: possible involvement of interleukin-6 and interleukin-8 in hematogenous metastasis. J Gastroenterol 29: 423–429.
19. Huang D, Ding Y, Zhou M, Rini BI, Petillo D, et al. Interleukin-8 mediates resistance to antiangiogenic agent sunitinib in renal cell carcinoma. Cancer Res 70: 1063–1071.
20. Baggiolini M, Moser B, Clark-Lewis I (1994) Interleukin-8 and related chemotactic cytokines. The Giles Filley Lecture. Chest 105: 95S–98S.
21. Baggiolini M, Loetscher P (2000) Chemokines in inflammation and immunity. Immunol Today 21: 418–420.
22. Stillie R, Farooq SM, Gordon JR, Stadnyk AW (2009) The functional significance behind expressing two IL-8 receptor types on PMN. J Leukoc Biol 86: 529–543.
23. Melero I, Vile RG, Colombo MP (2000) Feeding dendritic cells with tumor antigens: self-service buffet or a la carte? Gene Ther 7: 1167–1170.
24. Guo J, Zhu J, Sheng X, Wang X, Qu L, et al. (2007) Intratumoral injection of dendritic cells in combination with local hyperthermia induces systemic antitumor effect in patients with advanced melanoma. Int J Cancer 120: 2418–2425.
25. Triozzi PL, Khurram R, Aldrich WA, Walker MJ, Kim JA, et al. (2000) Intratumoral injection of dendritic cells derived in vitro in patients with metastatic cancer. Cancer 89: 2646–2654.
26. Alfaro C, Suarez N, Gonzalez A, Solano S, Erro L, et al. (2009) Influence of bevacizumab, sunitinib and sorafenib as single agents or in combination on the inhibitory effects of VEGF on human dendritic cell differentiation from monocytes. Br J Cancer 100: 1111–1119.
27. Verdijk P, Aarntzen EH, Lesterhuis WJ, Boullart AC, Kok E, et al. (2009) Limited amounts of dendritic cells migrate into the T-cell area of lymph nodes but have high immune activating potential in melanoma patients. Clin Cancer Res 15: 2531–2540.
28. de Vries IJ, Lesterhuis WJ, Barentsz JO, Verdijk P, van Krieken JH, et al. (2005) Magnetic resonance tracking of dendritic cells in melanoma patients for monitoring of cellular therapy. Nat Biotechnol 23: 1407–1413.
29. Melief CJ (2008) Cancer immunotherapy by dendritic cells. Immunity 29: 372–383.

30. Meyer TP, Zehnter I, Hofmann B, Zaisserer J, Burkhart J, et al. (2005) Filter Buffy Coats (FBC): a source of peripheral blood leukocytes recovered from leukocyte depletion filters. J Immunol Methods 307: 150–166.
31. Gasparini G (2001) Metronomic scheduling: the future of chemotherapy? Lancet Oncol 2: 733–740.
32. Ghiringhelli F, Menard C, Puig PE, Ladoire S, Roux S, et al. (2007) Metronomic cyclophosphamide regimen selectively depletes CD4+CD25+ regulatory T cells and restores T and NK effector functions in end stage cancer patients. Cancer Immunol Immunother 56: 641–648.
33. Balkwill F (2004) Cancer and the chemokine network. Nat Rev Cancer 4: 540–550.
34. Gross MD, Shapiro B, Fig LM, Steventon R, Skinner RW, et al. (2001) Imaging of human infection with (131)I-labeled recombinant human interleukin-8. J Nucl Med 42: 1656–1659.
35. Rossi D, Zlotnik A (2000) The biology of chemokines and their receptors. Annu Rev Immunol 18: 217–242.
36. Tirapu I, Huarte E, Guiducci C, Arina A, Zaratiegui M, et al. (2006) Low surface expression of B7-1 (CD80) is an immunoescape mechanism of colon carcinoma. Cancer Res 66: 2442–2450.
37. Rabinovich GA, Gabrilovich D, Sotomayor EM (2007) Immunosuppressive strategies that are mediated by tumor cells. Annu Rev Immunol 25: 267–296.
38. Zou W, Chen L (2008) Inhibitory B7-family molecules in the tumour microenvironment. Nat Rev Immunol 8: 467–477.
39. Suarez N, Alfaro C, Dubrot J, Palazon A, Bolanos E, et al. Synergistic effects of CTLA-4 blockade with tremelimumab and elimination of regulatory T lymphocytes in vitro and in vivo. Int J Cancer.
40. Belladonna ML, Orabona C, Grohmann U, Puccetti P (2009) TGF-beta and kynurenines as the key to infectious tolerance. Trends Mol Med 15: 41–49.
41. Rutella S, Danese S, Leone G (2006) Tolerogenic dendritic cells: cytokine modulation comes of age. Blood 108: 1435–1440.
42. Conejo-Garcia JR, Benencia F, Courreges MC, Kang E, Mohamed-Hadley A, et al. (2004) Tumor-infiltrating dendritic cell precursors recruited by a beta-defensin contribute to vasculogenesis under the influence of Vegf-A. Nat Med 10: 950–958 Epub 2004 Aug 2029.
43. Gabrilovich DI, Chen HL, Girgis KR, Cunningham HT, Meny GM, et al. (1996) Production of vascular endothelial growth factor by human tumors inhibits the functional maturation of dendritic cells. Nat Med 2: 1096–1103.
44. Aspord C, Pedroza-Gonzalez A, Gallegos M, Tindle S, Burton EC, et al. (2007) Breast cancer instructs dendritic cells to prime interleukin 13-secreting CD4+ T cells that facilitate tumor development. J Exp Med 204: 1037–1047.
45. Herber DL, Cao W, Nefedova Y, Novitskiy SV, Nagaraj S, et al. Lipid accumulation and dendritic cell dysfunction in cancer. Nat Med 16: 880–886.
46. Bell D, Chomarat P, Broyles D, Netto G, Harb GM, et al. (1999) In breast carcinoma tissue, immature dendritic cells reside within the tumor, whereas mature dendritic cells are located in peritumoral areas. J Exp Med 190: 1417–1426.
47. Kikuchi T, Moore MA, Crystal RG (2000) Dendritic cells modified to express CD40 ligand elicit therapeutic immunity against preexisting murine tumors. Blood 96: 91–99.
48. Miller PW, Sharma S, Stolina M, Butterfield LH, Luo J, et al. (2000) Intratumoral administration of adenoviral interleukin 7 gene-modified dendritic cells augments specific antitumor immunity and achieves tumor eradication. Hum Gene Ther 11: 53–65.
49. Nishioka Y, Hirao M, Robbins PD, Lotze MT, Tahara H (1999) Induction of systemic and therapeutic antitumor immunity using intratumoral injection of dendritic cells genetically modified to express interleukin 12. Cancer Res 59: 4035–4041.
50. Tirapu I, Arina A, Mazzolini G, Duarte M, Alfaro C, et al. (2004) Improving efficacy of interleukin-12-transfected dendritic cells injected into murine colon cancer with anti-CD137 monoclonal antibodies and alloantigens. Int J Cancer 110: 51–60.
51. Gabrilovich DI, Nagaraj S (2009) Myeloid-derived suppressor cells as regulators of the immune system. Nat Rev Immunol 9: 162–174.
52. van Gisbergen KP, Sanchez-Hernandez M, Geijtenbeek TB, van Kooyk Y (2005) Neutrophils mediate immune modulation of dendritic cells through glycosylation-dependent interactions between Mac-1 and DC-SIGN. J Exp Med 201: 1281–1292.
53. Melero I, Arina A, Murillo O, Dubrot J, Alfaro C, et al. (2006) Immunogenic cell death and cross-priming are reaching the clinical immunotherapy arena. Clin Cancer Res 12: 2385–2389.
54. Murillo O, Dubrot J, Palazon A, Arina A, Azpilikueta A, et al. (2009) In vivo depletion of DC impairs the anti-tumor effect of agonistic anti-CD137 mAb. Eur J Immunol 39: 2424–2436.
55. Melero I, Duarte M, Ruiz J, Sangro B, Galofre J, et al. (1999) Intratumoral injection of bone-marrow derived dendritic cells engineered to produce interleukin-12 induces complete regression of established murine transplantable colon adenocarcinomas. Gene Ther 6: 1779–1784.
56. Barnden MJ, Allison J, Heath WR, Carbone FR (1998) Defective TCR expression in transgenic mice constructed using cDNA-based alpha- and beta-chain genes under the control of heterologous regulatory elements. Immunol Cell Biol 76: 34–40.